Transactions of the ASME®

Editor, **T. H. OKIISHI (2003)**
Assistant to the Editor: **P. BUZZELL**
Associate Editors
Gas Turbine (Review Chair)
H. SIMMONS (2003)
Heat Transfer
T. ARTS (2005)
R. BUNKER (2003)
Turbomachinery
R. DAVIS (2005)
S. SJOLANDER (2005)

BOARD ON COMMUNICATIONS
Chair and Vice-President
OZDEN OCHOA

OFFICERS OF THE ASME
President, **S. H. SKEMP**

Executive Director, **VIRGIL R. CARTER**

Treasurer, **R. E. NICKELL**

PUBLISHING STAFF
Managing Director, Engineering
THOMAS G. LOUGHLIN
Director, Technical Publishing
PHILIP DI VIETRO
Manager, Journals
JOAN MERANZE
Production Coordinator
LYNN ROSENFELD
Production Assistant
MARISOL ANDINO

Transactions of the ASME, Journal of Turbomachinery (ISSN 0889-504X) is published quarterly (Jan., Apr., July, Oct.) by The American Society of Mechanical Engineers, Three Park Avenue, New York, NY 10016. Periodicals postage paid at New York, NY and additional mailing offices. POSTMASTER: Send address changes to Transactions of the ASME, Journal of Turbomachinery, c/o THE AMERICAN SOCIETY OF MECHANICAL ENGINEERS, 22 Law Drive, Box 2300, Fairfield, NJ 07007-2300.
CHANGES OF ADDRESS must be received at Society headquarters seven weeks before they are to be effective. Please send old label and new address.
STATEMENT from By-Laws. The Society shall not be responsible for statements or opinions advanced in papers or ... printed in its publications (B7.1, Par. 3).

INDEXED by Applied Mechanics Reviews and Engineering Information, Inc. Canadian Goods & Services Tax Registration #126148048

Journal of Turbomachinery

Published Quarterly by The American Society of Mechanical Engineers

VOLUME 125 • NUMBER 1 • JANUARY 2003

TECHNICAL PAPERS

(**Contents continued on inside back cover**)

This journal is printed on acid-free paper, which exceeds the ANSI Z39.48-1992 specification for permanence of paper and library materials. ♾™
♻ 85% recycled content, including 10% post-consumer fibers.

Journal of Turbomachinery **Volume 125, Number 1** **JANUARY 2003**

The ASME Journal of Turbomachinery is abstracted and indexed in the following:

Aluminum Industry Abstracts, Aquatic Science and Fisheries Abstracts, AMR Journal Article Abstracts Database, Ceramics Abstracts, Chemical Abstracts, Civil Engineering Abstracts, Compendex (The electronic equivalent of Engineering Index), Corrosion Abstracts, Current Contents, Ei EncompassLit, Electronics & Communications Abstracts, Energy Information Abstracts, Engineered Materials Abstracts, Engineering Index, Environmental Science and Pollution Management, Excerpta Medica, Fluidex, Fuel and Energy Abstracts, INSPEC, Index to Scientific Reviews, Materials Science Citation Index, Mechanical & Transportation Engineering Abstracts, Mechanical Engineering Abstracts, METADEX (The electronic equivalent of Metals Abstracts and Alloys Index), Metals Abstracts, Oceanic Abstracts, Pollution Abstracts, Referativnyi Zhurnal, Shock & Vibration Digest, Steels Alert

Time-Resolved Vane-Rotor Interaction in a High-Pressure Turbine Stage

R. J. Miller[1]
Whittle Laboratory,
University of Cambridge,
Cambridge, U.K. CB3 0DY

R. W. Moss[1]
Department of Marine Technology,
University of Newcastle,
U.K.

R. W. Ainsworth
Department of Engineering Science,
University of Oxford
Oxford, U.K. OX1 3PJ

C. K. Horwood
Rolls Royce plc.,
Derby, U.K. DE2 8BJ

This paper describes the time-varying aerodynamic interaction mechanisms that have been observed within a transonic high-pressure turbine stage; these are inferred from the time-resolved behavior of the rotor exit flow field. It contains results both from an experimental program in a turbine test facility and from numerical predictions. Experimental data was acquired using a fast-response aerodynamic probe capable of measuring Mach number, whirl angle, pitch angle, total pressure, and static pressure. A 3-D time-unsteady viscous Navier-Stokes solver was used for the numerical predictions. The unsteady rotor exit flowfield is formed from a combination of four flow phenomena: the rotor wake, the rotor trailing edge recompression shock, the tip-leakage flow, and the hub secondary flow. This paper describes the time-resolved behavior of each phenomenon and discusses the interaction mechanisms from which each originates. Two significant vane periodic changes (equivalent to a time-varying flow in the frame of reference of the rotor) in the rotor exit flowfield are identified. The first is a severe vane periodic fluctuation in flow conditions close to the hub wall and the second is a smaller vane periodic fluctuation occurring at equal strength over the entire blade span. These two regions of periodically varying flow are shown to be caused by two groups of interaction mechanisms. The first is thought to be caused by the interaction between the wake and secondary flow of the vane with the downstream rotor; and the second is thought to be caused by a combination of the interaction of the vane trailing edge recompression shock with the rotor, and the interaction between the vane and rotor potential fields. [DOI: 10.1115/1.1492823]

1 Introduction

Of the problems which an engine manufacturer faces when considering the aerothermal design of the modern high pressure turbine stage, it is unsteady blade row aerodynamic interaction which is the most difficult to overcome. The consequence of not considering blade row interaction is the inaccurate prediction of stage performance, high-cycle fatigue and thermal durability. For instance, in the case of the latter, unsteady interaction mechanisms govern the migration path of hot streaks, which leave the combustion chamber and enter the high-pressure turbine, differentially affecting parts of the blade annulus in terms of life. These three all cause a major increase in the development cost and risk for the aeroengine manufacturer, as well as in engine running costs for airlines. A detailed understanding of the unsteady flow physics of aerodynamic interactions within the high-pressure stage is required to address this.

The blade interaction mechanisms that occur in low-aspect ratio transonic turbine stages are different from those in high-aspect ratio subsonic turbines. In the high-aspect ratio subsonic blade, the flow can be considered to be two-dimensional over most of its span, and the dominant interaction mechanism is caused by the blade wake from one blade row impinging on a downstream blade row. In a transonic low-aspect ratio blade, in addition to blade wakes, the exit flow is dominated by secondary flows, strong potential fields, and trailing edge shocks. Thus, in designing a modern high-pressure turbine, the aerodynamicist must consider each of these sources of blade interaction. A considerable amount of research has been done to study each of these interaction mechanisms in isolation:

- periodic wake impingement on the downstream blade (e.g., Binder et al. [1] and Hodson [2]);
- periodic movement of the vane trailing edge shock-wave system (e.g., Doorly and Oldfield [3] and Giles [4]);
- periodic interaction between the vane potential field and the rotor flow-field (e.g., Lefcort [5] and Korakianitis [6]);
- convection of the vane secondary flow-field through the rotor (e.g., Binder [7]).

However, the difficulty in making measurements in transonic turbines has meant that little research has been carried out at engine representative conditions (correct Mach, Reynolds, and rotational numbers; temperature ratios) in a full high-pressure stage.

A number of experimental studies have been carried out in low speed facilities to investigate vane-rotor interaction. Dring et al. [8] measured the effect of vane-rotor interaction on the surface pressure profile around both vane and rotor blades. Joslyn and Dring [9] made measurements in a low-speed turbine stage and described in detail the time-averaged three-dimensional development of the flow. Sharma et al. [10], made time-resolved area aerodynamic traverse measurements of total pressure behind a low-speed single-stage turbine. It was found that the total pressure deficit associated with the hub secondary flow was strongly modulated by the presence of the upstream vane wake. They concluded that this showed that the upstream vane wakes reduced the strength of the rotor hub secondary flow. It was found that the upper passage vortex and tip leakage flow were found to be unaffected by the upstream vane. Zeschky and Gallus [11], made time-resolved measurements of velocity at the exit of a low speed subsonic turbine. They found that the non-uniform vane exit flow caused low-energy fluid to build up at the midspan of the rotor. The rotor exit velocity measurements showed that the vane had a significant effect on both the velocity and flow angle at rotor exit. Walraevens and Gallus [12] made measurements of velocity downstream of a low-speed subsonic turbine. They found that the rotor exit flow was dominated by hub secondary flow. The rotor

[1]Formerly at the Department of Engineering Science, University of Oxford.

Contributed by the International Gas Turbine Institute for publication in the JOURNAL OF TURBOMACHINERY. Manuscript received by the IGTI, June 20, 2000; revised manuscript received May 16, 2002. Associate Editor: S. Sjolander.

tip and casing secondary flow were also observed. Vane exit vorticity was observed to occur periodically in the rotor exit flow. Zaccaria and Lakshminaryana [13] made LDV measurements of velocity through the passage of a low-speed rotor. They observed that the rotor wakes were modulated by the position of the upstream vane.

A small number of papers have described investigations into blade row interaction in high-pressure turbines at engine representative conditions (Dietz and Ainsworth [14], Dunn et al. [15], Sheldrake et al. [16], Hilditch et al. [17], Denos et al. [18], Venable et al. [19], and Busby et al. [20]). However, these time-resolved measurements have concentrated on the vane rotor interaction along the midheight streamline and have not considered the three-dimensional interaction through the stage. The only investigations to study the three-dimensional interaction in a high-pressure turbine stage were Binder et al. [1] and Moss et al. [21]. Binder found that as the rotor cut the vane secondary flow, the turbulence level suddenly rose. Moss used a large number of rotor surface mounted Kulite pressure transducers to measure three-dimensional HP vane-rotor interaction. It was shown that the majority of the high loss fluid in the HP vane wake had migrated close to the hub end wall region upstream of the HP rotor inlet plane. This was shown to result in a large unsteady static pressure variation on the HP rotor crown close to the hub wall. However, none of these investigations has determined the effect of HP vane-rotor interaction on the development of the flow in the rotor passage. In particular, the effects of these interaction mechanisms on the key aspects of rotor flow field (such as rotor secondary flows; tip flows; trailing edge shock system and wake) remain objects for further investigation.

The current research program described in this paper has been conducted to address this void, employing both experimental and theoretical techniques. Firstly, use has been made of time-resolved area aerodynamic traverses, made downstream of the Oxford HP turbine stage using fast-response aerodynamic probes. Secondly, three-dimensional unsteady numerical predictions of the flow in the stage have also been conducted. The paper describes in detail the effect of vane-rotor interaction mechanisms on each of the four flow phenomena that dominate the exit flow of the rotor (shown in Fig. 1). It is shown that this behavior is split into two distinct regions: the first, close to the hub wall, is identified by a strong modulation of the low total pressure region associated with the rotor hub secondary flow and by a periodic disappearance of the rotor trailing edge shock, and the second, close to the rotor suction surface, which is identified by a smaller total pressure fluctuation over the entire span of the blade. The likely causes of these two distinct regions of the rotor exit flow are discussed and it is concluded that the first is caused by wake and secondary flow interaction, while the second is consistent with effects of shock or potential interaction.

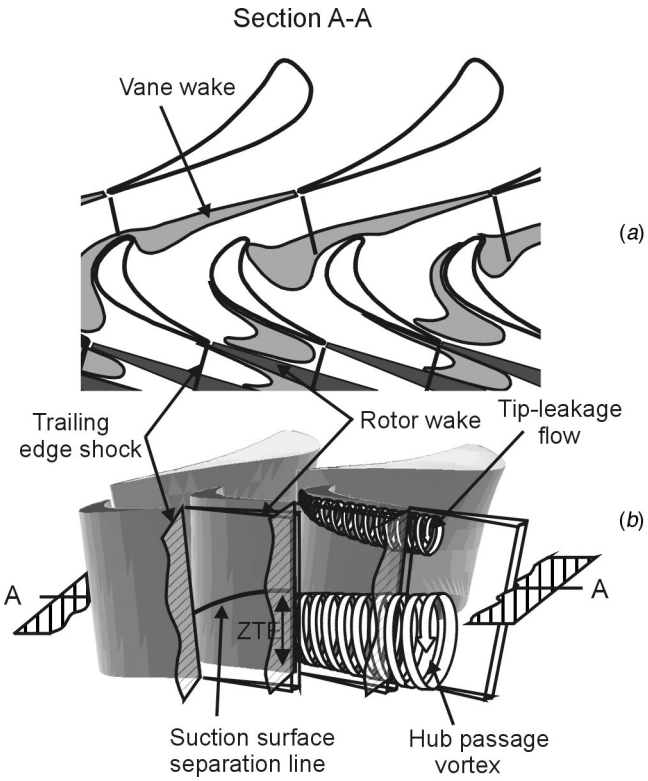

Fig. 1 (*a*) Schematic of two-dimensional vane rotor interaction, (*b*) schematic of the dominant rotor exit flow phenomena

2 Methodology

The experimental aerodynamic traverse measurements have been carried out in the Oxford Rotor Facility (Ainsworth et al. [22]), the aim being to measure the time-resolved three-dimensional flow downstream of the HP stage. The working section of the facility contains a 0.5-m-dia shroudless high-pressure turbine stage which allows the simulation of engine representative Mach and Reynolds numbers as well as the appropriate gas to wall temperature ratio (Table 1). A schematic of the turbine stage in the Oxford Rotor Facility is shown in Fig. 2.

Traverse measurements were made at a position corresponding to 25% of an axial chord downstream of the rotor trailing edge using a high bandwidth aerodynamic probe. Each traverse was completed in the 15 ms using an ultra-high-speed traverse mechanism driven by a large compression spring (Miller and Ainsworth [23]). The particular instrument used in the traverse mechanism was a high bandwidth three-dimensional pyramid probe (Fig. 3), which employed four surface mounted semi-conductor pressure sensors allowing time-varying quantities of Mach number, yaw angle, pitch angle and total pressure to be measured. It should be noted that at the exit of a turbine stage (in the absolute frame) the whirl angle varies by more than ± 30 deg and the size of the aerodynamic probe can cause blockage. It is therefore necessary to validate the accuracy of such a technique at engine conditions. This was done by measuring the same flow field with two entirely different geometries and sizes of probe and comparing the results.

The aerodynamic data presented in the forthcoming was derived from measurements made with the fast-response pyramid probe, the signals being ensemble filtered at blade passing frequency to remove the nonblade periodic components of the signal. The flow downstream of a turbine stage is composed both of time-resolved flow phenomena (such as vortex shedding and the blade trailing edge shocks, etc.) and time-unresolved flow phenomena (such as turbulence). The time-resolved component of the flow can be further divided into blade periodic components (such as the average blade shock and trailing edge wake) and nonblade

Table 1 Turbine stage data

	Vane	Rotor
Blade no.	36	60
Blade relative exit Mach no.	0.95	0.98
Midheight design turning angle	71.55	95.45
Rotational speed (RPM)	8910	
Vane exit Reynolds no. (axial chord)	1.55e6	
Gas to wall temperature ratio	1.3	
Rotor tip clearance (% height)	2	
Stage total static pressure ratio	3.12	
Stage temperature drop (°)	86.5	
Inlet total pressure (bar)	8.04	
Inlet total temperature (kelvin)	374.4	
Turbine output power	2.24MW	
Rotor exit hub to tip ratio	0.833	
Inter blade gap/axial chord	0.36	0.45
Rotor blade height/axial chord	1.76	

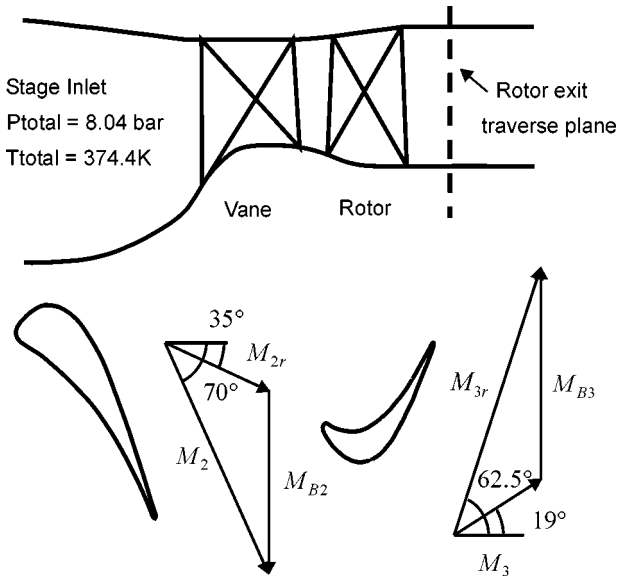

Fig. 2 Schematic of the turbine stage in the Oxford Rotor Facility

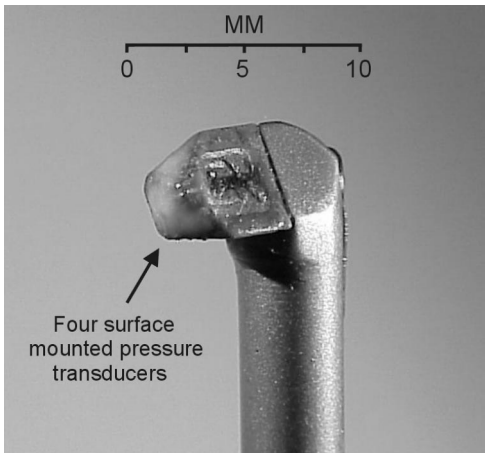

Fig. 3 Fast-response pyramid probe

periodic components (such as vortex shedding and blade to blade difference in the rotor trailing edge shock caused by small manufacturing and mounting variation in the blade geometry). In this work, only the blade periodic component of the flow have been considered. These flow measurements (made in the stationary frame of reference) were converted into the rotor relative frame using the blade Mach number.

Because of the complexity of the information available (involving both space and time) the format used for displaying time-resolved traverse data is important. A common method of representing time-resolved experimental measurements described in the literature has been to use phase-time diagrams, in which the vertical axis indicates the rotor relative phase at which each measurement was made and the horizontal axis the instant in time at which it was taken. However, the dominant interaction mechanisms that where measured in this program of research were found to occur at constant vane relative phase. On a phase-time diagram this would result in a diagonal stripe with a gradient equal to the ratio of the number of rotor blades to the number of vanes in the upstream stage. It is difficult to interpret deviations in gradient from this ideal behavior. In a phase-phase diagram (where the horizontal and vertical axes indicate the vane and rotor relative position at which each measurement was made), such structures would appear as a vertical feature, rendering interpretation an easier task (Fig. 4). It was therefore considered more useful to display results on phase-phase diagrams.

In practice, each phase-phase diagram presents the time-resolved aerodynamic measurements made at one radial height. The idealized structure of such a phase-phase interaction diagram at midspan rotor exit is shown in Fig. 5. The diagram shows the expected rotor relative phase of both the rotor trailing edge recompression shock and the rotor wake. At rotor exit the flow is also periodically affected by segments of vane wake fluid that have been chopped and distorted by the rotor. The lines with square markers on the right hand side of Fig. 5 indicates the absolute flow direction of the vane wake fluid. These lines may also be considered as the avenues along which vane wake fluid travels (Binder et al. [24]). The wake avenues are fixed relative to the upstream vanes and therefore cross the rotor exit traverse plane at a constant vane relative phase. The expected rotor and vane relative position of vane wake fluid at rotor exit is shown in Fig. 5.

On a phase-phase diagram a vertical line represents measurements made with a probe at a fixed position relative to the upstream vanes, while a horizontal line represents measurements made with a probe at a fixed position relative to the rotor. A

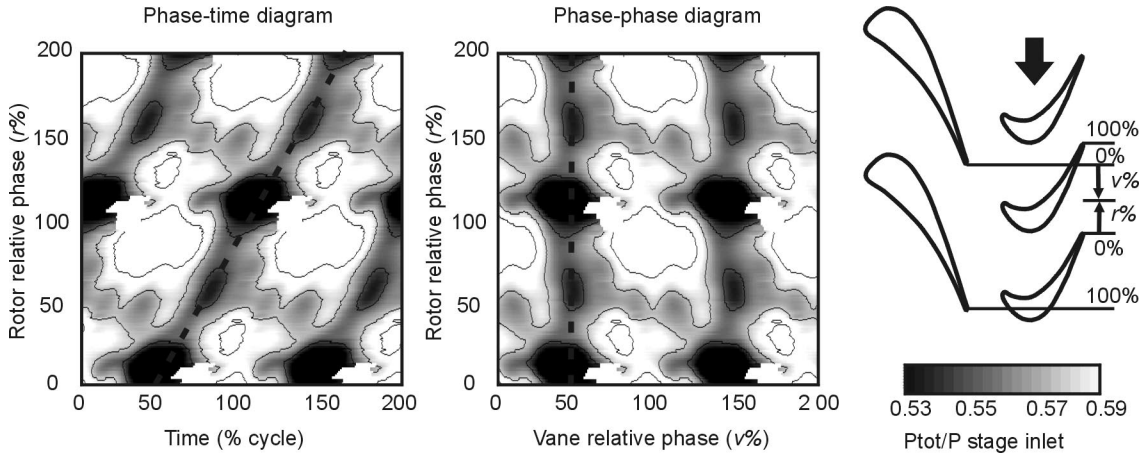

Fig. 4 Time-resolved total pressure measurements presented on both phase-time and phase-phase diagrams (measurements made along a circumferential arc close to the hub wall downstream of the HP stage)

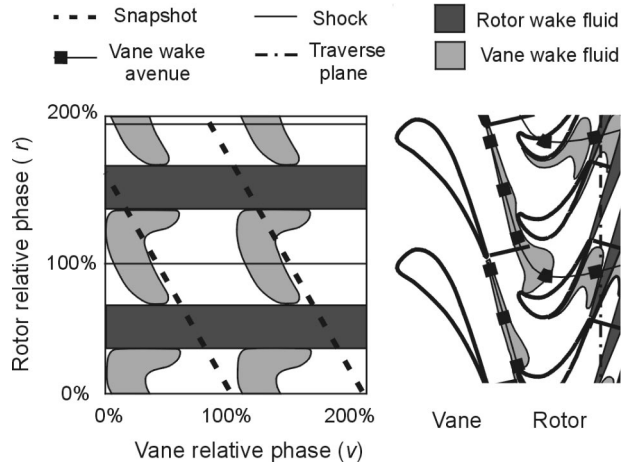

Fig. 5 Expected structure of the exit flow from the HP stage (displayed as a phase-phase interaction diagram)

snapshot of the rotor exit flow is obtained by looking at measurements along a diagonal line with a gradient of 5/3 (the ratio of rotor blades to vanes).

Numerical simulations were performed using a three-dimensional viscous time-unsteady code, Unstrest, developed by Denton [25] at Cambridge University. The code solves the Navier Stokes equations using a thin shear layer model with the viscous terms evaluated every time step, and turned into body force terms for momentum and source terms for energy. The structured grid is formed by the rotation of points defined in two dimensions (x,r) about the turbine axis; the (x,r) points are defined by meridional (pseudo-streamwise) and pseudo-radial vectors. The code uses a ''time-marching'' solution scheme in which one blade row gradually rotates relative to the other with flow parameters being interpolated across a sliding plane between the two grids.

Three meshes were used in this research: the first, used 0.4 million nodes, and included only rotor blades, the second, with no tip-clearance, used 0.8 million nodes and included a full stage, and the third, with the design tip clearance, used 1.6 million nodes and included the full stage. The correct 3:5 vane rotor repeat ratio was used in the second two solutions. The third grid, used in most of the analysis, has 300,000 elements per vane passage and 140,000 elements per rotor passage. The element to element expansion ratio was below 1.2 within the blade passage and below 1.3 between blade rows.

3 Time-Resolved Flow Downstream of the Stage

This section describes the time-resolved behavior of the dominant rotor flow phenomena, postulated as a result of the application of the experimental and theoretical methods outlined above. At rotor exit four major aerodynamic features (the trailing edge shock, the secondary flow, the wake and the tip-leakage flow) dominate the structure of the flow. A diagram showing each of these features simply marked over experimental measurements of rotor relative Mach number is shown in Fig. 6. No justification for this interpretation is made at this stage. However, each the four features is explained in Sections 3.1 to 3.4 and the diagram is referred to again in Section 4. Each of the following four sections combines a presentation of experimental data with an understanding of the flow physics to describe the time-resolved behavior of one of these aerodynamic features.

3.1 Shock Structure. As the rotor passes an upstream vane its trailing edge shock structure periodically changes. This effects blade loss and causes a change in the lift of a downstream vane. In this section area traverse measurements are used to interpret the time-resolved behavior of the rotor trailing edge shock. Three

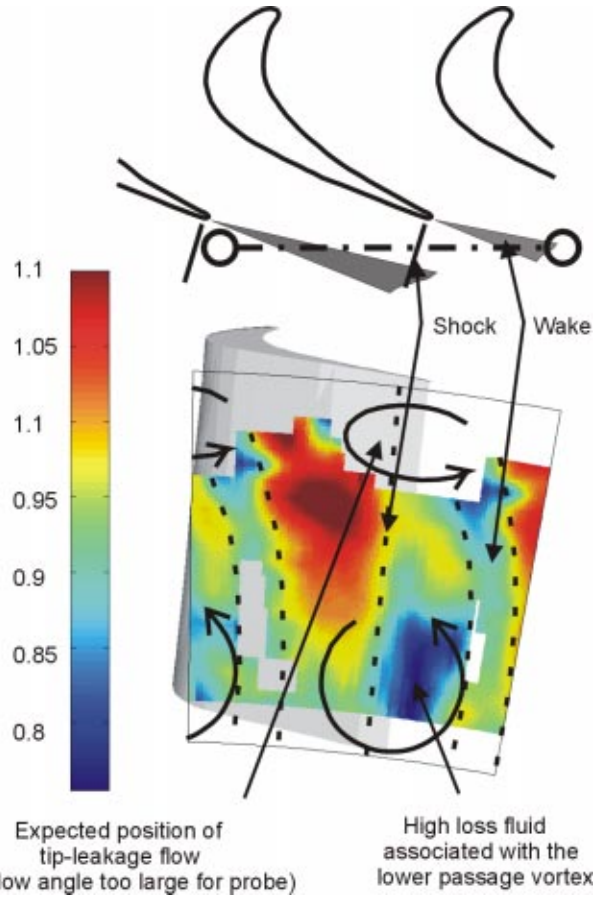

Fig. 6 Rotor exit Mach number measurements showing dominant structure of the flow (time-snapshot)

phase-phase interaction diagrams showing the rotor exit Mach number, total pressure and static pressure that were measured using the fast-response pyramid probe are shown in Figs. 7–9. Each diagram is made up of 18 phase-phase interaction diagrams, data being taken at differing radial heights. In the right-hand bottom corner of each figure is a phase-phase interaction diagram of the flow from an ideal HP stage, with no vane rotor interaction, to aid interpretation.

The time-resolved behavior of the rotor trailing edge shock can be interpreted by looking at the rotor exit Mach number traverse measurements shown in Fig. 7. In order to explain the structure of the time-resolved rotor exit flow, it is useful to discuss in detail three radial heights:

• Mid-height (traverse height 9). The structure of the midheight rotor phase-phase interaction diagram is very similar to the ideal phase-phase interaction diagram. At 60% vane relative phase the Mach number changes from 1.04 to 0.96 across the trailing edge shock (0% rotor relative phase). This corresponds to a static pressure rise of 10% (Fig. 9), which is consistent with a normal shock at the blade trailing edge. The region where the measured data is observed to differ significantly from the ideal phase-phase interaction diagram is between 0 and 25% rotor-relative phase (Marker **D**). The total pressure and the Mach number are observed to vary periodically with vane relative position. This variation in Mach and total pressure is observed at all traverse heights at the same rotor-relative phase. The cause of this ''two-dimensional'' (same phase at all radial heights) vane-rotor interaction phenomenon is discussed in more detail in Section 4.0. The interaction causes the Mach number downstream of the rotor trailing edge shock (0–30% rotor relative phase, marker **D**) to drop to between 0.88 and 0.9. This drop in Mach number downstream of the shock is not, however, associated with a rise in the Mach number upstream of

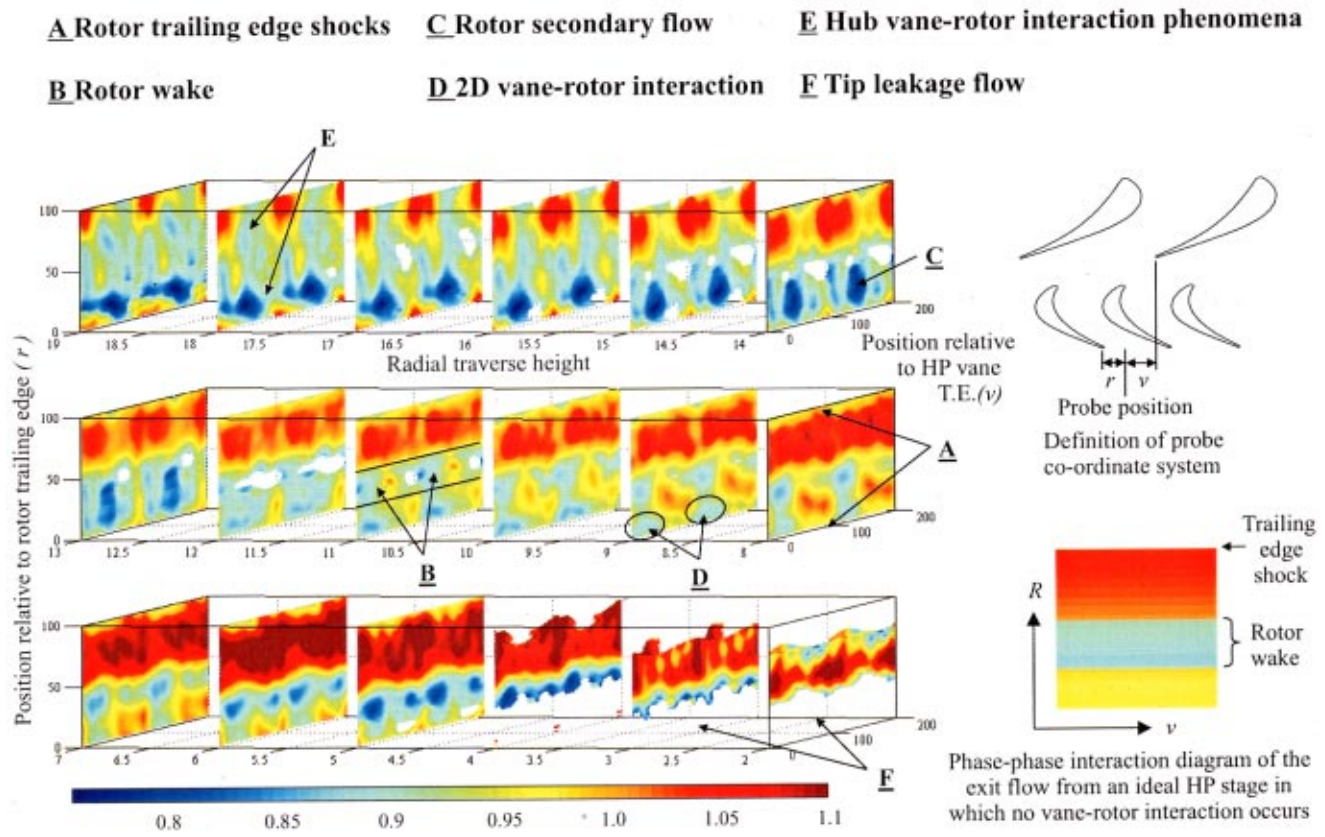

Fig. 7 Phase-phase interaction diagram—relative Mach number (height 2 is closest to the tip and height 19 is closest to the hub)

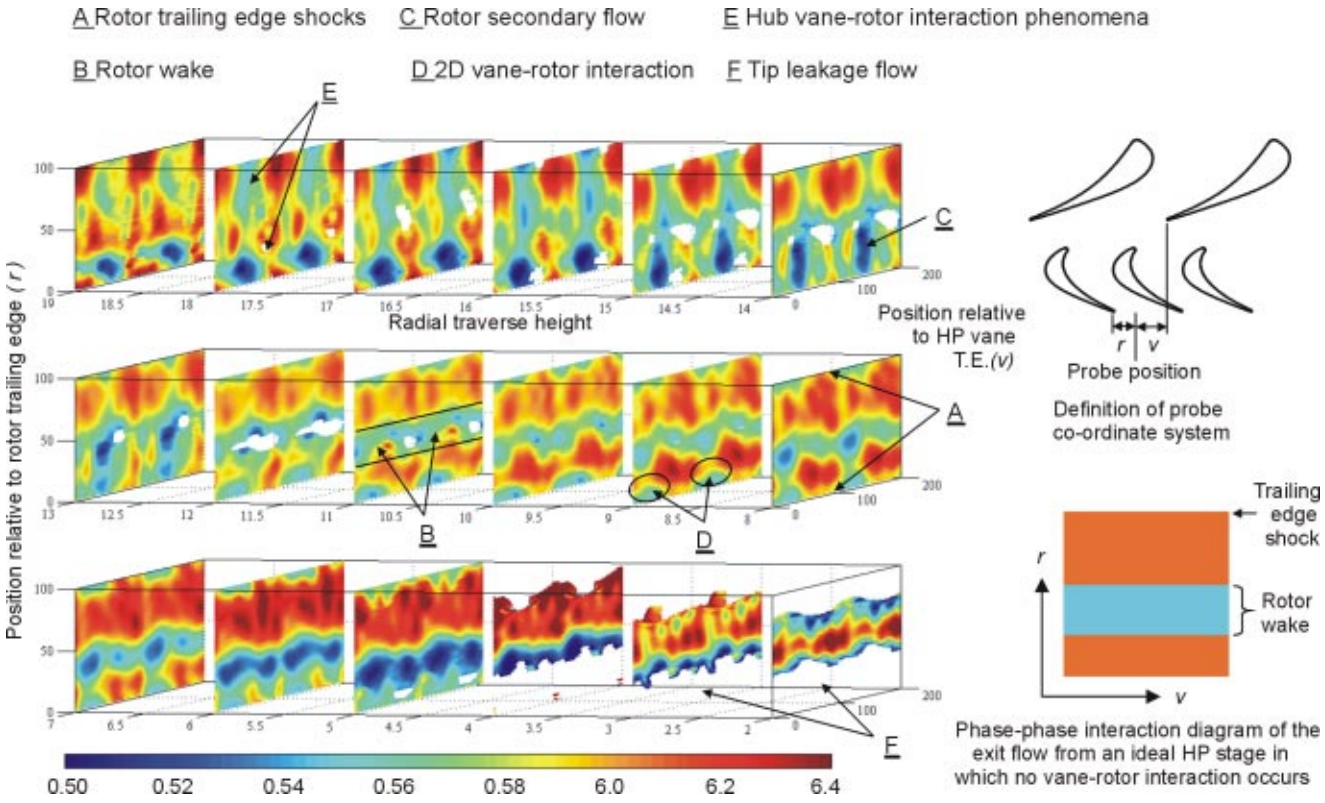

Fig. 8 Phase-phase interaction diagram—relative total pressure (height 2 is closest to the tip and height 19 is closest to the hub)

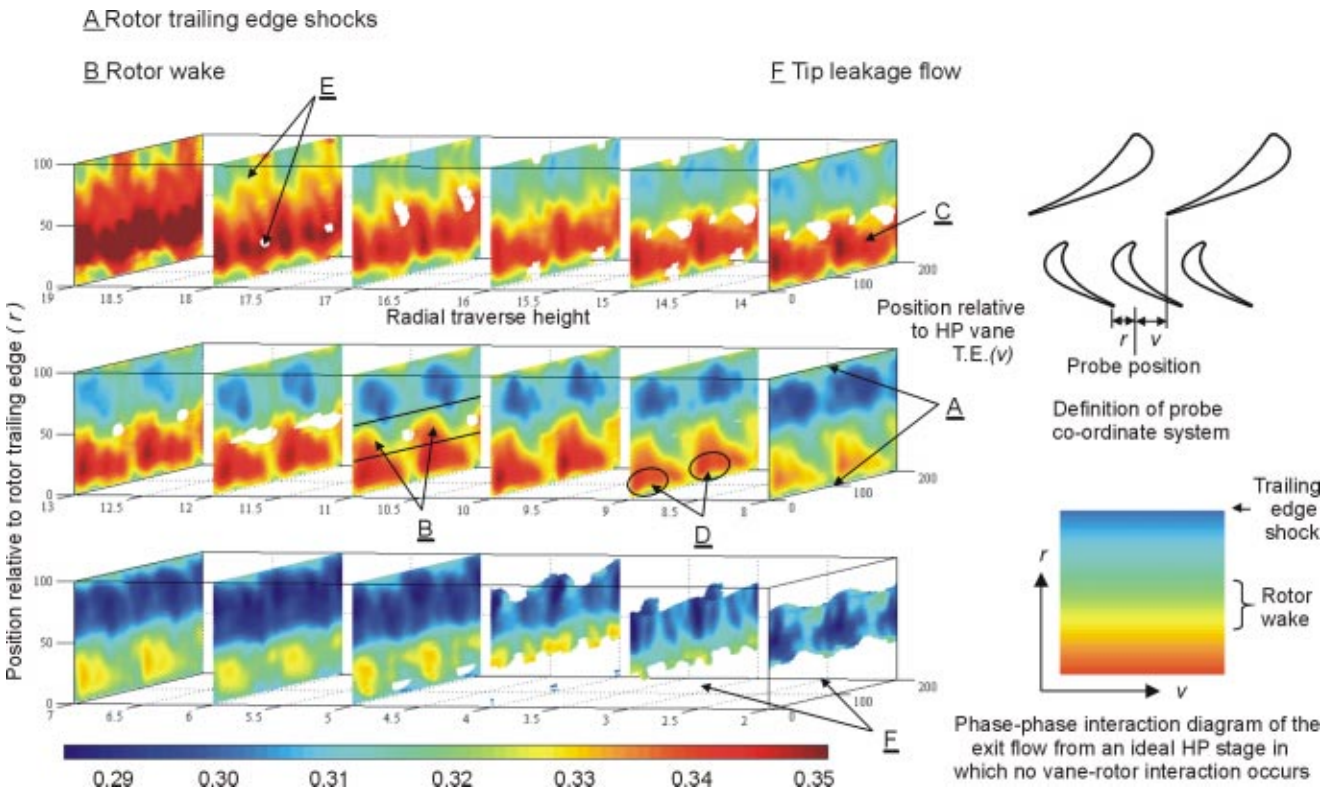

Fig. 9 Phase-phase interaction diagram—static pressure (height 2 is closest to the tip and height 19 is closest to the hub)

the shock (70–100% rotor relative phase). It is therefore likely that the strength of the rotor trailing edge shock is not significantly changed by the presence of the upstream vane. The simultaneous fluctuation of the total pressure and Mach number indicate that these Mach number fluctuations are caused either by periodic convection of vane loss fluid through the rotor or by an isentropic expansion or compression of the rotor fluid associated with vane periodic secondary fluid motion.

• Tip region (traverse height 5). This traverse height is the highest radial height that is not dominated by extreme flow angles associated with the tip-leakage vortex. The Mach number changes from 1.07 to 0.94 across the shock (0% rotor relative phase). This corresponds to a static pressure rise of 16%, which is consistent with a normal shock at the blade trailing edge.

• Hub region (traverse height 16). The structure of the phase-phase interaction diagram close to the hub wall is very different from the ideal interaction diagram. The diagram has a vertical stripe of low Mach number and total pressure between 25 and 65% vane-relative phase. This vane periodic phenomenon occurs between traverse heights 14 and 19 and affects all rotor-relative phases, dropping the rotor exit Mach number to 0.8, and thus causing the rotor trailing edge shock to disappear.

Considerable insight into the time-resolved structure of the rotor trailing edge shock was also obtained by looking at the change in the average rotor exit Mach number as the upstream vane moves through one vane pitch. The Mach number was averaged over a rotor pitch and its maximum and minimum plotted at each radial traverse height (Fig. 10). The four traverse heights close to the tip have not been plotted due to the large gaps in time-resolved measurements. The variation of rotor exit Mach number, shown in Fig. 10, indicates that from hub to tip the rotor exit Mach number rises monotonically. The amplitude of the change in rotor exit Mach number, during a vane passing cycle, has two distinct regions. Between traverse heights 5 and 12 (**A**, tip region) the amplitude variation is between 0.02 and 0.03, while between traverse heights 13 and 19 (**B**, hub region) the amplitude variation increases to 0.08.

To interpret the time-resolved trailing edge shock structure associated with these radial and temporal variations in the blade exit Mach number it is useful to compare Fig. 10 with schlieren photographs of the flow field around the rotor. Nicholson made a detailed study of the effects of varying the rotor exit Mach number

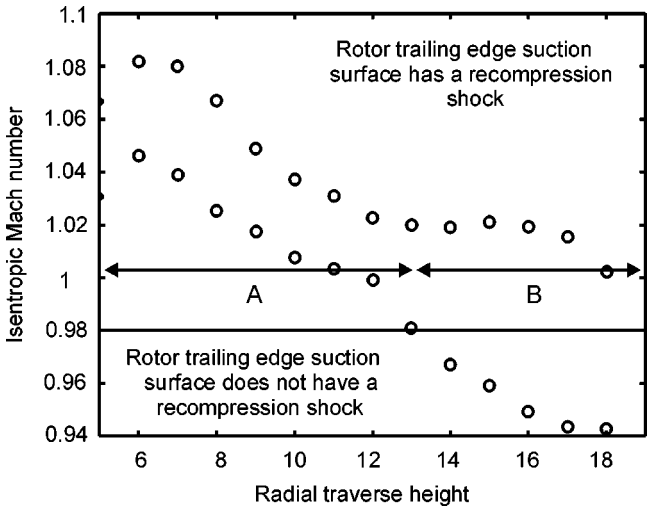

Fig. 10 The maximum and minimum (over a vane passing period) mean rotor exit isentropic Mach number (the line at Mach 0.98 signifies the approximate Mach number at which the rotor trailing edge shock forms)

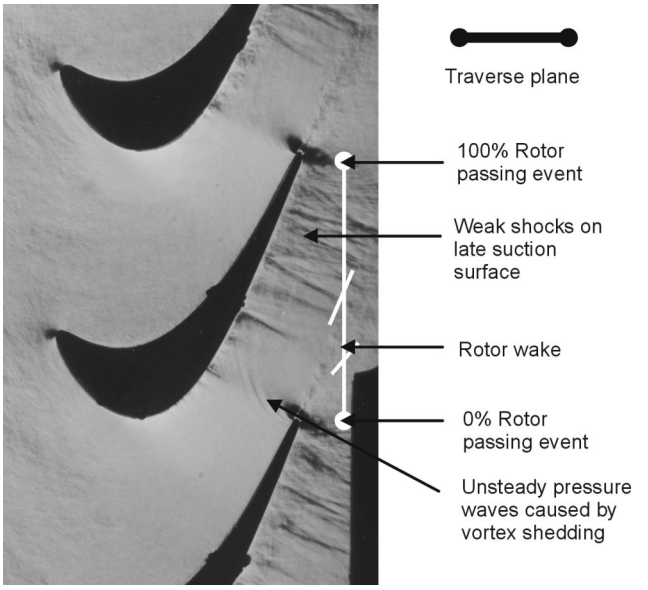

Fig. 11 Linear cascade schlieren photograph (isentropic exit Mach no.=0.96)

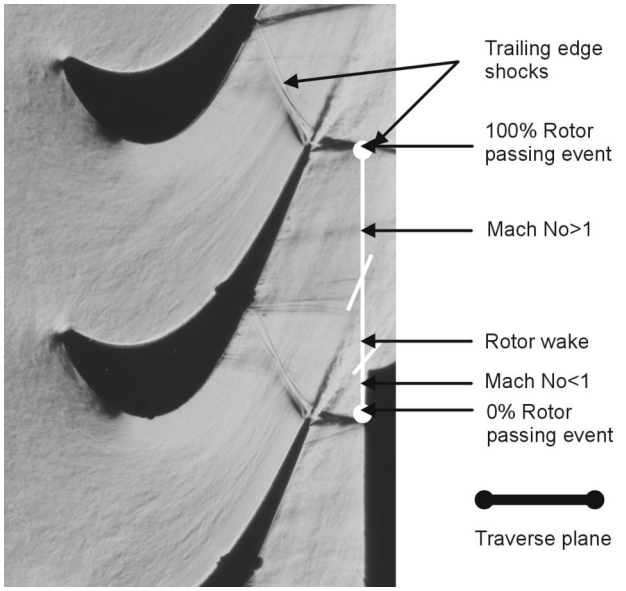

Fig. 12 Linear cascade schlieren photograph (isentropic exit Mach no.=1.1)

on trailing edge shock structure. His testing was done in a linear cascade of a two-dimensional blade of the same section as those used in the Oxford Rotor. His tests showed that the trailing edge shock structure was highly sensitive to blade exit Mach number.

Schlieren photographs of the rotor at two different exit Mach numbers ($M_{is}=0.96$ and 1.1) are shown in Figs. 11 and 12. The figures also show the relative position of the time-resolved rotor exit traverse carried out in the Oxford Rotor Facility. As the exit isentropic Mach number of the cascade of rotor blades was raised the flow was observed to pass through three distinct stages.

- Below $M_{is}=0.9$ the flow through the cascade was entirely subsonic.
- At $M_{is}=0.96$ the flow was just sonic over a portion of the suction surface and weak shock waves were found to start forming over the late suction surface (Fig. 11). These shocks were unsteady and often synchronized with the pressure waves caused by unsteady vortex shedding from the neighboring blade.
- As M_{is} approached 1.1 (Fig. 12) the peak suction surface Mach number reached 1.3. The suction surface shock structure moved to the blade trailing edge. The pressure surface shock reflected off the suction surface, and a weak reflected shock was incident on the blade wake.

Nicholson's results indicated that the critical isentropic Mach number at which the rotor trailing edge recompression shock started to form was approximately 0.98. Between traverse heights 5 and 12 (**A**, tip region in Fig. 10) the rotor exit Mach number remained above 0.98 over the whole vane passing cycle. This indicates that the strength of the rotor trailing edge shock may be altered by the presence of the upstream vane, but that the Mach number never drops low enough to stop the shock from forming. It should be noted that changes in the strength of the rotor trailing edge shock will result in a change in blade loss. Between traverse heights 13 and 19 (hub region) the vane exit Mach number is observed to drop periodically below the critical Mach number. This causes the rotor trailing edge shock to disappear periodically with the position of the upstream vane.

The traverse results thus showed that the strength of the rotor trailing edge shock increases monotonically with radial height and that in the mid-height and tip regions the trailing edge shock is unaffected by the position of the upstream vane. However, close to the hub the vane causes the rotor trailing edge shock periodically to disappear.

3.2 Secondary Flow. As the rotor passes an upstream vane the rotor passage secondary flows periodically change. This affects the secondary kinetic energy associated with the rotor flowfield and thus blade loss, as well as altering the inlet flow angle to a downstream vane. To aid interpretation of the rotor's secondary flow structure a numerical prediction of the flow within a rotor passage is shown in Fig. 13. Figure 13(*a*) shows the migration of high entropy fluid, while Fig. 13(*b*) shows the development of vorticity through the blade passage. The vorticity plots clearly show that the lower half of the rotor passage is dominated by hub secondary flow causing high entropy boundary layer fluid to migrate in a clockwise direction around the primary flow axis. A suitably low threshold level of entropy (0.1) has been set in the plotting such that only regions of significant loss are displayed. These plots show that between 30 and 40% blade height the clockwise migration of fluid results in high loss fluid separating from the blade surface and becoming entrained into the hub secondary flow.

To examine the size of the variation of the secondary flow, time-resolved rotor exit traverse measurements have been used. The low Mach number region, shown in Fig. 6 close to the suction surface, is caused by the hub secondary flow driving low-momentum fluid (high entropy fluid discussed in the foregoing) up the suction surface and then separating into the passage. The time-resolved behavior of the low Mach number and low total pressure fluid associated with the rotor hub secondary flow can be interpreted by examining the time-resolved area traverse measurements in Figs. 7 and 8. At traverse height 14 a vertical stripe of low total pressure (marker **C**) is observed at 40% vane relative phase (0–35% rotor relative phase). Between traverse heights 14 and 19 the low total pressure stripe becomes circular in shape and is located at 15% rotor relative phase. The origin of this low total pressure region is the same as the low Mach number region in Fig. 6. The phase-phase interaction diagrams (Fig. 8) indicate that the regions of low total pressure associated with the hub secondary flow disappear and reappear periodically at the vane passing frequency. This behavior was also observed in the numerical predictions. The predictions for two neighboring rotor passages with the upstream vane at different relative phases are shown in Fig. 14. In

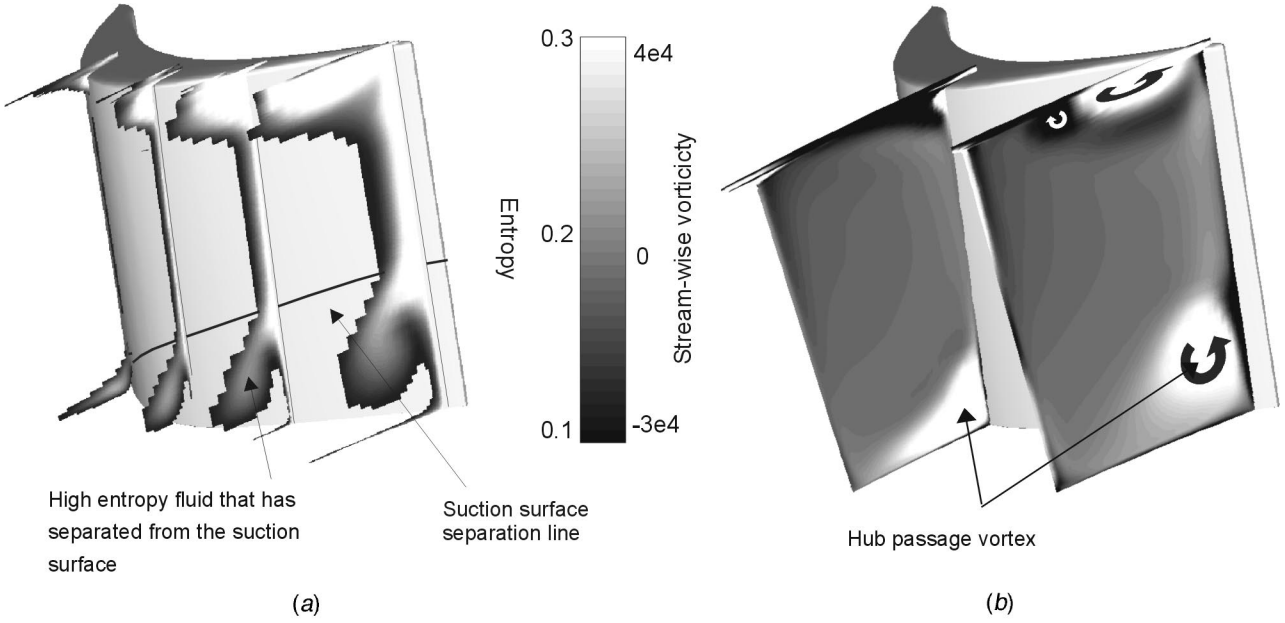

Fig. 13 Numerical predictions of entropy migration (*a*), and vorticity development (*b*) through a rotor passage (no upstream vanes present)—(*a*) four slices on entropy; (*b*) two slices of stream-wise vorticity

rotor passage **B** the low total pressure region associated with the hub secondary flow is clearly observed, while in passage **A** no low-pressure region is predicted.

The experimental results show that the total pressure in the center of the hub secondary flow changes by $21\pm3\%$ as the rotor moves through one vane pitch, while the numerical predictions show a 23% change. The secondary flow vectors, shown in Fig. 14, indicate that the strength of the hub secondary flow remains largely unaffected by the fluctuating total pressure.

To examine the time-resolved strength of the hub secondary flow and to compare the experimental measurements of its strength with numerical predictions it is useful to examine the penetration height of the hub suction surface separation line. In both the experimental results and numerical predictions the penetration depth of the suction surface separation line can be identified from the point at which the low momentum (high entropy) fluid leaves the suction surface of the rotor.

The low total pressure region, in the experimental results, associated with the hub separation line starts between traverse height 12 and traverse height 13 (Fig. 8). This indicates that the penetration depth of the suction surface separation line at the blade trailing edge is between 36 and 40% radial height. However, this is only true for 25–75% vane relative phase. Between 75 and 25% vane relative phase, no low total pressure region is observed. It is therefore impossible using the experimental measurements to estimate the penetration height of the suction surface separation line over half the vane passing cycle.

The time-resolved behavior of the suction surface penetration depth calculated from the numerical prediction is shown in Fig. 15. The results show that the penetration depth is not a strong function of vane relative position, varying by only 6% of blade height during a vane passing period. The numerical prediction of penetration depth was found to agree closely with the experimental measurements ($38\pm2\%$ experimentally and between 36 and 42% numerically).

Sharma [10] also observed this fluctuation in total pressure associated with the hub secondary flow in a low-speed turbine stage. However, unlike the results discussed in the foregoing, he concluded that this was caused by a fluctuation in the strength of the secondary flow. In contrast, the conclusions formed here are that vane-rotor interaction was found not to have a significant effect on the strength of the rotor secondary flow but was found to cause the high loss fluid close to the suction surface to fluctuate in total pressure and Mach number.

3.3 Rotor Wake. As the rotor passes an upstream vane, the width, phase and depth of its wake change. To examine the size of these variations the time-resolved traverse measurements have been used. The standard method of characterizing a wake is to calculate its semi-wake width and depth (Schlichting [26]) using downstream velocity measurements. However, at the trailing edge of a transonic blade, the wake can no longer be characterized by its velocity profile (Kurz [27]). The ideal method of characterizing a wake in compressible flow is by measuring the entropy profile downstream of the blade. However, to derive time-resolved entropy downstream of the rotor, it is necessary to measure both total temperature and total pressure

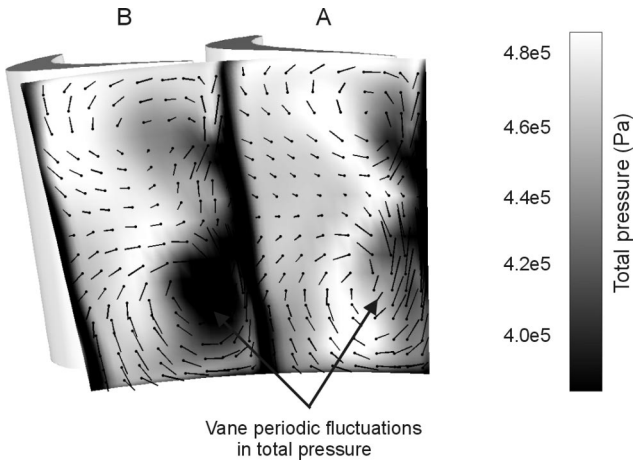

Fig. 14 Numerical prediction of the total pressure and secondary flow vectors downstream of the rotor

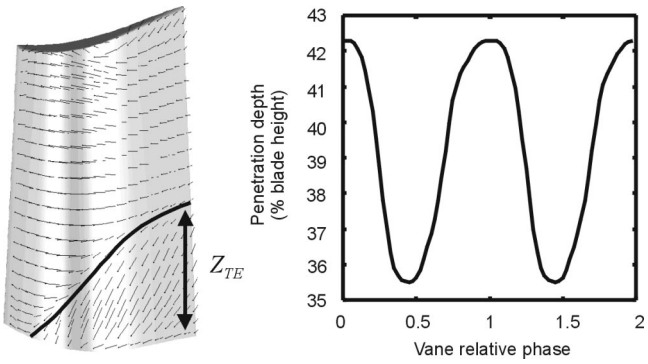

Fig. 15 Numerical prediction of the time-resolved behavior of the trailing edge penetration depth of the suction surface separation line

$$s - s_{\text{ref}} = C_p \ln\left(\frac{T}{T_{\text{ref}}}\right) - R \ln\left(\frac{P}{P_{\text{ref}}}\right)$$

In many cases, total temperature information may not be available. In a steady adiabatic flow, entropy is related directly to total pressure. In an adiabatic unsteady flow, total temperature fluctuations may be caused by variations in the static pressure field (unsteady work in the energy equation)

$$\frac{Dh_o}{Dt} = \frac{1}{\rho}\frac{\partial p}{\partial t}$$

Given that in this experiment time-resolved total temperature information was not available, total pressure was used to characterize the wake. Although the rotor wake is predominantly time-steady relative to the rotor, and the total temperature fluctuations may be small in an adiabatic flow, it should be realized that total pressure on its own will not allow a complete distinction between mixing and unsteady work processes.

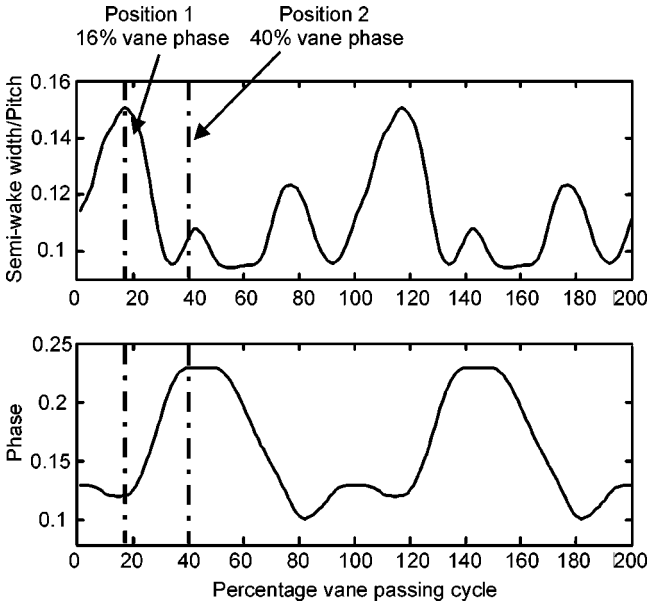

Fig. 16 Variation of width and phase of the rotor wake with HP vane phase (rotor midheight experimental measurements)

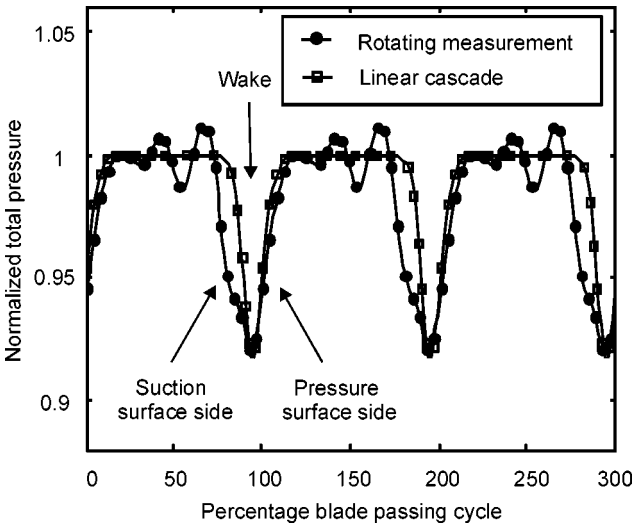

Fig. 17 Comparison of HP stage and linear cascade exit traverses (16% vane phase Fig. 16)

In order to explain the effect of the upstream vane on the rotor wake, data from total pressure traverses are presented in phase-phase diagrams (Figs. 7–9). Three radial heights from these are discussed in detail.

Midheight (Traverse Height 9). The total pressure deficit associated with the rotor wake crosses the traverse plane between 25 and 55% rotor relative phase (Fig. 8). The rotor wake corresponds to a 10% deficit in total pressure and a 17% deficit in Mach number. During a vane passing cycle, the rotor-relative phase at which the rotor wake occurs and the width and depth of the wake are observed to change. To interpret the effect of vane relative position on the size and phase of the rotor wake, the width of the wake (calculated as the semi-wake width) and phase were calculated (Fig. 16). The vane-rotor interaction was found to cause the semi-wake width to increase by 50% and the rotor relative phase to change by 10%. The maximum wake width was found to occur at 16% vane passing cycle. At this vane phase the wake is also observed to move toward the suction surface side of the blade. At 40% vane passing cycle the center line of the rotor wake was found to have moved across 10% of a rotor pitch (toward the pressure surface side) and the depth of the wake was found to drop to a value close to its minimum.

To interpret the causes of these changes in wake structure it is useful to compare the time-resolved total pressure measurements with measurements made downstream of a cascade. This allows the rotor wake structure to be examined with and without the effects of an upstream vane and the rotation of the blades. The cascade measurements used are those made by Mee et al. [28]. For comparison purposes the cascade measurements were interpolated onto the same plane on which the time-resolved traverse measurements were made. Comparison of the total pressure downstream of the rotor and the linear cascade are shown in Figs. 17 and 18. The figures show the rotor exit flow at 16 and 40% vane passing cycle (the two positions marked in Fig. 16). The first figure (Fig. 17) shows the point in the vane passing cycle at which the rotor wake is at its widest and when its center line is nearest to the suction surface side of the blade. The phase and depth of the wake agree closely with the measurements made in the cascade. However, the width of the wake was found to be double that measured in the cascade. It should also be noted that the cascade wake appears symmetric, while the one in the rotating rig is asymmetrical. This difference could be caused either by vane-rotor interaction or by the strong radial migration of wake fluid that occurs in a rotating blade row. The second figure (Fig. 18) shows the

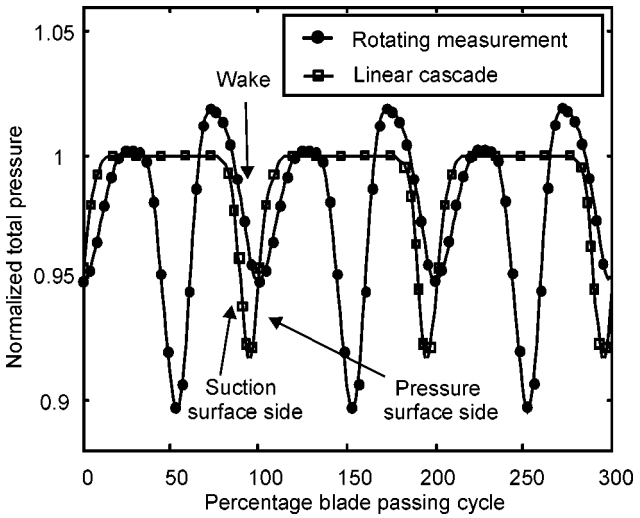

Fig. 18 Comparison of HP stage and linear cascade exit traverses (40% vane phase Fig. 16)

point in the vane passing cycle (40% vane relative phase in Fig. 16) when the rotor wake is close to its narrowest and when its centerline is nearest to the pressure surface side of the blade. The structure of the stage exit measurements is very different from the cascade measurements. The total pressure on the suction surface side of the wake has risen and a large drop in total pressure occurs in the nonwake fluid towards the suction side of the passage. It is at present not known whether these two phenomena are linked. However, two possible mechanisms that could cause such a change are a vane periodic convection of high entropy fluid through the rotor or a periodic isentropic compression or expansion of the fluid in the rotor (caused by the fluctuating static pressure field).

In Figs. 17 and 18 the wake depth is observed to halve during the vane passing cycle. Zaccaria and Lakshminarayana [13] investigated the effect of vane-rotor interaction on the wake characteristic downstream of a low-speed turbine. The velocity deficit associated with the rotor wake was found to change by 18% during a vane-passing period. In the Oxford transonic turbine stage the Mach number deficit associated with the wake changes by 60% (Fig. 7). As discussed above, characterizing a wake using Mach number or velocity profiles in transonic blades is highly inaccurate. However, it is clear that vane-rotor interaction has a far larger effect in the Oxford facility than than reported by Zaccaria and Lakshminarayana. It should be noted that the Zaccaria and Lakshminarayana facility had a hub to tip ratio very close to that of the Oxford rotor facility (10% smaller) and the turning angles in both the vane and rotor was within 1.5 deg. It is also of interest to note that the interblade gap was 33% small in Zaccaria and Lakshminarayana facility than in the Oxford rotor facility. The results thus indicate that blade interaction has a far larger effect on the characteristic of the rotor wakes in a transonic stage than it does in a low speed stage.

Tip Region (Traverse Height 5). The rotor wake crosses the traverse plane between 15 and 45% rotor relative phase, Figs. 7 and 8. The wake corresponds to approximately a 23% deficit in Mach number and a 16% deficit in relative total pressure. The center line of the wake was found to cross the traverse plane at 30% rotor relative phase. At mid-height the rotor wake crosses the traverse plane at 40% rotor relative phase. This implies that the rotor exit flow in the tip region (below the tip-leakage vortex) is underturned. This finding agreed with blade exit whirl angle measurements that were made at the exit of the stage (space precludes a detailed presentation of flow angle measurements). Thus, it can be seen that downstream of the stage the bound circulation in the flow causes the rotor wake to twist with its tip region moving toward the rotor suction surface. The rotor wake is also observed to get deeper close to the blade tip; this is caused by a radial outward migration of the low momentum wake fluid.

Hub Region (Traverse Height 16). No clear rotor wake is observed close to the hub wall. This is thought to be caused by the combined effect of the radial outward migration of the wake fluid and the hub secondary flow.

3.4 Rotor Tip-Leakage Flow. Between traverse heights 2 and 4 flow angles in excess of ± 50 deg were measured. Such changes in flow angle are too large to be measured accurately by the pyramid probe, and so gaps have been left in the measured data (Figs. 7–9). Future work is planned to include traversing in the near tip region using cross hot-wire probes. This will allow measurements to be made in regions of the flow where the amplitude of angle variations is too large to be measured accurately by fast-response aerodynamic probes.

The regions in which the flow has been measured exhibit strong rotor periodic behavior and show relatively little variation with vane relative position. The lack of vane periodic behavior close to the rotor tip is thought to be caused by the strong radially inward migration of vane wake fluid upstream of the rotor leading edge with the result that any circumferential variation of flow conditions at rotor inlet in the tip region is reduced.

4 Discussion of Interaction Mechanism

At the rotor trailing edge plane the flow exhibits time-unsteady behavior in two regions. In the first region, close to the hub wall (hub interaction region), a strong modulation of the low total pressure region associated with the rotor secondary flow (Section 3.2) and a periodic disappearance of the rotor trailing edge shock (Section 3.1) were observed. In the second region, a radial band close to the suction surface (two-dimensional interaction region), smaller total pressure and Mach number fluctuations were observed (Section 3.1). Both regions of the flow are labeled in Figs. 19 and 20. The figures show snapshots of the rotor exit total pressure and Mach number at a number of time intervals through the vane passing cycle. It should be noted that Fig. 6 is a single time-snapshot from Fig. 20 (86% vane relative phase), and shows the basic structure of the flow downstream of the rotor trailing edge. To allow a direct comparison of the relative size of phenomena at different vane relative positions, line plots of the rotor exit flow are also shown. The four heights at which the line plots are shown are marked H1 to H4. On each line plot the position of the rotor wake is marked using a blue band. Red and green colored bands are used to show the rotor relative position at which the hub and two-dimensional vane-rotor interaction regions of the flow occur. Each of the following sections discusses the probable causes of each of these two regions of the flow.

4.1 Hub Interaction. Close to the hub wall the rotor trailing edge shock and the total pressure deficit associated with the hub secondary flow both exhibit a strongly vane periodic behavior (discussed in Sections 3.1 and 3.2). In Figs. 19 and 20 the region of lowest total pressure and Mach number is observed when the rotor trailing edge is 86% across a vane passage and the region of highest total pressure and Mach number at 35%.

Any vane-rotor interaction mechanisms that exhibit such an affect must therefore only affect the rotor inlet flow close to the hub wall and do not occur in the mid-height or tip regions. This is likely to exclude both potential and shock interaction neither of which significantly increase in strength towards the hub wall. Downstream of the vane, low momentum, high loss fluid, has a lower swirl component than the core flow and so migrates towards the hub wall. Moss et al. [21], reported that in the Oxford Rotor the vane wake was found to pool onto the hub wall upstream of the rotor leading edge. This would result in wake interaction being

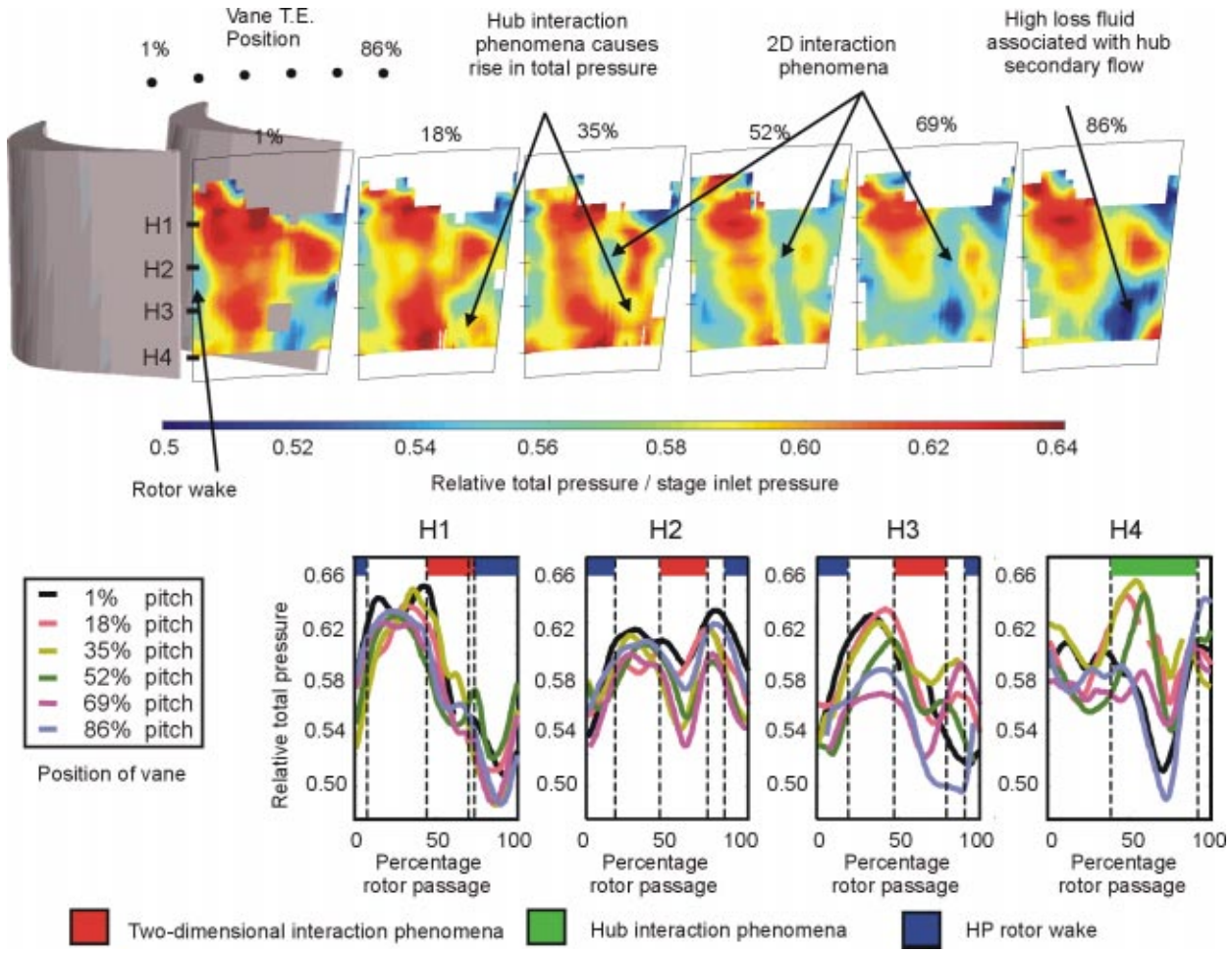

Fig. 19 Time-resolved rotor exit diagram—relative total pressure (H1–H4 show line plots at four radial heights as the upstream vane moves through one vane pitch

much stronger in the hub region than in the mid-height or tip regions. Another possible cause of hub interaction is the vane's secondary flow. However, in the Oxford vane the hub and casing secondary flows are of similar strength and no strong vane-rotor interaction has been measured close to the rotor tip region. It is thus thought likely that wake interaction, aided to a lesser extent by secondary flow interaction, is the cause of the hub interaction phenomena.

4.2 Two-Dimensional Interaction. At all radial heights the rotor exit traverse results show a fluctuating Mach number and total pressure between 0 and 30% rotor relative phase (Figs. 8, 9, marker **D**). This change in Mach number was highlighted in Section 3.1 as the major cause of the fluctuating rotor exit Mach number measured between the midheight of the annulus and the casing wall. In Figs. 19 and 20 this two-dimensional interaction phenomenon (marked with a red band) is observed between 45 and 75% rotor relative phase as a radial band of fluctuating total pressure and Mach number. The region of lowest total pressure and Mach number is observed to occur when the rotor trailing edge is 69% across a vane passage.

Any vane-rotor interaction mechanisms that exhibit such an effect must occur with the same strength at all radial heights. The wake fluid from the upstream vane twists as it convects downstream and migrates toward the hub wall. The rotor leading edge is thus subject to a different strength and vane relative phase of wake impingement at each radial height. It is therefore unlikely that wake impingement alone is responsible for this interaction. The two interaction mechanisms that occur with similar strength and phase at all radial heights are the interaction of the vane trailing edge shock system with the rotor and interaction between the potential fields of both the vane and rotor. The complexity and number of interaction mechanisms present within the stage indicate that it is unlikely that the ''two-dimensional interaction'' is caused by any single mechanism. However, at present, a detailed understanding of the mechanisms that cause this region has not been achieved.

5 Conclusion

The results described in the paper represent, to date, the most comprehensive experimental and computation data set that has been assembled on a transonic HP stage at engine representative conditions. The design of the stage is typical of modern HP turbines and the data set is thus of significant use in both validation of computation codes and giving insight into unsteady blade row interaction mechanisms. Future work will include further testing at engine operation conditions with the addition of a downstream vane. The following conclusions about the flow in a transonic HP turbine stage have been drawn from the discussions presented in this paper.

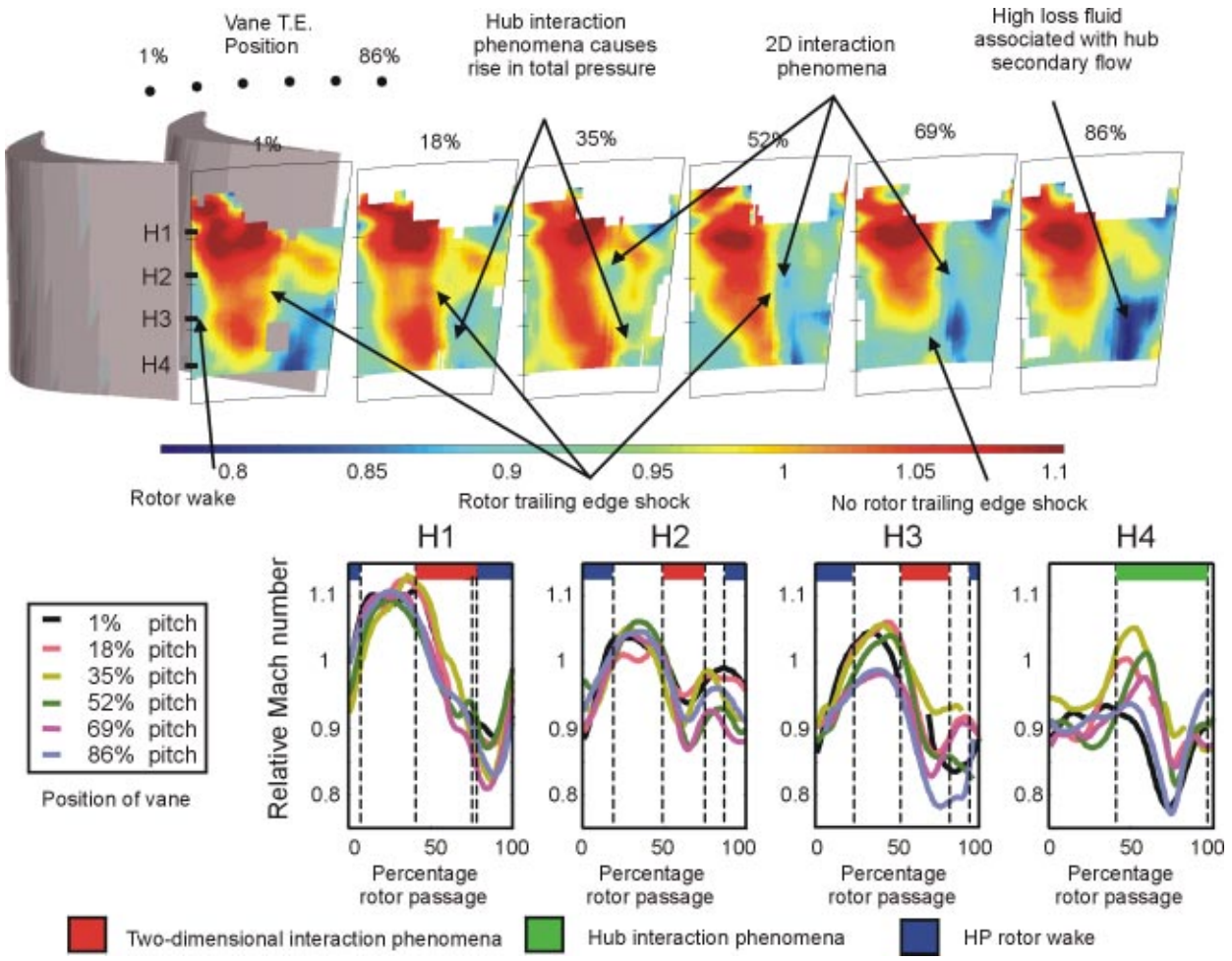

Fig. 20 Time-resolved rotor exit diagram—relative Mach no. (H1-H4 show line plots at four radial heights as the upstream vane moves through one vane pitch

Main Flow Features of Rotor Exit Flow

1. The exit flow from this transonic HP stage was found to be dominated by four flow features: the rotor tip-leakage flow, the rotor hub secondary flow the rotor trailing edge shock and the rotor wake.
2. The radial migration of wake fluid was such that, at 25% axial chord downstream of the rotor trailing edge, no definable wake structure was measured close to the hub wall.
3. The strength of the rotor trailing edge recompression shock was found to rise in strength linearly from hub to tip.

Vane-Rotor Interaction Mechanisms. Two significant vane periodic changes in the rotor exit flowfield have been identified. The first and most severe was found to occur close to the hub wall while the second was found to occur close to the rotor suction surface at all radial heights. The main features of these interaction mechanism are as follows:

1 *Hub interaction*, which is thought to be caused by the pooled vane wake segments aided to a lesser extent by vane secondary flow. The results of this interaction are as follows:

(a) The rotor trailing edge shock close to the hub wall periodically disappears with vane phase. This causes the time-resolved lift and inlet flow angle of a downstream vane to change.

(b) The low total pressure region associated with the hub passage vortex periodically disappears. The experimental measurements ($21\pm3\%$) and numerical predictions ($23\pm4\%$) of this change were found to agree closely.

(c) The strength of the hub secondary flow is not significantly changed. The penetration depth of the hub separation line was found to change by only 6%.

2 *Two-dimensional interaction*, which is thought to be caused by vane-rotor shock and potential flow interaction in addition to the remnants of the vane wake that has not pooled onto the hub wall upstream of the rotor leading edge. The interaction was found to result in a change in Mach number and total pressure at the same rotor and vane relative phase at all radial heights.

Time-Resolved Behavior of the Rotor Wake. The semi-wake width of the wake was found to change by 50% and the rotor relative phase of the wake was found to change by 10%. The change in the wake characteristic caused by vane-rotor interaction was found to be much greater than has been reported for subsonic stages. At present the mechanisms that cause this change are not understood. However, in compressible flow, it is known that the boundary conditions of the wake have a more severe effect on its characteristic.

Time-Resolved Behavior of the Tip-Leakage Flow. The tip-leakage flow was found to be largely unaffected by vane-rotor interaction.

Acknowledgments

All work was completed at the Southwell Laboratory in Oxford University. The authors gratefully acknowledge the support of K. J. Grindrod, John Allen, Nigel Brett and others from the Oxford Rotor Group. The authors also gratefully acknowledge the support of Rolls-Royce plc., DERA, MOD and DTI CARAD and their kind permission to publish this work.

Nomenclature

C_p = specific heat capacity at constant pressure
h = specific enthalpy
M = Mach no.
P = pressure
s = specific entropy
T = temperature
t = time
ρ = density

Subscripts

is = isentropic
ref = reference
o = total conditions

References

[1] Binder, A., Forster, W., Kruse, H., and Rogge, H., 1985, ''An Experimental Investigation into the Effect of Wakes on the Unsteady Turbine Flow,'' Trans. ASME, **107**, pp. 458–465.
[2] Hodson, H. P., and Dawes, W. N., 1996, ''On the interpretation of Measured Profile Losses in Unsteady Wake-Turbine Blade Interaction Studies,'' ASME 96-GT-494.
[3] Doorly, D. J., and Oldfield, M. L. G., 1985, ''Simulation of the Effect of Shock Waves on a Turbine Rotor Blade,'' ASME J. Eng. Gas Turbines Power, **107**, No. 4, pp. 998–1006.
[4] Giles, M. B., 1990, ''Stator-Rotor Interaction in a Transonic Turbine,'' J. Propul. Power, **6**, No. 5.
[5] Lefcort, M. D., 1965, ''An Investigation into Unsteady Blade Forces in Turbomachines,'' ASME J. Eng. Power, **87**, Oct., pp. 345–354.
[6] Korakianitis, T., 1993, ''On the Propagation of Viscous Wakes and Potential Flow in Axial Turbine Cascades,'' ASME J. Turbomach., **20**, pp. 657–674.
[7] Binder, A., 1985, ''Turbulence Production Due to Secondary Vortex Cutting in a Turbine Rotor,'' ASME 85-GT-193.
[8] Dring, R. P., Joslyn, H. D., Harding, L. W. and Wagner, J. H., 1982, ''Turbine Rotor-Stator Interaction,'' ASME 82-GT-3.
[9] Joslyn, D., and Dring, R., 1992, ''Three-dimensional Flow in an Axial Turbine: Part 1-Aerodynamic Mechanisms,'' ASME J. Turbomach., **114**, pp. 61–70.
[10] Sharma, O. P., Pickett, G. F., and Ni, R. H., 1992, ''Assessment of Unsteady Flows in Turbines,'' ASME J. Turbomach., **114**, pp. 79–90.
[11] Zeschky, J., and Gallus, H. E., 1993, ''Effects of Stator Wakes and Span-wise Non-uniform Inlet Conditions on the Rotor Flow of an Axial Turbine Stage,'' ASME J. Turbomach., **115** (1), Jan., pp. 128–136.
[12] Walraevens, R. E., and Gallus, H. E., 1995, ''Stator-Rotor-Stator Interaction in an Axial Flow Turbine and its Influence on Loss Mechanisms,'' AGARD-CP-571, Loss Mechanisms and Unsteady Flows in Turbomachines, Paper 39.
[13] Zaccaria, M. A. and Lakshminarayana, B., 1997, ''Unsteady Flow Field Due to Nozzle Wake Interaction With the Rotor in an Axial Flow Turbine,'' ASME 97-GT-206.
[14] Dietz, A. J., and Ainsworth, R. W., 1992, ''Unsteady Pressure Measurement on the Rotor of a Model Turbine Stage in a Transient Flow Facility,'' ASME 92-GT-156.
[15] Dunn, M. G., Bennett, W. A., Delaney, R. A., and Rao, K. V., 1992, ''Investigation of Unsteady Flow Through a Transonic Turbine Stage: Data/Prediction Comparison for Time-averaged and Phase-resolved Pressure Data,'' ASME J. Turbomach., **114**, pp. 91–99.
[16] Sheldrake, C. D., and Ainsworth, R. W., 1994, ''Rotating Hot-Wire Measurements in a Model Turbine Stage,'' Proc. 13th Symp. of Measurement Techniques for Transonic and Supersonic Flows in Cascades and Turbomachines.
[17] Hilditch, M. A., Smith, G. C., and Singh, U. K., 1998, ''Unsteady Flow in a Single Stage Turbine,'' ASME 98-GT-531.
[18] Denos, R., Sieverding, C. H., Arts, T., Brouckaert, J. F., Paniagua, G., and Michelassi, V., 1999, ''Experimental Investigation of the Unsteady Rotor Aerodynamics of a Transonic Turbine Stage,'' IMechE J. Power and Energy, **213** (A4), pp. 327–338.
[19] Venable, B. L., Delaney, R. A., Busby, J. A., Davis, R. L., Dorney, D. J., Dunn, M. G., Haldeman, C. W., and Abhari, R. S., 1999, ''Influence of Vane-Blade Spacing on Transonic Turbine Stage Aerodynamics—Part I: Time-Averaged Data and Analysis,'' ASME J. Turbomach., **121**, pp. 663–672.
[20] Busby, J. A., Davis, R. L., Dorney, D. J., Dunn, M. G., Haldeman, C. W., Abhari, R. S., Venable, B. L., and Delaney, R. A., 1999, ''Influence of Vane-Blade Spacing on Transonic Turbine Stage Aerodynamics, Part II: Time-Resolved Data and Analysis,'' ASME J. Turbomach., **121**, pp. 673–682.
[21] Moss, R. W., Ainsworth, R. W., Sheldrake, C. D., and Miller R. J., 1997, ''The Unsteady Pressure Field Over a Turbine Blade Surface: Visualisation and Interpretation of Experimental data,'' ASME 97-GT-474.
[22] Ainsworth, R. W., Schultz, D. L., Davies, M. R. D, Forth, C. J. P., Hilditch, M. A., and Oldfield, M. L. G., 1988, ''A Transient Flow Facility for the Study of the Thermofluid-Dynamics of a Full Stage Turbine Under Engine Representative Conditions,'' ASME 88-GT-144.
[23] Miller, R. J., and Ainsworth, R. W., 1994, ''An Ultra-High Speed Traverse System for Fast Response Aerodynamic Measurements in Transient Flow Facilities,'' Proc., 13th Symp. of Measurement Techniques for Transonic and Supersonic Flows in Cascades and Turbomachines.
[24] Binder, A., Schroeder, Th., and Hourmouziadis, J., 1989, ''Turbulence Measurements in a Multistage Low-Pressure Turbine,'' ASME J. Turbomach., **111**, pp. 153–161.
[25] Denton, J. D., 1990, ''The Calculation of Three-Dimensional Viscous Flow Through Multistage Turbomachines,'' ASME 90-GT-19.
[26] Schlichting, H., 1960, *Boundary Layer Theory*, McGraw Hill, New York, NY.
[27] Kurz, R., 1996, ''Characteristics of Wakes in Compressible Two-Dimensional Flows,'' ASME 96-GT-405.
[28] Mee, D. J., Baines, N. C., Oldfield, M. L. G., and Dickens, T. E., 1992, ''An Examination of the Contributions to Loss on a Transonic Turbine Blade in a Cascade,'' ASME J. Turbomach., **114** (1), Jan., pp. 155–162.

Blade Row Interaction in a High-Pressure Steam Turbine

V. S. P. Chaluvadi
A. I. Kalfas
H. P. Hodson

Whittle Laboratory,
Cambridge University Engineering Department,
Cambridge CB3 0DY, England

H. Ohyama
E. Watanabe

Turbine Engineering Department,
Mitsubishi Heavy Industries,
Takasago Machinery Works,
Takasago Hyogo 676, Japan

This paper presents a study of the three-dimensional flow field within the blade rows of a high-pressure axial flow steam turbine stage. Compound lean angles have been employed to achieve relatively low blade loading for hub and tip sections and so reduce the secondary losses. The flow field is investigated in a low-speed research turbine using pneumatic and hot-wire probes downstream of the blade row. Steady and unsteady numerical simulations were performed using structured 3-D Navier-Stokes solver to further understand the flow field. Agreement between the simulations and the measurements has been found. The unsteady measurements indicate that there is a significant effect of the stator flow interaction in the downstream rotor blade. The transport of the stator viscous flow through the rotor blade row is described. Unsteady numerical simulations were found to be successful in predicting accurately the flow near the secondary flow interaction regions compared to steady simulations. A method to calculate the unsteady loss generated inside the blade row was developed from the unsteady numerical simulations. The contribution of various regions in the blade to the unsteady loss generation was evaluated. This method can assist the designer in identifying and optimizing the features of the flow that are responsible for the majority of the unsteady loss production. An analytical model was developed to quantify this effect for the vortex transport inside the downstream blade. [DOI: 10.1115/1.1518504]

1 Introduction

The most significant contribution to the unsteadiness in a turbine is due to the periodic chopping of the wake (Hodson [1]) and secondary flow vortices from the upstream blade row by the downstream blade row (Sharma et al. [2], Boletis and Sieverding [3], Walraevens et al. [4], Ristic et al. [5]). As modern engine design philosophy places emphasis on higher blade loading and smaller engine length, the effects of these interactions become even more important. For a turbine with a low aspect ratio and high blade turning angle, secondary flow interactions could become more important than those due to wakes. It is possible for the incoming vortices to burst (Binder [6], Binder et al. [7]), giving rise to very high levels of free-stream turbulence. Sharma et al. [2,8] showed that the interaction of the first rotor secondary flows with the succeeding second stator blade row appears to dominate the flow field even at the exit of the second stator. In the turbine under investigation, the flow is subsonic. Thus the primary source of unsteadiness is the interaction of the blade row with the upstream blade wake and the secondary flow vortices.

This paper examines the impact of upstream streamwise vortices on the performance of the downstream blade row. This includes understanding the transport mechanism of the passage vortices inside the downstream blade row the mixing of the passage vortices unsteadily in the downstream blade row and finally translating this knowledge into design recommendations. These objectives are met by a comprehensive experimental testing and numerical simulation program.

2 Experimental and Numerical Approach

2.1 Test Rig and Instrumentation. The present work has been carried out in a subsonic large-scale, single-stage, axial flow high-pressure turbine with a casing diameter of 1.524 m and a hub-tip ratio of 0.8. Hodson [1] has described the test facility. Figure 1 shows the schematic diagram of the single-stage turbine test facility. The large scale of the rig makes it possible to measure the flow field inside the blade passage, upstream and downstream of the blade rows. Trip wires of 1.2 mm diameter are used to ensure that the boundary layers at the hub ($\delta^*/h=0.008, H=1.31$) and the casing ($\delta^*/h=0.0077, H=1.30$) are turbulent at the inlet to the stator row. These are located at two stator axial chords upstream of the stator blade row. Further details of the turbine are given in Table 1.

A Scanivalve system with integral pressure transducer is fitted to the rotor. Slip rings transfer power to and signals from the rotor mounted instruments. The rotor is designed to accommodate a three-axis relative frame traverse system in order to measure the flow field within and at the exit of the rotor. Area traverses were carried out downstream of the blade rows using a 5-hole, a 3-hole, or a Kiel probe. In all of the measurements, the probes were small relative to the blades having diameters of less than 1.5% of the blade pitch. The axes of the probes were aligned parallel to the mean flow direction in order to minimize the errors. The traversing was achieved using a computer-controlled stepper motor system. The probes were traversed radially from hub to tip in 26 steps and circumferentially over one pitch in 45 steps. Fine data grid resolution was used in the region of large gradients of total pressure such as the blade wake and secondary flows.

2.2 Hot Wire Anemometry. The development of the stator flow in the rotor blade passage was investigated using a rotating miniature three-axis hot wire probe. The probe had a measurement volume of 2 mm in diameter. Due to the length-diameter ratio of the hot wire sensors ($\sim$200), it was not appropriate to use the 'cosine law' or its modifications to represent the response of the sensors at different angles of attack (Champagne et al. [9]). For this reason, a technique similar to that used for calibrating a 5-hole pneumatic probe was developed. The technique relies on the interpolation of the data contained in a look-up table. Two non-dimensional coefficients, derived from the apparent velocities indicated by the three sensors were used as co-ordinates for the table. Each anemometer output signal was recorded at a logging frequency of 5.2 KHz using a computer controlled 12-bit transient-capture system.

All the measured voltages were converted to velocities before the determination of the statistical quantities. The acquisition of the data was triggered using a once-per-revolution signal. For the

Contributed by the International Gas Turbine Institute and presented at the International Gas Turbine and Aeroengine Congress and Exhibition, Amsterdam, The Netherlands, June 3–6, 2002. Manuscript received by the IGTI, December 12, 2002. Paper No. 2002-GT-30574. Review Chair: E. Benvenuti.

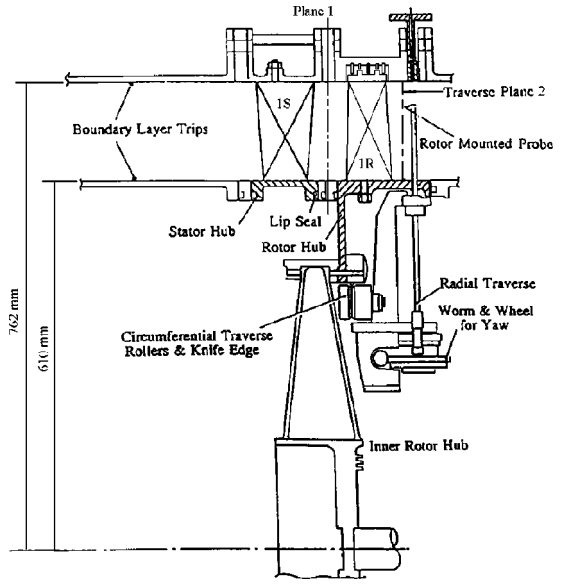

Fig. 1 Schematic diagram of the test configuration

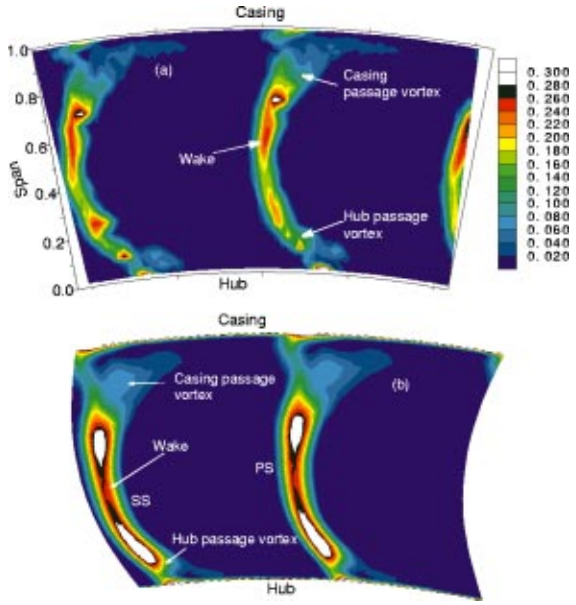

Fig. 2 Comparison of stagnation pressure loss coefficient (*Y*) at stator trailing edge (plane 1)—(*a*) measurements (*b*) steady CFD

phase-locked data measurements, 48 samples were recorded in the time taken for the rotor to move past three stator pitches. The data was ensembled over 200 revolutions and about 300 points (17 points pitchwise, 19 points radially), were taken within the area traverse.

2.3 Numerical Approach. The numerical simulations discussed in this paper were performed with a steady Navier-Stokes solver ''MULTIP81'' and time-accurate Navier-Stokes solver ''UNSTREST'' of Denton [10–12]. These codes solve the three-dimensional modified Reynolds averaged Navier-Stokes equations on a structured, nonadaptive mesh. The equations of motion are discretised to second-order accuracy and integrated forward in time. A mixing length model with wall function is used for modelling the turbulence in the flow. For the steady state calculations, a full multi-grid method and local time stepping are used to accelerate the convergence. In order to reduce the computation time and data storage, the unsteady simulations were carried out with 42 stator blades and 42 rotor blades instead of 36 and 42 blades of stator and rotor, respectively. This small variation in stator solidity may have some implications on exit angle distribution, blade lift and loss coefficient of the stator flow entering the rotor. It is assumed that this does not effect the transport behavior of the stator passage vortex inside the rotor. Agreement of the measured angles and losses at the exit of the rotor with unsteady simulations suggests that this difference is minimal. A sliding interface plane between the blade rows allows properties to pass from one blade row to another. The calculation is taken to be converged after a periodic solution is obtained in one blade passing period.

Table 1 Turbine geometry and test conditions

	Stator	Rotor
Flow Coefficient (V_{x1}/U_m)		0.35
Stage Loading ($\Delta h_0/U_m^2$)		1.20
Stage Reaction		0.5
Mid-Span upstream Axial Gap (mm)		41.2
Hub-Tip Radius Ratio	0.8	0.8
Number of Blades	36	42
Mean Radius (m)	0.6858	0.6858
Rotational Speed (rpm)		550
Mid-span Chord (mm)	142.5	114.5
Mid-span Pitch-Chord Ratio	0.84	0.896
Aspect Ratio	1.07	1.33
Radial Shroud Clearance (mm)		1.0
Inlet Axial Velocity (m/s)	13.85	
Mid-span Inlet Angle (from axial)	0.0^0	13.46^0
Mid-span Exit Angle (from axial)	71.03^0	-70.86^0
Chord based Reynolds Number	$5.24x10^5$	$4.12x10^5$
Inlet Free-Stream Turbulence	0.25%	

A grid of $41\times92\times45$ points for the stator and $41\times99\times45$ points for the rotor has been employed in these numerical simulations in the pitchwise, streamwise and spanwise directions, respectively. The grid expansion ratio determines the rate at which the grid is stretched away from the solid boundaries until the maximum permitted cell size is reached. Grid expansion ratio of 1.3 near the endwalls and 1.2 near the blade surfaces were used in these computations. In order to represent the vorticity accurately at inlet to the stator blade row, a total of 9 cells have been employed inside the endwall boundary layer thickness, which is of the order of 4% span. Unless otherwise indicated, all the experiments and computations have been carried out at the design operating condition.

3 Results and Discussion

3.1 Stator Exit Flow. The flow field at the stator exit is discussed with the help of measurements obtained at plane 1 located at a distance 13% of C_x downstream of the stator trailing edge. Figure 2 show the contour plots of the stagnation pressure loss coefficient (Y) and compared with computed results (steady flows assumed) over two stator pitches. The stagnation pressure loss is non-dimensionalised with a reference dynamic head.

The stator blade wake can be identified with the high loss region in the middle of the Fig. 2(*a*). Most of the loss over the span is associated with the blade wake, but there is also additional loss near the hub and the casing. The accumulation of the high loss fluid in these regions is a consequence of the hub and casing secondary flows. These loss cores can be identified at 10 and 90% of the blade span situated on the suction side of the blade passage. There is a good repeatability of the loss contours throughout the

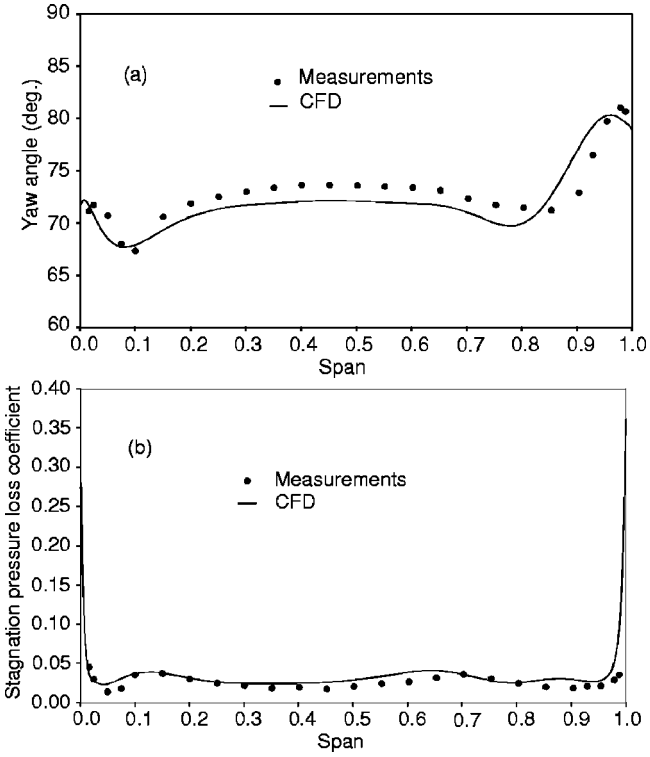

Fig. 3 Comparison of spanwise variations of pitchwise averaged flow field at stator trailing edge (plane 1)—(*a*) absolute yaw angle, (*b*) stagnation pressure loss coefficient (*Y*)

measurement domain of two stator passages. Figure 2(*b*) presents the loss coefficient predictions from steady numerical simulations. A comparison between the measured and computational results reveals a good qualitative and quantitative agreement with the main features of the stator flow being well captured. There is some discrepancy in the location and magnitude of the loss in the center of the wake at 20 and 70% of blade span, but the qualitative agreement is, nevertheless good. The computed width of the wake is more than the measured wake width. This may be due to the difference in the rate of mixing in the wake in the computations and in the experiments, which arises from the mixing model.

Figure 3 presents the radial distributions of the pitchwise averages of the absolute yaw angle and stagnation pressure loss coefficient at plane 1 behind the stator. The first plot (Fig. 3(*a*)) shows the absolute yaw angle distributions in the spanwise direction. It can be observed that there is a small variation of yaw angle from 30 to 65% of the span. However, near to the hub and the casing the familiar features of the passage vortex with overturning at the endwalls and underturning towards the midspan are observed. The second plot (Fig. 3(*b*)) shows the variation of the stagnation pressure loss coefficient in the spanwise direction. The loss coefficient is high at hub and casing due to the endwall boundary layers. The local increase in loss coefficient is observed corresponding to the secondary vortex cores near the hub and casing. There is a very good agreement between the measurements and the computations as can be seen in Fig. 3(*b*).

3.2 Rotor Flow

3.2.1 Static Pressure Distributions. Surface static pressure tappings were used to measure the pressure distributions along the stator and rotor blade surfaces. The static pressure coefficient (C_p, see Nomenclature for definition) distributions of the rotor blade, corresponding to five spanwise locations at 10, 50, and 90% of the blade span calculated from blade surface static pressure data, are shown in Fig. 4.

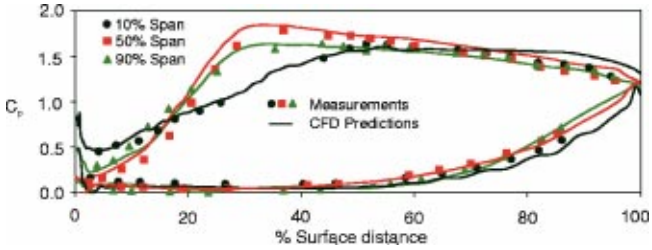

Fig. 4 Comparison of rotor surface static pressure coefficient distributions (C_p)

The symbols represent the data from measurements and the solid line from numerical simulations. The results indicate that the rotor blade is off-loaded near the endwalls ($C_{p,\max}$ of 1.64 at 10% blade span and 1.64 at 90% blade span) compared to the midspan region ($C_{p,\max}$=1.784 at 50% blade span) to reduce the rotor secondary flow. Also the rotor blade ends are aft-loaded (the peak suction is at 52% and 44% of surface distance at 10 and 90% blade span respectively) and the mid-span sections are front-loaded (peak suction is at 37% of surface distance). There is a very good agreement between the computations and the measurements indicating that the blade loading levels were represented correctly in the calculations.

3.2.2 Rotor Exit Flow. The flow field at the rotor exit is discussed with the help of 5-hole rotating probe measurements at plane 2, which is located at a distance of 26% rotor C_x downstream of the rotor trailing edge in the relative frame of reference. The loss coefficient (Y) contours of the relative stagnation pressure are presented in Fig. 5 and compared with the computed results. The data obtained from five radially disposed rotor leading edge Pitot tubes have been interpolated to provide a reference stagnation pressure for the traverse data at each radius.

The high loss region near the midspan is identified with the rotor blade wake. Figures 5(*a*), (*b*), and (*c*) have same level of contours and are given next to Fig. 5(*a*). The magnitude of the contours for Fig. 5(*d*) is given to the right of the figure.

Figure 5(*a*) shows that at least 45% of the blade span (from 20–65%) is occupied by two-dimensional flow, but there is additional loss near the hub and casing. The accumulation of the high loss fluid in these regions is a consequence of the hub and casing secondary flows and due to shroud leakage. At this measurement location, the shroud leakage loss dominates 15% of the blade height from casing. The casing secondary flow is pushed radially inwards by the growing tip leakage flow. At the hub, in addition to the loss core corresponding to the hub secondary flow on suction side of the blade, there is another loss core located near the pressure side of the blade (region 1). This is discussed further in Section 3.5 with the help of the unsteady measurements.

Figure 5(*b*) presents the contours of the loss coefficient predicted with a steady CFD calculation. The predicted hub and casing secondary flows are stronger than the measured values and are radially moved outward near the hub and inward near the casing. The loss core corresponding to the shroud leakage is not observed in this plot, as this feature is not modelled in this computation. The computation does not model the shroud leakage flow. The comparison of experimental data and computations revealed that this leakage flow is important and has to be modelled.

Further numerical simulations were carried out by including the modelling of shroud leakage flow (Denton [13]) and the associated loss. In this shroud leakage model, the leakage flow is estimated from the seal clearance and number of seals and is bled off from the main flow.

The change of angular momentum of the leakage flow due to friction on the shroud and casing are estimated using input values of the skin friction coefficient. The work done on the shroud by the leakage flow is also calculated. The leakage flow is then in-

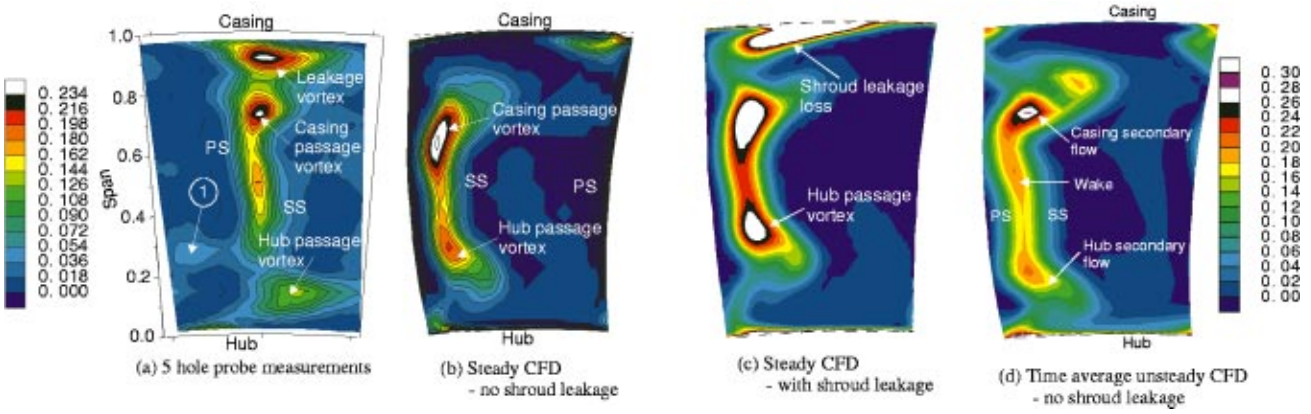

Fig. 5 Comparison of relative stagnation pressure loss coefficient at rotor trailing edge (plane 2)—(*a*) measurements; (*b*) steady CFD, no shroud leakage; (*c*) steady CFD, with shroud leakage; (*d*) time average unsteady CFD, no shroud leakage

jected into the main flow downstream of the blade row and the conservation equations determine the mixing loss. Figure 5(*c*) presents the results of this computation at the same measurement location. The loss core due to shroud leakage flow can now be observed very near the casing above the secondary flow loss as observed in the experiments. The computed magnitude of the shroud leakage loss is 20% more than the measured value. Given the simplicity of the model used for shroud leakage the comparison between the computations and experiments is thought to be very good especially in terms of the location and magnitude of this loss core corresponding to shroud leakage flow. The difference in efficiencies between the two simulations with and without shroud leakage modeling is 1.4%, indicating the importance of modeling the leakage flow in simulations. The tip clearance modeling of the shrouded blades is cumbersome and can be modeled only with multi-block methods or with an unstructured grid. This is a limitation of the present code as it is a structured single-block code. Alternatively, the modelling of source and sink terms often gives satisfactory results as shown in the present investigation.

The results of the three-dimensional time-accurate calculations (UNSTREST) have been used to give insight into the unsteady interactions occurring within the blade row. The same grid as that used for steady simulations was employed for unsteady simulations. The unsteady computation does not model the shroud leakage flow. The time-mean solution is obtained by averaging all the flow properties in one wake passing period (5188 iterations in this case). Figure 5(*d*) presents the contours of the relative stagnation pressure loss coefficient (Y) at the exit of the rotor. The difference between the mixing plane steady calculations and time mean calculations can be observed in the location of the rotor secondary flow at the hub and the casing. The loss core near the hub in this investigation is at a much lower radius than in the steady calculation. This unsteady calculation shows that the interaction between the stator flow and rotor flow is responsible for radial location of the hub secondary flow.

3.3 Unsteady Flow in the Rotor. The unsteady velocity field was measured using the stationary single slant hot-wire technique described by Kuroumaru et al. [14] and developed to work on the low-speed rotating compressor rig in the Whittle Laboratory by Goto [15]. An area traverse was performed over one stator pitch downstream of the rotor (26% C_x downstream of the rotor TE, plane 3) from 2.1 to 97.1% of the blade span in the absolute frame of reference. The measurement grid for the single slant hot-wire measurements consisted of 21 equispaced points in the pitchwise direction, 28 points in the spanwise direction and 300 points over two rotor pitches. This gave rise to a three-dimensional data (r,θ,t) set that can be viewed in various cutting planes.

Figure 6 presents the rotor exit absolute velocity contours in constant radius plane at blade midspan. The time variation of the ensemble averaged velocity trace at a point in the measurement grid was expressed as rotor pitch and plotted as abscissa. The circumferential probe location was plotted as a fraction of stator pitch. The rotor wake can be identified as a thin region of low absolute velocity surrounded by the higher velocity fluid as can be observed in Fig. 6(*a*). The variation, if any, of the velocity in the rotor wake in stator pitch direction can be attributed to the influence of the stator blade. One such region is observed between 75 to 100% of the stator pitch, associated with low velocity corresponding to the stator flow. At this stator pitch region, the rotor wake can not be identified separately.

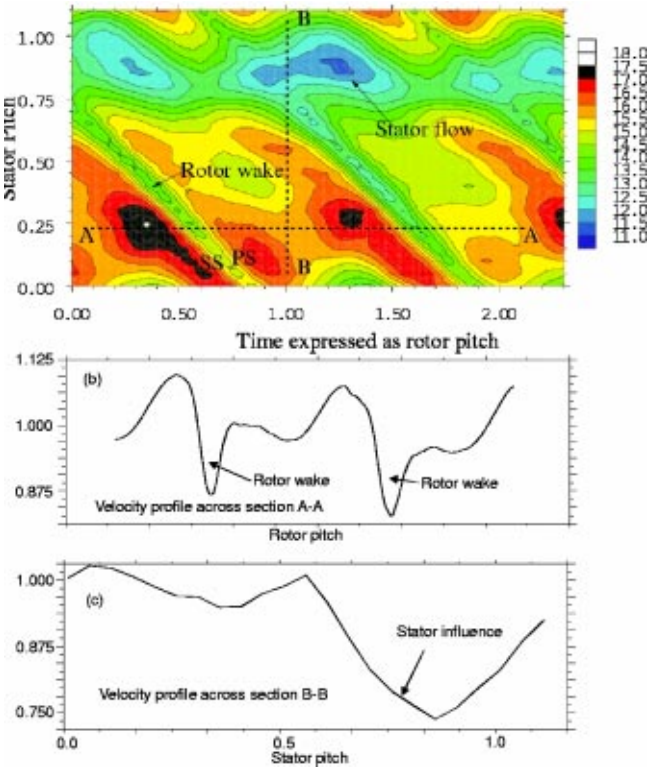

Fig. 6 Absolute velocity at rotor trailing edge measured with a SSHW at rotor midspan—(*a*) absolute velocity in rotor pitch, stator pitch plane; (*b*) velocity profile across section A-A; (*c*) velocity profile across section B-B

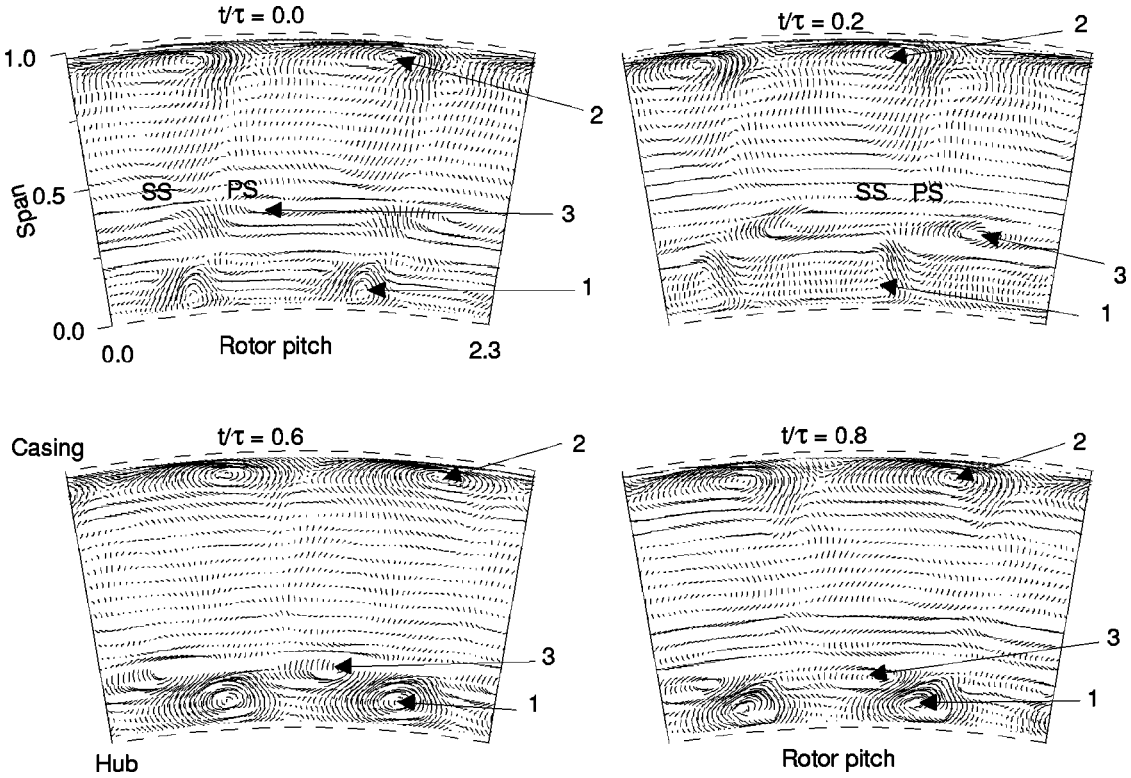

Fig. 7 Secondary flow lines at rotor trailing edge (plane 2) in relative frame of reference over one stator pitch

Figure 6(*b*) shows the variation of the absolute velocity of the flow with rotor pitch (across section AA) at 25% of the stator pitch. The narrow regions of low absolute velocity are due to the rotor wake. Averaging the absolute velocity at one stator pitch location and comparing the average velocity at various circumferential locations, the effect of stator flow influence on the rotor flow can be evaluated as shown in Fig. 6(*c*). The large velocity deficit corresponding to the stator flow interaction can be observed towards the rear end of the stator pitch (75–100%) as described earlier. The large magnitude of the velocity deficit indicates the significance of the unsteady interaction of the stator flow with the rotor.

The measurements carried out at various radial and circumferential locations in the area traverse were assembled together in the relative frame and presented over one rotor blade passing period in Fig. 7. Figure 7 presents the secondary flow lines in a quasi-orthogonal plane. The secondary flow lines were obtained by allowing the imaginary fluid particles to convect in the rotor exit secondary flow field for short period of time. The lines represent the response of the fluid particles to the secondary flow field at the traverse plane and are not a depiction of the flow development within the blade passage. The influence of the relative stator location on the rotor flow field can be understood from these plots. In these plots the stator flow features will be appearing and disappearing periodically at the frequency of the stator blade passing.

At $t/\tau=0.0$ (where τ is the stator blade passing period), the regions 1 and 2 correspond to the rotor passage vortices at hub and casing. At time $t/\tau=0.2$, the region 3 which is rotating opposite in direction to the rotor passage vortex can be observed on the pressure side of the blade. The same region 3 can be observed at a higher radius of 40% span when $t/\tau=0.0$ and at 24% span when $t/\tau=0.6$ and at 18% span when $t/\tau=0.8$. Further analysis of the absolute velocity and turbulence intensity data (not presented in the paper) at these spanwise locations corresponding to region 3 reveal that at time $t/\tau=0.2$, this rotating structure is strongest and the rotor passage vortex (region 1) is much smaller. At time $t/\tau=0.6$, the rotating structure (region 3) is smaller and the rotor hub passage vortex (region 1) is much larger. The sign of the rotation near the region 3 and its periodic nature indicate that this region may be due to the hub passage vortex of the previous stator. This was further analyzed with the help of three axis hot-wire measurements behind the rotor in the relative frame of reference.

3.4 Stator Wake and Vortex Transport. Figure 8 presents the instantaneous turbulence intensity (Tu) contours deduced from three axis hot-wire measurements downstream of the rotor (10% C_x downstream of the rotor TE, plane 3) plotted over one stator wake-passing period. Turbulence intensity can be used in tracking the stator flow inside the rotor as shown by Chaluvadi et al. [16].

The rotor wake and secondary flow features can be identified with the regions of high turbulence intensity (regions 1–3, respectively). It can be observed that region 4 is on the pressure side of the blade at 40% span is varying with period equal to that of stator passing. The maximum value of turbulence in the region 4 can be observed at $t/\tau=0.0$ and it gradually reduces to a minimum value at $t/\tau=0.50$. By observing the region 2 at all the time instants, it can be said that the rotor secondary flow at hub moves radially and circumferentially, varying in size in one stator blade-passing period. The loss measurements with a five-hole probe (Fig. 5) indicate that this region 4 correspond to a relatively higher loss. The yaw angles and secondary velocity vectors show that this region corresponds to a vortical flow rotating opposite in direction to the main rotor passage vortex. Furthermore, spectral analysis of the velocity trace in the center of this region 4 (not presented in the paper) showed a very strong stator blade passing frequency content indicating that this region is associated with the passage vortex of the stator at the hub. The location of this turbulence core on the pressure side is at a much higher radius than on the suction side. This is different from the vortex transport model proposed for the radially stacked blade by Chaluvadi et al. [16]. The present blade configuration is three dimensionally stacked with higher blade loading at the midspan and very low blade loading near the endwalls.

The stator passage vortex, when it convects to the downstream

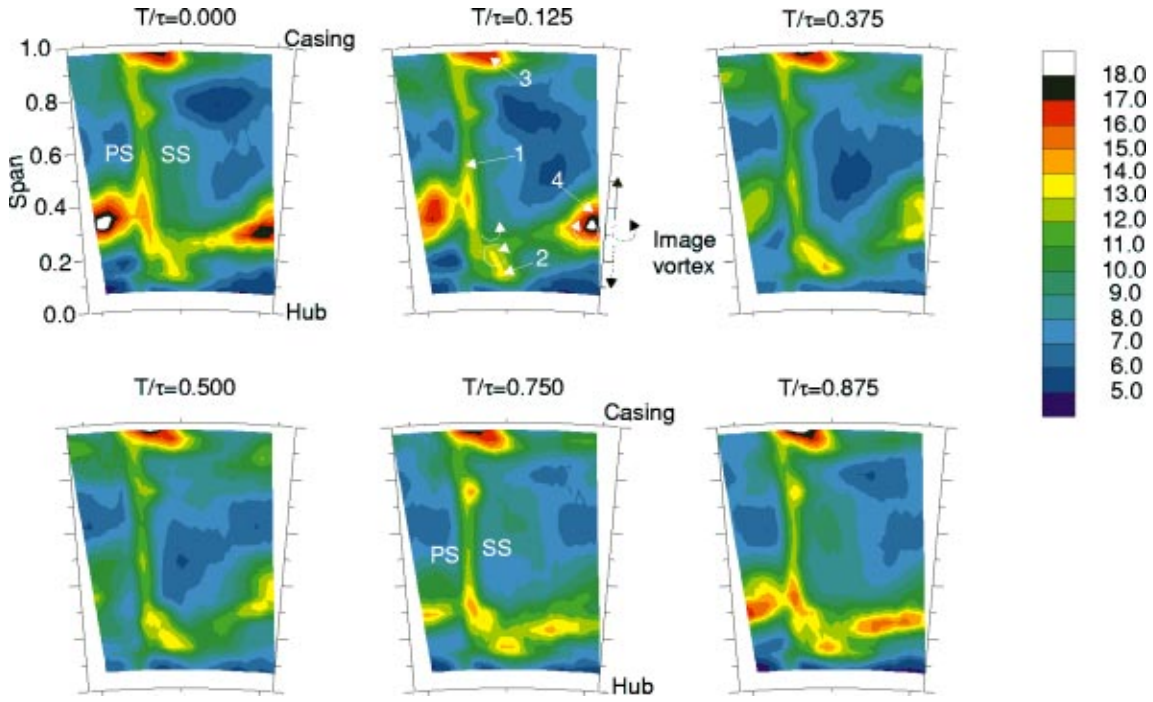

Fig. 8 Turbulence intensity contours at 10% *Cx* downstream of rotor trailing edge over one stator wake-passing period

rotor row, develops two counter rotating legs of the vortex on the pressure and suction surface of the rotor passage as shown in [16]. Both legs of the vortex convect downstream with the local flow velocities. At the exit of the rotor in the present investigation, the pressure leg of the stator passage vortex was radially displaced upwards and the suction leg was entrained into the rotor passage vortex. This is due to two different factors. The first factor stems from the three-dimensionality of the blade and the existing static pressure gradient, which drives the flow near the pressure surface towards the midspan. The larger radial migration of the vortex on the pressure surface than on the suction surface can also be explained with the help of vortex dynamics.

The vortical flows in the presence of solid surface are often analyzed with the help of *method of images*. The incoming stator passage vortex is rotating in the anticlockwise direction near the pressure surface, generates image vortex rotating opposite in direction inside the blade wall. The two vortices are of equal strength but rotating in opposite direction form a vortex pair as shown at $t/\tau=0.50$. Each induces a velocity of same magnitude and direction in the other and the vortex pair moves as a unit radially inwards in a fluid otherwise at rest. If a solid wall is placed at the central streamline of the figure at $t/\tau=0.50$, the vortices will start moving opposite in direction to the earlier one, i.e., radially outwards. This indicates that the pressure leg of the stator hub vortex will move radially out on the pressure surface and inwards on the suction surface, which concurs with the observation at the exit of the rotor blade as shown in figure $t/\tau=0.50$. If the stator hub passage vortex is stronger then the cross passage pressure gradient in the blade row will suggest that the pressure leg will travel to the suction side as suggested by Chaluvadi et al. [16] for a radially stacked blade.

4 Unsteady CFD Simulations

The results from the unsteady CFD simulations of the unsteady rotor flow field in one stator wake-passing period is presented at five instants in time separated by equal intervals. The unsteady computation does not model the shroud leakage flow. A comparison of the predicted pitchwise averaged unsteady flow field is made with the measurements from the five-hole probe traverse at the exit of the rotor (plane 2) in Fig. 9. The points indicate the results from the five-hole pneumatic probe measurements at the same plane.

The relative yaw angle distributions at the exit of the rotor are presented in Fig. 9(*a*). Near to the hub and the casing, the familiar features of the passage vortex with overturning at the endwalls and underturning towards the midspan are observed. There is a considerable variation in flow angle between the time instants near the hub region due to the transport of the stator secondary

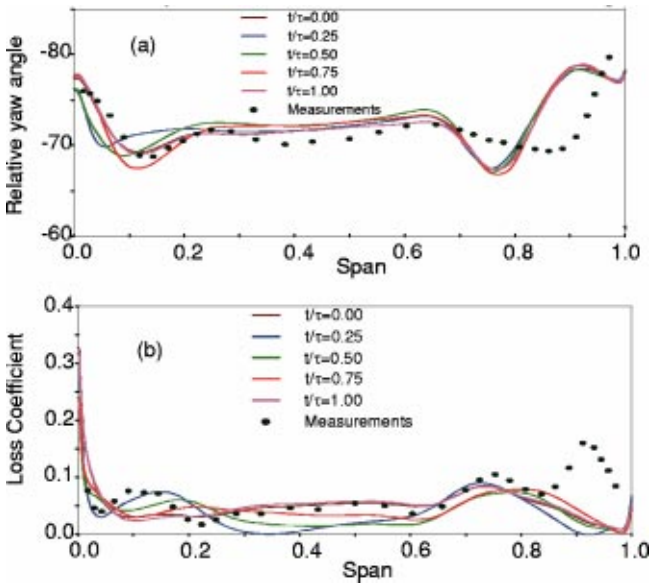

Fig. 9 Comparison of the pitch-wise averaged unsteady flow field between the five-hole probe measurements and unsteady CFD at rotor trailing edge—(*a*) relative yaw angle, (*b*) stagnation pressure loss coefficient

flow structures. The yaw angle variation between the time instants is observed from 25 to 70% span, but there is negligible difference in the corresponding mass flow distributions (not presented in the paper). This indicates that the difference in yaw angle is due to the variation in the lift of the rotor blade as the stator wake convects through the rotor blade. A very small variation in the yaw angles is observed between the various time instants from 70% span to the blade tip. A good comparison between the measurements and the unsteady numerical simulations can be observed up to 70% span from the hub. The difference between the measurements and the simulations near the casing is due to not modeling the shroud leakage flow in the unsteady simulations.

Finally, the spanwise variation of coefficient of relative stagnation pressure loss is presented in Fig. 9(*b*). The predicted relative stagnation pressure at the rotor inlet in the middle of the passage at various radial locations provided the reference stagnation pressure in evaluating the loss coefficient.

A large magnitude of the loss is predicted very near the hub due to the boundary layer on the hub endwall. The local increase in loss coefficient near the hub and casing secondary flow regions can be observed. A large difference in loss coefficient between the various time instants from 25 to 70% span is observed. This may be due to the stator wake interaction with the rotor blade row. Similarly, the difference between the five time instants near the hub region is due to the effect of the stator vortex transport through the rotor row. The predictions indicated the effect of unsteady flow on the exit yaw angles and the loss coefficient. The local increase in the loss can be observed at 75% blade span corresponding to the passage vortex. The difference between the predictions and the measurement from 73% span to the blade tip arises from not modelling the shroud leakage flow.

4.1 Loss Audit in the Turbine Stage. Denton [17] clearly illustrates that the only accurate measure of loss in a flow is entropy. Entropy is a particularly convenient measure because, unlike stagnation pressure, stagnation enthalpy or the kinetic energy, its value does not depend upon the frame of reference. By evaluating the entropy generation in a control volume and summing many such control volumes in a blade passage, it is possible to calculate the entropy increase for the whole blade row.

It can be shown from the energy equation (Hughes and Gaylord [18]) that for a volume of V, with a surface area A, the rate of entropy production due to viscous dissipation can be written as

$$\int_V \sigma d\text{vol} + \int_A \frac{k\nabla T}{T}\mathbf{n}dA = \frac{\partial}{\partial t}\int_V \rho s d\text{vol} + \int_A \rho s \mathbf{V}\mathbf{n}dA \quad (1)$$

where σ is the entropy production rate per unit volume due to viscous shear and k is the thermal conductivity. The unit normal vector **n** is positive when directed out of the volume and the velocity vector is denoted as **V**. As the present investigation is in a low-speed research turbine involving only incompressible and adiabatic flows, the entropy generation due to heat transfer is negligible and Eq. (1) becomes

$$\int_V \sigma d\text{vol} = \frac{\partial}{\partial t}\int_V \rho s d\text{vol} + \int_A \rho s \mathbf{V}\mathbf{n}dA \quad (2)$$

Since the numerical predictions were found to agree well with the experiments, the entropy production rate for the rotor and the stator blade rows was calculated from steady simulations. The intention was to identify the sources and regions of loss generation inside the blade row.

A typical control volume with the inlet and outlet entropy fluxes is depicted in Fig. 10. After evaluating the entropy fluxes into and out of each cell (control volume) of the computational domain, Eq. (2) was used to calculate the entropy production rate in that cell. Using the method of Jennings and Shin [19], the whole blade was divided into the number of regions as shown in Fig. 10. The 10% of the span from the endwalls of the blade are defined as the hub and the casing region such that it will contain most of the endwall boundary layers. The pitchwise extent of the ''pressure surface'' and ''suction surface'' was taken as 10% of the blade pitch so that it will contain most of the blade boundary layer. Two separate regions of upstream and downstream are also defined to account for the whole of upstream region from inlet to the blade leading edge and the downstream region from blade trailing edge to the mixing interface plane which is located midway between the stator and the rotor blade. The rate of entropy generated inside each blade row was taken as 100% and the entropy production rate in various regions of each blade was calculated as a percentage of the blade value.

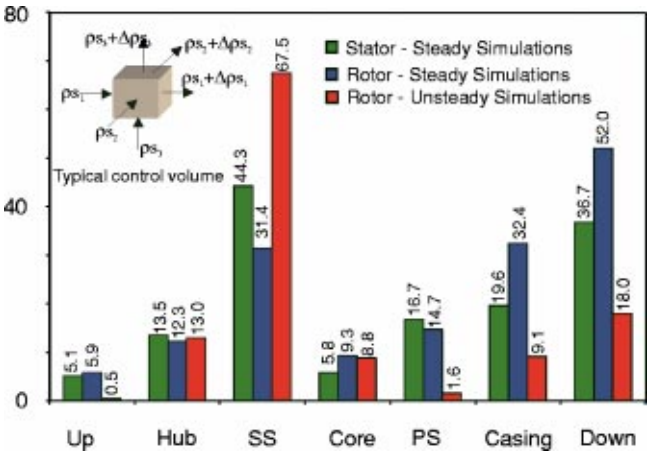

Fig. 10 Loss generation rate in various regions of the blade row

Figure 10 shows the rate of entropy generated in various regions of the flow in the stator and the rotor though the total values of the entropy generated in the stator and the rotor are different from the steady flow simulation. The maximum percentage of the rate of entropy is generated in the suction surface of the blade (44.3% for the stator, 31.4% for the rotor) compared to the other regions of the blade. The entropy generation rate in the casing region of the rotor (32.4% for the rotor, 19.6% for the stator) is much higher than the stator indicating a very strong rotor secondary flow at casing. The entropy generation rate in the ''downstream'' region corresponds to the wake and vortices mixing loss. The large magnitude of the mixing loss (36.7% for the stator, 52% for the rotor) is due to the larger downstream area considered in the analysis for the rotor. It is also due to the mixing of the deeper rotor wake and the passage vortices in the downstream of the rotor. This method of identifying the loss generating regions can be a useful tool for the blade designer as it enables the designer to focus on the relatively higher loss regions of the blade while optimizing the new blade design.

A similar analysis was carried out using unsteady numerical simulations, where the entropy generation rate in each control volume was integrated over one stator passing period. The unsteady computation does not model the shroud leakage flow. Hence, the magnitude of the entropy generation rate is not comparable to the ones from steady simulations but the qualitative conclusions can still be drawn from this analysis. The entropy generation rate for the suction surface region is 67.5% of the whole blade. This is higher in comparison to 31.4% for the same region from the steady simulations. The entropy generation rate in the core region is 8.8% of the total entropy generated in the rotor blade row. The reduction in entropy generation rate in the core region is due to not modeling the shroud leakage flow. The entropy generation rate in this region combined with some of the increase in suction surface region can be assumed to be due to the unsteady loss.

Figure 11 presents the contours of the time mean entropy generation rate per unit volume ($\dot{S}'''$) in the rotor blade row. The

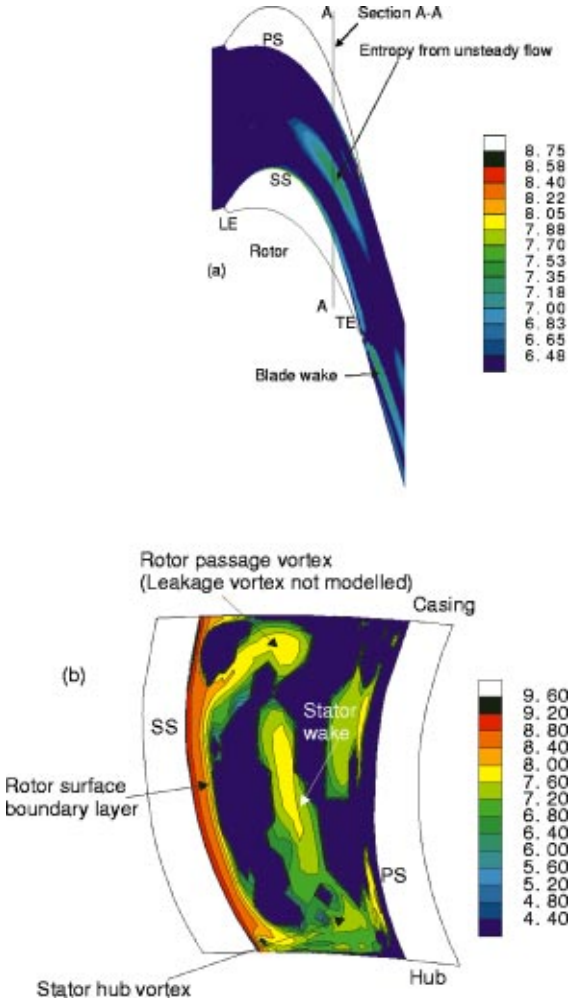

Fig. 11 Logarithm of the entropy generation rate per unit volume (J/s K m^3) in the rotor blade row from unsteady simulations—(*a*) at rotor midspan, (*b*) at section AA (80% rotor axial chord from LE)

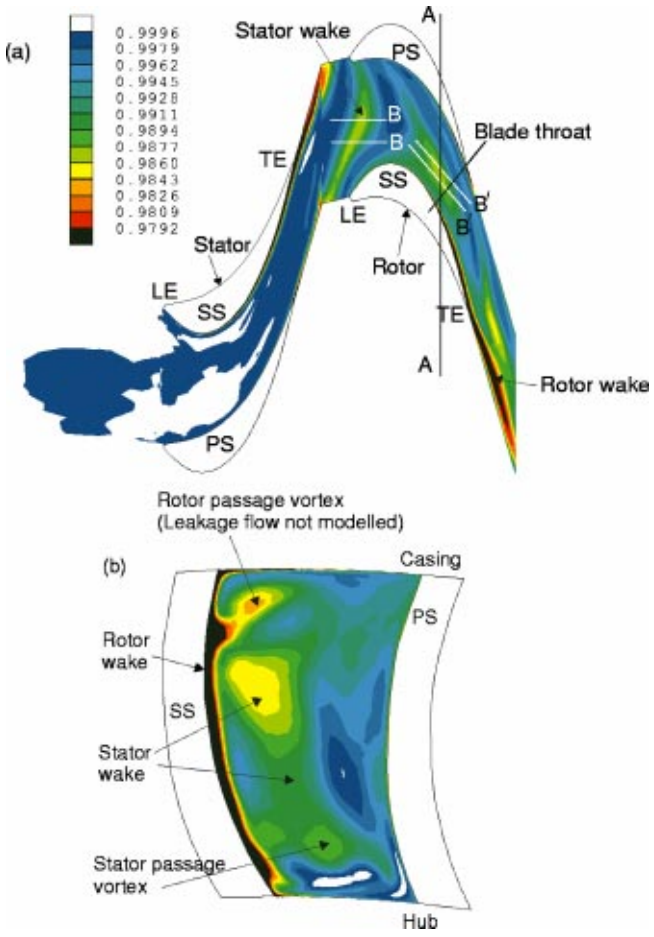

Fig. 12 Entropy function contours from unsteady numerical simulations—(*a*) in a blade-to-blade plane at midspan, (*b*) across section AA

magnitude of the entropy generation rate per unit volume being very large, logarithm of the same is presented in Fig. 11(*a*) at the rotor mid-span radius in the blade-blade plane. The entropy can be seen produced in the surface boundary layers of the rotor as well as during wake mixing with the free stream flow. In addition to these, the entropy generation can also be observed in the middle of the passage. Further investigation of the entropy generation rates was carried out at section A-A as shown in Fig. 11(*b*). The entropy generation can be observed on the rotor suction surface due to the surface boundary layers. The regions corresponding to the rotor hub and casing passage vortices can also be observed. In addition to the aforementioned regions, a region in the middle of the passage is also observed. This is the region that corresponded to the loss observed in Fig. 11(*a*) and is near the rotor blade throat. This unsteady loss-generating region may be due to the compression of the stator wake near the rotor throat region, while convecting in the rotor blade row. It is described as follows.

Figure 12(*a*) presents the instantaneous entropy function ($e^{-\Delta s/R}$) contours at the rotor midspan radius in the blade-blade plane. The stator wake can be identified in the middle of the rotor passage. The stretching of the stator wake near the rotor pressure surface and the shearing of the stator wake near the suction surface can be observed in this figure. Consider a segment BB of the stator wake at the rotor inlet, while convecting through the rotor blade from the conservation of mass flow inside the wake, it can be shown that it modifies to B′B′ near the rotor throat region. This results in the compression of the wake in the middle of the blade passage. If the wake is considered as being two vortex sheets, from Kelvin's theorem it can be shown that the velocity difference is amplified if the wake is compressed. This increased velocity difference inside the wake in turn increases the mixing losses and hence the generation of unsteady loss as predicted in Fig. 11(*b*).

Figure 12(*b*) presents the instantaneous entropy function contours across section AA of Fig. 12(*a*). In addition to the rotor wake and passage vortices, a region corresponding to the interaction between the stator flow (stator blade wake and passage vortices) and rotor can be observed in the middle of the passage. The two other entropy-generating regions observed in the middle of the blade passage in Fig. 11(*b*) can be identified to the stator hub and casing passage vortices from this figure. This unsteady loss generation is from the stretching of the stator passage vortices in the rotor blade and the loss generation can be observed at all the locations throughout the rotor blade. A secondary flow vortex from one blade row convects through a downstream blade row very much like a wake. However, the implications for the loss are very different. According to Kelvin's theorem, the circulation around a streamtube remains constant and so if stretching reduces the diameter of the tube, the streamwise vorticity is amplified. When a vortex is stretched (or compressed) longitudinally, it can be shown that its secondary kinetic energy will vary as the square of its length (Denton [17]). Hence, stretching a vortex will greatly

amplify its secondary kinetic energy and when this is subsequently dissipated by viscous effects to a uniform flow, it will generate additional loss.

This analysis has thus further demonstrated the use of the unsteady numerical simulations in identifying and understanding the mechanisms of unsteady loss generation in the turbine stage. Present measurement techniques restrict the measurement of entropy in the unsteady flow for the want of unsteady temperature measurement in experiments. Hence, the validation of the CFD predictions of entropy generation rate is out of the scope of the paper. The numerical scheme, grid, smoothing parameters and other control parameters being same for both the steady and the unsteady numerical simulations, the numerical diffusion, if any will also be identical for both of the calculation procedures. Hence, the difference between the steady and unsteady simulations can be assumed to be only due to the unsteadiness in the flow.

5 Analytical Model

The previous sections of this paper indicated that the vortex transport in the downstream blade row is complex. The vortex transport also generates additional losses in the process. It is helpful to use unsteady Navier-Stokes numerical simulations to calculate the contribution of unsteady losses from vortex interactions. Nevertheless, designers would like to know the global effects of the vortex interaction without resorting to full unsteady Navier-Stokes simulations. Hence, an attempt has been made to simplify various aspects of the vortex transport to find a simple analytical solution for the calculation of unsteady loss at the preliminary design stage.

One of the first studies of secondary flow generation using analytical modelling was proposed by Hawthorne [20]. He modelled the incoming boundary layer as a vortex filament in the tangential direction and showed that as this vortex filament convected through the downstream blade row, it produced secondary, trailing filament and trailing shed vorticity. Smith [21] presented a theory for the determination of secondary vorticity by considering the disposition of a vortex line as it moves through the blade passage with fluid particles. This model can be used for an inclined vortex filament unlike that of [20]. In the present investigation, a model similar to that used by Smith [21] was used for the transport of the vortex in the downstream blade row.

Figure 13 illustrates the kinematic model used in the present investigation. The incoming passage vortex (AP) can be considered as a concentrated vortex filament, which is at an angle to the main flow direction. The incoming freestream flow has a velocity of W_1 with inlet flow angle of θ_1. The exit flow has a velocity of W_2 with flow angle θ_2. The incoming vortex filament enters the downstream blade row inclined at an angle of γ_1 to the tangential direction as shown in Fig. 13. The assumptions used in the present analysis are (a) the flow is incompressible and inviscid, (b) there is one vortex tube per passage at any instant in time, (c) the mass flow associated with the trailing filament vorticity is small and can be neglected. There is no variation in blade loading in the spanwise direction resulting in negligible trailing shed vorticity, and (d) the vortex tube diameter is small compared to the blade chord. It will be represented as a straight line at exit. The vortical flow is convected by the mean flow of the passage.

As the vortex filament is inclined to the flow direction, it first encounters the blade leading edge near the pressure surface while convecting downstream. After traveling distance e with the freestream velocity W_1, the vortex filament now reaches the suction surface of the succeeding blade row. The vortex filament moves with the fluid downstream and satisfies the theorems of Kelvin and Helmholtz. The vortex will always be composed of the same particles and its motion may be followed until it is downstream of the blade row. Owing to the different velocities on the concave and convex surfaces of the blade, the vortex will take up different position at the exit of the row (DQ). The length and the

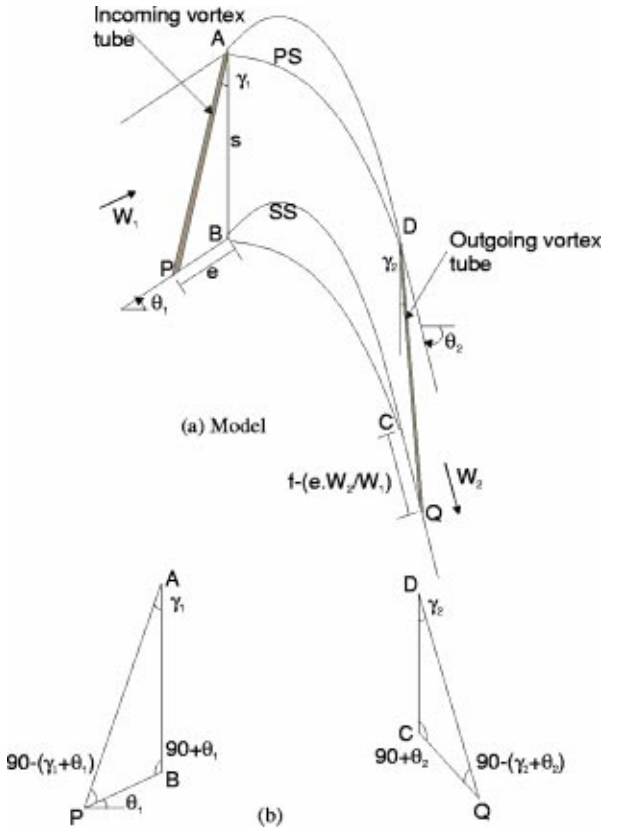

Fig. 13 Kinematic model illustrating the vortex transport through a turbine blade passage

orientation of the vortex segment leaving the blade row can then be determined from the difference between the times at which the pressure and suction side legs of the vortex are discharged.

The ratio of the exit vortex filament length to the inlet filament length can be defined as stretching ratio S_r and can be calculated from the inlet and exit velocity triangles as,

$$sr = \frac{\mathrm{DQ}}{\mathrm{AP}} = \frac{\mathrm{Cos}(\theta_2)}{\mathrm{Cos}(\theta_1)} \frac{\mathrm{Cos}(\gamma_1+\theta_1)}{\mathrm{Cos}(\gamma_2+\theta_2)} \tag{3}$$

The exit angle of the vortex filament γ_2 is evaluated from the relation

$$\frac{1}{(1/\mathrm{Tan}(\gamma_2)) - \mathrm{Tan}(\theta_2)} = \frac{4(\mathrm{Tan}(\theta_1)+\mathrm{Tan}(\theta_2))}{\{4+\{\mathrm{Tan}(\theta_1)-\mathrm{Tan}(\theta_2)\}^2\}} - \frac{\mathrm{Sin}(\gamma_1)\mathrm{Cos}(\theta_1)}{\mathrm{Cos}(\gamma_1+\theta_1)} \tag{4}$$

For the given blade geometry (s), inlet and exit flow angles (θ_1, θ_2) and vortex filament incidence angle at inlet (γ_1), the vortex filament angle at the blade exit and the stretching ratio can be calculated from Eqs. (4) and (3). The results of the filament exit angle and the stretching ratio of the vortex filament for the turbine under investigation is given in Fig. 14.

Figure 14 presents variation of the stretching ratio as a function of vortex inlet filament angle from Eq. (3). The lengths of the passage vortex filament at the rotor inlet and at the rotor exit were evaluated from the entropy contours in a blade-blade plane from unsteady numerical simulations for two turbine test cases are presented in Fig. 14. There is a reasonably good agreement between the simulations and the analytical model increasing the confidence in the analytical model. The effect of vortex stretching on the additional loss generation is discussed in the forthcoming.

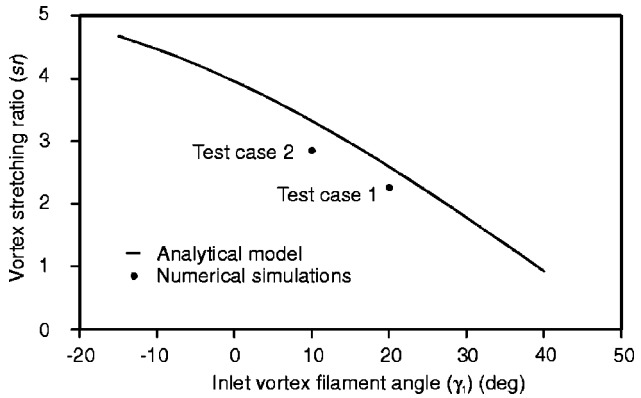

Fig. 14 Comparison of vortex stretching ratio between analytical model and numerical simulations

The vortex filament can be approximated as a Rankine's combined vortex consisting of a core region containing all the vorticity and an outer region containing the irrotational outer flow. Then the tangential velocity distribution across the vortex with radius is given as

$$V_\theta(r) = \left\{\frac{\Gamma}{2\pi\delta}\frac{r}{\delta}\right\} \quad 0 < r < \delta$$

$$= \left\{\frac{\Gamma}{2\pi r}\right\} \quad \delta < r < R \tag{5}$$

where δ and R corresponds to the rotational inner core radius and irrotational outer core radius of the vortex respectively. Now consider a finite sized vortex tube. The tube is stretched with tension forces from a length l_1 to a length

$$l_2 = S_r . l_1 \tag{6}$$

The total rotational kinetic energy for the vortex with length l_1 is given as

$$\text{Kinetic energy} = \frac{1}{2} m r^2 \Omega^2 = \frac{1}{2} m V_\theta^2$$

where V_θ is the tangential velocity inside the vortex and varies as per Eq. (5). The total rotational kinetic energy for this vortex tube can be calculated by integrating the velocity distribution over radius. It is given as

$$\text{Total rotational kinetic energy} = \left[\int_0^\delta \frac{\Gamma}{2\pi\delta}\frac{r}{\delta}dr + \int_\delta^R \frac{\Gamma}{2\pi r}dr\right]^2 \tag{7}$$

From the conservation of mass and angular momentum of the vortex tube before and after stretching gives rises to the relation after some algebraic manipulation

$$\text{Kinetic energy ratio} = \frac{17\Gamma/60\pi^2\delta_2}{17\Gamma/60\pi^2\delta_1} = \frac{\delta_1}{\delta_2} = \sqrt{S_r} \tag{8}$$

This relation shows that the increase in stretching ratio increases the secondary kinetic energy at blade exit. It can be shown that this total kinetic energy ratio for the vortex tube rotating as a body varies as the vortex-stretching ratio S_r. The stretching ratio (S_r) is only a function of turning in the blade row as can be observed from Eq. (3). It does not depend on the pitch or lift coefficient of the blade.

Combining this vortex transport model with the turbine design parameters demonstrates the significance of unsteady flow interaction for a given flow coefficient (V_x/U_m) and stage loading coefficient ($\Delta h_0/U_m^2$). The analysis is carried out for zero interstage swirl. Figure 15 illustrates the effect of flow coefficient and stage-loading coefficient on increased secondary kinetic energy ratio. A value of more than one signify increase in the secondary kinetic energy of the upstream vortex while traveling through the downstream blade. Figure 15 shows that the secondary kinetic energy ratio increases with the reduction in flow coefficient. On the other hand, the secondary kinetic energy ratio is a weak function of stage loading coefficient. Depending on the ratio of the secondary flow losses to the stage loss, one can calculate the additional losses generated due to the passage vortex transport and in turn to the stage efficiency. Despite the complexity of the actual vortex transport and the assumptions made in modeling the flow analytically, the presented model demonstrated the salient features of the vortex interaction. This can be a handy tool for the designers in selecting the turbine loading parameters from unsteady flow considerations.

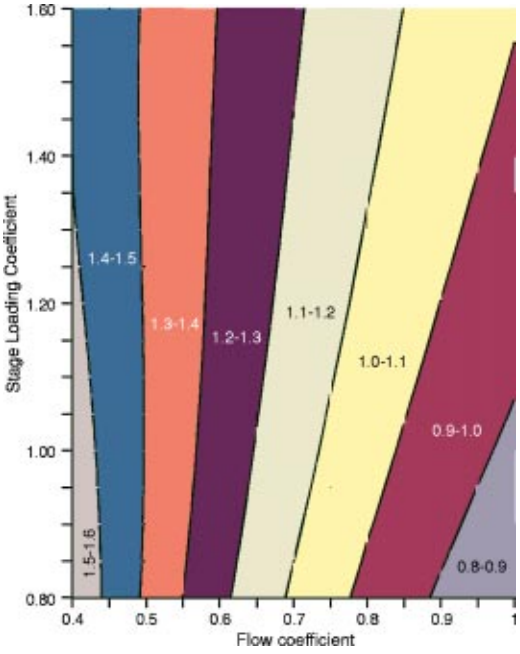

Fig. 15 Effect of flow coefficient and stage loading coefficient on vortex tube kinetic energy ratio

6 Conclusions

The development of the steady and the unsteady three-dimensional flow in the turbine has been described. The lower endwall loading and the three-dimensional stacking of the blades resulted in the reduced strength of the hub and casing passage vortices of the stator and the rotor. The passage vortices are also distributed over a large blade span.

The transport of the stator passage vortices inside the rotor blade is slightly different to the model proposed for the radially stacked blades. At the exit of the rotor in the present investigation, the pressure leg of the stator passage vortex was radially displaced upwards and the suction leg was entrained into the rotor passage vortex.

The agreement between the experimental and the computational results is good. The need for modelling secondary flows such as shroud leakage flows is also highlighted. Unsteady numerical simulations were found successful in accurately predicting the flow near the regions of secondary flow interaction.

A method to calculate the loss generation rate in the blade row was developed from numerical simulations. The contribution of various regions of the blade row towards the total blade loss was evaluated from steady numerical computations. The maximum percentage of the loss was generated near the suction surface of the blade. A similar analysis was carried out using unsteady numerical simulations, where the entropy generation rate in each control volume was integrated over one stator passing period. The unsteady loss generation from both the stretching of the stator

passage vortices in the rotor blade and the compression of the stator wake near the rotor throat in the midpitch region were demonstrated.

An analytical model was developed using the concepts of the kinematic vortex transport inside the downstream blade and assuming the incoming vortex to be as a concentrated vortex filament. The model was accurate enough in calculating the vortex filament exit angle and the increase in the exit secondary kinetic energy from vortex stretching inside the blade for the given blade parameters and inlet vortex angle. Despite the complexity of the actual vortex transport, the analytical model brought out the significant effects of vortex interaction with the downstream blade row very well.

Nomenclature

C = chord
C_p = static pressure coefficient $=\{P_{0in}-P\}/(1/2)\rho U_m^2$
h = enthalpy
H = blade span, boundary layer shape factor (δ^*/θ)
K = coefficient of thermal conductivity
N = total no. of realizations
P = pressure
R = universal gas constant, outer irrotational core radius
s = specific entropy, streamwise distance
$\dot{S}''$ = entropy generation rate per unit volume
S_r = ratio of vortex stretching
t = time from a datum point
T = temperature, wake passing period
Tu = turbulence intensity $=\sqrt{1/3(\langle V_x\rangle^2+\langle V_r\rangle^2+\langle V_0\rangle^2)}/V_{\text{ref}}$
U = blade speed
V = velocity, volume
x = axial distance
Y = stagnation pressure loss coefficient $=\{P_{01}-P_{02}\}/(1/2)\rho(V_{x1}/\text{Cos}\,74°)^2$
σ = entropy production rate per unit volume
δ = vortex inner core radius
δ^* = boundary layer displacement thickness
γ = vortex filament angle
θ = boundary layer momentum thickness, flow angle
τ = time for one wake passing period, time lag
Γ = circulation
ζ = vorticity

Subscripts

m = midspan
max = maximum
min = minimum
o,0 = stagnation
r = radial
ref = reference
x = axial
θ = tangential
1 = blade row inlet
2 = blade row exit

Superscripts

$'$ = perturbation of the quantity
- = time mean of the quantity

References

[1] Hodson, H. P., 1985, ''Measurements of Wake Generated Unsteadiness in the Rotor passages of Axial Flow Turbines,'' ASME J. Eng. Gas Turbines Power, **107**(2), Apr.
[2] Sharma, O. P., Renaud, E., Butler, T. L., Milsaps, K., Dring, R. P., and Joslyn, H. D., 1988, ''Rotor—Stator Interaction in Multistage Axial Flow Turbines,'' AIAA Pap., 88-3013 July 11–13.
[3] Boletis, E., and Sieverding, C. H., 1991, ''Experimental Study of the Three Dimensional Flow Field in a Turbine Stator Preceded by a Full Stage,'' ASME J. Turbomach., **113**(1), Jan., p. 1.
[4] Walraevens, R. E., Gallus, H. E., Jung, A. R., Mayer, J. F., and Stetter, H., 1998, ''Experimental and Computational Study of the Unsteady Flow in a 1.5 Stage Axial Turbine with Emphasis on the Secondary Flow in the Second Stator,'' ASME 98-GT-254, June 2–5.
[5] Ristic, D., Lakshminarayana, B., and Chu, S., 1999, ''Three-Dimensional Flow field Downstream of an Axial-Flow Turbine Rotor,'' J. Propul. Power, **15**(2), Mar.–Apr., pp. 334–344.
[6] Binder, A., 1985, ''Turbulence Production Due to Secondary Vortex Cutting in a Turbine Rotor,'' ASME J. Eng. Gas Turbines Power, **107**(4), Oct., pp. 1039–1046.
[7] Binder, A., Forster, W., Mach, K., and Rogge, H., 1986, ''Unsteady Flow Interaction Caused by Stator Secondary Vortices in a Turbine Rotor,'' ASME 86-GT-302.
[8] Sharma, O. P., Pickett, G. F., and Ni, R. H., 1990, ''Assessment of Unsteady Flows in Turbines,'' ASME 90-GT-150, June 11–14.
[9] Champagne, F. H., Schleicher, C. A., and Wehrmann, O. H., 1967, J. Fluid Mech., **28**, p. 153.
[10] Denton, J. D., 1986, ''The Use of a Distributed Body Force to Simulate Viscous Effects in 3-D Flow Calculations,'' ASME 86-GT-144.
[11] Denton, J. D., 1990, ''The Calculation of Three Dimensional Viscous Flow Through Multistage Turbomachinery,'' ASME 90-GT-19, June 11–14.
[12] Denton, J. D., 1997, *Multistage Turbomachinery Flow Calculation Program (MULTIP81)—User's Manual*, Whittle Laboratory, University of Cambridge, Apr.
[13] Denton, J. D., 1999, *Multistage Turbomachinery Flow Calculation Program (MULTIP99)—User's Manual*, Whittle Laboratory, University of Cambridge, April 1999.
[14] Kuroumaru, M., Inoue, M., Higki, T., Abd-Elkhalek, F. A.-E., and Ikui, T., 1982, ''Measurement of Three Dimensional Flow Field Behind an Impeller by means of Periodic Multi-sampling with a Slanted Hotwire,'' Bull. JSME, **25**(209), Nov., pp. 1674–1681.
[15] Goto, A., 1991, ''Three-Dimensional Flow and Mixing in an Axial Flow Compressor with Different Rotor Tip Clearances,'' ASME Paper 91-GT-89, June.
[16] Chaluvadi, V. S. P., Kalfas, A. I., Banieghbal, M. R., Hodson, H. P., and Denton, J. D., 2001, ''Blade Row Interaction in a High Pressure Turbine,'' J. Propul. Power, **17**(4), July–Aug., pp. 892–901.
[17] Denton, J. D., 1993, ''Loss Mechanisms in Turbomachines,'' IGTI Gas Turbine Scholar Lecture, ASME 93-GT-435.
[18] Hughes, W. F., and Gaylord, E. W., 1964, *Basic Equations of Engineering Science*, Schaum's Outline Series, McGraw Hill.
[19] Jennings, I. K., and Shin, C. T., 1993, ''An Exhaustive Study of the Flow in a Transonic Rotor,'' 2nd International Symposium on Experimental and Computational Aerothermodynamics of Internal Flows, Prague, July 12–15, pp. 315–327.
[20] Hawthorne, W. R., 1955, ''Rotational Flow Through Cascades,'' J. Mechanics Applied Maths., **8**.
[21] Smith, L. H., 1955, ''Secondary Flow in Axial-Flow Turbomachinery,'' Trans. ASME, **77**.

Predicting Bladerow Interactions Using a Multistage Time-Linearized Navier-Stokes Solver

W. Ning

Y. S. Li

R. G. Wells

ALSTOM Power,
UK Ltd.,
Lincoln LN5 7FD, UK

A multistage frequency domain (time-linearized/nonlinear harmonic) Navier-Stokes unsteady flow solver has been developed for predicting unsteady flows induced by bladerow interactions. In this paper, the time-linearized option of the solver has been used to analyze unsteady flows in a subsonic turbine test stage and the DLR transonic counter-rotating shrouded propfan. The numerical accuracy and computational efficiency of the time-linearized viscous methods have been demonstrated by comparing predictions with test data and nonlinear time-marching solutions for these two test cases. It is concluded that the development of efficient frequency domain approaches enables unsteady flow predictions to be used in the design cycles to tackle aeromechanics problems.
[DOI: 10.1115/1.1516570]

Introduction

In recent years, more and more attentions have been paid to increase gas turbine engine reliability, prolong life and lower maintenance costs. High cycle fatigue (HCF) caused by blade forced vibrations is one of the major reasons causing blade failures in gas turbine operation. For aeroengines HCF could risk the safety of an aircraft and for land based engines it could cause blackout of a city or factory. The traditional approach to avoid the unacceptable blade resonance vibrations is to rely on blade vibration characteristics and engine strain gauge test data. However, this approach can only reveal problems in the late stage of engine and component development programs. At this stage to rectify those problems is very costly. Various surveys of previous aeroengine development programs have found that HCF problems account for between 10 and 40% of total problems (Kielb [1]). Therefore, development of a blade forced response prediction system is important to reduce engine development cost and time. Furthermore, it could reduce the penalty on engine manufacturers incurred by poor reliability of products in the field.

A forced response prediction system involves integration of the aerodynamic and structure design methods. One essential part of the system is a fast and accurate CFD (computational fluid dynamics) solver to predict blade unsteady aerodynamic loading from bladerow interaction and the damping due to blade vibrations. To this end, in the last decade significant progress has been made on the unsteady turbomachinery CFD. The nonlinear time-marching unsteady flow solver is becoming more widely available. However, due to unequal blade counts in neighboring bladerows in a multistage compressor and turbine, an unsteady flow calculation using nonlinear time-marching method has to be carried out in a multiple blade passage domain that may extend to the whole annulus. This makes the calculation prohibitively expensive in computational time.

The active development of the time-linearized Euler/Navier-Stokes approaches for aeroelastic applications (Hall and Crawley [2], Halls et al. [3], Holmes and Chuang [4], Montgomery and Verdon [5], Marshall and Giles [6]) has provided a way to predict unsteady flows in turbomachinery very efficiently. By assuming that the unsteady flow is composed of a steady flow plus a harmonically varying component, solving unsteady flow is simplified by solving steady-state unsteady amplitude perturbation equations. By applying phase-shifted boundary conditions, an unsteady flow solution is realized in a single blade passage. The development of the nonlinear harmonic method and harmonic balance techniques (Ning and He [7], He and Ning [8], Hall et al. [9]) has enabled the frequency approaches to include some elements of the nonlinear effects and extended the application range of the frequency domain approaches considerably.

More recently the frequency domain approach has been extended into the multistage environment to predict bladerow interactions and time-averaged flows (Chen et al. [10]. He et al. [11]). By using these approaches, the CPU time for an unsteady flow solution in a multistage compressor and turbine is in similar scale to solving a single passage steady flow. This high computational efficiency makes these approaches attractive for use in design. The objective of this paper is to investigate the ability of the time-linearized method to predict subsonic and transonic bladerow interactions in the multi-bladerow environment. To this end, the unsteady flows in a subsonic turbine test stage and the DLR transonic counter-rotating propfan have been calculated. The accuracy and computational efficiency of the time-linearized Navier-Stokes approach on predicting bladerow interactions is demonstrated by comparing the predictions with the test data and the equivalent fully nonlinear time-marching solutions.

Theory

A three-dimensional multistage Navier-Stokes solver has been developed by He et al. at University of Durham in cooperation with ALSTOM Power UK Ltd.[11] for analysis of unsteady flows due to the bladerow interaction and blade vibrations. The solver provides three options for the unsteady solutions, fully nonlinear time-marching, time-linearized and nonlinear harmonic. For the linear solution the unsteady flow is decomposed into a steady flow plus harmonically varying flow unsteady perturbations. For the steady flow, the flow governing equations are discretized in space using a cell-centered finite volume scheme and solved by the time-marching using the explicit four-step Runge-Kutta scheme. The calculation is accelerated using local time-stepping and multigrid techniques. The mixing-plane approach uses a nonreflective procedure developed by Saxer and Giles [12] to transfer flow information between neighboring bladerows. The turbulence Reynolds stresses are closed by the Baldwin-Lomax mixing length model.

In the time-linearized solver, the harmonic perturbation equations are steady-state linear equations with coefficients based on the steady flow solutions. By making the perturbation amplitude time-dependent in a pseudo time, the perturbation equations can be solved by the same time-marching numerics used for the steady

Contributed by the International Gas Turbine Institute and presented at the International Gas Turbine and Aeroengine Congress and Exhibition, Amsterdam, The Netherlands, June 3–6 2002. Manuscript received by the IGTI, January 7, 2002. Paper No. 2002-GT-30309 Review Chair: E. Benvenuti.

flow solution. The impact of the blade count on the flow is taken into account by flow interblade-phase-angles in the bladerow. The unsteady flow amplitudes at inlet and outlet of the bladerow is obtained by Fourier analysis of steady flows in neighboring bladerows. The nonreflecting boundary conditions (Giles [13]) are applied at the inlet and outlet of the bladerow. The phase-shifted boundary conditions are used on periodical boundaries to solve the unsteady perturbation equations in a single passage. The turbulence viscosity in the perturbation equations is simply frozen to the steady value.

For the nonlinear harmonic method in the solver, different with linear method, the unsteady flow is decomposed into a time-averaged flow plus unsteady harmonic perturbations. The unsteady deterministic stresses are worked out from unsteady perturbation solutions. While the coefficients in the unsteady perturbation equations are time-averaged flow solutions. Therefore, the time-averaged equations and unsteady perturbation equations are solved simultaneously in a pseudo-time domain. The mixing loss at bladerow interface is removed by adding the unsteady deterministic stresses in the mixing plane treatment. The nonlinearity can be included in the coupled solution between time-averaged flow and unsteady perturbations. More details about this method can be found in [10] and [11].

Results

Case 1: A Turbine Test Stage. This is a subsonic turbine stage case for which unsteady pressure measurements were made on rotor blade surfaces (Hall et al. [14]). In the test, the turbine stage was inverted; i.e., the rotor bladerow was kept stationary and the vane bladerow was rotated in the opposite direction, to avoid the difficulty of unsteady data acquisitions in a rotating system. All blades are nontwist 2-D profiles representatives of root sections of an I.P. steam turbine. The stage has 32 nozzles and 55 rotor blades. The gap between the nozzle and rotor bladerow is 25% of the rotor blade axial chord. High-frequency response pressure transducers were embedded at seven chordwise locations on the rotor blade pressure surface and nine on the suction surface as shown in Fig. 1.

Due to the untwisted nature of the blades used in the test and as the measurements were only taken at midspan, the calculations are carried out by running the time-linearized Navier-Stokes solver in 2-D. In the calculation, the inverted stage of the rotating nozzle and stationary rotor is simulated. The computational mesh is a simple H-type mesh consisting of 79 mesh points in the axial direction, 31 in the pitchwise, and 2 in the radial direction per passage.

To demonstrate the accuracy and computational efficiency of the linear approach, a nonlinear time-marching calculation was also carried out. Due to the blade count, the nonlinear time-marching calculation is carried for the whole annulus consisting of 32 nozzle passages and 55 rotor blade passages. The nonlinear time-marching calculation is accelerated by the time-consistent multigrid technique (He [15]).

For the linear method, prior to the unsteady flow calculation, a single passage steady flow calculation with bladerow interface

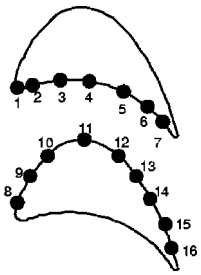

Fig. 1 Transducer locations

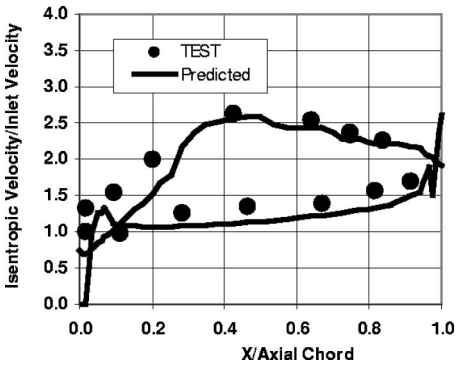

Fig. 2 Static pressure distribution on rotor blade surface

mixing plane is carried out. The predicted rotor surface steady pressure distribution in the form of isentropic velocity is compared with test data in Fig. 2. The comparison is reasonable and is similar to the prediction produced by other CFD code [14].

Figure 3 shows the instantaneous entropy contours reconstructed from the linear solutions. The convection of the nozzle wakes in the rotor bladerows is well captured. In the linear solution, the nozzle wake is resolved using the first three harmonics.

The nozzle wake migration process in the rotor blade passage is illustrated in Fig. 4. This shows the instantaneous velocity perturbation vector maps on the top of the instantaneous entropy contours. Once the wake enters the rotor passage, the low velocity inside the wake causes the low momentum wake fluid to migrate and collect near the suction surface forming so called ''negative jet'' when the wake is transported downstream (Hodson [16]).

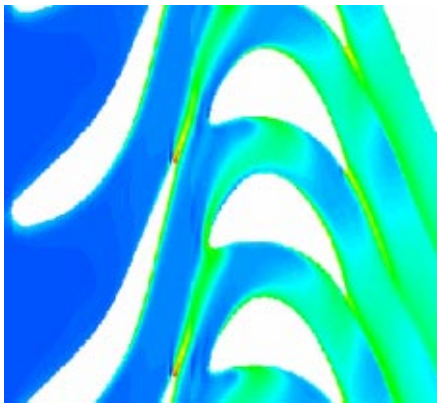

Fig. 3 Instantaneous entropy contours

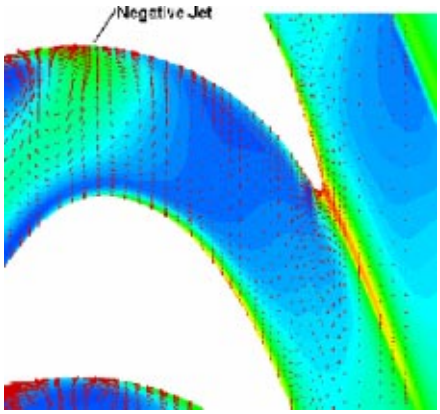

Fig. 4 Instantaneous unsteady velocity vectors

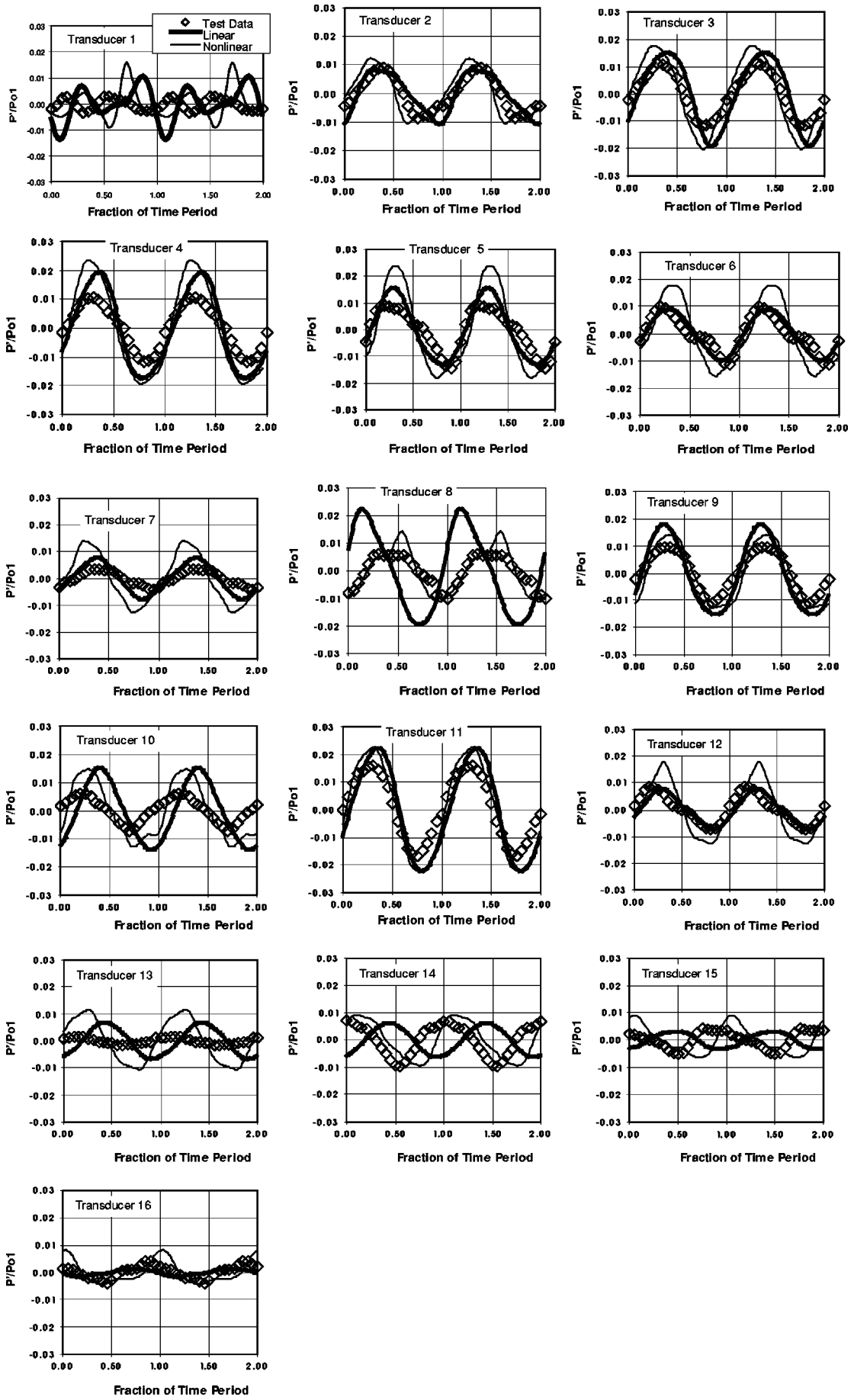

Fig. 5 Unsteady pressure time traces on rotor blade surfaces

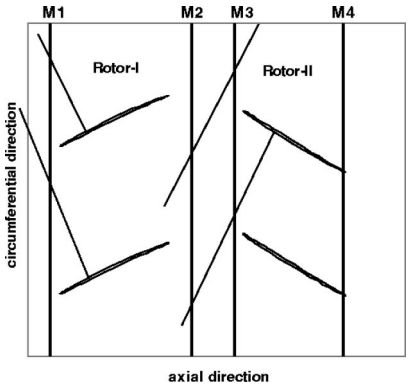

Fig. 6 Sketch of DLR transonic counter-rotating propfan

This ''negative jet'' generates a large pair of opposite vortices on each side of the wake. The linear method captures this complicated interaction mechanism quite well.

The predicted unsteady pressure time traces on the rotor blade surfaces over two nozzle wake passing periods from the linear method are compared to the test data and the nonlinear time-marching predictions. Figure 5 gives plot at each transducer locations. The P' represents the perturbation from steady/time-averaged value, $Po1$ is the total pressure at nozzle inlet. On the pressure surface, the unsteady pressure comparisons are good on whole surface. On the suction side, while both the linear and nonlinear time-marching predictions are good at the front part of the blade, however predicted phases seem shifted towards the trailing edge. Overall, the linear method compares favorably with both test data and nonlinear time-marching method for this subsonic turbine case.

In terms of computational efficiency, the linear solution takes about 13 min on a HP B2000 single processor workstation, while the whole annulus nonlinear time-marching calculation needs about 108 min for one nozzle passing period. The nonlinear time-marching needs to run at least 15 nozzle passing periods to obtain a periodic solution. Therefore, for this case, the linear method is about two orders magnitude faster than the nonlinear time-marching method, bearing in mind that the nonlinear time-marching solution is accelerated by the efficient time-consistent multigrid technique.

Case 2: DLR Transonic Counter-Rotating Shrouded Propfan. This DLR research fan stage consists of a pair of counter-rotating rotors as sketched in Fig. 6. The rotor-I has 10 blades and rotor-II has 12 blades. The flow in both rotors are highly transonic and complicated interactions exists between the two rotors. The test rig at DLR has 3-D geometry but all the unsteady measurements at four axial planes (M1-M4) using Laser-2- Focus (L2F) were made at a constant radius of 0.353 m (approximately 60% of rotor-I span). Only the geometry at this radius is released. More details about the test rig and measurements can be found in the paper by Wallscheid et al. [17].

This test case was previously numerically investigated by two groups of people from DLR and University of Florence (Schmitt, et al. [18]) using nonlinear time-marching codes to perform a 2-D run. Overall both CFD predictions compare reasonably well with time-averaged and unsteady data. Because of complicated and strong interactions between the two rotors, this case is deemed to be a challenge to the time-linearized approach.

In this paper, this test case is calculated using the time-linearized Navier-Stokes method. In the unsteady solution, the rotor-I wake is resolved by the first four harmonics and the upstream running potential wave from rotor-II is resolved by the first three harmonics. To demonstrate the accuracy and computational efficiency of the linear approach, the nonlinear time-marching solver was used to calculate this case. In the nonlinear time-marching calculation, the blade count is reduced to 5:6. Due to availability of the geometry, both linear and nonlinear time-marching calculations are carried out in 2-D with a specified streamtube height variation in the axial directions. The simple H-type mesh is used for the calculation which consists of about 9000 mesh points per passage.

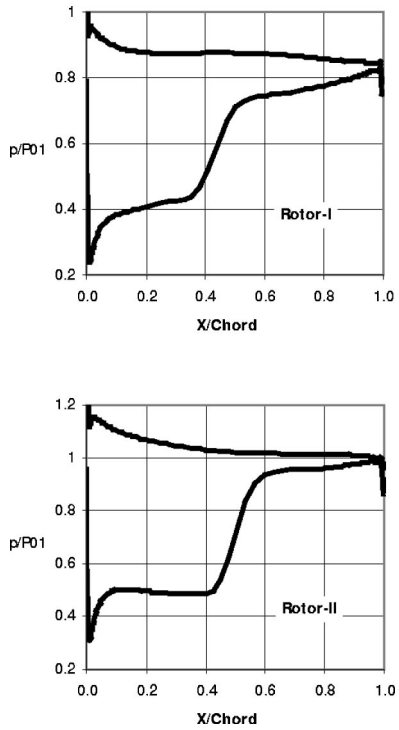

Fig. 7 Sketch of DLR transonic counter-rotating propfan

Similar to the turbine stage case, a steady flow calculation has to be carried out prior to solving the linear perturbation equations in the linear solver. The predicted static pressure distributions on blade surfaces are presented in Fig. 7. It can be seen that there is strong shock on rotor-I suction surface at around 45% axial chord and on rotor-II suction surface at around 50% axial chord.

The instantaneous pressure contours reconstructed from the time-linearized solutions are presented in Fig. 8. It compares very well with the instantaneous pressure contours produced from the nonlinear solution in Fig. 9. It can be seen that the rotor-II shock runs into rotor-I and is bowed in tangential direction, then chopped by rotor-I blades. The upstream running potential wave is suppressed by the rotor-I shock.

The instantaneous entropy contours constructed from the time-linearized solutions in Fig. 10 shows the rotor-I wakes are chopped by the rotor-II blades and then propagate downstream

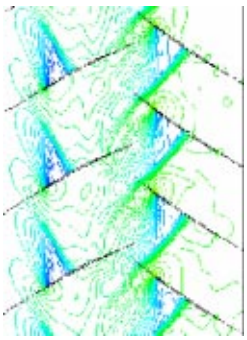

Fig. 8 Instantaneous pressure contours by linear method

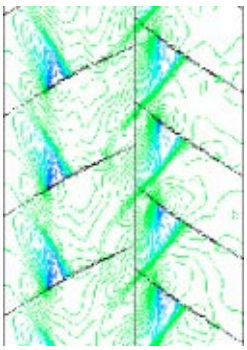

Fig. 9 Instantaneous pressure contours by nonlinear method

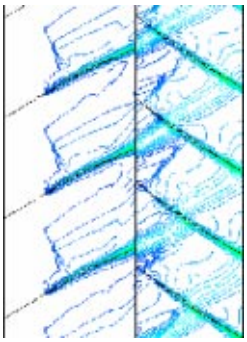

Fig. 10 Instantaneous entropy contours by linear method

inside the rotor-II passages. The pressure and entropy contours suggest that the essence of the rotor-I and rotor-II interactions are captured by the linear method.

As in the linear solution, the unsteady flow is composed of a steady flow plus the unsteady perturbations. The predicted steady flow results will be compared with the experimental time-averaged data. Figure 11 compares the predicted steady relative velocity and flow angle (rotor-I relative frame) with the test data at axial plane M1. In the figure, the pitchwise direction is from suction side (relative pitch 0) to pressure side (relative pitch 1).

The predicted relative velocity pitchwise distribution at this axial location suggests that the shock position in rotor-I is correctly predicted but the shock strength is over-predicted. The predicted unsteady amplitude of relative velocity and flow angle is compared with test data in Fig. 12.

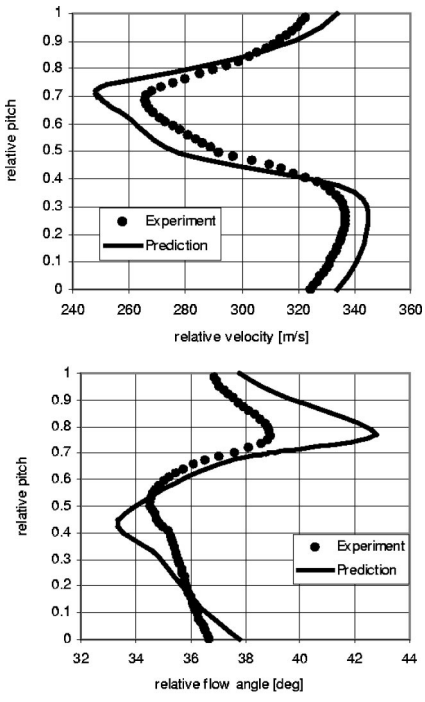

Fig. 11 Relative velocity and flow angle at axial plane M1

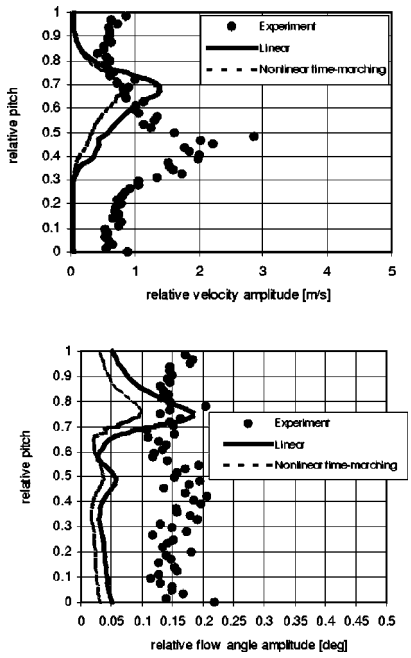

Fig. 12 Unsteady amplitude of relative velocity and flow angle at axial plane M1

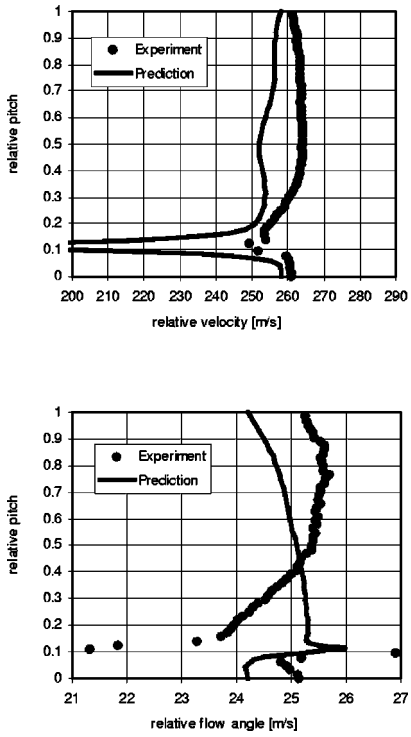

Fig. 13 Relative velocity and flow angle at axial plane M2

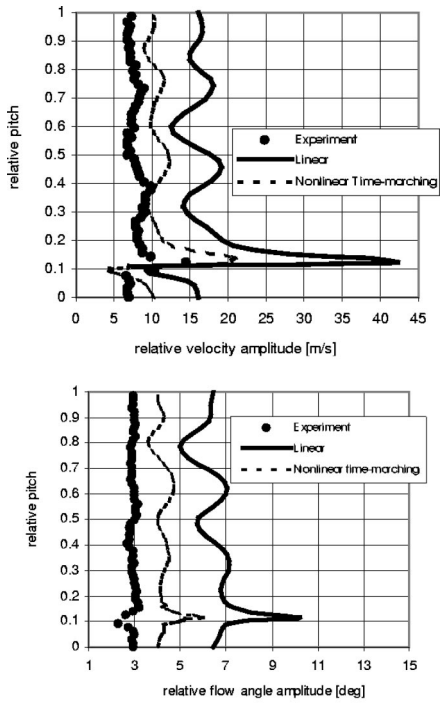

Fig. 14 Unsteady amplitude of relative velocity and flow angle at axial plane M2

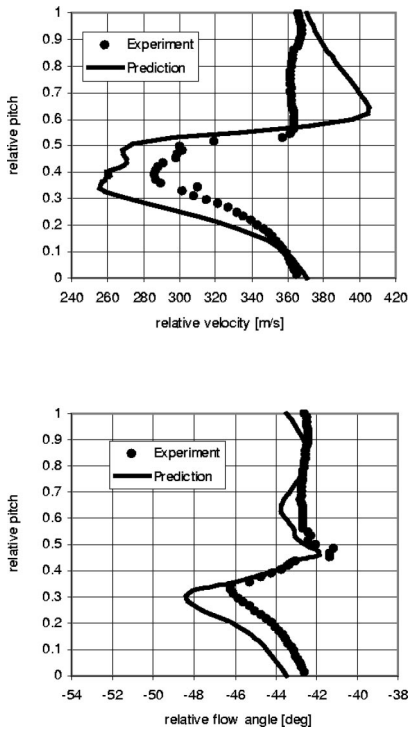

Fig. 15 Relative velocity and flow angle at axial plane M3

Due to the suppression of the unsteadiness from downstream by the rotor-I shock, the unsteady amplitude at axial plane M1 is very small.

The relative velocity and flow angle at axial plane M2 in Fig. 13 suggest that the rotor-I wake width is well predicted but the predicted velocity deficit is much higher.

The unsteady amplitude inside the gap between rotor-I and rotor-II at axial plane M2 is much higher than at plane M1 as shown in Fig. 14. Both linear and nonlinear time-marching methods overpredicts the unsteady amplitude at this location due to the overprediction of rotor-II shock strength (see Fig. 15). Meanwhile, the frequency domain method tends to overpredict unsteady impulse caused by shock moving. However, the shape of pitchwise distribution of the relative velocity and flow angle predicted by the linear method agrees well with nonlinear time-marching predictions.

The pitchwise distribution of relative velocity and flow angle (in rotor-II relative frame) at axial plane M3 in Fig. 15 suggests the shock position in rotor-II is correctly predicted, but the shock strength is overpredicted. The pitchwise direction in the figure is from pressure side (relative pitch 0) to suction side (relative pitch 1). The overprediction of the shock strength in rotor-I and rotor-II could be due to 2-D simplification of the flow. The shock strength is also overpredicted by other CFD solvers [18].

The unsteady amplitude near rotor-II leading edge at axial plane M3 is of a similar magnitude to that at plane M2 as shown in Fig. 16. The unsteady amplitude is well predicted by both linear and nonlinear time-marching methods.

The predicted relative velocity distribution at axial plane M4 near rotor-II trailing edge however dose not match the test data as shown in Fig. 17. The velocity near the suction side is predicted lower than the velocity near the pressure side. Due to the blade profiles on rotor-II, the loading towards the trailing edge of the blade is very small. Therefore, it is not surprised that the CFD predicts a locally inverse character of the pitchwise velocity distribution near to the trailing edge of the blade. This mismatch is also produced by other CFD solvers [18].

The unsteady amplitude of relative velocity and flow angle, however, are well predicted by the linear and nonlinear time-marching methods as presented in Fig. 18.

In Fig. 19, the amplitude and phase angle of first harmonic unsteady pressure on rotor-I and rotor-II blade surfaces predicted by the linear method are compared with the nonlinear time-

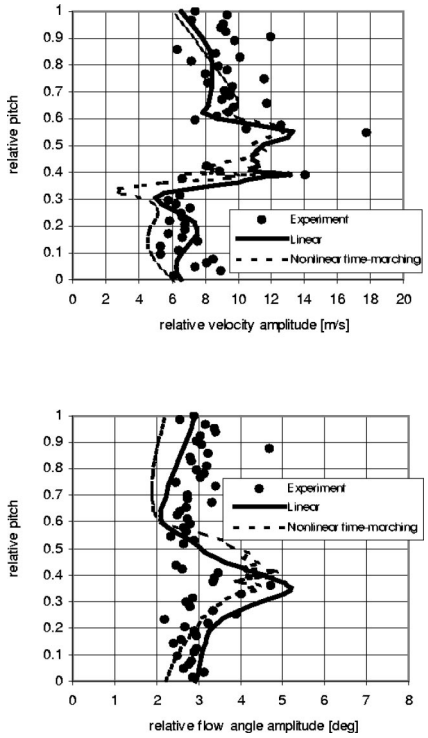

Fig. 16 Unsteady amplitude of relative velocity and flow angle at axial plane M3

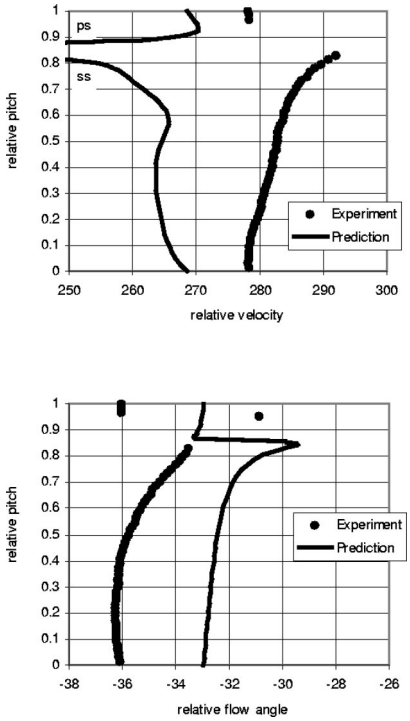

Fig. 17 Relative velocity and flow angle at axial plane M4

marching predictions. As expected, the unsteady pressure amplitude on rotor-I predicted by the linear method is higher than the nonlinear prediction as higher unsteadiness has been predicted by the linear method at the outlet of rotor-I (axial plane M2, as seen in Fig. 14). But the phase angles of the unsteady pressures compare well between the linear and nonlinear predictions. This implies that the linear method would make a more conservative prediction for a forced response analysis of rotor-I. The unsteady

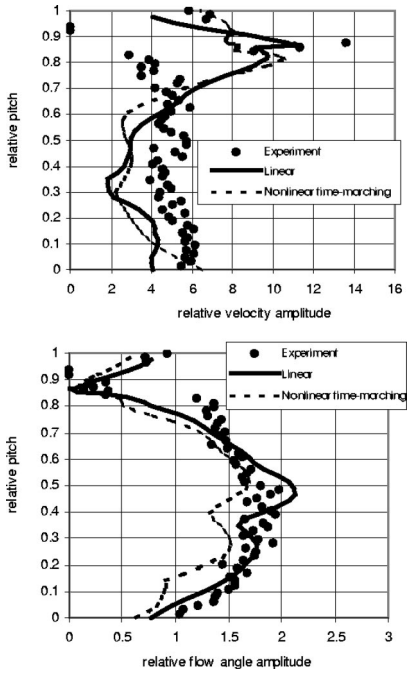

Fig. 18 Unsteady amplitude of relative velocity and flow angle at axial plane M4

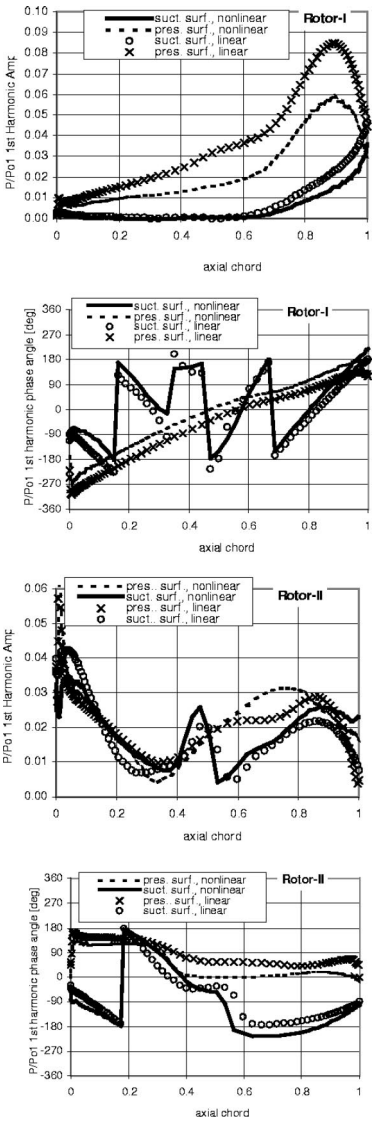

Fig. 19 1st harmonic unsteady pressure on blade surface

pressure on rotor-II predicted by the linear method compare well with nonlinear prediction both in amplitude and phase angle.

For this test case, the linear solution which contains 3 harmonics of potential waves of rotor-II and 4 harmonics of the rotor-I wakes is still about 4 times faster than the nonlinear time-marching calculation with the reduced blade count.

Conclusions

To investigate the capability of the multistage time-linearized method on predicting unsteady flows induced by bladerow interactions, the unsteady flows in a subsonic turbine test stage and the DLR transonic counter-rotating propfan have been calculated. The predicted unsteady flows have been compared with test data and solutions from a nonlinear time-marching analysis. The comparisons have demonstrated that the linear method is able to predict bladerow interactions (potential and wake) qualitatively and quantitatively. To the authors' knowledge, this is the first attempt to calculate bladerow interactions in a multi-bladerow environment using the frequency domain method against the test data. The advantage to couple the bladerows together in a linear solution is that the boundary condition specification for the unsteady perturbation equation is straightforward and more accurate.

A linear solution can be as much as two orders magnitude faster than a nonlinear time-marching calculation depending on the blade count and complexity of the flow. The development of the efficient time-linearized approaches has enabled the unsteady flow calculations be used in a multistage compressor and turbine design process for aeromechanics applications.

Acknowledgments

This work is partly funded by the European Union Framework V R&D project ''Development of Innovative Techniques for Compressor Aero-Mechanical Design (DITCAD),'' contract number ENK5-CT-2000-00086. The assistance from Prof. Li He on CFD codes used during this work is highly appreciated. The authors would like to thank Mr. Stephen Dewhurst and Dr. David Bell of ALSTOM Steam Turbines for providing the turbine stage data and useful discussions. The authors are also grateful to Dr. Stefan Schmit at DLR's Institute of Propulsion Technology in Cologne for providing the DLR test data.

References

[1] Kielb, R. E., 1999, ''Aeroelasticity in Axial Flow Turbomachines,'' VKI Lecture Series 1999-05, von Karman Institute for Fluid Dynamics. May 3–7.
[2] Hall, K. C., and Crawley, E. F., 1989, ''Calculation of Unsteady Flows in Turbomachinery Using the Linearized Euler Equations,'' AIAA J., **27**, No. 6.
[3] Hall, K. C., Clark, W. S., and Lorence, C. B., 1994, ''A Linearized Euler Analysis of Unsteady Transonic Flows in Turbomachinery,'' ASME J. Turbomach., **116**.
[4] Holmes, D. G., and Chuang, H. A., 1993, ''2D Linearized Harmonic Euler Flow Analysis for Flutter and Forced Response,'' *Unsteady Aerodynamics, Aeroacoustics, and Aeroelasticity of Turbomachines and Propellers*, ed., H. M. Arassi, Springer-Verlag, New York, NY.
[5] Montgomery, M. D., and Verdon, J. M., 1997, ''A 3-D Linearized Euler Analysis for Blade Rows. Part 1: Aerodynamic and Numerical Formulations and Part II: Unsteady Aerodynamic Response Predictions,'' *Unsteady Aerodynamics and Aeroelasticity of Turbomachines*, ed., T. H. Fransson, Kluwer Academic Publishers.
[6] Marshall, J. G., and Giles, M. B., 1997, ''Some Applications of a Time-Linearized Euler Method to Flutter & Forced Response in Turbomachinery,'' *Unsteady Aerodynamics and Aeroelasticity of Turbomachines*, ed., T. H. Fransson, Kluwer Academic Publishers.
[7] Ning, W., and He, L., 1998, ''Computation of Unsteady Flows Around Oscillating Blades Using Linear and Non-linear Harmonic Euler Methods,'' ASME J. Turbomach., **120**(3).
[8] He, L., and Ning, W., 1998, ''Efficient Approach for Analysis of Unsteady Viscous Flows in Turbomachines,'' AIAA J., **36**(11).
[9] Hall, K. C., Thomas, J. P., and Clark, W. S., 2000, ''Computation of Unsteady Nonlinear Flows in Cascades Using a Harmonic Balance Technique,'' 9th International Symposium on Unsteady Aerodynamics, Aeroacoustics and Aeroelasticity of Turbomachines, Lyon, France.
[10] Chen, T., Vansanthakumar, P., and He, L., 2001, ''Analysis of Unsteady Blade Row Interaction Using Nonlinear Harmonic Approach,'' J. Propul. Power, **17**(3).
[11] He, L., Chen, T., Well., R. G., Li, Y. S., and Ning, W., ''Analysis of Rotor-Rotor and Stator-Stator Interferences in Multi-Stage Turbomachines,'' ASME Turbo Expo' 2002, Amsterdam.
[12] Saxer, A. P., and Giles, M. B., 1993, ''Quasi-Three-Dimensional Nonreflecting Boundary Conditions for Euler Equations Calculations,'' J. Propul. Power, **12**(2).
[13] Giles, M. B., 1990, ''Nonreflecting Boundary Conditions for Euler Equation Calculations,'' AIAA J., **28**(12).
[14] Hall, D. M., McGuire, P. M., and Price D. W., 1981, ''Excitation of Blade Vibration,'' GEC Turbine Generators Report No. AGR 131/F.
[15] He, L., 1993, ''New Two-Grid Acceleration Method for Unsteady Navier-Stokes Calculations,'' J. Propul. Power, **9**(2).
[16] Hodson, H. P., 1984, ''An Inviscid Blade-to-Blade Prediction of a Wake-Generated Unsteady Flow,'' ASME Paper 84-GT-43.
[17] Wallscheid, L., and Eulitz, F., 1997, ''Investigation of Rotor/Rotor Interaction,'' Proc., 13th International Symposium on Air Breathing Engines (ISABE), 7th–12th, September 1997, Chattanooga, TN.
[18] Schmitt, S., Eulitz, F., Wallscheid, L., Amone, A., and Marconcini, 2001, ''Evaluation of Unsteady CFD Methods By Their Application To a Transonic Propfan Stage,'' ASME Paper 2001-GT-0310.

Wake, Shock, and Potential Field Interactions in a 1.5 Stage Turbine—Part I: Vane-Rotor and Rotor-Vane Interaction

R. J. Miller[1]
Whittle Laboratory,
University of Cambridge,
Cambridge, CB30 DY, UK

R. W. Moss[1]
Department of Marine Technology,
University of Newcastle,
Newcastle upon Tyne NE1 7RU, UK

R. W. Ainsworth
Department of Engineering Science,
University of Oxford,
Oxford OX1 3PJ, UK

N. W. Harvey
Rolls Royce plc.,
Derby DE24 8BJ, UK

The composition of the time-resolved surface pressure field around a high-pressure rotor blade caused by the presence of neighboring blade rows is investigated, with the individual effects of wake, shock and potential field interaction being determined. Two test geometries are considered: first, a high-pressure turbine stage coupled with a swan-necked diffuser exit duct; secondly, the same high-pressure stage but with a vane located in the downstream duct. Both tests were conducted at engine-representative Mach and Reynolds numbers, and experimental data was acquired using fast-response pressure transducers mounted on the mid-height streamline of the HP rotor blades. The results are compared to time-resolved computational predictions of the flowfield in order to aid interpretation of experimental results and to determine the accuracy with which the computation predicts blade interaction. The paper is split into two parts: the first investigating the effect of the upstream vane on the unsteady pressure field around the rotor (vane-rotor interaction), and the second investigating the effect of the downstream vane on the unsteady pressure field around the rotor (rotor-vane interaction). The paper shows that at typical design operating conditions shock interaction from the upstream blade row is an order of magnitude greater than wake interaction and that with the design vane-rotor inter-blade gap the presence of the rotor causes a periodic increase in the strength of the vane trailing edge shock. The presence of the potential field of the downstream vane is found to affect significantly the rotor pressure field downstream of the Mach one surface within each rotor passage. [DOI: 10.1115/1.1508386]

1 Introduction

The relative motion of turbine rotor blades and vanes introduces two forms of unsteadiness into the flow: random (time-unresolved) fluctuations such as turbulence and deterministic (time-resolved) fluctuations such as blade wakes and shock waves. When the flow unsteadiness experienced by a blade occurs at frequencies close to one of the blades' natural frequencies a significant vibration can occur. Over time this can cause high cycle fatigue (HCF) and eventually, if not identified, to a catastrophic blade failure. Wisler [1] reported that HCF problems accounted for between 10 and 40% of engine development problems and the half that were not uncovered during extensive development testing accounted for 5% of total field maintenance costs. A detailed understanding of unsteady flow physics within turbine stages is thus clearly of great importance to engine manufacturers.

The aim of this research is to understand the unsteady interaction mechanisms within a one and a half-stage turbine. The turbine is representative of the first one-and-a-half stages of civil aeroengines; its design, as a research turbine, is intended to be relevant to future engine design. The design of downstream vane used in this set of tests is a large low aspect ratio vane positioned in a swan-necked diffuser with a hade angle. The duct geometry used is modeled on proposals for future interstage diffuser designs. The continued pressure to design higher bypass ratio aeroengines has led to a continual increase in the diameter of the engine fan blades. To achieve this whilst still preserving the tip speed of the fan its rotational speed must be reduced. A corresponding increase in the diameter of the low-pressure turbine is then required to maintain turbine performance. This design requirement within a fixed engine length has led to increases in the hade angle within turbine diffusers. The large size of the second stage vane is caused by the necessity to route service ducts through the vane core and to use it as a rear engine support strut.

The transonic nature of modern first and second stage turbines and the large size of the second stage vane leads to particularly strong blade row interactions. The trailing edge shocks from upstream vanes cause a large unsteady pressure field around the rotor leading edge and the potential field of the downstream vane causes pressure fluctuations around the rotor trailing edge. The aim of this research is to investigate the strength of these interactions and to understand in detail the mechanisms which cause them.

A considerable amount of research has been done to study individual interaction mechanism in turbine stages:

- periodic wake impingement on the downstream blade (e.g., Binder et al. [2] and Hodson [3]);
- periodic movement of the vane trailing edge shock-wave system (e.g., Doorly and Oldfield [4] and Giles [5]);
- periodic interaction between the vane potential field and the rotor flow-field (e.g., Lefcort [6] and Korakianitis [7]);
- convection of the vane secondary flow-field through the rotor (e.g., Binder [8]).

However, the difficulty in making measurements in transonic turbines has meant that little research has been carried out at engine representative conditions (correct Mach, Reynolds and rotational numbers; temperature ratios) in a full high-pressure stage. A small number of papers have described investigations into blade

[1]Formerly at the Department of Engineering Science, University of Oxford.

Contributed by the International Gas Turbine Institute and presented at the International Gas Turbine and Aeroengine Congress and Exhibition, Amsterdam, The Netherlands, June 3–6, 2002. Manuscript received by the IGTI, January 31, 2002. Paper No. 2002-GT-30435. Review Chair: E. Benvenuti.

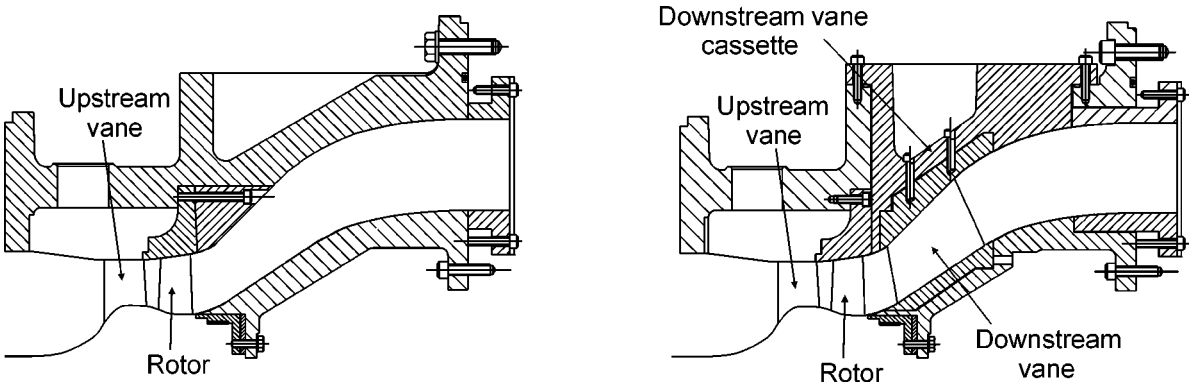

Fig. 1 The two test sections with and without a downstream vane

row interaction in high-pressure turbines at engine representative conditions (Dietz and Ainsworth [9]; Hilditch et al. [10], Dunn et al. [11], Moss [12], Denos et al. [13], Sheldrake et al. [14], Venable et al. [15] and Busby et al. [16]). These papers have resulted in a good understanding of the interaction mechanism within the first turbine stage. None of these investigations, however, has investigated vane-rotor-vane interaction at engine representative conditions; in particular, the effects of a large low aspect ratio (engine representative) second vane on interaction within the first stage turbine has not previously been studied.

The research program described in this paper has been conducted to address this void. Use has been made of time-resolved surface pressure sensors mounted on the rotor surface to measure blade interaction with and without the presence of a downstream vane. The paper describes first the mechanisms that cause vane-rotor interaction in an HP stage, then goes on to describe the effect of adding a large low-aspect ratio downstream vane to the stage and investigates how this affects the rotor pressure field.

2. Methodology

The experimental measurements described in this paper were carried out in the Oxford Rotor Facility (Ainsworth et al. [17]), the aim being to measure the time-resolved surface static pressure around a high-pressure rotor, with and without the presence of a downstream vane. The working section of the facility contains a 0.5-m-dia shroudless high-pressure turbine stage and allows the simulation of engine representative Mach and Reynolds numbers as well as the appropriate gas to wall temperature ratio.

The working section of the facility was rebuilt twice: first to include a plain swan-necked duct at rotor exit and secondly to include a second vane within the swan-necked duct. Schematics of the working sections used in these tests are shown in Fig. 1. The upstream row of vanes had 36 blades with an exit Mach number of 0.95 and an exit Reynolds number, based on axial chord, of 1.55×10^6. The rotor disc had 60 blades with an exit Mach number of 0.98 and the rotational speed of the rotor disk was 8910 rpm. The tip clearance on the rotor was 2% of blade height. The downstream row of vanes had 21 blades with an exit Mach number of 0.86. The axial gap between the upstream vane and rotor was 0.36 of the upstream vane axial chord and the axial gap between the rotor and downstream vane was 0.88 of the rotor axial chord.

Experimental measurements were made using three blades instrumented with surface mounted pressure sensors. The location of the sensors is shown in Fig. 2. A photograph of an instrumented rotor blade is shown in Fig. 3. Measurements were made over two rotor revolutions and each set of tests was repeated three times.

To obtain the vane dependent deterministic component at each vane passing frequency the measurements were ensemble averaged over six revolutions. The discussion of blade interaction mechanisms in this paper centres around four key suction surface pressure sensors (2, 7, 8, and 11) that characterize the structure of downstream vane interaction within the upstream stage.

Numerical simulations were performed using a three-dimensional viscous time-unsteady code, Unstrest, developed by Denton [18] at Cambridge University. The code solves the Navier Stokes equations using a thin shear layer model with the viscous terms evaluated every time step, and turned into body force terms for momentum and source terms for energy. The structured grid is formed by the rotation of points defined in two dimensions (x,r) about the turbine axis; the (x,r) points are defined by meridional (pseudo-streamwise) and pseudo-radial vectors. The code uses a ''time-marching'' solution scheme in which one blade row gradually rotates relative to the other with flow parameters being interpolated across a sliding plane between the two grids.

The mesh that was used in this research had 1.6 million nodes and included only the upstream vane and rotor. The correct 3:5 vane-rotor repeat ratio was used in the solution. The grid has 300,000 elements per vane passage and 140,000 elements per rotor passage. The element to element expansion ratio was below 1.2 within the blade passage and below 1.3 between blade rows.

3 Vane-Rotor Interaction (HP Stage)

3.1 Rotor Suction Surface Measurements. This section describes the time-resolved pressure field around the rotor with no downstream vane present. Experimental measurements and com-

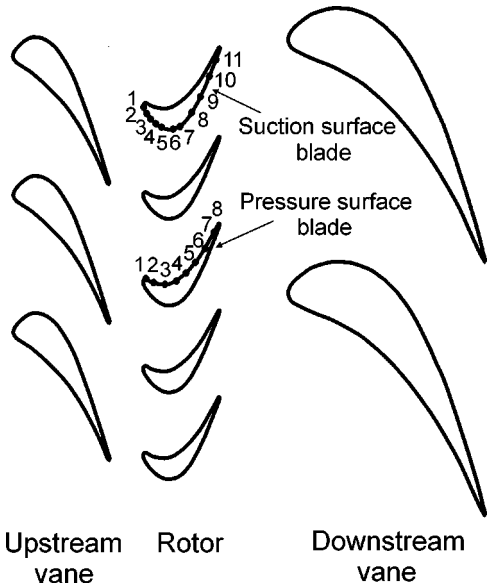

Fig. 2 Location of pressure sensors

Fig. 3 Photograph of instrumented blade

putational predictions of the time-resolved surface pressure around the rotor are shown in Figs. 4 and 5. The figures show a time history of the blade surface pressure as the rotor passes an upstream vane. The horizontal axis is plotted as vane relative phase and three vane passing events are shown.

The structure of the rotor mid-height time-resolved pressure field is affected by two main unsteady interaction phenomena: firstly shock and potential field interaction and secondly wake interaction. The structure of shock interaction is shown in the two schematics in Figs. 6(*a*) and 6(*b*). In the schematics the shock first contacts the rotor suction surface around sensor 7 and then moves forward over the blade surface until it reaches the blade leading edge. This effect can be observed in the experimental measurements, Fig. 4, as a diagonal line of high pressure gradient starting at sensor 7 and moving toward the right as it approaches the rotor leading edge.

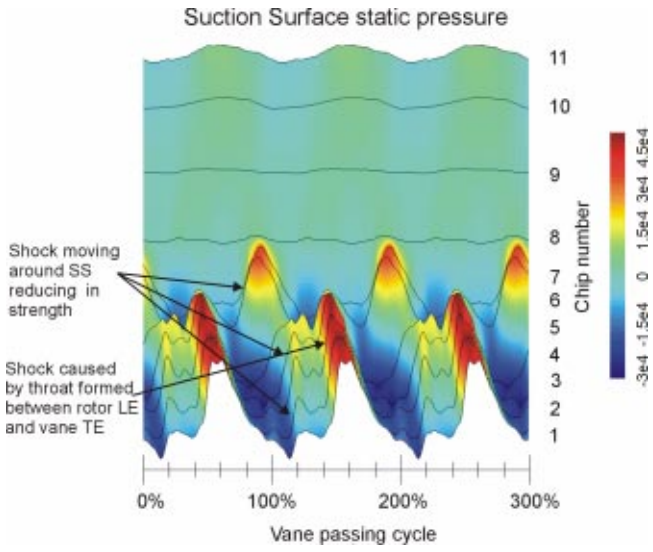

Fig. 4 Experimental measurement of suction surface static pressure

To interpret the shock interaction in more detail it is useful to look at the computational predictions shown in Fig. 5. To aid interpretation three stills from the computational prediction are shown on the right of the figure. Each shows a snapshot of the unsteady component (the time-resolved pressure minus the time averaged pressure) of the rotor surface pressure as the rotor passes through an upstream vane pitch. A description of the three snapshots follows:

- **Time Step 1.** The vane trailing edge shock impinges on crown of the suction surface (sensor 7) raising the surface pressure.
- **Time Step 2.** The impingement point of the vane trailing edge shock moves upstream along the suction surface. As the trailing edge shock moves around the suction surface the vane trailing edge and the rotor leading edge form an effective throat ([13]). The formation of this throat is shown in the schematic that accompanies each snapshot. This acts as a convergent divergent nozzle and raises the vane exit Mach number. As a rotor blade moves past a vane the divergent part of the effective nozzle gets shorter and the vane trailing edge Mach number is observed to drop. The computational prediction in Fig. 5 shows only a small drop in pressure change across the shock between timesteps 1 and 2. However, in the experimental results shown in Fig. 4, the vane trailing edge shock is observed to weaken significantly between sensor 7 and sensor 1, causing the size of the static pressure rise across the shock to decrease.
- **Time Step 3.** As the vane trailing edge shock approaches the rotor leading edge the effective throat area between the vane trailing edge and rotor reduces sharply. This causes a sudden rise in the strength of the vane trailing edge shock and causes a 60% rise in the rotor surface pressure. An equal rise was observed on both the experimental results and computational predictions.

The experimental results (Fig. 4) show the same structure as observed in the computational predictions. The measurements show both a reduction in the strength of the first shock as it moves around the rotor leading edge and the formation of a second stronger shock as a result of the effective throat set up between the vane and rotor. However, at the point where the vane trailing edge shock first contacts the surface of a rotor blade the experimental results show a much larger pressure rise than observed in the computational simulation. This is to be expected, as the grid resolution in the computational prediction is not sufficient to accurately predict shocks so far downstream of the vane trailing edge.

The second interaction phenomena that affects the flowfield in the rotor is wake interaction. As the vane wake is cut by the rotor leading edge, segments convect through the blade row at the free stream velocity. A schematic of wake interaction is shown in the top right of Fig. 6(*b*). The wake segments results in two regions of secondary circulation of an opposing sign (the negative jet effect). This raises the velocity on the suction surface downstream of the wake (lowering the static pressure) and reduces it upstream (raising the static pressure); Hodson and Dawes [19]. These regions of raised and lowered static pressure convect with the wake through the blade row at the free stream velocity.

A phenomena travelling through the rotor at the free stream velocity would appear on the surface pressure diagrams in Figs. 4 and 5 as a diagonal stripe from bottom left to top right. It should be noted that the convection of a phenomenon from the rotor leading edge to trailing edge takes more than one vane passing cycle. The space-time diagrams of suction surface pressure, shown in Figs. 4 and 5, show no such characteristic striping. It is therefore concluded that the upstream vane wakes have a negligible effect on the rotor unsteady surface pressure and thus blade loading.

Between sensor 8 and blade trailing edge the unsteady rotor surface pressure field is observed to be much weaker than up-

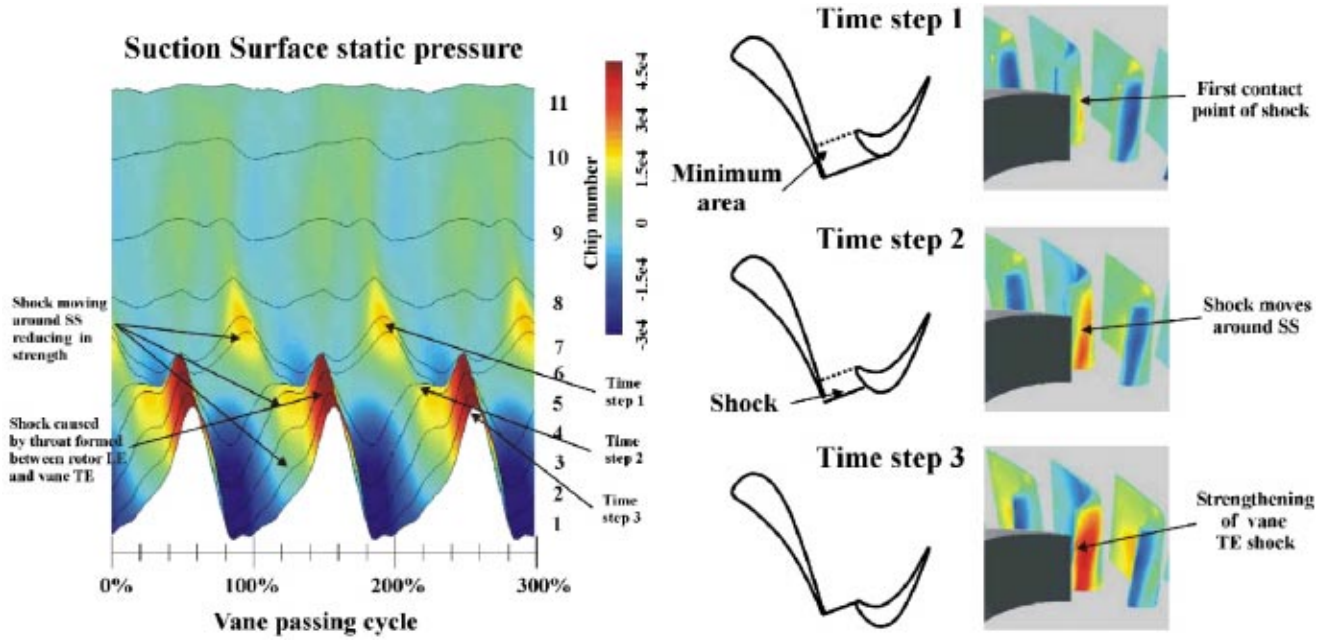

Fig. 5 Computational prediction of the suction surface static pressure

stream of sensor 7. Over the late suction surface the pressure field is observed to show little phase variation. As described in the foregoing, pressure fluctuations caused by wake interaction should be represented by diagonal lines from bottom left to top right. Neither the computation nor the experimental results show such a fluctuation. This indicates that the pressure fluctuations on the late suction surface are caused by the upstream vanes shock and potential field and not by wake interaction.

3.2 Rotor Pressure Surface Measurements. The size of pressure fluctuations on the rotor pressure surface are much lower than those observed on the early suction surface. This is because the geometry of the stage is such that the vane trailing edge shock cannot impinge directly on the rotor pressure surface. Similar results for the Oxford Rotor have been presented before [12] and space precluded their inclusion in this paper. However, it is of interest to note that the pressure fluctuations showed little phase variation over the entire surface indicating that the presence of the vanes potential field and trailing edge shock are the dominant cause of the unsteady pressure field around the pressure surface. An example of the unsteady pressure field measured by one of the pressure surface pressure sensors is shown in Figs. 7 and 8.

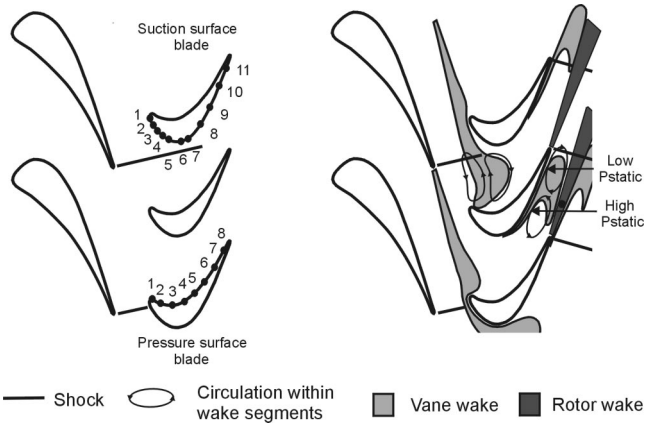

Fig. 6 (*a*) Sensor location, (*b*) schematic of flow structure

4 Rotor-Vane Interaction (HP Rotor and Downstream Vane)

In the following section a comparison is made between the time-resolved rotor surface pressure measurements with and with-

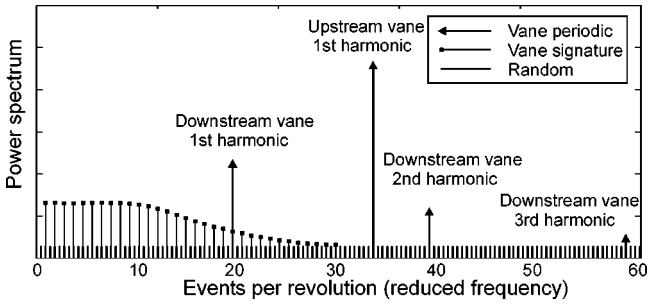

Fig. 7 Power spectrum of an idealized rotor surface pressure measurement

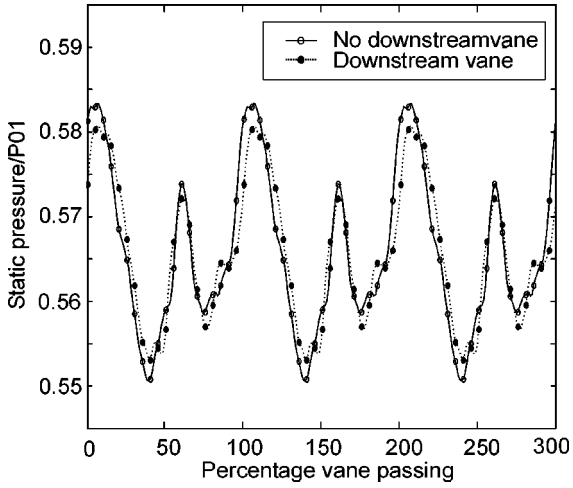

Fig. 8 Sensor 6 pressure surface (ensemble average)

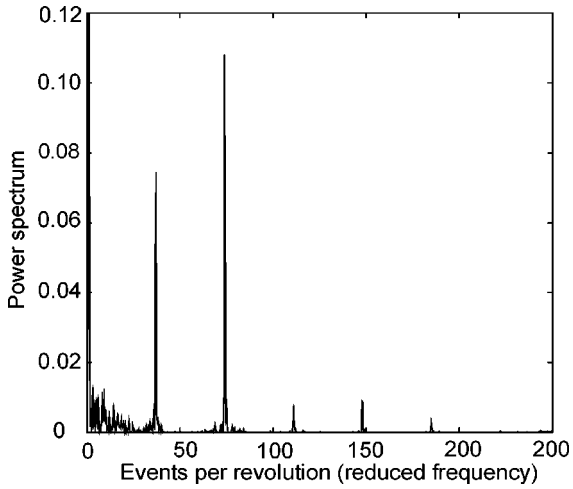

Fig. 9 Sensor 6 pressure surface (power spectrum)

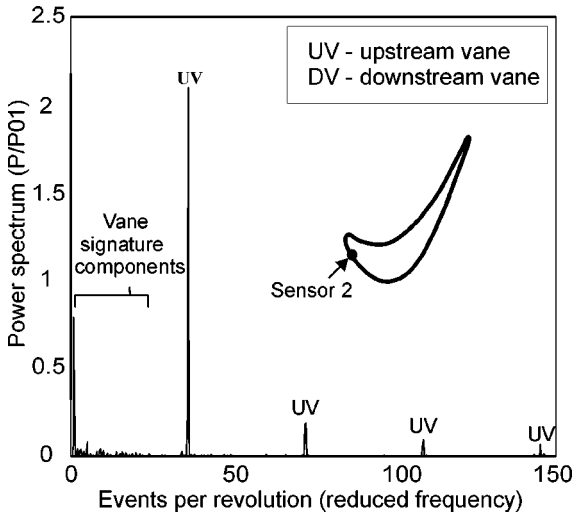

Fig. 10 Suction surface pressure sensor 2

out a downstream vane. These results are then used to interpret the effect of the downstream vane on the pressure field experienced by the upstream rotor. It is extremely important when investigating stage interaction in a transonic turbine to ensure that the correct operating conditions have been achieved. Small changes in stage pressure ratio and nondimensional speed can result in a large change in the strength of the upstream vane's trailing edge shock and can therefore cause a large change in the time-resolved static pressure field around the rotor. For the two sets of tests described in this paper (with and without downstream vane) the facility was rebuilt twice and the resulting testing was completed over 2 yr. A detailed comparison of the operating conditions simulated in the two sets of tests is given in Miller et al. [20]. The paper shows that the difference in average HP vane exit Mach numbers simulated in the two tests was 0.007, which is smaller that the vane to vane difference around the annulus. It was therefore considered that the operating conditions had been accurately reproduced.

To interpret the structure and size of such an interaction it is important to understand the composition of the pressure field around the surface of the rotor. To aid this understanding a schematic showing the power spectrum of an idealised pressure measurement (obtained in the rotor-relative frame) is shown in Fig. 9. Three distinct components can be observed: the vane periodic deterministic component, the vane signature component and the random component. A description of the structure and origin of each component follows:

- The vane periodic deterministic component: this is observed to occur at frequencies corresponding to multiples of up and downstream blade passing frequencies (36 and 21 events per revolution).
- The vane signature deterministic component: this is caused by small blade to blade variations in the throat area and trailing edge thickness of each vane. These differences, though very small, result (within a transonic blade row) in a relatively large variation in the vane exit shock structure and therefore the strength of its interaction with a downstream rotor. The power spectrum of the vane signature component (in the rotor-relative frame) is made up of harmonics of the rotor revolution frequency. The idealised power spectrum shown in Fig. 9 is that which would be expected from a pressure measurement recorded over two revolutions. The vane signature component is therefore observed to occur at multiples of twice the minimum measurable frequency (since the minimum measurable frequency has a period of two rotor revolutions). There is a characteristic drop in the power spectrum at higher frequencies, shown in Fig. 9, which arises for the following reasons. An individual vane signature is created largely by the substantive flow features (vane trailing edge shocks and wakes). These flow structures affect the entire exit flow from the passage in which they occur. The vane signature component, as defined, results from differences in these signatures (vane to vane). The vane exit flow structures result in a high correlation between sampled pressure measurements in the same vane passing cycle. A higher correlation in the temporal domain is equivalent to a lowering of the bandwidth in the frequency domain, and hence the power spectrum of the vane signature component is attenuated at higher frequencies.
- The random component: this is observed to occur at all frequencies. However, depending on the length scale of the random unsteadiness this will drop off at high frequencies (not shown in Fig. 9).

Two analysis methods are used to analyze each blade surface pressure measurement:

- The first method involves ensemble averaging the pressure measurements over the up and downstream vane passing period. This removes any component not at harmonics of the vane passing frequency and therefore removes the vane signature and random components leaving only the vane periodic component.
- The second method involves taking the power spectrum of the raw pressure signal. This allows the relative size of each of the three components, discussed above, to be determined. However, it should be noted that taking the power spectrum removes the phase relationship of the various components in the signal and is therefore of no use when interpreting detailed flow structures.

In this section the structure of the unsteady pressure field around the suction surface of the rotor is examined. The pressure surface was found to be unaffected by the presence of the downstream vane and is therefore not presented. An example showing the unsteady pressure measured by sensor 6 on the late pressure surface is shown in Figs. 7 and 8. Figure 7 shows the vane periodic component of the pressure measurements made with and without the downstream vane present. Figure 8 shows the power spectrum of the pressure measured by sensor 6. It should be noted that the power spectrum shows no peak at 21 events per revolution and therefore it can be concluded that the downstream vane has no effect on the pressure surface pressure field.

The relative effects of the upstream and downstream vanes on the time-resolved pressure field around the rotor suction surface

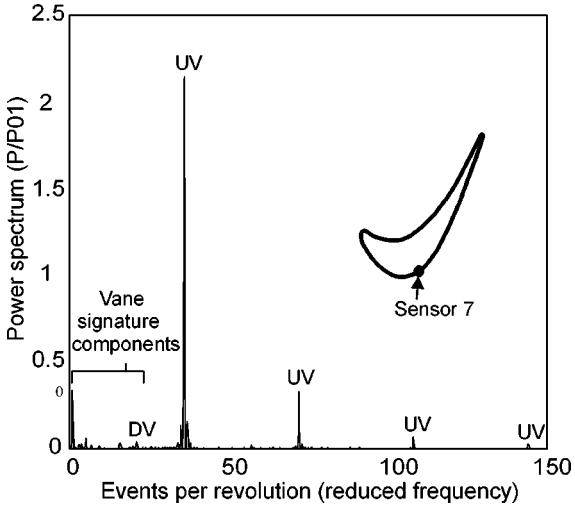

Fig. 11 Suction surface pressure sensor 7

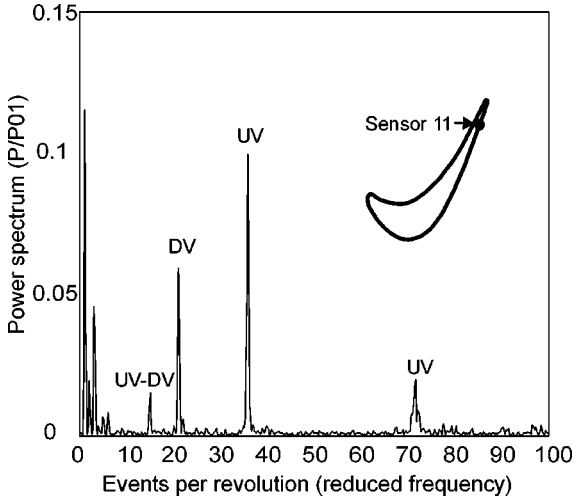

Fig. 13 Suction surface sensor 11 (expanded)

were evaluated by examining the spectral content of the signal from each pressure sensor. Figures 10–13 are used in the following description. The figures show the power spectra measured on sensors 2, 7, 8, and 11. The structure of the measured power spectra shows that the unsteady pressure fluctuations over the suction surface is split into three regions.

- Close to the leading edge (Sensors 1–4) the first four harmonics of the upstream vane passing frequency are clearly observed (Fig. 10 shows the power spectrum for sensor 2). No distinct peaks in the power spectrum were observed at the downstream vane passing frequency. From the leading edge up to sensor 7 the components of the power spectra at the upstream vane passing frequency show little change in magnitude (compare for instance Figs. 10 and 11). However, by sensor 7 a clear peak is observed in the power spectrum at the first harmonic of the downstream vane passing frequency (Fig. 11).
- From sensor 7 to sensor 8 a large change is observed in the strength of both the up and downstream vanes' pressure fields. The power spectra of the pressure measurements made with sensors 7 and 8 are shown in Figs. 11 and 12. The rms pressure fluctuations associated with the upstream vane are observed to drop by a factor of 3.5, while the rms pressure fluctuations associated with the downstream vane rise by 40 percent.
- From sensor 8 to sensor 11 the rms pressure fluctuations at the downstream vane passing frequency are observed to drop by 16%. The power spectra of the pressure measurements made with sensors 11 plotted in Fig. 13. In addition to the peaks in the power spectrum at frequencies corresponding to multiples of the upstream and downstream vane passing frequencies a peak in the power spectrum is observed at a frequency corresponding to the difference in the upstream and downstream vane passing frequencies. The origin of this extra component of vane-rotor-vane interaction is discussed in part two of this paper.

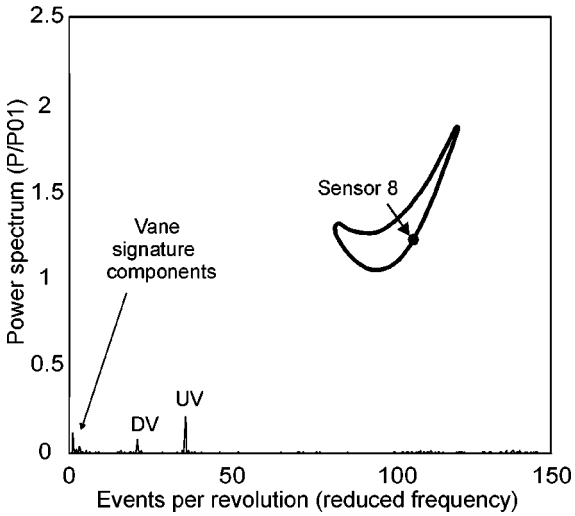

Fig. 12 Suction surface pressure sensor 8

It should be noted that the sudden drop in the effect of the upstream vane between sensors 7 and 8 is caused by the location of the impingement point of the upstream vane's trailing edge shock on the rotor suction surface [12]. After making contact the shock moves upstream around the rotor suction surface to the rotor leading edge. This explains why only a small change in the rms upstream vane component was observed between sensors 1 and 7.

The drop in the effect of the potential field of the downstream vane between sensor 7 and 8 is discussed in Miller et al. [21]. In addition to the upstream and downstream vane passing frequencies (vane-rotor and rotor-vane interaction), Fig. 13 shows a peak in the power spectrum at the difference between the upstream vane and the downstream vane passing frequencies. This is caused by the interaction between the upstream vanes flowfield with the downstream vanes potential field in the rotor relative frame (vane-vane interaction). The size and cause of vane-vane interaction is discussed in the second part of this paper [21].

5. Conclusions

- Upstream of its crown the rotor suction surface pressure field is dominated by the upstream vanes potential field and shock. As the vane trailing edge approaches the rotor leading edge an effective throat is set up between the two blades causing the vane trailing edge shock to strengthen. This effect reduces in strength as the vane shock moves around the surface of the rotor. As the vane trailing edge approaches the rotor leading edge a second stronger shock is observed to occur.
- The computational solution of the upstream stage has been shown to accurately predict vane-rotor interaction. However,

at the contact point of the vane trailing edge shock with the rotor suction surface (close to sensor 7) the amplitude of the unsteady pressure field is underestimated. It is expected that a much finer grid resolution would allow the vane trailing edge shock to be accurate prediction inside the rotor passage and would result in the correct amplitude of the unsteady pressure field at this location.

- In transonic turbine stages wake interaction has been shown not to cause a significant change in the rotor surface pressure field. It may therefore be ignored from an aeroelastic perspective.
- The presence of the downstream vane does not affect the pressure field around the suction surface leading edge or the pressure surface.
- The presence of the downstream vane causes a change in the pressure field downstream of the rotor's geometric throat. The size of this effect is comparable with that caused by the upstream vane.

Acknowledgments

All work was completed at the Southwell Laboratory in Oxford University. The authors gratefully acknowledge the support of K. J. Grindrod, John Allen, Nigel Brett and others from the Oxford Rotor Group. The authors also gratefully acknowledge the support of Rolls-Royce plc., DERA, MOD and DTI CARAD and their kind permission to publish this work.

Nomenclature

M = Mach no.
P = pressure
T = temperature
t = time
x = axial component, input signal
y = circumferential coardinate
X = Fourier transform of x
Y = Fourier transform of y
λ = convolution variable
is = isentropic
o = total conditions

References

[1] Wisler, D. C., 1998, Blade Row Interference effects in Axial Turbomachinery Stages. von Karman Institute lecture notes.
[2] Binder, A., Forster, W., Kruse, H., and Rogge, H., 1985, ''An Experimental Investigation into the Effect of Wakes on the Unsteady Turbine Rotor Flow,'' ASME J. Eng. Gas Turbines Power, **107**, pp. 458–466.
[3] Hodson, H. P., 1984, ''Measurements of Wake Generated Unsteadiness in the Rotor Passages of Axial-Flow Turbines,'' ASME 84-GT-189.
[4] Doorly, D. J., and Oldfield, M. L. G., 1985, ''Simulation of the Effect of Shock Waves on a Turbine Rotor Blade,'' ASME J. Eng. Gas Turbines Power, **107(4)**, pp. 998–1006.
[5] Giles, M. B., 1990, ''Stator-Rotor Interaction in a Transonic Turbine,'' J. Propul. Power, **6(5)**.
[6] Lefcort, M. D., 1965, ''An Investigation into Unsteady Blade Forces in Turbomachines,'' ASME J. Eng. Power, **87**, pp. 345–354.
[7] Korakianitis, T., 1993, ''On the propagation of Viscous Wakes and Potential Flow in Axial Turbine Cascades,'' ASME J. Turbomach., **115**, pp. 115–127.
[8] Binder, A., 1985, ''Turbulence Production due to Secondary Vortex Cutting in a Turbine Rotor,'' ASME 85-GT-193.
[9] Dietz, A. J., and Ainsworth, R. W., 1992, ''Unsteady Pressure Measurement on the Rotor of a Model Turbine Stage in a Transient Flow Facility,'' ASME 92-GT-156.
[10] Hilditch, M. A., Smith, G. C., and Singh, U. K., 1998, ''Unsteady Flow in a Single Stage Turbine,'' ASME 98-GT-531.
[11] Dunn, M. G., Bennett, W. A., Delaney, R. A., and Rao, K. V., 1992, ''Investigation of Unsteady Flow Through a Transonic Turbine Stage: Data/Prediction Comparison for Time-averaged and phase-Resolved Pressure Data,'' ASME J. Turbomach., **114**, pp. 91–99.
[12] Moss, R. W., Ainsworth, R. W., Sheldrake, C. D., and Miller R. J., 1997, ''The Unsteady Pressure Field Over a Turbine Blade Surface: Visualisation and Interpretation of Experimental Data,'' ASME 97-GT-474.
[13] Denos, R., Sieverding, C. H., Arts, T., Brouckaert, J. F., Paniagua, G., and Michelassi, V., 1999, ''Experimental Investigation of the Unsteady Rotor Aerodynamics of a Transonic Turbine Stage,'' IMechE Conf. Trans., Third European Conference on Turbomachinery.
[14] Sheldrake, C. D., and Ainsworth, R. W., 1994, ''Rotating Hot-Wire Measurements in a Model Turbine Stage,'' Proc., 13th Symposium of Measurement Techniques for Transonic and Supersonic Flows in Cascades and Turbomachines.
[15] Venable, B. L., Delaney, R. A., Busby, J. A., Davis, R. L., Dorney, D. J., Dunn, M. G., Haldeman, C. W., and Abhari, R. S., 1999, ''Influence of Vane-Blade Spacing on Transonic Turbine Stage Aerodynamics—Part I: Time-Averaged Data and Analysis,'' ASME J. Turbomach., **121**, pp. 663–672.
[16] Busby, J. A., Davis, R. L., Dorney, D. J., Dunn, M. G., Haldeman, C. W., Abhari, R. S., Venable, B. L., and Delaney, R. A., 1999, ''Influence of Vane-Blade Spacing on Transonic Turbine Stage Aerodynamics—Part II: Time-Resolved Data and Analysis,'' ASME J. Turbomach., **121**, pp. 673–682.
[17] Ainsworth, R. W., Schultz, D. L., Davies, M. R. D., Forth, C. J. P., Hilditch, M. A., and Oldfield, M. L. G., 1988, ''A Transient Flow Facility for the Study of the Thermofluid-Dynamics of a Full Stage Turbine Under Engine Representative Conditions,'' ASME 88-GT-144.
[18] Denton, J. D., 1990, ''The Calculation of Three-Dimensional Viscous Flow Through Multistage Turbomachines,'' ASME 90-GT-19.
[19] Hodson, H. P., and Dawes, W. N., 1996, ''On the interpretation of Measured Profile Losses in Unsteady Wake-Turbinc Blade Interaction Studies,'' ASME 96-GT-494.
[20] Miller, R. J., Moss, R. W., Ainsworth, R. W., and Harvey, N. W., 2001, ''Time-Resolved Vane-Rotor-Vane Interaction in a Transonic One and a Half Stage Turbine,'' 4th European Conference of Turbomachinery Fluid Dynamics and Thermodynamics, ATI-CST-081/01, pp. 937–949.
[21] Miller, R. J., Moss, R. W., Ainsworth, R. W., and Harvey, N. W., 2002, ''Wake, Shock and Potential Field Interactions in a 1.5 Stage Turbine—Part II: Vane-Vane Interaction and Discussion of Results,'' ASME J. Turbomach., **124**, pp. 40–47.

Wake, Shock, and Potential Field Interactions in a 1.5 Stage Turbine—Part II: Vane-Vane Interaction and Discussion of Results

R. J. Miller[1]
Whittle Laboratory,
University of Cambridge,
Cambridge CD30DY, UK

R. W. Moss[1]
Department of Marine Technology,
University of Newcastle,
Newcastle upon Tyne NE1 7RU, UK

R. W. Ainsworth
Department of Engineering Science,
University of Oxford,
Oxford OX13PJ, UK

N. W. Harvey
Rolls Royce plc.
Derby DE24 8BJ, UK

The composition of the time-resolved surface pressure field around a high-pressure rotor blade caused by the presence of neighboring blade rows is investigated with the individual effects of wake, shock and potential field interaction being determined. Two test geometries are considered: first, a high-pressure turbine stage coupled with a swan-necked diffuser exit duct; secondly, the same high pressure stage but with a vane located in the downstream duct. Both tests were conducted at engine-representative Mach and Reynolds numbers and experimental data was acquired using fast-response pressure transducers mounted on the mid-height streamline of the HP rotor blades. The results are compared to time-resolved computational predictions of the flow field in order to aid interpretation of experimental results and to determine the accuracy with which the computation predicts blade interaction. In the first half of this paper it is shown that, in addition to the two main interaction mechanisms (upstream vane-rotor and rotor-downstream vane interactions, presented in Part I of this paper) a third interaction occurs. This new interaction mechanism is shown to be caused by the interaction between the downstream vane's potential field and the upstream vane's trailing edge potential field and shock. The unsteady rotor surface static pressure fluctuations caused by this interaction are shown to occur on the late rotor suction surface at a frequency corresponding to the difference in the numbers of upstream and downstream vanes. The second part to the paper discusses the mechanisms that cause vane-rotor-vane interaction. The rotor's operating point is periodically altered as it passes the downstream vane. It is shown that for a large downstream vane, the flow conditions in the rotor passage, at any instant in time, are close to being steady state.
[DOI: 10.1115/1.1508387]

1 Introduction

The motion of the rotor, relative to the upstream vane and downstream vane causes the surface of the rotor to be subjected to an unsteady pressure field. When the flow unsteadiness experienced by a blade occurs at frequencies close to one of the blades' natural frequencies a significant vibration can occur. Over time this can cause high cycle fatigue (HCF) and eventually, if not identified, to a catastrophic blade failure. In Part I of this paper [1] the pressure field produced by both vane-rotor and rotor-vane interaction was presented.

In addition to the passing frequencies of both the upstream and downstream vane rows (vane-rotor and rotor-vane interaction) the unsteady pressure field is found to contain frequencies that correspond to the sum and difference of the passing frequencies of the vane's in the upstream and downstream blade rows. These extra frequency components in the rotor's forcing function are caused by the interaction between the upstream vane's flow field (trailing edge shocks and wakes) and the downstream vane's potential field within the passage of the rotor. A schematic of the structure of the flow in the passage of the rotor is shown in Fig. 1.

In a number of modern aeroengines the second stage vane is used both as the rear engine support strut and to route service ducts. This means that the vane is typically of a low aspect ratio and low number off and thus has a strong potential field. Small inter-stage spacing means that the downstream vane's potential field stretches into the passage of the upstream rotor (Korakianitis [2]). The combination of the transonic nature of modern first and second stage turbines and the large size of the second stage vane leads to particularly strong interaction between the upstream vane's flow field and the downstream vane's potential field (vane-vane interaction).

In [1] it was shown that the unsteady pressure field around the rotor leading edge is dominated by the contact of the upstream vane trailing edge shock with the surface of the rotor. Downstream of the rotor crown, Miller et al. [1] showed that the downstream vane and upstream vane contribute equally to the unsteady pressure field. In this paper it is shown that over a section of the rotor suction surface, close to the blades geometric throat, the unsteady pressure field caused by vane-vane interaction is comparable in amplitude to the unsteady pressure field caused by the downstream vane alone (rotor-vane interaction).

The generation of rotor forcing functions at frequencies that differ from the passing frequency of either the upstream or the downstream vane row is of particular importance for blade vibration. If the number of vanes in the upstream and downstream vane rows is similar then this interaction results in a forcing function at extremely low frequencies. It is therefore of importance to understand the cause of vane-vane interaction and to ensure during the design process that its affects are considered.

No literature, to the authors' knowledge, has presented experimental measurements of vane-vane interaction within a transonic multistage turbine operating at engine representative conditions.

[1]Formerly at the Department of Engineering Science, University of Oxford.

Contributed by the International Gas Turbine Institute and presented at the International Gas Turbine and Aeroengine Congress and Exhibition, Amsterdam, The Netherlands, June 3–6, 2002. Manuscript received by the IGTI, January 31, 2002. Paper No. 2002-GT-30436. Review Chair: E. Benvenuti.

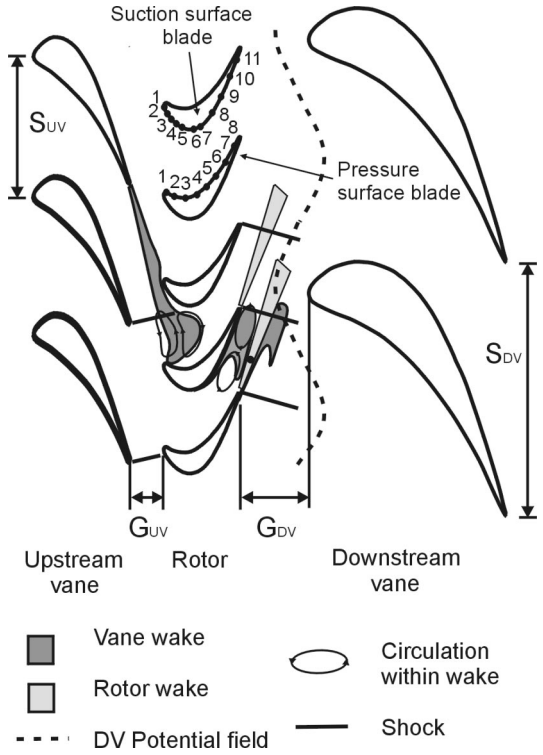

Fig. 1 Schematic showing the structure of the unsteady flow field

The aim of this paper to understand the mechanisms that cause interaction between the upstream vane and the downstream vane (vane-vane interaction) in a transonic one and half stage turbine.

2 Methodology

The experimental measurements described in this paper were carried out in the Oxford Rotor Facility using fast response pressure sensors mounted on the surface of the rotor blades. Detailed information about the instrumentation and the test facility were presented in [1]. The location of the surface-mounted pressure sensors on the rotor are shown in Fig. 1. The working section of the facility was rebuilt twice: first to include a plain swan-necked duct at rotor exit and secondly to include a second vane within the swan-necked duct. A comparison of the results from the two sets of tests was then used to compare the effect of the downstream vane on the unsteady pressure field around the rotor blade. It should be noted that the facility simulated engine representative Mach and Reynolds numbers. The axial gap between the upstream vane and rotor, G_{UV} in Fig. 1, was 0.36 of the upstream vane axial chord and the axial gap between the rotor and downstream vane, G_{DV}, was 0.88 of the rotor axial chord.

Numerical simulations were performed using a three-dimensional viscous time-unsteady code, Unstrest, developed by Denton [3] at Cambridge University. The code solves the Navier-Stokes equations using a thin shear layer model with the viscous terms evaluated every time step, and turned into body force terms for momentum and source terms for energy. The structured grid is formed by the rotation of points defined in two dimensions (x,r) about the turbine axis; the (x,r) points are defined by meridional (pseudo-streamwise) and pseudo-radial vectors. The code uses a ''time-marching'' solution scheme in which one blade row gradually rotates relative to the other with flow parameters being interpolated across a sliding plane between the two grids.

The mesh that was used in this research had 5.2 million nodes and included the upstream vane, the rotor and the downstream vane. The simulation spanned a repeat period of three upstream vanes, five rotors, and two downstream vanes, thus achieving the correct 3:5 vane rotor repeat ratio over the first two blade rows and the correct lift and time-mean pressure distribution for *all* blade rows. Flow properties (pressure, temperature and polar velocity components) are interpolated from the rotor grid onto the downstream vanes grid as if they covered the same circumferential extent: this allows the vane grid to span two passages (34.3 deg) instead of the ideal 1.75 passages (30 deg). This approximation allows a sufficiently fine grid for the calculation to resolve detailed secondary flow and tip leakage structures with available computational and time resources; the equivalent grid over the ideal 12:20:7 (120 deg) repeat ratio would have required nearly 20 million nodes and 4 Gb memory.

Between the leading and trailing edges of each row the grid has 242,000 nodes per vane passage, 135,000 per rotor passage and 408,000 per downstream vane passage. The annulus is modeled for 3.2 axial chords beyond the downstream vane to ensure accuracy of the streamlines at the trailing edge. The element to element expansion ratio was less than 1.18 in the axial direction and less than 1.1 in the radial and circumferential directions.

3 Vane-Vane Interaction (HP Vane and Downstream Vane)

The presence of the downstream vanes has two effects on the unsteady pressure field around a rotor blade. The first, described in [1], is caused by the rotor's flow field being changed by the presence of the downstream vane and causes pressure fluctuations at multiples of the downstream vane passing frequency. The second is caused by the upstream vane's exit flow field being changed within the rotor passage by the presence of the downstream vane. In this section experimental and computational results are used to determine the size of this ''vane-vane'' interaction. It should be noted that, as shown in [1], the downstream vane does not affect the unsteady pressure field around the rotor pressure surface and therefore the discussion in this paper will concentrate on the pressure field around the rotor suction surface.

The structure of the unsteady pressure field presented in [1], and used in the remainder of this paper, is summarized in the following:

- **Sensors 1–7.** Large unsteady pressure fluctuations caused by the upstream vane's trailing edge shock.
- **Sensors 1–6.** No measurable component of the unsteady pressure field at multiples of the downstream vane passing frequency
- **Sensor 7.** Small component of the unsteady pressure field at multiples of the downstream vane passing frequency.
- **Sensors 8–11.** Sharp drop in the size of the unsteady pressure field at multiples of the upstream vane passing frequency. Rise in the size of the component of the unsteady pressure field at multiples of the downstream vane passing frequency. Sensor 8 was found to have the largest component at multiples of the downstream vane passing frequency.

In this section, the measured and computationally predicted power spectrum of the suction surface pressure field is used both to analyze the composition of the unsteady pressure field and to investigate the accuracy of the computation prediction.

3.1 Experimental Measurements. Before examining the spectral composition of the pressure measurements made over the entire suction surface, the structure of the power spectrum measured by the trailing edge suction surface sensor (sensor 11) will be examined in detail. The power spectrum measured by this sensor is shown in Fig. 2. The power spectrum can be seen to be made up of a number of peaks. All but one of these peaks is observed to occur at frequencies that correspond to multiples of the upstream vane passing frequency (vane-rotor interaction) and downstream vane passing frequency (rotor-vane interaction). The remaining peak is observed to occur at 15 events per revolution.

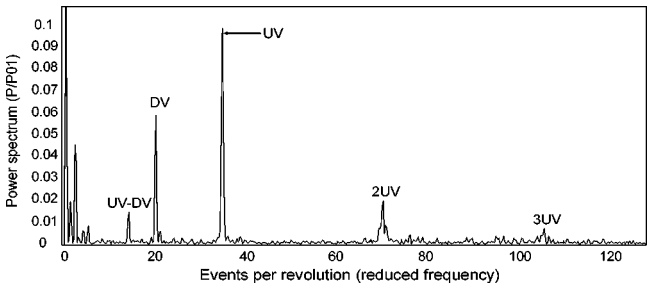

Fig. 2 Power spectrum calculated using measurements from suction surface sensor 11

The peaks in the power spectrum at multiples of the upstream and downstream vane passing frequency correspond to a simple superposition of the downstream vane's flow field with that set up by the upstream vane. It is, however, important to understand whether, in addition to such a simple superposition, the two flow fields interact in a more complex fashion. Such an interaction is likely to take the form of an amplification or attenuation of one flow field by the other. Such effects are highly important in turbomachinery as multiplication and division are nonlinear processes, and thus result in forcing functions that occur at frequencies that differ from the harmonic frequencies associated with the passing of either the upstream or downstream blade rows.

The remaining peak in the power spectrum occurs at a frequency of 15 events per rotor revolution. This frequency is consistent with an interaction (amplification or attenuation) between the downstream and upstream vane rows in the rotor-relative frame. Multiplication of two signals can be thought of as the scaling or modulation of one signal by the other. The modulation theorem (Oppenheim et al. [4]) states that the multiplication of two signals in the time-domain corresponds to convolution in the frequency domain.

The convolution of two signals involves time-reversing the second signal and sliding it relative to the first. At each position the new signal (the result of the convolution) is obtained by integrating the product of the two signals.

$$X(\omega)^{*}Y(\omega)=\int_{-\infty}^{\infty}X(\lambda)\cdot Y(\omega-\lambda)\cdot d\lambda$$

The Fourier transform of the pressure field created by each vane row alone is simply made up of a series of impulses at multiples of the particular vane passing frequency. Convolving two signals, each made up of a series of impulses, creates another signal made up of impulses at frequencies corresponding to the sum and difference of the frequencies in the original signal. The convolution process is complex to visualise; it is presented in detail in [4]. To simulate the amplification of the upstream component by the downstream component, or vice versa, two idealised pressure signals were both added and multiplied together. The power spectra

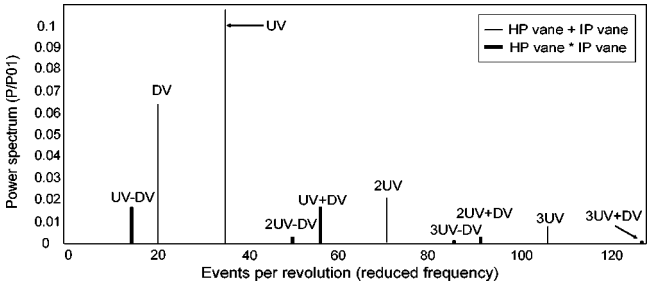

Fig. 3 Power spectrum created by idealized interaction between upstream and downstream vane

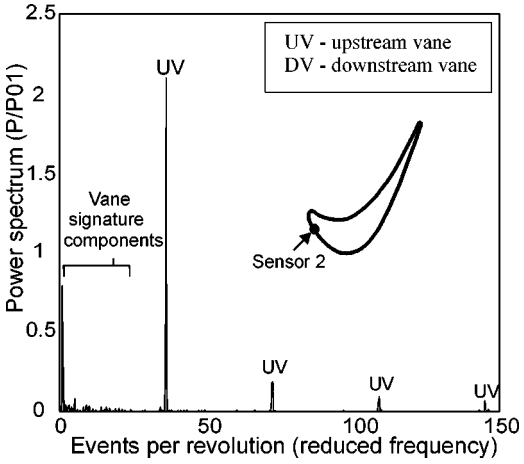

Fig. 4 Suction surface pressure sensor 2

of the two resulting signals are shown in Fig. 3. With 36 upstream vanes and 21 downstream vanes it is clear the peak in the measured power spectrum at 15 events per revolution corresponds to an interaction between the flow fields of the two vanes in the rotor relative frame.

The idealized upstream/downstream vane interaction, shown in Fig. 3, results in the rotor pressure field containing components at six new frequencies. One of these peaks is (as indicated by the idealised vane interaction) actually observed in the measured power spectrum shown in Fig. 2. It is clear that some of the idealized interaction frequencies are measured on the rotor blade surface and others are not. It is important to note that a simple amplification or attenuation of the flow field associated with one vane by that of the other is unlikely to occur. It is more likely that different individual structures within the flow field interact in different ways, some being simply superimposed on each other, while others are both superimposed on and attenuated by each other.

It has been shown in the foregoing that in addition to the upstream and the downstream vane passing frequencies, the unsteady pressure field measured by sensor 11 contains a component at the difference between the upstream and downstream vane passing frequencies. As shown in [1] sensor 7 to 11 all experience a component of the unsteady pressure field at the downstream vane passing frequency, caused by the potential field of the downstream vane, with sensor 8 measuring the largest fluctuations. In the remainder of this section it is shown that this potential field interacts with the upstream vane's flow field and causes sensors 7 to 11 to experience unsteady pressure fluctuations at the difference between the upstream and downstream vane passing frequencies (vane-vane interaction). The power spectrum of the unsteady pressure measured by four key pressure transducers on the rotor suction surface, sensors 2, 7, 8, and 11, are shown in Figs. 4 to 7. Figures 5 to 7 have been expanded so that the size of the vane-vane interaction can be clearly observed.

Between sensors 11 and 8 the structure of the power spectrum is not observed to alter significantly. The size of the upstream vane component is observed to drop but the size of the downstream vane component rises. Both sensor 8 and 11 show a peak in the power spectrum at the difference between the upstream and downstream vane passing frequencies but neither show a peak at the sum of the upstream and downstream vane passing frequencies. The size in the peak power spectrum at the difference in the upstream and the downstream vane passing frequencies is observed to rise by 10% between sensor 11 and sensor 8. This rise in strength of the vane-vane interaction between these two sensors is consistent with the increase in the strength of the rotor-vane interaction measured between the same two sensors [1].

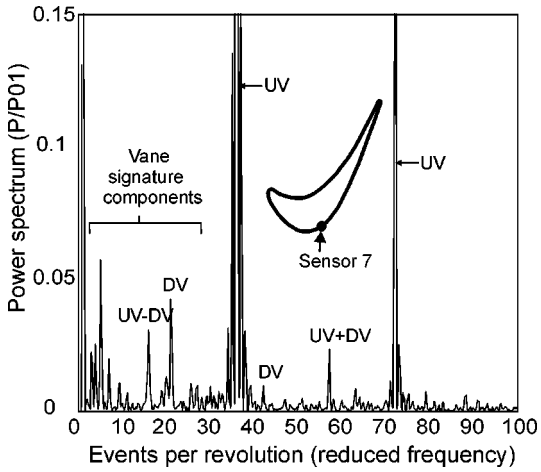

Fig. 5 Suction surface sensor 7 (expanded)

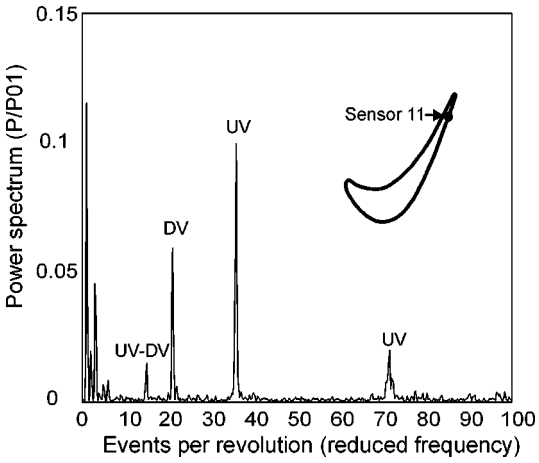

Fig. 7 Suction surface sensor 11 (expanded)

Between sensors 8 and 7 a significant change is observed in the structure of vane-vane interaction (Figs. 5 and 6). The peak power spectrum at the difference between the upstream and downstream vane passing frequencies is observed to rise by 67% and a second peak in the power spectrum is observed at the sum of the upstream and downstream vane passing frequencies. Upstream of sensor 7 the pressure field was not found to contain components at multiples of the downstream vane passing frequency (rotor-vane interaction) or the sum or difference of the upstream and downstream vane passing frequencies (vane-vane interaction). The power spectrum measured by sensor 2 is shown in Fig. 4.

In this section it has been shown that, between sensors 7 and 11, vane-vane interaction causes an unsteady pressure field to occur at a frequency corresponding to the difference between the upstream and downstream vane passing frequencies. Between senor 8 and 11 vane-vane interaction was found to be smaller than both vane-rotor and rotor-vane interaction. The largest vane-vane interaction was found to occur on sensor 7. At this location the unsteady pressure fluctuations caused by vane-vane interaction were found to be comparable in size to those caused by rotor-vane interaction. The cause of the increase in vane-vane interaction on sensor 7 is discussed in the Section 4.

3.2 Computational Predictions. To examine the accuracy with which vane-vane interaction can be computationally predicted, the power spectrum of the predicted unsteady pressure field at each grid point along the rotor mid-height suction surface streamline was calculated. The square root of the power spectrum is shown plotted in Fig. 8. The square root was chosen instead of the power spectrum itself so that the vane-rotor, rotor-vane and vane-vane interactions could be clearly observed on the same graph. It should also be noted that the square root of the power spectrum allows the amplitudes of the unsteady pressure fluctuations associated with each interaction to be directly compared. A number of black lines have been added to Fig. 8 to mark the location of the experimental pressure sensors.

As discussed in Section 2 the row to row interpolation used in the computation implies an effective downstream vane spacing slightly different to that occurring in the test facility. The apparent downstream vane passing frequency in the computation is 24 per revolution compared with the ideal 21; the frequencies of the UV, UV−DV and UV+DV peaks in Fig. 8 are thus slightly different to those in previous figures.

The computational prediction of the power spectrum (Fig. 8) shows the same structure as the experimental measurements described in Section 3.1. Close to the rotor leading edge the unsteady pressure field is dominated by vane-rotor interaction and downstream of the rotor crown all three interactions (vane-rotor,

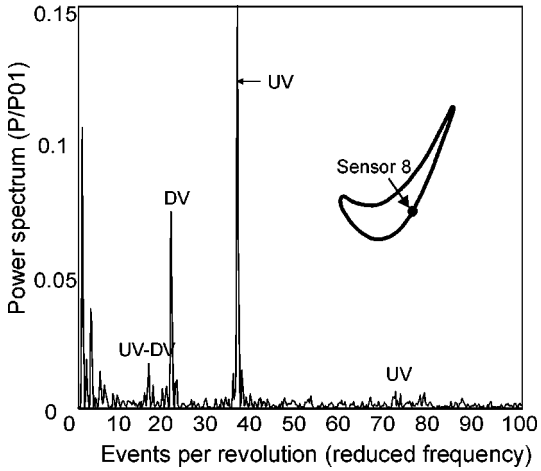

Fig. 6 Suction surface sensor 8 (expanded)

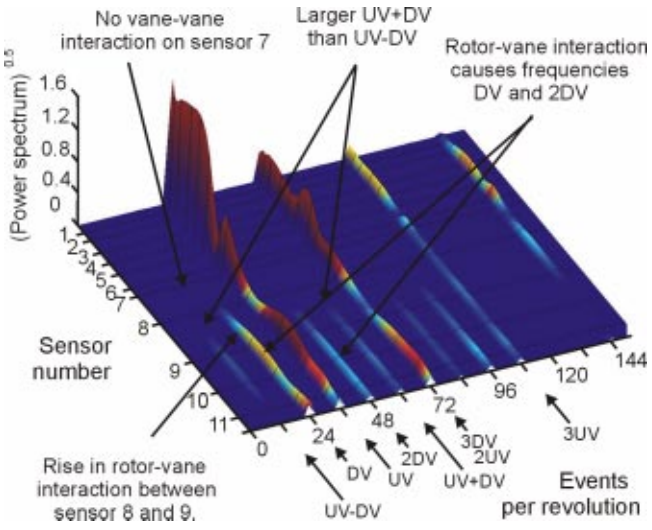

Fig. 8 Computational prediction of the square root of the power spectrum (suction surface)

rotor-vane and vane-vane) are observed. However, the computational predictions differ from the experimental results in a number of ways (labeled in Fig. 8).

- In the computational prediction rotor-vane interaction causes a peak in the power spectrum at both the fundamental frequency and the first harmonic of the downstream vane passing frequency (DV and 2DV in Fig. 8). In the experimental measurements the first harmonic of the downstream vane passing frequency was not observed (2DV in Figs. 6 and 7). The experimental results therefore indicate that the potential field of the downstream vane is close to sinusoidal while the computational predictions indicate a non-sinusoidal potential field. This is discussed in more detail in Section 4.
- In the experimental results it was shown that rotor-vane interaction increased in strength sharply between sensor 7 and 8 (Figs. 5 and 6). The computation predicts that the rotor-vane interaction increases between sensor 8 and 9.
- In the experimental results it was shown that the strongest vane-vane interaction was measured by sensor 7; however, the computation predicts that sensor 7 is not affected by the presence of the downstream vane.
- In the experimental results, vane-vane interaction was not found to cause a peak in the power spectrum, between sensors 8 and 11, at the upstream vane plus the downstream vane passing frequency (UV+DV). In the computation the strongest component of vane-vane interaction was found to occur at the upstream vane plus the downstream vane passing frequency (UV+DV).

The general agreement between the computational prediction and the experimental measurements is good. However, a number of differences, especially in the prediction of vane-vane interaction, have been highlighted. The causes of these differences are discussed in Section 4. The grid resolution used in the computational prediction presented in this paper is as good as, and possibly better than, those used in current engine design. This direct comparison between experiment and computational prediction is thus useful in highlighting the accuracy with which a designer is likely to predict each of the three interaction mechanisms.

4 Discussion of Interaction Mechanisms

The presence of the downstream vane has been shown to cause the rotor's pressure field to contain two distinct groups of frequency components: the first at harmonics of the downstream vane passing frequency (rotor-downstream vane interaction, [1]) and the second group at the sum and difference of the upstream and downstream vane passing frequencies (vane-vane interaction, Section 3). In this section the interaction mechanisms that cause these two groups are discussed.

The locations of the key pressure sensors used in this discussion are shown in Fig. 9(*a*). The unsteady pressure field experienced by each sensor is summarized in the following:

- **Sensor 2.** Large upstream vane effect. Unaffected by the presence of the downstream vane.
- **Sensor 7.** Large upstream vane effect, small downstream vane effect and the largest inter-vane interaction (UV+DV and UV−DV).
- **Sensor 8.** Small upstream vane effect, 40% rise in downstream vane effect and a 40% drop in the strength of vane-vane interaction (UV−DV only).
- **Sensor 11.** Small upstream vane effect, 16% drop in downstream vane effect and a 10% drop in the strength of the vane-vane interaction (UV−DV only).

As the rotor exit pressure field is altered by the presence of the downstream vane the flow field in each rotor passage changes as it passes each downstream vane. The effect of a steady state change in the exit conditions of the Oxford rotor blades was investigated by Mee et al. [5]. He measured the pressure profile around the blade while altering its exit static pressure. The Oxford rotor blade operating at four isentropic exit Mach numbers is shown in Fig. 10. Above an exit Mach number of 0.9 the blade pressure surface and early suction surface (upstream of the Mach 1 line) can be

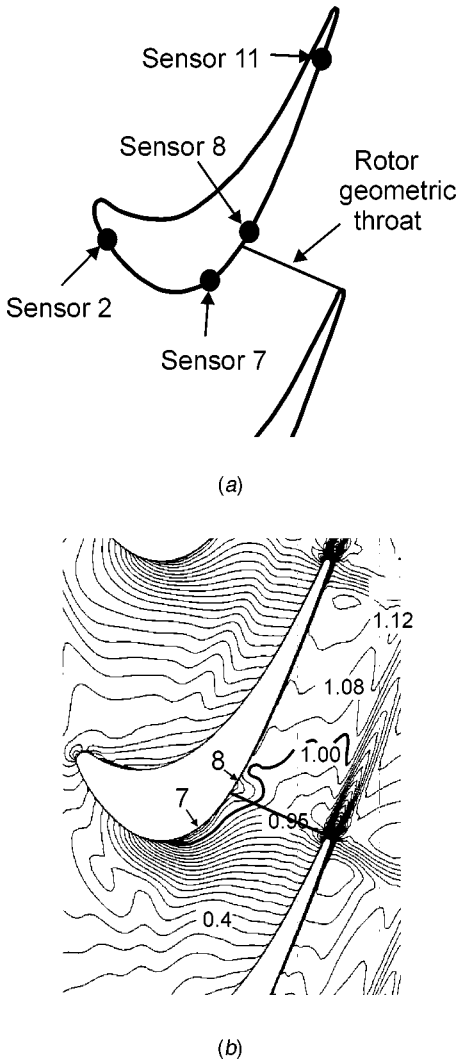

Fig. 9 (*a*) Location of key surface pressure sensors; (*b*) rotor relative Mach number (Mach 1 line highlighted)

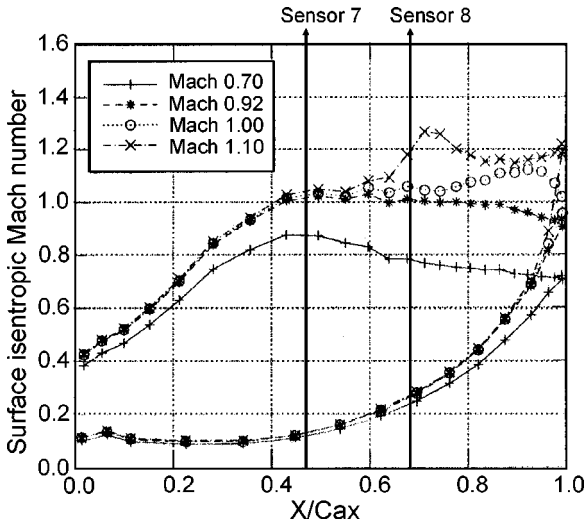

Fig. 10 Blade surface isentropic Mach number distribution [5]

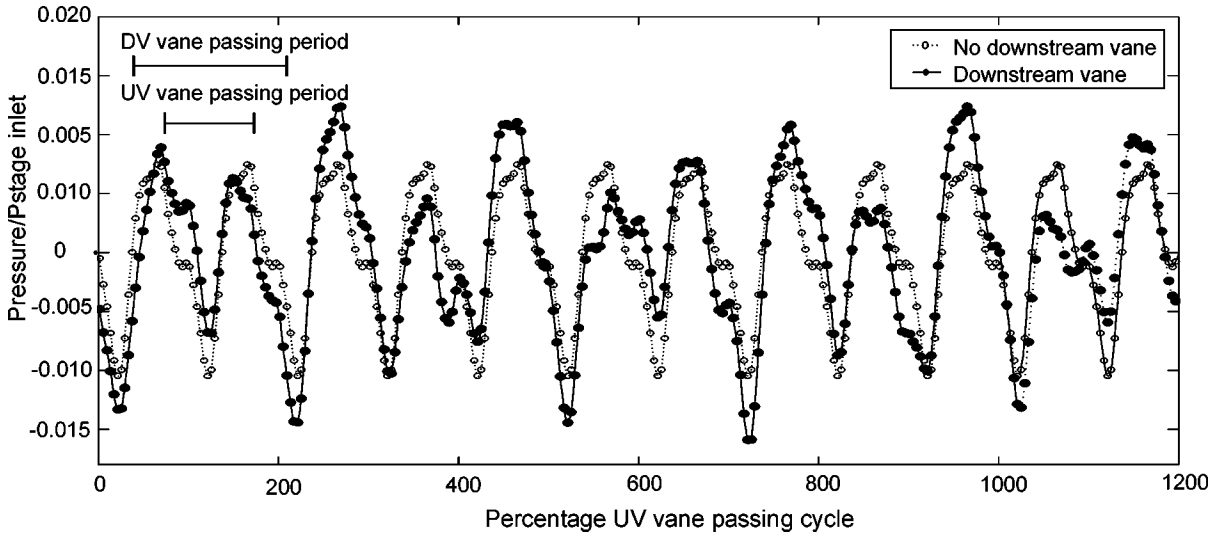

Fig. 11 Deterministic component of pressure measurements made using sensor 11 at both upstream and downstream passing frequencies

seen to be insensitive to the blade exit conditions. A computational prediction calculated, using Mike Giles Unsflo code (two-dimensional, viscous, unsteady Unsflo prediction, Giles [6]), of the rotor relative Mach number showing the position of the Mach **1** line is shown in Fig. 9(*b*). Mee's steady tests indicate that if the presence of a downstream vane simply alters each rotor blade's exit conditions then sensor 7, 8 and 11 should show a downstream vane component while sensor 2 should be unaffected.

Mee's results also indicate that the pressures at some points on the rotor suction surface are more sensitive than at others to changes in the blade exit static pressure. Close to the blade geometric throat (0.6 to 0.8 axial chord, Mach 1.1 in Fig. 10) a small region of supersonic flow can be observed. The static pressure in this region is most sensitive to changes in the blade exit conditions. As the blade exit Mach number is raised this region of high sensitivity moves backward along the blade surface towards the trailing edge. The computation in Fig. 9(*b*) shows that at the design operating condition of the Oxford Rotor, this region lies just upstream of sensor 8. This indicates that sensor 8 should be more sensitive to variations in the rotor operating conditions than any of the other sensors. This agrees with the findings of the experimental results that show that the downstream vane component of the unsteady pressure field on sensor 11 is 16% small than on sensor 8 [1].

It should, however, be noted that the rotor is not simply exposed to steady state changes in its operating point. The exit of each rotor blade is subjected to temporal and spatial variations in static pressure as it passes the downstream vane. To investigate the time taken for the pressure field in the rotor downstream of the Mach one line to be altered by the presence of the downstream vane, it is useful to examine the relative phase of the downstream vane component of the unsteady pressure field measured by pressure sensors 8 (just downstream of the Mach one line) and 11 (close to the rotor trailing edge).

In Section 3.1 the structure of the pressure field measured by these two sensors was interpreted by calculating their power spectrum. The power spectrum is very useful for interpreting the strength of individual flow components, but is not of use in studying the time-resolved structure of the flow field; to do this it is necessary to ensemble the pressure measurements to obtain the vane-periodic component. The locations of the four pressure sensors that will be discussed are shown in Fig. 9(*a*).

Before discussing the relative phase of the pressure field caused by the downstream vane it is useful to compare the pressure field measured by the trailing edge suction surface pressure sensor (sensor 11) with and without the downstream vane (Fig. 11). When the upstream and downstream vane components of the flow field are considered then the pressure field is observed to repeat over one third of the annulus (the up and downstream vane repeat ratio). The presence of the downstream vane is observed to modulate the flow field set up by the upstream vane causing the amplitude of the unsteady pressure field to change by 50%.

The ensemble averaged downstream vane components from sensors 8 and 11 are shown in Fig. 12. Upstream of Sensor 8 it was impossible to accurately extract the downstream vane-periodic component by ensemble averaging. This was due to the small size of the downstream vane component relative to the size of the deterministic upstream vane component. The signals, in Fig. 12, show the 16% drop in the RMS pressure fluctuations from sensor 8 to 11 indicated by the power spectrum in [1]. However, it is interesting to note that both the phase and structure of the unsteady pressure field does not change over the late suction surface.

A computational prediction of the pressure on the late rotor suction surface (sensors 9, 10, and 11) is shown in Fig. 13. As

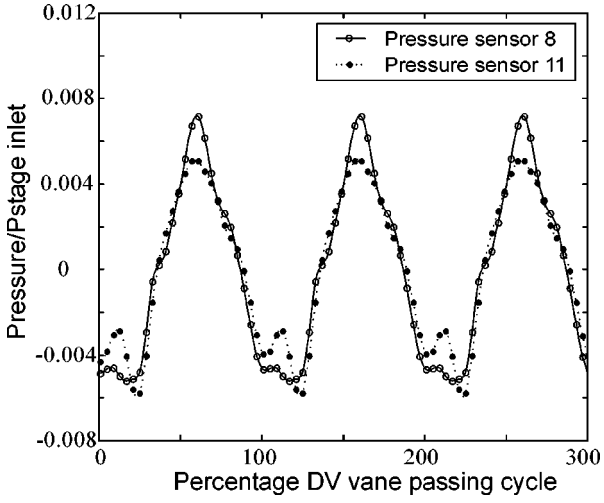

Fig. 12 Experimental measurement of the pressure on the late suction surface (ensemble averaged at downstream vane passing frequency)

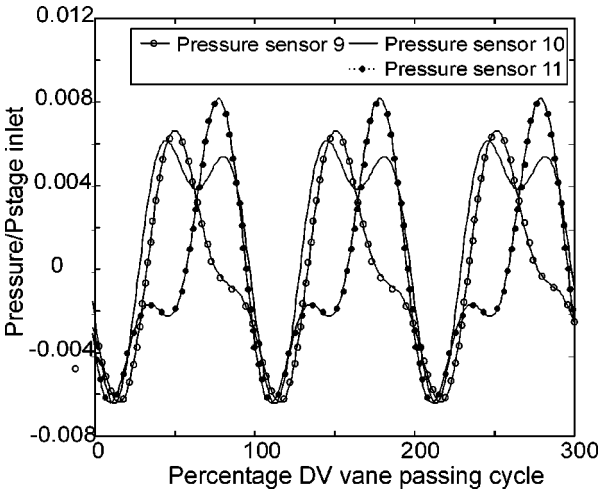

Fig. 13 Computational prediction of pressure on late suction surface (1st two harmonics of downstream vane passing frequency)

discussed in Section 3 the computational solution and the experimental measurements disagree about the point on the suction surface at which the size of the downstream vanes pressure field drops. The experimental results show the drop in the strength of rotor-vane interaction occurring between sensors 8 and 7 and the computational predictions show the drop between sensors 9 and 8. The amplitude of the unsteady pressure field predicted by the computation is very close to the amplitude measured experimentally. However, unlike the experimental results the structure of the computationally predicted pressure field was found to vary along the suction surface. Between sensors 9 and 11 (Fig. 13) the peak in the unsteady pressure field at 45% downstream vane passing cycle is observed to drop and the pressure at 80% downstream vane passing cycle to rise. This change in the structure of the pressure field caused by the downstream vane was not observed in the experimental measurements and its cause is at present not understood.

The computation results show only a small difference in phase between sensor 9 and 11, with sensor 11 leading sensor 9 by 5 percent of the downstream vane passing period. The experimental results show no phase difference between the pressure field measured by sensors 8 and 11. Sensors 8 and 11 are located at circumferential positions that are 25% of a downstream vane pitch apart. If the downstream vanes' potential field were simply superimposed on the rotor flow field then Figures 12 and 13 indicate that iso-surfaces of static pressure associated with the vanes' potential field must lie parallel to the late suction surface of the rotor. It is, however, unlikely that a simple superposition of the blade potential fields is the only interaction that occurs.

A change in the blade's exit pressure requires time to propagate upstream toward the Mach 1 line in side the rotor passage and thus takes time to alter the operating point of the entire blade. To indicate the relative time required for the rotor to respond to a change in exit pressure field caused by its movement relative to the downstream vane it is convenient to note the distance a pressure wave would travel in the time taken for a rotor to travel across one downstream vane pitch. If the wave is considered as propagating upstream against an average flow speed of Mach 0.5 then in one downstream vane passing period it would travel through a distance of three rotor axial chords. This indicates that the time taken for the rotor operating point to change due to a change in its exit condition is much smaller than the time taken for the rotor to pass through one downstream vane pitch. This agrees with both the computational and experimental results that show that the there is little phase difference between the unsteady fluctuations measured downstream of the Mach one line. It is thus likely that the effect of the downstream vane on the rotor's pressure field can be considered as close to steady state.

The vane-vane interaction is caused, as discussed in Section 3, by an amplification and attenuation of one vane's flow field by the other. It is interesting to note that in the experiment this phenomenon is stronger on sensor 7 than on either sensor 8 or 11, where the direct interaction of the downstream vane is at its strongest. It is also interesting to note that sensor 7 measured beat frequencies at both DV−UV and DV+UV passing frequencies while sensors 8 and 11 show no sign of the UV+DV passing frequency. The detailed mechanisms that cause these interaction are at present not understood but it is clear that the vane-vane interaction is strongest just downstream of the contact point of the Mach 1 line with the rotor surface.

The strength of the interaction in this region is thought to be caused by the interaction between the vane trailing edge shock and the downstream vane potential field. The region on the suction surface between the Mach 1 line and contact point of the upstream vane's trailing edge shock is therefore the region of strongest vane-vane interaction. The fact that this large vane-vane interaction on sensor 7 is not shown in the computational solution (Fig. 8) is of no surprise. In [1] the experimental results showed that the upstream vane trailing edge shock caused a large pressure fluctuation on sensor 7, but the computational solution showed only a small pressure fluctuation. This was because the grid resolution in the computation was insufficient to accurately resolve the vane trailing edge shock deep inside the rotor passage. It is therefore likely that an extremely fine computational grid would be required to resolve the increased vane-vane interaction measured on sensor 7.

It should be noted that if a turbine stage were designed in which the contact point of the upstream vane's trailing edge shock with the rotor suction surface was close, or downstream of, the rotor's geometric throat then it is likely that the strength of vane-vane interaction would increase significantly causing an extremely low frequency rotor forcing function (UV−DV frequency) and a new higher frequency forcing function (UV+DV).

5 Conclusions

- The pressure component created by the downstream vane on the late rotor suction surface was found to be close to sinusoidal and no phase lag was measured between the pressure sensors close to the rotor geometric throat and close to the trailing edge. The results indicate that the downstream vane is causing a quasi-steady change in the operating conditions of each rotor passage.
- The computation was found to accurately predict the phase and amplitude of the downstream unsteady pressure field and was found to predict vane-vane interaction. However, the structure of the predicted and experimental vane-vane and rotor-vane interactions were found to differ.
- As well as the up and downstream vane passing frequencies the rotor suction surface experiences a new frequency component caused by the interaction of the up and downstream vanes in the relative frame. This new component was found to be at a frequency corresponding to the difference in the up and downstream vane passing frequencies.
- Vane-vane interaction was found to be strongest between the contact point of the Mach 1 line and the contact point of the upstream vane's trailing edge shock with the rotor suction surface. The results indicate that transonic stages should not be designed so that the vane trailing edge shock contacts the rotor suction surface downstream, or close to, the rotor's geometric throat. The grid resolution in the computation was insufficient to resolve this interaction. It is thought that extremely fine grids would be required to accurately resolve this component.

- Results indicate that vane-vane interaction is likely to be strongest in low reaction transonic stages.

Acknowledgments

All work was completed at the Southwell Laboratory in Oxford University. The authors gratefully acknowledge the support of K. J. Grindrod, John Allen, Nigel Brett and others from the Oxford Rotor Group. The authors also gratefully acknowledge the support of Rolls-Royce plc., DERA, MOD and DTI CARAD and their kind permission to publish this work.

Nomenclature

G = interblade gap
M = Mach no.
P = pressure
S = blade pitch
T = temperature
t = time
x = axial component, input signal
y = circumferential coordinate
X = Fourier transform of x
Y = Fourier transform of y
λ = convolution variable
is = isentropic
o = total conditions
UV = upstream vane
DV = downstream vane

References

[1] Miller, R. J., Moss, R. W., Ainsworth, R. W., and Harvey, N. W., 2002, ''Wake, Shock and Potential Field Interactions in a 1.5 Stage Turbine—Part I: Vane-Rotor and Rotor-Vane Interaction,'' ASME 2002-GT-30435, ASME J. Turbomach., **124**, pp. 33–39.
[2] Korakianitis, T., 1993, ''On the Propagation of Viscous Wakes and Potential Flow in Axial Turbine Cascades,'' ASME J. Turbomach., **115**, pp. 115–127.
[3] Denton, J. D., 1990, ''The Calculation of Three-Dimensional Viscous Flow Through Multistage Turbomachines,'' ASME 90-GT-19.
[4] Oppenheim, A. V., Willsky, A. S., and Withian, T. Y. 1983, *Signals and Systems*. Prentice Hall International Editions.
[5] Mee, D. J., Baines, N. C., Oldfield, M. L. G., and Dickens, T. E., 1992, ''An Examination of the Contributions to Loss on a Transonic Turbine Blade in a Cascade,'' ASME J. Turbomach., **114**.
[6] Giles, M. B., 1990, ''Stator-Rotor Interaction in a Transonic Turbine,'' J. Propul. Power, **6**(5).

Controlling Secondary-Flow Structure by Leading-Edge Airfoil Fillet and Inlet Swirl to Reduce Aerodynamic Loss and Surface Heat Transfer

T. I-P. Shih

Y.-L. Lin

Department of Mechanical Engineering,
Michigan State University,
East Lansing, MI 48824-1226

Computations, based on the ensemble-averaged compressible Navier-Stokes equations closed by the shear-stress transport (SST) turbulence model, were performed to investigate the effects of leading-edge airfoil fillet and inlet-swirl angle on the flow and heat transfer in a turbine-nozzle guide vane. Three fillet configurations were simulated: no fillet (baseline), a fillet whose thickness fades on the airfoil, and a fillet whose thickness fades on the endwall. For both fillets, the maximum height above the endwall is positioned along the stagnation zone/line on the airfoil under the condition of no swirl. For each configuration, three inlet swirls were investigated: no swirl (baseline) and two linearly varying swirl angle from one endwall to the other (+30 to −30 deg and −30 to +30 deg). Results obtained show that both leading-edge fillet and inlet swirl can reduce aerodynamic loss and surface heat transfer. For the conditions of this study, the difference in stagnation pressure from the nozzle's inlet to its exit were reduced by more than 40% with swirl or with fillet without swirl. Surface heat transfer was reduced by more than 10% on the airfoil and by more than 30% on the endwalls. When there is swirl, leading-edge fillets became less effective in reducing aerodynamic loss and surface heat transfer, because the fillets were not optimized for swirl angles imposed. Since the intensity and size of the cross flow were found to increase instead of decrease by inlet swirl and by the type of fillet geometries investigated, the results of this study indicate that the mechanisms responsible for aerodynamic loss and surface heat transfer are more complex than just the intensity and the magnitude of the secondary flows. This study shows their location and interaction with the main flow to be more important, and this could be exploited for positive results. [DOI: 10.1115/1.1518503]

Introduction

Secondary flows in airfoil passages such as horseshoe, passage, and corner vortices are generally considered detrimental to the performance and reliability of gas turbines (Langston [1]). This is because secondary flow gets its energy from the main flow, and so is a source of aerodynamic loss. Also, they entrain higher-temperature gas in the main flow to the airfoils and the endwalls, and this can increase surface heat transfer. On film cooling, secondary flows can advect and lift film-cooling jets away from surfaces that they are intended to protect. These potentially adverse effects can be especially severe for low-aspect ratio, high-pressure turbines, and highly loaded, low-pressure turbines.

A number of design concepts have been advanced to minimize the intensity and size of secondary flows. One promising concept is endwall contouring, especially the contouring, which accelerates the main flow upstream of the airfoil and continues the acceleration throughout the airfoil passage (see, e.g., Deich et al. [2], Ewen et al. [3], Dossena et al. [4] Duden et al. [5], Burd and Simon [6], Shih et al. [7], and Lin et al. [8,9]). Though promising, this design concept can only be applied to the first-stage stator, where there is a contraction in cross-sectional area from the combustor to the turbine.

Another promising design concept is contouring the airfoil next to the endwalls, often referred to as airfoil fillets. This design concept has the advantage of being applicable to airfoil passages in any stage. Most of the research on airfoil fillets has been on wing/body junctures (see, e.g., Pierce et al. [10], Davenport et al. [11], Pierce and Shin [12], and references cited there). These studies were primarily concerned with the elimination of horseshoe vortices. They found that a pointed/sharp fillet on the leading edge of the airfoil (Fig. 1(*a*)) could reduce or eliminate horseshoe vortices. But, the ''pointedness and sharpness'' of the fillet must be aligned with the stagnation flow. For rounded fillets (Fig. 1(*b*)), they found the intensity and size of horseshoe vortices to increase with the radius of the fillet. They also found the horseshoe vortex structure to be displaced further upstream of the leading edge.

Very few studies have reported the use of airfoil fillets in gas turbines, where there are not only horseshoe-type vortices, but also Dean-type vortices induced by the pressure difference between the pressure and suction sides of adjacent airfoils. Using leading-edge fillets to eliminate horseshoe vortices was recently proposed by Bancalari and Nordlund [13], and then reiterated by Shih [14]. Zess and Thole [15] reported a combined numerical and experimental study on leading-edge airfoil fillet, and found that the pointed/sharp-type of fillet shown in Fig. 1(*a*) can indeed eliminate horseshoe vortices. They also noted that the turbulent kinetic energy is greatly reduced in the endwall region. Sauer et al. [16] studied a different type of fillet, one that enhances instead of diminishes horseshoe vortices. Their fillet, a bulb-type (Fig. 1(*c*)), is intended to intensify horseshoe vortices on the suction side in order to reduce the pressure-side-to-suction-side secondary flow.

Thus, most research on secondary flows has been on how to

Contributed by the International Gas Turbine Institute and presented at the International Gas Turbine and Aeroengine Congress and Exhibition, Amsterdam, The Netherlands, June 3–6, 2002. Manuscript received by the IGTI, January 3, 2002. Paper No. 2002-GT-30529. Review Chair: E. Benvenuti.

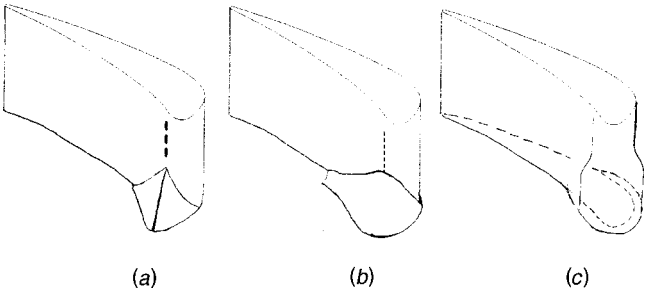

Fig. 1 Basic leading-edge fillet geometries—(*a*) sharp/pointed, (*b*) rounded, (*c*) bulb type

suppress or minimize the intensity and size of secondary flows. In this study, that is not the objective. Instead, it is to investigate how secondary flows can be harnessed to produce positive results—even if secondary flows intensify. More specifically, the objective is to use computational fluid dynamics (CFD) to explore secondary flows induced by leading-edge airfoil fillet and inlet swirl in a nozzle guide vane and their effects on aerodynamic loss and surface heat transfer. Three leading-edge fillets are studied: no fillet (baseline), a fillet whose thickness fades on the airfoil, and a fillet whose thickness fades on the endwall. Since swirl can be quite high in magnitude at combustor exit (see, e.g., Goebel et al. [17]- and van Fossen and Bunker [18]), three inlet swirls were studied for each fillet configuration: no swirl (baseline) and two linearly varying swirl angle from one endwall to the other (+30 to −30 deg and −30 to +30 deg). These swirls are taken to simulate flow conditions from can-type combustors with fuel/air swirlers.

Problem Description

A schematic diagram of one periodic section of the nozzle guide vanes studied is shown in Fig. 2. A three-dimensional (3-D) rendering is shown in Fig. 3. For this linear cascade, the airfoil is two-dimensional (2-D) with an axial chord length C_x of 19.883 cm. The actual chord length C is 31.8 cm. The pitch P between airfoils is 31.8 cm. On the endwalls, one is flat, and another is contoured. For the contoured endwall, the profile is made up of straight line with a 45-deg slope and a 45-deg arc with radius R of 24.41 cm. Note that all of the contouring is upstream of the airfoil (Figs. 2 and 3). This is the more traditional design in which contouring is not utilized to modify the flow within the airfoil passage. The distance from the inlet to the beginning of contouring

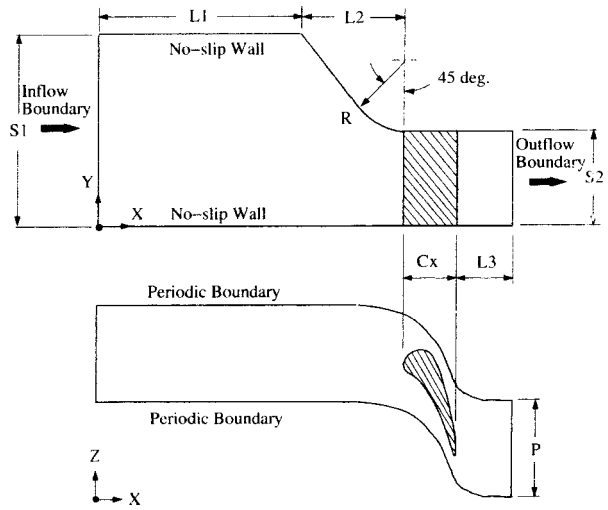

Fig. 2 Schematic of the nozzle vane studied (not drawn to scale)

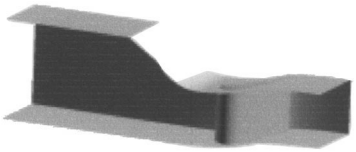

Fig. 3 Three-dimensional rendering of the nozzle vane studied

L1 is 58.4 cm; the distance of the contouring L2 is 35.8 cm; and the distance from the airfoil's trailing edge to the outlet L3 is 23.8 cm. The nozzle has an inlet height S1 of 44.45 cm and an outlet height S2 of 24.41 cm.

For this 2-D airfoil, three different leading-edge fillets were studied (Fig. 4): no fillet (baseline; referred to as C1 configuration), a fillet whose thickness diminishes on the airfoil surface (C2 configuration), and a fillet whose thickness diminishes on the endwall (C3 configuration). For both fillets, the maximum height above the endwall is positioned along the stagnation zone/line on the airfoil for the case with no swirl. Note that the two fillets studied are of the rounded type (Fig. 1(*b*)), which are known to increase horseshoe vortices instead of reducing them.

The flow through the nozzle is air. At the nozzle inlet, the air temperature is uniform at $T_i = 300$ K. The X-component (streamwise) velocity at the nozzle inlet has a one-seventh power-law profile. Though this profile may not be the most realistic, it is no worse than any other profile in serving as a reference. In an actual combustor, the velocity profile at the turbine inlet can be incredibly complicated with large-scale turbulence structures, depending on the combustor design and operation. In this study, the averaged inlet Mach numbers based on the X-component velocity M_x is 0.05. With an inlet temperature T_i of 300 K, the corresponding averaged X-component velocity U_i is 17.4 m/s, which give rise to a Reynolds numbers (Re) based on C_x of 438,000. The turbulence intensity and the turbulent viscosity at the nozzle inlet are taken to be 10% of U_i and 100 times the laminar viscosity, respectively [6]. The X-component velocity at the inflow boundary is kept constant when swirl is added.

In this study, swirl is introduced at the nozzle inlet by setting the Y-component velocity y to zero, by keeping the X-component

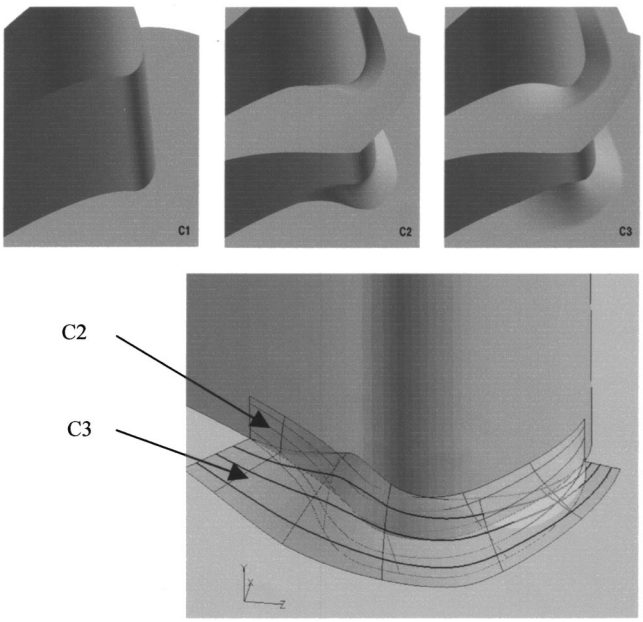

Fig. 4 Fillet configurations studied—C1: no fillet, C2: merge on airfoil, C3: merge on endwall

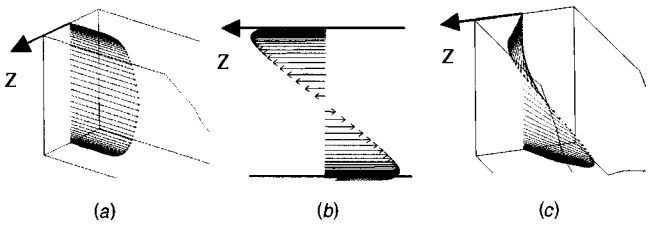

Fig. 5 Illustration of swirls investigated—(*a*) no swirl with 1/7th profile; (*b*) S1 swirl (2-D view); (*c*) S1 swirl (3-D view). S2 is just the opposite of S1 and so is not shown.

velocity u the same as the no swirl case, and by adjusting the Z-component velocity w to produce the desired swirl angle ($\theta = \tan^{-1} w/u$). Three swirls were simulated (Fig. 5): no swirl (baseline; referred to as NS), one linearly varying swirl angle with $\theta = +30$deg on the upper contoured endwall and -30 deg on the lower flat endwall (S1 swirl), and one linearly varying swirl angle with $\theta = -30$deg on the upper endwall and $+30$ deg on the lower endwall-(S2 swirl). The S1 swirl (Figs. 5(*b*) (*c*)) produces positive angles of attack on the airfoil from midspan to the upper endwall, and negative angles of attack from the midspan to the lower endwall. The S2 swirl produces negative angles of attack on the airfoil from mid-span to the upper endwall, and positive angles of attack from the midspan to the lower endwall.

All surfaces of the airfoil and endwalls are maintained at a constant temperature T_w of 270 K. The average static pressure at the nozzle outlet is maintained at 1 atm ($P_{\text{ref}} = 101325$ Pa). A summary of the cases studied is given in Table 1.

Problem Formulation

The flow and heat transfer in the nozzle guide vane described in the previous section are modeled by the ensemble-averaged conservation equations of mass (continuity), momentum (compressible Navier-Stokes), and total energy for a thermally and calorically perfect gas with Sutherland's model for viscosity and a constant Prandtl number. These ensemble-averaged equations were closed by the shear-stress-transport (SST) turbulence model (Menter [19,20]). The SST model is a blend of the k-ω model in the near-wall region and the k-ε model further away from the wall. Though the SST model uses the k-ω model in the near-wall region, dependence on freestream k has been eliminated. Also, a limiter is introduced to control overshoot in k with adverse pressure gradients so that separation is predicted more accurately.

The SST model does not require explicit damping in the near-wall region because ω becomes very large as the wall is approached. In this study, integration of the conservation equations as well as the turbulence model is made all the way to the wall (i.e., wall functions are not used). The boundary conditions (BCs) used on all walls are no-slip (zero velocity), isothermal walls

Table 1 Summary of cases studied[1]

Case No.	Fillet Configuration	Swirl Angle (degrees)
C1-NS	no fillet	no swirl
C1-S1	no fillet	S1: +30 to −30
C1-S2	no fillet	S2: −30 to +30
C2-NS	merge on airfoil	no swirl
C2-S1	merge on airfoil	S1: +30 to −30
C2-S2	merge on airfoil	S2: −30 to +30
C3-NS	merge on endwall	no swirl
C3-S1	merge on endwall	S1: +30 to −30
C3-S2	merge on endwall	S2: −30 to +30

[1] $M_x = 0.05$, $T_i = 300$ K, $T_w = 270$ K, $P_{\text{ref}} = 101325$ Pa

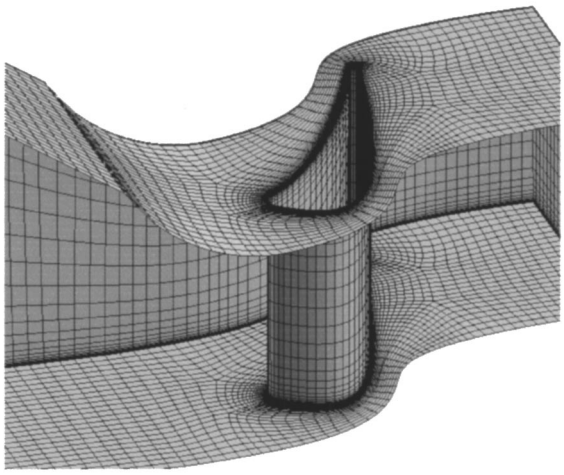

Fig. 6 Multiblock grid system used (not all grid lines shown)

(constant T_w), and zero turbulent kinetic energy. The dissipation rate per turbulent kinetic energy, ω, on the wall is set to $60_v/\beta\xi^2$, where β equals 3/40 and ξ is the normal distance of the first grid point from the wall in which that first point must be within a y^+ of one. Other BCs are as follows (see Fig. 2): At the inflow (nozzle inlet), the velocity, temperature, k, and ω are specified (see Problem Description). At the outflow (nozzle outlet), the average static pressure is specified, but the pressure gradients in the Y and Z directions are extrapolated. Also, extrapolated are density, velocity, k, and ω. At the two planes denoted as periodic boundaries, periodic boundary conditions are imposed.

Numerical Method of Solution

Solutions to the conservation equations were obtained by using a cell-centered finite-volume code called CFL3D (see Thomas et al. [21] and Rumsey and Vatsa [22]). This research code, developed at NASA-Langley Research Center, is widely used in the aerodynamics community, and has been validated by the authors for gas-turbine heat transfer studies (see, e.g., Lin et al. [23], Lin and Shih [24] and Shih and Sultanian [25]). In this code, all inviscid terms are approximated by the third-order flux-difference splitting of Roe [26] with limiters. Flux-difference was used so that numerical diffusion would be much smaller than physical diffusion. All diffusion terms are approximated conservatively by differencing derivatives at cell faces. Since only steady-state solutions are of interest, time derivatives were approximated by the Euler implicit formula. The systems of nonlinear equations that resulted from the aforementioned approximations to the space- and time-derivatives were analyzed by using a diagonalized alternating-direction implicit scheme (Pulliam and Chaussee [27]) with local time-stepping and three-level V-cycle multigrid (Anderson et al. [28]).

The domain of the nozzle-guide vane investigated (region within the solid lines in Fig. 2) is represented by a multi-block structured grid system made up of five H-H grids. Figure 6 shows the overall grid for the case without fillets, and Fig. 7 shows the grids with the fillets. The number of grid points used is 1,658,685 for all cases summarized in Table 1. The number and distribution of the grid points used were obtained by satisfying a set of rules established by developers of numerical methods and turbulence models to ensure accuracy. These rules include having at least five grid points within a y^+ of 5 with the first point within a y^+ of unity and having constant grid spacing next to walls for at least three grid points to resolve turbulent boundary layers. Other rules include aligning grid lines with flow direction as much as possible and keeping grid-aspect ratio near unity in regions with recirculating flow. As a further test, grids were refined by a factor of 25%

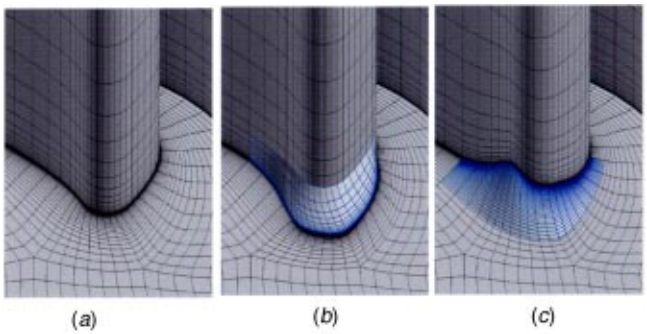

Fig. 7 Grid system about the airfoil/flat-endwall junction (not all grid lines shown)—(*a*) C1, (*b*) C2, (*c*) C3

in each direction for Cases C1-NS, C2-NS, and C3-NS. This test showed the predicted pressure difference in the stagnation pressure from inflow to outflow boundary normalized by the stagnation pressure at the inflow boundary to vary by less than 2% when compared to the more refined grids.

Results and Discussion

The objective of this study is to use CFD to investigate secondary flows induced by leading-edge airfoil fillet and inlet swirl and how they affect aerodynamic loss and surface heat transfer in a nozzle guide vane. The goal is not to minimize secondary flows, but rather to see if secondary flows can be harnessed in a positive way. To accomplish this, nine CFD simulations were performed (see Table 1). Results of these simulations are summarized in Table 2 and displayed in Figs. 8 to 14. In the following, we first examine if fillets and swirl can affect aerodynamic loss and surface heat transfer in a positive way. Afterwards, we examine the mechanisms involved.

Aerodynamic Loss and Surface Heat Transfer. Table 2 summarizes a number of integrated results obtained from all simulations performed: the change in the average stagnation pressure from the nozzle inflow boundary to the nozzle outflow boundary ($\Delta P_{\text{stagnation}}$), the net surface heat transfer rate (Q) on the airfoil and the two endwalls, and the percent change in mass flow rate through the nozzle guide vane relative to the baseline case of C1-NS (i.e., $\Delta\dot{m}/\dot{m}=(\dot{m}-\dot{m}_{\text{C1-NS}})/\dot{m}_{\text{C1-NS}}$). $\Delta P_{\text{stagnation}}$ is taken to be a measure of the aerodynamic loss. From this table, the effects of inlet swirl and leading-edge fillets on aerodynamic loss and surface heat transfer can be assessed.

Table 2 Summary of aerodynamic loss surface heat transfer, and change in mass flow rate[1]

Case No.	$\Delta P_{\text{stagnation}}$ (Pa)	Q_{contour} (W)	Q_{flat} (W)	Q_{airfoil} (W)	$\frac{\Delta\dot{m}}{\dot{m}}$
C1-NS	3006.2	3104.6	3075.1	2214.9	0.00%
C1-S1	1707.8	2076.9	2033.0	1948.8	1.74%
C1-S2	1668.8	1697.1	1727.3	1804.4	1.92%
C2-NS	1714.2	2083.7	2077.9	1909.6	1.74%
C2-S1	1865.2	1843.2	1773.2	1832.7	1.87%
C2-S2	1718.8	1830.7	1811.5	1819.1	1.87%
C3-NS	1688.7	1976.5	1953.6	1847.6	1.81%
C3-S1	1682.4	1803.0	1708.0	1810.0	1.90%
C3-S2	1706.3	1767.4	1763.5	1792.6	1.90%

[1]$\Delta P_{\text{stagnation}}$ is the change in stagnation pressure from nozzle inlet to exit (Fig. 2). Q_i is the net heat transfer rate from surface i (i denoted airfoil. contoured and flat endwall). $\Delta\dot{m}/\dot{m}=(\dot{m}-\dot{m}_{\text{C1-NS}})/\dot{m}_{\text{C1-NS}}$ is increase in mass flow rate relative to baseline case C1-NS.

The effects of inlet swirl without the complication of fillets can be evaluated by comparing C1-NS (baseline: no fillets and no swirl) with C1-S1 (no fillets, S1 swirl) and C1-S2 (no fillets, S2 swirl). This comparison shows that when swirl is added, $\Delta P_{\text{stagnation}}$ is reduced by 43.2% for S1 and by 44.5% for S2. Surface heat transfer is also greatly reduced by swirl. On the airfoil, Q is reduced by 12.0% for S1 and 18.5% for S2. On the endwalls, the reduction in Q is even more, 33.5% for S1 and 44.6% for S2. Thus, both S1 and S2 swirls are quite effective in reducing aerodynamic loss and surface heat transfer. Though aerodynamic loss is greatly reduced with S1 and S2 swirls, the increase in mass-flow rate through the nozzle-guide vane is quite small, less than 2%. This is because the boundary layers next to solid surfaces account for a small fraction of the flow-path cross section. Note that the results for S1 and S2 differ because of the contouring of one endwall upstream of the airfoil. Basically, if the contouring is on the top wall, then it is more advantage to have a swirl that produces a negative angle of attack for that endwall.

The effects of leading-edge fillets on aerodynamic loss and surface heat transfer can be evaluated by comparing C1-NS (baseline: no fillets and no swirl) with C2-NS (C2 fillet, no swirl) and C3-NS (C3 fillet, no swirl). This comparison shows that $\Delta P_{\text{stagnation}}$ is reduced by 42.9% for the C2 fillet and by 43.8% for the C3 fillet. For surface heat transfer on the airfoil, it is reduced by 13.8% for the C2 fillet and 16.6% for the C3 fillet. The reduction in Q on the endwalls is even more, 32.7% for C2 fillet and 36.4% for C3 fillet. Again, though aerodynamic loss decreases considerably, increase in mass flow rate is less than 2%.

Thus, it can be seen that both leading-edge airfoil fillet and inlet swirl can significantly reduce aerodynamic loss and surface heat transfer on its own. The effects of having both swirl and fillet can also be evaluated. By comparing, C2-S1 and C3-S1 with C1-S1, we see the C2 fillet tends to increase and the C3 fillet tends to decrease aerodynamic loss slightly. Both C2 and C3 fillets further reduced surface heat transfer with C3 fillet reducing slightly more. By comparing, C2-S2 and C3-S2 with C1-S2, we see both C2 and C3 fillets tend to increase instead of decrease aerodynamic loss and surface heat transfer by a small percentage. The poorer performance of C2 and C3 fillets for S2 swirl may indicate that fillet shape needs to be optimized with respect to swirl. Since the reduction in aerodynamics loss and surface heat transfer is small when we have both swirl and fillets,

Induced Secondary Flows. In this section, we examine the size and intensity of the secondary flows induced by inlet swirl and leading-edge fillets.

Since a reduction in aerodynamic loss and surface heat transfer for a given airfoil configuration/passage is often attributed to reduced secondary flows, we examine the secondary flows induced by inlet swirl and fillets. Figure 8 shows the cross-flow velocity vector and magnitude in an A-A plane perpendicular to the airfoil flow passage near the trailing edge of the pressure surface. From part (a) of this figure, the following can be observed. For the case without fillet and without swirl (C1-NS), the cross flow is asymmetric because of the contouring on the upper endwall. By adding S1 swirl (which produces greater positive angle of attack at the upper endwall), this asymmetry is greatly enhanced with a corresponding increase in size and intensity of the cross flow. With the S2 swirl (which produces a negative angle of attack at the upper endwall), the asymmetry is reversed with the cross flow being larger near the lower endwall (denoted as flat) instead of the upper endwall (denoted as contoured). Though S2 swirl produces considerably less cross flow than S1 swirl, both S1 and S2 produce more cross flow than the case without swirl.

By comparing C2-NS and C3-NS with C1-NS in Figs. 8(*a*), (*b*), and (*c*), it can be seen that adding fillets also does not reduce the cross flow. Cross-flow size and magnitude increased slightly with the C2 fillet and decreased slightly with the C3 fillet. If swirl is added with the fillets, then cross flows are enhanced but less than when there are no fillets.

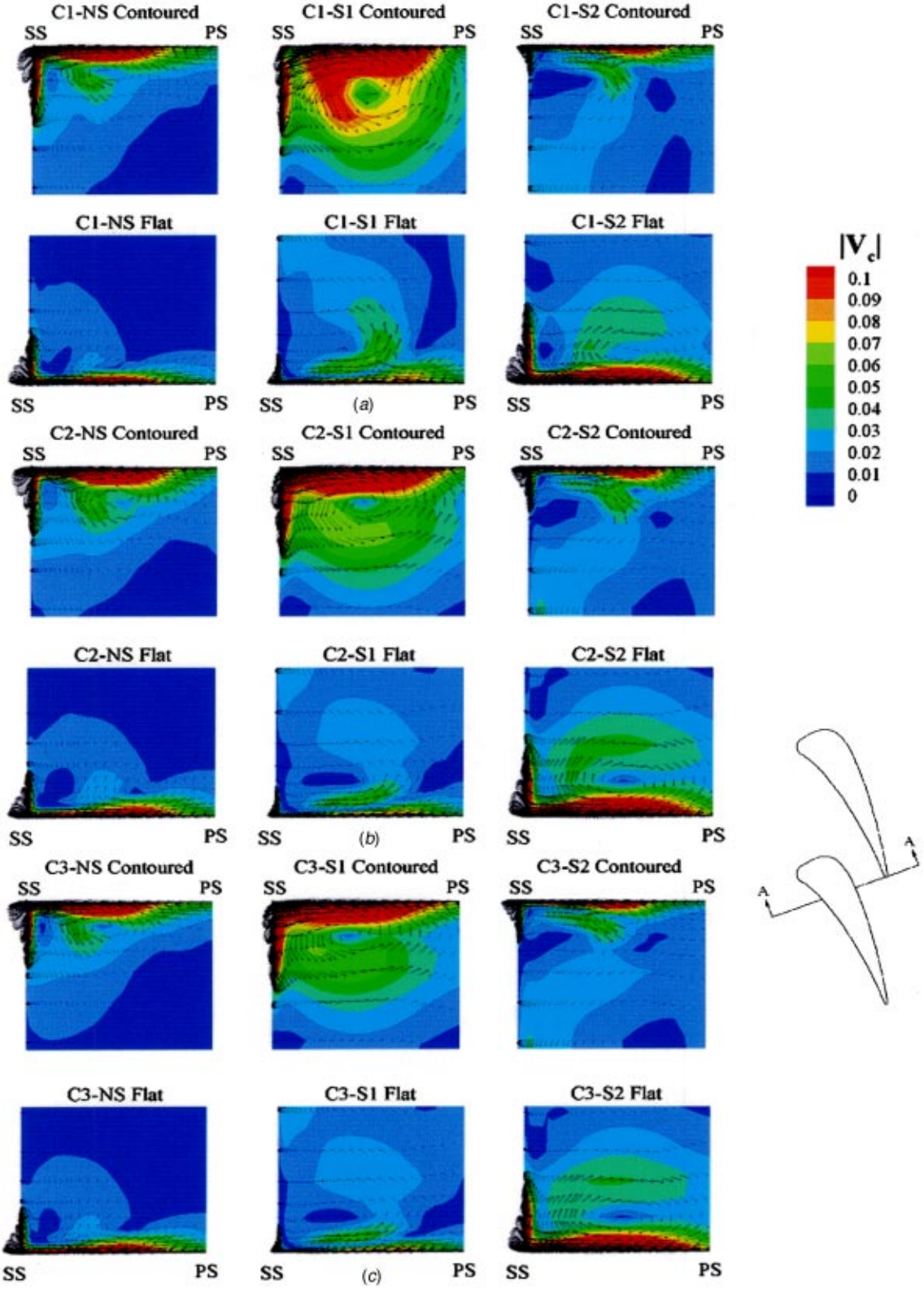

Fig. 8 Cross-flow velocity vector and magnitude in plane A-A

Figure 9 shows streamlines approaching the airfoil's leading edge near the airfoil/flat-endwall junction. From that figure, it can be seen that the fillets investigated do not eliminate or minimize horseshoe vortices. Not shown is that the swirls investigated also do not eliminate or reduce horseshoe vortices. Both swirl and fillet tend to push the horseshoe-vortex structure further upstream of the airfoil's leading edge. This is consistent with the observations made by previous investigators; e.g., [10–12].

Since horseshoe vortices at the airfoil's leading edge/endwall junction and cross flows at the airfoil's trailing edge were not

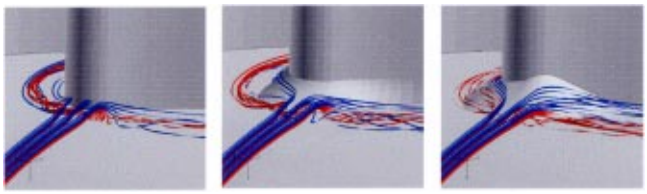

Fig. 9 Streamlines approaching the airfoil/flat-endwall junction, showing the generation of horseshoe vortices

diminished and yet aerodynamic loss and surface heat transfer are reduced significantly, this must mean that the mechanism responsible for reduction is much more complex than just the size and intensity of secondary flows. The fact that the size and intensity of secondary flow alone do not tell the whole story should not be unexpected. This is because the streamwise component of the velocity is so much greater than the cross-flow components. But, secondary flows, especially those near the airfoil/endwall junctions, could affect the flow structure and the evolution of the boundary layers, which do affect significantly the aerodynamic loss and surface heat transfer.

Flow-Structure Near Endwalls and Airfoil Surface. In this section, we examine the flow structure near the airfoil/endwall junction with and without swirl and with and without fillets. Figure 10 shows the pressure contours on the airfoil/flat endwall and the velocity vectors very close to those surfaces (y^+ between 10 and 20). From this figure, it can be seen that both swirl and fillets increase the pressure and the size of the high-pressure (stagnation) region on the endwall about the airfoil's leading edge. When there is no fillet, even S1 swirl with negative angle of attack increases the pressure there. With S2 swirl, which provides a positive angle of attack at the flat endwall, the increase is even more substantial. The imposed S1 and S2 swirls increase the magnitude and the size of the high-pressure region on the endwalls about the airfoil's leading edge because they increase the kinetic energy of the approaching flow, especially in the region close to the endwall (see Fig. 5). The fillets investigated increase the extent of the stagnation region on the endwalls by geometrically extending the airfoil forward. This increased pressure, whether from swirl or from the fillet, is why horseshoe vortices form further upstream of the airfoil. Figure 11 shows how swirl affects the streamlines very close to the endwalls. From this figure, the extent of the upstream influence of the airfoils's leading edge can clearly be seen. The increased size of the stagnation zones on the endwalls about the airfoil's leading edge lowers the flow speed and velocity gradients there, which in turns reduces turbulence production. This could be one of the main reasons for the reduced aerodynamic loss and surface heat transfer on the endwall. However, there may be other reasons or a point of diminishing returns. This is because Fig. 10 shows C2-S1, C2-S2, C3-NS, C3-S1, and C3-S2 to have larger regions of higher pressure on the endwall than those from C1-S1 or C2-NS, but have comparable aerodynamic loss and surface pressure.

On the airfoil surface, the swirls and fillets investigated shift the location of maximum pressure on the airfoil surface further downstream of the geometric leading edge near the endwalls. Moving the location of the stagnation zone downstream of the geometric leading edge, where the airfoil is flatter, can be significant. This is because the boundary-layer thickness at the stagnation zone is finite (>0), whose value depends on the surface curvature. As a first approximation, that thickness is $2.4\sqrt{\nu/\lambda}$ from the similarity solution of the Hiemenz flow, where ν is the effective kinematic

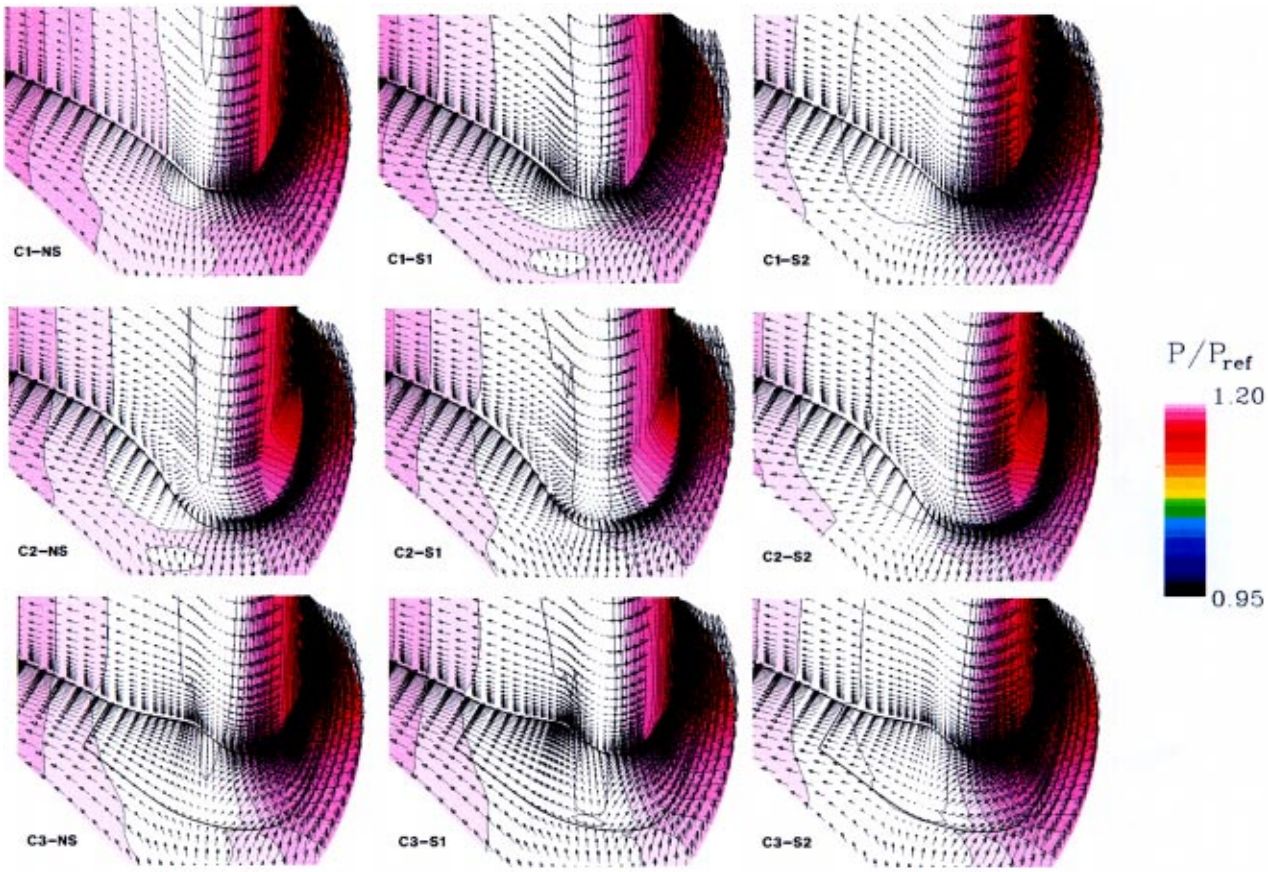

Fig. 10 Surface pressure and velocity vector near surface ($y+$ between 10 and 20) at airfoil/flat-endwall junction

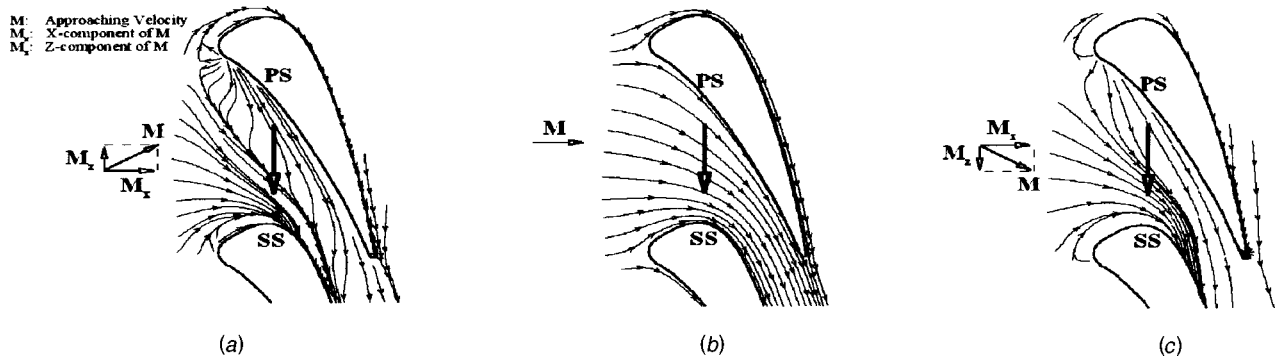

Fig. 11 Streamlines near the endwalls and the midplane with S1 swirl (no fillets)—(*a*) contoured endwall, (*b*) midplane, (*c*) flat endwall

viscosity and λ depends on surface curvature. If the surface is flat, then $\lambda = U_\infty$, where U_∞ is the speed of the approaching flow far upstream of the surface. For a cylindrical surface of radius r_0, λ can be approximated by $2U_\infty/r_0$. Thus, the flatter the surface, the larger is the boundary-layer thickness at the stagnation zone. With a larger boundary-layer thickness, the boundary-layer development on the airfoil from the stagnation zone will be different since the gradients will be less. This could explain why aerodynamic loss is reduced on the airfoil.

When there is swirl, Fig. 8 shows the cross flow from the pressure to the suction surface reaches the suction surface if the angle of attack from swirl is positive near that endwall. This is because when the angle of attack is positive, static pressure on the pressure surface near the endwall is increased, which increases the pressure difference between the pressure and suction surfaces. If the angle of attack is negative near an endwall, then Fig. 8 shows the cross flow to not reach the suction surface. This is because when the angle of attack is negative, the pressure on the suction surface near the endwall is increased. This increased pressure diverts flow away from the suction surface, causing the cross flow from the pressure surface to lift off from the endwall before reaching the suction surface. This can be seen in Figs. 8 and 11.

Distribution of Heat Transfer Coefficient. Figures 12–14 show the computed heat transfer coefficient on the airfoil and the endwall surfaces. When there is no swirl and fillets, Fig. 12 (C1-NS) shows that the heat-transfer coefficient is high on the airfoil's suction surface near the blade-to-blade throat region (i.e., where the normal distance between blades is the minimum) because of the high-speed flow there. Heat transfer rate is also high on the parts of the suction surface airfoil next to the endwalls because of the small-scale secondary flows there, transporting hotter fluid from the mainstream to the airfoil surface. On the endwalls, the heat transfer rate is high everywhere except about the stagnation region next to the pressure surface of the airfoil, where the velocities near the surface have been reduced. The foregoing explanations are the traditional ones, which apply for the case without swirl and fillets.

When there is swirl and fillet, Figs. 12–14 show that the locations of where heat transfer rate (q) are high and low are similar to the case without swirl and fillets with two exceptions. The first is the reduced size of the region with higher q, and the second is markedly reduced magnitudes of higher q. These differences can be linked to the secondary flow structures induced by swirl and fillets.

When there is swirl, fillet, or both, Figs. 12–14 show q to be reduced on the endwall about the airfoil's leading edge because of the increased size of the high-pressure (stagnation) region, which produced lower flow speeds and gradients. The maximum q on the airfoil's suction surface near the blade-to-blade throat region is reduced as well. Either swirl or fillet was also found to reduce q on the airfoil's pressure surface near the trailing edge.

When there is only the fillet and no swirl, q is still high on the parts of the suction surface airfoil next to the endwalls because of the small-scale secondary flows there, which is similar to the case without swirl and fillet (compare C1-NS with C2-NS and C3-NS). With swirl, q there can be reduced considerably, especially on the suction surface next to the flat (lower) endwall (compare C1-NS with C1-S1 and C1-S2).

When there is swirl and no fillet, Fig. 12 (C1-S1 and C1-S2) shows q to be higher on the lower or upper part of the airfoil suction surface depending upon S1 or S2 swirl. Also, one endwall has lower q than the other. The asymmetric heat transfer coefficient on the airfoil surface and endwalls is a clear sign of the effects of a large-scale secondary flow with a continuous versus a broken thermal boundary layer along the airfoil and endwalls. Swirl also reduces cross flow on one endwall.

Summary

Computations performed show that inlet swirl and leading-edge fillet can reduce significantly aerodynamic loss and surface heat transfer. This study shows that the size and the intensity of the secondary flows alone do not tell the whole story about aerodynamic and heat transfer. The swirls and fillets investigated were

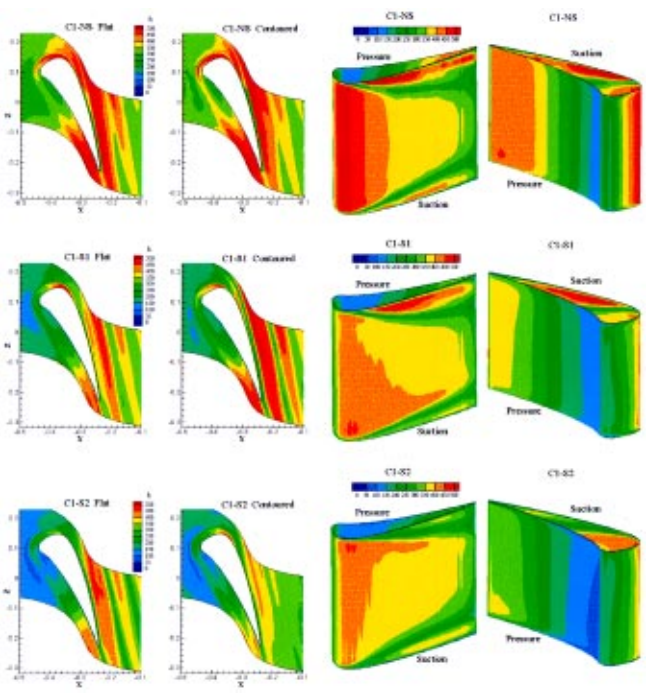

Fig. 12 Heat transfer coefficient: no fillet with and without swirl

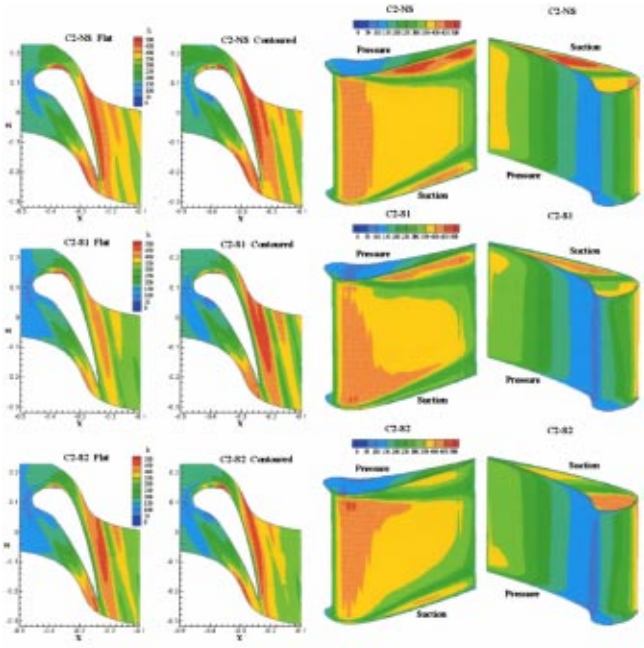

Fig. 13 Heat transfer coefficient: C2 fillet with and without swirl

found to increase the size of the stagnation region on the endwall about the airfoil's leading edge. It also modified the stagnation region on the airfoil pressure surface and the boundary development from there. Fillets accomplish this geometrically. Swirl accomplishes this by increasing kinetic energy near the endwall region and by modifying the angles of attack.

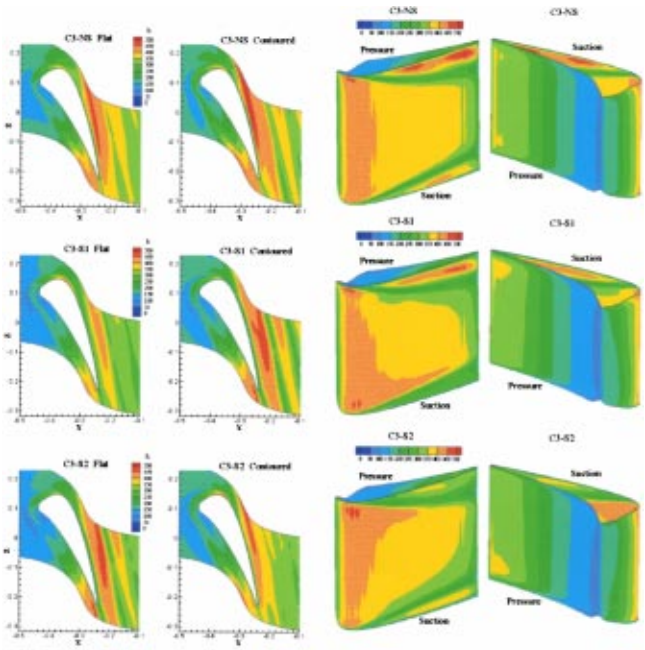

Fig. 14 Heat transfer coefficient: C3 fillet with and without swirl

Acknowledgment

This research was supported by the U.S. Department of Energy's AGTSR Program with Dr. R. Wenglarz and Dr. L.P. Golan as the Technical Monitors. The authors are grateful for this support.

Nomenclature

C1 = no airfoil fillet (Fig. 4)
C2 = fillet whose thickness fades on airfoil (Fig. 4)
C3 = filet whose thickness fades on endwall (Fig. 4)
C_x = airfoil chord length projected on X-coordinate
h = heat transfer coefficient ($h = q''/(T_w - T_i)$)
k = turbulent kinetic energy
M_x = average inlet Mach no. based on X-component velocity
NS = no swirl
P = static pressure or pitch (Fig. 2)
P_{ref} = reference static pressure (pressure at nozzle exit)
q'' = surface heat transfer per unit area ($-\kappa \partial T/\partial n$)
S1, S2 = nozzle inlet/outlet height (Fig. 2); also swirl 1/2 (Fig. 4)
T_w = wall temperature
T_i = hot gas temperature at nozzle inlet
ρ_i = inlet averaged density
U_i = average X-component velocity of mainflow at nozzle inlet
U_τ = friction velocity of mainflow ($\sqrt{\tau_w/\rho_w}$)
X, Y, Z = coordinate direction defined in Fig. 1 ($X = 0$ at nozzle exit)
y^+ = normalized distance normal to wall ($\rho U_\tau Y/\mu$)
κ = thermal conductivity
ν = kinematic viscosity
ρ = density
θ = swirl angle ($\cos^{-1} M_x/M_i$)
ω = dissipation rate per unit k

Subscripts and Superscripts

i = inlet conditions
w = wall

References

[1] Langston, L. S., 2000, "Secondary Flows in Axial Turbines—A Review," Int Symp Heat Transfer in Gas Turbine Systems.
[2] Deich, M. E., Zaryankin, A. E., Fillipov, G. A., and Zatsepin, M. F., 1960, "Method of Increasing the Efficiency of Turbine Stages and Short Blades," *Teploenergetika*, No. 2, Transaction No. 2816, Associated Electrical Industries (Manchester) Ltd., Apr.
[3] Ewen, J. S., Huber, F. W., and Mitchell, J. P., 1973, "Investigation of the Aerodynamic Performance of Small Axial Turbines," ASME Paper 73-GT-3.
[4] Dossena, V., Perdichizzi, A., and Savini, M., 1999, "The Influence of Endwall contouring on the Performance of a Turbine Nozzle Guide Vane," ASME J. Turbomach., **121**, pp. 200–208.
[5] Duden, A., Raab, I., and Fottner, L., 1999, "Controlling the Secondary Flow in Turbine Cascade by Three-Dimensional Airfoil Design and Endwall Contouring," ASME J. Turbomach., **121**, pp. 191–199.
[6] Burd, S. W., and Simon, T. W., 2000, "Flow Measurements in a Nozzle Guide Vane Passage with a Low Aspect Ratio and Endwall Contouring," ASME Paper 2000-GT-0213.
[7] Shih, T. I-P., Lin, Y.-L., and Simon, T. W., 2000, "Control of Secondary Flow in Turbine Nozzle Guide Vane by Endwall Contouring," ASME Paper 2000-GT-0556, May.
[8] Lin, Y.-L., Shih, T. I-P., Chyu, M. K., and Bunker, R. S., "Effects of Gap Leakage on Fluid Flow in a Contoured Turbine Nozzle Guide Vane," ASME Paper 2000-GT-0555, May 2000.
[9] Lin, Y.-L., Shih, T. I-P., Stephens, M. A., and Chyu, M. K., 2001, "A Numerical Study of Flow and Heat Transfer in a Smooth and a Ribbed U-Duct with and without Rotation," ASME J. Heat Transfer, **123**, pp. 219–232.
[10] Pierce, E. J., Frangistas, G. A., and Nelson, D. J., 1988, "Geometry-Modification Effects on a Junction-Vortex Flow," *Proc Symp Hydrodynamics Performance Enhancement for Marine Applications*, Oct. pp. 37–44.
[11] Davenport, W. J., Agarwal, N. K., Dewitz, M. B., Simpson, R. L., and Poddar, K., 1990, "Effects of a Fillet on the Flow Past a Wing-Body Junction," AIAA J., **28**(12), pp. 2017–2024.
[12] Pierce, E. J., and Shin, J., 1992, "The Development of a Turbulent Junction Vortex System," ASME J. Fluids Eng., **114**, pp. 559–565.

[13] Bancalari, E., and Nordlund, S., 1999, DOE AGTSR Aero-Heat Transfer Workshop III, Austin, Texas, February 10–12.
[14] Shih, T. I.-P., 2000, DOE AGTSR Aero-Heat Transfer Workshop IV, Minneapolis, Minnesota, October 11–13.
[15] Zess, G. A., and Thole, K. A., 2001, ''Computational Design and Experimental Evaluation of Using a Leading Edge Fillet on Gas Turbine Vane,'' ASME Paper 2001-GT-0404, June.
[16] Sauer, H., Mueller, R., and Vogeler, K., 2000, ''Reduction of Secondary Flow Losses in Turbine Cascades by Leading Edge Modifications at the Endwall,'' ASME Paper 2000-GT-0473, May.
[17] Goebel, S. G., Abuaf, N., Lovett, J. A., and Lee, C. P., 1993, ''Measurements of Combustor Velocity and Turbulence Profiles,'' Paper 93-GT-228, June.
[18] van Fossen, G. J., and Bunker, R. S., 2001, ''Augmentation of Stagnation Region Heat Transfer Due to Turbulence from a DLN Can Combustor,'' ASME J. Turbomach., **123**, pp. 140–146.
[19] Menter, F. R., 1991, ''Performance of Popular Turbulence Models for Attached and Separated Adverse Pressure Gradient Flows,'' AIAA J., **30**(8), pp. 2066–2071.
[20] Menter, F. R., 1993, ''Zonal Two-Equation k-ω Turbulence Models for Aerodynamic Flows,'' AIAA Pap. 93–2906.
[21] Thomas, J. L., Krist, S. T., and Anderson, W. K., 1990, ''Navier-Stokes Computations of Vortical Flows over Low-Aspect-Ratio Wings,'' AIAA J., **28**(2), pp. 205–212.
[22] Rumsey, C. L., and Vatsa, V. N., 1993, ''A Comparison of the Predictive Capabilities of Several Turbulence Models Using Upwind and Central-Difference Computer Codes,'' AIAA Pap. 93–0192.
[23] Lin, Y.-L., Schock, H. J., Shih, T. I-P., and Bunker, R. S., 2001, ''Effects of Inlet Conditions on Flow and Heat Transfer in Contoured Turbine Nozzle Guide Vanes,'' ASME Paper IMECE2001/HTD-24312, Nov.
[24] Lin, Y.-L., and Shih, T. I.-P., 2001, ''Film Cooling of a Semi-Cylindrical Leading Edge with Injection through Rows of Compound-Angled Holes,'' ASME Journal Heat Transfer, **123**, pp. 645–654.
[25] Shih, T. I.-P., and Sultanian, B., 2001, ''Computations of Internal and Film Cooling,'' *Heat Transfer in Gas Turbines*, ed., B. Suden and M. Faghri, WIT Press, Ashurst, Southhampton, Chapt. 5, pp. 175–225.
[26] Roe, P. L., 1986, ''Characteristic Based Schemes for the Euler Equations,'' Ann. Review of Fluid Mechanics, **18**, pp. 337–65.
[27] Pulliam, W. R., and Chaussee, D. S., 1981, ''A Diagonal Form of an Implicit Approximate Factorization Algorithm,'' J. Computational Physics, **39**, pp. 347–363.
[28] Anderson, W. K., Thomas, J. L., and Whitfield, D. L., 1988, ''Multigrid Acceleration of the Flux-Split Euler Equations,'' AIAA J., **26**(6), pp. 649–654.

Assessment of Various Film-Cooling Configurations Including Shaped and Compound Angle Holes Based on Large-Scale Experiments

J. Dittmar
e-mail: jan.dittmar@its.uni-karlsruhe.de

A. Schulz

S. Wittig

Institut für Thermische Strömungsmaschinen,
Universität Karlsruhe (TH),
76128 Karlsruhe, Germany

The demand of improved thermal efficiency and high power output of modern gas turbine engines leads to extremely high turbine inlet temperatures and pressure ratios. Sophisticated cooling schemes including film cooling are widely used to protect vanes and blades from failure and to achieve high component lifetimes. Besides standard cylindrical cooling hole geometry, shaped injection holes are used in modern film cooling applications in order to improve cooling performance and to reduce the necessary cooling air flow. However, complex hole shapes may lead to manufacturing constraints and high costs. This paper evaluates some film-cooling injection geometry with different complexity. The comparison is based on measurements of the adiabatic film-cooling effectiveness and the heat transfer coefficient downstream of the injection location. In total, four different film-cooling hole configurations are investigated: a single row of fanshaped holes with and without a compound injection angle, a double row of cylindrical holes and a double row of discrete slots both in staggered arrangement. All holes are inclined 45 deg with respect to the model's surface. During the measurements, the influence of coolant blowing ratio is determined. Additionally, the influence of cooling air feeding direction into the fanshaped holes with the compound injection angle is investigated. An infrared thermography measurement system is used for highly resolved mappings of the model's surface temperature. Accurate local temperature data is achieved by an in-situ calibration procedure with the help of single thermocouples embedded in the test plate. A subsequent finite elements heat conduction analysis takes three-dimensional heat fluxes inside the test plate into account. [DOI: 10.1115/1.1515337]

Introduction

In modern gas turbines sophisticated cooling schemes including film cooling are widely used to protect the vanes and blades of the first turbine stages from failure and to achieve high life cycles. In film-cooling applications, injection from discrete holes is commonly used to generate a coolant film on the blade's surface. In an attempt to improve the cooling process, recent attention has been given to contouring the injection hole geometry. Modern manufacturing technologies like precise electric-discharge machining or laser drilling enable form the injection hole in more complex shapes.

Many of the earlier studies of film cooling considered injection from a single row of discrete holes. Due to the three-dimensional character of the flow field downstream of the coolant injection the cooling effectiveness decreases compared to injection from a continuous slot. In order to improve the lateral distribution of the injected coolant and to approach a two-dimensional film-cooling situation, more studies were focused on the injection from a double row of cylindrical holes (Jabbari et al. [1], Jubran and Brown [2], Jubran and Maiteh [3]). In general, the results show that for the same injected mass flow rate per unit span the double row arrangement provides better cooling effectiveness compared to injection from a single row. Staggered rows show better performance than rows with inline arrangement. The gain in effectiveness is attributed to the lower penetration of the coolant jets because of lower momentum ratio resulting from the increased injection area and better lateral spreading of the cooling air. Increasing the distance between the two rows give a significant decrease to both local and lateral averaged effectiveness, especially close behind the downstream row. A compound angle orientation of the holes, especially of the second row, increases cooling effectiveness (Ligrani et al. [4]). Recent studies on film-cooling holes with a diffuser-shaped expansion at the exit portion of the hole (''fan-shaped'' holes) have shown a promising improvement of the film cooling performance. Various research groups (Goldstein et al. [5], Gritsch et al. [6,7] Makki and Jakubowski [8], Yu et al. [9], Reiss and Bölcs [10]) investigated film-cooling effectiveness with injection from different hole shapes, including holes with a lateral or forward expanded exit part. They all found higher effectiveness values for the shaped holes compared to cylindrical holes with the same arrangement. The lateral expanded holes show much better lateral spreading of the injected coolant and hence more uniform distribution of effectiveness. Due to the reduced jet exit momentum, shaped holes show less penetration of the coolant jet into the mainstream and reduced velocity gradients in the mixing region (Thole et al. [11]). Nevertheless, increased manufacturing effort has to be done when using shaped hole geometry.

The achievable surface temperature reduction by using film cooling on a turbine blade depends not only on the injection hole geometry, but also on the overall design of the film-cooling configuration. The present study aims to assess the cooling performance of two simple hole geometry, arranged in an optimum way as a staggered double row and two shaped geometry arranged in a

Contributed by the International Gas Turbine Institute and presented at the International Gas Turbine and Aeroengine Congress and Exhibition, Amsterdam, The Netherlands, June 3–6, 2002. Manuscript received by the IGTI, November 21, 2001. Paper No. 2002-GT-30176. Review Chair: E. Benvenuti.

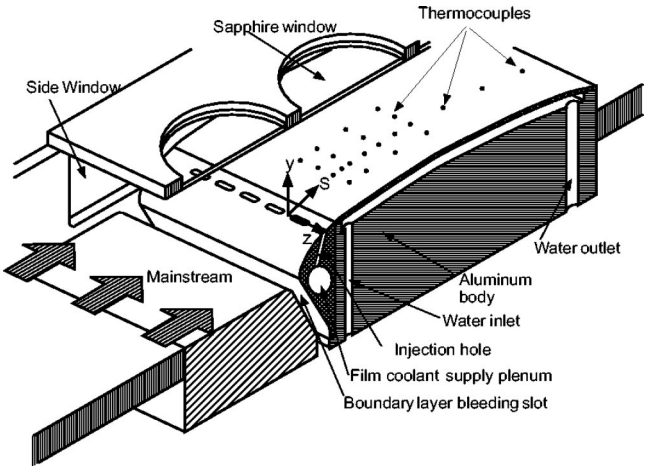

Fig. 1 Experimental setup and large-scale film-cooling model

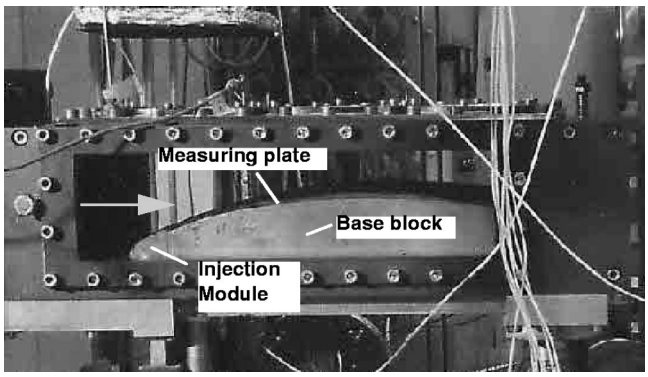

Fig. 3 Photo of assembled suction side film-cooling test section

single row. Adiabatic effectiveness and heat transfer coefficient results are compared for equal injected coolant mass flow per unit span.

Experimental Setup

The experiments presented in this paper are conducted on a model of a suction side of an actual turbine guide vane assembled in an open loop atmospheric wind tunnel, see Fig. 1. Its contoured shape has been designed in order to simulate almost realistic distributions of Reynolds number and acceleration parameter k on the model's surface, as shown in Fig. 2. The Reynolds number based on chord length at the location of injection is about 5.5×10^5 and about 7330 based on the injection hole diameter. The model basically consists of three parts: a base block, an interchangeable injection module, and a contoured test plate for surface temperature measurements. The test plate is made of a high-temperature plastic (TECAPEEK©) with a low thermal conductivity of about 0.43 W/m·K. In the top wall three sapphire windows are inserted to enable optical access to the test model. Figure 3 shows a photo of the contoured test model assembled inside the test section. In this study the cooling performance of four different injection configurations is compared: a double row of cylindrical holes (CONF1), a double row of discrete slots (CONF2), a single row of straight fan-shaped holes (CONF3) and a single row of compound angle fan-shaped holes (CONF4).

Details of the hole geometry are shown in Fig. 4. The holes are placed at 10% of the chord length referring to the stagnation point of the blade model and feature a streamwise injection angle of 45 deg. In each row the holes are separated 4 diameters in lateral direction. The total length of the holes is 6 diameters. All holes have a diameter of 4 mm at the inlet part of the hole except for the slot configuration. In this case, the slot height B is 2.5 mm, the slot width is 3.06 mm, which results in the same inflow cross section compared to the cylindrical holes. The two fan-shaped hole configurations feature a cylindrical hole inlet with a length of two diameters. Following, the hole is laterally expanded with an opening angle of 14 deg on each side. The injection configuration CONF4 comprises a compound angle orientation. The additional lateral injection angle is 35 deg with respect to the incoming mainstream flow. The film cooling holes for CONF1-CONF3 are supplied with cooling air by means of a large cylindrical chamber inside the nose part of the model to provide for plenum conditions. In case of CONF4 with the compound angle orientation, two different feeding crossflow directions are investigated: case CONF4.1 represents ''direct'' coolant inflow and case CONF4.2 represents ''opposing'' coolant inflow (see Fig. 4, CONF4).

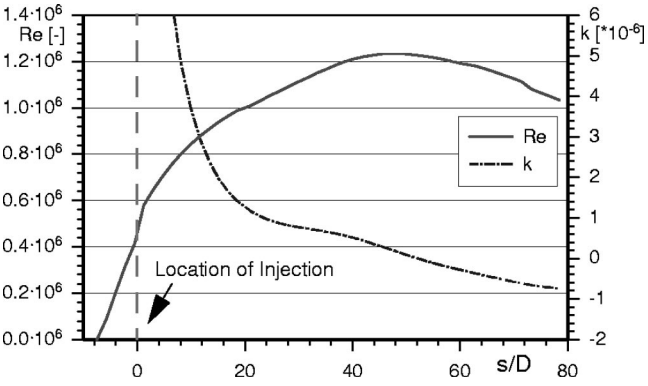

Fig. 2 Distributions of Reynolds number and acceleration parameter *k*

Measurement Technique and Data Processing

Surface temperature measurements are performed by means of an infrared thermography system (AGEMA© Thermovision 900 SW). The IR-system consists of a optical scanner which directs the incoming infrared radiation line by line onto the detector working in a wavelength bandwidth of 2–5.4 μm. The scanner is mounted above the test section of the wind tunnel and reads the surface temperature information through the sapphire windows. The output signal of the IR-detector is digitized by a processing computer in a frame of 136×272 pixels corresponding to a spatial resolution of 0.65×0.65 mm with the optical setup used in the experiments. The surface of the contoured test plate is covered with a black paint with a well-known emissivity of $\varepsilon = 0.95$. In order to get quantitatively accurate wall temperature data, the radiation data from the IR-system is re-calibrated using 12 thermocouples embedded flush with the surface. A calibration routine has been developed taking reflected ambient radiation as well as transmission losses into account. A detailed description of the applied IR-calibration procedure is presented in Dittmar et al. [12].

In contrast to two-temperature heat transfer problems, film cooling is dominated by three temperatures: the temperature of the hot gas, the temperature of the injected cooling film, and the resulting wall temperature. The heat transfer to a film-cooled surface is commonly described by

$$\dot{q}_w = h_f \cdot (T_{aw} - T_w) \tag{1}$$

with the adiabatic wall temperature T_{aw} as a reference temperature. The adiabatic wall temperature is typically presented in terms of the nondimensional film-cooling effectiveness (Goldstein [13])

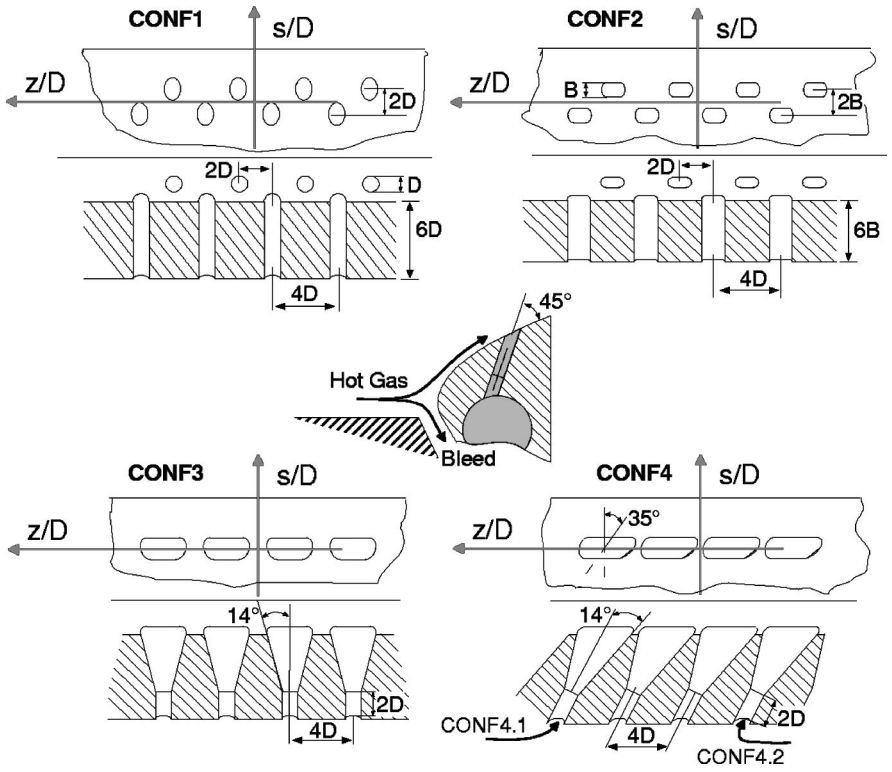

Fig. 4 Investigated film-cooling injection configurations

$$\eta = \frac{T_m - T_{aw}}{T_m - T_c} \tag{2}$$

Thus, the film-cooling effectiveness describes the cooling potential of the injected film without any heat flux into the wall. The heat transfer coefficient h_f in Eq. (1) considers the influence of the coolant injection on the heat transfer process due to the modified fluid dynamics. It does not depend on the temperature boundary layer condition. Both of these two parameters have to be known to calculate the wall heat flux accurately.

In a real film-cooling situation it is not possible to separate the two parameters η and h_f. Alternatively, the heat transfer to the wall can be describes as follows:

$$\dot{q}_w = h(\theta) \cdot (T_m - T_w) \tag{3}$$

where T_m denotes the mainstream temperature as a reference value. Here, all the effects of the cooling film are described with the value of the heat transfer coefficient $h(\theta)$ as a function of the nondimensional wall temperature θ (Choe et al. [14])

$$\theta = \frac{T_m - T_c}{T_m - T_w} \tag{4}$$

Metzger et al. [15] and Gritsch et al. [16] proved, that the relationship $h(\theta)$ is linear and valid even in realistic gas turbine conditions. The linear function can be specified by the equation

$$h(\theta) = h_f \cdot (1 - \eta\theta) \tag{5}$$

which is visualized in Fig. 5. The point of intersection of the straight line with the abscissae represents the reciprocal value of the film cooling effectiveness (adiabatic condition). The intersection with the ordinate represents the heat transfer coefficient h_f. Within the experiments, the linearity of Eq. (5) is used to determine the two basic film cooling parameter η and h_f. Therefore, two different sets of measurements of the surface temperature are performed. The first one is made at nearly adiabatic conditions without any additional cooling of the test plate. At identical flow conditions, a second measurement is made where the bottom side of the test plate is cooled with water in order to reduce the wall temperature T_w, and thereby the value of θ. In both cases the surface temperature data obtained with the IR-camera system is subsequently used to perform a three dimensional finite element heat flux analysis of the test plate. The calculated heat flux is then used to determine local values for $h(\theta)$ at each case. The radiative heat exchange inside the test section is taken into account to correct all the heat transfer data. Finally, the two $h(\theta)$-values are fitted with a straight line and the film-cooling effectiveness η as well as the heat transfer coefficient h_f are extrapolated using the fitted line. An estimation of the uncertainty level using a one dimensional heat flux analysis determines an overall error of 10% for the h_f value.

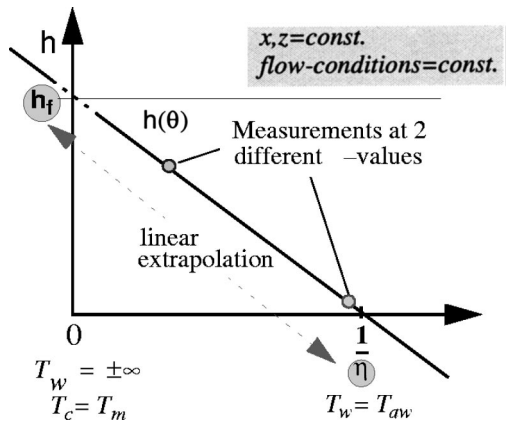

Fig. 5 Using the linear superposition principle for the determination of η and h_f

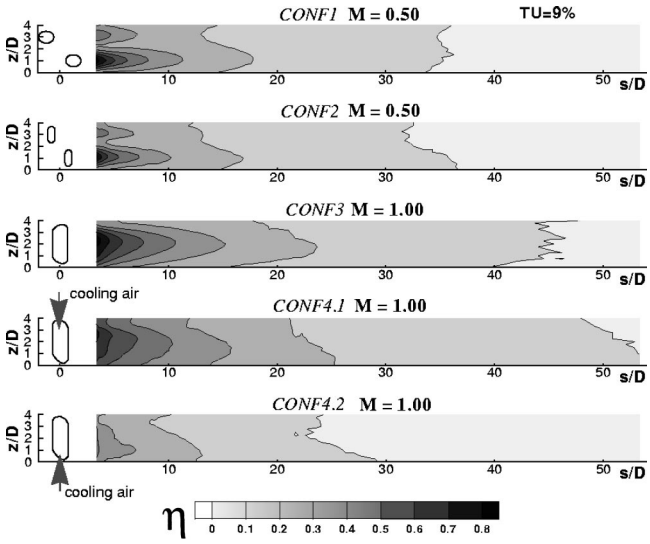

Fig. 6 Local adiabatic effectiveness η at low blowing rate

Results and Discussion

Using the measurement technique and post processing procedure described above, film-cooling effectiveness and heat transfer coefficient data is determined for all of the injection hole geometry. During the experiments the blowing ratio M was varied in the range of 0.2 to 1.5 in case of the double row configurations and in the range of 0.5 to 3.0 for the single row configurations. The definition of the blowing rate M which is given in the Nomenclature, is based on the inlet area of the injection holes as a reference area. The inlet mainstream turbulence level has been adjusted to 9% by the use of a special grid in front of the test model. The temperature ratio of mainstream gas to coolant gas T_m/T_c has been kept constant at a value of 1.3 during all the experiments by heating up the mainstream gas to about 440 K using electrical heaters.

Adiabatic Film-Cooling Effectiveness Results. Figures 6 and 7 show local pattern of the adiabatic film-cooling effectiveness downstream of the point of injection up to $s/d=50$. Results for a low and a high blowing rate value are plotted. For the single rows with fan-shaped holes blowing rate values of $M=1.0$ and 3.0 has been chosen. For the double rows a blowing rate of $M=0.50$ and 1.5 has been chosen, which represents the same amount of total injected coolant mass flow per unit span for all hole configurations.

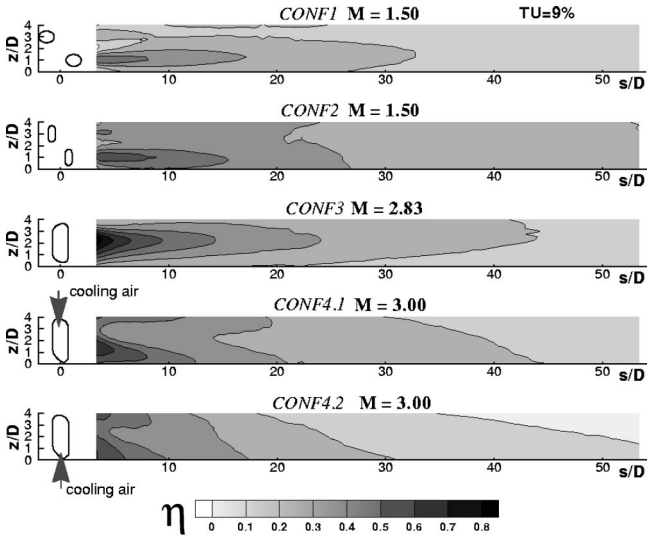

Fig. 7 Local adiabatic effectiveness η at high blowing rate

For the low blowing rate of $M=0.50$ or 1.0, respectively, the shaped holes of CONF3 and CONF4.1 show the best effectiveness results. Due to the lateral expansion of the holes, the injected coolant is evenly spread which results in a quite uniform surface temperature distribution. The most uniform distribution of the injected cooling air is found for CONF4.1. Due to the compound angle injection, the lateral spreading of the coolant on the surface is improved which results in higher effectiveness values and a homogeneous temperature distribution. The results for CONF4.2 with the ''bent'' coolant inflow into the cooling holes show substantially lower effectiveness values compared to CONF4.1 with the direct coolant feeding direction. The effectiveness is even lower than for the straight fan-shaped hole CONF3. This indicates that the coolant crossflow direction has an considerable effect on the cooling performance of injection holes with a lateral injection angle. If the cooling air is provided from the ''opposing'' direction, the inflow into the cooling hole is disturbed and the coolant does not follow the contour of the shaped holes precisely which results in decreased surface temperature protection.

Compared to the fan-shaped configurations CONF3 and CONF4.1 the double row with the cylindrical holes CONF1 shows in general lower effectiveness values. Especially in the near-hole region, the coolant is not as uniform distributed as in case with the fan-shaped holes. The cold streaks of the single coolant jets are clearly visible and there is a small region between the holes with little cooling performance. Further downstream, the lateral effectiveness distribution is more uniform and is approaching the performance for the fanshaped holes. Looking at the double slot configuration CONF2 at a blowing rate of $M=0.50$ a similar surface temperature pattern is found. Due to the stretching of the holes and the staggered arrangement of the two rows a wider geometrical coverage is achieved. However, the results show an improved lateral spreading of the cooling air, but little smaller local effectiveness values.

Figure 7 shows effectiveness results at high blowing rates of $M=1.5$ and $M=3.0$, respectively. Here, the fan-shaped hole configurations show the advantage of the reduced jet exit momentum due to the increased hole exit area. The coolant jet stays attached to the surface and gives a good protection, especially in the near holes region. CONF4.1 shows similar effectiveness performance compared to CONF3, even though the cooling air is not that concentrated in the middle axis, but more laterally distributed. As in the case with the low blowing rate, CONF4.2 show worse effectiveness performance which is caused by the harmful cooling air inlet conditions. The cylindrical hole configuration CONF1 shows a distinctive decrease in effectiveness in the near-hole region. Due to the high exit momentum, the cooling jets start to separate from the wall which is more pronounced for the first row due to a blockage effect of the second row. A wake region right behind the injection is established and hot mainstream gas is transported to the wall caused by complex vortex generation, mainly in the shear layer between jet and mainstream. The use of a double row of slots in CONF2 seems to find a remedy for this problem at high blowing rates. Even though the jet exit momentum is the same for both double row configurations, the slots show much better effectiveness data. Due to the lateral extension of the slot and the increased corroding surface for the hot mainstream the jet is better deflected and stays closer to the surface.

The different performance of the configurations 1–4 at small, moderate, and high blowing rates is emphasized looking at the lateral averaged effectiveness data, see Figs. 8(*a*), (*b*), and (*c*). The averaging is done over the range of 1 pitch including a distance of four hole diameters

$$\eta_{\mathrm{Lat}}=\frac{1}{4}\cdot\int_{z/D=0}^{z/D=4}\eta(s/D,z/D)d(z/D) \tag{6}$$

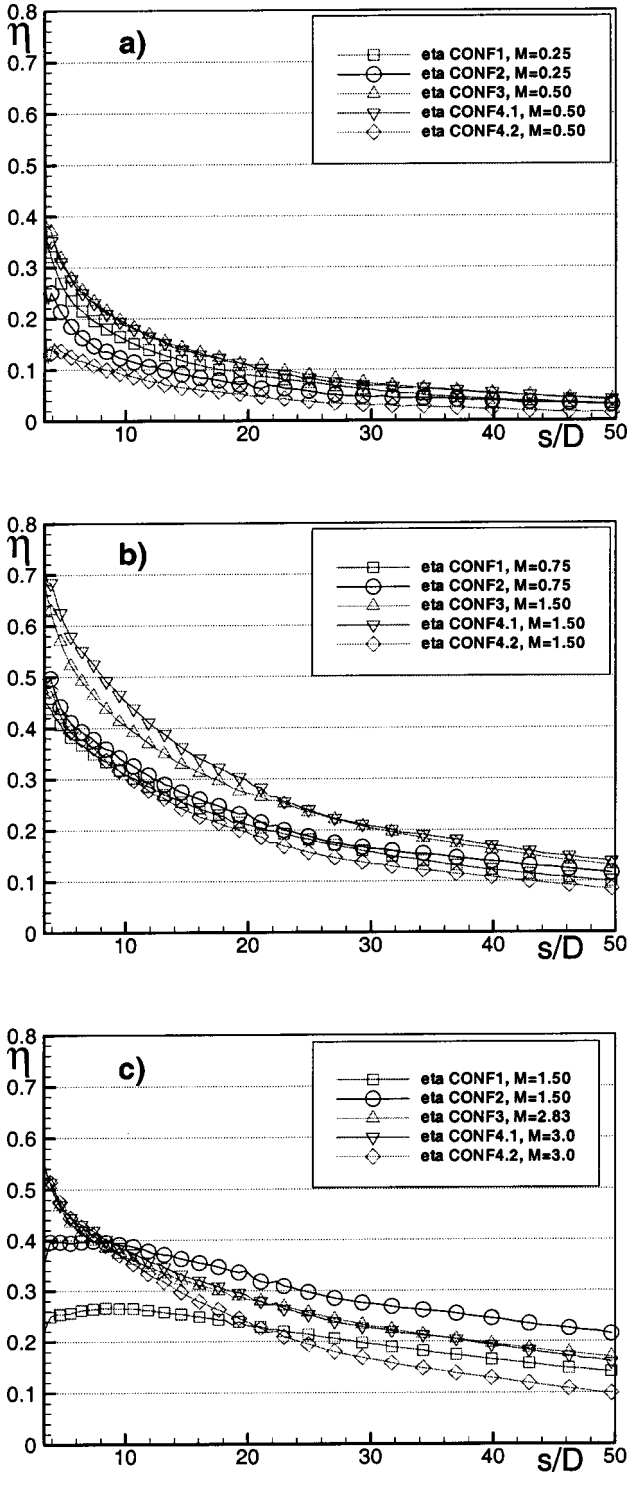

Fig. 8 Lateral averaged adiabatic effectiveness for small (*a*), medium (*b*), and high (*c*) blowing rate

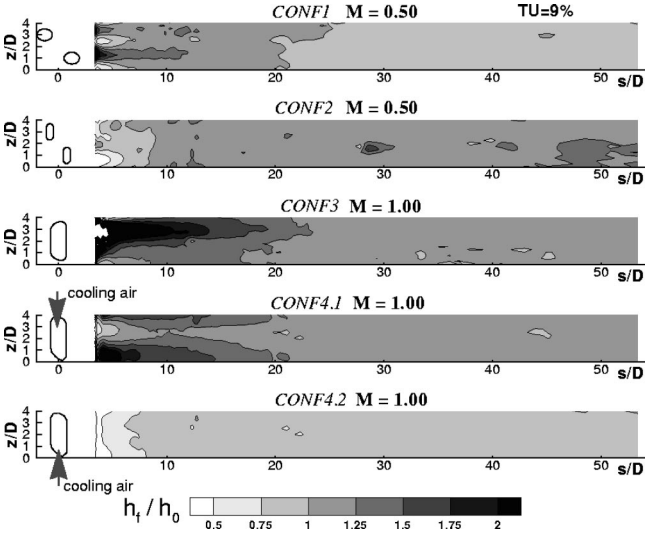

Fig. 9 Nondimensional local heat transfer coefficient h_f/h_0 at a blowing rate of $M=0.5$ and 1.0 respectively

At low blowing rates all configurations show quite similar lateral averaged effectiveness performance. At medium blowing rates the fan-shaped holes show best effectiveness data except for CONF4.2 where the disadvantageous coolant inflow causes a severe drop in effectiveness. The improvement in lateral averaged adiabatic film-cooling effectiveness when using shaped holes is caused mainly by the increased lateral spreading of the injected cooling air and the better coverage of the surface. At high blowing rates the shaped hole configurations show clearly improved effectiveness data compared to the cylindrical holes in CONF1 which is caused by the depressed jet lift off. This jet lift-off behavior can be drastically improved when using slots instead of holes (CONF2). Figure 8(*c*) indicates the improvements achieved by the double row of slots. Close behind the injection the effectiveness in still lower than for the shaped holes. But due to the higher coolant momentum the cooling film is well transported downstream and the decay of effectiveness in streamwise direction is not as strong as for the shaped holes. This results in high effectiveness values of 0.3 even at $s/D=30$ compared to about 0.25 for CONF3 and 4.2.

Heat Transfer Coefficient Results. Besides the effectiveness data the heat transfer coefficient with coolant injection h_f is of interest when discussing the total film-cooling performance. The parameter h_f gives information about the influence of the coolant injection on the heat transfer process due to changes in the fluid dynamic situation in the boundary layer. It is not dependent on the cooling air temperature, but only on the fluid dynamic boundary conditions. The heat transfer coefficient data is determined by using the linear relationship in Eq. (5) and is extrapolated from the two single measurements at different θ-values.

Figures 9 and 10 show local heat transfer coefficient pattern for all investigated hole configurations exemplarily for two blowing rates. Here, the heat transfer coefficient with film injection h_f is normalized with the value without any injection h_0 and with covered filmholes to visualize the local influence of the coolant injection on the heat transfer behavior. The reference case h_0 was measured within a separate experimental run. A very thin aluminum tape was used to thoroughly cover the filmholes. The mainstream turbulence level was again adjusted to 9% during the measurements.

The results show different influence of the hole geometry on the development of the heat transfer coefficient. In general, one can say that the impact of the injection is mostly pronounced in an area close behind the injection. CONF1 show an increase in heat transfer on the surface up to a streamwise distance of $s/D=20$. In contrast to this, the slot configuration CONF2 show a little decrease of h_f in this area despite the fact that the hole arrangement is very similar. This is attributed to the different flow field character and the different jet-mainstream interaction of the cylindrical holes and slots. The coolant injection from cylindrical holes causes strong shear layers and a strong kidney vortex pair which is directing hot mainstream gas beneath the coolant jet (Thole et al. [11]). On the other hand, the slot configuration seems to generate much weaker kidney vortex pairs which results in re-

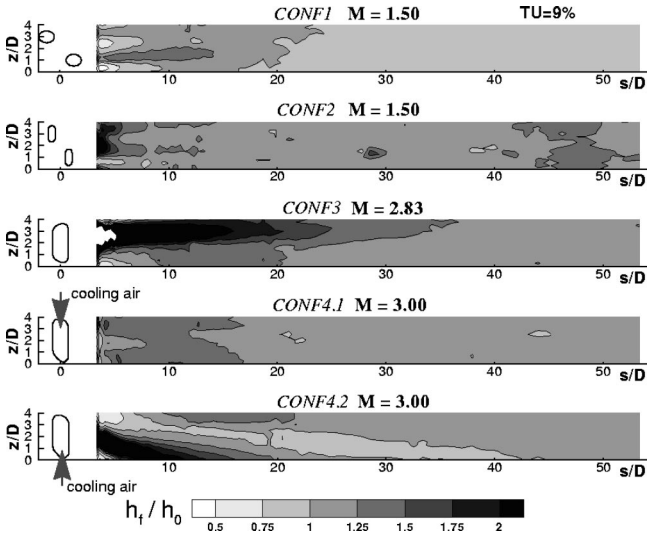

Fig. 10 Nondimensional local heat transfer coefficient h_f/h_0 at a blowing rate of $M=1.5$ and 3.0, respectively

duced heat transfer coefficients on the surface. At higher blowing rates the two double row configurations show similar values for h_f/h_0 in the near hole region. The two fan-shaped configurations CONF3 and 4 both show a significant increase in the heat transfer coefficient when cooling air is injected. In case of CONF3, this increase in heat transfer is reinforced at high blowing rates. In case of CONF4.1, high blowing rates of $M=3.0$ show lower values of h_f/h_0 compared to low and medium blowing rates. The strong dependency of the heat transfer coefficient on the coolant injection in case of the shaped holes is attributed to the transport of increased turbulent kinetic energy which is produced inside the holes. As the holes comprise a large lateral expansion angle of 14 deg and an additional lateral injection angle of 35 deg, the flow field inside the holes is quite complex and flow separation might occur at some locations. The increased turbulent kinetic energy inside the hole is transported into the boundary layer with the cooling air downstream of the injection, and thus causes higher heat transfer values.

In contrast to CONF3 and 4.1, CONF4.2 shows decreased heat transfer values at low blowing rates, but significantly increased values at high blowing rates. This is again attributed to the nonideal flow inside the hole, especially in this case, where the cooling air feeding direction is unfavorable.

Figure 11 show lateral averaged data for the nondimensional heat transfer coefficient. Like for the adiabatic effectiveness results in Fig. 8, curves are presented for a low (*a*), medium (*b*), and high (*c*) blowing rate. Increasing the blowing rate causes an increase in h_f. Especially the medium blowing rate of $M=0.75$ shows high heat transfer data for two fan-shaped geometries. The heat transfer augmentation is mainly pronounced in the area close to the injection holes, where the heat transfer coefficient can increase up to 60 %. More downstream the heat transfer enhancement is weak and in the magnitude of 10–15% for most of the measured cases, except for CONF2 that shows a heat transfer enlargement of about 20% even at the end of the measuring plate. It is remarkable that the double row configuration CONF1 show a decrease in the heat transfer coefficient in the far downstream region even at high blowing rates. This is in contrast to the single row configuration CONF3 and CONF4.1 where the coolant injection always causes an increase in heat transfer. This opposed behavior might be attributed to the different interaction with the mainstream boundary layer at the point of injection. As the boundary layer is very thin ($\delta_{99}/D \approx 0.2$) the injection of cooling air causes an increase in the boundary layer thickness. In case of an injection with low turbulence transport and production, this causes

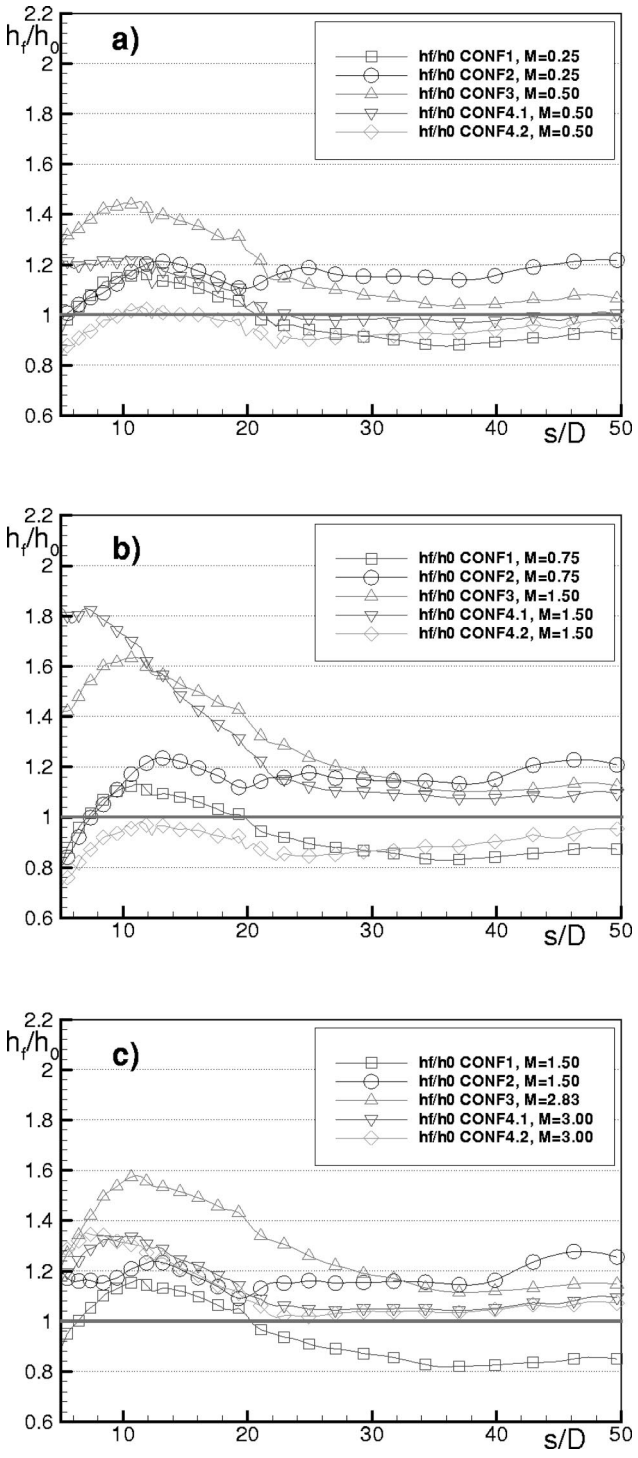

Fig. 11 Nondimensional lateral averaged heat transfer coefficient h_f/h_0 for small (*a*), medium (*b*), and high (*c*) blowing rate

a decrease in heat transfer as in the case of CONF2. On the other hand, if more turbulent kinetic energy is transported into the boundary layer as it assumed for CONF3 and 4.1 due to coolant separation inside the filmholes, the heat transfer is increasing. The flow situation for CONF4.2 is more complex. Here, the results show low heat transfer at low blowing rates and increase values at a blowing rate of $M=3.0$. To fully understand the complex interaction of injected cooling air and the boundary layer situation and its influence on the heat transfer coefficient, more detailed flow studies including the flow inside the cooling holes are necessary.

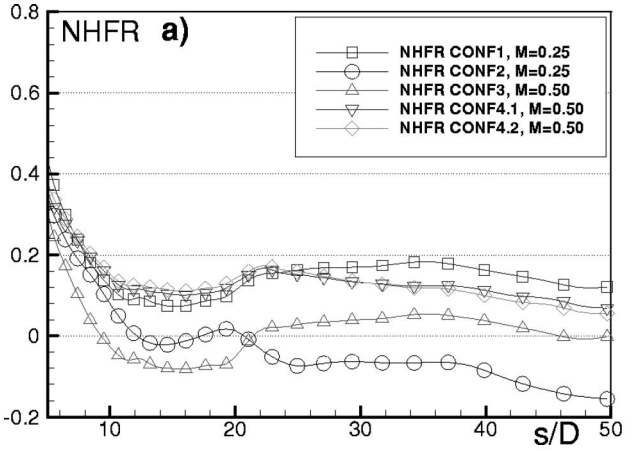

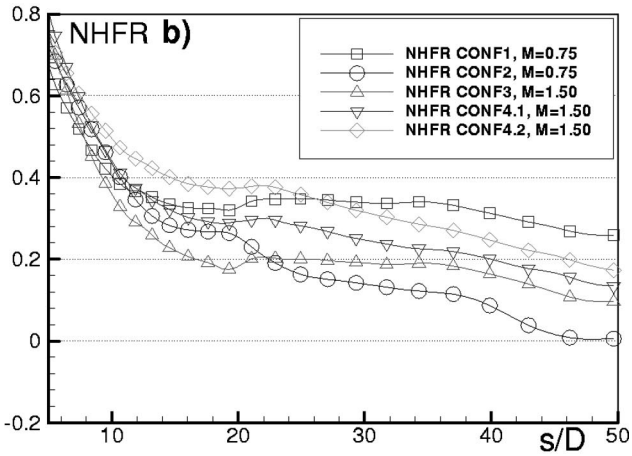

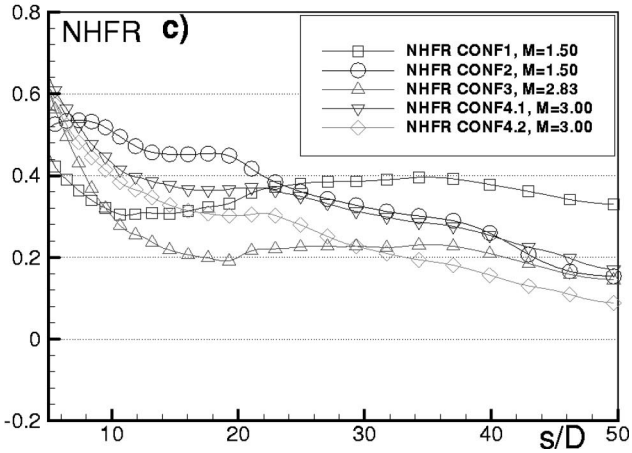

Fig. 12 Lateral averaged net heat flux reduction parameter NHFR for small (*a*), medium (*b*), and high (*c*) blowing rate

Overall Film-Cooling Performance. In order to get an overall validation of film cooling, the adiabatic film-cooling effectiveness and the heat transfer augmentation have both to be considered. Therefore, an overall film-cooling parameter, the net heat flux reduction parameter is defined (Sen et al. [17])

$$\mathrm{NHFR} = \frac{\dot{q}_0 - \dot{q}_w}{\dot{q}_0} = 1 - \frac{\dot{q}_w}{\dot{q}_0} \tag{7}$$

Using the film effectiveness η and the heat transfer coefficient h_f leads to

$$\mathrm{NHFR} = 1 - \frac{h_f}{h_0} \cdot (1 - \eta\theta) \tag{8}$$

As the NHFR parameter combines both major thermal effects it is suitable to compare two different injection configurations by using only one parameter. Here, a θ-value of 1.5 is used for the calculation of NHFR. Figure 12 shows the distribution of the lateral averaged NHFR parameter for the various blowing rates investigated.

Conclusions

Adiabatic film-cooling effectiveness and heat transfer coefficient measurements for four different injection geometry have been conducted. A typical distribution of Reynolds number and acceleration parameter *k* has been realized by using a scaled guide vane suction side model. The injection geometry comprises a double row of cylindrical holes, a double row of discrete slots and two single row configurations with fan-shaped holes, including one with a compound angle arrangement. In case of the compound angle holes, the influence of the cooling air feeding direction has been investigated.

It is found that all configurations show similar film-cooling effectiveness at low blowing ratios. In case of the fan-shaped holes with compound angle injection, a strong influence of the cooling air crossflow direction has been observed for all blowing rates. A bent inflow into the cooling holes has a clearly negative effect on the adiabatic effectiveness. At moderate and high blowing ratios the fan-shaped holes show very good effectiveness values, especially in the near hole region. The compound angle injection increases the effectiveness slightly, if the direct-cooling air inflow is chosen. Fan-shaped holes provide good effectiveness values even at high blowing rates. Here, effectiveness decreases drastically for the cylindrical holes which was attributed to coolant jet separation from the surface. In case of the double row of discrete slots, this jet separation seems to be understated, which results in good effectiveness values also at higher blowing rates in the near hole region. Further downstream, the double row of discrete slots show the best effectiveness results at high blowing rates for all the investigated configurations.

The heat transfer coefficient with film cooling is found to be quite different for the various cooling hole geometries. For two of the shaped holes, an increase in the heat transfer coefficient up to 60% near the holes has been observed with coolant injection. The double row configurations on the other hand show decreased heat transfer values. This different behavior was attributed to the certain flow conditions inside the cooling holes. If coolant separation occurs inside the diffuser part of the holes more turbulent kinetic energy is transported into the boundary layer which increases the heat transfer.

Acknowledgments

This study was partly funded by the Ministry of Research and Technology BMBF of the Federal Republic of Germany through the joint research program 'AG-Turbo' and the MTU Aero Engines GmbH, Munich, Germany.

Nomenclature

D = injection hole diameter
h = heat transfer coefficient
k = acceleration parameter: $k = du/ds \cdot \nu/u^2$
L = total chord length of model
M = blowing rate: $M = (\rho_c \cdot u_c)/(\rho_m \cdot u_m)$
NHFR = net heat flux reduction parameter Eq. (8)
$\dot{q}$ = wall heat flux

Re = Reynolds no., $\mathrm{Re}=(u(s)\cdot L)/\nu$
s = streamwise coordinate
TU = mainstream turbulence intensity: $\mathrm{TU}=\sqrt{1/3\cdot(\overline{u'^2}+\overline{v'^2}+\overline{w'^2})}/u_{\mathrm{mean}}$
u, v, w = streamwise, normal, and lateral velocity component
z = lateral coordinate
ε = emissivity of the painted test plate
η = adiabatic film-cooling effectiveness, Eq. (2)
ν = kinematic viscosity
θ = dimensionless wall temperature, Eq. (4)

Subscripts

f = with film injection
0 = without film injection
m = mainstream gas
c = coolant gas
w = wall
aw = adiabatic wall
Lat = lateral averaged

References

[1] Jabbari, M. Y., and Goldstein, R. J., 1978, ''Adiabatic Wall Temperature and Heat Transfer Downstream of Injection Through Two Rows of Holes,'' ASME J. Eng. Power, **100**, Apr., pp. 303–307.
[2] Jubran, B., and Brown, A., 1985, ''Film Cooling From Two Rows of Holes Inclined in the Streamwise and Spanwise Directions,'' ASME J. Eng. Gas Turbines Power, **107**, Jan., pp. 84–91.
[3] Jubran, B. A., and Maiteh, B. Y., 1999, ''Film Cooling and Heat Transfer From a Combination of Two Rows of Simple and/or Compound Angle Holes in Inline and/or Staggered Configurations,'' Heat Mass Transf., **34**, pp. 495–502.
[4] Ligrani, P. M., Wigle, J. M., Ciriello, S., and Jackson, S. M., 1994, ''Film-Cooling From Holes With Compound Angle Orientations: Part1–Results Downstream of Two Staggered Rows of Holes With 3D Spanwise Spacing,'' J. Heat Mass Transf., **116**, May, pp. 341–352.
[5] Goldstein, R. J., Eckert, E. R. G., and Burggraf, F., 1974, ''Effects of Hole Geometry and Density on Three-Dimensional Film Cooling,'' Int. J. Heat Mass Transf., **17**, pp. 595–607.
[6] Gritsch, M., Schulz, A., and Wittig, S., 1997, ''Adiabatic Wall Effectiveness Measurements of Film Cooling Holes with Expanded Exits,'' ASME Paper 97-GT-164.
[7] Gritsch, M., Schulz, A., and Wittig, S., 1998, ''Heat Transfer Coefficient Measurements of Film Cooling Holes With Expanded Exits,'' ASME Paper 98-GT-28.
[8] Makki, Y., and Jakubowski, 1986, ''An Experimental Study of Film Cooling From Diffused Trapezoidal Shaped Holes,'' AIAA Pap. .
[9] Yu, Y., Yen, C-H., Shih, T. I-P., Chyu, M. K., and Gogineni, S., 1999, ''Film Cooling Effectiveness and Heat Transfer Coefficient Distribution Around Diffusion Shaped Holes,'' ASME Paper 99-GT-34.
[10] Reiss, H., and Bölcs, A., 1999, ''Experimental Study of Showerhead Cooling on a Cylinder Comparing Several Configurations Using Cylindrical and Shaped Holes,'' ASME Paper 99-GT-123.
[11] Thole, K., Gritsch, M., Schulz, A., and Wittig, S., 1996, ''Flow Field Measurements for Film Cooling Holes With Expanded Exits,'' ASME Paper 96-GT-174.
[12] Dittmar, J., Jung, I. S., Schulz, A., Wittig, S., and Lee, J. S., 2000, ''Film Cooling From Rows of Holes—Effect of Cooling Hole Shape and Row Arrangement on Adjabatic Effectiveness,'' Ann. N.Y. Acad. Sci., **934**, pp. 321–328.
[13] Goldstein, R. G., 1971, ''Film Cooling,'' Adv. Heat Transfer, **7**, pp. 312–379.
[14] Choe, H., Kays, W. M., and Moffat, R. J., 1974, ''The Superposition Approach to Film Cooling,''ASME Paper 74-Wa/GT-27.
[15] Metzger, D. E., Carper, H. J., and Swank, L. R., 1968, ''Heat Transfer With Film Cooling Near Non-Tangential Injection Slots,'' ASME J. Eng. Power, **90**, pp. 157–163.
[16] Gritsch, M., Baldauf, S., Martiny, M., Schulz, A., and Wittig, S., 1999, ''The Superposition Approach to Local Heat Transfer Coefficients in High Density Ratio Film Cooling Flows,'' ASME Paper 99-GT-168.
[17] Sen, B., Schmidt, D. L., and Bogard, D. G., 1996, ''Film Cooling With Compound Angle Holes: Heat Transfer,'' ASME J. Turbomach., **118**, pp. 800–806.

Free-Stream Turbulence Effects on Film Cooling With Shaped Holes

Christian Saumweber
e-mail: Christian.Saumweber
@its.uni-karlsruhe.de

Achmed Schulz

Sigmar Wittig

Lehrstuhl und Institut für Thermische
Strömungsmaschinen,
Universität Karlsruhe (T.H.),
Karlsruhe, Germany

A comprehensive set of generic experiments has been conducted to investigate the effect of elevated free-stream turbulence on film cooling performance of shaped holes. A row of three cylindrical holes as a reference case, and two rows of holes with expanded exits, a fanshaped (expanded in lateral direction), and a laidback fanshaped hole (expanded in lateral and streamwise direction) have been employed. With an external (hot gas) Mach number of $Ma_m = 0.3$ operating conditions are varied in terms of free-stream turbulence intensity (up to 11%), integral length scale at constant turbulence intensity (up to 3.5 hole inlet diameters), and blowing ratio. The temperature ratio is fixed at 0.59 leading to an enginelike density ratio of 1.7. The results indicate that shaped and cylindrical holes exhibit very different reactions to elevated free-stream turbulence levels. For cylindrical holes film cooling effectiveness is reduced with increased turbulence level at low blowing ratios whereas a small gain in effectiveness can be observed at high blowing ratios. For shaped holes, increased turbulence intensity is detrimental even for the largest blowing ratio ($M = 2.5$). In comparison to the impact of turbulence intensity the effect of varying the integral length scale is found to be of minor importance. Finally, the effect of elevated free-stream turbulence in terms of heat transfer coefficients was found to be much more pronounced for the shaped holes. [DOI: 10.1115/1.1515336]

Introduction

Todays trend in gas turbine design is towards increasing pressure ratios, higher turbine inlet temperatures to increase cycle efficiency, and less turbine stages. Therefore, the thermal and mechanical loads on the components exposed to the hot gas—particularly the turbine blades—are increased as well, which necessitates extremely efficient cooling configurations. State-of-the-art film-cooling schemes with shaped holes of various geometry are employed in advanced high-pressure turbines. To achieve maximum benefit from the expended cooling air accurate information on the impacts of all quantities that affect film-cooling performance is required. Among others, turbulence intensity is one such parameter of major importance.

At the exit of a gas turbine combustor turbulence levels can range from 7 to 20% [1] and vary widely with combustor geometry. Goebel et al. [2] measured turbulence profiles and swirl velocity downstream of a small-scale combustor. They found, that combustion decreased the turbulence level in case of a high swirl nozzle and that turbulence levels are almost not affected by combustion in case of a low swirl nozzle. The turbulence levels without combustion ranged from 8–12% in most of the combustor exit area and increased towards the edge up to 20%. Combustor exit turbulence level is the inlet turbulence boundary condition for the first stage vane along which the free-stream turbulence intensity will be further reduced due to strong acceleration inside the vane passage. Therefore, free-stream turbulence levels in the range of 8–12% appear to be reasonable for the investigation of turbulence intensity effects on film cooling when the area around the leading edge is excluded, where free-stream turbulence intensity might be larger.

Since the majority of film cooling investigations have been performed with low turbulence intensity conditions, in recent years several studies have been conducted that particularly address the effect of increased turbulence level on film-cooling performance. In the following, a brief review on experimental investigations related to this topic will be given, whereas only generic test facilities are considered that exclude additional effects of acceleration and surface curvature.

Kadotani and Goldstein [3,4] investigated the effect of mainstream turbulence intensity ranging from 0.3 to 20.6% and the impact of small integral length scales between 0.06 and 0.33 film-cooling hole diameters. They used a row of cylindrical holes inclined 35 deg with respect to the mainstream, and a length to diameter (L/D) ratio of 62. The density ratio ρ_c/ρ_m was 0.95 for all tests. At low blowing ratios a decrease of centerline effectiveness was found at elevated turbulence intensity whereas for high blowing ratios centerline effectiveness increased with turbulence intensity due to enhanced mixing of coolant with mainstream air and smaller penetration of the jets into the hot gas flow. The laterally averaged effectiveness showed a similar but less pronounced tendency with varying turbulence level. Furthermore, for low turbulence intensity it was found that the lateral distribution of effectiveness becomes more uniform with increasing length scale.

Jumper et al. [5] examined the mechanisms that influence film-cooling effectiveness for turbulence intensities in the range of 14 to 17% and compared their data to results acquired with low free-stream turbulence conditions. Coolant was injected at low density ratio conditions into a wall jet flow through a row of cylindrical holes inclined 30 deg with respect to the mainstream and a hole length of 6 diameters. The turbulence levels of 14–17% resulted in pronounced reductions of film cooling effectiveness and the effective cooling film length. The range of optimum blowing ratios was found to be much broader and shifted towards larger values of M for flow conditions with increased turbulence intensity.

Bons et al. [6] presented film cooling effectiveness data for free-stream turbulence intensities up to 17.4% downstream a row of cylindrical holes inclined 35 deg with an L/D-ratio of 3.5. The facility was run with a density ratio of $\rho_c/\rho_m = 0.95$ for all tests. At elevated levels of free-stream turbulence film cooling effectiveness was decreased by up to 70% in regions immediately downstream of the hole exit for low to moderate blowing ratios.

Contributed by the International Gas Turbine Institute and presented at the International Gas Turbine and Aeroengine Congress and Exhibition, Amsterdam, The Netherlands, June 3–6, 2002. Manuscript received by the IGTI, September 27, 2001. Paper No. 2002-GT-30170. Review Chair: E. Benvenuti.

However, between the holes the high free-stream turbulence produced a 50–100% gain in film cooling effectiveness at the same time due to accelerated spanwise diffusion of coolant resulting in an earlier merger of jets from adjacent holes.

Schmidt and Bogard [7] studied free-stream turbulence intensity effects on film cooling in the range of 0.3 to 17%. They used a row of cylindrical film cooling holes inclined at 30 deg with respect to the free-stream and a hole length of 6 hole diameters. Film cooling effectiveness tests were conducted with a density ratio of $\rho_c/\rho_m=2.0$ whereas heat transfer measurements were conducted at a density ratio of 1.0. The results indicate a significantly decreased adiabatic effectiveness by up to 50% close to the hole for high turbulence levels and low to moderate momentum flux ratios. At large momentum flux ratios high free-stream turbulence conditions lead to an increase in adiabatic effectiveness. The greater dispersion of the coolant caused by the high free-stream turbulence results in less detachment of the jet and a movement of coolant back to the surface. Furthermore no significant differences in effectiveness occurred when the turbulence intensity was increased from 10 to 17%.

A row of 35 deg inclined cylindrical holes with a pitch to diameter ratio of 3 was employed by Drost and Bölcs [8] to study film cooling effectiveness and heat transfer for two turbulence levels and two hot gas Mach numbers. An enginelike density ratio of 1.6 was established using foreign gas ejection. Similar to the findings mentioned before the elevated turbulence intensity resulted in a decrease of effectiveness for low to moderate blowing ratios whereas at high blowing ratios effectiveness was increased due to better dispersion of the detached jets.

Kohli and Bogard [9] used a high frequency response temperature sensor to study the dispersion of coolant jets for two different turbulence levels (0.5 and 20%). Cylindrical holes inclined 35 deg with respect to the mainstream were used to eject coolant at a momentum flux ratio of $I=0.156$ and a density ratio of $\rho_c/\rho_m=1.05$. The results indicate that the process of coolant dispersion is completely different at low and high free-stream turbulence intensity conditions. For low main-flow turbulence levels the shear layer between mainstream and coolant jet generates strong intermittent flow structures that cause mixing of coolant and main-flow. In case of high free-stream turbulence main-flow fluid penetrates through the core of the coolant jet towards the wall, causing rapid mixing of coolant and main-flow and a pronounced degradation of the jet.

Hot wire anemometer measurements at a density ratio of $\rho_c/\rho_m=1$ were undertaken by Burd et al. [10] in order to study the flow field downstream of film cooling holes with different L/D-ratios. A row of cylindrical holes inclined at 35 deg with respect to the mainstream was investigated at two turbulence levels of 0.5 and 12%. The L/D-ratio was varied from 2.3 to 7. With low free-stream turbulence and short holes the coolant is ejected farther from the wall and spreads more into the spanwise direction than with a long hole. The pronounced differences in the flowfield between long and short hole ejection diminish when high turbulence levels prevail in the hot gas. The authors conclude that the L/D-ratio has to be taken into account additionally when turbulence intensity effects on film cooling are to be investigated.

The study by Burd et al. [10] implies, that in general the geometry of the film-cooling hole plays an important role when free-stream turbulence effects on film cooling are considered. The authors state that short and long-hole injection produce fundamentally different velocity profiles at the hole exit which will result in a different interaction of coolant and mainstream. However, the same is true about the shape of the hole exit, which has not been considered in previous investigations on free-stream turbulence effects and which as well is the reason for vastly different velocity profiles. It can, therefore, be expected that shaped holes are sensitive to elevated hot gas turbulence levels in a manner different from cylindrical holes. The purpose of the present study is to quantify these differences and to provide a data-set for film cooling with shaped holes at elevated free-stream turbulence conditions, which is up to now not available in the open literature.

Experimental Facility and Test Conditions

The present investigation is carried out in a continuous flow wind tunnel at the Institut für Thermische Strömungsmaschinen (ITS), University of Karlsruhe. The film-cooling test rig consists of a primary loop representing the external flow and a secondary loop representing the internal flow of an airfoil. Pressure, temperature and crossflow velocity in both loops can be set independently. Primary and secondary loop can be oriented to each other with arbitrary angles, constituting flow conditions typically found in turbine vanes or blades, respectively (see Fig. 1). At the bottom side of the primary loop an interchangeable test plate is assembled carrying the film-cooling hole specimen. A boundary layer bleed at the entry of the hot gas wind tunnel facilitates to control the boundary layer thickness. More details on the experimental facility are given in [11].

Turbulence grids of various geometry can be placed in front of the hot gas part at different streamwise positions. Hence, it is possible within a certain range to control turbulence intensity and length scale at the ejection location by varying the distance and the bar size of the turbulence grid simultaneously. Turbulence intensity decay with streamwise length and development of dissipation length scale is quantified using a DANTEC© LDV system. A 2-D fiber flow probe equipped with a 400 mm transmitting lens together with a 150-mm focal length receiver unit are operated in forward scatter mode. Data processing is achieved using two DANTEC© Enhanced Burst Signal Analyzers. The measured turbulence intensity, decay shows very good agreement with correlations given in the literature [12,13]. In terms of dissipation length scale, satisfying agreement of experimental data and correlations [13] is observed as well.

The tests are carried out using hole inserts with a row of three scaled up film-cooling holes with an inclination angle of 30 deg. Three types of hole geometry are tested. They comprise a cylindrical hole and two holes with an expanded exit portion (fan-shaped hole and laidback fan-shaped hole, see Fig. 2). The diameter of the cylindrical hole and the diameter of the cylindrical inlet portion of the shaped holes is 5 mm. Both shaped holes are expanded in lateral direction with an angle of 14 deg resulting in a hole width of 15 mm at the hole exit. The laidback fan-shaped hole has an additional forward expansion of 15 deg which increases the hole length at the exit to 20 mm. The exit-to-entry area ratio of the fanshaped and the laidback fanshaped hole is 3.0 and 3.1, respectively. The length-to-diameter ratio L/D is 6, the pitch-to-diameter ratio is kept constant at 4. Entry and exit of the holes are sharp edged. The interior surfaces are aerodynamically smooth. Each hole geometry is tested with three different free-stream turbulence intensities (Tu=3.5, 7.5, and 11%). For each turbulence intensity five different blowing ratios are established. A complete set of the operating conditions is given in Table 1.

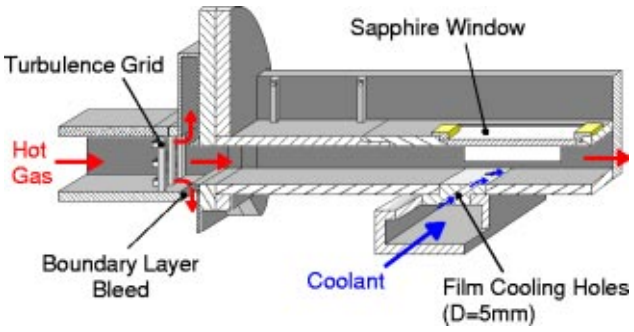

Fig. 1 Test section

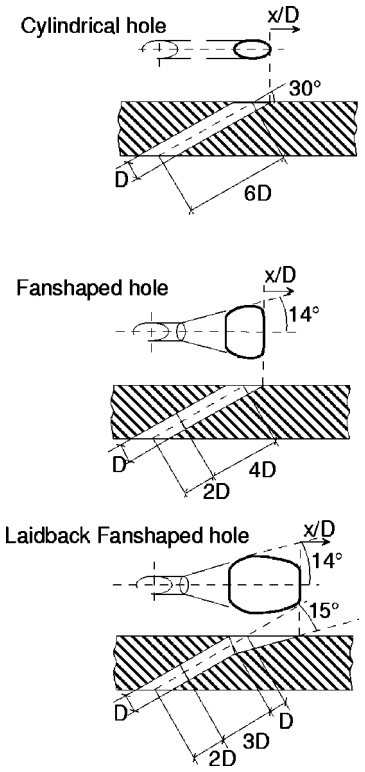

Fig. 2 Hole geometry tested

The first quantity of interest is the discharge coefficient C_D, which is used to quantify the throughflow losses of film-cooling holes. It is defined as the ratio of actual and ideal mass flow rate through the hole. The ideal mass flow rate is calculated assuming an isentropic, one-dimensional expansion from the total pressure in the coolant plenum to the hot gas static pressure at the hole exit

$$C_D=\frac{\dot{m}_c}{p_{tc}\left(\frac{p_m}{p_{tc}}\right)^{\kappa+1/2\kappa}\sqrt{\frac{2\kappa}{(\kappa-1)RT_{tc}}\left(\left(\frac{p_{tc}}{p_m}\right)^{\kappa-1/\kappa}-1\right)}\frac{\pi}{4}D^2} \tag{1}$$

For the expanded holes the discharge coefficient is based on the cylindrical cross section at the hole inlet. This makes it more convenient to evaluate the effect of expanding the hole exit since the discharge coefficients can be directly compared to those of the cylindrical holes.

The second quantity of interest is the adiabatic film-cooling effectiveness, which is defined by

Table 1 Operating conditions

Coolant Pressure	p_{tc}	< 2 bars
Coolant Temperature	T_{tc}	310 K
Hot Gas Temperature	T_{tm}	540 K
Blowing Ratio		
a) Cylindrical Holes	M	0.5, 0.75, 1.0, 1.25, 1.5
b) Shaped Holes	M	0.5, 0.75, 1.0, 1.5, 2.5
Density Ratio	ρ_c/ρ_m	1.7
Turbulence Intensity	Tu	3.6%, 7.5%, 11%
Integral Length Scale	L	2.1D, 2.7D, 3.5D
Hot Gas Mach Number	Ma_m	0.3
Hot Gas Reynolds Number	$Re_{D,m}$	$0.25\ 10^5$

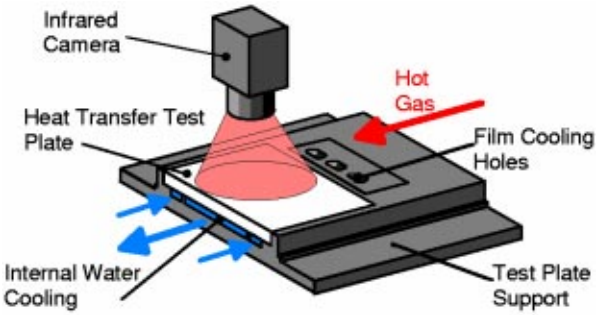

Fig. 3 Principal arrangement for heat transfer tests

$$\eta_{aw}=\frac{T_{\mathrm{rec},m}-T_{\mathrm{aw}}}{T_{\mathrm{rec},m}-T_{tc}} \tag{2}$$

To measure adiabatic film cooling effectiveness it is required to establish thermal boundary conditions as close as possible to adiabatic. The test plate used for these experiments is made of the high temperature thermoplastic material TECAPEEK which has a low thermal conductivity of 0.3 W/(mK) and a maximum operating temperature of about 570 K.

The superposition approach of film cooling [14–20] is used in order to determine the local heat transfer coefficients

$$h(\theta)=h_f\cdot(1-\eta_{aw}\theta) \tag{3}$$

with

$$\theta=\frac{T_{tc}-T_{\mathrm{rec},m}}{T_w-T_{\mathrm{rec},m}} \tag{4}$$

In general, to acquire the linear relation between h and θ of Eq. (3), two measurements of h at two different θ have to be performed. The first data set is given by the film-cooling effectiveness measurements. For a given flow field data points at $h=0$ and $\theta=\theta_{aw}=1/\eta$ are generated. The second data set has to be acquired with a dimensionless temperature different from $1/\eta$ but at the same flow conditions as for the film cooling effectiveness tests, particularly the same temperature ratio. For that reason θ is varied by varying the wall temperature only. The test plate used for these experiments is machined out of titanium-aluminum with a thermal conductivity of 7.2 W/(mK) at ambient temperature, which increases up to 8.5 W/(mK) at a temperature of 470 K. The temperature-dependence of the thermal conductivity is taken into account by a subsequent finite element (FE) analysis. To enhance the heat flux through the test plate internal water cooling is applied. A simplified sketch of the setup is shown in Fig. 3.

For both, film-cooling effectiveness and heat transfer tests, surface temperature mappings on the test plates are acquired by an infrared camera system (AGEMA 900), that has proven its accuracy and reliability in previous studies [21,22]. The infrared camera provides a two-dimensional distribution of temperatures that is digitized into an array of 272 times 136 pixels. According to the optical setup used in the experiments, this results in a spatial resolution of 0.8 mm times 0.8 mm per pixel. The hot gas surface of each test plate is covered by a black paint with a well-known emissivity of 0.95. Seven 0.5 mm NiCr-Ni-thermocouples are embedded flush with the surface in order to in-situ calibrate the infrared camera readings [23]. The temperatures on the back surface of each test plate are monitored by further 12 NiCr-Ni thermocouples. The measured temperatures are interpolated onto a FE mesh of the respective test plate (Fig. 4). The FE model extends half a pitch to either side of the symmetry plane to the midspan between the center hole and each adjacent hole. A steady-state thermal analysis is performed in order to calculate the three-dimensional heat flux distribution of the test plate. The surface temperatures of the film cooling effectiveness tests together with

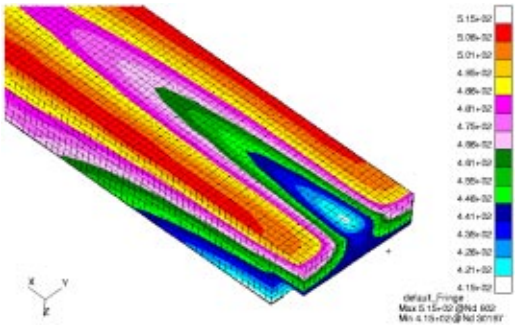

Fig. 4 Finite element mesh of the low thermal conductivity test plate

the respective heat flux distribution from the FE analysis allow to perform a correction for remnant heat fluxes and to calculate the adiabatic wall temperature. The surface temperature distribution of the heat transfer test together with the heat flux distribution of the respective FE calculation is employed to calculate the heat transfer coefficients with film cooling. They are used together with the two-dimensional distribution of the adiabatic film-cooling effectiveness to extrapolate the temperature-independent heat transfer coefficient with film cooling h_f according to Eq. (3).

Experimental Uncertainties

Uncertainties are estimated according to the procedure proposed by Kline and McClintock [24]. Mach number is kept constant within $\pm 1.6\%$. Uncertainty in setting the blowing ratio is $\pm 2\%$. Density ratio uncertainty is $\pm 1.7\%$. The uncertainty in the values of C_D is found to be less than 2% in most of the cases considered, increasing up to 4.5% for very low pressure ratios. Based on an accuracy of ± 0.5 K for the temperature measurement, the uncertainty in adiabatic effectiveness amounts to $\pm 4\%$ and heat transfer coefficient uncertainty to $\pm 15\%$.

Results

Discharge coefficients for the three hole shapes are presented in Fig. 5. The measurements have been conducted with four different turbulence levels, whereas each geometry was tested with five different pressure ratios. For the turbulence levels 7.5 and 3.6% the integral length scale was kept constant at $2.7D$. At a turbulence level of 5.1% the integral length scale was varied from 2.1 to $3.5D$.

The discharge coefficients for a given operating condition are largest for the laidback fan-shaped holes and smallest for the cylindrical holes. The discharge coefficients of the fan-shaped holes are in general slightly lower than those of the laidback fan-shaped holes which might result from the smaller area ratio $A_{\text{exit}}/A_{\text{inlet}}$ (3.0 vs 3.1). For the cylindrical holes there is obviously no dependence of the discharge coefficient neither on turbulence level nor on turbulence length scale. All runs pretty much collapse on the same curve. For fan-shaped and laidback fan-shaped holes the differences from one test series to the next are larger than for the cylindrical holes. However, since the deviations are still quite small and since there is no uniform tendency, it might as well be concluded that neither the turbulence level nor the length scale does have significant impact on the discharge coefficients for fan-shaped and laidback fan-shaped holes.

In order to validate the measurement procedure of the aerothermal tests, adiabatic effectiveness data is compared to results of previous studies for cylindrical holes in Fig. 6. Centerline data is used rather than laterally averaged data because hole pitches differ significantly. Since the investigations have been conducted with different density ratios, centerline effectiveness is plotted versus momentum flux ratio instead of blowing ratio. Despite the fact, that only reasonable match of experimental conditions and ejection configuration can be obtained, the data agree well with the results from Bons et al. [6] and Schmidt and Bogard [7].

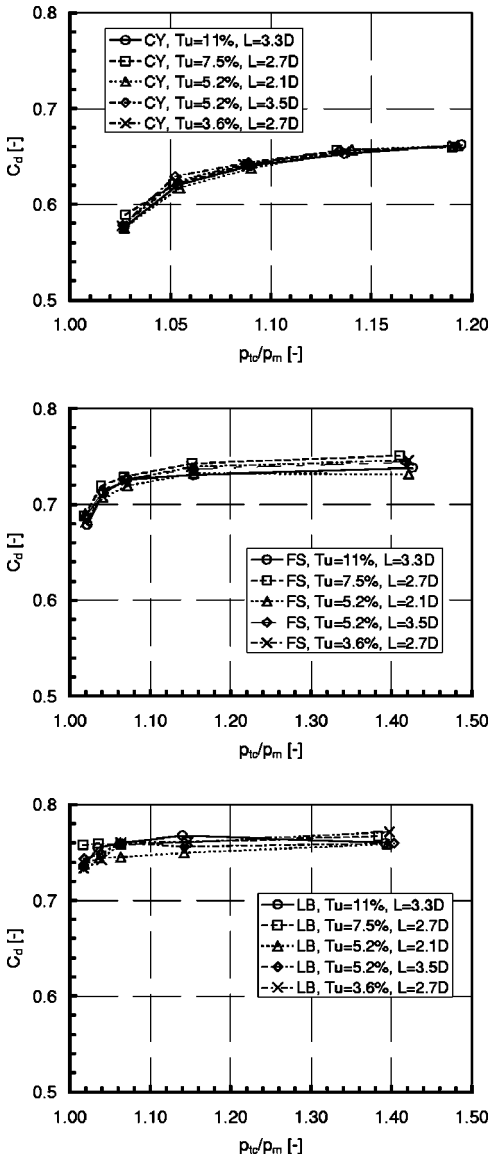

Fig. 5 Discharge coefficient C_D versus pressure ratio p_{tc}/p_m

Figure 7(*a*) shows local values of the adiabatic film cooling effectiveness for the cylindrical holes. At low blowing ratios

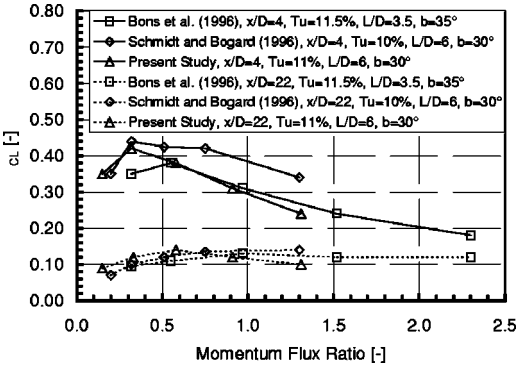

Fig. 6 Comparison of centerline effectiveness with published data, cylindrical holes

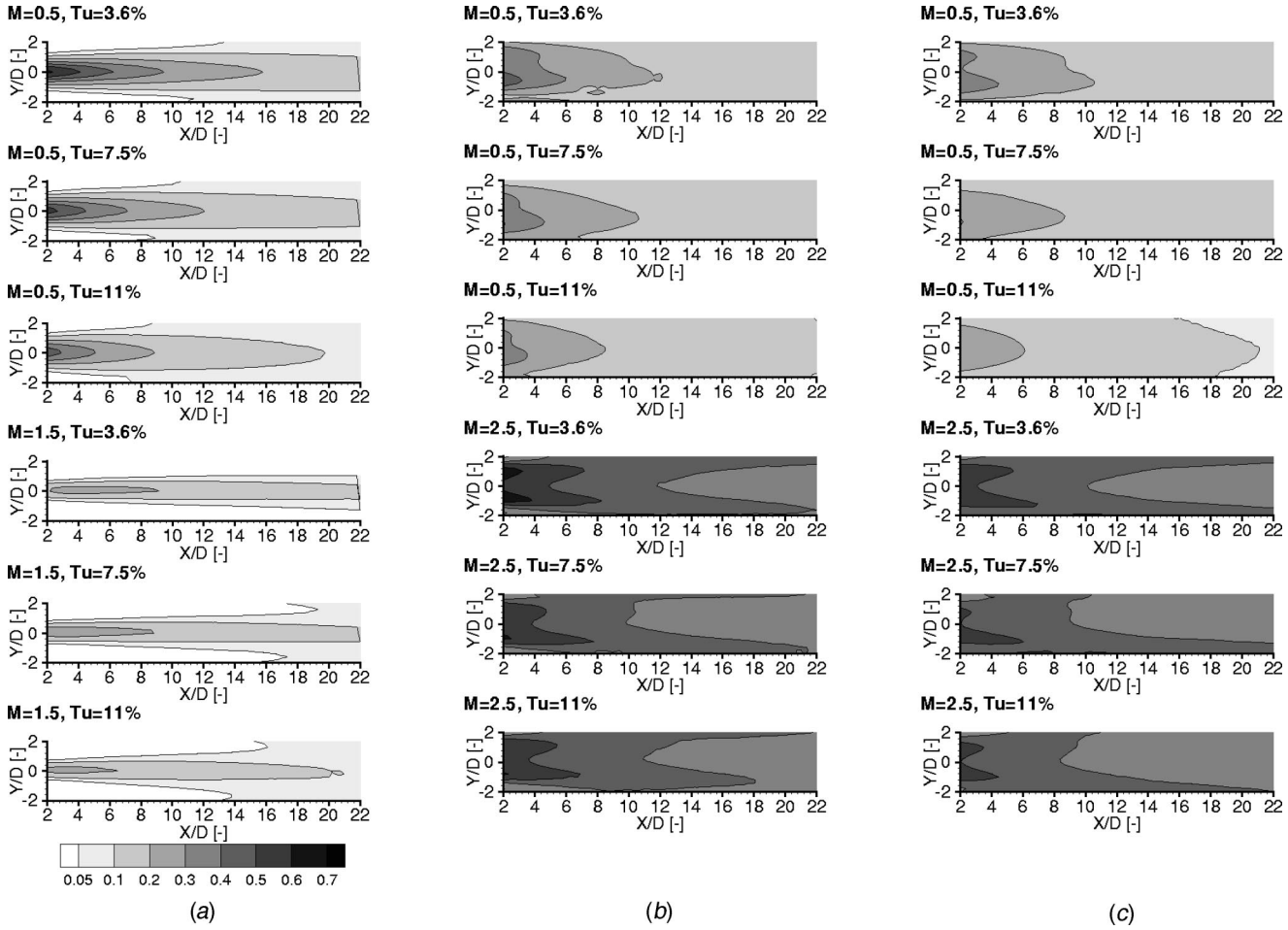

Fig. 7 Local adiabatic film-cooling effectiveness—(*a*) cylindrical holes, (*b*) fan-shaped holes, (*c*) laidback fan-shaped holes

($M=0.5$) a continuous decrease in effectiveness is observed in the near hole region when free-stream turbulence intensity is raised from 3.6 to 7.5%, and finally 11%. Centerline effectiveness is reduced by up to 30% close to the hole and up to 40% further downstream. The strong decrease in centerline effectiveness is partially compensated by an improved lateral spreading of coolant at higher turbulence levels. At high blowing ratios ($M=1.5$) an increase of free-stream turbulence intensity from 3.6 to 7.5% at constant length scale actually leads to minor benefits in terms of effectiveness which are amplified by the improved lateral distribution of coolant. Additionally, the plots indicate a reduced tendency of the jets to detach from the surface. Further downstream effectiveness levels are quite the same for both turbulence intensities. A further increase of turbulence intensity to 11% at high blowing ratios again leads to a reduction of centerline effectiveness.

The fan-shaped holes exhibit a characteristic different from the cylindrical holes. Figure 7(*b*) shows, that film-cooling effectiveness is reduced for all blowing ratios when the turbulence level is increased from 3.6 to 7.5%, and finally 11%. The gain in effectiveness at larger blowing ratios caused by increased turbulence intensity, that has been observed for the cylindrical holes, is not visible for the fan-shaped holes. This phenomenon might be explained by the fact that the effectiveness increase for the cylindrical holes is—as previously mentioned—mainly due to enhanced mixing which forces more coolant back towards the wall in regions, in which the jet would exhibit lift-off at lower turbulence levels. Additionally, higher turbulence levels improve the lateral distribution of coolant for the cylindrical holes. In case of the fanshaped holes there is obviously no tendency to detach at low turbulence levels even for the highest blowing ratio of $M=2.5$. As a result of the lateral expansion of the hole exit, the lateral distribution of coolant is already excellent for the tight pitch (pitch $=4D$) considered in this study. Therefore, there is no potential to improve the spreading of coolant in lateral direction. In other words, both mechanisms that might cause a gain in effectiveness for the cylindrical holes are ineffective for the fan-shaped holes. Consequently, elevated free-stream turbulence intensity can only result in reduced film-cooling effectiveness for all blowing ratios investigated due to stronger mixing within the shear layer of coolant and hot gas.

The laidback fan-shaped holes perform quite similar to the fan-shaped holes, as can be seen from the contour plots of Fig. 7(*c*). Film-cooling effectiveness is reduced with increasing turbulence intensity for all blowing ratios tested. The fact, that film-cooling effectiveness of the laidback fan-shaped holes is lower than for the fan-shaped holes is partially caused by the shift of the ejection location with respect to the nominal origin of the coordinate system. The distance of the point, at which the hole axis intersects the hot gas surface, to the holes trailing edge, where the origin of the coordinate system is located, is $3D$ in case of the laidback fan-shaped holes and only $1D$ in case of the cylindrical and the fan-shaped holes (compare Fig. 3). When taking this shift of two hole diameters into account it can be seen that the performance of the two shaped holes is fairly the same.

In Fig. 8 laterally averaged film-cooling effectiveness distributions downstream the cylindrical holes are presented. Lateral averaging was performed over one hole pitch downstream the center hole of the row. The plot clearly indicates the different reactions of the cylindrical holes to elevated turbulence intensity at low and

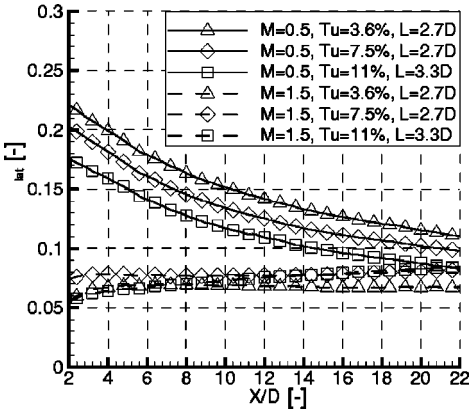

Fig. 8 Laterally averaged effectiveness; cylindrical hole

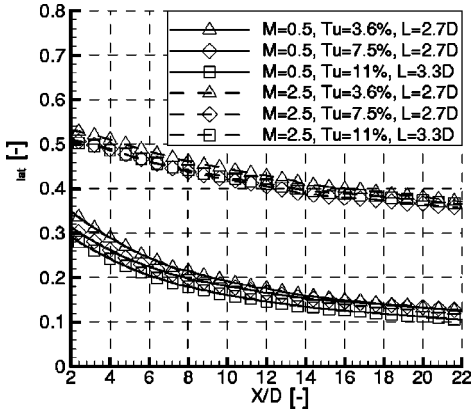

Fig. 10 Laterally averaged effectiveness; fan-shaped hole

high blowing ratios. Whereas at low blowing ratios laterally averaged effectiveness is reduced by up to 25%, increased turbulence intensity leads to a gain at high blowing ratios, though on a very poor overall level. The characteristic of the cylindrical holes at elevated free-stream turbulence levels might be summarized by Fig. 9, which shows the adiabatic film-cooling effectiveness averaged over an area of one pitch in width and 20 hole diameters in streamwise length. In order to exclude an impact of the length scale, only the cases with the same integral length scale are plotted. At low blowing ratios the low turbulence case indicates superior performance whereas at high blowing ratios increased turbulence levels lead to a gain in effectiveness. Furthermore, this figure shows that the optimum blowing ratio in both cases is around $M=0.75$. However, since the shape of the effectiveness versus blowing ratio curve is less steep for the higher turbulence level, it might be suspected that a deviation from the optimum blowing ratio results in a less significant reduction of effectiveness at elevated turbulence intensity. Furthermore, it seems reasonable to assume that the optimum is shifted towards a slightly higher blowing ratio in case of elevated turbulence levels. The ''resolution'' in terms of blowing ratio though is too coarse to show this in Fig. 9. In general it can be stated that the results obtained for cylindrical holes confirm and are in accordance with the findings of previous studies [3–8].

Laterally averaged effectiveness distributions downstream the fan-shaped holes are presented in Fig. 10. Figure 11 shows the corresponding spatial averages. As already mentioned when discussing the local effectiveness distributions, increased turbulence intensity lowers laterally averaged effectiveness for all blowing ratios tested. However, at larger blowing ratios the effect is less significant. Furthermore Fig. 10 indicates that increasing blowing ratio with fanshaped holes in general leads to increased effectiveness for the range of blowing ratios considered in this study- a behavior that is typical for shaped holes.

By comparing Fig. 12 with Fig. 10 and Fig. 13 with Fig. 11 the very similar performance of laidback fan-shaped and fan-shaped holes becomes evident. Particularly at high blowing ratios, laterally averaged values of effectiveness are fairly the same for both shaped holes. As for the fan-shaped holes, the impact of increased free-stream turbulence is detrimental for all blowing ratios, but becomes less pronounced at high blowing ratios.

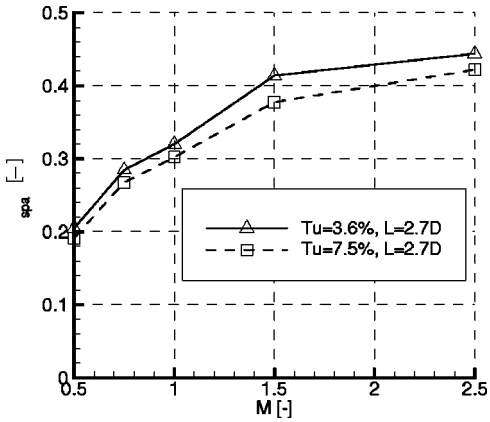

Fig. 11 Spatially averaged effectiveness; fan-shaped hole

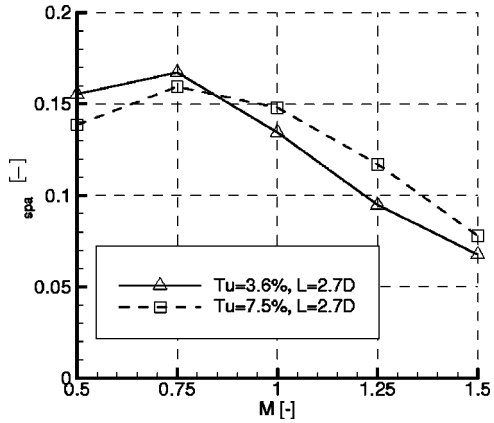

Fig. 9 Spatially averaged effectiveness; cylindrical hole

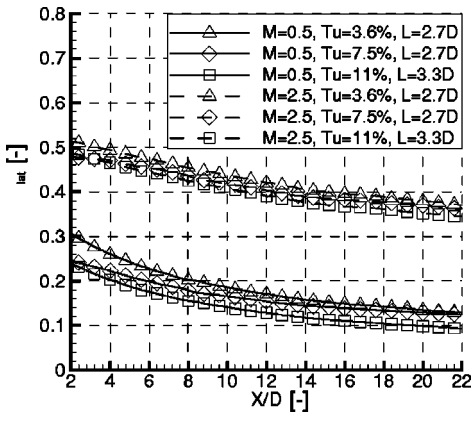

Fig. 12 Laterally averaged effectiveness; laidback fan-shaped hole

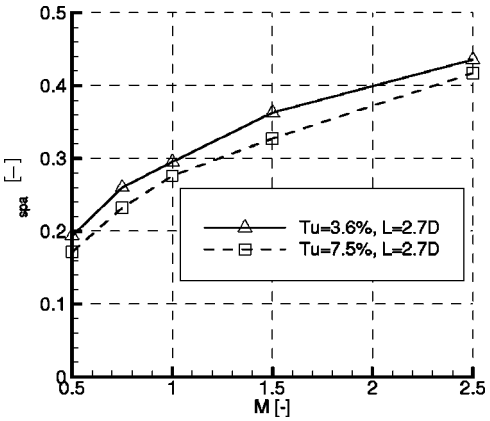

Fig. 13 Spatially averaged effectiveness; laidback fan-shaped hole

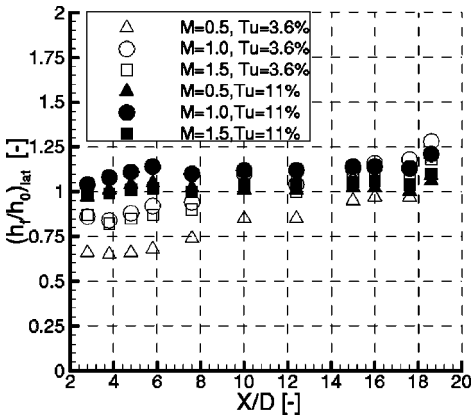

Fig. 15 Laterally averaged heat transfer coefficient ratio; cylindrical hole

An attempt has been made to quantify the effect of integral length scale on film-cooling effectiveness. Additional tests at constant turbulence intensity of 5.1% with two different length scales of 2.1*D* and 3.5*D* have been performed. From two-dimensional distributions of film-cooling effectiveness, which are not shown, an improvement of lateral spreading and slightly increased centerline effectiveness close to the hole could be observed. Both effects together lead to a higher laterally averaged effectiveness for the case with larger length scale, which is visible in Fig. 14. As compared to the impact of turbulence intensity though, the effect of changing the integral length scale from 2.1*D* to 3.5*D* is rather small.

The results of the heat transfer measurements are presented in terms of laterally averaged heat transfer coefficients with film cooling, h_f, normalized with a laterally averaged baseline heat transfer coefficient for the flat plate, h_0. The laterally averaged baseline heat transfer coefficients h_0 have been derived from additional measurements without film cooling. A dummy insert without holes instead of the film-cooling hole specimen was used for these tests in order to avoid disturbances caused by the holes, that can significantly affect the near wall aerodynamics. The baseline heat transfer coefficients were compared to a correlation for a flat plate with unheated starting length given by Kays and Crawford [25]. For the low turbulence case (Tu=3.6%) satisfying agreement of correlation and measured data with maximum deviations of about 10% was found. For conditions with elevated free-stream turbulence levels strong increases of the heat transfer coefficient in comparison to the correlation can be expected according to the literature [26,27]. The data for the baseline heat transfer coefficients at highest free-stream turbulence intensity indicated raises up to 40% as compared to the low turbulence intensity data.

In Fig. 15 the laterally averaged heat transfer coefficient ratios for the cylindrical holes are shown. For the case with low free-stream turbulence intensity the heat load increases with blowing ratio. For all blowing ratios a maximum could be detected by about 19*D* streamwise distance from the ejection location. 20*D* downstream the heat transfer enhancement ranges between 6% for the lowest blowing ratio of $M=0.5$ and 21% for the largest blowing ratio of $M=1.5$. Raising the turbulence level to 11% clearly results in a decreased sensitivity of the heat transfer coefficients to a change in blowing ratio. Furthermore, close to the holes the heat transfer coefficient ratio is increased and no maximum at a certain streamwise position can be detected. Instead, heat load for a given blowing ratio is pretty much on a constant level up to 20*D* distance from the ejection location.

For the fan-shaped holes the heat transfer coefficient ratios exhibit a completely different characteristic and show a much stronger dependency on free-stream turbulence level, see Fig. 16. In contrast to the cylindrical holes, a raise of the turbulence intensity from 3.6 to 11% obviously enlarges the spread between the cases with different blowing ratio. An increase of the blowing ratio leads to higher heat transfer coefficients for both turbulence levels but the maximum heat load is located closer to the hole exit in case of high free-stream turbulence intensity. Similar to the results of the cylindrical holes, the heat transfer coefficient ratios close to the holes are larger for the high turbulence level.

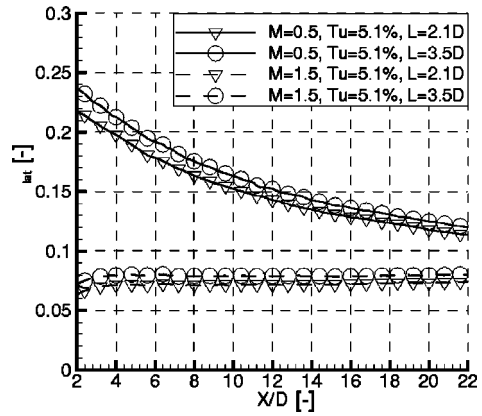

Fig. 14 Laterally averaged effectiveness; cylindrical hole

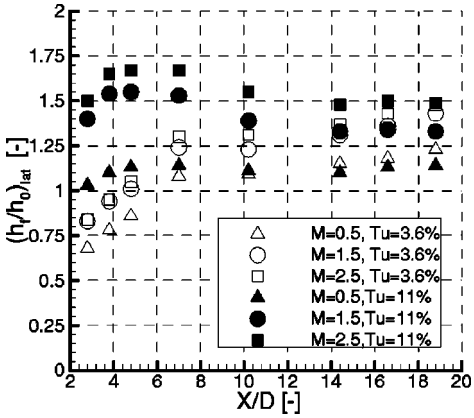

Fig. 16 Laterally averaged heat transfer coefficient ratio; fan-shaped hole

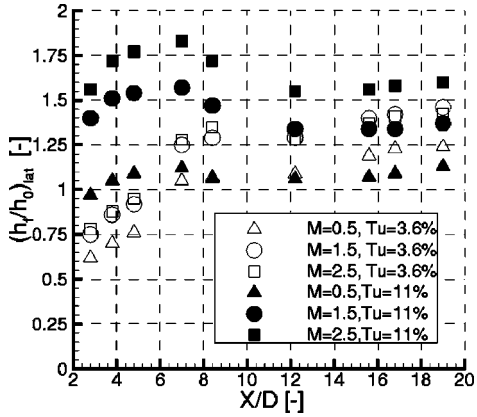

Fig. 17 Laterally averaged heat transfer coefficient ratio; laid-back fan-shaped hole

In terms of heat transfer coefficient ratio the similarity of laid-back fanshaped and fanshaped holes again becomes apparent, compare Fig. 16 with Fig. 17. In general the heat transfer coefficient ratios of both shaped holes show a much stronger dependency on free-stream turbulence level. Furthermore, the impact of blowing ratio is much more pronounced for the shaped holes, which exhibit much stronger impacts on the heat transfer than the cylindrical holes. This phenomenon might be explained by the fact, that the surface area, in which the hot gas flow is ''disturbed'' by the presence of coolant is far larger for the shaped holes than for the cylindrical holes. In fact, for the—in terms of shaped holes—tight pitch considered in the present study, the lateral distribution of coolant is so excellent, that no part of the surface is exposed to hot gas only (see Fig. 7). This, however, implies that there is no region on the surface in which the hot gas flow is not altered by coolant. Additionally, it might be hypothesized, that the jets from shaped holes are narrowed by neighboring jets in case of a pitch-to-diameter ratio of $P/D=4$. Since the spread of coolant in lateral direction is obstructed, the interaction with the hot gas has to be intensified. Coolant vortices cannot expand in lateral direction such as in case of larger pitches which results in a smaller scale of the vortices and consequently an increase of vorticity that finally enhances the heat load. For the cylindrical holes on the other hand, a pitch-to-diameter ratio of 4 is relatively large. Figure 7 shows that close to the holes ($x/D<8$) there is no interaction between the jets at all. Most data presented in the literature has been acquired with a smaller pitch of $P/D=3$ and additionally slightly steeper ejection angles (e.g., [[8], [28–30]]). Therefore, it can be expected for the present study that the heat transfer coefficients downstream of the cylindrical holes are on a lower level in comparison to most data in the open literature.

Conclusions

An experimental study has been performed to investigate the impact of various hot gas turbulence conditions on film-cooling performance of shaped holes in comparison to simple cylindrical holes. The key findings might be summarized as follows:

- Pressure losses quantified by means of discharge coefficients are not significantly affected by changes of turbulence level and integral length scale.
- For cylindrical holes, elevated free-stream turbulence intensity lowers adiabatic film-cooling effectiveness at small to moderate blowing ratios. Reductions up to 40% for local effectiveness and 25% for laterally averaged effectiveness are found when the turbulence intensity is raised from 3.6 to 11%. In accordance to previous studies, at high blowing ratios, a gain in effectiveness is observed which results from an improved lateral spreading of coolant and a diminished tendency to detach from the surface.
- At low turbulence levels both shaped holes do not show any indication to detach even at the highest blowing ratio. Therefore, the high turbulence intensity can only result in a stronger exhaustion of coolant due to intensified mixing with the hot gas. Because of the laterally expanded hole exit and the tight pitch considered in this study, coolant jets from both shaped holes interact with each other immediately downstream of the ejection location and form a closed cooling film. For that reason, the lateral spreading of coolant can not be improved by elevated free-stream turbulence intensity. Consequently, the effect of increased turbulence level is detrimental at all blowing ratios for the shaped holes. Laterally averaged effectiveness is reduced up to 30% when the turbulence intensity is increased from 3.6 to 11%. The effect is more pronounced at smaller blowing ratios.
- As compared to the effect of elevated free-stream turbulence intensity, the impact of increasing the integral length scale from 2.1 to 3.5D at constant turbulence intensity of 5.1% is not very pronounced.
- For cylindrical holes, the heat transfer data indicate a reduced sensitivity with respect to the blowing ratio when turbulence intensity is raised. For the shaped holes the opposite is true. The impact of blowing ratio becomes more significant at higher free-stream turbulence levels.
- Both shaped holes show a very similar characteristic. No superior performance due to an additional layback is observed.

Acknowledgments

This study was partly funded by the European Union through grant by the BRITE EURAM program ''Turbine Aero-Thermal External Flows'' under Contract No. BRPR-CT97-0519.

Nomenclature

C_D = discharge coefficient
D = film-cooling hole diameter
$h(\theta)$ = heat transfer coefficient according to Eq. (3)
h_f = heat transfer coefficient with film cooling
h_0 = heat transfer coefficient without film cooling
L = film-cooling hole length measured along centerline, integral length scale
M = blowing ratio
Ma = Mach number
$\dot{m}_c$ = mass flow rate through film-cooling hole
p_m = static pressure hot gas
p_{tc} = total pressure coolant
R = gas constant
Re_D = Reynolds number based on hole diameter
T_{aw} = adiabatic wall temperature
$T_{\mathrm{rec},m}$ = recovery temperature hot gas
T_{tc} = total temperature coolant
Tu = turbulence intensity
κ = ratio of specific heats
θ = dimensionless temperature ratio (Eq. (4))
ρ_c = coolant density
ρ_m = hot gas density
η_{aw} = adiabatic film-cooling effectiveness

References

[1] Ames, F. E., 1998, ''Aspects of Vane Film Cooling with High Turbulence: Part I—Heat Transfer,'' ASME J. Turbomach., **120**, pp. 768–776.
[2] Goebel, S. G., Abuaf, N., Lovett, J. A., and Lee, C.-P., 1993, ''Measurements of Combustor Velocity and Turbulence Profiles,'' ASME Paper No. 93-GT-228.
[3] Kadotani, K., and Goldstein, R. J., 1979, ''On the Nature of Jets Entering a Turbulent Flow Part A—Jet-Mainstream Interaction,'' ASME J. Eng. Power, **101**, pp. 459–465.
[4] Kadotani, K., and Goldstein, R. J., 1979, ''On the Nature of Jets Entering a

Turbulent Flow Part B—Film Cooling Performance,'' ASME J. Eng. Power, **101**, pp. 466–470.
[5] Jumper, G. W., Elrod, W. C., and Rivir, R. B., 1991, ''Film Cooling Effectiveness in High Turbulence Flow,'' ASME J. Turbomach., **113**, pp. 479–483.
[6] Bons, J. P., MacArthur, C. D., and Rivir, R. B., 1996, ''The Effect of High Free-Stream Turbulence on Film Cooling Effectiveness,'' ASME J. Turbomach., **118**, pp. 814–825.
[7] Schmidt, D. L., and Bogard, D. G., 1996, ''Effects of Free-Stream Turbulence and Surface Roughness on Film Cooling,'' ASME Paper No 96-GT-462.
[8] Drost, U., and Bölcs, A., 1997, ''Utilization of the Transient Liquid Crystal Technique for Film Cooling Effectiveness and Heat Transfer Investigations on a Flat Plate and a Turbine Airfoil,'' ASME Paper No. 97-GT-26.
[9] Kohli, A., and Bogard, D. G., 1998, ''Effects of Very High Free-Stream Turbulence on the Jet-Mainstream Interaction in a Film Cooling Flow,'' ASME J. Turbomach., **120**, pp. 785–790.
[10] Burd, S. W., Kaszeta, R. W., and Simon, T. W., 1998, ''Measurements in Film Cooling Flows: Hole L/D and Turbulence Intensity Effects,'' ASME J. Turbomach., **120**, pp. 791–797.
[11] Wittig S., Schulz A., Gritsch M., and Thole K. A., 1996, ''Transonic Film-Cooling Investigations: Effects of Hole Shapes and Orientations,'' ASME Paper 96-GT-222.
[12] Baines, W. D., and Peterson, E. G., 1951, ''An Investigation of Flow Through Screens,'' Trans. ASME, July, pp. 467–480.
[13] Roach, P. E., 1987, ''The Generation of Nearly Isotropic Turbulence by Means of Grids,'' Heat Fluid Flow, **8**(2), pp. 82–92.
[14] Metzger, D. E., Carper, H. J., and Swank, L. R., 1968, ''Heat Transfer with Film Cooling near Nontangential Injection Slots,'' ASME J. Eng. Power, **90**, pp. 157–163.
[15] Metzger, D. E., and Fletcher, D. D., 1971, ''Evaluation of Heat Transfer for Film-Cooled Turbine Components,'' J. Aircr., **8**, pp. 33–38.
[16] Metzger, D. E., Takeuchi, D. I., and Kuenstler, P. A., 1973, ''Effectiveness and Heat Transfer With Full-Coverage Film Cooling,'' ASME J. Eng. Power, **95**, pp. 181–184.
[17] Choe, H., Kays, W. M., and Moffat, R. J., 1974, ''The Superposition Approach to Film Cooling,'' ASME Paper No 74-WA/HT-27.
[18] Eckert, E. R. G., 1984, ''Analysis of Film Cooling and Full Coverage Film Cooling of Gas Turbine Blades,'' ASME J. Eng. Gas Turbines Power, **106**, pp. 207–213.
[19] Forth, C. J. P., Loftus, P. J., and Jones, T. V., 1985, ''The Effect of Density Ratio on the Film Cooling of a Flat Plate,'' Heat Transfer and Cooling in Gas Turbines, AGARD-CP-390. Paper 10.
[20] Teekaram, A. J. H., Forth, C. J. P., and Jones, T. V., 1989, ''The Use of Foreign Gas to Simulate the Effects of Density Ratios in Film Cooling,'' ASME J. Turbomach., **111**, pp. 57–62.
[21] Gritsch, M., Schulz, A., and Wittig, S., 1998, ''Adiabatic Wall Effectiveness Measurements of Film-Cooling Holes with Expanded Exits,'' ASME J. Turbomach., **120**, pp. 568–574.
[22] Baldauf, S., Schulz, A., and Wittig, S., 2001, ''High Resolution Measurements of Local Effectiveness by Discrete Hole Film Cooling,'' ASME J. Turbomach., **123**, pp. 758–765.
[23] Martiny, M., Schiele, R., Gritsch, M., Schulz, A., and Wittig, S., 1996. ''In Situ Calibration for Quantitative Infrared Thermography,'' QIRT '96 Eurotherm Seminar No. 50.
[24] Kline, S. J., and McClintock, F. A., 1953, ''Describing Uncertainties in Single Sample Experiments,'' Mech. Eng. (Am. Soc. Mech. Eng.), **75**, pp. 3–8.
[25] Kays, W. M., and Crawford, M. E., 1980, *Convective Heat and Mass Transfer*, McGraw Hill, New York, NY.
[26] Blair, M. F., 1983, ''Influence of Free-stream Turbulence on Turbulent Boundary Layer Heat Transfer. Part I and II,'' ASME J. Heat Transfer, **105**, pp. 33–47.
[27] Moffat, R. J., and Maciejewski, P. K., 1985, ''Heat Transfer with Very High Free-stream Turbulence,'' Proceedings of HOST Conference, NASA Conf. Publ. 2405, NASA LeRC, pp. 203–215.
[28] Hay, N., Lampard, D., and Saluja, C. L., 1985, ''Effects of Cooling Films on the Heat Transfer Coefficient on a Flat Plate with Zero Mainstream Pressure Gradient,'' ASME J. Eng. Gas Turbines Power, **107**, pp. 105–110.
[29] Makki, Y. H., and Jakubowski, G. S., 1986, ''An Experimental Study of Film Cooling from Diffused Trapezoidal Shaped Holes,'' AIAA Pap., 86–1326.
[30] Ammari, H. D., Hay, N., and Lampard, D., 1990, ''The Effect of Density Ratio on the Heat Transfer Coefficient from a Film-Cooled Flat Plate,'' ASME J. Turbomach., **112**, pp. 444–450.

Flow and Heat (Mass) Transfer Characteristics in an Impingement/Effusion Cooling System With Crossflow

Dong Ho Rhee

Jong Hyun Choi

Hyung Hee Cho
e-mail: hhclo@yonsei.ac.kr

Department of Mechanical Engineering,
Yonsei University,
Seoul, 120-749 Korea

The present study is conducted to investigate flow and heat/mass transfer characteristics in an impingement/effusion cooling system with crossflow. To simulate the impingement/effusion cooling system, two perforated plates are placed in parallel and staggered arrangements with a gap distance of two times of the hole diameter, and initial crossflow passes between the plates. Both the injection and effusion hole diameters are 10 mm, and the Reynolds number based on the hole diameter and hole-to-hole pitch are fixed to 10,000 and six times of the hole diameter, respectively. To investigate the effect of crossflow, the flow rate of crossflow is changed from 0.5 to 2 times of that of the impinging jet, and the results of impingement/effusion cooling with crossflow are compared with those of the crossflow in the channel and of an array of impingement jets and the effusion cooling system. A naphthalene sublimation method is used to determine the local heat/mass transfer coefficients on the upward facing surface of the effusion plate. The flow patterns are calculated numerically using a commercial package. With the initial crossflow, the flow and heat/mass transfer characteristics are changed significantly from the results without the crossflow. Jet flows ejected from the injection plate are deflected by the crossflow, so that the stagnation points of the impinging jets move downstream. The heat/mass transfer rates on the effusion (target) plate decrease as the velocity of crossflow increases, since the crossflow induces the locally low transfer regions formed at the mid-way between the effusion holes. However, the impingement/effusion cooling with crossflow presents higher heat/mass transfer rates than the array jet impingement cooling with the same initial crossflow. [DOI: 10.1115/1.1519835]

Introduction

The thermal efficiency and specific power of gas turbine systems depend strongly on turbine inlet temperature. The inlet temperature is limited by the potential structural failure of the engine components mainly attributable to high thermal stresses and reductions in material strength due to high wall temperature. The wall temperature can be reduced by various cooling techniques such as internal convection cooling, jet impingement cooling and film cooling. In recent years, impingement/effusion cooling, which is one of the advanced cooling schemes, is developed and used in gas turbine engines. In this cooling scheme, the inner surfaces of hot components, such as combustor wall or blade surface, are cooled by the impingement of cooling air and outer surfaces which contact with hot gases are protected by effusion film cooling. This includes two flow situations, such as jet impingement on a plate and effusion flow through the holes of the target plate.

Some basic studies about impingement/effusion cooling have been performed for the last few decades. Hollworth and Dagan [1] and Hollworth et al. [2] measured the average and local heat transfer coefficients of arrays of turbulent air jets impinging on perforated target surfaces, and reported that arrays with staggered vents consistently yield higher heat transfer rates than do the impinging jets on the solid plates. Cho and Goldstein [3] investigated the effect of hole arrangements on the local heat/mass transfer characteristics inside the effusion plate. They found that the high transfer rate is induced by strong secondary vortices and flow acceleration, and the overall transfer rate is approximately 45 ~55% higher than that for the impingement cooling alone. Cho and Rhee [4] and Cho et al. [5] investigated heat/mass transfer and flow characteristics of an impingement/effusion cooling system with various experimental conditions.

In actual situations of combustor wall or turbine blade cooling, crossflow exists in the internal passages. Therefore, to improve cooling performance on the hot components, one should know the basic heat transfer characteristics of the impingement/effusion cooling with crossflow.

The studies related to the effects of crossflow are mainly concerned to the array jet impingement on the solid plate. Metzger and Korstad [6] and Florschuetz et al. [7] investigated the effects of crossflow on heat transfer/flow characteristics of array jet impingement, and reported that heat transfer is decreased at upstream region due to initial crossflow. Haiping et al. [8] studied flow/heat transfer characteristics for impinging jets with initial crossflow in numerical method. Cho et al. [9] investigated the effect of crossflow on heat transfer characteristics for array impinging jets and compared with the cases with effusion holes on the injection plate.

In the present study, heat/mass transfer characteristics on the effusion plate for an impingement/effusion cooling with initial crossflow are investigated for various operating conditions, and compared with those for a convective cooling (crossflow only) and an array jet impingement with initial crossflow.

To prevent hot spots and obtain better cooling performance, not only information of overall heat transfer coefficient but also its local variation is required [10]. Therefore, a naphthalene sublimation method is used to measure local heat/mass transfer coefficients on the effusion plate. This technique eliminates the conduc-

Contributed by the International Gas Turbine Institute and presented at the International Gas Turbine and Aeroengine Congress and Exhibition, Amsterdam, The Netherlands, June 3–6, 2002. Manuscript received by the IGTI, November 17, 2001. Paper No. 2002-GT-30474. Review Chair: E. Benvenuti.

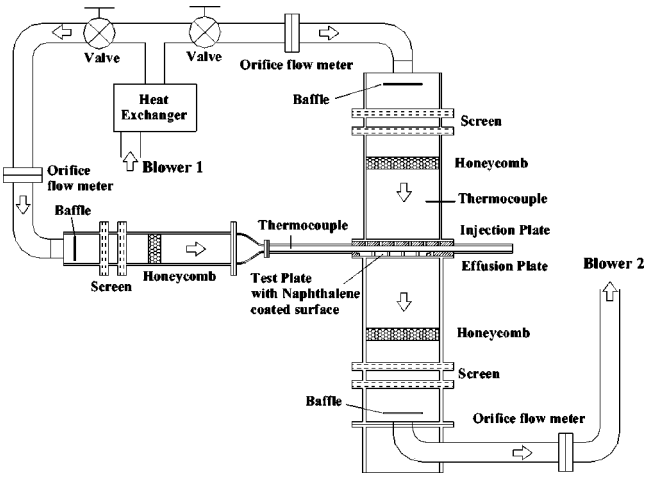

Fig. 1 Schematic view of experimental apparatus

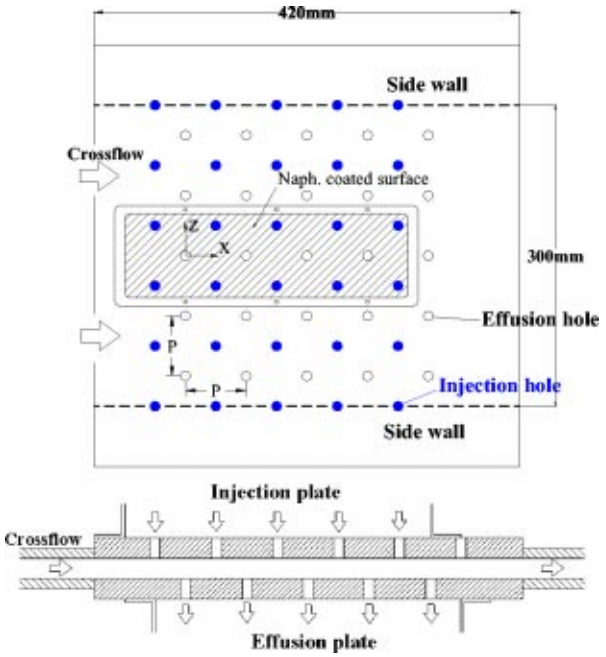

Fig. 2 Schematic diagrams of injection and effusion hole arrangement

tion and radiation errors inherent in heat transfer experiments. The surface boundary condition is analogous to an isothermal surface in a corresponding heat transfer experiment.

The flow characteristics should be obtained to understand local heat/mass transfer characteristics on the surface of effusion plate. Therefore, the present computational simulations using a commercial program (FLUENT) are accomplished to understand the flow patterns in the impingement/effusion cooling with initial crossflow.

Experimental Apparatus and Procedure

Experimental Apparatus and Operating Conditions

Experimental Apparatus. Figure 1 shows the schematic view of experimental apparatus. The experimental apparatus is composed of three parts: impinging jet, flow effusion, and crossflow supply parts. Two inverter-controlled blowers (Blowers 1 and 2) are used to obtain the designed operating conditions. Blower 1 (10HP) supplies air to the impinging jet and the crossflow plenum chambers, and the flow rate through each part is controlled by gate valves. Flow in the test section (between the injection and effusion plates) is sucked through the effusion holes by Blower 2. Three orifice flow meters are installed to measure the flow rates of the crossflow, the injected jets and the effused flow. Temperature of air in each plenum chamber is measured by *T*-type thermocouples, and is controlled using a heat exchanger to maintain the difference between the room temperature and temperature of air in the plenums within 0.2°C. In each plenum chamber, baffles, screens and honeycombs are installed to obtain uniform flow conditions. Cho and Goldstein [11] reported that heat/mass transfer coefficients on inside surface of the effusion plate are the same with and without crossflow over the outer surface of effusion plate (i.e., mainstream), therefore the effect of mainstream is not considered in the present study

The crossflow duct is located between the injection and the effusion plenum chambers. Room air from Blower 1 enters the crossflow plenum chamber, and then is discharged into the room through the duct. The cross section of duct is 300 mm (W) $\times$20 mm (H), and the hydraulic diameter (D_h) of the crossflow duct is 37.5 mm. The contraction section of which the area ratio is 6:1 is installed to obtain a uniform flow at the inlet of crossflow duct, and the distance between the inlet of duct and the first row of injection holes is set to be 400 mm ($10.7\,D_h$).

The coordinate system and injection and effusion hole arrangements are presented in Fig. 2. The diameters of the injection and the effusion holes are 10 mm, and the thickness of plates is 20 mm ($t/d=2.0$). The injection and effusion plates have 25 (5×5) holes of square array, and the ratio of hole spacing to the diameter (P/d) is 6.0.

A staggered hole arrangement between the injection and the effusion plates is used in this study. The naphthalene coated test plate is installed on the effusion plate for local mass transfer measurements as shown in Fig. 2. Four effusion holes are located in the test plate and the effusion holes are protected with the aluminum rim to maintain the circular hole shapes. The naphthalene-coated area in the test plate is $8.4d\times28d$ and A *T*-type thermocouple is installed in the test plate to measure precisely the naphthalene surface temperature.

Test Parameters and Operating Conditions. In this study, the effects of the initial crossflow are investigated for various ratios of the flow rate of the crossflow to the impinging jets with the fixed flow rate of impinging jets. The blowing rate represents a ratio of the flow rate of the crossflow to the impinging jets, and is defined as Eq. (1).

$$M=Q_c/Q_i \tag{1}$$

The experiments are performed with various blowing rates of 0.5 to 2.0 ($\mathrm{Re}_{Dh}=6{,}000\sim25{,}000$) in the present study. The gap distance between the injection and the effusion plate is fixed at $H/d=2.0$. Flow rates of air through the injection holes and the effusion holes are set to be constant, and the Reynolds numbers of the flow through the injection and effusion holes are fixed at $\mathrm{Re}_d=10{,}000$. Details of the test parameters and operating conditions are listed in Table 1.

Data Acquisition. In order to obtain the local mass transfer coefficients, the profile of the naphthalene surface coated on the test plate is scanned by an automated surface measuring system before and after exposure to air flow. Sublimation depth during the run is calculated from the difference of the surface profiles. The measuring system consists of a depth gage, a linear signal conditioner (LUCAS ATA-101), a digital multimeter (Keithley model 2001), two stepping-motor driven positioners, a motor controller, and a personal computer with GPIB (IEEE-488) board. The depth gage is a linear variable differential transformer (LVDT) made by Schaevitz Engineering (LBB-375TA-020),

Table 1 Test parameters

Cooling scheme	M	MR	I	Re_d	Re_{Dh}	d	D_h	H/d
Crossflow only	-	-	-	-	6,130 12,270	-	37.5 mm	2.0
Array impinging jet	0.5 1.0	0.164 0.327	0.027 0.107	10,000	6,130 12,270	10 mm	37.5 mm	2.0
Impingement/effusion cooling with initial crossflow	0.5* 1.0* 1.5* 2.0	0.164 0.327 0.491 0.654	0.027 0.107 0.241 0.428	10,000	6,130 12,270 18,400 24,540	10 mm	37.5 mm	2.0

(*: numerical simulations are also performed)

which has a resolution of 0.025 μm. Error of the LVDT measurements on a flat plate is less than 1% of an average sublimation depth of 40 μm during the run. The automated system typically obtains more than 2000 data points in an hour.

Heat/Mass Transfer Coefficient. The local mass transfer coefficient is defined as:

$$h_m = \frac{\dot{m}}{\rho_{v,w} - \rho_{v,\infty}} = \frac{\rho_s (dy/d\tau)}{\rho_{v,w}} \tag{2}$$

since incoming flow contains no naphthalene, $\rho_{v\infty} = 0$ in the present study. Therefore, the mass transfer coefficient is calculated from the local sublimation depth of naphthalene (dy), run time ($d\tau$), density of solid naphthalene (ρ_s), and naphthalene vapor density ($\rho_{v,w}$). The naphthalene vapor pressure is obtained from a correlation of Ambrose et al. [12]. Then, the naphthalene vapor density, $\rho_{v,vy}$ is calculated from the perfect gas law.

The Sherwood number can be expressed as

$$\mathrm{Sh} = h_m D_h / D_{\mathrm{naph}} \tag{3}$$

D_{naph} is based on the discussion of naphthalene properties given by Goldstein and Cho [13]. The mass transfer coefficients can be converted to the heat transfer coefficients using the heat and mass transfer analogy per Eckert [14]. Prandtl number is 0.71 for air and the Schmidt number is 2.28 for the naphthalene vapor in air at 25°C. The experiments are conducted at room temperature, and the Lewis number (Pr/Sc) for this study is about 0.307.

$$\frac{\mathrm{Nu}}{\mathrm{Sh}} = \left(\frac{\mathrm{Pr}}{\mathrm{Sc}}\right)^{0.4}, \quad \mathrm{Nu} = 0.624 \;\; \mathrm{Sh} \tag{4}$$

Uncertainty of the Sherwood numbers using the Kline and McClintock's [15] method for single sample experiments, considering the measured temperature, depth, position and correlation equations, is within $\pm 7.1\%$ in the entire operating range of the measurement, based on a 95% confidence interval. This uncertainty is attributed mainly to the uncertainty of properties of naphthalene, such as the naphthalene saturated vapor pressure (3.8%), and diffusion coefficient of naphthalene vapor in the air (5.1%). However, the uncertainty due to the sublimation depth measurement is only 0.7%. The other uncertainties are 0.2%, 1.1% and 4.9% for T_w, ρ, and h_m, respectively.

Numerical Analysis

Numerical simulations using a commercial code (FLUENT) are accomplished to understand the flow patterns in an impingement/effusion cooling system. The computation domain is modeled by the geometry used in the experimental study. The symmetry boundary conditions are imposed on injection/effusion hole planes to reduce grid size and calculation time. The computation domain grids are created using the GAMBIT solid modeling, and the number of grid points is about 500,000. Different grids are used to verify the grid independence of the solution at Reynolds number of 10,000. The steady solutions for turbulent flow field in the impingement/effusion cooling system are calculated using a RNG k-ε model with a standard wall function for the near wall region. In the present numerical simulations, the flow characteristics for the impingement/effusion cooling with initial crossflow are investigated with the various blowing rates ($M = 0.5$, 1.0, and 1.5) at $\mathrm{Re}_d = 10{,}000$ and $H/d = 2.0$.

Results and Discussion

In this study, the flow patterns and heat/mass transfer characteristics are investigated for the impingement/effusion cooling with an initial crossflow, and compared with those for the convective cooling (crossflow only) and the impingement cooling of jet array.

1 Convection in Crossflow Channel. The distributions of the Sherwood numbers are measured in the crossflow channel (convective cooling only) to obtain the baseline data (Fig. 3). The Reynolds numbers (Re_{Dh}) of the crossflow are the same as those for the impingement/effusion cooling with initial crossflow at $M = 0.5$ and 1.0. Local Sherwood numbers are high at the inlet region and decrease monotonously as the flow moves downstream because the concentration (thermal) boundary layer develops.

In Fig. 3, the Sherwood numbers for fully developed turbulent flow and laminar flow are presented to compare with the experimental data. The Dittus-Boelter correlation [16] of the Sherwood number for fully developed turbulent flow ($\mathrm{Sh} = 0.023\,\mathrm{Re}^{0.8}\,\mathrm{Sc}^{0.4}$) and the constant value for laminar flow inside a smooth circular pipe are used. It is noted that the Sherwood numbers are switched to Sh based on the hole diameter (d) in Fig. 3. For $\mathrm{Re}_{Dh} = 12{,}270$ ($M = 1.0$), the Sherwood number converges to the value for the fully developed turbulent flow. However, for $\mathrm{Re}_{Dh} = 6{,}130$ ($M = 0.5$), the Sherwood number is lower than that for the fully developed turbulent flow and converges to the value between the laminar flow and the turbulent flow. The higher value may be due to the difference in geometry and near a transient duct

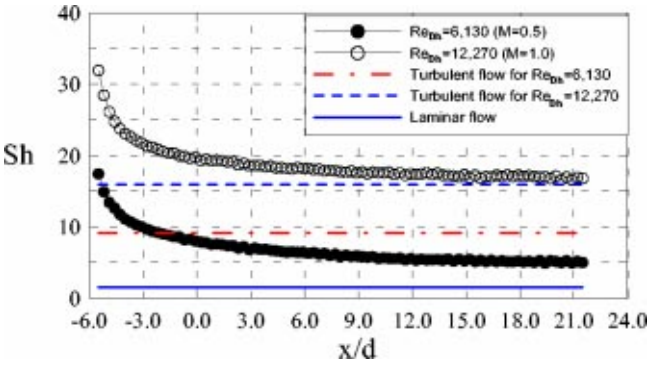

Fig. 3 Distributions of Sh for crossflow only (without impingement/effusion flow)

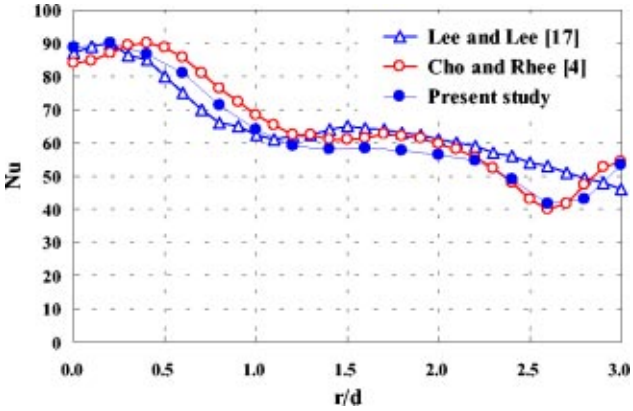

Fig. 4 Comparison with other results near the stagnation point for $H/d=2.0$ and $Re_d=10{,}000$

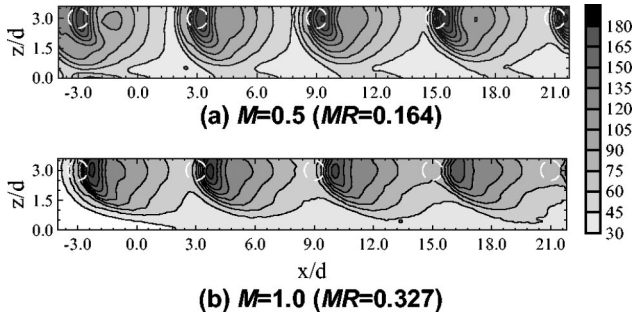

Fig. 5 Contour plots of Sh for array jet impingement with initial crossflow at $Re_d=10{,}000$ and $H/d=2.0$. (*a*) $M=0.5$ ($MR=0.164$), (*b*) $M=1.0$ ($MR=0.327$)

flow regime ($Re_H \simeq 3300$). It is also noted that the laminar duct flow has the longer flow developing entrance length.

The tested flow with the array jet impingements or impingement/effusion is expected to be in a turbulent flow regime whether the crossflow at the inlet is laminar or turbulent. It is because the crossflow is disturbed vigorously by the impinging jets and effusion holes.

2 Array Jet Impingement Cooling With an Initial Crossflow. To verify the experimental apparatus, the experiment of the array jet impingement without crossflow is conducted. Figure 4 shows the local distributions of Nusselt number obtained by the heat/mass transfer analogy (Eq. (4)) of the present study and other results for $H/d=2.0$ and $Re_d=10{,}000$. The data of the present study are taken in the region of $9.0 \leqslant x/d \leqslant 12.0$ to minimize the effect of crossflow generated by spent air. Some discrepancies are observed among the results for the same jet Reynolds number because the heat/mass transfer pattern near the stagnation point is affected by the impinging jet flow condition at the hole exit. However, there is a favorable agreement on the results. In addition, the additional peak values are observed at $r/d=3.0$ for the array jets due to the interaction between the adjacent wall jets and these values are almost the same for both cases.

Figure 5 presents the contour plots of Sh for the array jet impingement cooling with an initial crossflow at $M=0.5$ and 1.0. It is noted that the white dotted circles mean the projected positions of the injection holes in contour plots. In general, a crossflow is formed by the spent air from the array impinging jets in a confined space even when there is no initial crossflow, and the amount of the crossflow increases as flow moves downstream. Therefore, the stagnation points of the impinging jets move downstream, and the heat/mass transfer rates decrease at the midway region because the thermal boundary layer develops with the crossflow [9].

With the initial crossflow, the effects of the crossflow start at the first row of impinging jets as shown in Fig. 5. Asymmetric distributions of Sh are formed on the stagnation regions due to the initial crossflow. For $M=0.5$, the high transfer regions spread laterally, and the additional peaks at the mid-way region are shifted toward the downstream side and decrease with increasing x/d. For $M=1.0$, the overall contour pattern of Sh is similar to that for $M=0.5$. However, Sh at the stagnation points are lower than those for $M=0.5$ and the locations of the peak values move downstream. In addition, the additional peak at the midway region is not observed due to increased amount of the crossflow.

The local distributions of Sh for the array jet impingement with initial crossflow are presented in Fig. 6. At $z/d=3.0$, the local values of Sh at the stagnation points increase as x/d increases for $M=0.5$ because the turbulence intensity of jet core flow is elevated by the interaction with the crossflow. The peak values are about eight times higher than that of the channel flow (convective cooling). However, for $M=1.0$, the Sherwood numbers at the stagnation points decrease and the locations of the peak values move downstream with increasing x/d because the crossflow sweeps the impinging jets resulting in weak impingements on the target plate.

At $z/d=0.0$, the additional peak values are observed for $M=0.5$ due to the interaction between the adjacent wall jets, and these peaks decrease as x/d increases due to increasing effect of the crossflow. For $M=1.0$, the additional peaks are not seen clearly because the wall jets of the adjacent impinging jets are swept by the strong crossflow, hence the interaction between the wall jets does not appear at the midway region.

3 Impingement/Effusion Cooling With Initial Crossflow

3.1 Flow Field. Figure 7 presents velocity vector plots at the injection plane ($z/d=3.0$) for the impingement/effusion cooling with initial crossflow with various blowing rates. For $M=0.5$, the effects of the initial crossflow are not shown clearly except the upstream region of the impinged jets. The impinging jets are not deflected significantly and the vortex due to the interaction between the wall jet and the crossflow is formed at the upstream region of the impinging jet. Small recirculation regions are formed at the downstream side of impinging jets due to the flow reentrainment, which is a typical flow pattern in a confined jet.

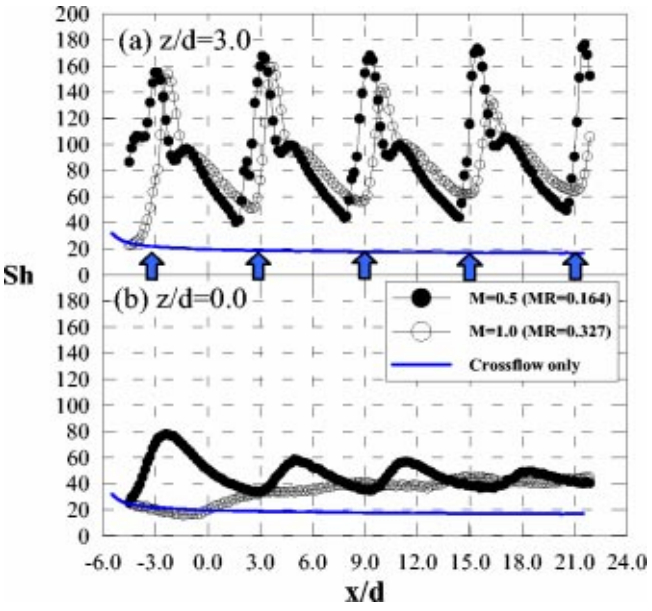

Fig. 6 Local distributions of Sh for array jet impingement with initial crossflow at $Re_d=10{,}000$ and $H/d=2.0$.

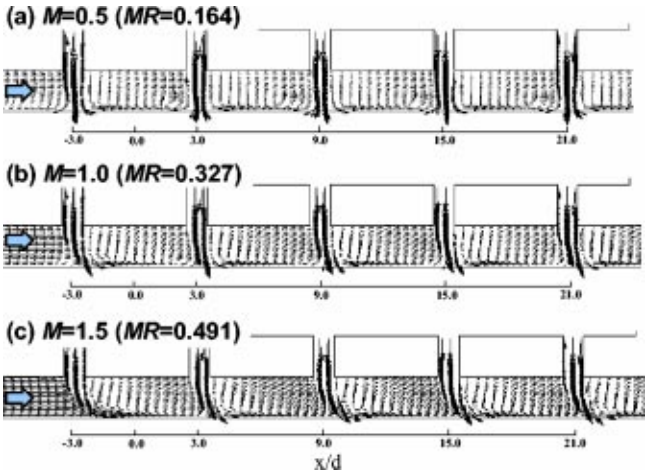

Fig. 7 Calculated velocity vector plots at the injection plane ($z/d=3.0$) for impingement/effusion cooling with initial crossflow at $Re_d=10{,}000$ and $H/d=2.0$

For relatively higher blowing rates of $M=1.0$ and 1.5, the injected jets are deflected toward the downstream side due to the strong crossflow effect. For example, at $M=1.5$, the injected jets are swept away by the crossflow rather than impinge on the effusion plate at the entrance region. The injected jets of the first row ($x/d=-3.0$) impinge weakly on the effusion plate at $x/d \cong -1.5$. The stagnation points of the other impinging jets are shifted about $1d$ from the center of the impinging jet locations without crossflow. In addition, the large recirculation regions are formed at the downstream side of the impinging jets for higher blowing rates. This recirculation is related to the blockage effect of impinging jets for the strong crossflow.

Figure 8 presents velocity vector plots at the effusion plane ($z/d=0.0$) for the impingement/effusion cooling with initial crossflow at various blowing rates. For the low blowing rate of $M=0.5$, the upward flow pattern is observed due to the interaction between the adjacent wall jets as reported by Cho and Rhee [4], and then the flow is discharged through the effusion holes. Therefore, the effects of the crossflow are weak and the periodic flow patterns are observed in the whole domain. However, for the high

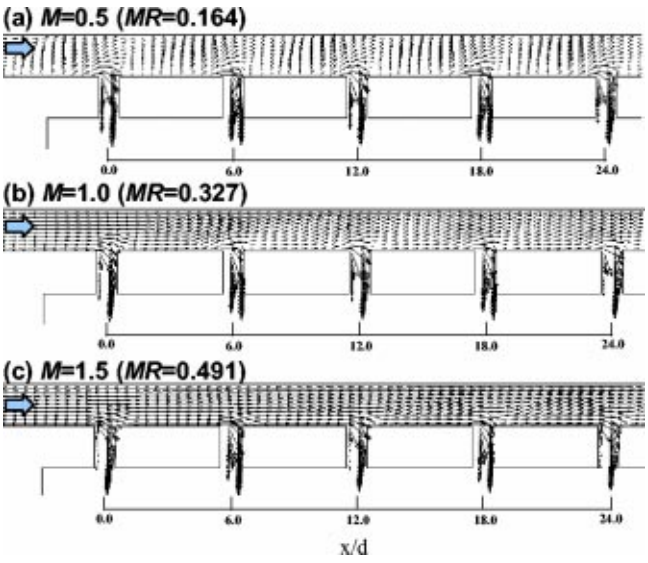

Fig. 8 Calculated velocity vector plots at the effusion plane ($z/d=0.0$) for impingement/effusion cooling with initial crossflow at $Re_d=10{,}000$ and $H/d=2.0$

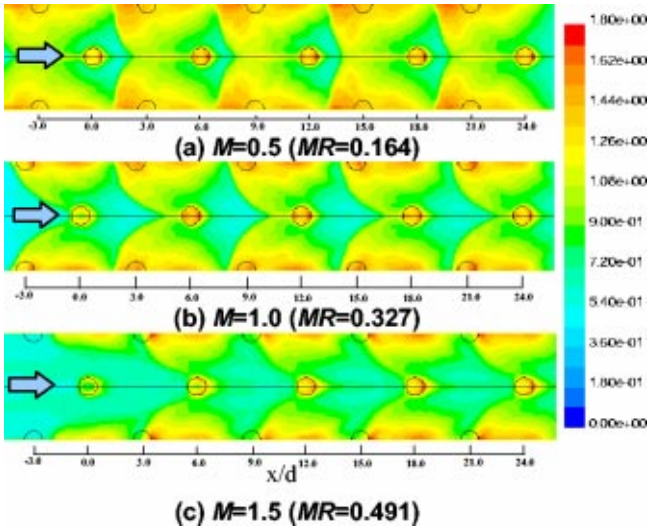

Fig. 9 Contour plots of calculated turbulence intensity (%) on the plane $0.1d$ apart from the effusion plate for various blowing rates at $Re_d=10{,}000$ and $H/d=2.0$

blowing rates, the overall flow patterns are similar to that for a smooth duct except near the inlet of the effusion holes. Near the inlet region of effusion holes, the channel flow is disturbed and impinges on the inside wall of the effusion holes. Therefore, relatively high heat/mass transfer rates can be observed on this region [17]. For $M=1.5$, the wall jets are swept, thus the interactions of the wall jets are not generated and the upward flow patterns are not observed in Fig. 8(c).

Figure 9 shows the contour plots of turbulence intensity on the plane 1 mm ($0.1d$) apart from the bottom wall for the various blowing rates. Overall turbulence intensity for $M=0.5$ is higher than that for higher blowing rates of $M=1.0$ and 1.5. The reason is that most of the injected jet is swept by the strong crossflow and the effects of the jet impingement and the wall jet are reduced for higher blowing rates.

For the low blowing rate of $M=0.5$, a region of high turbulence intensity is divided into four regions: 1) the upstream region of the stagnation points (impinging jets) due to the interaction between the crossflow and the wall jets, 2) the downstream region of the stagnation points (impinging jets) due to the flow transition to turbulent flow with the small gap distance, 3) the midway region due to the interaction of wall jets, and 4) the inlet region of the effusion holes due to the disturbance of flow by the effusion hole. However, the low turbulence intensity distributions are observed at the downstream region of the effusion holes. Therefore, the low heat/mass transfer region may be formed at this region.

As the blowing rate increases, the regions of the high turbulence intensity at the upstream and downstream regions of the stagnation points are shifted toward the downstream side due to the deflection of the impinging jets. Especially, for $M=1.5$, the turbulence intensity around the first impinging jets is significantly lower and the region affected by the impingement jet is narrower with the strong crossflow. At the midway region, a region of the low turbulence intensity increases with increasing the blowing rate because most of the wall jets are swept by the strong crossflow.

3.2 Local Heat/Mass Transfer Characteristics. Figure 10 presents the contour plots of Sh for the impingement/effusion cooling with initial crossflow of various blowing rates at $Re_d=10{,}000$ and $H/d=2.0$. White dotted circles and the small half circles (full circles for $M=1.0$) in the contour plots represent the projected positions of injection hole and the effusion holes with the aluminum rim between two circles, respectively.

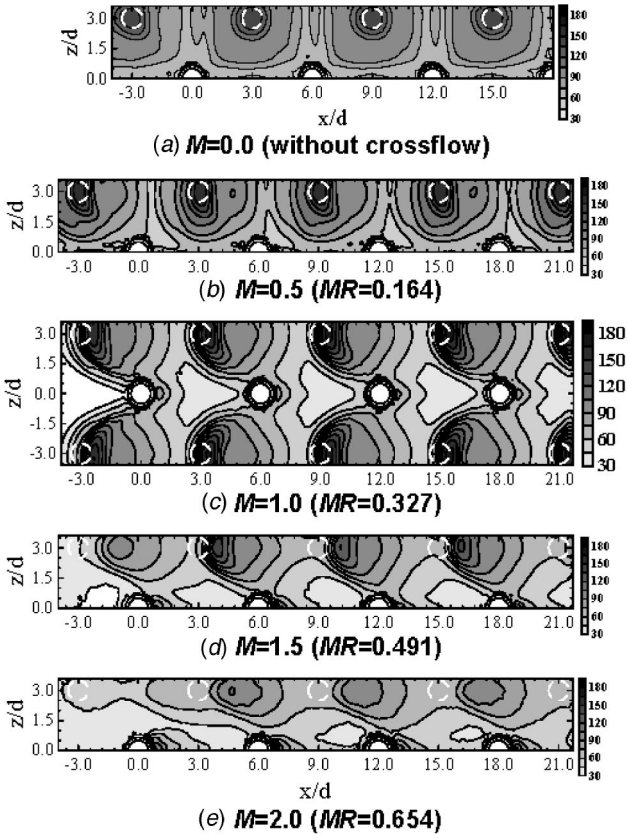

Fig. 10 Contour plots of Sh for various blowing rates at Re_d = 10,000 and H/d=2.0

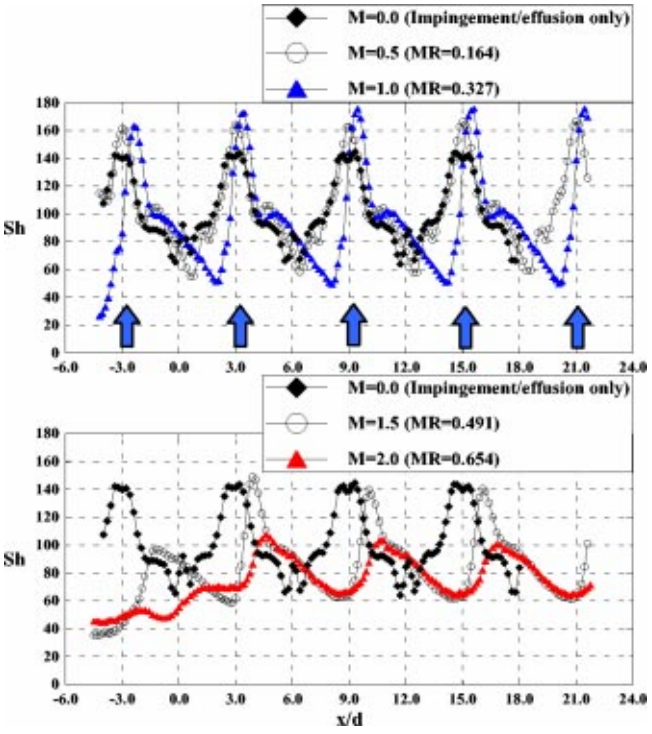

Fig. 11 Local distributions of Sh for impingement/effusion cooling with initial crossflow at z/d=1.0

For the case without initial crossflow (Fig. 10(*a*)), the pattern of local Sh shows a good symmetry. The Sherwood numbers are high around the stagnation points and decrease as the wall jet boundary layer develops after the impingement. Also, the additional peak values of Sh are observed along the midline (at $x/d=0.0$, 6.0, and 12.0) due to the secondary vortices induced by the interaction of the adjacent wall jets and the flow acceleration toward the effusion holes [4].

For the low blowing rate of $M=0.5$, the distribution of Sh is similar to that without the crossflow because the effect of the crossflow is weak. However, the stagnation points are shifted slightly toward the downstream side and the high transfer region spreads in the lateral direction. Also, the additional peaks at the mid-way region between the impinging jets are not observed clearly due to the weak interaction of the wall jets.

For the cases of relatively high blowing rates, the heat/mass transfer patterns are totally different from those without the initial crossflow. The injected jets are deflected and the wall jets are swept away by the crossflow. Therefore, the Sherwood number contours show nonuniform and asymmetric distributions. For $M=1.0$, the regions of high heat/mass transfer at the stagnation points are bended and deflected toward the downstream direction. However, the Sherwood number contour shows a periodic distribution except the first row of injection holes because a certain amount of the crossflow and the spent air is discharged through the effusion holes and the balance between the flow entrance and exhaust is preserved. The additional peaks shown in the cases of $M=0.0$ and 0.5 are not observed for $M=1.0$, and the heart-shaped low transfer regions are formed between the effusion holes. It is because the wall jets swept by the crossflow are sucked by the effusion holes and the flow field is similar to that in a duct at this region (Fig. 8). The heat/mass transfer pattern shows the similar trend as the distribution of the turbulence intensity shown in Fig. 8. The locally high heat/mass transfer coefficients are observed around the inlet of effusion holes due to the flow disturbance and the flow acceleration toward the effusion holes.

For relatively high blowing rates of $M=1.5$ and 2.0, the regions affected by the impinging jets are reduced significantly and the overall levels of Sh are lower than the cases for $M\leqslant 1.0$. Especially, the heat/mass transfer enhancement by the first row of impinging jets is decreased greatly due to the strong crossflow effect with the weak jet impingement. However, the heat/mass transfer coefficients at the region between the effusion holes are higher than those for $M=1.0$ because the flow disturbance around the effusion hole is increased with increasing crossflow velocity.

The local distributions of Sh for the impingement/effusion cooling with initial crossflow at $z/d=3.0$ and 0.0 are presented in Figs. 11 and 12, respectively. For $M=0.5$, the levels of peak values at the stagnation points are almost the same in spite of the crossflow. The secondary peaks due to the flow transition of the wall jet to turbulent flow [18] are observed at the downstream region of the stagnation points and these peaks are even higher than those without crossflow. However, the small peaks at the upstream region of the stagnation points are observed. This pattern is caused by the deflections of the impinging jet and the wall jets. Some of the wall jets at the upstream region are blocked and swept by crossflow, so the most part of wall jets are directed toward the downstream region. Therefore, the flow rate of wall jets toward the downstream region is increased with some initial crossflow and the secondary peaks at downstream region is higher than those without crossflow.

The overall pattern of the Sherwood numbers is similar to that of $M=0.0$ (without the initial crossflow), except at the stagnation region. The higher values at the stagnation regions are caused by the increased turbulence intensity of the jet core flow.

For $M=1.0$, the peak values at the stagnation points increases slightly as the flow moves downstream because the interaction between the impinging jets and the crossflow enhances the turbulence intensity of jets. However, the secondary peaks at the down-

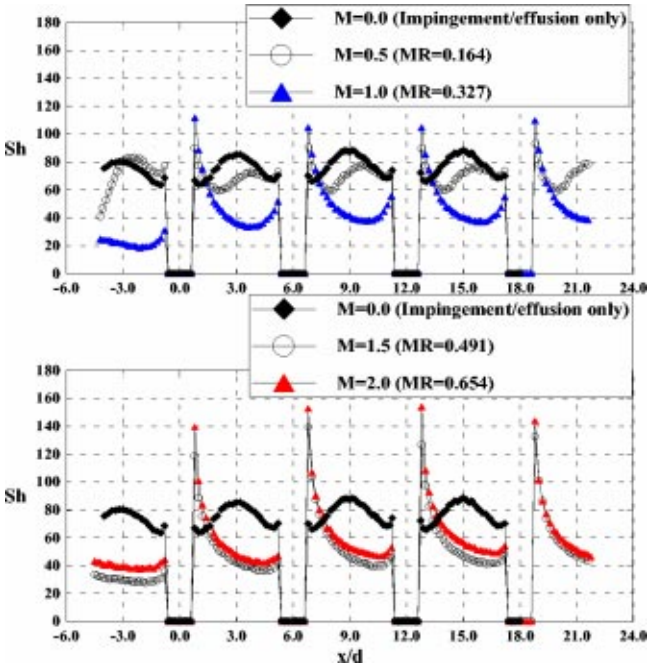

Fig. 12 Local distributions of Sh for impingement/effusion cooling with initial crossflow at $z/d=0.0$

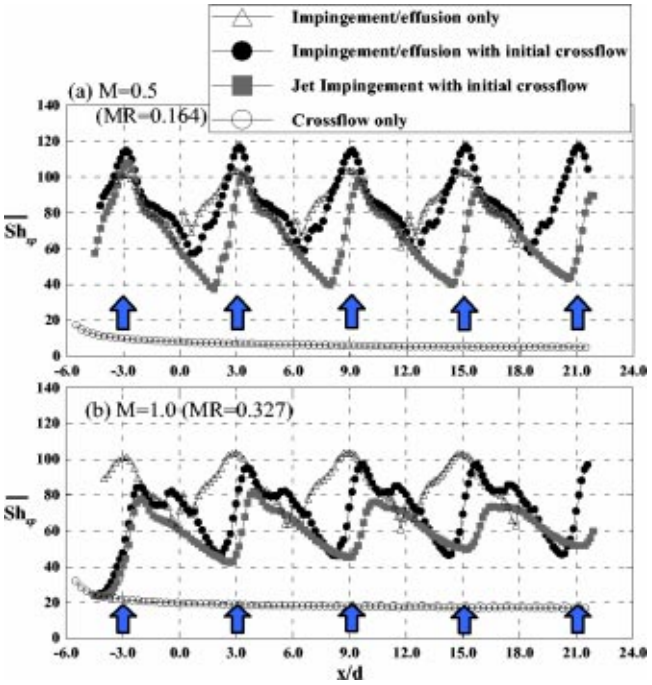

Fig. 13 Distributions of spanwise averaged Sh for various cooling schemes at Re_d=10,000 and $H/d=2.0$

stream regions of the stagnation points are lower than those for $M=0.5$ and the peaks at the upstream region disappear.

As the blowing rate increases more, the effect of the crossflow becomes dominant. The heat/mass transfer rates at the inlet region decrease significantly and the Sherwood numbers at the inlet region for $M=1.5$ and 2.0 are only 30~60% of those for $M \leqslant 1.0$. This trend is preserved at the downstream region. The peaks at the stagnation points are shifted toward the downstream direction. The peak Sherwood number is the highest at the second row and then decreases slightly going downstream and the values are 20~40% lower than those for $M \leqslant 1.0$.

At $z/d=0.0$, relatively high Sherwood numbers are observed between the effusion holes for $M=0.5$ (Fig. 12). This is due to the interaction between the adjacent wall jets. However, these peaks disappear as the blowing rate increases. For relatively higher blowing rates ($M \geqslant 1.0$), the Sherwood numbers have peak values at the trailing edge (downstream) of the effusion holes, and then decrease monotonously. The reason is that the effusion flow through the holes removes the high concentration (temperature) air of the mass (thermal) boundary layer and the duct core flow attaches on this region as shown in the velocity vector plot (Fig. 8). The mass (thermal) boundary layer redevelops as the flow goes to the upstream side of the next effusion hole. The level of Sh increases slightly as the blowing rate increases due to the increased Reynolds number of duct.

4 Average Heat/Mass Transfer. Figure 13 presents the spanwise averaged Sherwood numbers on the effusion plate for the various cooling schemes at $M=0.5$ and 1.0. The averaged values are obtained by taking the local data in the region of $0.0 \leqslant z/d \leqslant 3.0$. The arrows indicate the locations of the impinging jets. As expected, the average Sherwood numbers for the impingement/effusion cooling show the highest values for all the tested cases, because the effects of crossflow and the flow re-entrainment of spent air are reduced. For the array jet impingement, the flow rate of the crossflow increases with increasing x/d and the thermal boundary layer is thickened. Thus, the flow re-entrainment of the spent air into the impinging jets also increases. Therefore, the average Sh decreases and the peak values move downstream as the flow moves toward the downstream side. However, for the impingement/effusion cooling, a certain amount of the crossflow and/or the spent air is discharged through the effusion holes and hence the effects of the crossflow and the flow re-entrainment are reduced in the whole domain except the inlet region. Consequently, the distributions of the average Sherwood number have the periodic patterns and the levels of peak Sherwood number are almost the same in the whole domain for both cases (with and without initial crossflow).

Figure 14 presents the spanwise averaged Sherwood numbers on the effusion plate for the impingement/effusion cooling with initial crossflow for various blowing rates. For $M=0.5$, the aver-

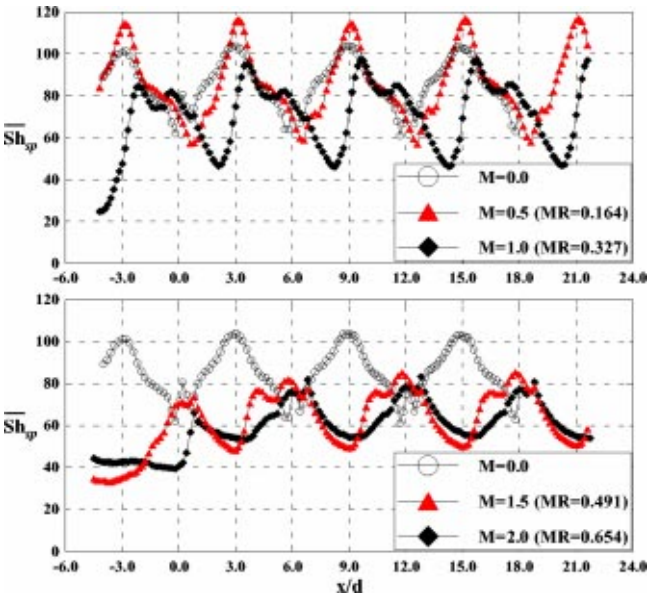

Fig. 14 Distributions of spanwise averaged Sh for impingement/effusion cooling with initial crossflow of various blowing rates at Re_d=10,000 and $H/d=2.0$

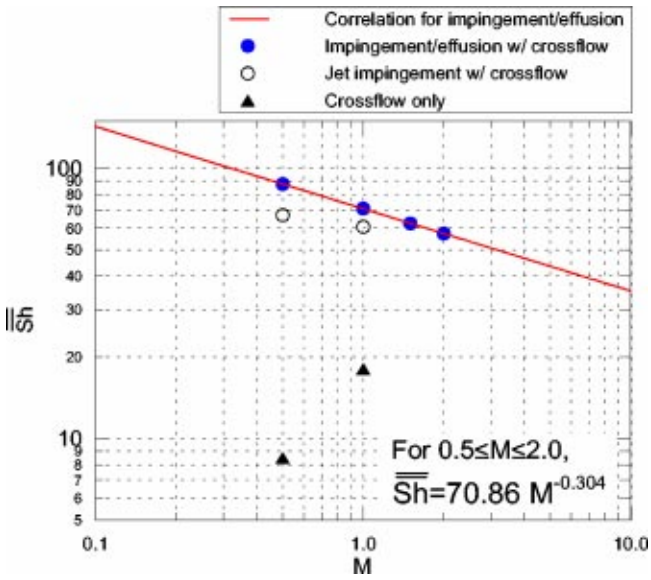

Fig. 15 Overall averaged Sh for various cooling schemes and blowing rates at Re_d=10,000 and H/d=2.0

age values at the stagnation points are about 20% higher than those without the initial crossflow due to the elevated turbulence intensity of the impinging jets. However, the average Sherwood numbers at the upstream region of the stagnation points are lower because the impinging jets are shifted slightly toward the downstream side and the interaction between the wall jets is weakened. For $M=1.0$, two peaks and one valley are observed in one pitch. Two peaks are mainly due to the jet impingement on the stagnation points and the flow disturbance around the effusion holes, respectively. The valley is related to the heart-shaped low transfer region as shown in Fig. 10(*c*) due to the low velocity near the surface. For $M=2.0$, the average Sherwood number shows peak values at the region where the effusion holes are located rather than the stagnation points. The reason is that the effect of the jet impingement is weakened significantly, while the heat/mass transfer is enhanced due to the flow disturbance with the strong crossflow.

Figure 15 shows the overall averaged Sherwood numbers on the effusion plate for various cooling schemes and blowing rates. The impingement/effusion cooling shows 20~30% higher cooling performance than the array jet impingement and 3.5~9 times higher than the convective cooling (crossflow only). For the impingement/effusion cooling and the array jet impingement, the overall averaged Sh for $M=1.0$ is lower than that for $M=0.5$. This implies that the large amount of the crossflow reduces the heat/mass transfer on the effusion plate in spite of the more flow rates of the coolant.

For the impingement/effusion cooling with initial crossflow, the average value for $M=0.5$ is almost the same as that without the initial crossflow, but the average Sh decreases as the blowing rate increases. Therefore, it is necessary to reduce the blowing rates as possible to obtain the high cooling performance. For the impingement/effusion cooling with initial crossflow, the overall averaged Sherwood number on the effusion plate is fitted as the following equation for $M=0.5$ to $M=2.0$ at $Re_d=10{,}000$ and $H/d=2.0$:

$$\overline{\overline{Sh}} = 70.86\ M^{-0.304}$$

$$\overline{\overline{Sh}} = 50.40\ (MR)^{-0.304} \quad (5)$$

Conclusions

In the present study, the flow and heat/mass transfer characteristics for the impingement/effusion cooling with initial crossflow are investigated and compared with those for the convective cooling and the array jet impingement. The results are summarized as follows:

Effects of the Initial Crossflow on Impingement/Effusion Cooling. With the initial crossflow, the flow and heat/mass transfer characteristics are changed significantly from the results without the crossflow. Jet flows ejected from the injection plate are disturbed by the crossflow, and the interaction between the adjacent wall jets is weakened by the crossflow.

For the low blowing rate, the cooling performance is similar to that without the initial crossflow. However, the heat/mass transfer rates on the effusion (target) plate decrease as the blowing rate increases, and the crossflow induces the locally low transfer regions formed at the midway region between the effusion holes. Therefore, it is necessary to reduce the crossflow rates to obtain the high cooling performance.

Variation of Cooling Schemes. With the initial crossflow, the impingement/effusion cooling shows 20~30% higher cooling performance than the array jet impingement and 3.5~9 times higher than the convective cooling (crossflow only) due to the reduction of the effect of crossflow and the spent air reentrainment.

Acknowledgments

The authors wish to acknowledge support for this study by Ministry of Science and Technology through National Research Laboratory program.

Nomenclature

- d = injection and effusion hole diameter
- dy = local sublimation depth of naphthalene
- D_h = hydraulic diameter of test duct
- D_{naph} = mass diffusion coefficient of naphthalene vapor in air
- H = gap distance between injection and effusion plates
- h_m = local mass transfer coefficient
- I = local momentum flux ratio of crossflow and impinging jets, $\rho_c V_c^2/\rho i V_i^2$
- $\dot{m}$ = local naphthalene mass transfer per unit area and time
- M = blowing rate (total mass flow ratio of crossflow and impinging jets), Q_c/Q_i
- MR = local mass flux ratio of crossflow and impinging jets, $\rho_c V_c/\rho_i V_i$
- Nu = Nusselt no. based on hole diameter, hd/k
- Pr = Prandtl no.
- P = pitch of array holes
- Q_c = mass flow rate of crossflow
- Q_i = mass flow rate of injected jet or effused flow
- Re_d = Reynolds no. based on hole diameter and average velocity in hole
- Re_{Dh} = Reynolds no. based on hydraulic diameter of duct and average velocity of crossflow
- Sc = Schmidt no.
- Sh = Sherwood no. based on hole diameter, $h_m d/D_{\text{naph}}$
- $\overline{Sh}_{sp}$ = spanwise average Sherwood no.
- $\overline{\overline{Sh}}$ = overall average Sherwood no.
- t = thickness of injection and effusion plates
- V_c = mean velocity of crossflow
- V_i = mean velocity of impinging jet
- x, z = distance from center of effusion hole (Fig. 2)
- ρ_c = density of crossflow
- ρ_i = density of impinging jet flow
- ρ_s = density of solid naphthalene

$\rho_{v,w}$ = naphthalene vapor density on surface
$\rho_{v,\infty}$ = naphthalene vapor density of injected jet
τ = test duration

References

[1] Hollwarth, B. R., and Dagan, L., 1980, ''Arrays of Impinging Jets with Spent Fluid Removal through Vent Holes on the Target Surface Part 1: Average Heat Transfer,'' ASME J. Eng. Power, **102**, pp. 994–999.

[2] Hollwarth, B. R., and Lehmann, G., and Rosiczkowski, J., 1983, ''Arrays of Impinging Jets with Spent Fluid Removal through Vent Holes on the Target Surface Part 2: Local Heat Transfer,'' J. Eng. Power, **105**, pp. 393–402.

[3] Cho, H. H., and Goldstein, R. J., 1996, ''Effect of Hole Arrangements on Impingement/Effusion Cooling,'' *Proc. 3rd KSME-JSME Thermal Engineering Conference*, pp. 71–76.

[4] Cho, H. H., and Rhee, D. H., 2001, ''Local Heat/Mass Transfer Measurement on the Effusion Plate in Impingement/Effusion Cooling System,'' ASME J. Turbomach., **123**, pp. 601–608.

[5] Cho, H. H., Choi, J. H., and Rhee, D. H. 2001, ''The Effects of Hole Arrangements on Heat/Mass Transfer of Impingement/Effusion Cooling System,'' *Proc. ExHFT-5*, pp. 975–980.

[6] Metzger, D. E., and Korstad, R. J., 1992, ''Effects of Cross flow in Impingement Heat Transfer,'' ASME J. Eng. Power, **94**, pp. 35–41.

[7] Florschuetz, L. W., Metzger, D. E., and Su, C. C., 1984, ''Heat Transfer Characteristics for Jet Array Impingement With Initial Crossflow,'' ASME J. Heat Transfer, **106**, pp. 34–41.

[8] Haiping, C., Wanbing, C., and Taiping, H., 1999, ''3-D Numerical Simulation of Impinging Jet Cooling with Initial Crossflow,'' ASME Paper No. 99-GT-256.

[9] Cho, H. H., Yoon, P. H. and Rhee, D. H., 2001, ''Heat/mass Transfer Characteristics of Arrays of Impingement Jets with Effusion Holes,'' *Proc. ExHFT-5*, pp. 955–960.

[10] Cho, H. H., and Goldstein, R. J., 1997, ''Total Coverage Discrete Hole Wall Cooling,'' ASME J. Turbomach., **119**(2), pp. 320–329.

[11] Cho, H. H., and Goldstein, R. J., 1995, ''Heat (Mass) Transfer and Film Cooling Effectiveness With Injection Through Discrete Holes—Part I: Within Holes and on the Back Surface,'' ASME J. Turbomach., **117**, pp. 440–450.

[12] Ambrose, D., Lawrenson, I. J., and Sparke, C. H. S., 1975, ''The Vapor Pressure of Naphthalene,'' J. Chem. Thermodyn., **7**, pp. 1173–1176.

[13] Goldstein, R. J., and Cho, H. H., 1995, ''A Review of Mass Transfer Measurement Using Naphthalene Sublimation,'' Exp. Therm. Fluid Sci., **10**, pp. 416–434.

[14] Eckert, E. R. G., 1976, *Analogies to Heat Transfer Processes, in Measurements in Heat Transfer*, ed., E. R. G. Eckert, and R. J. Goldstein, pp. 397–423, Hemisphere Pub., New York, NY.

[15] Kline, S. J., and McClintock, F., 1953, ''Describing Uncertainty in Single Sample Experiments,'' Mech. Eng. (Am. Soc. Mech. Eng.), **75**, p. 3–8.

[16] Dittus, P. W., and Boelter, L. M. K., 1930, Univ. Cal. Pebl. Engng, **2**(13), pp. 443–461; 1985, reprinted in Int. Commun. Heat Transfer, **12**, pp. 3–22.

[17] Goldstein, R. J., Cho, H. H., and Jabbari, M. Y., 1997, ''Effect of Plenum Crossflow on Heat (Mass) Transfer Near and Within the Entrance of Film Cooling Holes,'' ASME J. Turbomach., **119**, pp. 761–769.

[18] Cho, H. H., Lee, C. H., and Kim, Y. S., 1997, ''Characteristics of Heat Transfer in Impinging jets by Control of Vortex Pairing,'' ASME Paper No. 97-GT-276.

The Measurement of Full-Surface Internal Heat Transfer Coefficients for Turbine Airfoils Using a Nondestructive Thermal Inertia Technique

Nirm V. Nirmalan
Mem. ASME

Ronald S. Bunker
Fellow ASME

Carl R. Hedlund

Global Research Center,
General Electric Company,
Niskayuna, NY 12309

A new method has been developed and demonstrated for the non-destructive, quantitative assessment of internal heat transfer coefficient distributions of cooled metallic turbine airfoils. The technique employs the acquisition of full-surface external surface temperature data in response to a thermal transient induced by internal heating/cooling, in conjunction with knowledge of the part wall thickness and geometry, material properties, and internal fluid temperatures. An imaging Infrared camera system is used to record the complete time history of the external surface temperature response during a transient initiated by the introduction of a convecting fluid through the cooling circuit of the part. The transient data obtained is combined with the cooling fluid network model to provide the boundary conditions for a finite element model representing the complete part geometry. A simple 1-D lumped thermal capacitance model for each local wall position is used to provide a first estimate of the internal surface heat transfer coefficient distribution. A 3-D inverse transient conduction model of the part is then executed with updated internal heat transfer coefficients until convergence is reached with the experimentally measured external wall temperatures as a function of time. This new technique makes possible the accurate quantification of full-surface internal heat transfer coefficient distributions for prototype and production metallic airfoils in a totally nondestructive and non-intrusive manner. The technique is equally applicable to other material types and other cooled/heated components. [DOI: 10.1115/1.1515798]

Introduction

The increasing efficiency and performance of gas turbine engines relies on the combination of many disciplines, including aerodynamics, combustion, cooling technology, rotor dynamics, aeromechanics, manufacturing, and materials science to name only a few. The quality of components and systems is assured through a network of tasks, beginning with the fundaments in research and development, incorporation of sound design practices, evaluations in engine testing, and many quality inspection methods. During the early development stages, the primary inspection methods are those involving the destruction of materials and parts to measure actual physical properties and their statistical distributions. In the latter stages of development, and especially in the production and operation of engines, non-destructive evaluation (NDE) methods must be relied upon. Typical techniques other than simple visual inspection include ultrasound, X-ray, digital X-ray, fluoro-penetrant inspection, and flash Infrared thermography. The objective of these techniques is the detection and measurement of cracks, wall thickness, feature dimensions, porosity, and coating flaws, on the internal and external surfaces, as well as through the wall.

High-pressure turbine blade internal cooling in advanced engines is typically composed of very complex flow circuits containing many 3-D geometrical features, including passage aspect ratio changes, multi-channels, rib rougheners, pedestals or pin-fins, film cooling extraction, impingement, and turning regions. As a result, the internal cooling distribution in the form of local heat transfer coefficients is also highly 3-D in nature. While designs are typically formulated with the aid of semi-empirical heat transfer correlations for specific types of internal cooling, these tools cannot fully predict the correct 3-D thermal response for an as-built blade cooling configuration. Test techniques such as liquid crystal thermography have the ability to obtain maps of the internal heat transfer coefficients, but generally only on scaled-up models of the blades using materials such as acrylics, rather than the actual cast blades. Such methods are very useful, but have inherent limitations with respect to the as-produced cast parts.

The inspection of component heat transfer or cooling quality, particularly for cooled turbine airfoils, has been performed by a number of techniques, none of which are capable of direct quantitative measurement of the internal heat transfer coefficients in a nondestructive manner. In the production of cooled turbine airfoils, it is common practice to inspect the part, a portion of the part or assembly of parts, by flowing air or water through the cooling circuit. This inspection method is known as a ''flow check.'' The flow obtained for a specific part as a function of pressure ratio is compared to a desired or required flow. Acceptance of the part is based upon the flow check falling within the upper and lower specification limits. The specification limits are determined by design in conjunction with the testing of prototype parts. This technique is relatively simple and fast. However, for highly cooled airfoils with complex internal flow circuits and/or parallel flow circuits, the flow check does not guarantee that the internal heat transfer distribution at all regions within the part is adequate. A ''heat transfer check'' method is required for this purpose.

Other indirect heat transfer inspection methods for as-fabricated turbine airfoils involve semi-predictive schemes, which combine steady, nonintrusive measurements with modeling to determine

Contributed by the International Gas Turbine Institute and presented at the International Gas Turbine and Aeroengine Congress and Exhibition, Amsterdam. The Netherlands, June 3–6, 2002. Manuscript received by the IGTI, October 4, 2001. Paper No. 2002-GT-30199. Review Chair: E. Benvenuti.

the internal thermal performance. External surface temperatures may be obtained using Infrared pyrometry, thermographic phosphor coatings, luminescent barometry, thermal paints, liquid crystals, or thermocouples. Coupling such steady data to models of the external and internal flows, and a model of the solid, can lead to a prediction of the internal heat transfer. These techniques are commonly referred to as ''data matching,'' since one or more variables must typically be adjusted to obtain agreement with the measurements.

For turbine airfoils which are placed on a flow check test stand or similar apparatus, imaging infrared (IR) thermography using transient or ''flash'' heating/cooling methods has been recently developed. An early version of this method shown by Bantel and Mack [1] and also Bantel [2], preheated an airfoil on a flow test stand, and then introduced cooling flow through the part to produce a thermal transient. Comparison of the thermal response of the part with a ''known standard''part provided the indirect evaluation of the internal heat transfer distribution. A very recent twist on this technique is an extension of IR flash wall thickness and flow detection. As described by Daniels [3], IR flash methods utilize a Dirac delta input of high-intensity thermal radiation (e.g., flash lamps) to heat a part, and then measure the thermal response of the external surface using high-speed IR thermography. The wall thickness and thermal properties, including any local flaws, determine the temporal response of the surface temperatures, hence the local thermal decay is used as a direct measure of such quantities. This method has been extended, as described by Beckeiz et al. [4] and Stiglich et al. [5], by the simple introduction of cooling fluid inside the part after the heating of the part. By heating the part with quartz lamps or other means, the introduction of internal flow induces a thermal transient carrying information about the internal heat transfer distribution. In the methods of [4] and [5], the thermal response of the part is still compared to a ''known standard'' to provide the indirect evaluation of the internal heat transfer distribution.

The present research has developed a transient IR thermography technique capable of providing direct quantitative measurement of the internal heat transfer distribution within a cooled turbine airfoil. This NDE method, referred to as thermal inertia HTC (heat transfer coefficients), uses measured flow rates and part geometry in conjunction with transient IR data and inverse conduction analysis to determine full-surface internal HTCs. A patent application has been field with the U.S. Patent and Trademark Office for protection of the intellectual property associated with this measurement technique.

Measurement Technique

The method demonstrated in this study begins with the placement of a metal airfoil, or other component with an internal flow circuit, on a flow test stand. The airfoil need not be metallic, but this is used in this example to represent a common as-fabricated production component. A controlled thermal transient is induced by flowing a cooling medium through the component from some known initial thermal state at time $t=0$. In this case, a controlled thermal transient is one in which the initial component temperature distribution is known throughout the part, the heat source is a known value everywhere, and the coolant temperature and flow rate are known. In the simplest form of such a transient, the component would be at a uniform initial temperature throughout, the heat source would be either a uniform constant value or zero for time $t>0$, and the coolant inlet temperature and flow rate would be constants. The part could either be preheated to a known condition and then cooled transiently, or pre-cooled to a known condition and heated transiently. During such a transient, an imaging Infrared camera records the external surface temperature distribution of the part to obtain $T_S(x,y,z,t)$. For a single camera, the camera array is of course capturing a two-dimensional image, which must then be transformed per the three-dimensional part surface geometry. The transient thermal history of each location on the surface contains the response data related to the internal surface heat transfer coefficients.

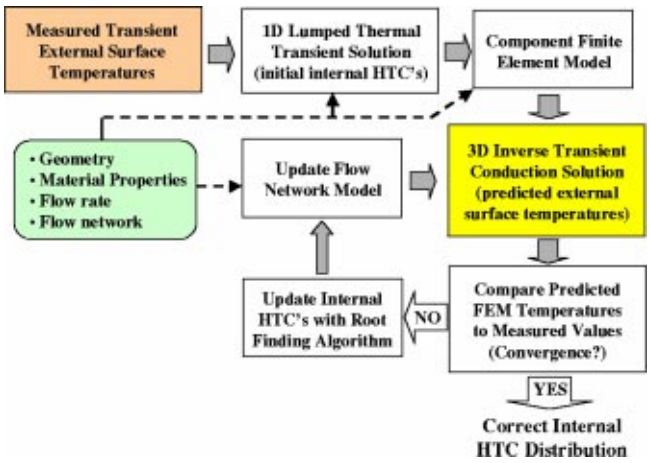

Fig. 1 Analysis process

Assuming first that the component may be represented or approximated by a simple 1-D wall of finite thickness, neglecting conduction laterally within the wall, then a lumped thermal capacity model of the form

$$[T_S(t)-T_{\text{initial}}]/[T_{\text{coolant}}-T_{\text{initial}}]=e^{-at}$$

$$a=h/\rho lC_p$$

may be used to determine the internal heat transfer coefficient h. This simple representation assumes that thermal resistance due to conduction through the wall is negligible by comparison with the internal convective heat transfer, and also that the external surface is insulated. This lumped parameter solution may be enhanced greatly by two additional steps, accounting for the 1-D temperature difference across the finite wall thickness, and a simple heat balance between adjacent elements to approximate the corrections due to lateral conduction. While these assumptions may be very limiting, the enhanced lumped parameter solution does provide an approximate solution, which may be quite satisfactory for many purposes.

The simple enhanced solution referred to here as 1-D also serves another function, it is an excellent initial solution for more involved 2-D or 3-D numerical models. The complete method for a complex internally cooled part is depicted in Fig. 1, where the 1-D lumped thermal transient solution is shown as providing the initial HTCs for the finite element model (FEM). Use of this solution as the FEM initial condition is not required, but it will greatly reduce the time to convergence. The part geometry and material properties are modeled by FEM (e.g., an ANSYS model) to obtain full 3-D corrections for the local effects of conduction and the spatial variation in internal heat transfer. Using either an adiabatic external surface boundary condition, or some other known external boundary condition, as well as the internal surface initial HTC's and coolant temperature, the 3-D model is executed for the transient conduction period matching the data time period. The output of the 3-D model is a prediction of the solid temperatures at all nodes, including the external surface temperatures. These predicted temperatures are then compared to the measured IR temperatures. Agreement will only be obtained if the lumped parameter solution is indeed representative of reality. Otherwise, the local differences in the predicted and measured external temperatures are then used to improve the internal HTCs. Any of a number of stable root-finding algorithms may be used to advance the HTCs for the next 3-D transient solution.

At this stage of the calculation, a flow network model may be used to update the local internal coolant temperatures, if war-

ranted by the complexity of the component. Such a network model may in fact be directly linked to the FEM. The primary purpose of the flow network model is to account for iterative changes in the internal HTCs as they affect heat transfer to the fluid, and therefore change the local temperature potentials from fluid to wall. A network model may be as simple as a 1-D incompressible model with heat balance, or as complicated as a CFD model. Simple flow and geometry configurations, such as that used in the present study, may not require the use of a flow network model at all. Iteration of this method continues until agreement is reached to within some specified convergence criteria. It is important to note that this method only requires a finite transient time period of data, which may be very short or long depending on the thermal response rate and the fidelity of the data acquisition system. Additionally, one or more time segments from a single transient may be used to calculate the same resulting HTCs, or used in conjunction to reduce stochastic errors. Other complexities due to nonconstant or locally varying conditions may also be incorporated into this method, provided the conditions are reasonably well known.

One further note should be made concerning the uniqueness of such solutions. Provided all boundary conditions are known or set such that only the internal HTC distribution is allowed to change, the solution will be unique. Nonuniqueness will result if at least one other condition, for example the local coolant temperature, is also allowed to vary. Another nonunique case may occur when the internal (or external) geometry of the part contains ''hidden'' surfaces. An example of a hidden surface is an internal rib within an airfoil, whose convective surface faces each contribute to a common external location response. If the number of external transient data locations used to define convergence is not detailed enough in comparison to the complexity of internal HTC surfaces or elements, then multiple solutions may be possible via alteration of the conditions on the internal surfaces. A detailed external map will allow resolution of the complete internal HTC distribution.

While the present test cases did not require optimization of numerical processing to reduce computational time, an indication of computational resources can be given by another example. For a multi-pass serpentine cooling design of an actual turbine blade involving an FEM model of some 7500 elements, real-time computations using a single processor required about 50 iterations for convergence, and about 150 min total time. This example started from a constant internal initial HTC rather than the 1-D solution, and made some blade section averaging simplifications. Much of the computing time was consumed in I/O for iteration results comparisons.

Experimental Apparatus

A simple test setup was made to demonstrate the methodology described in the foregoing. Figure 2 shows a plenum flow chamber with a component affixed on top. The plenum is supplied by house compressor air, which is metered upstream by a calibrated sonic venturi. The inlet air pressure and temperature are continuously monitored. Screens are provided within the plenum to assure a uniform low velocity flow entering the test piece. The test part is fixed to a base plate, which is insulated from the plenum by gasket sealing material. A heater jacket is shown in-place, completely covering the part during the pre-heat portion of the test. At time $t=0$, a solenoid valve causes the pre-heater to be quickly lifted away ($\sim$0.1 s), while at the same time initiating data acquisition. An AGEMA Thermovision ® 900 Infrared imaging camera and support computer are used to obtain the external surface temperatures as a function of time. The camera imaging array is 272 by 136 pixels. For the present tests, each pixel corresponds to a surface dimension of 0.764 mm. The burst RAM of this system allows images to be recorded at a rate of 15 frames per second.

Figure 3 shows the ''airfoil'' used for this study. The airfoil is a simple elliptic shape containing an impingement insert for cooling. The airfoil is 2.03-mm thick stainless steel with the outer dimensions shown. The exterior surface finish is a nonreflective, diffuse type produced by wire electro-discharge machining. For consistent IR images, this surface is coated with a high temperature black paint of 0.97 emissivity. A series of coolant exit holes are located in the trailing edge of the airfoil having total flow area greater than that of the impingement array. The inner impingement insert is a 1-mm-thick sleeve of stainless steel with major diameter of 9.21 cm, and minor diameter of 1.59 cm. The gap between the insert and the inner surface of the airfoil is 2.03 mm. The insert contains a bell-mouth entry, which is sealed inside the top of the plenum chamber. The impingement geometry is a square 10×10 array of jets with diameters of 1.27 mm. The spacing of the jets is $X/D=Y/D=5$. The target distance Z/D is then 1.6. As shown in the inset photo of Fig. 3, a gap is present between the top of the insert and the airfoil tip. This gap was sealed for these tests, forcing the post-impingement air to flow strictly laterally in both directions to the trailing edge exit holes. Air is exhausted from the airfoil directly to the room.

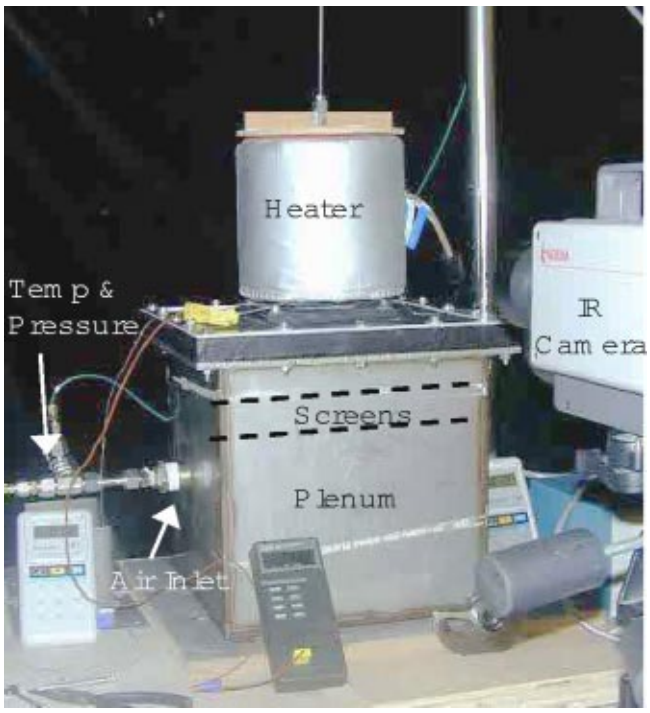

Fig. 2 Flow stand and heater test arrangement

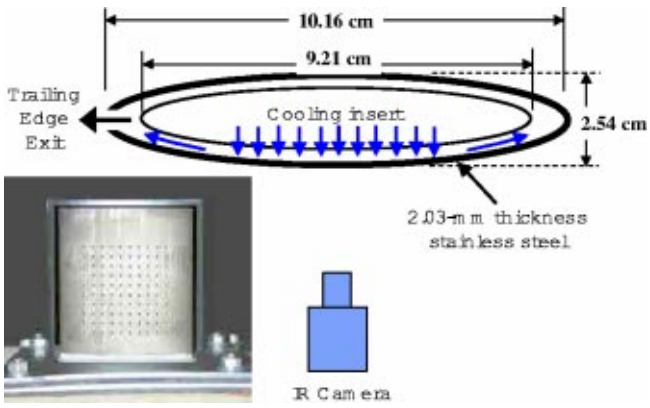

Fig. 3 Elliptic airfoil with Impingement cooling (insert photo shows the array size and location)

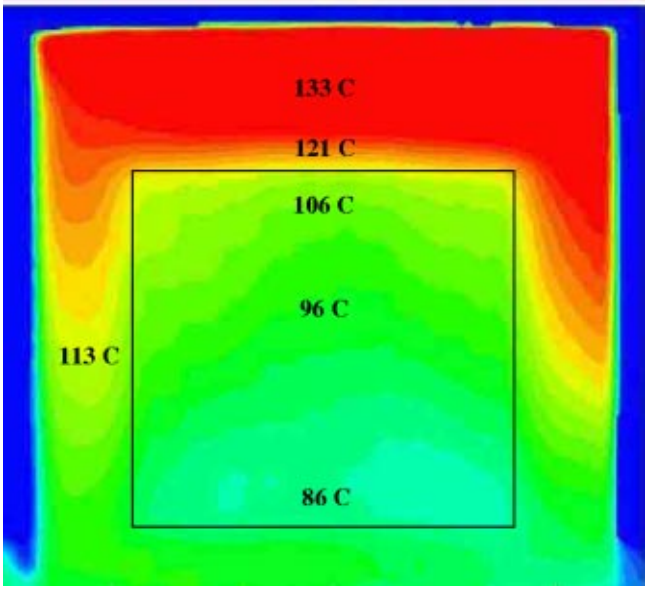

Fig. 4 Typical surface temperatures at some time during transient test

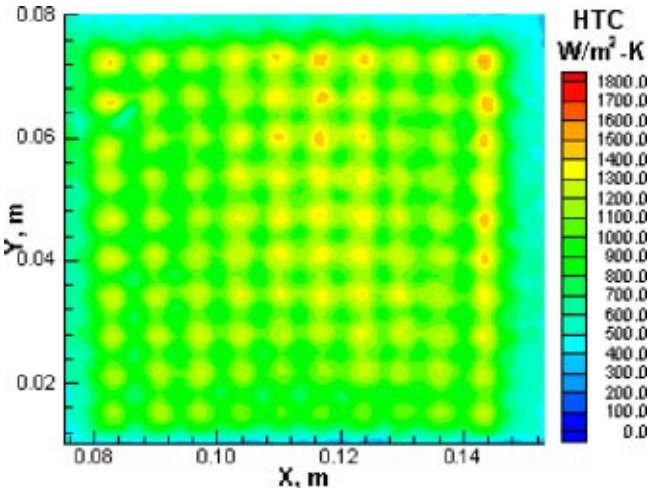

Fig. 5 Experimental data for jet average Re of 16,636 as reduced with 1-D lumped capacity model (W/m2/K)

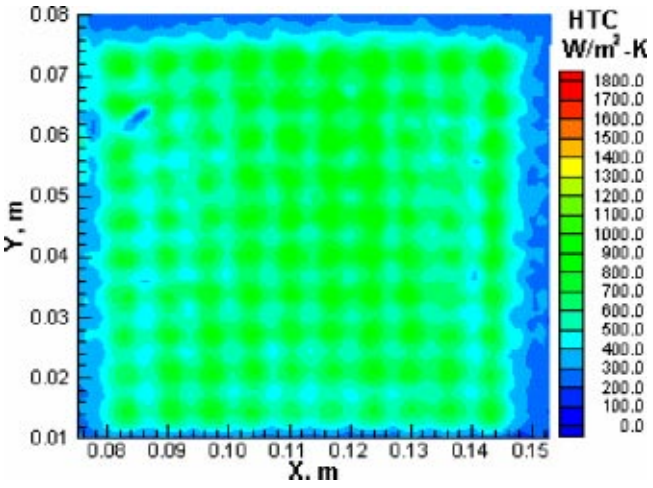

Fig. 6 Experimental data for jet average Re of 7,016 as reduced with 1-D lumped capacity model (W/m2/K)

A typical transient test begins by heating the airfoil (and insert) to approximately 150°C. The initial temperature of the airfoil is not precisely uniform, but this is not a requirement. The initial temperature distribution is steady, and recorded by the IR camera. For the present test airfoil, a typical temperature distribution at some time during a transient is shown in Fig. 4. The outlined box region is the location of the jet array. A gradient of about 20°C is present from top to bottom due primarily to the initial heating condition. The tip region of the airfoil is seen to be at an elevated temperature due to the lack of direct cooling flow.

For the condition of a constant coolant temperature everywhere (i.e., no flow network model is used), the experimental uncertainty is driven by three factors, the accuracy of the IR device, the uncertainty in surface emissivity (as this affects surface temperature), and the precision of the local wall thickness/geometry. In the present elliptic airfoil test, the wall thickness accuracy is ± 0.05 mm, and the surface emissivity results in a ± 1°-C uncertainty due to calibration by a standard thermocouple. The accuracy of the IR sensor array contributes negligible error by comparison. Also negligible is the uncertainty in time. The resulting uncertainty in the heat transfer coefficient is $\pm 12\%$ for the tests of this study, as determined by the method of Kline and McClintock [6]. About one-third of this uncertainty is due to the wall thickness, and the other two-thirds is due to surface temperature as caused by emissivity. While the uncertainty can be driven down by more accurate knowledge of surface and thickness values, more complex geometries may introduce additional uncertainty due to local coolant temperature. The magnitude of the driving temperature potential for the transient must also be weighed against the expected magnitude of the resulting heat transfer coefficients. In the present treatment, numerical accuracy is not considered to be part of the uncertainty.

Results and Discussion

1-D Lumped Thermal Capacity Method. A series of tests were executed using the elliptic airfoil and jet array impingement insert previously described. Each test was begun by pre-heating the airfoil to a steady initial condition without internal flow. Thermocouples glued to the nonviewed side of the ellipse verified the initial condition as steady. At time $t=0$, cooling air was introduced into the impingement insert via the plenum, and IR imaging was started at the rate of 15 frames per second. The first few seconds of data for any test are not used in data reduction, since this period is required to allow the flow conditions to stabilize to a steady state.

Figure 5 shows the internal HTC map which results from a 1-D analysis of the transient data with an average jet Reynolds number of 16,636, a plenum temperature of 27°C, and a total flow rate of 31.4 g/s. A constant exterior surface heat transfer coefficient of 4 W/m2/K was applied in the analysis as the estimated natural convection around the test airfoil. Since this external coefficient is very very small compared to the magnitude of the expected internal heat transfer coefficients, it has a negligible impact on the thermal response. The orientation of Fig. 5 shows the inlet on the bottom, and the trailing edge exit region on the left. Each of the 100 jets is clearly seen in this representation. This is a bounded impingement array fed from a restricted insert region, hence uniformity of impingement jet heat transfer is not to be expected. Since the flow is constrained to exit on the left and right sides of the impingement array (the right side flow traversing around the back of the insert), the center rows of jets are expected to have the least crossflow and hence the highest heat transfer, and this is indeed the case. The extreme jet rows on the left and right also show higher heat transfer due to their proximity to the exit pres-

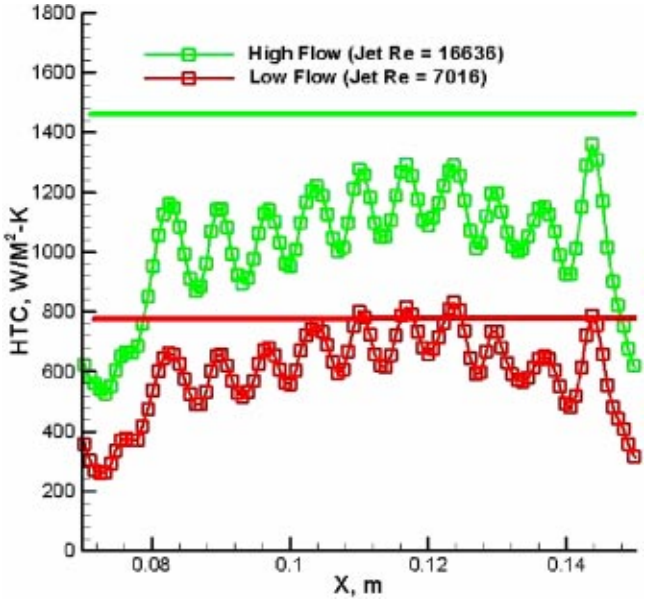

Fig. 7 Comparison of 1-D results with impingement array correlation of Florschuetz et al. [7] (W/m2/K)

sure. The inlet appears to have some flow separation, causing a locally lower heat transfer along the bottom-most jets.

Figure 6 shows another example of this same geometry with a jet average Reynolds number of 7016 and a total flow rate of 13.2 g/s. The HTC scale is the same as in Fig. 5 for direct comparison. Overall, this 1-D result is the same as that of the higher Re, merely at a lower heat transfer magnitude.

These jet array 1D results are compared to the correlation for in-line jet array impingement developed by Florschuetz et al. [7]. Figure 7 shows the correlation of [7] as flat lines at 1460 and 780 W/m2/K, respectively for average jet Re of 16,636 and 7016. While the correlation of [7] can be used to determine streamwise row-averaged heat transfer coefficients, since the present directional flow involves no more than five rows, the overall average jet Re was used for comparison purposes. The 1-D data shown in Fig. 7 represent a horizontal zone of pixels in the center of the array, covering a single spanwise periodic section of jets.

Both the correlation and the present results use the preimpingement air temperature as the fluid temperature. In the impingement region, the comparison for Re of 7016 is very good. At the higher Re of 16,636, the 1-D data fall about 15% below the correlation value. The differences are due to two effects here: 1) the present impingement array is not precisely the same constrained flow case as that of [7], and 2) the lateral thermal gradients due to impingement create strong 3-D conduction within the wall. The latter effect is analyzed in the forthcoming.

3-D Transient Inverse Conduction Method. The transient IR data used to arrive at the 1-D results shown in Fig. 5 with Re of 16,636 were analyzed using the procedure outlined in Figure 1. The 1-D distribution was used as the initial condition for internal heat transfer coefficients in the ANSYS model of the ellipse wall. As in the 1-D solution, the 3-D solution of the present case does not use a flow model. The FEM was a simple flat wall layer of elements, which corresponded to the test material and thickness. The FEM number of elements in the lateral and longitudinal directions corresponded to the number of IR camera data pixels. As in the 1-D analysis, a constant coolant temperature of 27°C was used. The method for updating the internal HTCs used in each subsequent iteration was to apply the ratio

$$\frac{[T_S(x,y,t=0)-T_{S,\text{measured}}(x,y,t)]}{[T_S(x,y,t=0)-T_{S,\text{predicted}}(x,y,t)]}$$

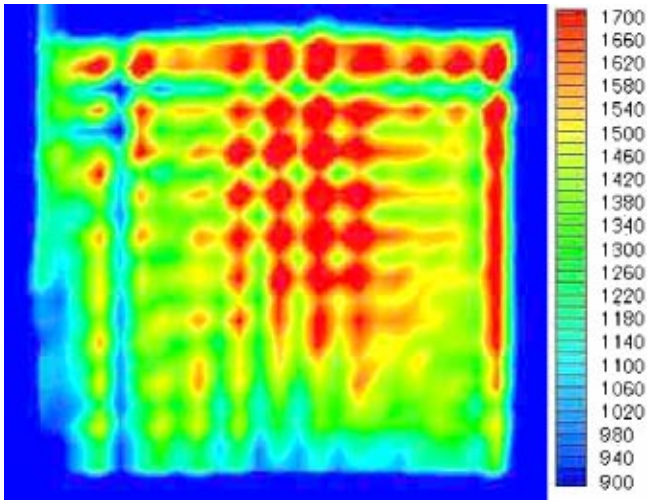

Fig. 8 3-D ANSYS results for internal HTCs with convergence criteria of 0.5°C and 4×4 pixel averaging (W/m2/K)

to each location. Other root finding algorithms could be used, but this was found to be sufficient and simple for the present case. No flow network model was utilized for this geometry.

Figure 8 shows the converged 3-D result for internal heat transfer coefficients. The convergence criterion applied to all locations of external surface temperature was 0.5°C. This criterion was applied to the last time step in an 8-s transient, not to every time step. To reduce the amount of computational time, the IR pixels were averaged as 4×4 sets for the 3-D analysis. The impingement array is reasonably visible in this result, yet it is apparent that regions of too high and too low heat transfer exist, such as the low strip just before the last row of jets on the left side. The overall and local HTCs are consistent with the 1-D results. Additional resolution can be obtained by tightening the convergence criterion (both in magnitude and number of time steps), and by using more of the specific pixel data from the IR camera. Figure 9 shows the 3-D result with only a 3×3 averaging of the IR pixels. The high and low regions take on more realistic values, and the individual jet impingement definition becomes sharper for all of the 100 jets.

Figure 10 shows the effect of temperature convergence criterion in a comparison of the midspan heat transfer coefficients for three

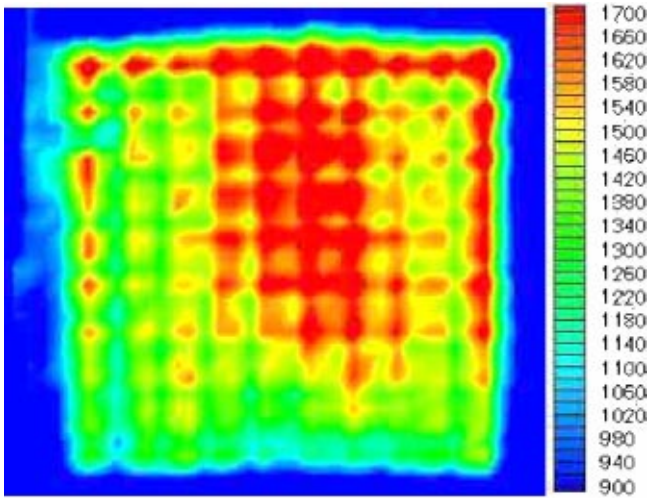

Fig. 9 3-D ANSYS results for internal HTCs with convergence criteria of 0.5°C and 3×3 pixel averaging (W/m2/K)

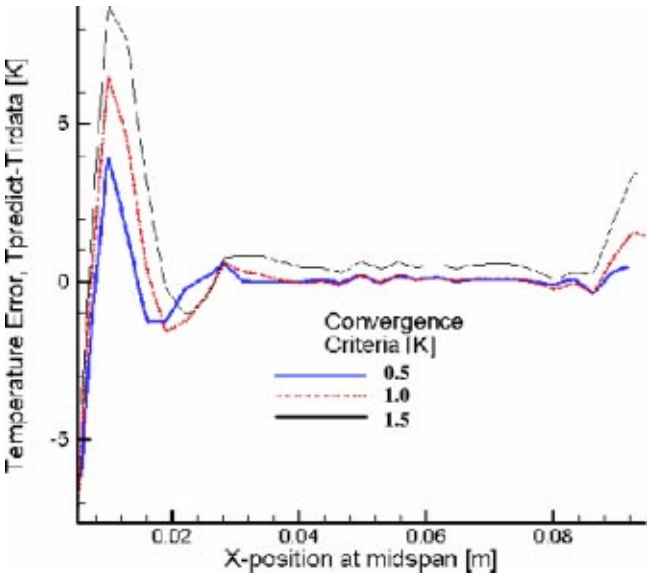

Fig. 10 Effect of surface temperature convergence criterion

values of surface temperature criterion. While the central region appears to be well converged in all cases, the edge regions clearly require a tighter convergence criterion.

The magnitude of internal heat transfer coefficient change due to the incorporation of 3-D conduction by FEM can be seen in Fig. 11. Here both the midspan results of Figs. 5 and 8 are plotted together, using the spanwise-averaged values representing one impingement jet periodic region. Concentrating attention on the central region, away from the nonconverged edge areas, the 3-D corrections are seen to result in an increased average heat transfer coefficient of about 40% over the 1-D result. Needless to say, this correction represents a significant change in the final results. The overall average value of heat transfer coefficient is now in much better agreement with the correlation of [7]. Additional accuracy (i.e., agreement) would be obtained with finer spatial resolution, increased time step data convergence, and an accounting for local fluid temperature rise through the model.

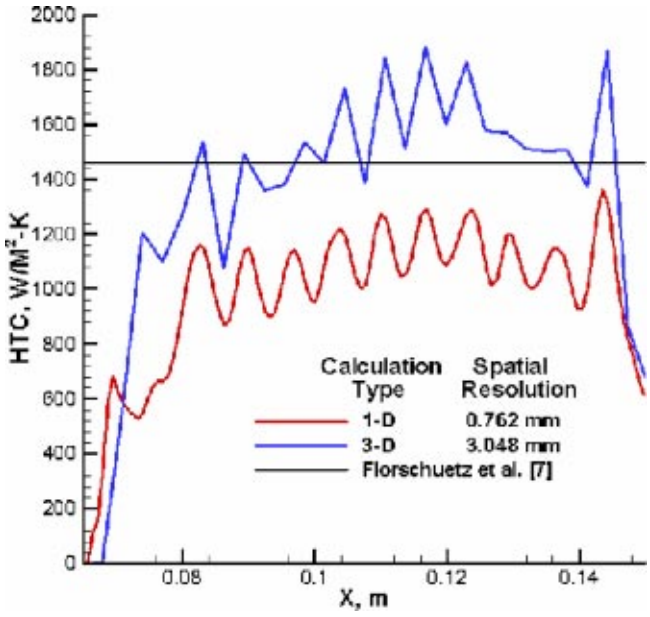

Fig. 11 Comparison of 1-D and 3-D results

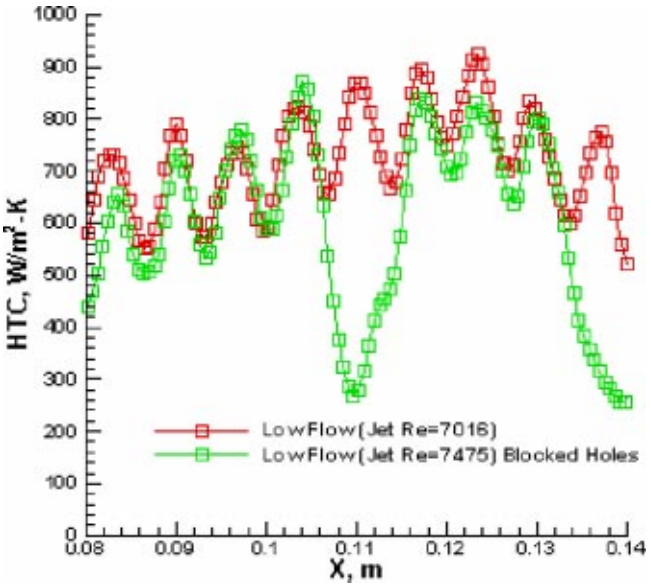

Fig. 12 Internal heat transfer coefficients with blocked impingement holes (W/m2/K)

Quantification of Inadequate Internal Heat Transfer. As noted in the Introduction, the measurement and analysis technique demonstrated here has particular significance in the quantification of out-of-specification or marginal thermal performance of parts. As an example of this application, the jet array impingement test of Fig. 6 was run with five of the 100 impingement holes closed with epoxy. While a simple IR transient test can detect such a condition, the present method allows a quantification of the affected local heat transfer.

Figure 12 shows the altered internal heat transfer for a location containing two blocked jets. The analysis has been carried out by the enhanced 1-D method for consistency in comparison. The two blocked jets are very apparent. The local heat transfer coefficients at the peak locations have been reduced to nearly 30% of the original magnitudes. Such information is not available through the use of design correlations, and can be invaluable in assessing the effects of non-conformances on temperatures, stress, and life.

Conclusions

The present study introduces a new method for the *quantification* of internal heat transfer coefficient distributions within complex parts such as cooled turbine airfoils. This new technique utilizes transient infrared imaging of a cooled or heated airfoil, together with flow rate measurements and geometry, to produce a map of internal heat transfer for an as-fabricated airfoil in a completely nondestructive manner. The method differs from previous practice by the incorporation of 1-D or 3-D analysis to arrive at quantified heat transfer coefficients rather than qualitative results. The current investigation has demonstrated this technique on a simple model airfoil with impingement array cooling. *The level of detailed information obtained corresponds to that expected of full-field optical methods such as liquid crystals, but does so with measurements from the exterior surface of the airfoil*. An extension of this method to the quantification of internal heat transfer abnormalities has also been demonstrated. This method satisfies a growing need within the gas turbine community for thermal performance quality inspections of complex, expensive hot gas path components.

Acknowledgment

This study was prepared with the support of the U.S. Air Force, Aero Propulsion and Power Directorate, under Contract F33615-

98-C-2893, and also the NASA Glenn Research Center, Ultra Efficient Engine Program, under contract NAS3-27720. However, any opinions, findings, conclusions, or recommendations expressed herein are those of the author and do not necessarily reflect the views of the USAF or NASA. The authors would also like to thank Dr. R. Bergholz of GE Aircraft Engines for his support of this work.

Nomenclature

A_h = internal surface area
C_p = specific heat of component material
D = jet diameter
h = internal heat transfer coefficient, $Q/(A_h^*(T_{\text{internal}} - T_{\text{coolant}}))$
HTC = heat transfer coefficient
k = thermal conductivity of air (W/mK)
l = local wall thickness
m = mass flow rate
Q = heat flux
Pr = Prandtl no.
Re_{jet} = average jet Reynolds no. = $\text{Re}=(4m)/(D/\mu)$
t = time
T_C = coolant supply temperature
T_S = external wall temperature
x, y, z = space coordinates
X = axial jet spacing
Y = lateral jet spacing
Z = let plane to target plate distance
μ = viscosity
ρ = density

References

[1] Bantel, T. E, and Mack, D. C., 1987, "Cooling Hole Inspection," US Patent No. 4,644,162, assigned to General Electric Co.
[2] Bantel, T. E., 1992, "Apparatus and Method for Inspecting Cooling Holes," US Patent No. 5,111,046, assigned to General Electric Co.
[3] Daniels, A., 1996, "Nondestructive Pulsed Infrared Quantitative Evaluation of Metals," Thermosense XVIII: An International Conference on Thermal Sensing and Imaging Diagnostic Applications, Society of Photo-Optical Instrumentation Engineers, SPIE Vol. 2766, pp. 185–201.
[4] Beckeiz, E., Sperling, A., and Carl, V., 1998, "Thermography Inspection System for Gas Turbine Blades," 7th ECNDT, Copenhagen, Denmark.
[5] Stiglich, J. J., Bishop, C. C., Daleo, J. A., Boone, D. H., and Eelkema, T. E., 1998, "The Thermal Inertia Analysis Technique in Gas Turbine Component Reliability Assessment," presented at the ASM Gas Turbine Materials Technology Conference, Rosemont IL.
[6] Kline and McClintock, 1953, "Describing Uncertainties in Single-Sample Experiments," Mech. Eng. (Am. Soc. Mech. Eng.), Jan.
[7] Florschuetz, L., Truman, C., and Metzger, D., 1981, "Streamwise Flow and Heat Transfer Distributions for Jet Array Impingement with Crossflow," ASME J. Heat Transfer, **103**, pp. 337–342.

Effects of Tip Geometry and Tip Clearance on the Mass/Heat Transfer From a Large-Scale Gas Turbine Blade

M. Papa
Department of Mechanical Engineering,
University of Rome 'Tor Vergata,'
Rome, Italy

R. J. Goldstein
Mem. ASME
Department of Mechanical Engineering,
University of Minnesota,
Minneapolis, MN 55455

F. Gori
Department of Mechanical Engineering,
University of Rome 'Tor Vergata,'
Rome, Italy

An experimental investigation has been performed to measure average and local mass transfer coefficients on the tip of a gas turbine blade using the naphthalene sublimation technique. The heat/mass transfer analogy can be applied to obtain heat transfer coefficients from the measured mass transfer data. Flow visualization on the tip surface is provided using an oil dot technique. Two different tip geometries are considered: a squealer tip and a winglet-squealer tip having a winglet on the pressure side and a squealer on the suction side of the blade. Measurements have been taken at tip clearance levels ranging from 0.6 to 3.6% of actual chord. The exit Reynolds number based on actual chord is approximately 7.2×10^5 for all measurements. Flow visualization shows impingement and recirculation regions on the blade tip surface, providing an interpretation of the mass transfer distributions and offering insight into the fluid dynamics within the gap. For both tip geometries the tip clearance level has a significant effect on the mass transfer distribution. The squealer tip has a higher average mass transfer that sensibly decreases with gap level, whereas a more limited variation with gap level is observed for the average mass transfer from the winglet-squealer tip.
[DOI: 10.1115/1.1529190]

Introduction

In gas turbine engines, the clearance between the tip of the rotating blades and the stationary casing provides a path for hot gas to flow from the pressure side to the suction side of the blades. This leakage flow causes a reduction of the blade aerodynamic performance and generates high heat transfer rates on and near the blade tip.

The high thermal load caused by the leakage flow represents a severe condition for the engine. Blade tips are exposed to hot gases on all sides and are very difficult to cool through conventional film cooling techniques. The high operating temperature causes oxidation and erosion. Internal to external thermal gradients, as well as nonuniformity of heat transfer coefficients on the surface, can result in high thermal stresses and cracking. During transient operation, blade tips can also be subject to rubs against the casing, resulting in removal of material and increased gap levels at other operating conditions. All these factors make the blade tip one of the regions of the turbine that requires the most frequent inspection and repair.

It has been recognized that the use of special blade tip geometries can be effective in reducing the leakage flow. One blade tip design in current use consists of a recessed tip and is known as squealer tip. Adopting this geometry, the tip gap can be made smaller without the risk of catastrophic failure in case of rubs against the casing. The recess is also believed to act as a labyrinth seal, increasing the resistance to the flow. Other blade tip geometries make use of winglets, features that extend perpendicularly from the blade.

It is evident that blade tip design cannot only be based on aerodynamic performance considerations, but has to take into account several other factors. Heat transfer is undoubtedly one of the most important, since blade tips are subject to burn-out. The distribution of heat transfer coefficients on the tip surface is therefore precious information for the designer. None-the-less, relatively few studies that quantify the heat transfer from a blade tip are available in literature. An extensive review on blade tip heat transfer can be found in Bunker [1]. Bunker et al. [2] obtained the heat transfer distribution for a flat blade tip of a high pressure turbine using a transient liquid crystals technique in a high-speed linear blade cascade. They show the existence of a region of low heat transfer, termed the ''sweet spot,'' near the leading edge of the blade. The entire stationary cascade of Bunker et al. [2] was modeled numerically by Ameri and Bunker [3] and CFD predictions were performed for the same flow conditions, finding good agreement with the experimental results. Azad et al. [4] also performed experiments with liquid crystals for a flat tip blade in a high-speed linear cascade, finding consistent heat transfer distributions with the work of Bunker et al. [2]. Pressure measurements detected a contained leakage flow in the leading region of the blade, resulting in low heat transfer coefficients. The pressure difference between the two sides of the blade was found to become large starting from the midchord region toward the trailing edge, causing high velocities and much higher heat transfer coefficients. Teng et al. [5] reported detailed blade tip heat transfer measurements in a large-scale low-speed wind tunnel facility, using a transient liquid crystals technique. Effects of upstream unsteady wakes on tip heat transfer were investigated at different clearance levels.

The first detailed heat transfer measurements on a squealer tip blade were performed by Azad et al. [6]. Experiments were conducted with a transient liquid crystals technique in a high-speed wind tunnel facility using the profile of a GE-E^3 turbine blade. The squealer height was equal to 3.77% of the blade span, and three gap levels were investigated: 1, 1.5, and 2.5% of the blade span. High heat transfer was observed in the front-central portion of the cavity floor, attributed to flow impingement, and on the pressure side and suction side rims, due to the flow entrance and exit effects. A recirculating dead-flow region was observed in the downstream end of the cavity, toward the trailing edge, causing

Contributed by the International Gas Turbine Institute and presented at the International Gas Turbine and Aeroengine Congress and Exhibition, Amsterdam, The Netherlands, June 3–6, 2002. Manuscript received by the IGTI, October 18, 2001. Paper No. 2002-GT-30192. Review Chair: E. Benvenuti.

low heat transfer rates. The overall heat transfer for the squealer tip decreased with gap level and was found to be smaller than that observed for the flat tip geometry. Ameri et al. [7] performed a computational study to investigate the heat transfer distribution for a squealer tip blade using the geometry and flow conditions of a real GE-E^3 first-stage turbine. Two squealer heights were considered, equal to 2 and 3% of blade span, at a gap level of 1% of blade span. High heat transfer coefficients on the cavity floor were found by the pressure side and near the leading edge of the blade.

In the present work, detailed distributions of mass transfer coefficient on the blade tip surface are obtained from naphthalene sublimation for two blade tip geometries: a squealer tip and a winglet-squealer tip having a winglet on the pressure side and a squealer on the suction side. Mass transfer coefficients can be related to heat transfer coefficients using the heat/mass transfer analogy. The experiments are conducted in a large-scale low-speed wind tunnel facility. Four different tip clearance levels are tested for both tip geometries. Average mass transfer coefficients are measured directly for each configuration, and the results compared to area averaged local coefficients to verify the accuracy of the method. Flow visualization is provided for both blade tip geometries using an oil dot technique.

The naphthalene sublimation technique, widely used in mass transfer studies, allows a high spatial resolution in the determination of local transfer coefficients. The great level of detail allows flow field prediction and is valuable to validate numerical codes. This study provides mass transfer data for a traditional squealer tip design and for a new design featuring a winglet on the suction side and a squealer on the pressure side of the blade. Flow visualization experiments performed for both tip geometries offer insight on the flow field near and within the gap and provide an interpretation of the mass transfer distributions. This information is essential to develop efficient tip film cooling schemes and introduce new high performance tip designs.

Experimental Apparatus and Method

Experiments are conducted in a blowing-type wind tunnel with a five-blade linear cascade in a blade-centered configuration. Details of the facility can be found in Jin and Goldstein [8]. The blades are large-scale aluminum models of a first stage rotor blade of a GE high-performance turbine aircraft engine. They have an actual chord of 18.4 cm and a high turning angle of 107.5 deg. The blade pitch of the cascade is 13.8 cm, giving a solidity of 0.75. The maximum span of the blades (configuration with no tip clearance) is 45.7 cm. The cascade is therefore characterized by a high aspect ratio (span/actual chord) of 2.48, larger than that typically found in turbine engine, allowing a clear separation of the endwall effects (platform and tip) on flow within the cascade. The three central blades can be removed from the test section, and spacers added on the bottom of each blade to vary the tip clearance. The clearance levels tested in the present study are 0.6, 1.1, 2.0, and 3.6%, based on actual chord. The exit Reynolds number based on actual chord is approximately 7.2×10^5 for all measurements.

The naphthalene sublimation technique is used to determine local and average mass transfer coefficients on the blade tip. It consists in coating the specimen with a layer of naphthalene and exposing it to the flow in the wind tunnel. The naphthalene sublimation depth is then measured locally to enable calculation of the local nondimensional mass transfer coefficient, the Sherwood number. This number can be related to the nondimensional convective heat transfer coefficient, the Nusselt number, through the heat/mass transfer analogy. The specimen can also be weighed before and after the experiment to determine directly the total mass loss and calculate the average mass transfer coefficient. A comprehensive review of the naphthalene sublimation technique can be found in Goldstein and Cho [9].

Blade Tip Models. The central test blade of the cascade is composed of stackable components so the tip geometry can be modified substituting the terminal component of the stack. In order to facilitate the naphthalene coating and the measurement of sublimation depth, the blade tips are an assembly of three separate components: a support, a central component and an outer component, as illustrated in Fig. 1 for the squealer tip. Figure 2 is a cross sectional view of the two blade tip assemblies.

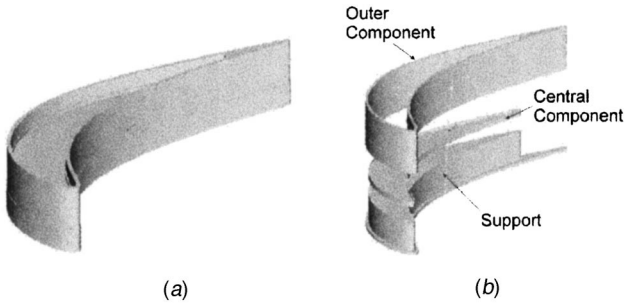

Fig. 1 Squealer tip assembly—(*a*) exploded view, (*b*) assembled view

This design offers several advantages. The squealer tip and the winglet-squealer tip, as well as other geometries that might be used in future investigations, can be obtained exchanging just the outer component of the assembly. Naphthalene can be easily cast inside the central component, which represents the cavity bottom of the squealer tip, since the mold can be constituted of two flat plates. The outer component can be removed when measuring the naphthalene profile on the central component before and after the run, so that the probe can take measurements over a larger area without interference from the squealers. The central component is very light, and can be weighed before and after the run with a precision balance to measure the total mass loss due to naphthalene sublimation and calculate the overall mass transfer coefficient directly. The outer component, for which a casting procedure would be more complicated, can be coated painting a thin layer of naphthalene on it. Its light weight also allows overall measurements with a precision balance. The outer component can be made nonactive in the mass transfer process, simulating an adiabatic surface for the heat/mass transfer analogy, simply applying a layer of paint in place of the naphthalene.

The squealers on both the squealer tip and the winglet-squealer tip have a height of 4.8% and a width of 1.2% of actual chord. The winglet width, or extent away from the original surface is equal to 3% of actual chord, while the radial extent of the feature is equal

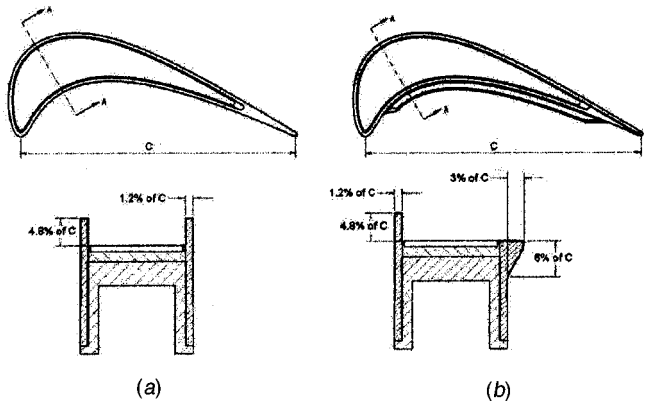

Fig. 2 Top view and cross-sectional view of blade tip Assemblies—(*a*) squealer tip, (*b*) winglet-squealer tip

to 6%. For both tip geometries, the clearance is measured as the spanwise distance between the squealer's top surface and the wind tunnel top panel.

Experimental Procedure. The experimental procedure starts with the preparation of the naphthalene coated specimen. Naphthalene is melted and cast into the central component of the blade tip assembly using a mold. Once the naphthalene has solidified, the component is removed from the mold and placed into an air-tight container, to limit losses due to natural convection. If the outer component has to be made active in the mass transfer process, a thin layer of naphthalene is applied on it using a paint-brush, and the component is placed in the container. The specimens are taken to the measurement room. They are weighed on a precision balance, and time and room temperature are noted. The central component is then positioned on a measurement table where the initial naphthalene profile is measured with an LVDT (linear variable differential transformer) probe. The precision limit of the instrument found after calibration is equal to ± 0.36 μm at a 95% confidence level in a linear range of ± 0.25 mm. When measurements are completed, the components are assembled together, put in the air-tight container and taken to the wind tunnel room.

The wind tunnel is turned on in advance and left running for at least 1 h to ensure the desired steady state conditions when the blade tips are ready to be mounted. A thermocouple and a Pitot tube placed upstream of the test section are used to monitor freestream temperature and velocity. Tests are performed at room temperature, and the value of freestream temperature is on average 25°C. The freestream velocity is adjusted accordingly, in order to obtain the desired value of $Re_{ex}=7.2\times10^5$. The average value for the cascade inlet velocity is 23 m/s, giving a cascade exit velocity of 63 m/s. When the blade tip is brought in from the measurement room, the wind tunnel is stopped and the blade tip is mounted. The wind tunnel is restarted and the time is noted. The run time can vary from 15 to 25 min, depending on the tip geometry and the gap level. This is done to keep the average sublimation depth at approximately 70 μm. If the sublimation depth is too small, natural convection losses as well as uncertainty in sublimation depth measurement can be significant. If the sublimation depth is too large, geometric variations of the naphthalene surface might affect the measurement, and some sublimation peaks might be out of the LVDT linear range.

Two thermocouples embedded in the naphthalene, with their beads close to the surface, measure naphthalene temperature at the interface with air. All thermocouples used in this study are T-type thermocouples. Their signals are transfered to a digital multimeter having a resolution of 0.1 μV through a multiple scanner. The system is controlled by a Linux workstation through an IEEE-488 (GPIB) bus. A numerical noise rejection and a correction for the multimeter zero drift are applied. Each thermocouple reads one temperature value per minute. The accuracy of the temperature acquisition system found after calibration is 0.04°C at a 95% confidence level. It is important to get accurate temperature readings, since the value of naphthalene saturated vapor pressure, which affects the naphthalene sublimation rate during wind tunnel operation, is strongly dependent on temperature (approximately 10% variation/°C, Goldstein and Cho [9]). It is also important to verify that the naphthalene temperature and the air temperature remain constant and equal during the course of the run. In all measurements taken in the present study, naphthalene and freestream temperature were never more than 0.2°C apart and individually varied less than 0.2°C during the course of the run.

When the measurement time has expired, the wind tunnel is stopped, the blade tip unmounted and put back in the container, noting the time. The blade tip assembly is brought back to the measurement room where the final weight and profile are measured.

All physical parameters recorded during the experiment, as well as the LVDT voltage readings for the naphthalene initial and final profile are stored in input files to a data reduction program. This program first calculates the local sublimation depth and the total mass loss. It then estimates the natural convection losses that occur during profile measurement, storage, and setup in order to obtain the net local values of sublimation depth due to forced convection and the net mass loss. The average natural convection loss is approximately 1 μm for an average total sublimation depth of about 70 μm. The net sublimation depth is used to calculate the local value of the nondimensional mass transfer coefficient, the Sherwood number. The value of the overall Sherwood number is determined from the value found for the net mass loss.

The uncertainty for the local Sherwood number is estimated to be approximately 8% at a 95% confidence level. It should be pointed out that a good part of this value has to be attributed to the uncertainty in the correlations used to determine the naphthalene mass diffusion coefficient (5.1%) and the naphthalene vapor pressure (3.77%).

Mass Transfer Measurements

In this section, results of local and global mass transfer measurements on the central component are presented. An interpretation of the mass transfer distributions is given in the next section, with the aid of the flow visualization results. All reported mass transfer plots are relative to experiments performed without coating the outer component with naphthalene, thus keeping it non active in the mass transfer process. At least two runs are performed for each configuration to check for repeatability.

Squealer Tip. Local measurements are taken at four different gap levels: 3.6, 2.0, 1.1, and 0.6% of actual chord. Results are shown in the form of contour plots (Fig. 3) and three-dimensional plots (Fig. 4). For all gap levels, the highest mass transfer peak is observed on the cavity floor in a region very close to the leading edge, at a distance of approximately one squealer height (4.8% of *C*) from the step formed by the squealer. As the gap level decreases, the peak moves slightly away from the leading edge and gets closer to the suction side squealer. High mass transfer coefficients are observed along a line (essentially the same location as line 2 on Fig. 8) that runs on the cavity floor, starting from the leading edge, and meets the suction side squealer at a distinct chordwise location. From this location on to the trailing edge, high mass transfer coefficients are measured near the suction side squealer. As the gap level decreases, the line meets the suction side squealer at earlier chordwise locations. A second mass transfer peak is always observable on the line, as clearly shown in the 3-D plots. Its intensity decreases with the gap level, and its position shifts toward the leading edge. Effects of secondary flows are also distinguishable on the mass transfer plots. They will be discussed in the next section with the aid of flow visualization results.

Previous investigations on heat transfer distributions for a squealer tip blade have been performed by Azad et al. [6] and Ameri et al. [7] and are briefly described in the introduction section. They use different blade profiles, squealer dimensions and flow conditions from those used in this work, not allowing a direct comparison. The trend of the presented squealer tip results, however, is in good agreement with the experimental work of Azad et al. [6], with the exception of the leading edge peak that was not found in their study. The numerical simulation performed by Ameri et al. [7] predicted a heat transfer peak by the leading edge of the blade.

Winglet-Squealer Tip. The mass transfer coefficients distributions obtained for the winglet-squealer design are substantially different from the ones reported for the traditional squealer design. Results are reported in Figs. 5 and 6. Very low mass transfer coefficients are found in a large region near the leading edge. High coefficients are observed in the trailing part of the blade, by the suction side squealer, as best seen in the 3-D plots. For each gap level, two high mass transfer streaks are observed on the top

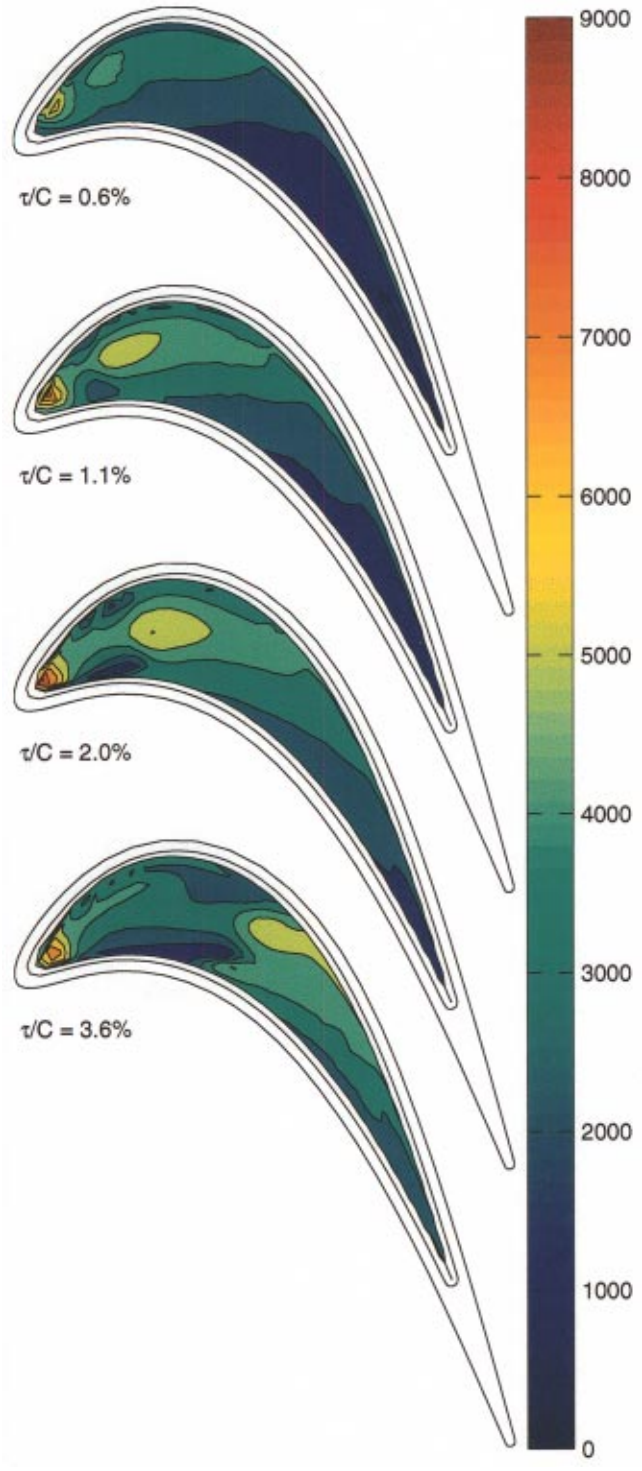

Fig. 3 Contour plot of Sherwood number distribution for the squealer tip

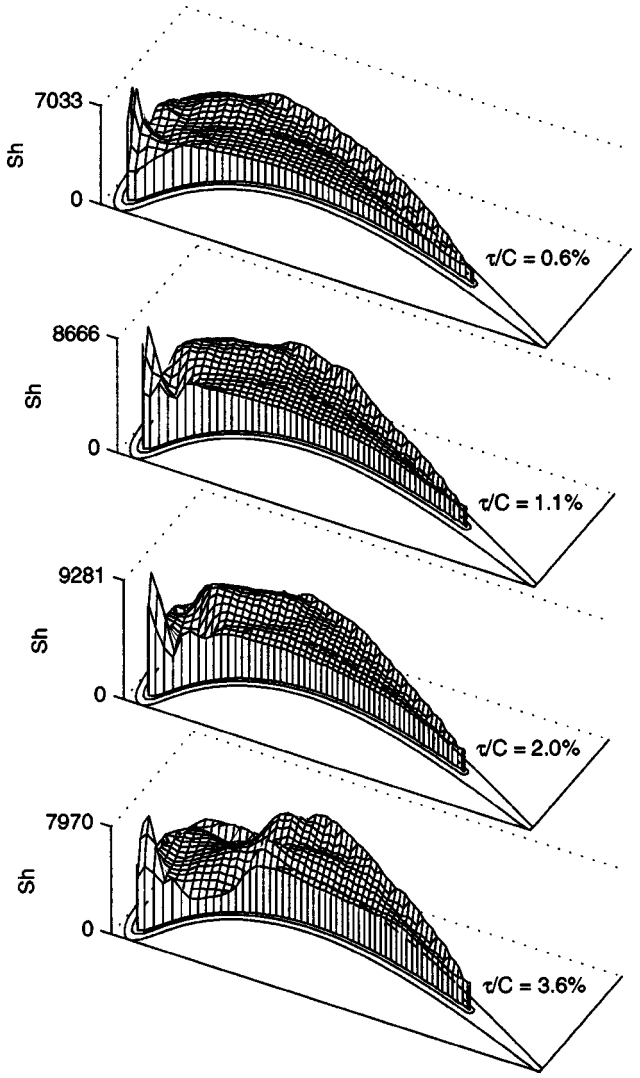

Fig. 4 3-D plot of Sherwood number distribution for the squealer tip

surface, starting from the pressure side and running toward the suction side squealer. The extension of the low mass transfer area in the leading part of the blade decreases with gap level, and the two streaks move toward the leading region of the blade, unloading the trailing edge.

Overall Measurements. The average mass transfer coefficient can be obtained in two ways. With the first method, the coefficient is calculated weighing the specimen before and after the experiment and dividing the net total mass loss by the run time and the naphthalene surface area. With the second method, the local mass transfer coefficients calculated from the naphthalene sublimation depth measurements are integrated over the whole surface and then divided by the total area. On average, values obtained with the two methods differ from each other by 2.1%. The fact that the overall Sherwood number obtained from the integration of the local coefficients is almost always smaller than the one obtained from the direct mass measurement might indicate that the value used for the density of solid naphthalene, which influences only the value of local transfer coefficients, might be slightly underestimated. The two measurements, however, show very good agreement and confirm the validity of the experimental approach.

The behavior of overall mass transfer as a function of geometry and gap level is well described in Fig. 7, where the results of the direct mass transfer measurements are plotted. The squealer tip shows a reduction of the overall coefficient when the gap level is reduced, whereas a more limited variation is observed for the winglet-squealer tip. The values of the overall mass transfer coefficient for the squealer tip are consistently greater than those observed for the winglet-squealer tip, even though they become comparable at the lowest gap level.

The estimate of the standard deviation for the direct measure-

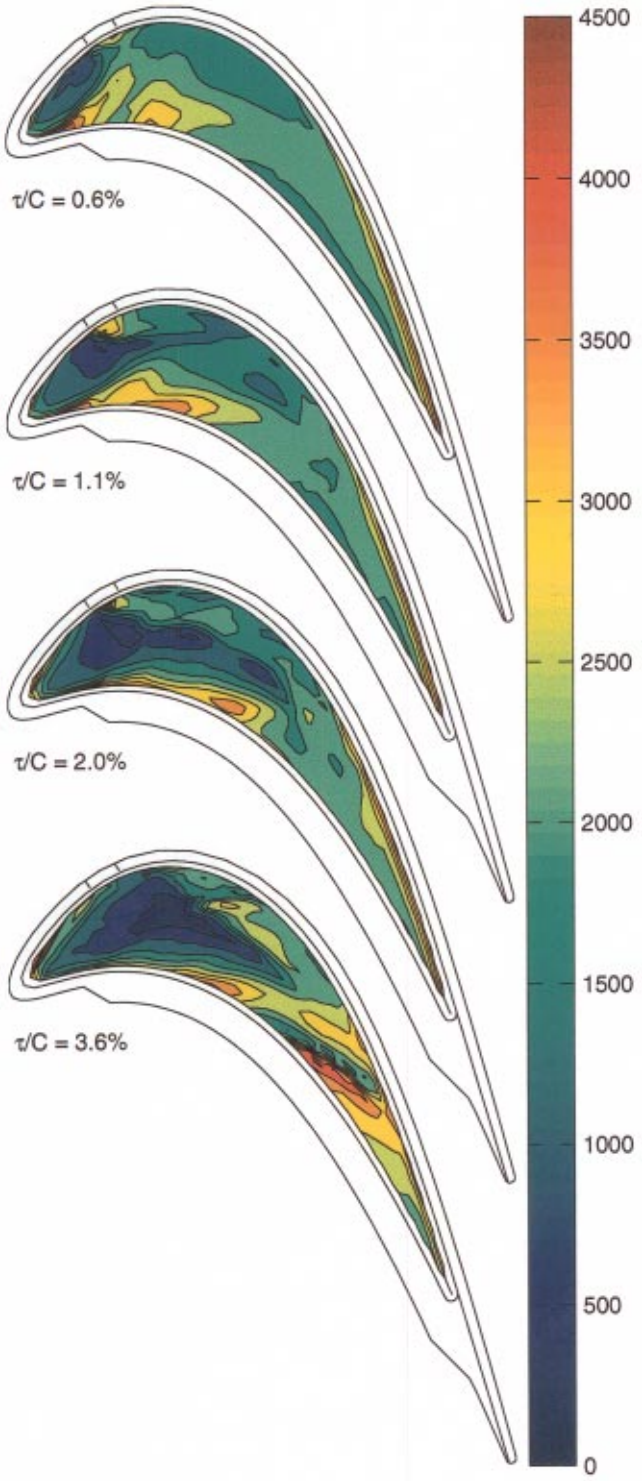

Fig. 5 Contour plot of Sherwood number distribution for the winglet-squealer tip

ment is calculated using results of repeated measurements taken at each nominal condition. The data for all measurements can be pooled together, assuming that the causes of randomness associated with each measurement are the same, to calculate the first-order precision limit for the overall nondimensional Sherwood numbers. This value, calculated at a 95% confidence level, was found to be equal to 1.2% of the mean value of all average mass transfer measurements.

Influence of an Active Outer Component. Measurements at one nominal condition were taken coating the outer component of the squealer tip assembly with a painting technique, making it ''active'' in the mass transfer process. Naphthalene was applied on the inner and top surface of the squealers, and on the outer profile of the blade. Local Sherwood numbers obtained for the cavity floor of the squealer tip at $\tau/C=2.0\%$ are compared to the results obtained at the same nominal conditions with a nonactive outer

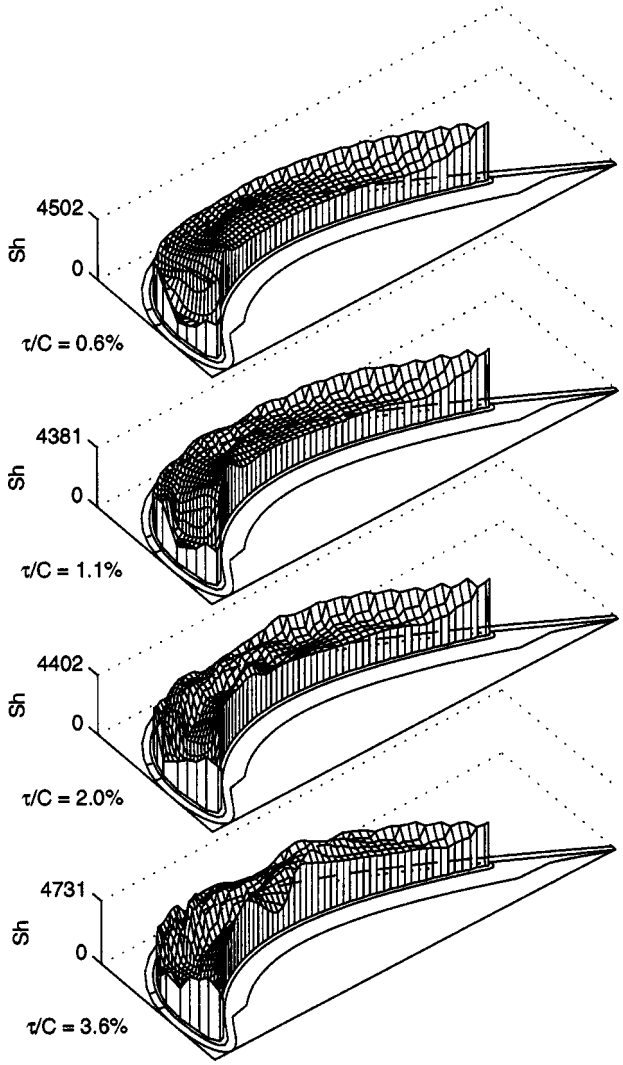

Fig. 6 3-D plot of Sherwood number distribution for the winglet-squealer tip

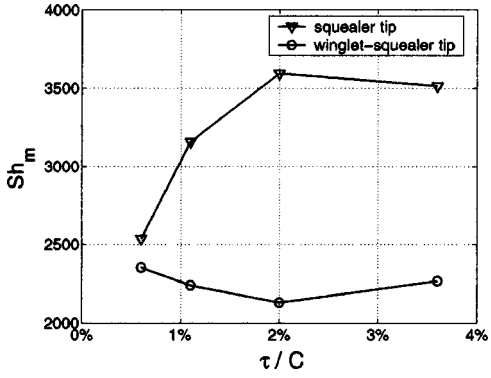

Fig. 7 Average Sherwood number as a function of tip clearance

component. The effect of the active outer component on the mass transfer from the cavity floor is shown to be noticeable but minor, confirming that the leakage flow is composed essentially of mainstream fluid, as found by previous investigators. The mass transfer phenomena are therefore dominated by the fluid dynamics and thickness of boundary layers, and are very slightly influenced by the transfer phenomena in the upstream portion of the tip, namely the pressure side of the blade and the pressure side squealer. The mass transfer distribution remains qualitatively unchanged when the outer component is made active, and the average value of Sh_m is reduced by 2.9%. As previously stated, the repeatability of overall measurements was found to be 1.2% at a 95% confidence level, indicating that the measured reduction has some significance.

Flow Visualization and Interpretation of Mass Transfer Distributions

Flow visualization on the tip surface is performed with an oil-lampblack technique. The tip surface of the test blade is covered with a sheet of adhesive paper impermeable to oil. A mixture of motor oil and lampblack powder is prepared and small oil dots are applied on the tip surface with a syringe. The blade is exposed to the flow in the wind tunnel, and pictures are taken to record the movement of the oil dots. The lampblack has the purpose of leaving a visible trace of dots trajectories on the paper. With this technique, the direction of the flow on the tip surface can be identified at different locations. Also, dots that are subject to higher shear stress start moving before others and usually leave longer streaks.

Pictures of flow visualization for the squealer and winglet-squealer tip at the highest gap level are presented in Fig. 8. The two pictures are relative to the final configuration of the dots, i.e., after a long exposure time to the flow in the wind tunnel. Results can be compared to the mass transfer distributions obtained for the two geometries at the same flow conditions and for $\tau/C=3.6\%$ (Figs. 3, 4, 5, 6).

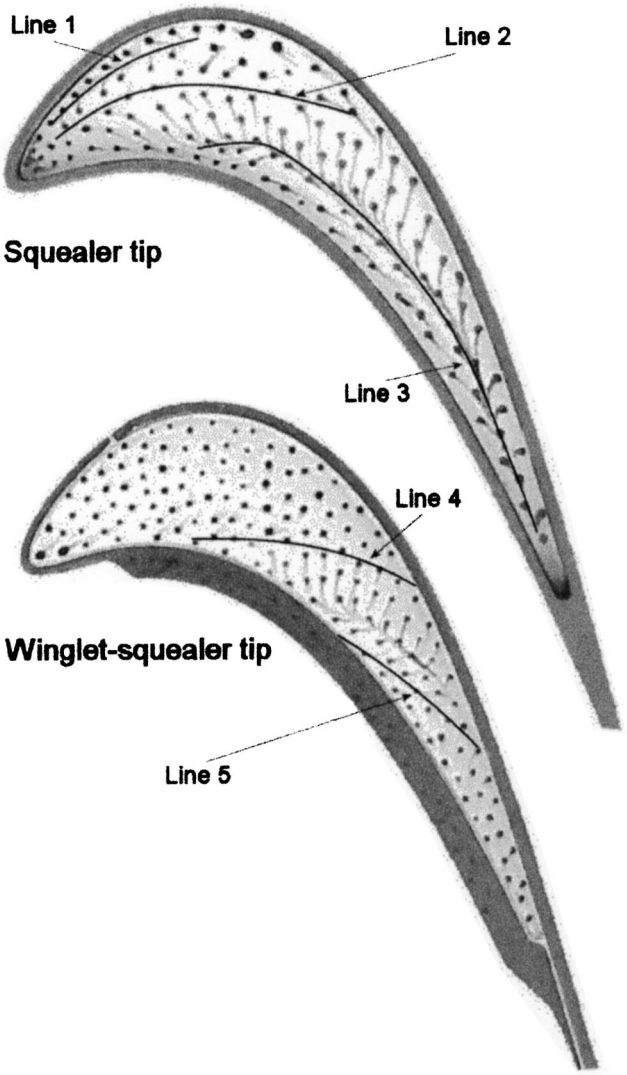

Fig. 8 Flow visualization for blade tips ($\tau/C=3.6\%$)

Squealer Tip. For all gap levels, the highest mass transfer coefficients are observed near the leading edge of the blade, at a distance of approximately one squealer height (4.8% of C) from the step formed by the squealer. The flow visualization reported in Fig. 8 clearly shows that the flow is impinging in this region. The dots that are closest to the leading edge are pushed back towards the squealer, while downstream of the impingement location the dots are pushed forward and to the sides.

The oil dots part from line 2, in the mid region of the cavity floor, indicating the occurrence of flow impingement. The local mass transfer measurements validate this inference, reporting enhanced mass transfer around this line. Line 2 shifts closer to the suction side squealer as the gap level is decreased, indicating that the starting point for tip leakage formation moves forward with decreasing clearance. A similar conclusion was reached by Sjölander and Amrud [10], who measured pressure on a flat tip blade.

Line 1 runs parallel and close to the suction side squealer and is located in the leading part of the blade. Oil dots coming from line 2 and oil dots moving away from the suction side squealer collect around this line. Lower mass transfer coefficients are observed along line 1 where two flows meet with resulting stagnation. The movement of the dots from the suction side squealer is believed to be due to an induced counterrotating vortex that might entrain some air flowing over the suction side squealer by the leading edge of the blade.

A stagnation region is located after the end of line 1. The fluid that impinges on line 2 and flows toward the suction side stagnates against the squealer. Part of it is pushed downstream and joins the recirculating impinging flow at the end of line 2, curling up in a large vortex that extends until the trailing end of the cavity. If line 2 is prolonged until it meets the suction side squealer, a distinct chordwise location can be identified. Downstream of this location the leakage flow entering from the pressure side is believed to hit the inner surface of the suction side squealer instead of impinging directly on the cavity floor, and is entrained in the main vortex system enclosed between line 2 and a third line marked as line 3. Downstream of this location, in fact, the highest mass transfer coefficients are observed by the suction side squealer.

Line 3 starts from the pressure side squealer and then runs parallel to the pressure side rim. Oil dots clearly collect around this line. The dots located downstream of line 2 are pushed toward the pressure side squealer by the main vortex, but cannot reach it because of the action of part of the leakage flow that is not caught in the main vortex system and reaches the cavity floor in the region between the pressure side rim and line 3. This interpretation is suggested by the direction of the oil streaks and is supported by the mass transfer results. Focusing attention on the beginning of line 3, a low mass transfer region is observed around the line and immediately upstream of it. The flow reaches this region only after having impinged on the cavity floor and the boundary layer has grown thicker, accounting for the reduced mass transfer rate. On the opposite side of the line, higher mass transfer rates are observed, indicating that some naphthalene-free mainstream flow is reaching the cavity floor in the vicinity of the pressure side squealer.

Winglet-Squealer Tip. Hardly any dot movement is observed in the leading region of the winglet-squealer blade, indicating a low level of shear stress (Fig. 8). Consistently, low mass transfer coefficients are observed in this region (Fig. 5 for $\tau/C = 3.6\%$).

High mass transfer coefficients are observed in the trailing region of the blade, by the suction side squealer. Flow visualization runs indicate that in this region the mainstream flow might recirculate over the cavity floor after having impinged on the inner surface of the suction side squealer.

The mass transfer measurements also show two high mass transfer streaks, particularly evident at the highest gap level, that run from the pressure side to the suction side. From the flow visualization runs it is evident that the flow impinges in these locations, marked as lines 4 and 5. The appearance of two impingement lines seems to be caused by the discontinuity of the winglet on the pressure side, which starts only at 20% of the axial chord. At the highest gap level oil dots pushed downstream of line 4 and upstream of line 5 collect around a visible line. The naphthalene sublimation measurements indicate a region of low mass transfer along this line, as would be expected in a region of low shear stress.

With decreasing gap levels, the same trend described for the squealer tip is observed: the starting point of tip leakage formation moves toward the front part of the blade. The extension of the region of low heat transfer in the leading region of the blade gradually decreases as the gap level is reduced.

Conclusions

Local and overall mass transfer measurements on the tip of a gas turbine blade have been conducted in a linear cascade for a squealer tip and a winglet-squealer tip geometry, at different clearance levels. The flow on the tip surface is visualized with an oil-lampblack technique. Based on the experimental evidence, the following conclusions can be drawn:

1 The cavity floor of the squealer tip is subject to higher mass transfer rates than the corresponding region of the winglet-squealer tip.

2 The overall Sherwood number for the cavity floor of the squealer tip decreases with decreasing gap level, while the influence of gap level on mass transfer from the winglet squealer tip is weak.

3 The mass transfer that occurs on the pressure side of the blade has a negligible influence on the mass transfer that occurs downstream, within the gap, indicating that the leakage flow is essentially composed of mainstream fluid.

The local mass transfer distributions for the two tips are substantially different. The main features observed for the squealer tip are summarized in the following points:

1 The incoming flow impinges on the cavity floor along a line that runs from the leading edge and meets the suction side squealer at around midchord. The high mass transfer rates along this line have two maximums. The first is located by the leading edge, approximately one squealer height away from the beginning of the cavity, and the second further downstream.

2 After impinging on the cavity floor, part of the mainstream flow rolls up into a vortex that fills most of the cavity and part is directed toward the suction side squealer. In the trailing region of the blade, the incoming flow might impinge on the inner surface of the suction side squealer and recirculate over the cavity floor, taking part to the main vortex system. In this region the highest mass transfer coefficients are in fact observed by the suction side squealer.

3 Part of the flow entering from the pressure side is not caught in the main vortex system and reaches the cavity floor by the pressure side squealer. In the leading region a flow acting from the suction side squealer toward the camber line is identified. This is believed to be due to an induced counterrotating vortex that might cause some flow to enter the gap from the suction side of the blade.

4 Increasing the gap level moves the starting point of the leakage flow rearward. The size of the recirculation region in the trailing part of the blade is also reduced and impingement occurs over a larger portion of the cavity floor, accounting for the increased overall mass transfer rate.

The main features observed for the winglet-squealer tip are summarized in the following points:

1 An extended low mass transfer region is located in the leading edge region of the blade, where the flow over the tip surface is characterized by very low velocity and might stagnate against the suction side squealer.

2 The leading edge region is separated from the trailing region by an impingement line that originates from the pressure side and meets the suction side squealer near midchord High mass transfer coefficients are observed on this impingement line.

3 The trailing region of the blade is characterized by high mass transfer coefficients that decrease moving from the suction side toward the pressure side. In this region, the flow appears to recirculate over the tip surface after hitting the squealer.

4 The starting point of the leakage flow moves rearward with increasing clearance, extending the size of the low mass transfer area. The increased leakage flow results in higher mass transfer rates in the trailing edge region, keeping the overall mass transfer coefficient fairly constant.

Acknowledgment

This research was supported by the U.S. Department of Energy-Federal Energy Technology Center through the AGTSR Program and by the University of Rome 'Tor Vergata', under grant MIUR No. 200209 3829. Information on tip geometry was provided by Dr. Ronald S. Bunker of GE R&D Center. His help and suggestions have been greatly appreciated and are acknowledged.

Nomenclature

C = actual chord, 18.4 cm in present study
Re_{ex} = Reynolds no. based on cascade exit velocity and actual chord
Sh = Sherwood no. based on actual chord
Sh_m = area averaged Sherwood no.
τ = tip clearance=tip gap

References

[1] Bunker, R. S., 2001, "A Review of Turbine Blade Tip Heat Transfer," *Heat Transfer in Gas Turbine Systems*, R. J. Goldstein, ed., Annals of the New York Academy of Sciences, New York, NY, Vol. 934, pp. 64–79.
[2] Bunker, R. S., Bailey, J. C., and Ameri, A. A., 1999, "Heat Transfer and Flow on the First Stage Blade Tip of a Power Generation Gas Turbine—Part 1: Experimental Results," ASME 99-GT-169.
[3] Ameri, A. A., and Bunker, R. S., 1999, "Heat transfer and Flow on the First Stage Blade Tip of a Power Generation Gas Turbine—Part 2: Simulation Results," ASME 99-GT-283.
[4] Azad, G., Han, J.-C., and Teng, S., 2000, "Heat Transfer and Pressure Distribution on a Gas Turbine Blade Tip," ASME 2000-GT-194.
[5] Teng, S., Han, J.-C., and Azad, G. S., 2001, "Detailed Heat Transfer Coefficient Distributions on a Large-Scale Gas Turbine Blade Tip," ASME J. Heat Transfer, **123**, pp. 803–809.
[6] Azad, G., Han, J.-C., and Boyle, R. J., 2000, "Heat Transfer and Flow on the Squealer Tip of a Gas Turbine Blade," ASME 2000-GT-195.
[7] Ameri, A. A., Steinthorsson, E., and Rigby, D. L., 1997, "Effect of Squealer Tip on Rotor Heat Transfer and Efficiency," ASME 97-GT-128.
[8] Jin, P., and Goldstein R. J., 2002, "Local Mass/Heat Transfer on a Turbine Blade Tip," *ISROMAC-9*, Honolulu, HI, February 10–14.
[9] Goldstein, R. J., and Cho, H. H., 1995, "A Review of Mass Transfer Measurements Using Naphthalene Sublimation," Exp. Therm. Fluid Sci., **10**, pp. 416–434.
[10] Sjölander, S. A., and Amrud, K. K., 1987, "Effects of Tip Clearance on Blade Loading in a Planar Cascade of Turbine Blade," ASME J. Turbomach., **109**, pp. 237–244.

Turbine Tip and Shroud Heat Transfer and Loading—Part A: Parameter Effects Including Reynolds Number, Pressure Ratio, and Gas-to-Metal Temperature Ratio

Marc D. Polanka
Donald A. Hoying
Matthew Meininger
Charles D. MacArthur

Air Force Research Laboratory,
AFRL/PRTT,
Wright-Patterson AFB, OH 45433

Turbine tip and shroud flow and heat transfer are some of the most complex, yet important, issues in turbine design. Most of the work performed to date has been performed in linear cascades and has investigated such items as the effect of tip geometries and turbulence on tip and shroud pressure and heat transfer. There have been very few full annulus or rotating measurements in the literature. Experimental measurements have been made on a single stage high pressure turbine at the US Air Force Turbine Research Facility (TRF) to aid in the understanding of this phenomena. The TRF is a full scale, rotating rig that operates at matched flow conditions to the true turbine environment. Heat flux measurements were acquired with both Pyrex insert strip and button gages, while the pressure measurements were taken with surface-mounted Kulite® pressure transducers. This paper presents one of the first full rotating, simultaneous pressure and heat transfer measurements to be taken in the turbine tip shroud region. These measurements provide some of the details needed for accurately quantifying the true flow condition in this complex flow regime. Comparisons between the present data and the existing 2-D cascade data were made. This investigation quantified the effects of Reynolds number, inlet temperature, turbine pressure ratio and inlet flow temperature profiles. This provides a benchmark data set for validation of numerical codes. [DOI: 10.1115/1.1515338]

Introduction

Two competing desires for gas turbine engines are increased performance and reduced operating cost. The performance can typically be achieved through increases in turbine inlet temperature; but coupling this temperature increase with the commonly used, experienced-based design approach rapidly consumes the built in durability margin. This results in increased inspection, repair and/or part replacement. In addition, if the design tip to shroud clearance is not maintained throughout the duty cycle, the operating cost and performance can be adversely affected. A better fundamental understanding of the complex flow and thermal environment in the blade tip region is key to improving the predictive capability that will allow minimization of cooling at required durability and performance levels.

The blade tip flowfield region, comprising the near tip airfoil surfaces, the blade tip and the adjacent stationary shroud, has been the subject of many aerodynamic and heat transfer studies in models, cascades, and full-scale rotating rigs over the last 20 yr. Bunker [1] and Dunn [2] provide an extensive review of known blade tip region studies. Some of the earliest work was done by Allen and Kofskey [3] visualizing the character of the tip flow in a low-speed rotating rig. Booth, et al. [4] performed tip flowfield visualization and measured tip leakage and losses for many tip geometries. Moore et al. [5] studied laminar to transonic flat tip region flows and compared their predictions of flow characteristics and heat transfer with experimental data. Mayle and Metzger [6] conducted some of the earliest published tip heat transfer experiments. They used a simulated tip model and found that the tip leakage flow to be related strongly to the airfoil tip pressure distribution and weakly to the relative motion between blade tip and shroud. Further experimental studies by Metzger and Rued [7] showed the flow field and heat transfer characteristics of the near tip airfoil surfaces. They observed on the shroud that the leakage flow characteristics resulted in very strong near-gap heat transfer enhancements of up to 200% with the pressure side sink flow and also with the suction side source flow.

Experimental data on the blade tip flowfield and heat transfer in stationary cascades has provided valuable insight into the area distribution of heat transfer. Bunker et al. [8] studied turbine tip heat transfer and flow in a linear cascade typical of a first-stage power generation turbine. They obtained near full surface heat transfer data on flat tips with various edges, three clearances and two turbulence levels. These effects had up to 20% augmentation depending on the chord location. Additionally, pressure distributions were measured for the blade tip, near-tip and shroud surfaces. The tip and shroud pressure measurements agreed well with design predictions. Ameri et al. [9] performed computations for the same geometry and showed good agreement with the data. Azad et al. [10] also studied detailed flat tip heat transfer and flow in a linear cascade. The effects of clearance and turbulence varied along the leakage flow path, with notable entrance effects on the pressure side.

Some research groups have measured blade tip/shroud heat transfer and shroud pressure in full-scale rotating turbine rigs. Dunn and Hause [11], Dunn et al. [12,13] studied various effects including rotating speed, Reynolds number, and gas-to-wall temperature ratio on the tip/shroud heat transfer. The tip Stanton num-

Contributed by the International Gas Turbine Institute and presented at the International Gas Turbine and Aeroengine Congress and Exhibition, Amsterdam, The Netherlands, June 3–6, 2002. Manuscript received by the IGTI, October 30, 2001. Paper No. 2002-GT-30186. Review Chair: E. Benvenuti.

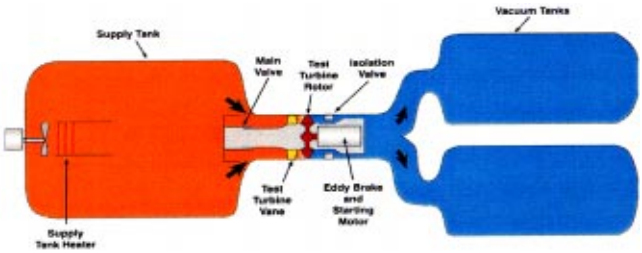

Fig. 1 Schematic of turbine research facility

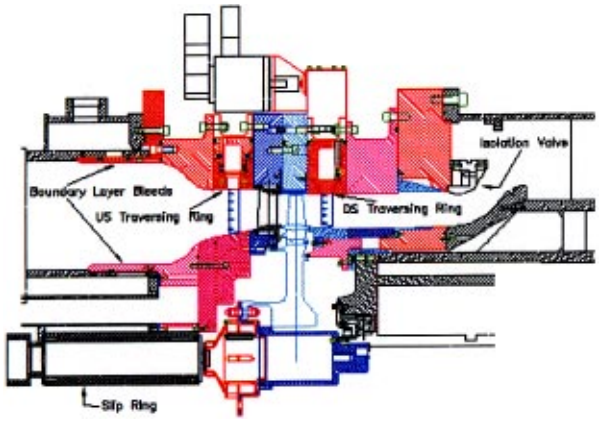

Fig. 2 Cross section of TRF test section

bers were similar to those for inlet guide vane leading edges and the shroud heat flux levels exceeded the blade levels. Epstein et al. [14] measured time-averaged and time-resolved heat flux and pressure to the shroud. The time averaged heat flux dropped by a factor of 5 along the blade chord and varied little with corrected speed. Peak heat flux levels were equal to those for the nozzle guide vane leading edge. Heat flux levels under the blade tips were 5–6 times that of the airfoil passage. In a low-speed rotating rig, Blan [15] measured the near tip heat transfer and noted that the suction side was 100% higher than that measured at the aft portion of the blade at midspan. The pressure side near tip heat transfer was only 10% higher than measured at blade midspan. Flow visualization in the same rig confirmed the transverse tip leakage path and showed the extent of the tip leakage vortex, which affected the near tip heat transfer.

This study is presented in two parts: Part A examines the time-averaged pressure and heat transfer measurements in the tip region of a full-scale rotating turbine blade, while Part B describes the time-resolved measurements and computations for the same geometry (Polanka et al. [16]). The turbine represents a modern first-stage high pressure turbine used for aircraft application. The turbine stage was comprised of the turbine vane presented by Joe et al. [17] and its matching highly loaded turbine rotor. The blade tip geometry has a sharp edged, flat tip with a nominal tip to shroud clearance of approximately 0.5% of blade height. Time averaged heat transfer and surface pressure are presented for the blade tip, shroud, and the near tip (96.5% span) airfoil surfaces. Data is presented for three stage pressure ratios, five Reynolds numbers, four inlet radial temperature profiles and four gas-to-wall temperature ratios.

Experimental Apparatus

Facility. The experimental apparatus used was the Air Force Research Laboratory Turbine Research Facility (TRF) (Haldeman et al. [18]) a transient ''blow down'' device that operates for several seconds at the same Mach and Reynolds numbers of the turbines of actual engines. (The reference cited above describes the TRF by its former name, the Advanced Turbine Aerothermal Research Rig.) The TRF, shown schematically in Fig. 1, operated as follows. Before the start of a test the entire facility was evacuated and the fast acting valve between the supply tank and test section was closed. The supply tank can be filled with a mixture of N_2 and CO_2 whose composition is set to simulate the same specific heat ratio (γ) as that of vitiated air at the engine operating conditions. For these tests only nitrogen was used resulting in $\gamma = 1.4$ and a $\mathrm{Pr} = 0.71$. This was reasonably close to the desired Prandtl number of high temperature air (about 0.68).

The nitrogen was heated with an internal electric heater until the gas temperature to room temperature metal ratio, representative of the engine ratio was reached. The tank pressure was adjusted until the density was correct for the turbine engine Reynolds number. Before the start of the run, the isolation valve was set to the proper throat area to control the pressure ratio across the stage when the gas was released from the tank. The turbine was spun up with an air motor to a speed slightly above the point for the correct velocity triangles and the correct Mach number of the engine.

The air drive motor was turned off and the turbine (still in vacuum) coasted slowly downward until the desired test speed. At this point the fast acting supply tank valve opened and flow proceeded through the turbine for about three seconds at the correct engine parameter conditions. The turbine was prevented from over speeding by an electric eddy current brake connected to the downstream side of the rotor beyond the choke valve. The brake current was controlled via an active feedback loop. This control circuit read the turbine speed and the supply tank total temperature and calculated the corrected speed. This value is compared to a set point and the brake adjusts to reach the desired set point. The Reynolds number is the only one of the five controlling nondimensional parameters (Re, M, γ, T_g/T_m, Pr) that changed significantly, about 20%, over a typical 3-s run. Fortunately the data was acquired at rates of tens to hundreds of thousands of samples per second. This resulted in data records of sufficient duration to achieve good statistical averaging over a short portion of the overall run. These small windows were then averaged to create nearly 'steady state' data.

A cross section of the test section holding the turbine is shown in Fig. 2. Gas flowing from the heated supply tank undergoes a substantial contraction before entering the vane set. Total temperature and total pressure profiles were measured with two rakes of five element probes in the inlet plane. Additional information about the probes is forthcoming. The inlet turbulence for this facility was less than 1% and the inlet Mach number to the vane was about 0.08. Behind the turbine a similar set of rakes measure the exit temperature and pressure profiles. These rakes were traversed 90 deg in the circumferential direction during the test and sample the flow about 1.3 axial chords behind the rotor.

Figure 2 also shows the position of the boundary layer bleed ports located just before the contraction. These full annular openings, one at the outer diameter and one at the inner, directed gas from the main flow path to a by-pass collection system designed to remove the boundary layer formed upstream of the contraction. The amount of flow bled off was set by a calibrated critical flow venturi between the bleed exit and the vacuum tanks. By adjusting the bleed flows the inlet flow profiles were controlled.

Instrumentation. The primary data acquired for this program were surface heat transfer and pressure measurements. The heat flux between the main flow gas and the turbine blades was measured by Pyrex® insert ''button'' and ''strip'' gages. These gages measure the rate of temperature rise at the surface of a small insert of Pyrex glass made flush with the surrounding metal surface. The recorded temperature-time profile, along with the assumption that

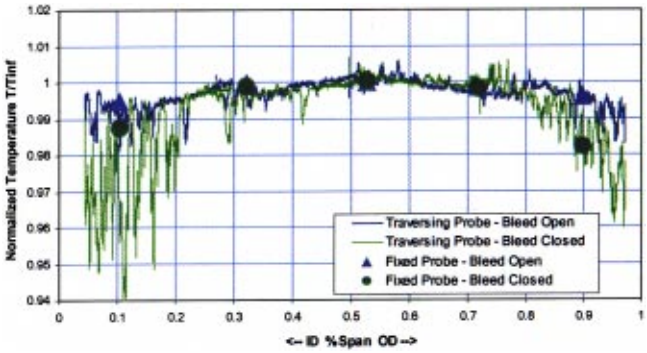

Fig. 3 Radial inlet temperature profiles

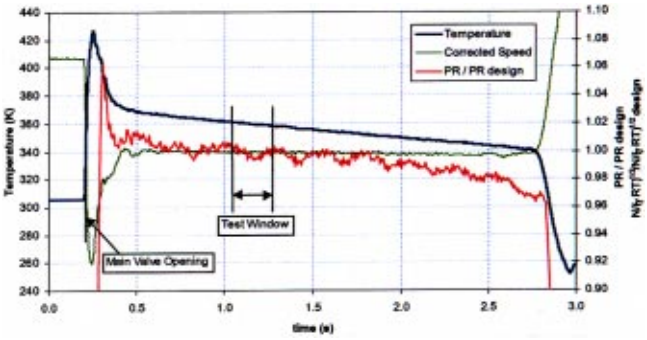

Fig. 4 Test window showing "steady" flow regime

the heat conduction into the glass is one dimensional and semi-infinite can be processed in several ways to obtain the heat flux, q'', as a function of time. The operation of these gages has been described (Dunn et al. [19]). The pressure loading on the airfoils and tip shroud was measured locally by using Kulite® miniature pressure sensors. Data for the surface mounted pressure transducers were acquired at a sampling rate of 100 kHz, whereas the heat transfer gages were acquired at 20 or 50 kHz.

The upstream and downstream flow conditions were measured with total temperature and pressure rakes. The total temperature was measured with two identical rakes each with five 1 mil type E thermocouples located in Kiel heads. Similarly, the total pressure was obtained by similar Kiel heads with tubing routing the pressure to external transducers. This limited gage frequency response but enhanced the accuracy. These fixed radial probes traversed circumferentially to characterize the flow. An additional probe further quantified the inlet flow by translating radially across the inlet duct height. This probe consisted of four Kiel heads with 1 mil E-type thermocouples and was located at the same axial position as the inlet temperature and pressure rakes. During the test, the probe moved radially inward with the first Kiel head starting near the OD wall and moved until the fourth Kiel head was almost at the ID wall. In this manner the full inlet temperature profile was mapped.

Experimental Conditions

Several measurements were taken to quantify the turbine operating environment. These included detailed measurements of the inlet flow approaching the turbine vane as well as detailed measurements of the rotor tip clearance. As described in more detail in the companion paper, the tip clearance was found to be 0.24 mm for the gages located on the shroud and 0.32 mm for the gages on the blade tip.

Inlet Flow. The inlet flow was characterized during a series of tests performed with only the vane installed in the test section. The radially traversing probe showed a relatively thick boundary layer growth on both the OD and ID walls as well as a highly unsteady boundary layer. The boundary layer thickness varied in time between 1.0 and 2.2 cm. Taking a mean value of 1.5 cm for both surfaces resulted in about 20% of the flow in the boundary layer. These experimental results were confirmed with the TEXSTAN (Crawford [20]) boundary layer code. Of the 20% core flow. TEXSTAN showed that 1/3 was in the ID while 2/3 was in the OD boundary layer.

This study led to the design of the boundary layer bleed system described in the foregoing. A series of tests were run removing 6, 12, and 18% of the core flow through the bleed system. Figure 3 shows both the time varying fluctuations acquired with the radially traversing probe and the time-averaged results obtained with the fixed five headed total temperature rake. The figure only compares the full open bleed with the bleed system closed for clarity. The bleed system significantly reduced the thickness and the fluctuations in the thermal boundary layer. The thickness of the boundary layer along the OD wall decreased substantially with just 33% of the max bleed flow removed (not shown), but did not reach a ''flat'' profile shape until the full bleed case. Measurements were also taken of the total pressure profiles both with and without bleeds. These measurements showed that even without the bleeds, the total pressure profile was flat to within 0.2% and did not contain high oscillations. The lower frequency response of the pressure transducers would have the tendency to dampen this response though. It was expected that the static pressure profile was also improved with the implementation of the boundary layer bleeds but this was not quantified.

Test Conditions. In this investigation fourteen total runs were performed independently varying four parameters. An averaging time window of 740 to 980 ms after the main valve opened was used. This provided for a ''steady'' portion of the blowdown where all start up transients have concluded and the pressure ratio and corrected speed have been accurately achieved as shown in Fig. 4. This window was also early enough to ensure that the semi infinite assumption was true for the Pyrex insert gages. For the baseline case, the initial inlet conditions were a pressure of 450 kPa, temperature of 480 K, Mach number of 0.08 and turbulence intensity of less than 1%. Table 1 outlines the averaged conditions for the test runs. The first parameter varied was the gas to metal temperature ratio. The second investigation focused on Reynolds number effects. The Reynolds number provided was based on turbine exit conditions and blade axial chord. The third set of tests varied the pressure ratio while the last focused on inlet total temperature profile effects.

Table 1 Averaged test conditions for 740 to 980 ms

Case / Variable	Exp	Base	Repeat	-21 % Tg/Tm	-17 % Tg/Tm	-11 % Tg/Tm	-69 % Re	-39 % Re	+8 % Re	+13 % Re	-10 % Pr	+12 % Pr	-100% Bleed	-66 % Bleed	-33 % Bleed
Tg /Tm		1.47	1.47	1.16	1.22	1.31	1.47	1.48	1.46	1.48	1.46	1.49	1.46	1.47	1.45
Re_{ac} exit	10^5	3.79	3.76	3.46	3.61	3.69	1.19	2.33	4.10	4.30	3.49	3.92	3.90	3.90	3.89
Pres Ratio		2.76	2.77	2.75	2.76	2.76	2.76	2.80	2.86	2.67	2.48	3.09	2.75	2.72	2.73
$\%m_{core}$		18	18	18	18	18	18	18	18	18	18	18	0	6	12

Data Analysis and Uncertainty

The reference length for the data to follow varied with the location and type of data. For the pressure transducers the ratio of axial length to axial chord was used consistent with most loading diagrams. For the 96.5% span heat flux gages, the surface length normalized by the total surface length was used for comparisons with boundary layer analyses. For both the tip and shroud gages, the hydraulic diameter (D_h) was used for reducing the data to Nusselt number. The hydraulic diameter was taken to be two times the tip gap height. This was plotted against the axial length normalized by the axial chord.

For all runs the rotor relative total conditions were utilized in obtaining the data. For instance, the pressure loading data was plotted against rotor inlet relative pressure based on local radius at the gage. Subsequently, Nusselt numbers were calculated based on the measured heat flux with a driving temperature being the rotor inlet relative total temperature. This value was chosen as it was the closest available value to the true driving temperature. The local relative total temperature was the actual driving temperature for heat flux but this was a value that was unobtainable experimentally. Computationally this was shown and will be discussed more in the companion paper. This local value could only be obtained from the computations which were not performed for all fourteen cases. Therefore the inlet rotor relative conditions were the best measurable representation of the true environment. With this, the Nusselt number was calculated as follows:

$$\mathrm{Nu}_s = hs/k \quad \text{or} \quad \mathrm{Nu}_{Dh} = hD_h/k \tag{1}$$

where s was the surface distance from the stagnation point for the surface gages and D_h was the hydraulic diameter of the tip gap for the tip and shroud gages (0.64 mm and 0.48 mm, respectively) and the heat transfer coefficient was defined as

$$h = q''/(T_{trel} - T_m) \tag{2}$$

The pressure transducers were calibrated in situ prior to and after each run. A Ruska 7010 pressure standard monitored the test section pressure while it was filled and evacuated. A typical calibration uncertainty for the static transducers was less than 0.05% full scale. The rotating transducers on the blade had higher uncertainties closer to 0.20% due to slip ring noise. A few transducers experienced larger hysteresis thus increasing their overall uncertainty. In comparing the calibrations prior to and post test, the Kulite® gages drifted. A transducer voltage difference of about 0.40% was found between the pre and post calibration coefficients. In reducing the data, only the set of coefficients closer to the actual test, usually within an hour, was used, thus minimizing the uncertainty.

The pressure data on the rotor needed a further correction due to g-loading on the wheatstone bridge in the Kulite transducers. This resulted in artificial pressures being recorded by the transducers. A correction calibration was performed by spinning the rotor from zero to test speed while in a vacuum. The voltages were recorded and a calibration of voltage versus speed was obtained to correct the data. The correction varied between $+2000$ and $-25{,}000$ Pa with the tip gages experiencing the greatest changes. This was believed to be due to the orientation of the transducers with respect to the rotational axis. This correction resulted in an additional uncertainty in the rotor pressure measurements due to the uncertainty in this bias shift of 150 Pa (or less than 0.01% of the full scale) for the majority of the transducers.

The uncertainties in the normalized data were determined primarily with the propagation of errors methods of Kline and McClintock [21]. The uncertainty for most of the rotor pressure transducers was $\pm 0.45\%$. The uncertainty in the relative total properties were determined from the upstream total pressure and temperature along with the turbine speed. This was determined to be about 0.15%. Based on the uncertainties in the measurement of the gage resistance and the uncertainty in calibration from resistance to temperature, the surface temperature uncertainty for the heat flux measurement was calculated to be ± 0.8 K for the heat flux gages. A jitter analysis was then performed (Moffat [22]) through the reduction scheme to obtain the uncertainty in the surface heat flux. This resulted in uncertainties in q'' between 700 and 2000 W/m^{2}K depending on the gage. With q'' and T_m, the heat transfer coefficient uncertainty was determined to be about 30 W/mK for the Pyrex gages based on an uncertainty in $T_g = 0.7$ K. This resulted in Nusselt number uncertainties between 5 and 9% depending on location. For the tip and shroud, button gages were utilized and the heat island effect was analyzed. Based on the results of Zilles and Abhari [23] for the short boundary layer development distances and the low local Reynolds numbers, the maximum expected error for these gages was estimated to be 2%. Since this was less than the overall uncertainty for the measurements, no correction was applied.

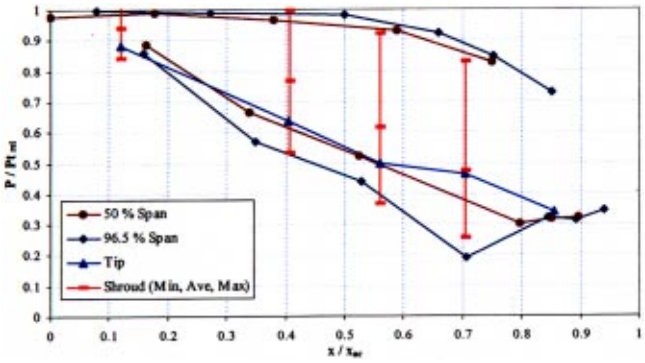

Fig. 5 Baseline case loading

Results

Pressure Results. Discrete static pressure measurements were taken with high-response surface-mounted Kulite transducers. Five transducers were located along the mean camber line of the turbine blade tip and five transducers were mounted into the shroud spaced along the blade tip axial chord. Furthermore, an array of transducers were mounted at the 96.5% span location along the airfoil surface. These included six sensors on the pressure surface and seven along the suction surface. This adequately defined the loading on the airfoil surface. A further array was located at 50% span which included five pressure side gages and six suction side gages.

Figure 5 shows the baseline pressure loading at 50, 96.5%, and along the midcamber line of the blade tip. This airfoil was highly loaded with somewhat greater loading near the tip as expected. This loading suggested some shock interactions along the aft portion of the suction side. This was more evident at 50% due to the higher concentration of gages, but was believed to occur at 96.5% as well. The tip surface pressures are closer to the suction side values and display the same acceleration characteristics.

Also shown on Fig. 5 is the shroud data. The average values as well as the maximum and minimum values are presented. The blade shroud displayed higher average pressures than the blade tip, as opposed to that measured by Bunker et al. [8] in a stationary cascade. This was because of the unsteady range of pressures as the blades pass. The shroud gages varied from a maximum very close to the pressure side value to a minimum close to the suction side value. The slight difference from the 96.5% pressure distribution to the shroud confirms that less work is being done in the tip gap as expected. The losses in the tip gap were relatively minimal for this turbine design. The relationship between the shroud pressures and the tip pressures was difficult to quantify without the aid of CFD since the tip gages only represent one position on the tip. With the high pressure gradient on the tip, these gages did not measure the ''average'' pressure on the tip. In

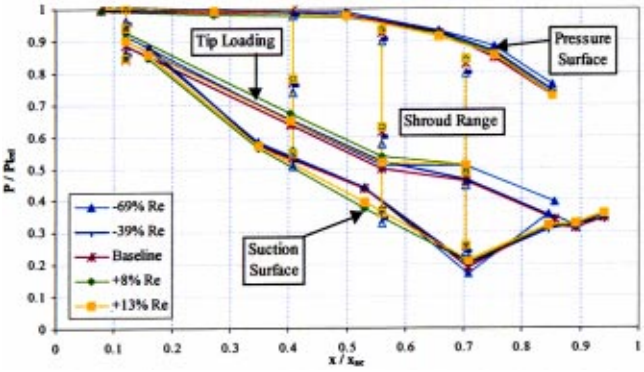

Fig. 6 Effects of Reynolds number on blade loading at 96.5% span

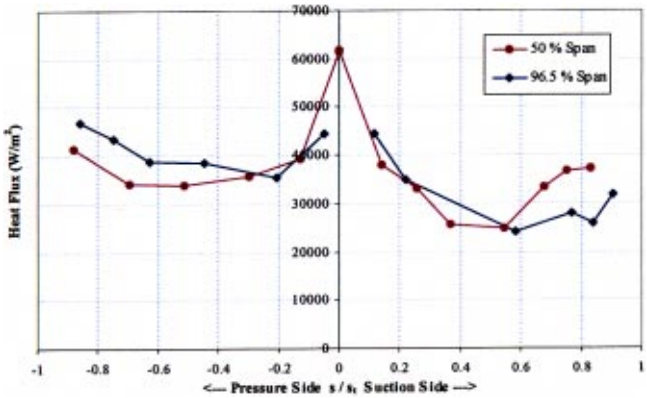

Fig. 8 Local heat flux at 50 and 96.5% span for the baseline case

contrast, the shroud gages were time dependant and experienced the full range of pressures within the tip gap region and as such do not represent the mean camber line pressure. For comparison, CFD was utilized in the companion paper to investigate the shroud data while it is directly over the tip gages.

Of the four primary parameters varied in this investigation, altering the bleed flow and the gas-to-metal temperature ratio were not expected to affect the blade loading since these parameters primarily affected the total temperature. This was found true as the data was within the experimental uncertainty for these conditions.

The parameters that were expected to affect the loading on the airfoil were the Reynolds number and the pressure ratio. Figure 6 shows the results of the five Reynolds numbers run with this turbine. Little change in loading at 96.5% span was evident for the exit Reynolds numbers tested. The higher Reynolds numbers had somewhat lower pressures at $x/x_{ac}=0.5$ suggesting higher velocities around the suction side. Decreasing the inlet Reynolds resulted in slightly increased pressures on the aft portion of the pressure side. The tip gages displayed no consistent change with Reynolds number. Overall, the Reynolds number had a rather minimal effect on the loading characteristics of this airfoil. Interestingly, the endwall shroud showed a decrease in the minimum, maximum, and average pressure as the Reynolds number decreased as shown in Fig. 6. This could be indicative of extra losses in this region at lower Reynolds numbers.

Figure 7 shows changes in loading due the overall pressure ratio at 96.5% span. The primary effect was along the aft portion of the suction side where an increase in pressure ratio resulted in higher loading and a decrease in pressure ratio yielded lower overall loading. No significant changes were evident on the blade tip as the pressure ratio was varied. One possible explanation was that the flow was choked in the tip region, as indicated by the

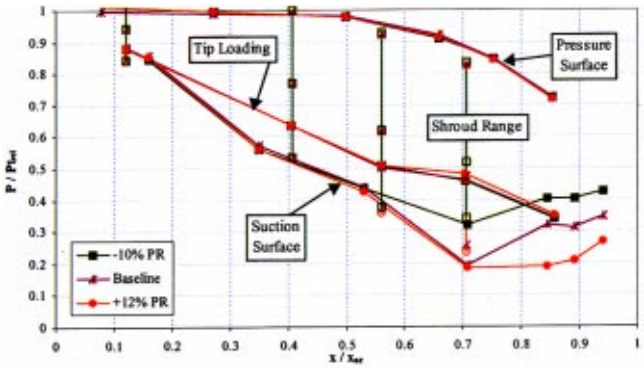

Fig. 7 Effects of pressure ratio on blade loading at 96.5% span

local static pressure, and changes in the suction side back pressure did not alter the flow over the tip. Matching the suction side pressure condition may have resulted in additional downstream losses; however, this was not measured. Figure 7 shows no significant change for the forward shroud gages with pressure ratio. The fourth shroud gage does begin to reflect the changes in the suction side pressure. A higher average and minimum pressure are recorded for the lower pressure ratio consistent with the suction side results. With the majority of the pressure ratio influence occurring near the trailing edge of the blade, the fifth endwall gage (which was not functional) would have been necessary to better see this impact on the shroud. The effects were more evident in the heat transfer results.

96.5% Span Heat Transfer Results. The heat transfer data was acquired simultaneously with the pressure data at coincident locations, albeit on different airfoils. Figure 8 shows the local heat flux at 50 and 96.5% span for both the pressure and suction surfaces for the baseline condition. There was a high heat load at the stagnation point. The suction side exhibited a subsequent decrease followed by an increase toward the trailing edge typical of a transitional boundary layer flow along the airfoil surface. The pressure side heat load remained high and nearly constant once away from the stagnation point. Only a slight rise in heat flux occurred suggesting a turbulent boundary layer. Comparing the heat loads at the two spans, the pressure side displayed a higher heat flux at 96.5% span by approximately 10 to 20% from the midchord to trailing edge locations. The loading was slightly higher in the near tip and may contribute to this augmentation. This trend was observed in the pressure side near tip region by Blair [15] in a low-speed rotating rig and by Metzger and Rued [7] in a simulated tip model. As these researchers note, the pressure-surface boundary layer near the tip was thinned and apparently relaminarized, resulting in higher heat transfer rates. The suction surface heat transfer data at midspan and near-tip were similar up to 60% chord, after which the midspan appears to transition earlier than the near-tip region. The pressure distribution does not reveal why an earlier transition would result. The midspan heat transfer data was approximately 20 to 30% higher than that measured in the near-tip from midchord to the trailing edge. No localized enhancement due to the tip leakage flow over the near tip suction surface was observed, as compared to that shown by Blair [15] where there was a 100% increase. This may be attributed to the present low tip clearances and low flow spilling over the tip to the suction side.

Plotting local Nusselt number versus local Reynolds number (Fig. 9) for the 96.5% span gages reveals that the suction surface started laminar and transitioned to turbulent over the airfoil length. The pressure side begins turbulent and appears to relaminarize somewhat with downstream distance. Also shown on Fig. 9

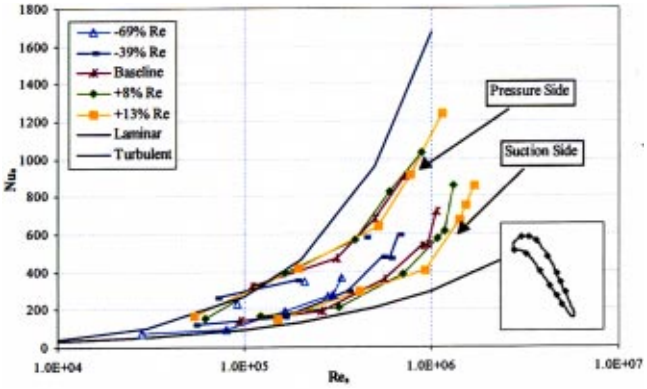

Fig. 9 Boundary layer state of blade at 96.5% span

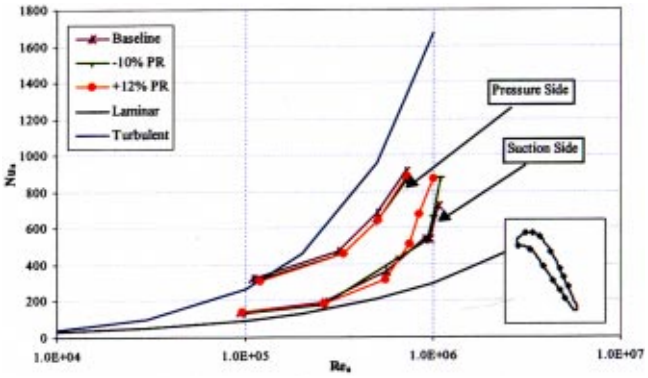

Fig. 11 Pressure ratio effect at 96.5% span

is that the heat transfer increased as the local Reynolds number increased. The pressure side followed a consistent relationship between local Reynolds number and local Nusselt number. In contrast, the suction side Nusselt number begins laminar and starts to transition for all cases further downstream. Both Figs. 9 and 10 show, for each Reynolds number case, the last suction side gage displays a significantly higher heat flux. This was probably due to a slightly separated flow near the trailing edge of the blade resulting in a high heat region transfer. Inset to both of these figures is a schematic displaying the location of the heat flux gages. These locations are identical to the pressure gages presented earlier.

Figure 10 also shows two variations in pressure ratio from the design point. Both a lower pressure ratio and a higher pressure ratio resulted in enhanced heat transfer along the aft portion of the suction side of the blade. This region was expected to be affected as the pressure distribution was only altered here. While the pressure distribution was clearly changed in this region of the airfoil, the local Reynolds numbers were nearly constant for the three cases (Fig. 11). This was due to the decrease (or increase) in density to counteract the increase (or decrease) in the local velocity. Therefore, the change in Nusselt number was not a velocity effect. The increase in Nusselt number for lower pressure ratio can be explained by separation occurring in this region of the airfoil thus increasing the heat transfer. The increase in Nusselt number for the higher pressure ratio was believed to be due to a change in the local driving temperature. The heat flux increased because the local relative total temperature increased but since the data was reduced using the upstream relative total temperature, this was not accounted for in reducing the data to Nusselt number.

Decreasing the gas to metal temperature ratio resulted in a substantial decrease in suction side and pressure side heat transfer. Plotting the same data as a Nusselt number (Fig. 12) resulted in a collapse of the pressure side data suggesting no influence of inlet temperature. In contrast, the suction side displayed a decrease in Nusselt number as the inlet temperature decreased. This decrease is attributed to not accounting for the work extraction through the turbine. In reducing the data, T_{trel} was merely the upstream conditions corrected for the average losses across the vane and then converted to relative conditions based on local radius and turbine speed. It is not the local relative total temperature at the gage. For the aft gages on the suction side, the local temperature was significantly less than the upstream value.

As the gas to metal temperature ratio decreased, the difference between the driving temperature and the metal temperature decreased dramatically. At the lowest inlet temperatures, the local T_{trel} was lower than $T_{m'}$. This resulted in negative heat transfer coefficients being recorded. Since the data reduction scheme used the upstream T_{trel} value, which was still larger than T_m, negative Nusselt numbers were output. In this case, the negative Nusselt numbers represent that the average heat transfer was actually from the blade to the freestream. Had the correct driving temperature been used, a negative denominator would have been calculated in Eq. (2) and the resultant Nusselt number would have been positive.

Obviously the difficulty lies in the inability to measure this local driving temperature. Unfortunately, only the upstream total temperature was quantifiable. This results in inaccurate results as shown in Fig. 12. This is a problem that is not easily corrected. CFD can help in providing the proper driving temperature, but that requires that the computations model all the physics properly and that simulations are performed for each test condition. This local driving temperature was calculated for the baseline case and

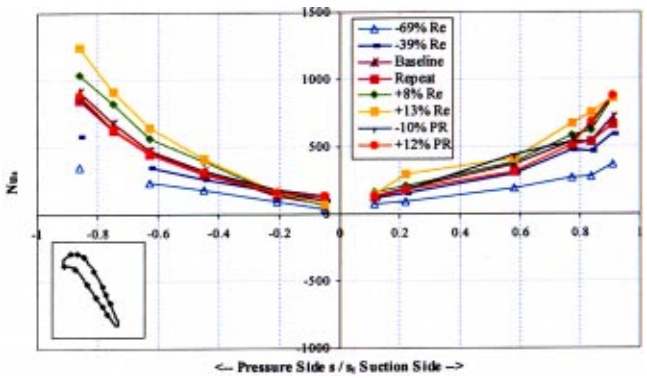

Fig. 10 Effects of pressure ratio and Reynolds number on local Nusselt number at 96.5% span

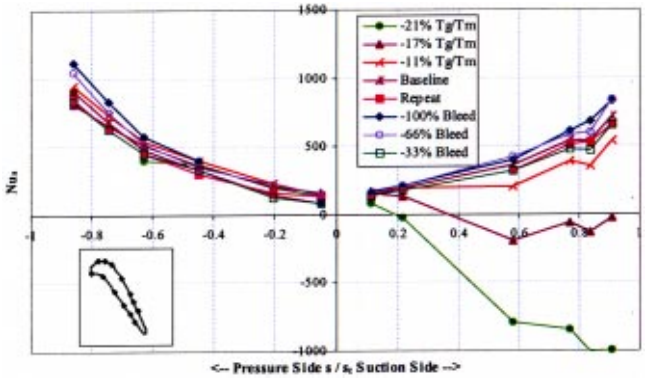

Fig. 12 Effect of inlet temperature and inlet profile on local Nusselt number at 96.5% span

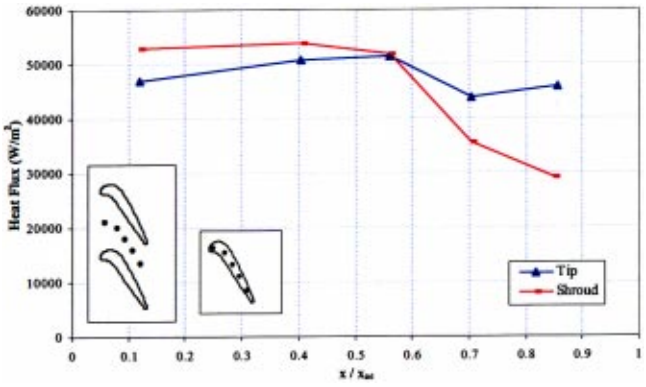

Fig. 13 Heat flux distribution on the tip and shroud for the baseline case

an attempt to correct this data was made in the companion paper. Without the computational input, a general correction is not available.

Removing the upstream boundary layer resulted in a substantial decrease in the heat transfer rate for all the gages in the tip region. Looking specifically at the 96.5% span data (Fig. 12) shows a decrease in Nusselt number as more boundary layer was removed. As the inlet temperature profile flattened, the local total temperature in this region of the flow increased which would imply that the heat flux should increase. But as just mentioned, even though the heat flux increased with inlet temperature, the heat transfer, i.e., the Nusselt number, remained constant. Therefore, based completely on the local temperature, no effect should be seen. Also, the local Reynolds number remained nearly constant as the amount of bleed was varied.

This suggested that it was the shape of the temperature profile in this passage, and its influence on the secondary flows, that was contributing to the effect observed. As shown by Hermanson and Thole [25], a flat total pressure and temperature profile convected through the airfoil passage cleanly, whereas a parabolic-shaped profile enabled the formation of the leading edge horseshoe vortex and the subsequent passage vortex. This led to a distortion of the flow moving hotter fluid toward the endwalls of the pressure surface and cooler fluid toward midspan of the suction side. It also resulted in a thinner boundary layer along the pressure side. While Hermanson and Thole's [25] investigation was looking at a vane cascade, the implications of the vortex formation could be transferred to the rotating case. The thinner pressure side boundary layer and not accounting for the hotter fluid being carried toward the tip in the data reduction resulted in higher heat transfer coefficients and higher calculated Nusselt numbers on the pressure side. The increase in suction surface Nusselt number with a more parabolic profile was thought to be a result of the hotter pressure side gases being convected over the tip and then impinging on the suction side as described by Blair [15].

Tip and Shroud Heat Transfer Results. The tip and shroud heat flux data shows elevated levels as seen in Fig. 13. The tip values are as high as the 96.5% span stagnation point heat flux (Fig. 8). The shroud has similar initial levels which then decrease along the length of the airfoil. These high heat fluxes were due to the reformation of the boundary layer along the tip. With the streamlines crossing the tip from pressure side to suction side, every gage was located a short distance from the start of a new boundary layer. These streamlines were predicted for the baseline condition as shown in Fig. 14. From this plot the local streamline length from the pressure side tip edge was determined.

With this information a comparison of local Nusselt numbers was made against thermal entry length laminar and turbulent correlations, Figures 15(*a*) and (*b*), respectively. The data does not follow the same trend as the laminar entry region flow as shown in

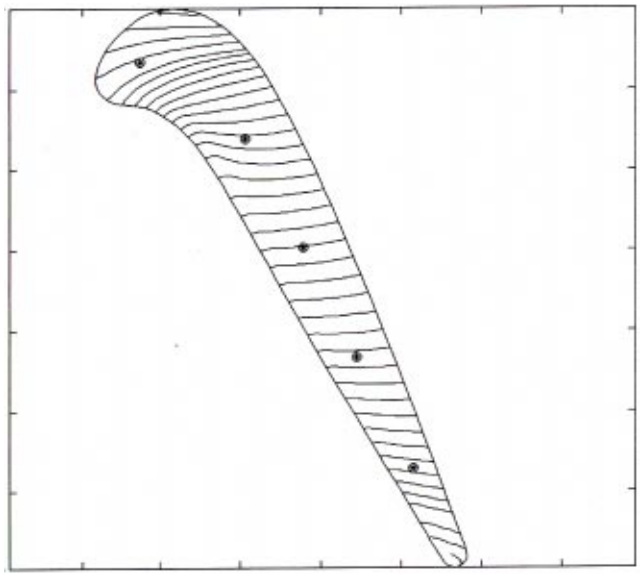

Fig. 14 Tip streamlines—gage locations indicated

Fig. 15(*a*). The laminar correlation compared to was for parallel planes with a constant heat rate as given by Kays and Crawford (Eq. 8–24) [24]

$$\mathrm{Nu}_i = \mathrm{Nu}_{ii}/(1-(q_o''/q_i'')\Theta_i^*) \tag{3}$$

Figure 13 provided the ratio between the outer (shroud) and inner

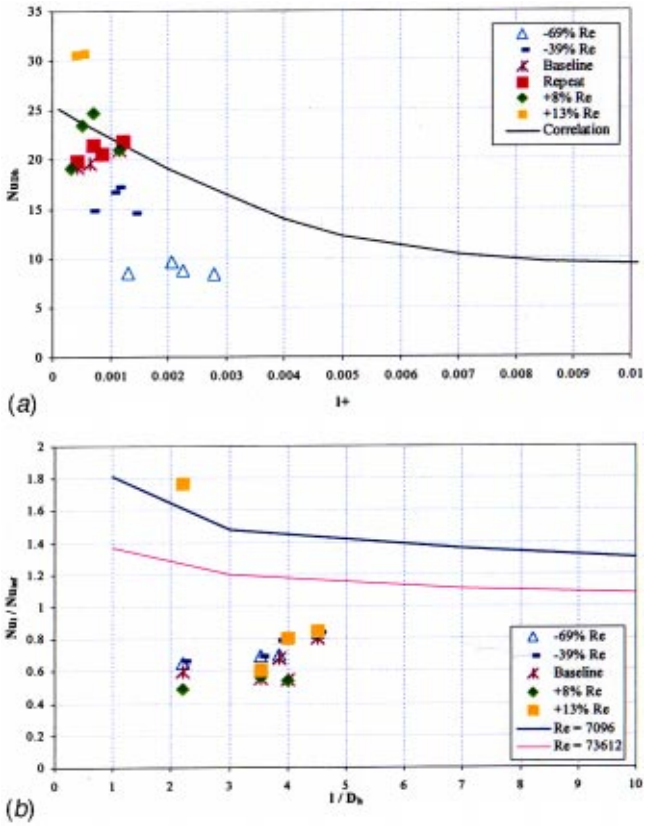

Fig. 15 Comparing tip Nusselt numbers to (*a*) laminar correlation (*b*) turbulent correlation

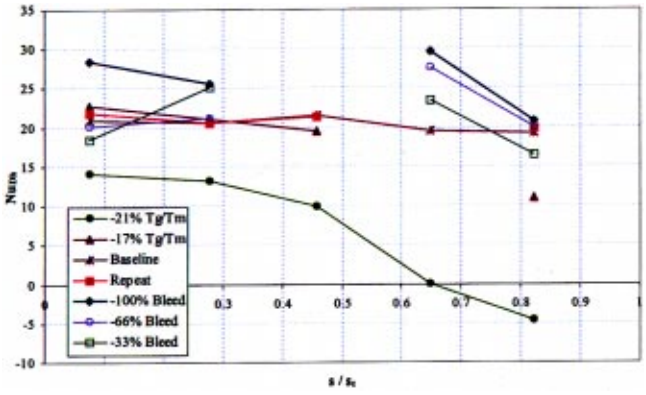

Fig. 16 Tip Nusselt numbers comparing gas to metal Temperature and inlet profile effects

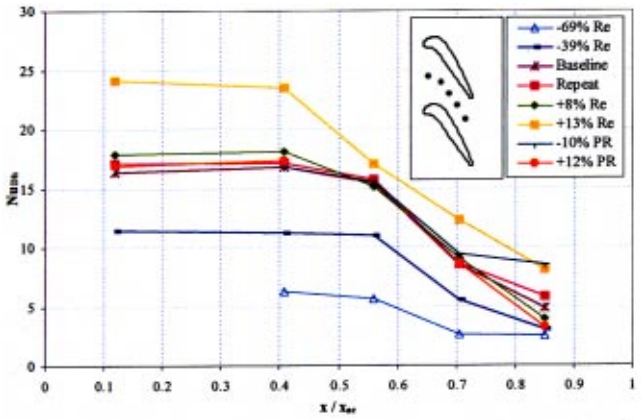

Fig. 17 Effects of Reynolds number and pressure ratio on shroud Nusselt number

(tip) surfaces. Nu_{ii} and Θ_i^* were taken from Table 8-10 in [24]. For the laminar correlation, the length was normalized per [24], as follows:

$$l^+ = 2(l/D_h)/\mathrm{RePr} \tag{4}$$

where l represents the length of the streamline along the blade tip and D_h is the hydraulic diameter.

Comparing the same data against the correlation given in Table 13-9 [24] clearly shows that the tip data clearly does not follow a typical turbulent entry region flow either (Fig. 15(*b*)). Reynolds numbers of 7096 and 73612 are shown for reference. These two Reynolds numbers were in the correct range for this turbine. The lowest local gap Reynolds number based on hydraulic diameter ranged from 2700 to 5000, while the highest gap Reynolds number varied from 10,000 to 20,000. These correlations did not incorporate that the shroud was moving in the tip frame of reference and thus the velocity profile and the thermal profile are not developing as these correlations assume. This highlights the need for better prediction of the tip flow. The standard 2-D correlations do not apply to this complicated flowfield. The rotational aspect of tip with respect to the shroud along with the overall three dimensionality of the flow makes this a difficult region to understand.

Decreasing the gas to metal temperature ratio resulted in smaller tip heat transfer rates and subsequently lower Nusselt numbers (Fig. 16) similar to the effect noticed along the suction side of the airfoil. The same issues concerning utilizing the proper driving temperature occurred for the tip flow. Again this became more obvious for the lower T_g/T_m temperature ratios. The impact of changing the inlet temperature profile is also shown in Fig. 16. While there appears to be some variation in the data, a trend of increasing Nusselt number as the bleed was decreased was evident, particularly for the last two gages. This was consistent with the results at 96.5% span and further suggests that there was more mixing and probably more unsteadiness in the tip region flow with a non flat approach boundary layer into the tip gap region. The unsteadiness will be addressed more in the companion paper. Also, it was believed that the shape of the inlet profile would have an effect on the boundary layer formation mechanism along the blade tip. From an energy balance, the heat transfer coefficient can be determined from

$$h = k_m dT/dy(T_{\mathrm{trel}} - T_m) \tag{5}$$

With a flatter profile, dT/dy approaches zero resulting in lower heat transfer coefficients. As the profile steepens, so does dT/dy and therefore higher heat transfer coefficients result.

While the tip maintained a relatively constant Nusselt number along the meanline for the baseline case, the shroud Nusselt number dropped by a factor of 2 to 3 down the blade chord, most of which occurred aft of the airfoil gage point. This reduction in shroud heat transfer was consistent with, although smaller in magnitude than, data published [14] who observed a factor of 4 to 5 reduction down the blade chord for a much higher loaded turbine (pressure ratio=4). This reduction was due to shape of the blade tip. For the more downstream gages, the percent of time that the shroud gages were directly over the tip was reduced due to the thinner width of the tip in the circumferential direction. While in the ''freestream'' flow, lower heat transfer coefficients were experienced. This will be shown directly in the companion paper.

Increasing the chord Reynolds number increased the Nusselt number (Fig. 17) along the shroud as it did at 96.5% and on the tip. Similar to the 96.5% span data, the pressure ratio only had an effect on the aft portion of the shroud. Again the lower pressure ratio resulted in a higher Nusselt number again believed to be due to possible separation in the aft portion of the blade. This would have the impact of changing the flowfield in the tip gap and would enhance the heat transfer along the shroud. The measured decrease in Nusselt number with increasing pressure ratio was again attributed to not utilizing the true driving temperature. This was especially complicated for the nonrotating shroud. The relative inlet temperature was chosen for reducing the heat flux data to Nusselt number based primarily on the good collapse of the pressure data when reduced in this manner; but, as discussed earlier, the changes in relative total temperature through the passage are not captured. Also, the tip gap velocities are not uniform both along the chord and in time.

Investigation of the gas to metal temperature ratio further revealed the difficulty with knowing what driving temperature should be used to reduce the data. While the heat flux maintained the shape shown in Fig. 13 as these parameters were varied, clearly the Nusselt number profile revealed a significant difference as shown in Fig. 18. As the gas-to-metal temperature decreased, the shroud Nusselt number slope changed dramatically. This was explained mostly by comparing the relative total temperature to the metal temperature. For the -21% T_g/T_m case, the metal temperature approached the same value as the relative total temperature at the leading portions of the shroud. This makes sense in that the leading edge region was virtually stagnant in velocity. Therefore high heat transfer coefficients were expected and for the low freestream temperature, the temperature differential was not very large. This resulted in high calculated Nusselt numbers. Further downstream the work done through the rotor passage resulted in a change in the local total temperature. Therefore, using the inlet relative total temperature may not be the correct choice for reducing the shroud heat flux to Nusselt number for this region. Using a local total temperature, that would be decreasing with downstream distance, would result in less divergence of the Nusselt numbers. This would also counteract the apparent reduction in

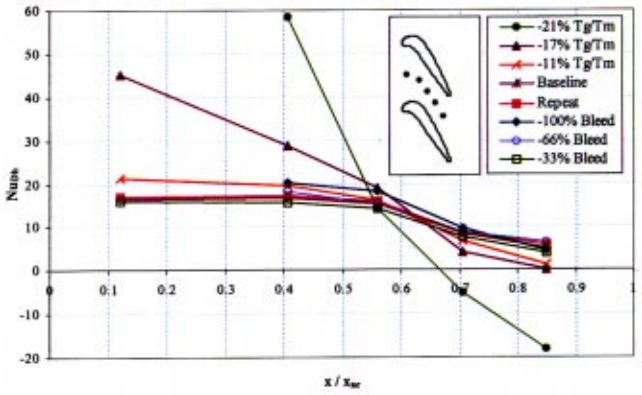

Fig. 18 Effects of gas to metal temperature and inlet profile on shroud Nusselt number

Nusselt number with downstream distance. This calculation was performed and will be discussed in the companion paper.

Interestingly, variations in the inlet temperature profile had minimal effect on the shroud Nusselt number. While no changes were measured in the pressure distribution as more flow was bled off, the thermal boundary layer was expected to change. As shown in Fig. 18 only for the no bleed case was the Nusselt number different, being slightly higher. With the large variation in flow along the shroud as each blade passes, it can be suspected that the boundary layer always has to restart itself and may not be affected by the upstream condition.

Conclusions

This work represents one of the first fully rotating investigations into both pressure loading and heat transfer in the tip region of a turbine blade. This study obtained data simultaneously in a quasi steady-state portion of a blowdown rig test. Data comparisons were made between the shroud, the blade tip, and along the blade surface at 96.5% span. This enabled a full picture of the loading and heat load in this region of a blade. The tip region was highly loaded and the relatively small clearance resulted in low flow rates and minimal losses over the blade tip. Very high heat transfer rates were measured on both the blade tip and the shroud with levels as high as the stagnation region on the airfoil itself. The Nusselt numbers on the blade suggested that this airfoil is transitional on the suction surface and turbulent on the pressure surface.

This investigation focused on the effects of varying several key parameters such as the exit chord Reynolds number, the turbine pressure ratio, the gas to metal temperature ratio and the inlet temperature profile. The Reynolds number had a minimal effect the loading, but a significant effect on the heat transfer. Lower Reynolds numbers reduced the heat load to the airfoil in all regions. The pressure ratio only had an effect on the aft portion of the suction side. Higher pressure ratios increased the overall loading of the airfoil, while lower pressure ratios decreased the loading. In contrast, both the higher and lower pressure ratios resulted in higher Nusselt numbers on aft portion of the suction side and the blade tip. The lower pressure ratio was believed to have resulted in some separation in this region, thus acting to increase the heat transfer. Conversely, the high pressure ratio was believed to have resulted in a local change in the driving temperature which resulted in higher heat transfer rates.

The inlet temperature had a strong influence on the local heat transfer in this regime. But reducing the data to Nusselt number collapsed the pressure side data. For the very low T_g/T_m temperature ratios the work extraction resulted in local relative total temperatures that were close to if not lower than the metal temperature. Neglecting this change in driving temperature resulted in apparent negative Nusselt numbers. This effect highlighted the need to fully understand the true driving temperature for reduction of heat transfer data to Nusselt number. This is a significant problem for understanding the true heat load on rotating components and needs to be further addressed in the future. The inlet total temperature profile had the effect of changing the secondary flow structure in the turbine passage. While this was not quantified it was understood that a flat inlet profile resulted in less vortical motion and thus lower mixing and lower heat transfer rates. As the profile became more parabolic, the horseshoe vortex and the passage vortices resulted in higher overall Nusselt numbers particularly on the aft portions of both the pressure and suction surfaces.

Acknowledgments

The authors would like to thank Michael Kobelak of the Turbine Engine Division, Curt Rice of Wyle Labs, and Matthew Streby of Adtech Inc. for their dedication in carrying out the experiments. We also acknowledge John Clark of Pratt and Whitney for supporting this effort with computational results.

Nomenclature

D_h = hydraulic diameter (m)
h = heat transfer coefficient (W/m^2-K)
k = thermal conductivity (W/m-K)
l = distance along streamline (m)
M = Mach no. (−)
Pr = Prandtl no. (−)
q'' = heat flux (W/m^2)
Re = Reynolds no. (−)
T = temperature (K)
s = surface streamwise distance (m)
x = axial distance (m)

Subscripts

ac = axial chord (m)
g = conditions of freestream gas
m = conditions of metal
t = total thermodynamic properties, total surface length
rel = relative to rotor frame of reference

References

[1] Bunker, R. S., 2000, ''A Review of Turbine Blade Tip Heat Transfer,'' A Review of Turbine Blade Tip Heat Transfer,'' presented at Turbine 2000 Int. Symp. Heat Transfer in Gas Turbine Systems, Izmir, Turkey.
[2] Dunn, M. G., 2001, ''Convective Heat Transfer and Aerodynamics in Axial Flow Turbines,'' ASME Paper 2001-GT-0506.
[3] Allen, H. W., and Kofskey, M. G., ''Visualization Study of Secondary Flows in Turbine Rotor Tip Regions,'' NACA TN 3519.
[4] Booth, T. C., Dodge, P. R., and Hepworh, H. K., 1982, ''Rotor-Tip Leakage: Part I-Basic Methodology,'' ASME J. Eng. Power, **104**, pp. 154–161.
[5] Moore, J., Moore, J. G., Henry, G. S., and Chaudhry, U., 1989, ''Flow and Heat Transfer in Turbine Tip Gaps,'' ASME J. Turbomach., **111**, pp. 301–309.
[6] Mayle, R. E., and Metzger, D. E., 1982, ''Heat Transfer at the Tip of an Unshrouded Turbine Blade,'' Proc. 7th Int. Heat Transfer Conference, vol. 3, pp. 87–92.
[7] Metzger, D. E., and Rued, K., 1989, ''The Influence of Turbine Gap Leakage on Passage Velocity and Heat Transfer Near Blade Tips: Part I-Sink Flow Effects on Blade Pressure Side,'' ASME J. Turbomach., **111**, pp. 284–292.
[8] Bunker, R. S., Bailey, J. C., and Ameri, A. A., 2000, ''Heat Transfer and Flow on the First-Stage Blade Tip of a Power Generation Gas Turbine: Part 1—Experimental Results,'' ASME J. Turbomach., **122**, pp. 263–271.
[9] Ameri, A. A., and Bunker, R. S., 2000, ''Heat Transfer and Flow on the First-Stage Blade Tip of a Power Generation Gas Turbine: Part 2-Simulation Results,'' ASME J. Turbomach., **122**, pp. 272–277.
[10] Azad, Gm S., Han, J. C., Teng, S., and Boyle, R. J., 2000, ''Heat Transfer and Pressure Distributions on a Gas Turbine Blade Tip,'' ASME Paper 2000-GT-194.
[11] Dunn, M. G., and Hause, A., 1982, ''Measurement of Heat Flux and Pressure in a Turbine Stage,'' ASME J. Eng. Power, **104**, pp. 215–223.
[12] Dunn, M. G., Rae, W. J., and Holt, J. L., 1984, ''Measurement and Analyses of Heat Flux Data in a Turbine Stage: Part II—ASME Discussion of Results and Comparison With Predictions,'' ASME J. Eng. Gas Turbines Power, **106**, pp. 234–240.
[13] Dunn, M. G., Martin, H. L., and Stanek, M. J., 1986, ''Heat-Flux and Pressure

Measurements and Comparison With Prediction for a Low-Aspect-Ratio Turbine Stage,'' ASME J. Turbomach., **108**, pp. 108–115.
[14] Epstein, A. H., Guenette, G. R., Norton, R. J. G., and Yuzhang, C., 1985, ''Time Resolved Measurements of a Turbine Rotor Stationary Tip Casing Pressure & Heat Transfer Field,'' AIAA Pap., No. 85–1220.
[15] Blair, M. F., 1994, ''An Experimental Study of Heat Transfer in a Large-Scale Turbine Rotor Passage,'' ASME J. Turbomach., **116**, pp. 1–13.
[16] Polanka, M. D., White, A. L., Meininger, M., Clark, J. P., and Praisner, T. S., 2002, ''Turbine Tip and Shroud Heat Transfer and Loading Part B: Experimental and Computational Comparisons Including Unsteady Effects,'' submitted to IGTI 2003.
[17] Joe, C. R., et al., 1998, ''High Pressure Turbine Vane Annular Cascade Heat Flux and Aerodynamic Measurements with Comparisons to Predictions,'' ASME Paper 98-GT-430.
[18] Haldeman, C. W., et al., 1992, ''The USAF Advanced Turbine Aerothermal Research Rig,'' AGARD Propulsion and Energetics Panel Conference Proc. 527, Antalya, Turkey.
[19] Dunn, M. G., Rae, W. J., and Holt, J. L., 1984, ''Measurement and Analyses of Heat Flux Data in a Turbine Stage: Part I—Description of Experimental Apparatus and Data Analysis,'' ASME J. Eng. Gas Turbines Power, **106**, pp. 229–233.
[20] Crawford, M. E., 1986, ''Simulation Codes for Calculation of Heat Transfer to Convectively-Cooled Turbine Blades,'' *Convective Heat Transfer and Film Cooling in Turbomachinery*, VKI Lecture Series 1986-06.
[21] Kline, S. J., and McClintock, F. A., 1953, ''Describing Uncertainties in Single Sample Experiments,'' Mech. Eng. (Am. Soc. Mech. Eng.), **75**, pp. 3–8.
[22] Moffat, R. J., 1982, ''Contributions to the Theory of a Single-Sample Uncertainty Analysis,'' ASME J. Fluids Eng., **107**, pp. 153–160.
[23] Zilles, D. A., and Abhari, Reza S., 1999, ''Influence of Non-Isothermal Button Gage Surface Temperature in Heat Flux Measurement Applications,'' Proc. IMECE 99, Nashville, TN.
[24] Kays, W. M., and Crawford, M. E., 1980, *Convective Heat and Mass Transfer*, McGraw-Hill, New York, NY.
[25] Hermanson, K., and Thole, K. A., 2000, ''Effect of Inlet Profiles on Endwall Secondary Flows,'' J. Propul. Power, **16**(2), pp. 286–296.

Predictions of External Heat Transfer for Turbine Vanes and Blades With Secondary Flowfields

K. Hermanson

S. Kern

G. Picker

S. Parneix

Alstom Power (Switzerland),
CH-5401 Baden, Switzerland

Detailed heat transfer distributions on the endwall and along the vane/blade surface are essential for component mechanical integrity and life predictions. Due to secondary flows, high gradients in heat transfer are present at the endwall and at the vane or blade surface itself where the passage vortex influences the mainstream flow. This paper documents the benchmarking of three turbulence models: 1) k-ε realizable with wall functions, 2) k-ε realizable with two layer model, and 3) the V2F model for endwall and surface heat transfer and flowfield predictions. Benchmark experimental data from a scaled-up low speed rig for both a stator and rotor geometry are used for comparisons of heat transfer and flowfield. While the k-ε realizable turbulence models give a good prediction of the secondary flow pattern, the heat transfer at the endwall and at the surface is not well predicted due to the inadequate modeling of near wall turbulence. The V2F model gives better agreement with the experiments on the endwall and vane midspan heat transfer is also well predicted, although transition occurs too far upstream on the suction surface. The results from this study represent the feasibility of CFD utilization as a predictive tool for local heat transfer distributions on a vane/blade endwall. [DOI: 10.1115/1.1529201]

Introduction

For meeting demands of increased power output and efficiency in modern gas turbine engines, accurate predictions of heat transfer on critical components are essential. The vane or blade platform is a particular region with high local gradients in heat load primarily due to the horseshoe and passage vorticies. The understanding of secondary flows and consequent heat transfer patterns for detailed predictions allows an improved design of critical components.

Secondary flows not only affect the leading edge and endwall region, but also a substantial portion of the span of the airfoil, most notably on the suction surface due to the interaction of the passage, horseshoe and corner vortices. Several flow models exist which describe this interaction based on measurements and flow visualization; for example, Langston [1], Sharma and Butler [2], Goldstien et al. [3].

Kang and Thole [4] demonstrated the secondary flow development through a stator vane passage with LDV measurements and presented the measured heat transfer on the endwall showing large gradients due to the secondary flowfield, Kang et al. [5]. In addition, Radomsky and Thole [6] measured the heat transfer at the midspan of the same vane geometry at both low and high freestream turbulence levels. Cho et al. [7] presented mass transfer measurements in a low-speed rig for a blade geometry with large secondary flows. These independent experimental data sets will be referenced in this paper.

Utilization of computational fluid dynamics (CFD) could provide detailed predictions of heat transfer on both endwalls and airfoils for a range of inlet parameters, or airfoil configurations. Hermanson and Thole [8] benchmarked several turbulence models using a commercial CFD code and reported secondary flowfields. The RNG k-ε model gave good agreement to the secondary flow development, however, no accompanying heat transfer results were presented. Giel et al. [9] reported combined experimental and numerical results from a transonic cascade. A 3-D Navier Stokes code with a 2-layer algebraic turbulence model (Chima et al. [10]) provided heat transfer results which varied in prediction accuracy depending on the region of the airfoil surface and turbulence intensity simulated. Langston [11] recently provided a review of research in secondary flow outlining the progress made in the last 25 years. A detailed review of research prior to that period is published in Sieverding [12].

The goal of this study is to evaluate the predictive capabilities of CFD for flowfield and heat transfer on turbine airfoils and endwalls. The computational methodology and an evaluation of the results will be presented focusing on the feasibility of utilizing CFD in design.

Modeling Description

Before utilizing CFD to predict airfoil/endwall heat transfer on different geometries or with varying inlet conditions, several turbulence models were benchmarked against data from a low-speed, scaled-up stator vane rig at low turbulence (0.6%) (Kang and Thole [4]). For all computations, the hybrid meshing program Centaur [13] and the commercial package Fluent 5.4 [14] were used with a module for the V2F turbulence model from Cascade Inc. [15]

Three turbulence models were considered in this study:

- realizable k-ε model with wall functions (Launder and Spaulding [16])
- realizable k-ε, (RKE), model with the 2-layer near-wall approach (Shih, et al., [17])
- V2F model (Durbin [18], Durbin et al. [19], Parneix et al. [20], Durbin et al. [21]).

A detailed description of the wall function versus the 2-layer approach, as well as the V2F turbulence model considered in this study, can be found in Hermanson et al. [22]. The work applies to internal cooling of gas turbines. Numerically, the incompressible formulation within Fluent [14], with the segregated solver and constant air-properties, was utilized. Convergence was assumed to be reached when all normalized residuals were smaller than 10^{-4}, except energy smaller than $5 \cdot 10^{-7}$. The heat transfer coefficient on the endwall was also monitored to ensure convergence whereby there was less than 0.5% change over $N-500$ iterations in the average value, where N is the number of iterations to

Contributed by the International Gas Turbine Institute and presented at the International Gas Turbine and Aeroengine Congress and Exhibition, Amsterdam, The Netherlands, June 3–6, 2002. Manuscript received by the IGTI November 5, 2001. Paper No. 2002-GT-30206. Review Chair: E. Benvenuti.

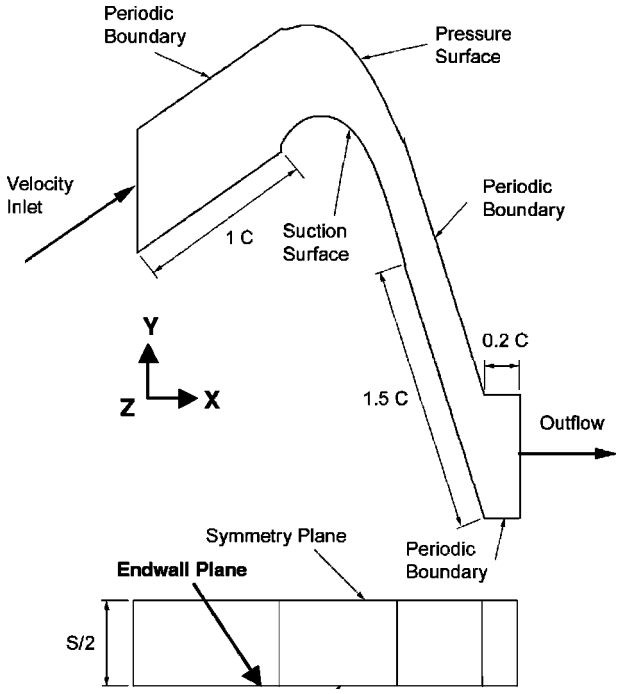

Fig. 1 Computational domain for rotor blade benchmarking

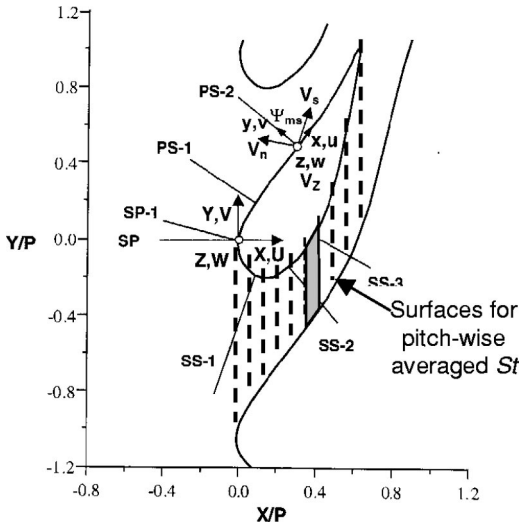

Fig. 2 Stator vane geometry with analysis planes

convergence, and less than 3% change over the final $N/2$ iterations. Second order discretization was used on all equations. As an essential part of the benchmarking, grid independence was addressed.

Computational domains were constructed similarly to those reported in Hermanson and Thole [8]. Periodicity and symmetry boundary conditions were utilized to minimize the required number of computational cells, and inlet/outlet boundary conditions are placed far enough upstream/downstream so as not to affect the flowfield in the passage between two airfoils. The outflow boundary condition is placed $0.2C$ along the X direction in Fig. 1 to avoid highly skewed cells at the outflow plane resulting from the small angle to the suction side periodic boundary. The boundary layer code TEXSTAN, Crawford [23], was used to generate a turbulent inlet boundary layer profile for velocity (U_{inlet}), k, and ε at low turbulence. This profile matches the experimental boundary layer thickness, freestream inlet Reynolds number and turbulence intensity. To match experimental conditions, the vane geometry was simulated with a constant wall heat flux and the blade geometry with a constant wall temperature.

Reference Geometry and Analysis. The characteristics of both airfoils and the corresponding inlet conditions are summarized in Table 1. Both reference experiments are performed in linear, low-speed scaled-up, cascades.

Table 1 Inlet conditions and airfoil descriptions for both benchmark cases

	Quantity	Vane geometry	Blade geometry
Airfoil	C (m)	0.594	0.16
	C/S	1.08	0.82
	C/P	1.3	1.43
	θ	72 deg	136 deg
Inlet	δ/S ($X/C=1$)	0.091	0.1
	Ma_{inlet}	0.012	0.02
	U_{inlet} (m/s)	5.85	8
	Re_{ex}	1.06×10^6	2.1×10^5
	Tu (%)	0.6	0.7

The planes used for flowfield benchmarking of the stator vane geometry are shown in Fig. 2. Note that the vane trailing edge is located at $X/P=0.63$ or $X/C=0.485$. This figure also defines areas used for pitchwise averaging of heat transfer through the passage. The results are presented in Fig. 3(a).

Grid Independence. The results for the stator were checked for grid independence for all turbulence models. A measurement plane was selected which is parallel to the inlet flow direction and

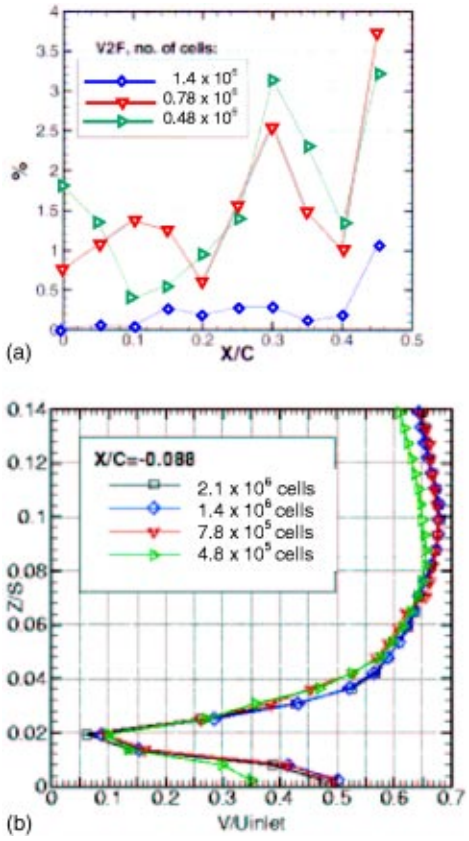

Fig. 3 (a) Pitchwise averaged Stanton number presented as % difference from baseline grid (2.1×10^6 cells); (b) normalized velocity magnitude in plane SP on a spanwise line at $X/C=-0.088$

intersects the vane stagnation, plane SP in Fig. 2. This plane intersects the leading edge horseshoe vortex and the developing passage vortex. For this plane, spanwise lineplots characterized by large velocity gradients were extracted. The second measure was a comparison of the pitchwise-averaged Stanton numbers on the endwall. Results are presented as % difference from a very fine grid, which is considered to be finer than the resolution required for resolving the endwall secondary flows. Results for the grid independence study with of the V2F model are shown in Figs. 3(*a*)–(*b*) where a common number of data points regardless of mesh size is plotted for evaluation purposes.

Figure 3(*b*) shows that the smallest mesh size of 480,000 cells shows diffusion in the velocity profile compared with the larger meshes very near the wall. The next largest mesh of 780,000 cells shows good agreement with the finer meshes in the resolution of velocity gradients. The deviation of pitchwise-averaged Stanton numbers is also under 3% for most of the passage, therefore, this mesh is considered to be grid independent. Note that the first prismatic layer was chosen to achieve average y^+ levels of approximately 1 with a maximum value on the passage endwall and airfoil of 2.5. The grids represented in Fig. 3 were generated by varying meshing parameters such as surface mesh stretching ratio, maximum tetrahedral length scale, and number of prism layers.

A similar judgment of grid independence was carried out for the other turbulence models, however for the Stanton number predictions on the endwall with wall functions the heat transfer levels can be sensitive to the value of y^+ on the wall. Therefore, grid independence was limited to judgment based on resolution of velocity gradients. After completing the grid independence study on one geometry meshing standards for quality and resolution could be set for other geometries.

CFD Benchmarking—Stator Geometry

Benchmarking of the turbulence models considered was focused on the stator vane geometry. Hermanson and Thole [8] focused on benchmarking of flowfield for the stator vane geometry and already showed that the standard k-ε model is not capable of correctly predicting the leading edge horseshoe vortex roll-up, and is consequently unable to simulate the development of the passage vortex. In the present study, the benchmarking is also evaluated on the basis of heat transfer predictions on the endwall, both locally and pitchwise-averaged. Results for flowfield, endwall heat transfer, and airfoil heat transfer are presented and discussed.

Flowfield. Before evaluating the heat transfer results from each turbulence model, predictions were made of the flowfield and results were compared with experimental data. Accurate predictions of the flowfield associated with the horseshoe vortex and passage vortex is essential for accurate prediction of local heat transfer results. Predictions on a plane intersecting the vane stagnation, plane SP, show the prediction of the horseshoe vortex roll-up at the leading edge in Figs. 4(*a*)–(*d*).

The RKE model with wall functions does predict the roll-up of the vortex, however with a weaker intensity, and the center of the vortex is located approximately $X/C=0.033$ closer to the vane stagnation than in the experiments. The RKE two-layer and V2F models show better agreement with the experimental measurements. The V2F model predicts the vortex center slightly further from the vane stagnation than the realizable k-ε 2-layer model. This difference may be attributed to near wall modeling where the V2F model can predict the anisotropy of turbulence at the wall that could result in a stronger vortex roll-up.

Detailed comparisons were made on all seven measurement planes located perpendicular to the vane on both the pressure and suction surfaces (Fig. 2). Further downstream, in the vane passage all models predict the secondary flow pattern as documented in Kang and Thole [4], but the k-ε realizable with wall functions gives an underprediction in secondary velocities. The secondary flow vectors yielded very similar results for both turbulence models with resolution to the wall. For a more quantitative comparison of the flowfield, pitch angles, ϕ, are plotted in Fig. 5 on plane PS-2 [24].

This quantity gives a measure of the spanwise velocity component prediction. Plane PS-2 shows the passage vortex; the reader is referred to Kang and Thole [4] for the flowfield vector plot. Both models show an underprediction in the peak flow turning toward the wall ($\phi<0$) near the pressure surface which is reflected in local underprediction of heat transfer in the upcoming section. The line of zero spanwise component ($\phi=0$) intersects the endwall further from the pressure surface. The V2F model shows a better prediction of the movement of the passage vortex away from the endwall ($\phi>0$) at $y/P>0.15$. These near-wall differences in the velocity influence the qualitative and quantitative heat transfer predictions.

Heat Transfer—Endwall. Since the major focus of this study is to evaluate the feasibility of CFD as a predictive tool of local heat transfer on endwalls and airfoils, this quantity was the most important in the benchmarking of turbulence models.

Before presentation of the complex, detailed heat transfer pattern on the endwall, the heat transfer results averaged across the pitch from pressure to suction side in strips along the axial chordwise direction (see Fig. 2) are presented (Fig. 6). These results give a first understanding of the quantitative values of the endwall predictions relative to the measurements.

It is clear that the V2F model provides the best agreement throughout the passage with the experimental results. Note that the experimental setup uses a flexible wall around a central measurement vane which may influence results at the downstream portion of the passage ($X/C>0.4$) providing an explanation for the deviation in this region. The results from the RKE models both give a similar prediction of heat transfer in the passage, with an overprediction of the rate of increase of heat transfer in the passage from $0<X/C<0.3$. A similar trend for the k-ε RNG and Reynolds stress models computed on unstructured meshes was shown by Hermanson [25].

Although the flowfield was predicted well by the 2-layer, RKE model, the heat transfer results are still on the same level as those with wall functions. This is a clear demonstration that for accurate heat transfer predictions, the key factor is not only resolution of the flow down to the wall, but also the scaling of turbulence near the wall. Since the V2F model employs scaling of turbulence by the square of the normal fluctuating velocity component it can be expected to provide better heat transfer predictions.

Local distributions of heat transfer are shown in Fig. 6 only for the RKE 2-layer and V2F models in comparison with experimental measurements. Since RKE 2-layer and RKE wall function results are similar, (shown in Fig. 6) the RKE wall function results have been omitted from Fig. 7.

In Fig. 7, a good qualitative agreement between both models and the measurements can be seen. Again, note that the experiments show good repeatability between the two vane passages; however, the levels far downstream in the passage may be influenced by the flexible wall. The reason for overprediction by the RKE 2-layer model of pitchwise-averaged heat transfer can be seen more clearly on the local distribution. There is an overprediction of Stanton number on the endwall near the suction surface where there is a large acceleration of fluid and where the suction-side horseshoe vortex travels around the airfoil. Also, further down stream there is a general overprediction of heat transfer along the pressure surface, extending into the midpassage. Both CFD results show a more defined heat transfer pattern than seen in the experimental contours on the endwall. The underprediction of the heat transfer near the pressure surface in Fig. 7(*b*) (PS-2 location) corresponds with the flowfield shown in Fig. 5.

Heat Transfer—Airfoil. In order to achieve heat transfer predictions on the endwall, the flow must be modeled to the midspan

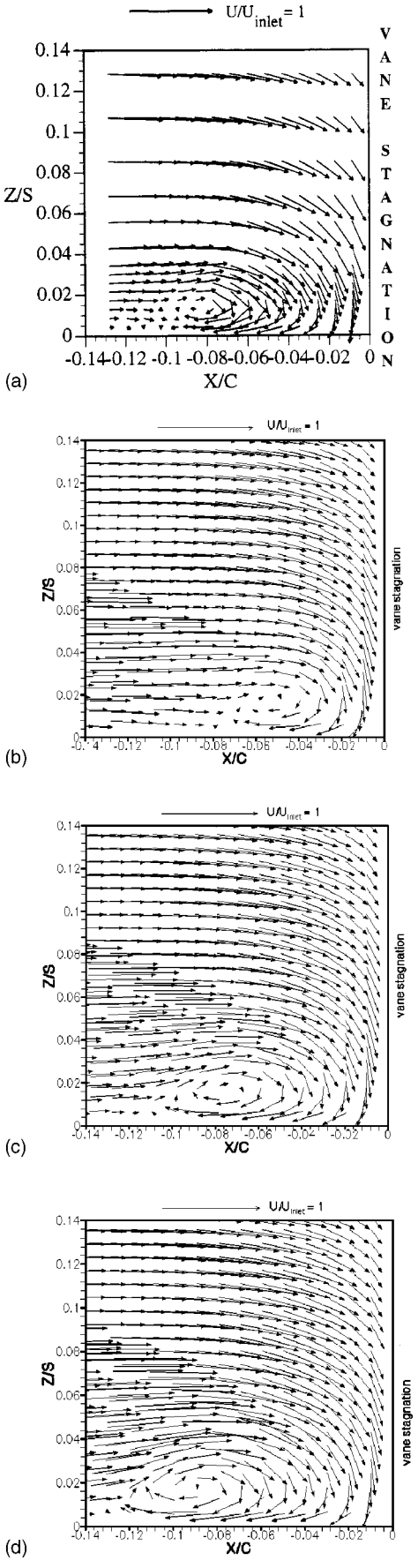

Fig. 4 Leading edge horseshoe vortex roll-up in plane SP—(*a*) measurements [4], (*b*) realizable k-ε with wall functions, (*c*) realizable k-ε two-layer model, (*d*) V2F model

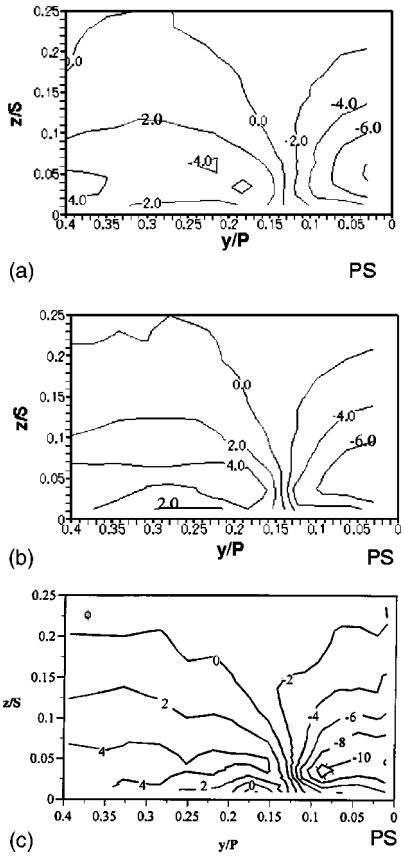

Fig. 5 Pitch angles, ϕ, on plane PS-2—(*a*) realizable k-ε two-layer model, (*b*) V2F model, (*c*) measurements [24]

for a 2-D airfoil geometry. This means that, with appropriate mesh resolution, heat transfer can also be evaluated in the freestream, at midspan, as well as near the endwall/airfoil junction. Flow visualization and measurements have shown that the complex interaction of the passage, suctionside horseshoe vortex, and corner vorticies have the potential to create high gradients in heat transfer on the suction side of the endwall/airfoil junction (Graziani et al. [26], Giel et al. [9]).

First, Fig. 8 presents the predictions of heat transfer at the midspan for the RKE and V2F models in comparison with experimental measurements (Radomsky and Thole [6]). The V2F model again shows good agreement with the experiment, with transition occurring too far upstream on the suction side. Most important is that the levels of Stanton number before and after transition are correctly predicted, as with engine components, roughness or film

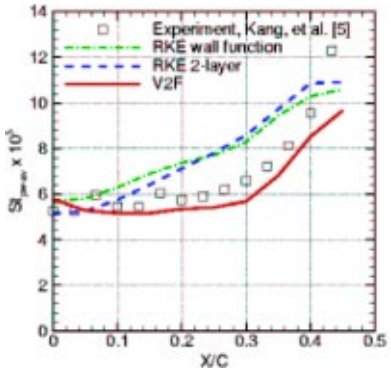

Fig. 6 Pitchwise-averaged Stanton numbers

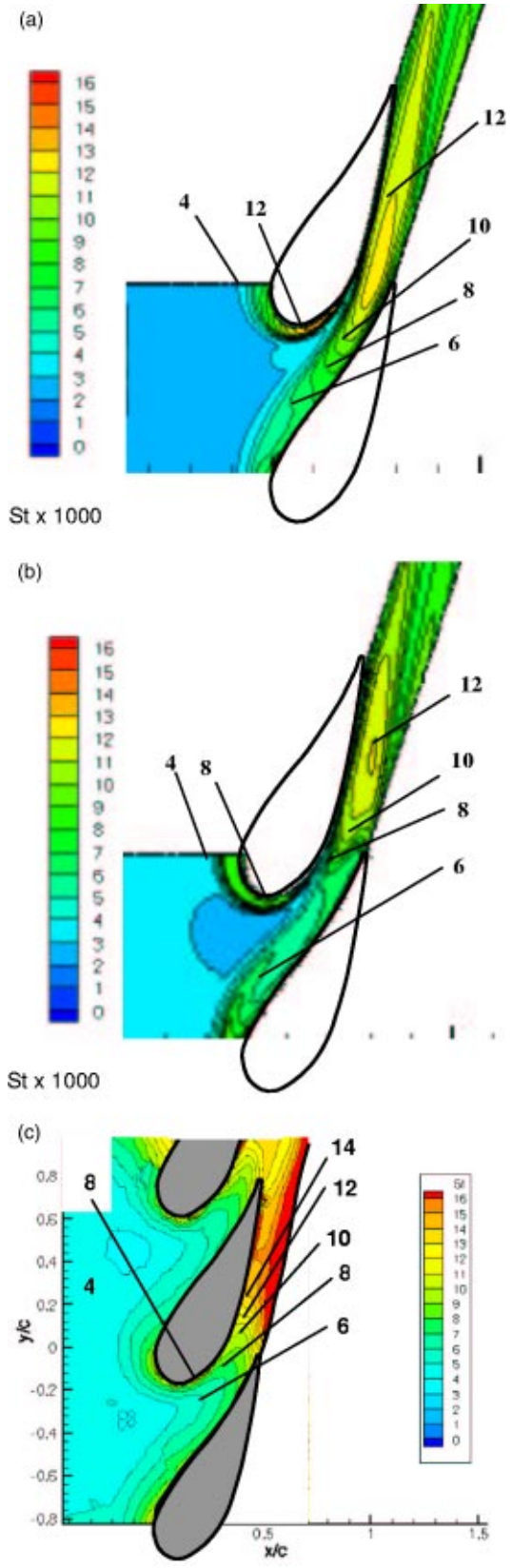

Fig. 7 Contours of Stanton number on the endwall—(*a*) RKE 2-layer, (*b*) V2F, (*c*) experimental measurements [5]

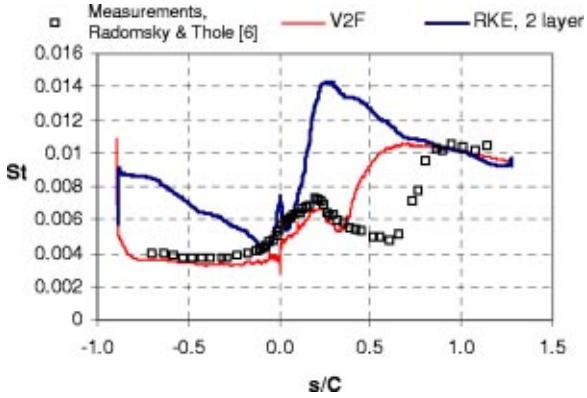

Fig. 8 Heat transfer at midspan

cooling are likely to affect the onset of transition. The RKE 2-layer model clearly demonstrates a large mismatch in Stanton number, most notably at the suction side shoulder where the k-ε models are known to have an overproduction of turbulent kinetic energy. This trend was demonstrated by Walters and Leylek [27]. Although the RKE model had less turbulence production than the standard or RNG k-ε models, it still showed a larger production relative to the Reynolds stress model results reported.

After presenting good agreement of the V2F model with experiment on the endwall and at the midpsan it is rational to present the heat transfer on the entire span of the suction surface where the flow is highly three-dimensional and boundary layer codes fail. Figure 9 shows the detailed Stanton number pattern on the suction surface.

Even for this geometry which has a relatively low turning angle compared to blade geometries, a large influence of secondary flows over up to about 15% of span, has been demonstrated. These results are consistent with the previous studies.

Rotor Blade Geometry

Upon completion of the benchmarking and evaluation of the successful predictions of heat transfer by the V2F model, the model was tested on a typical rotor blade geometry. This geometry, measured by Cho et al. [7] has a larger flow turning angle and the potential to create larger secondary flowfields and increased heat transfer gradients on both the endwall and airfoil surfaces. For this purpose, the calculated secondary flowfield will be presented along with heat transfer results on the endwall and along airfoil span.

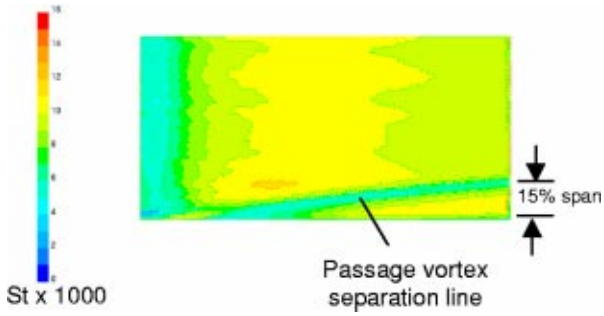

Fig. 9 Contours of heat transfer on the suction surface of the vane

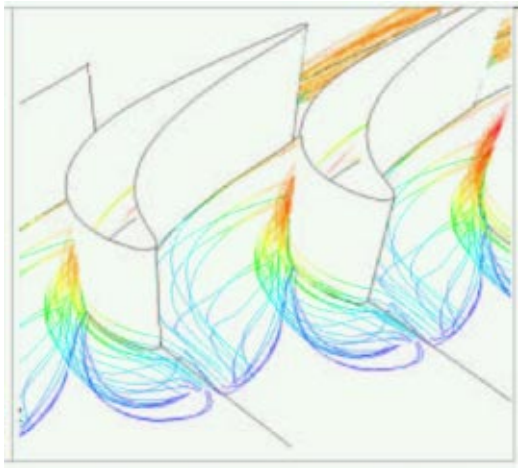

Fig. 10 Secondary flow in blade geometry

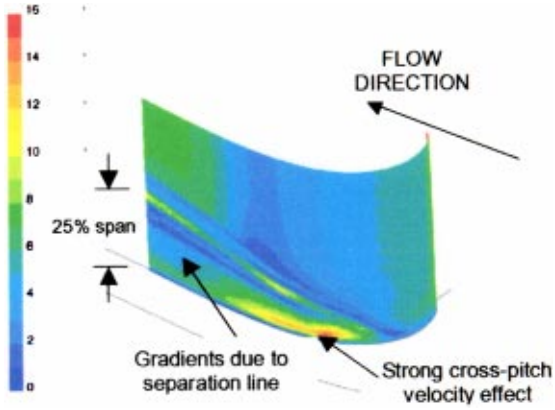

Fig. 12 Heat transfer along the span of the suction side of the airfoil

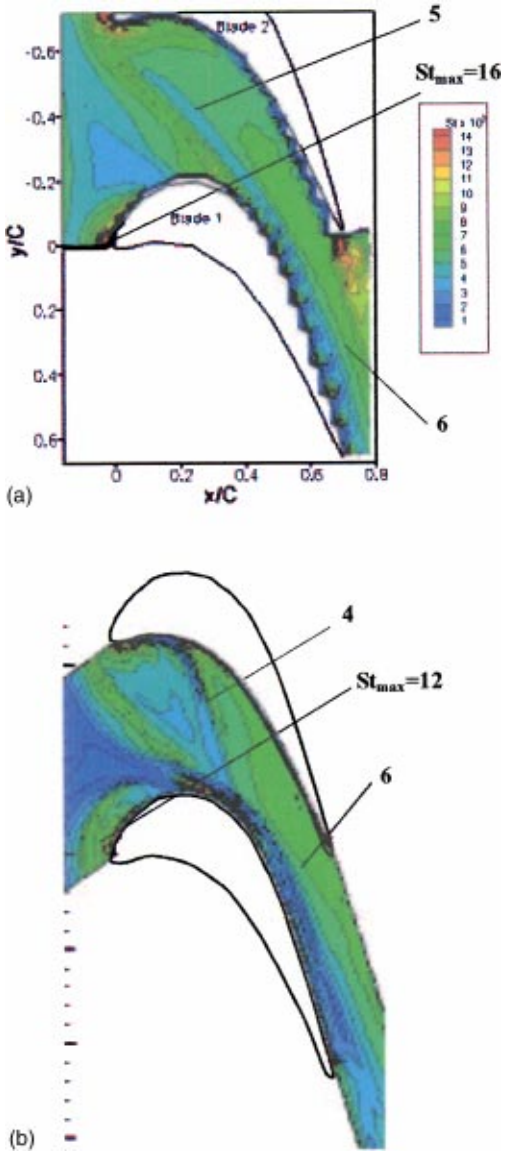

Fig. 11 Contours of Stanton number on the endwall for the rotor blade geometry—(*a*) experiment [7], (*b*) V2F model

Figure 10 presents pathlines released upstream of the blade stagnation region which reveal the complex and large secondary flows that occur for this geometry. Compared to a similar plot presented in Hermanson and Thole [8], the secondary flow is significantly stronger than in the stator vane flowfield. There is apparent stronger cross flow from the pressure to the suction side near the endwall and the suction side horseshoe vortex structure occupies a greater portion of the passage.

The heat transfer pattern corresponding to the large secondary flows is shown experimentally and numerically in Figs. 11(*a*)–(*b*). Quantitatively, the values are slightly underpredicted, most notably at the leading edge stagnation region and downstream of the trailing edge. It should be noted that these experiments were performed using the mass transfer measurement technique. Besides the experimental uncertainty of the measurements, there is additional uncertainty associated with conversion to Stanton number values. The simulation shows a distinct low heat transfer path moving across the passage that can likely be associated with the separation line of the passage vortex. Qualitatively, the augmentation of heat transfer at the leading edge and across the upstream region of the passage from pressure to suction side due to secondary flows is in good agreement.

Although there was no mass transfer recorded on the surface of the airfoil, values were computed and are plotted on Fig. 12 along the suction surface similar to those presented in Fig. 9, in order to assess the effects of secondary flow. Prediction of such high gradient heat loads could contribute to an improvement in durability of components. Note that the blade is shown from endwall to midspan.

The high heat transfer along the suction side shoulder is a result of the large amount of flow crossing the passage and impinging upon the airfoil surface. This 3-D nature of the passage flow cannot be captured with boundary layer codes. Compared to the stator case, the low heat transfer associated with separation of the passage vortex penetrates at least 25% more of the span. This is attributed to the large difference in airfoil geometry and aspect ratio. Notice that there appears to be two lines of low heat transfer associated with this large secondary flowfield. The line nearest the midspan could be associated with the lift-off of the suction side horseshoe vortex, as suggested in the flow model by Goldstein and Spores [3].

Conclusions and Recommendations

Benchmarking of CFD predictions to flowfield and heat transfer measurements in a stator vane geometry at low turbulence showed good agreement in flowfield and heat transfer for the V2F turbulence model on the endwall as well as at the airfoil midspan.

Although the RKE 2-layer model was capable of predicting the flow pattern, the heat transfer was overpredicted due to near wall scaling of turbulence.

Although further benchmarking of heat transfer with experiments along the airfoil span should be documented, preliminary results reveal high gradients in heat transfer dependent on the strength of the secondary flows. Further benchmarking at higher turbulence levels representing typical combustor exit values should be investigated.

The results from this study represent the feasibility for CFD to be utilized as a predictive tool for local heat transfer distributions on a vane/blade endwall. Such a tool also provides heat transfer data on the vane surface and, most importantly, provides heat transfer distributions at the endwall/surface junction which are not achievable using a boundary layer code. Such heat transfer distributions are significant to component design.

Acknowledgments

Prof. K. Thole and Prof. H. H. Cho are gratefully acknowledged for providing the experimental benchmark data documented in this paper.

Nomenclature

C = true chord
k = turbulent kinetic energy
Ma = Mach no.
p = static pressure
P = vane/blade pitch
Re = Reynolds no., $\rho UC/\mu$
s = surface distance along airfoil
S = span
St = Stanton no. normalized by inlet properties
Tu = turbulence level based on U_{inlet}
T_{wall} = temperature on the endwall
u,v,w = in-plane velocity components
U = inlet freestream velocity
$\mathbf{X},\mathbf{Y},\mathbf{Z}$ = global coordinate system
y^+ = normalized distance from wall
δ = 99 % boundary layer thickness
ε = turbulent dissipation
ϕ = flow pitch angle, $\tan-1(w/u)$
μ = fluid viscosity
ρ = density
θ = flow turning angle

Subscripts

av = average
ex = exit quantity
inlet = inlet quantity
pw = pitchwise

References

[1] Langston, L. S., 1980, ''Crossflows in a Turbine Cascade Passage,'' ASME J. Turbomach., **109**, pp. 186–193.
[2] Sharma, O. P., and Butler, T. L., 1987, ''Predictions of Endwall Losses and Secondary Flows in Axial Flow Turbine Cascades,'' ASME J. Turbomach., **109**, pp. 229–236.
[3] Goldstein, R. J., and Spores, R. A., 1988, ''Turbulent Transport on the Endwall in the Region Between Adjacent Turbine Blades,'' ASME J. Heat Transfer, **110**, pp. 862–869.
[4] Kang, M., and Thole, K. A., 2000, ''Flowfield Measurements in the Endwall Region of a Stator Vane,'' ASME J. Turbomach., **122**, pp. 458–466.
[5] Kang, M., Kohli, A., and Thole, K. A., 1999, ''Heat Tranfser and Flowfield Measurements in the Leading Edge Region of a Stator Vane Endwall,'' ASME J. Turbomach., **121**(3), pp. 558–568.
[6] Radomsky, R., and Thole, K. A., 2000, ''Highly Turbulent Flowfield Measurements Around a Stator Vane,'' ASME J. Turbomach., **122**, pp. 255–262.
[7] Cho, H. H., Rhee, D. H., and Choi, J. H., 2001, ''Heat/Mass Transfer Characteristics on Turbine Shroud With Blade Tip Clearance,'' Heat Transfer Gas Turbine Systems, Annals of the N.Y. Academy of Sciences, **934**, pp. 281–288.
[8] Hermanson, K., and Thole, K., 1999, ''Effect of Inlet Conditions on Endwall Secondary Flows,'' AIAA Power Turbomachinery, **16**(2), pp. 286–296.
[9] Giel, P. W., Van Fossen, G. J., Boyle, R. J., Thurman, D. R., and Civinskas, K. C., 1999, ''Blade Heat Transfer Measurements and Predictions in a Transonic Turbine Cascade,'' ASME Paper 99-GT-125 (NASA TM-209296).
[10] Chima, R. V., Giel, P. W., and Boyle, R. J., 1993, ''An Algebraic Turbulence Model for Three-Dimensional Viscous Flows,'' AIAA Pap., Paper No. 93-0083 (NASA TM-105931).
[11] Boyle, R. J., 2001, ''Secondary Flows in Axial Turbines—A Review,'' Heat Transfer in Gas Turbine Systems, Annals of the N.Y. Academy of Sciences, **932**, pp. 11–26.
[12] Sieverding, C. H., 1985, ''Recent Progress in the Understanding of Basic Aspects of Secondary Flows in Turbine Blade Passages,'' ASME J. Eng. Gas Turbines Power, **107**, pp. 248–257.
[13] Khawaja, A., Kallinderis, Y., Irmisch, S., Lloyd, J., Walker, D., and Benz, E., 1999, ''Adaptive Hybrid Grid Generation for Turbomachinery and Aerospace Applications,'' AIAA Paper, , Paper No. 99-0916.
[14] FLUENT User's Guide, Version 5.1. 1999. **I–IV**, Fluent Inc.
[15] Cascade Inc. 1999. www.turbulentflow.com.
[16] Launder, B. E., and Spaulding, D. B., 1974, ''The Numerical Computation of Turbulent Flows,'' Comput. Methods Appl. Mech. Eng., **3**, pp. 269–289.
[17] Shih, T. H., Liou, W. W., Shabbir, A., and Zhu, J., 1995, ''A New k-ε Eddy-Viscosity Model for High Reynolds Number Flows-Model Development and Validation,'' Comput. Fluids, **24**(3), pp. 227–238.
[18] Durbin, P. A., 1991, ''Near-Wall Turbulence Closure Modeling Without Damping Functions,'' Theor. Comput. Fluid Dyn., **3**, pp. 1–13.
[19] Durbin, P. A., 1993, ''Application of a Near-Wall Turbulence Model to Boundary Layers and Heat Transfer,'' Int. J. Heat Fluid Flow, **14**, pp. 316–323.
[20] Parneix, S., Durbin, P. A., and Behnia, M., 1998, ''Computation of 3-D Turbulent Boundary Layers Using the V2F Model,'' Flow, Turbul. Combust., **60**, pp. 19–46.
[21] Durbin, Kalitzin, and Iaccarino, 2001, http://www-fpc.stanford.edu/Durbin/Turbine.html.
[22] Hermanson, K., Parneix, S., Von Wolfersdorf, J., and Semmler, K., 2001, ''Prediction of Pressure Loss and Heat Transfer in Internal Blade Cooling Passages,'' Heat Transfer in Gas Turbine Systems, Annals of the N.Y. Academy of Sciences, **932**, pp. 448–455.
[23] Crawford, M. E., 1986, ''Simulation Codes for Calculation of Heat Transfer to Convectively-Cooled Turbine Blades,'' set of 4 lectures in Convective Heat Transfer and Film Cooling in Turbomachinery, ed., T. Arts, Lecture Series 1986-06, von Karman Institute for Fluid Dynamics, Rhode-Saint-Genese, Belgium.
[24] Kang, M., 1998, ''Detailed Measurements in the Endwall Region of a Gas Turbine Stator Vane,'' Master of Science thesis, University of Wisconsin-Madison.
[25] Hermanson, K., 1999, ''Effect of Inlet Conditions on Endwall Secondary Flows,'' Master of Science thesis, University of Wisconsin-Madison.
[26] Graziani, R. A., Blair, M. F., Taylor, J. R., and Mayle, R. E., 1980, ''An Experimental Study of Endwall and Airfoil Surface Heat Transfer in a Large Scale Turbine Blade Cascade,'' ASME J. Eng. Power, **102**, pp. 257–267.
[27] Walters, D. K., and Leylek, J. H., 2000, ''Impact of Film-Cooing Jets on Turbine Aerodyamic Losses,'' ASME J. Turbomach., **122**, pp. 537–545.

Aaron R. Byerley
Department of Aeronautics,
USAF Academy,
Colorado Springs, CO 80840

Oliver Störmer
Bundesamt fur Wehrtechnik und Beschaffung,
Manching, Germany

James W. Baughn
Mechanical and Aeronautical Engineering,
University of California,
Davis, CA

Terrence W. Simon
Department of Mechanical Engineering,
University of Minnesota,
Minneapolis, MN

Kenneth W. Van Treuren
Department of Engineering,
Baylor University,
Waco, TX

Jörg List
Bundesamt fur Wehrtechnik und Beschaffung,
Manching, Germany

Using Gurney Flaps to Control Laminar Separation on Linear Cascade Blades

This paper describes an experimental investigation of the use of Gurney flaps to control laminar separation on turbine blades in a linear cascade. Measurements were made at Reynolds numbers (based upon inlet velocity and axial chord) of 28×10^3, 65×10^3 and 167×10^3. The freestream turbulence intensity for all three cases was 0.8%. Laminar separation was present on the suction surface of the Langston blade shape for the two lower Reynolds numbers. In an effort to control the laminar separation, Gurney flaps were added to the pressure surface close to the trailing edge. The measurements indicate that the flaps turn and accelerate the flow in the blade passage toward the suction surface of the neighboring blade thereby eliminating the separation bubble. Five different sizes of Gurney flaps, ranging from 0.6 to 2.7% of axial chord, were tested. The laser thermal tuft technique was used to determine the influence of the Gurney flaps on the location and size of the separation bubble. Additionally, measurements of wall static pressure, profile loss, and blade-exit flow angle were made. The blade pressure distribution indicates that the lift generated by the blade is increased. As was expected, the Gurney flap also produced a larger wake. In practice, Gurney flaps might possibly be implemented in a semi-passive manner. They could be deployed for low Reynolds number operation and then retracted at high Reynolds numbers when separation is not present. This work is important because it describes a successful means for eliminating the separation bubble while characterizing both the potential performance improvement and the penalties associated with this semi-passive flow control technique. [DOI: 10.1115/1.1518701]

Introduction

This work describes the control of laminar separation on turbine cascade blades at low Reynolds number through the use of Gurney flaps. A Gurney flap is a mechanically simple device consisting of a short, flat plate attached to the pressure side of an airfoil near the trailing edge. Race car driver Dan Gurney used this type of flap to increase the ''down force'' and thus the traction generated by the inverted wings on his race cars. Numerous wind tunnel tests on Gurney flaps attached to airfoils have been performed [1–4]. These investigations have shown that the Gurney flap increases the effective camber of the airfoil. The result is a significant increase in lift with only a small increase in drag as long as the flap height scales with the local boundary layer thickness.

To the authors' knowledge, there have been only a few previous investigations of Gurney flaps in turbomachinery applications. Janus [5] performed a two-dimensional computational investigation of Gurney flaps on industrial fan blade designs. Fuglsang et al. [6] and Yen et al. [7] both investigated Gurney flaps for wind turbine blades. Yen's study used micro-electromechanical (MEM) translational tabs for active load control on utility-scale wind turbines. The situation in the present work is different from [5–7] in that blade-to-blade flow interaction is present and important in a cascade flow. The Gurney flap was selected for evaluation because of its simplicity and its demonstrated ability to enhance lift and control separation on airfoils. Furthermore, it might be possible to build on Yen's concept by deploying the Gurney flaps during low Reynolds number operation and retracting or stowing them during high Reynolds number operation. Possible control mechanisms might be based upon MEMs, as in Yen's work, or by other means such as positive displacement (using internal blade channel pressure) or through shape-memory-alloys.

Low Reynolds number performance is of interest because of unexpected aerodynamic losses that have occurred in gas turbine engines during high-altitude (low-density) flight conditions. These losses have caused fuel consumption to be 1% greater than predicted and have been attributed to flow separation on the blade suction surfaces, particularly in the low pressure-turbine as noted by Rivir [8]. Previous investigations of low Reynolds number aerodynamic behavior have included Van Treuren et al. [9], who demonstrated in the present facility that counterrotating vortex generators placed upstream of the separation zone were effective at controlling separation down to inlet Reynolds numbers of 22×10^3. Lake et al. [10] evaluated the effectiveness of both v-grooves and dimples to control boundary layer separation on the Pak-B turbine blade. He demonstrated that dimples were effective across a wide range of Reynolds numbers and freestream turbulence intensities because they generated streamwise vorticity. While Van Treuren and Lake both examined passive control techniques that involved modifying the surface upstream of the separation point, Murawski and Vafai [11] investigated the effect of adding tail extensions. They demonstrated that the addition of tail extensions delayed the onset of boundary layer separation on the suction surface of the neighboring blade by decreasing the region of uncovered diffusion.

The purpose of the present work was to determine the effect of Gurney flaps for three Reynolds number conditions. Separation was expected at the two lower Reynolds numbers of 28×10^3 and 65×10^3. Fully attached flow was expected at 167×10^3. The freestream turbulence was held constant at 0.8% during these experiments.

Experimental Apparatus

The test facility at the United States Air Force Academy (USAFA) is a closed loop wind tunnel facility specifically designed

Contributed by the International Gas Turbine Institute and presented at the International Gas Turbine and Aeroengine Congress and Exhibition, Amsterdam, The Netherlands, June 3–6, 2002. Manuscript received by the IGTI, January 29, 2002. Paper No. 2002-GT-30662. Review Chair: E. Benvenuti.

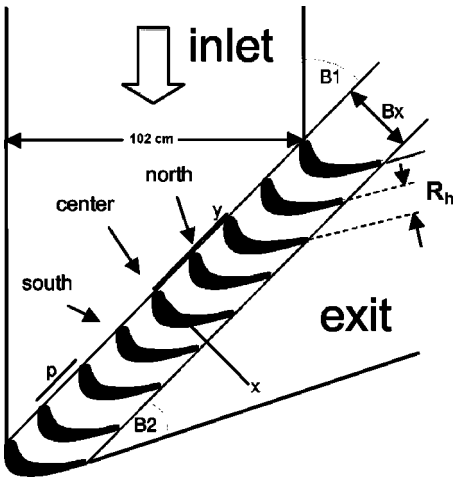

Fig. 1 Cascade geometry

for use as a linear cascade. It was previously described in [12–14]. The tunnel is capable of velocities from 3 m/s up to approximately 75 m/s, and is adjusted by moving variable pitch fan blades on a 200-hp electric motor. Speed control is also available by a variable frequency drive which allows a variation in blade rpm. The tunnel operates near ambient pressure and temperature (typically 78 kPa and 20–22°C). The tunnel air temperature can be controlled by adjusting the water flow rate through a fin-and-tube heat exchanger. The geometry of the linear cascade test section is shown in Fig. 1 with the corresponding parameters given in Table 1. The *x*-axis is defined in the axial direction and cascade angles are defined relative to the *y*-axis. The USAFA tunnel was modified to accept seven blades (nine including sidewalls) with a high aspect ratio of 3.97 which achieves uniform two-dimensional flow over the test portion of the blades. The Langston turbine blade geometry is that of a heavily loaded machine with a design flow coefficient of 0.78, stage loading coefficient of 2.8, and 34% static pressure reaction [15,16]. The turbine blade has an inlet mean camber line angle of 44 deg and an exit mean camber line of 26 deg. The air inlet angle is 46 deg. The hydraulic radius of the blade row exit passage is 71.5 mm.

Locations on the turbine blade were measured relative to a geometric zero, which is determined by placing a straight edge across the concave portion of the turbine blade. The tangent point near the leading edge is used as the reference point ($s=0$). Note, this location is not the stagnation point, although, this reference location is easier to duplicate and is consistent with [15,16]. The tunnel freestream turbulence was measured with a hot-film anemometer and found to be 0.8%.

Table 1 Cascade Parameters

Operation	Closed Loop
Axial Chord (B_x)	171 mm
Blade Pitch (p)	163 mm
Pitch/Axial Chord	0.95
Span/Axial Chord	3.86
Inlet Camber Angle	44°
Exit Camber Angle	26°
Air Inlet Angle (B_1)	46°
Air Exit Angle (B_2)	26°
Hydraulic radius of blade row exit (R_h)	71.5 mm

Fig. 2 Gurney flap detail

The center blade was made from polystyrene and coated with Mylar™, flat-black paint, and thermochromic liquid crystal (Hallcrest™ R23C5W) to support the laser thermal tuft, an optical surface flow diagnostic described in the forthcoming. The blades labeled ''north'' and ''south'' in Fig. 1 have 41 static pressure ports each. Wall static pressure and profile loss (wake) measurements were made and presented for both of these blades as a check for cascade periodicity.

The Gurney flaps themselves were made from stainless steel tubing of circular cross section and placed 10 mm upstream of the blade trailing edge as shown in Fig. 2. Flaps made from flat strips were used first but they lacked the required mechanical stiffness. The flaps were placed on all seven blades in the cascade test section to ensure flow passage periodicity. Cellophane tape was applied to the length of each flap (in the spanwise direction) to form a right-angle between the Gurney flap edge and the blade surface.

Experimental Methods and Data Reduction

Four different types of measurements were made to investigate the effect of Gurney flaps on the cascade flow. Laser thermal tufts were used on the center blade for detecting surface flow direction. Wall static pressure and profile loss were measured on both the ''north'' and the ''south'' blades. The blade row exit flow angle was measured in the two passages on either side of the center blade. The experimental methodology for these measurements is described below.

Laser Thermal Tuft Measurements. The laser tuft technique was first described in [12] and later in [14] and Rivir et al. [17]. The laser tuft works by heating a small (3 mm) spot on an insulated test surface with an IR laser. The heated laser spot shows up on the video image as a round dot because the reflected infrared radiation saturates the red color in a RGB camera. The test surface was coated with a thermochromic liquid crystal that changes color over a range 23–28°C. Energy is advected away from the laser spot in the direction of the surface flow. This produces a ''comet tail'' created by the liquid crystal color change as shown in Fig. 3. In a region of reverse flow, the ''comet tail'' will point toward the blade leading edge (to the left in the present work). At the point where the boundary layer separates, the laser tuft is circular and

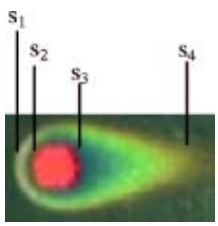

Fig. 3 Laser thermal tuft for attached flow (downstream is to the right)

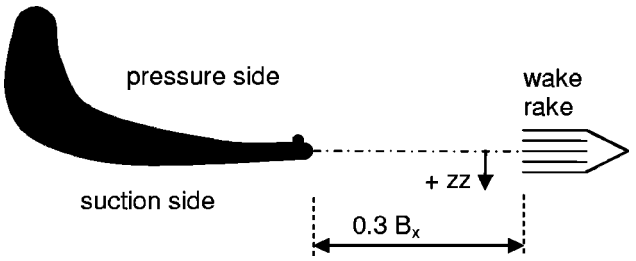

Fig. 4 Profile loss measurement details

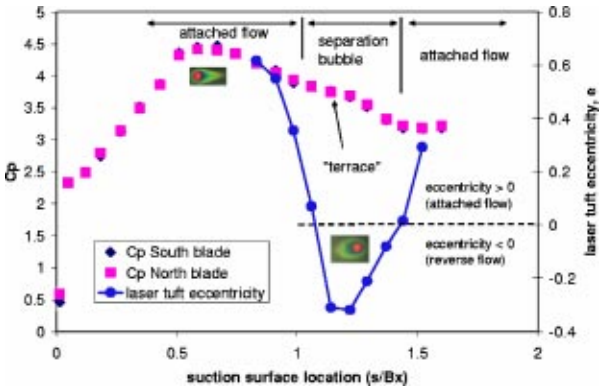

Fig. 5 Evidence of boundary layer separation at Re=28×10³ without Gurney flaps. Pressure coefficient and laser thermal tuft eccentricity distributions.

centered about the laser spot. To quantify the strength of this directional feature, a laser tuft eccentricity factor was defined by Eq. (1)

$$e = \frac{(s_4 - s_3) - (s_2 - s_1)}{(s_4 - s_1)} \tag{1}$$

Positive values of eccentricity indicate attached flow moving toward the blade trailing edge. Negative values of eccentricity indicate reverse flow that is typically found within a separation bubble. Values of zero indicate either the point of separation or of reattachment. The color images were videotaped, digitized, enlarged, and printed. The length values in Eq. (1) were measured with a ruler. The overall uncertainty in the eccentricity factor was less than ± 0.04 for all cases.

Wall Static Pressure Measurements. Wall static pressure measurements were made with MKS Baratron™ differential pressure transducers with full scale pressure ranges matched carefully to the expected pressure values. A Scanivalve™ pressure switching arrangement was used so that a single transducer could be used in taking the readings. All surface static pressure measurements were made relative to the upstream total pressure and nondimensionalized according to Eq. (2). Values were plotted against wetted surface distance in the streamwise direction for ease of comparison with flat-plate results.

$$Cp(s/B_x) = \frac{(P_{T\text{inlet}} - P(s/B_x))}{(P_{T\text{inlet}} - P_{\text{inlet}})} = \left(\frac{V(s/B_x)}{V_{\text{inlet}}}\right)^2 \tag{2}$$

For the low subsonic flows (Mach<0.07) tested in the present work, the value of *Cp* relates the local freestream velocity to the inlet velocity as shown in Eq. (2). The overall uncertainty in *Cp* was less than ± 0.18 for all cases.

Profile Loss Measurements. The profile loss associated with the boundary layer growth over the blade profile was measured with a 31-element pressure rake positioned at a location 54 mm ($0.3\ B_x$) downstream of the ''north'' and the ''south'' blade trailing edges as shown in Fig. 4. The loss is presented in terms of the loss coefficient given by Eq. (3) as defined by Horlock [18].

$$\gamma(zz) = \frac{(P_{T\text{inlet}} - P_T(zz))}{\frac{1}{2}\rho V_{\text{exit}}^2} \tag{3}$$

The exit velocity used in (3) was determined from the *Cp* measurement taken at the last pressure port on the suction surface near the trailing edge and then corrected for the trailing edge thickness. For the plane-blade case, this yielded an exit-to-inlet velocity ratio of 1.64 which, as expected, is equal to the ratio of the inlet-to-exit flow area. Finally, the effects of the Gurney flaps were also expressed in terms of the overall integrated loss coefficient given by Eq. (4).

$$\overline{\gamma} = \int_{-0.5}^{+0.5} \gamma(zz/R_h)\, d(zz/R_h) \tag{4}$$

The overall uncertainty in profile loss was less than ± 0.04 for all cases.

Exit Angle Measurements. Exit angle measurements were made using a yaw meter constructed from circular tubing (O.D. 18 mm) with static pressure ports placed at ± 45 deg relative to the stagnation point as described by Benedict [19]. The yaw meter was placed in the inviscid flow region in the center of the flow passage 300 mm ($1.75\ B_x$) downstream of the blade row exit. Differential pressure measurements were made at 1.0 degree increments across a range of -3 to $+3$ deg on either side of the trailing edge camber line. For this type of yaw meter, the relationship between the pressure differences of the static ports and the flow angle is linear. The exit angle was found by taking the x-intercept of the resultant plot. The yaw meter was calibrated by placing it upstream of the test section and aligning it with the tunnel centerline. The overall uncertainty was estimated to be less than ± 0.7 deg for all cases.

Uncertainty Analysis. Estimates of experimental uncertainty for all four types of measurements were made using the methodology outlined by Coleman and Steel [20]. The overall uncertainty at a 95% confidence level consists of both systematic and random components. To lessen the systematic component, three different ranges of differential pressure gauges were used in the wall static pressure, the profile loss, and the exit angle measurements. The full-scale ranges of 0.027, 0.133, and 1.33 kPa were carefully matched to the expected pressure measurements. The accuracy of each transducer was $\pm 0.3\%$ of full scale. The signals from the transducers were scanned at 100 Hz for 20 s by an HP 3852 data acquisition system and then averaged.

Experimental Results and Discussion

Baseline Case: Plane Blade (no Gf) at Re=28×10³. To establish the basis of comparison, measurements were made for the inlet Reynolds number of 28×10^3 for the blades without the Gurney flaps. At this Reynolds number, a large laminar separation bubble is present between s/B_x of 1.08 and 1.45 on the suction surface as indicated by the *Cp* and laser tuft measurements shown in Fig. 5.

The relationship between the terraced region of the *Cp* curve and the separated region identified by the laser tufts agrees with the findings of [11]. The peak marking the end of the terrace region is attributed to separated-flow transition where transition to turbulent flow proceeds in the free-shear-layer flow above the separation bubble. Reattachment occurs just downstream of this peak. The elimination of the large separation bubble is the focus of the present work.

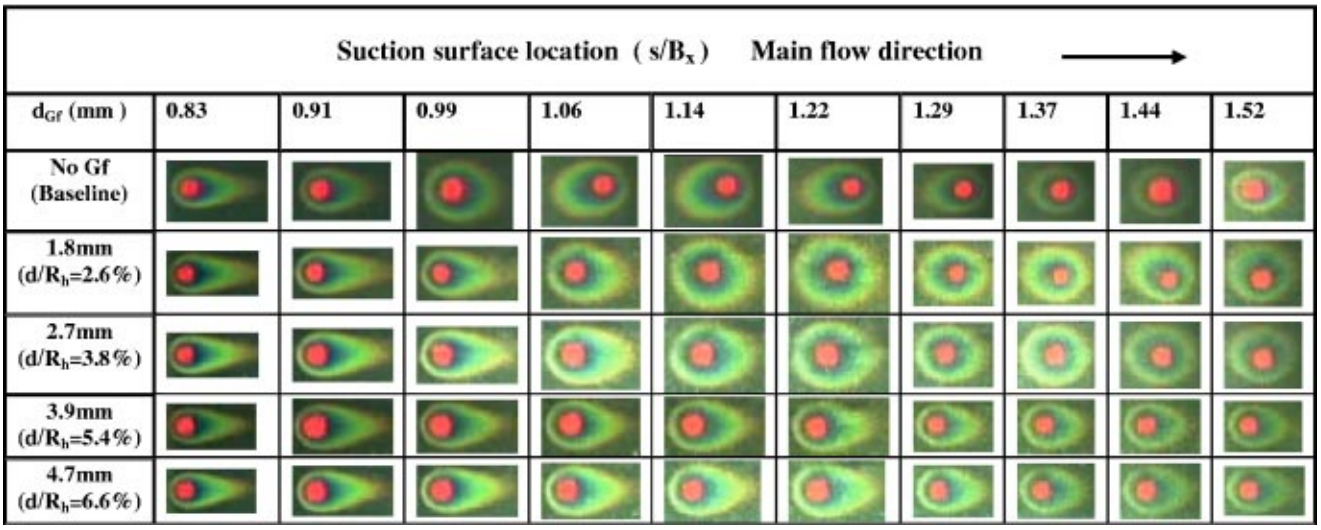

Fig. 6 Laser tufts on the suction surface of the cascade blade for different sizes of Gurney flaps

After establishing the baseline case, the next step was to determine the smallest Gurney flap that would eliminate separation. The laser thermal tuft technique was used for five different Gurney flap sizes while maintaining the inlet Reynolds number at 28×10^3. Representative laser tuft images from these tests are shown in Fig. 6 and the corresponding plot of eccentricity factors are shown in Fig. 7. Figure 7 shows that the effect of increasing the Gurney flap diameter is to move the point of separation further downstream. For the 2.7 mm Gurney flap, the location of separation is moved back to $s/B_x=1.36$. The flow is reattached by $s/B_x=1.50$. The next largest Gurney flap (3.9 mm) successfully eliminated the separation bubble so this was the size that was investigated in further detail.

Measurements With and Without Gurney Flap. To further characterize the effect the 3.9 mm Gurney flaps had on the cascade flow, detailed measurements were made at three Reynolds numbers both with and without the Gurney flaps installed. The lower two Reynolds numbers were expected to have separation present. The highest Reynolds number was expected to have fully attached flow. The test cases are shown in Table 2. Both the inlet Reynolds number and the Reynolds number based upon the NASA Glenn definition (wetted surface length, exit velocity) are shown. Since the Gurney flaps increase the exit velocity, the Re_{NASA} were different even though the inlet Reynolds number was the same.

Wall Static Pressure Distributions. The wall static pressure distributions for both the north and south blades are shown in Fig. 8 for each of the test cases. For the ''no Gf'' cases the terraced region moved upstream and decreased in size as Reynolds number increased. While there appears to be a very small terraced region at $s/B_x=1.05$ for Re=167 k, the laser thermal tuft showed that the flow was attached at this point. It is speculated that this is the location of transition. For each Reynolds number, the effect of the Gurney flaps is to increase the exit velocity over the ''uncovered''

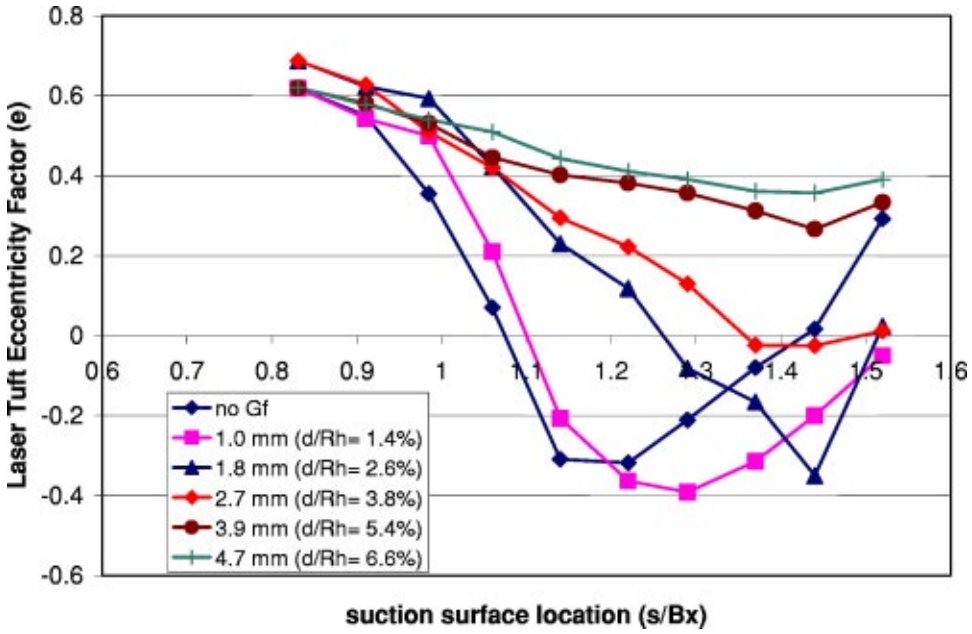

Fig. 7 Effect of Gurney flap diameter on boundary layer separation as indicated by laser tuft eccentricity (positive values of e indicate attached flow)

Table 2 Test cases: three Reynolds numbers with and without the 3.9 mm Gurney flap.

Re (x 10^3)	no Gf	with Gf	ReNASA (x 10^3)
28	x		78
28		x	88
65	x		182
65		x	207
167	x		464
167		x	528

region of the suction surface by approximately 14%. A momentum analysis indicates that this exit velocity increase results in an increased lift force of approximately 9%.

Profile Loss Coefficients. Profile loss measurements were made on both the north and south blades for each of the test cases

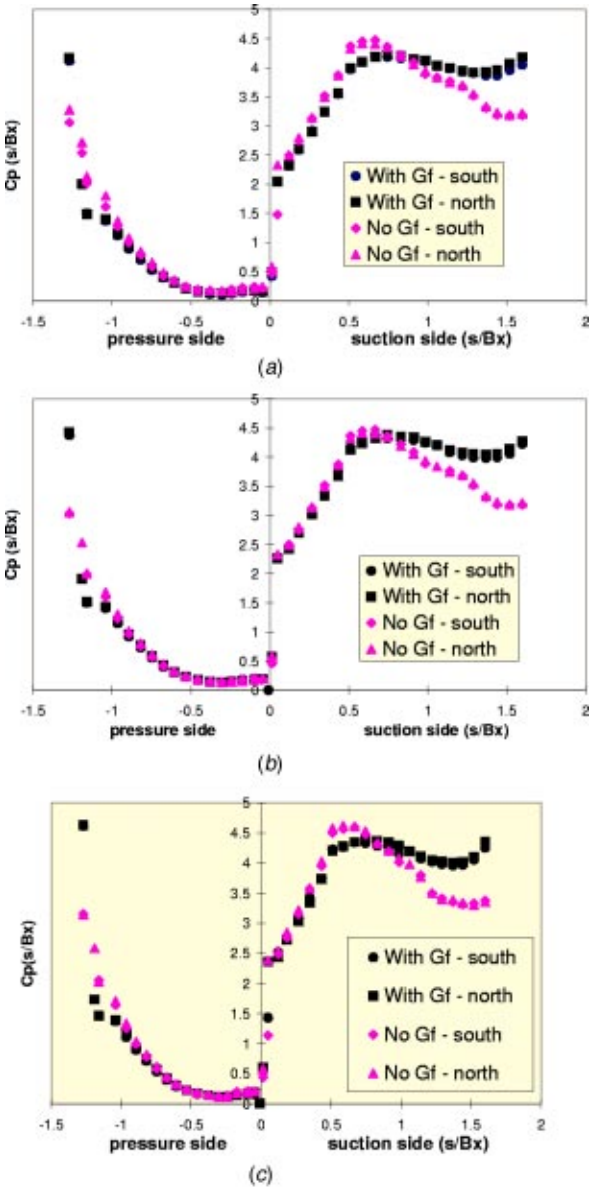

Fig. 8 Effect of Gurney flaps on wall static pressure—(*a*) (Re =28×10^3), (*b*) (Re=65×10^3), (*c*) (Re=167×10^3)

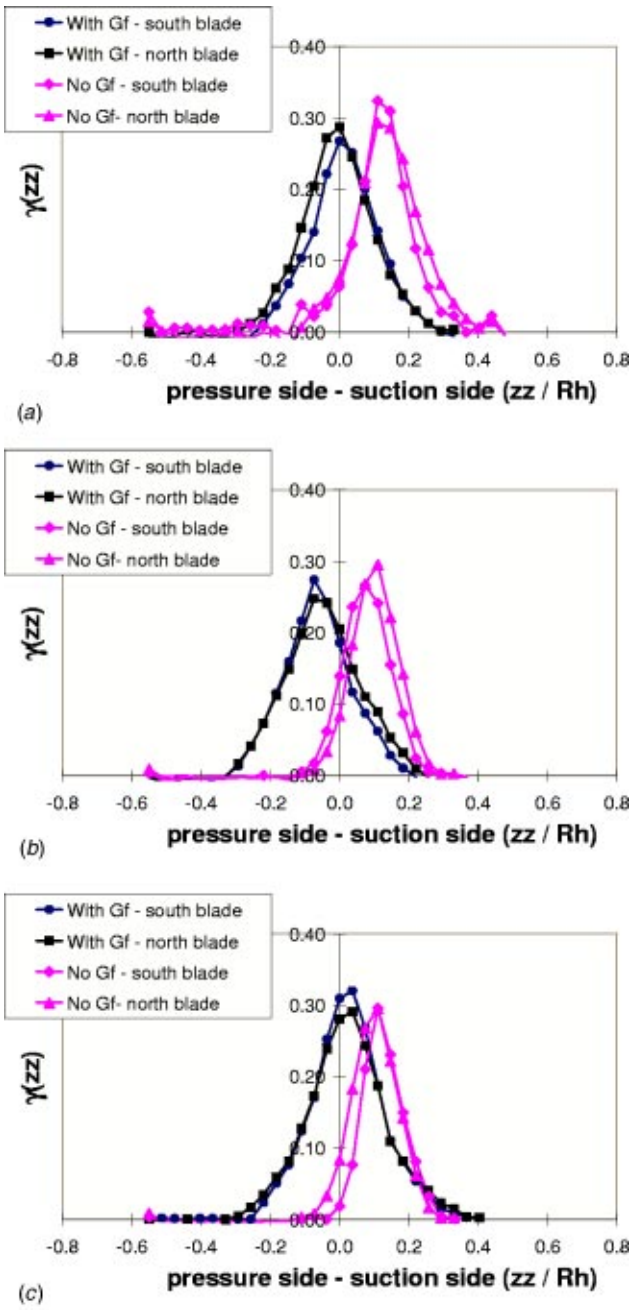

Fig. 9 Effect of Gurney flaps on profile loss—(*a*) (Re=28 ×10^3), (*b*) (Re=65×10^3), (*c*) (Re=167×10^3)

and are shown in Fig. 9. Without the Gurney flap, the center of the wake is offset to the suction side because of the thicker boundary layer on that side. The effect of the Gurney flaps was to shift the wake center closer to the trailing edge camber line ($zz=0$). Another effect, as expected, was the widening of the wake region.

The areas under the loss coefficient curves were integrated and plotted versus Reynolds number as shown in Fig. 10. At Re $=167\times10^3$, the value matched that predicted by the Ainsley correlation given in Horlock [18] within the range of uncertainty (0.041 versus 0.046). At Re$=28\times10^3$, the loss with the Gurney flaps was the same as without within the range of uncertainty. As Reynolds number was increased, the losses for the plane blade dropped as expected. However, with Gurney flaps, the losses at the higher Reynolds numbers were much greater. This finding reinforces the need to retract the Gurney flap for cases when the Reynolds number is high enough that separation is not present.

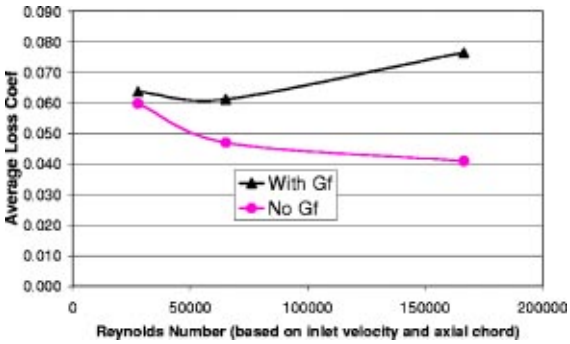

Fig. 10 Effect of Gurney flaps on average profile loss as a function of Reynolds number

Blade Row Flow Exit Angle. The effect of the Gurney flaps on the exit angle is shown in Fig. 11. As expected, the Gurney flap turned the flow in the direction of the suction surface of the neighboring blade although only by a small amount (0.8 deg). Although this amount is only slightly larger than the experimental uncertainty (0.7 deg), the effect was consistent for all three Reynolds numbers.

Conclusions

The following conclusions are submitted based upon the data presented:

1. Gurney flaps with $d/R_h = 5.4\%$ were successful at eliminating the laminar separation bubble for inlet Reynolds numbers as low as 28×10^3.
2. The Gurney flaps increased the exit velocity of the blade row passage by 14%. This results in a lift force increase of approximately 9%.
3. The Gurney flaps increased the profile loss coefficient for all Reynolds numbers above 28×10^3.
4. The center of the wake region shifted from the suction surface side towards the pressure surface side when the Gurney flaps were installed.
5. The Gurney flaps turned the flow approximately 0.8 deg towards the direction of the suction surface of the neighboring blade.

Acknowledgments

The authors thank Cadets Richard Janssen and Nathan Loucks for assisting in these measurements. Dr. Richard Rivir of the Air Force Research Lab Propulsion Directorate provided financial support. The authors are very grateful for the machine shop support provided by Mr. Jim Philp and Mr. Bobby Hatfield. Both the German government and the USAF AFOSR are thanked for supporting the "Engineer and Scientist Exchange Program" that made it possible for Mr. Oliver Störmer and Mr. Jörg List to participate in this research. Finally, Mr. Bob Humes of the USAF Academy Library must be thanked for the great document search and retrieval service that he provided.

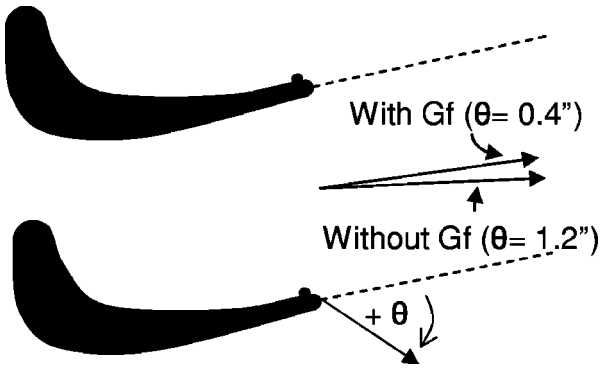

Fig. 11 Effect of Gurney flaps on exit angle

Nomenclature

B_x = airfoil axial chord, mm
B_1 = air inlet angle, deg
B_2 = air exit angle, deg
Cp = coefficient of pressure
d = Gurney flap diameter, mm
e = laser thermal tuft eccentricity factor
P = pressure, Pa
p = pitch distance between turbine blades, mm
R_h = $p \sin B_2$, hydraulic radius at blade row exit, mm
Re = Reynolds no. based on inlet conditions and axial chord
$\mathrm{Re}_{\mathrm{NASA}}$ = Reynolds no. based on exit velocity and suction surface length
s = wetted surface length, mm
V = velocity, m/s
x = distance measured in axial chord direction, mm
y = distance measured perpendicular to axial chord, mm
zz = distance measured parallel to hydraulic radius at blade row exit, mm
$\gamma(zz)$ = loss coefficient at location zz
$\overline{\gamma}$ = profile loss coefficient
ρ = density, kg/m^3
θ = flow exit angle, deg

Subscripts

center = center blade
exit = blade row exit
inlet = upstream of airfoil row
Gf = Gurney flap
north = north blade
south = south blade
T = total property
Tinlet = total property at inlet
Tdown = total property downstream of blade row

References

[1] Jeffrey, D., and Zhang, X., 2000, "Aerodynamics of Gurney Flaps on a Single-Element High-Lift Wing," J. Aircr., **37**(2).
[2] Myose, R., Papadakis, M., and Heron, I., 1998, "Gurney Flap Experiments on Airfoils, Wings, and Reflection Plane Model," J. Aircr., **35**(2).
[3] Selig, M. S., and Guglielmo, 1997, "High-Lift Low Reynolds Number Airfoil Design," J. Aircr., **34(1)**.
[4] Storms, B. L., and Jang, C. S., 1994, "Lift Enhancement of an Airfoil Using Gurney Flap and Vortex Generators," J. Aircr., **31**(3).
[5] Janus, J. M., 2000, "Analysis of Industrial Fan Designs With Gurney Flaps," AIAA Pap., AIAA-2000-0983.
[6] Fuglsang, P., and Bak, C., 2001, "Design and Verification of the New Riso-Al Airfoil Family for Wind Turbines," AIAA Pap., AIAA-2001-0028.
[7] Yen, D. T., van Dam, C. P., Smith, R. L., and Collins, S. D., 2001, "Active Load Control for Wind Turbine Blades Using MEM Translational Tabs," AIAA Pap., AIAA-2001-0031.
[8] Rivir, R. B., 1996, "Transition on Turbine blades and Cascades at Low Reynolds Numbers," AIAA Pap., AIAA-96-2D79.
[9] Van Treuren, K., Simon, T., Von Koller, M., Byerley, A. R., Baughn, J. W., and Rivir, R., 2001, "Measurements in a Turbine Cascade Flow Under Ultra Low Reynolds Number Conditions." ASME Paper 2001-GT-164, June.
[10] Lake, J. P., King, P. I., and Rivir, R. B., 2000, "Low Reynolds Number Loss Reduction on Turbine Blades With Dimples and V-Grooves," AIAA Pap., AIAA-00-0738.
[11] Murawski, C. G., and Vafai, K., 1999, "Effect of Variable Axial Chord on a Low-Pressure Turbine Blade," J. Propul. Power, **15**(5), Sept-Oct.
[12] Baughn, J. W., Butler, R. J., Byerley, A. R., and Rivir, R. B., 1995, "An Experimental Investigation of Heat Transfer, Transition and Separation on Turbine Blades at Low Reynolds Number and High Turbulence Intensity," ASME Paper 95-WA/HT-25.
[13] Welsh, S. T., Barlow, D. N., Butler, R. J., Van Treuren, K. W., Byerley, A. R., Baughn, J. W., and Rivir, R. B., 1997, "Effect of Passive and Active Air-Jet Turbulence on Turbine Blade Heat Transfer," ASME Paper 97-GT-131.

[14] Butler, R. J., Byerley, A. R., Van Treuren, K. W., and Baughn, J. W., 2000, ''The Effect of Turbulence Intensity and Length Scale on Low Pressure Turbine Blade Aerodynamics,'' Int. J. Heat Fluid Flow, Nov.
[15] Blair, M. F., Dring, R. P., and Joslyn, H. D., 1989a, ''The Effects of Turbulence and Stator/Rotor Interactions on Turbine Heat Transfer. Part 1-Design Operating Conditions,'' ASME J. Turbomach., **111**, pp. 87–96.
[16] Blair, M. F., Dring, R. P., and Joslyn, H. D., 1989b, ''The Effects of Turbulence and Stator/Rotor Interactions on Turbine Heat Transfer. Part 2-Effects of Reynolds Number and Incidence,'' ASME J. Turbomach., **111**, pp. 97–103.
[17] Rivir, R., Baughn, J., Townsend, J., Butler, R., and Byerley, A. R., 1999, ''*Thermal Tuft Fluid Flow Investigation Apparatus with a Color Alterable Thermally Responsive Liquid Crystal Layer*,'' U.S. Patent 5,963,292, U.S. Patent Office, Washington, D.C., 5 Oct.
[18] Horlock, J. H., 1966, *Axial Flow Turbines*, Butterworths Publishing Company, London.
[19] Benedict, R. P., 1984, *Fundamentals of Temperature, Pressure, and Air Flow Measurement*, 3rd Edition, John Wiley & Sons, New York, NY.
[20] Coleman, H. W., and Steele, W. G., 1999, *Experimentation and Uncertainty Analysis for Engineers*, 2nd Edition, John Wiley & Sons, New York, NY.

The Investigation of Turbine and Exhaust Interactions in Asymmetric Flows— Blade-Row Models Applied

J. J. Liu[1]

T. P. Hynes

Whittle Laboratory,
University of Cambridge,
Cambridge CB3 0DY, UK

This paper describes the blade-row models applied to the asymmetric flow-field coupling between turbine and exhaust system. Numerical actuator disk is applied to represent a turbine blade row around the whole annulus and flow properties across the disk can jump to achieve required flow turning and entropy rise. The derivation of disk boundary conditions and the implementation in CFD solvers are described in detail. Validation of the actuator disk model and sample application of the present numerical approach are presented. [DOI: 10.1115/1.1516812]

Introduction

Exhaust system of steam turbines and industrial gas turbines consists of an annular diffuser and a collector (volute). The system is used to transfer the turbine leaving kinetic energy to potential energy while guiding the flow from turbine exit plane to the downstream component. It has been recognized that the pressure recovery performance of diffuser, as is the performance of the whole exhaust system, is strongly influenced by diffuser inflow conditions such as flow swirl and total pressure profile distortion, which are set up by the operation of the last stage turbine. On the other hand, the one-side discharge of the exhaust results in asymmetric flow at the turbine exit. Turbine blade rows may experience varying back pressure at different circumferential locations. It is essential to allow for the flow-field coupling between the turbine and exhaust in order to obtain proper inflow conditions for the diffuser and therefore make realistic predictions of the flow in the exhaust.

The diffuser inlet corresponds to the entire annulus of the turbine exit plane. Due to the nonaxisymmetric hood structure, the diffuser experiences asymmetric inflows in the actual environment. That assumption of axisymmetric flow at the turbine exit plane such that only one blade passage is considered in the calculation of turbine and exhaust interactions (in the sense of steady flow) does not reflect the flow characteristic of asymmetry at this plane. An obvious method of resolving this problem is to include all the blade passages in the whole annulus in the calculation.

Difficulties arise when all the blade passages of a blade row are taken into account in the calculation of turbine and exhaust interactions. It is very CPU-intensive and costly if a fully 3-D calculation is performed for each of the dozens of turbine blade passages. Some researchers have tried various models to represent the turbine. Mainly they use fully 3-D calculation of *one* or *several* blade passages to simulate the blade to blade flow (e.g., Benim et al., [1]). The fully 3-D calculation for blade rows and the calculation for the exhaust system are either internally coupled via a mixing plane or externally coupled in an iterative manner. These approaches are still computationally expensive and it is not easy to maintain the compatibility of the flow between the turbine and exhaust system.

It is noticed that the circumferential length scale of diffuser is dramatically larger than a blade pitch. The circumferential variation of flow properties within a blade passage cannot be felt numerically by the diffuser, unless the circumferential mesh size of diffuser matches that of the blade passage. The matching of circumferential mesh size between the diffuser and blade passage rarely happens because of the limitation of computer resources and also that the length scale of interest associated with the turbine and exhaust interactions in asymmetric flows is larger than a blade pitch. This suggests that it may not be necessary to use fully 3-D blade row models to represent the turbine.

Actuator disk is one of the most effective models in simulating the presence of blade rows in asymmetric flows. Joo and Hynes [2] developed an actuator disk model to represent the low hub-to-tip ratio fan or compressor blade rows in turbofan engine. The model was successfully applied to the calculations of the flow in turbofan installations (Joo and Hynes [3]) and liftfan installations (Taylor [4]).

This paper presents the *extension* of the actuator disk model to represent the turbine blade rows with *highly flared annuli*. After this introduction, the actuator disk model and disk boundary conditions are described. The CFD method used for the calculation and the implementation of disk boundary conditions are presented. The present actuator disk model is compared with the early one. The investigation of turbine and exhaust interactions by using the present actuator disk model is presented in the companion paper (i.e., Liu and Hynes [5]).

Actuator Disk Model

Basic Idea of Actuator Disk Model. In this model, a blade row is contracted into a zero-thickness disk. The disk has two sides. One side corresponds to the inlet of the blade row, the other side to the exit of the blade row. The flow variables across the disk can jump in order to achieve the flow turning and entropy rise occurred within the blade row.

Numerically speaking, an actuator disk is a boundary that is geometrically continuous and physically discontinuous, as shown in Fig. 1. The left side of the disk belongs to the left computational domain and the right side to the right domain. The two flow fields separated by the disk can be calculated, respectively, by 3-D flow solvers and connected by disk boundary conditions.

Actuator Disk Boundary Conditions. The disk boundary conditions should preserve the conservation of mass flow, momentum and energy. But it is not obvious how to use the 3-D conservation equations as numerical boundary conditions for the disk. Simplification of these 3-D conservation relations must be

[1]Current address: Institute of Engineering Thermophysics, Chinese Academy of Sciences, Beijing 100080, China.

Contributed by the International Gas Turbine Institute and presented at the International Gas Turbine and Aeroengine Congress and Exhibition, Amsterdam, The Netherlands, June 3–6, 2002. Manuscript received by the IGTI, revised manuscript received October 2, 2001. Paper No. 2002-GT-30342. Review Chair: E. Benvenuti.

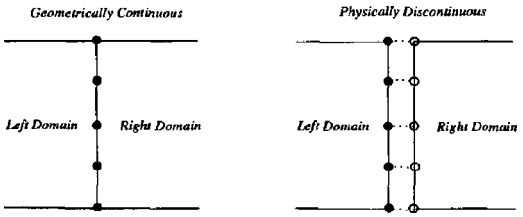

Fig. 1 Illustration of actuator disk model

made. In the present approach, it is assumed that the streamlines across an actuator disk are *continuous* in the meridional plane. Along a streamline across the disk, the total rothalpy should be constant; and the entropy can either be constant or increase, depending upon the loss correlations applied for the blade row. The assumption of continuous streamlines (across a disk) in the meridional plane implies that the mass flow is conserved in this plane. Referring to Fig. 2, m denotes a streamline passing through an actuator disk at any circumferential and radial location L (also R), l is a *quasi-orthogonal* line to m; λ is the angle between l and the radial direction. The continuity equation in the meridional plane is $\int \rho V_x dr + \int \rho V_r dx = \text{constant}$. Applying this equation to the two sides of the disk by integrating the equation along the l direction, gives

$$(\rho V_x)^L \Delta l \cos(\lambda) + (\rho V_r)^L \Delta l \sin(\lambda) = (\rho V_x)^R \Delta l \cos(\lambda) + (\rho V_r)^R \Delta l \sin(\lambda) \quad (1)$$

i.e,

$$(\rho V_x)^L = \frac{[1+\tan(\lambda)\tan(\beta_r^R)]}{[1+\tan(\lambda)\tan(\beta_r^L)]} (\rho V_x)^R \quad (2)$$

where $\beta_r^L = \arctan(V_r/V_x)^L$, $\beta_r^R = \arctan(V_r/V_x)^R$. In general, $(\beta_r)^L$, $(\beta_r)^R$ and λ are independent.

There are many ways to apply the continuity equation by imposing numerical boundary conditions for the disk, according to Eq. (2). We shall assume that the slope of a streamline is also continuous at the two sides of the disk, which implies $(\beta_r)^L = (\beta_r)^R$. Regardless of the integration path l, two numerical boundary conditions for the disk are obtained as follows:

$$(\beta_r)^L = (\beta_r)^R$$
$$(\rho V_x)^L = (\rho V_x)^R \quad (3)$$

Noting the definition of β_r, Eq. (3) is equivalent to

$$(\rho V_r)^L = (\rho V_r)^R$$
$$(\rho V_x)^L = (\rho V_x)^R \quad (4)$$

The five disk boundary conditions are then completed by specifying relative outlet swirl angle β_θ, loss ΔS and the rotating speed Ω, which reflect the characteristic of the blade row, and by using the relation of constant total rothalpy I_0 across the disk.

Instead of Eq. (3), the following disk boundary conditions were proposed in the previous research (e.g., Joo [6])

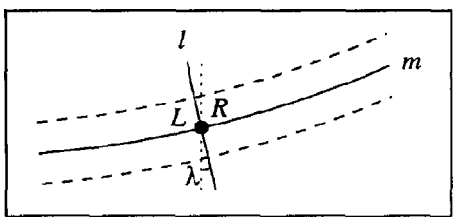

Fig. 2 Streamline and quasi-orthogonal line in the meridional plane

$$(V_r)^R = (V_r)^L$$
$$(\rho V_x)^L = (\rho V_x)^R \quad (5)$$

in which the axial continuity equation and radial momentum equation are applied, with the assumption of zero radial blade force for a disk that is perpendicular to the x-axis.

Actuator disk boundary conditions should, as far as possible, represent the total effect of the blade row on the local flow. The four boundary conditions of conservation of mass and of rothalpy, a condition on relative exit flow angle and on loss are relatively natural ways of ensuring that the actuator disk achieves the same mass flow rate, energy input, swirl and entropy rise as the blade row. The fifth boundary condition is intended to achieve the same radial flow migration across the disk. It is not obvious how to achieve this since one could take the view that all radial redistribution should be concentrated at the disk itself, in which case a condition on the radial blade force at the disk would seem natural. On the other hand, within the blade row region, the annulus contraction as well as blades themselves will have a significant effect on constraining the flow in the radial direction. The effect of the annulus contraction is not modeled as being concentrated at the disk, but happens naturally in the region of the flow domain that the blades would occupy.

It appears that concentrating the radial effect of the blades at the disk, as Joo did, introduces a problem at the end walls, where the condition of no change in radial velocity is not compatible with the condition of no flow through the end walls on either side of the disk. For the case of relatively small rates of annulus contraction studied by Joo, this incompatibility is probably not significant and, in addition, the cell-centered scheme helped him to confine this problem to the immediate vicinity of the end wall cells. The study reported later will indicate that a more satisfactory view is to regard the spanwise force effects of the presence of the blade row not to be concentrated at the disk, but to be considered to take place within the full axial extent of the blades. The boundary conditions of Eq. (3) represent continuity of streamline meridional slope at the disk, rather than zero radial blade force, and *are* fully compatible with no flow through the end walls.

Implementation of the Disk Model

A good numerical implementation of an actuator disk model will obtain clean jumps in flow properties across the disk and good convergence rates. The implementation detail of a disk model differs from one solver to another, depending upon the simplification made to the conservation equations and also upon the algorithms employed. Previous researchers have gained useful experience in implementing disk boundary conditions for a structured cell-centered solver [6] and for an unstructured cell-vertex solver [4]. The numerical implementation of the present disk boundary conditions for a structured cell-vertex solver are described in this section.

CFD Method. A fully 3-D flow solver, DiscRow, is developed for the simulation of asymmetric flow in turbine exhaust systems. The Reynolds averaged Navier-Stokes equations are solved by using the cell-vertex finite-volume TVD Lax-Wendroff scheme (Roe [7]) incorporating Roe's approximate Riemann solver (Roe [8]). It is generally recognized that minimal numerical dissipation is introduced in a TVD scheme in order to stabilize the calculation, and that Roe's Riemann solver resolves both shear layer and flow discontinuity very well (Van Leer et al. [9]). As a result, mesh independent numerical solutions can be easily obtained.

The turbulent eddy viscosity is estimated by using the Baldwin-Lomax model. In this two-layer algebraic model a turbulent boundary layer is divided into an inner and an outer region. The eddy viscosity for each region is computed by using the corresponding formula. In practice, both inner-layer viscosity and outer-layer viscosity are computed for the entire boundary layer

and the smaller one is taken as the actual eddy viscosity. For a complicated physical domain, two solid walls may intersect. The eddy viscosity in which case is first computed according to each of the two walls and then weighted by the distance from the wall to form the effective eddy viscosity. Standard coefficients due to Baldwin and Lomax [10] are used for this model.

The boundary conditions applied in the present solver are of the prediction-modification type, similar to that of Ni [11]. It is assumed that the TVD Lax-Wendroff scheme gives correct prediction of flow properties at the numerical boundaries (such as inlet, outlet, solid wall and periodic boundary). The predicted properties are then modified to satisfy the enforced boundary conditions.

The V-cycle multigrid algorithm [11] is applied in the present solver to speed up the convergence to a steady state. Multiblock method is also incorporated to deal with complicated physical domains. The details of the CFD method and the validations against some analytical solutions can be found in Liu [12].

Implementation Details. The calculation is carried out in a Cartesian system in the absolute frame. Whereas the disk boundary conditions are applied in a cylindrical system in the relative frame. Let V_x, V_θ and V_r denote the three components of relative velocity and $\theta=\arctan(y/z)$. The following relations apply:

$$\begin{pmatrix} \rho \\ V_x \\ V_\theta \\ V_r \\ p \end{pmatrix}_p = \begin{pmatrix} \rho \\ u \\ v\cos\theta - w\sin\theta - \Omega r \\ v\sin\theta + w\cos\theta \\ p \end{pmatrix}_p \tag{6}$$

$$\begin{pmatrix} \rho \\ u \\ v \\ w \\ p \end{pmatrix}_{\text{new}} = \begin{pmatrix} \rho \\ V_x \\ (V_\theta+\Omega r)\cos\theta + V_r\sin\theta \\ -(V_\theta+\Omega r)\sin\theta + V_r\cos\theta \\ p \end{pmatrix}_{\text{new}} \tag{7}$$

where $(\cdot)_p$ refers to the predicted variables and $(\cdot)_{\text{new}}$ the new variables after imposing boundary conditions. The total rothalpy and entropy are given by

$$I_0=\frac{\gamma}{\gamma-1}\frac{p}{\rho}+\frac{1}{2}[V_x^2+V_\theta^2+V_r^2-(\Omega r)^2] \tag{8}$$

$$S=\frac{p}{\rho^\gamma} \tag{9}$$

Suppose subsonic axial flow is from left to right. On the downstream (right) side of the disk, four variables need to be specified. Making use of continuous streamlines across a disk and Eq. (3), three of the four variables are total rothalpy I_0^L, entropy S^L, and pitch angle β_r^L, which are transformed from the upstream (left) side, the fourth variable is the previously specified swirl angle β_θ, gives

$$\begin{aligned} (I_0^R)_{\text{new}} &= (I_0^L)_p \\ (S^R)_{\text{new}} &= (S^L)_p + \Delta S \\ (\beta_\theta^R)_{\text{new}} &= \beta_\theta \\ (\beta_r^R)_{\text{new}} &= (\beta_r^L)_p \end{aligned} \tag{10}$$

Applying the above four conditions to the downstream side of the disk, new primary variables on this side can be obtained. The new velocity components are

$$\begin{aligned} (V_x^R)_{\text{new}} &= (V_{p_n}^R)_p l_x \\ (V_\theta^R)_{\text{new}} &= (V_{p_n}^R)_p l_\theta \\ (V_r^R)_{\text{new}} &= (V_{p_n}^R)_p l_r \end{aligned} \tag{11}$$

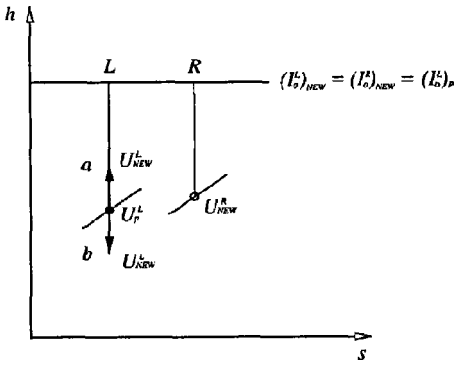

Fig. 3 Diagram for disk boundary condition

where $\vec{l}$ is the unit velocity vector determined by angles $(\beta_\theta^R)_{\text{new}}$, and $(\beta_r^R)_{\text{new}}$, and $V_{p_n}^R=(V_x^R)_p l_x+(V_\theta^R)_p l_\theta+(V_r^R)_p l_r$ is the magnitude of the predicted velocity.

The new density and pressure are obtained by solving the following equations:

$$(I_0^R)_{\text{new}}=\frac{\gamma}{\gamma-1}\frac{p_{\text{new}}^R}{\rho_{\text{new}}^R}+\frac{1}{2}[(V_x^R)_{\text{new}}^2+(V_\theta^R)_{\text{new}}^2+(V_r^R)_{\text{new}}^2-(\Omega r)^2] \tag{12}$$

$$S_{\text{new}}^R=\frac{p_{\text{new}}^R}{(\rho_{\text{new}}^R)^\gamma} \tag{13}$$

It has been pointed out by Joo and Hynes [2] that two solutions for density exist in the above equations. One density corresponds to subsonic relative flow and one to supersonic relative flow. In the present approach, the magnitude of the total velocity at the downstream side of the disk is determined by the numerical solution from the internal flowfield connecting to this side of the disk. Once this total velocity (either subsonic or supersonic) is obtained, the density and the static pressure can be uniquely determined from Eqs. (12) and (13). The difficulty of two values for density is thus avoided.

Upstream of the disk, we set (according to Eq. (3))

$$(\rho^L V_x^L)_{\text{new}}=(\rho^R V_x^R)_{\text{new}} \tag{14}$$

the additional conditions are

$$(V_r^L)_{\text{new}}=\frac{(V_x^L)_{\text{new}}}{(V_x^L)_p}(V_r^L)_p \tag{15}$$

$$(I_0^L)_{\text{new}}=(I_0^L)_p \tag{16}$$

$$(S^L)_{\text{new}}=(S^L)_p \tag{17}$$

Equations (14) to (17) are solved in an iterative manner. The iteration starts by guessing a ρ_{new}^L (for example, set $\rho_{\text{new}}^L=\rho_p^L$) for Eq. (14), and ends by obtaining a new ρ_{new}^L from Eqs. (16) or (17). It usually takes less than ten iterations by using under-relaxation to make the two values identical. Theoretically, two solutions for density could be obtained from Eq. (14). However, by setting the initial density $\rho_{\text{new}}^L=\rho_p^L$, the final density ρ_{new}^L will converge to a solution that is near ρ_p^L (it is unlikely that the density ρ_{new}^L will converge to another solution when the total velocity in the upstream side is away from sonic).

This approach is illustrated in the enthalpy-entropy diagram of Fig. 3. When the new state of the right side of disk is obtained, the new axial mass flow rate is imposed on the left side (see Eq. (14)) to determine the new state of this side. If the new axial velocity calculated from Eq. (14) is larger than the predicted one, the new state of the left side of the disk will move towards *b*; otherwise, it

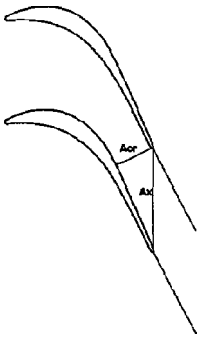

Fig. 4 Choking model for a turbine blade passage

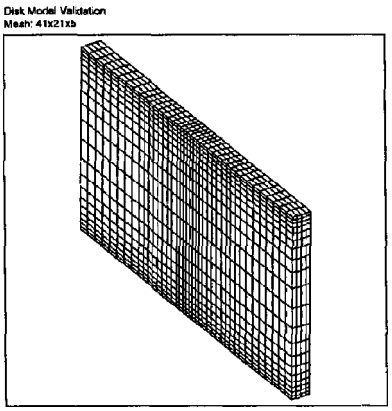

Fig. 5 Mesh used for disk-model validation

will move towards *a*. In either case, the total rothalpy and entropy do not change (see Eqs. (17) and (16). Equation (15) keeps the pitch angle unchanged.

The foregoing implementation will ensure that left and right states of the disk are matched by the disk boundary conditions at *each time step*, i.e., there is no lagging in time between the properties on the two sides of the disk.

For steady calculations, local time steps are employed and transient results are not of interest. However, the foregoing treatment ensures that multigrid methods work properly. This can be explained as follows, if the procedure described in the foregoing is repeatedly applied to the left and right side of the disk by using the newly obtained variables, the flow states will not be changed; if there is a time lag between the two new states, the repeated application of the disk boundary conditions will result in varied new states and the process may not be stable. The boundary conditions used on the fine mesh are also used on coarse meshes, if the multigrid routine is invoked, the repeated imposition of disk boundary conditions on coarse meshes will enlarge this time-gap and calculation with multigrid may fail to converge. For time-accurate calculation, the no-time-lagging disk boundary conditions will give correct variable jumps across the disk at each time step, and therefore correct transient results within the limitations of the actuator disk approach.

The inherent advantage of the present solver makes the implementation of the foregoing conditions very easy. Due to cell-vertex storage, the flow variables are already stored on each side of the disk; no interpolation is required. The numerical smoothing can be terminated at a disk boundary, and the two computational domains on each side of the disk are only connected by the disk boundary conditions. By doing so, no oscillation is introduced into the regions immediately upstream and downstream of the disk, as sometimes happens using other methods.

Choking Model. The flow in a blade row may be choked at a certain section. The mass flow passing through this choked section will be limited by which passing through the blade throat. Joo and Hynes [2] proposed a simple model, for a blade passage of fan or compressor, to allow the actuator disk to account for such a choking effect.

Applying the similar choking model to a turbine blade passage, as illustrated in Fig. 4, the maximum value of axial mass flux passing the streamtube at the blade exit is given by

$$(\rho V_x)_{\max} = \frac{F^* P_{02}^{\mathrm{rel}}}{\sqrt{C_p T_{02}^{\mathrm{rel}}}} \frac{A_{cr}}{A_x} \tag{18}$$

where F^* is the appropriate compressible flow function, A_x and A_{cr} are the streamtube axial cross-sectional area at actuator disk and throat cross-sectional area, respectively.

For a turbine blade row, the actuator disk is usually placed at the blade trailing edge. At each time step, the axial mass flux at the disk downstream side is compared with the maximum value given by Eq. (18). If the mass flux is larger than the maximum value, the mass flux at disk downstream side is set to this maximum value and this choked mass flux is also imposed to the disk upstream side.

Compared With Other Solutions

Compared With Analytical Solution. A reliable way of validation is to compare numerical results with analytical test cases. For this purpose, the foregoing disk model has been used for a 3-D channel which is a hexahedron with three pairs of parallel walls, as shown in the Fig. 5. A mesh of $41\times21\times5$ in *i*, *j*, *k* directions is used for this test case. Two disks, which are used to represent a turbine stage, are located at $i=9$ and $i=25$, respectively.

The inflow is along the axial direction. Periodic boundary conditions are applied in the *y* direction. A slip condition is used for the hub and tip. With two disks present, the flow inside the channel is like the flow going through two 2-D cascades. By specifying uniform inflow and uniform back pressure, the channel is separated by the two disks into three uniform flow subdomains.

The first disk represents a stator and the specified boundary conditions are: outlet swirl angle $\beta_{\theta_1}=50$ deg; entropy increase $\Delta S_1=0.0$ and wheel speed is zero. The second disk represents a rotor and the specified boundary conditions are: outlet swirl angle $\beta_{\theta_2}=-50$ deg; entropy increase $\Delta S_2=0.0$ and wheel speed is 117.3 m/s. The exit static pressure is 0.784 of the inlet total pressure. The wheel speed is chosen in a way such that the absolute swirl angle at rotor exit is small. The analytical solution is acquired by using conservation of total rothalpy and axial massflow, and the relation of entropy. For this turbine stage, the flow coefficient V_x/U_{rotor} is 0.9; the blade loading coefficient $\Delta H_0/U_{\mathrm{rotor}}^2$ is 1.1 and the absolute swirl angle at rotor exit is 4.5 deg. The numerical and analytical results are shown in Figs. 6–8.

Crisp discontinuity of flow variables across the two disks is observed and there is no oscillation on the upstream or downstream sides of the disks. The comparison between numerical and analytical solutions is excellent.

Compared With the Previous Model. In order to investigate the difference between Eq. (3) (referred as Model A) and Eq. (5) (*the previous model*, referred as Model B), a low-speed and a high-speed test are carried out for a turbine and its following axial-radial diffuser. A mesh of $53\times21\times5$ is used in the streamwise, radial and circumferential directions, respectively. The meridional mesh of 53×21 is shown in Fig. 9. Two actuator disks are located at $i=9$ and $i=13$ where the grid lines are perpendicular to the *x*-axis. The Mach number distributions for the low-speed test case are shown in Fig. 10. The highest Mach number in the flowfield is about 0.2. Difference in the Mach number distribution between the two disk models is noticed at the tip end wall where

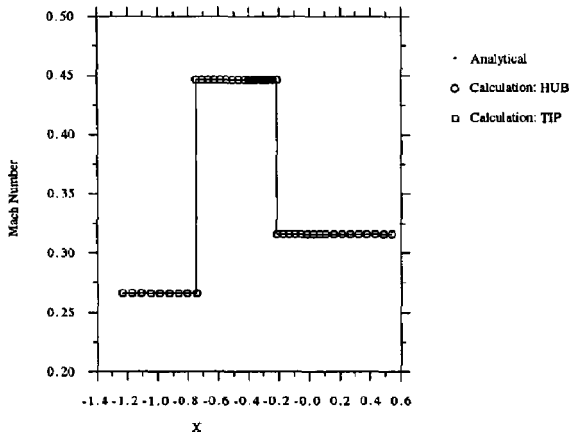

Fig. 6 Mach number distribution across actuator disks

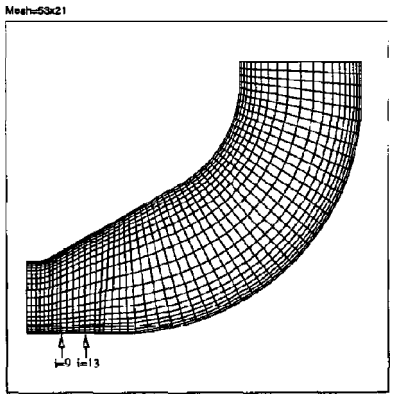

Fig. 9 Mesh used for the comparison of disk boundary conditions; two disks are located at $i=9$ and $i=13$

the radial velocity is not zero and the flow is not absolutely incompressible (even though the Mach number is very low). The mass flow error from the diffuser outlet to the turbine inlet is 0.19% using equation 3 and it is 0.86% using Eq. (5). For the high speed test case, as shown in Fig. 11, the difference in the Mach number distribution between the two disks is negligible at the hub end wall where the radial velocity is zero. The difference is increased at the tip end wall, compared with the low-speed test case. The mass flow error from the diffuser outlet to the turbine inlet is 0.12% using Eq. (3) and it is 6.16% using Eq. (5). It may be concluded from the foregoing test cases that the disk boundary conditions of Eq. (5) are equivalent to those of Eq. (3) for incompressible flow or for the flow with zero radial velocity. For compressible flow or for the flow with nonzero radial velocity, Eq. (5) will cause significant mass flow error, and oscillations in flow properties at end walls.

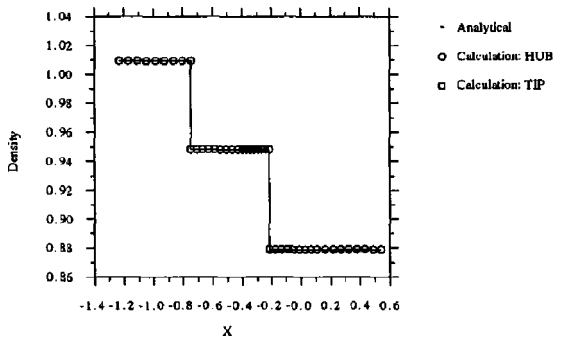

Fig. 7 Density distribution across actuator disks

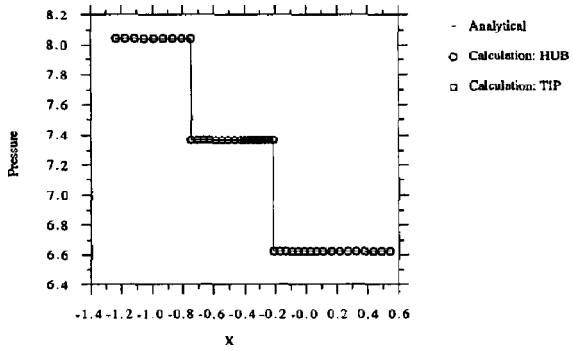

Fig. 8 Pressure distribution across actuator disk

The solutions of the previous actuator disk model have been compared with three-dimensional calculations by Joo and Hynes [2]. It is believed that the present disk model can work equally well.

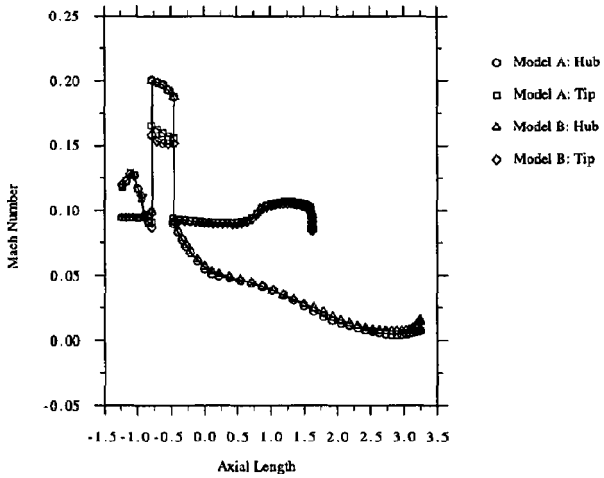

Fig. 10 Mach number distributions for low-speed flow, the mass flow error is 0.19% using Eq. (3) (Model A), and it is 0.86% using Eq. (5) (Model B)

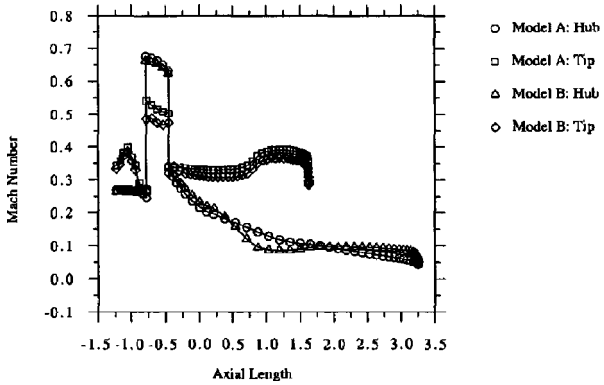

Fig. 11 Mach number distributions for high-speed flow, the mass flow error is 0.12% using Eq. (3) (Model A), and it is 6.16% using Eq. (5) (Model B)

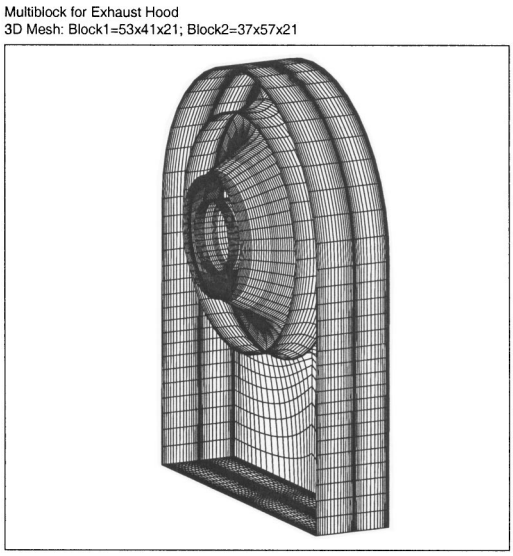

Fig. 12 Multiblock mesh used for an exhaust hood

Sample Application

The numerical approach described in the foregoing has been used for the simulation of turbine and exhaust interactions in asymmetric flows. A sample application to a steam turbine exhaust hood is presented in this section. The 3-D structured mesh for the one-stage turbine and its following hood is given in Fig. 12. Two blocks of mesh are applied, one block for the turbine and diffuser, the other for the collector. Two actuator disks are positioned at $i=13$ and $i=21$ in the first block to represent the two turbine blade rows, respectively.

Uniform total pressure, total temperature, swirl and pitch flow angle are specified at the turbine inlet. Averaged static pressure is specified at the hood outlet. The computed stream ribbons starting from four radial lines at the diffuser inlet (also turbine exit) are given in Fig. 13. The Mach contours at a plane of $\theta=0$ degree are given in Fig. 14. It can be seen that the flow field in the turbine region is separated by the two actuator disks.

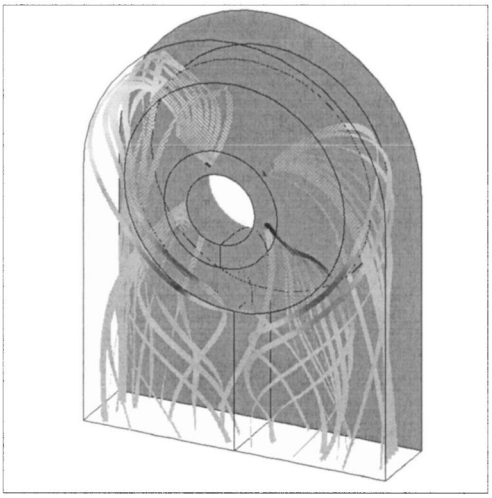

Fig. 13 Stream ribbons starting from four radial lines at the diffuser inlet in the exhaust hood

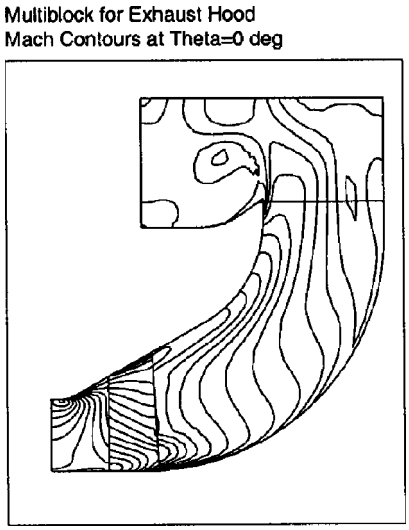

Fig. 14 Mach contours at a plane of $\theta=0$ deg in the exhaust hood

Conclusions

The actuator disk model for the turbine blade rows with highly flared annuli has been developed. The implementation of the disk boundary conditions in the cell-vertex CFD solver is described in detail. The sample calculation is presented to demonstrate the capability of the present numerical method in the simulation of the asymmetric flow between turbine and exhaust system. The conclusions are:

i. A novel actuator disk boundary condition (compare Eq. (4) with (5)) is derived by assuming that the streamline across the actuator disk and the slope of the streamline at the disk are continuous. The present assumption, compared with the previous zero radial blade force, is fully compatible with no flow through the end walls.

ii. With the new disk boundary conditions of Eq. (4) (or (3)), the present actuator disk model can be used for blade rows with large levels of annulus expansion or contraction regardless the disk orientation. In contrast, the previous disk model is only suitable for relatively small levels of annulus expansion or contraction and the disk has to be perpendicular to the x-axis.

iii. The present implementation of the disk model usually gives clean jump of flow properties across the disk.

Acknowledgment

The first author would like to thank the awarding bodies of SBF scholarship and ORS awards for the financial support during his study in Cambridge University. He also gratefully acknowledges the support of CUED and Rolls Royce plc for completing this research. Thanks are due to Professor Liping Xu for the discussions on the actuator disk model described in this paper.

Nomenclature

I_0 = total rothalpy
L = left side of actuator disk
p = static pressure
R = right side of actuator disk
S = entropy, p/ρ^{γ}
u,v,w = velocity components in Cartesian system
V_x, V_θ, V_r = velocity components in cylindrical system
x,y,z = directions of Cartesian coordinate
x, θ, r = directions of cylindrical coordinate
β_r = pitch angle, $\arctan(V_r/V_x)$
β_θ = swirl angle, $\arctan(V_\theta/V_x)$

ρ = density
Ω = rotating speed

References

[1] Benim, A. C., Geiger, M., Doehler, S., Schoenenberger, M., and Roemer, H., 1995, ''Modelling the Flow in the Exhaust Hood of Steam Turbines Under Consideration of Turbine-Exhaust Hood Interaction,'' 1st European Congress, Turbomachinery Fluid Dynamic and Thermodynamic Aspects, March 1–3.

[2] Joo, W. G., and Hynes, T. P., 1997, ''The Simulation of Turbomachinery Blade Rows In Asymmetric Flow Using Actuator Disks,'' ASME J. Turbomach., **119**, pp. 723–732.

[3] Joo, W. G., and Hynes, T. P., 1997, ''The Application of Actuator Disks to Calculations of the Flow in Turbofan Installations,'' ASME J. Turbomach., **119**, pp. 733–741.

[4] Taylor, J., 1997, personal communication.

[5] Liu, J. J., and Hynes, T. P., 2002, ''The Investigation of Turbine and Exhaust Interactions in Asymmetric Flows: Part 2—Turbine-Diffuser-Collector Interaction,'' ASME Paper 2002-GT-30343.

[6] Joo, W. G., 1994, ''Intake/Engine Flowfield Coupling in Turbofan Engines,'' PhD thesis, Cambridge University Engineering Department, United Kingdom.

[7] Roe, P. L., 1984, ''Generalized TVD formula for Lax-Wendroff Scheme,'' ICASE Report, No. 84-53.

[8] Roe, P. L., 1981, ''Approximate Riemann Solvers, Parameter Vectors and Difference Schemes,'' J. Comput. Phys., **43**, pp. 357–372.

[9] Van Leer, B., Thomas, J. L., Roe, P. L., and Newsome, R. W., 1987, ''A Comparison of Numerical Flux Formulas for the Euler and Navier-Stokes Equations,'' AIAA Pap. 87–1104. Honolulu, Hawaii.

[10] Baldwin, B. S., and Lomax, H., 1978, ''Thin Layer Approximation and Algebraic Model for Separated Turbulent Flows,'' AIAA Pap., No. 78–257.

[11] Ni, R. H., 1989, ''Prediction of 3D Multi-Stage Turbine Flow Field Using a Multiple-Grid Euler Solver,'' AIAA Pap., 89–0203.

[12] Liu, J. J., 1998, ''The Calculation of Asymmetric Flow in Turbine Exhaust Systems,'' Ph.D. thesis, Cambridge University Engineering Department, United Kingdom.

A New Tailpipe Design for GE Frame-Type Gas Turbines to Substantially Lower Pressure Losses

Richard Golomb

Vivek Sahai
e-mail: vsahai@chengfluid.com

Dah Yu Cheng

Cheng Fluid Systems,
Mountain View, CA 94040

Many GE frame gas turbines have a unique 90-deg tailpipe exhaust system that contains struts, diffusers, and turning vanes. As confirmed in a recent report by GE and other authors, it is known in the industry that this tailpipe design has large pressure losses. In this recent report a pressure loss as high as 60 in. of water (0.15 kgs/sqcm) was cited. Due to the flow separations they create, the report indicates that the struts can cause very high-pressure losses in the turbine. The report also states that these pressure losses can vary with different turbine load conditions. Cheng Fluid Systems and Cheng Power Systems have conducted a study aimed at substantially reducing these pressure losses. Flow control technology introduced to the refinery industry, i.e., the Cheng Rotation Vane (CRV) and the Large Angle Diffuser (LAD) can be used to mitigate the flow separation and turbulence that occurs in turns, bends, and large sudden expansions. Specifically the CRV addresses the flow separations in pipe turns, and the LAD addresses the flow problems that occur with large sudden expansion areas. The paper will introduce the past experience of the CRV and LAD, and will then use computer simulations to show the flow characteristics around a new design. First, the study meticulously goes through the entire GE exhaust system, starting with the redesign of the airfoil shape surrounding the struts. This new design has a larger angle of attack and minimizes the flow separations over a much wider operating range. Second, the pros and cons of the concentric turning vanes are studied and it is shown that they are more flow restrictive, rather than flow enhancing. Third, it is shown that the highly turbulent rectangular box-type exhaust ducting design, substantially contributes to high noise levels and pressure losses. In this paper a completed design will be shown that incorporates a new airfoil shape for the struts, and by using CRV flow technology in combination with the LAD flow technology, the pressure recovery can be enhanced. If the pressure losses could be reduced by 40 inches of water (0.10 kgs/sqcm), the turbine efficiency could be increased by 5%, and the power output could be increased by 6%. [DOI: 10.1115/1.1515335]

Introduction

With the current need for more efficient power generation cycles, the designs of many gas turbine exhaust systems are being examined in order to try and improve the turbines performance. An improvement in the exhaust system can lead to lower pressures at the turbine outlet. This lower pressure then translates into the gas turbines higher output, efficiency, and lower heat rate. It is the achievement of this goal that has led us to develop an improved design for the GE frame engine gas turbine exhaust system.

The current design of most GE frame-type gas turbines have a unique 90-deg turn in their tailpipe exhaust system, that contains struts, turning vanes, diffusers, and a rectangular exhaust plenum. The schematic of this system showing the exhaust gas path is shown in Fig. 1. After the gas exits the last stage of the turbine, it enters into an expanding diffuser area. The gas then passes over a series of struts. Inside the struts are posts that help transmit the weight load to the journal bearing. Downstream of the struts the gas continues to slow down in the diffuser, and then it makes a sharp 90-deg turn into the exhaust plenum, guided into this area by a series of concentric turning vanes. These turning vanes are used to help deflect the flow from the axial to the radial direction. The gas flow then rapidly expands into the rectangular shaped exhaust plenum, which is located immediately downstream of the turning vanes.

It is known in the industry that this type of tailpipe design causes separated flows, and flow turbulence, which can account for higher-pressure losses, high noise levels, and decreased turbine efficiency. As confirmed in a recent report by GE and other authors [1], pressure losses as high as 60 in. of water (0.15 kg/sqcm) were cited. The report indicated that the position and design of the struts cause very large pressure losses, due to the flow separations that they create. In a GE Frame Gas Turbine, as the swirling gas leaves the turbine and passes through and over the struts (these struts were not designed to account for any swirling flow), they separate and the flow turbulence increases. Downstream of these struts the gas then makes a sharp 90-deg turn out of the turbine, and the upper half of the gas is guided through concentric turning vanes into the exhaust plenum, while the lower half of the gas has to find its own flow path into the exhaust plenum. The report showed that these concentric turning vanes account for another pressure drop within the exhaust system, and they further increase the flow turbulence [1]. Finally, the exhaust gas as it passes through the turning vanes, and enters into the sudden expansion of the exhaust plenum, is subject to further separation, reverse flows, and increased turbulence. The report showed that these losses can vary widely under different turbine load conditions [1].

Contributed by the International Gas Turbine Institute and presented at the International Gas Turbine and Aeroengine Congress and Exhibition, Amsterdam, The Netherlands, June 3–6, 2002. Manuscript received by the IGTI, October 9, 2001. Paper No. 2002-GT-30149. Review Chair: E. Benvenuti.

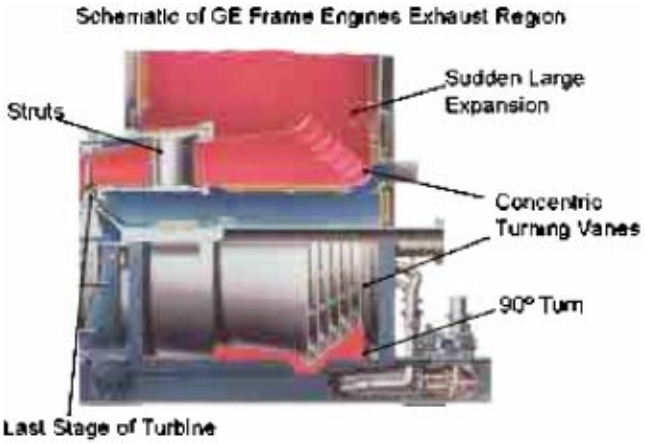

Fig. 1 A schematic of GE frame gas turbine showing the exhaust gas path and areas where large pressure losses occur

Cheng Fluid Systems and Cheng Power Systems have conducted a study aimed at substantially reducing these pressure losses and improving the exhaust system performance. This can be accomplished by using rotation vane technology and source and sink concepts to design an advanced diffuser. This flow turbulence control technology has been introduced to the refinery and chemical industry almost a decade ago [2]. The flow turbulence control technology can mitigate the flow separation and turbulence caused by turns, bends, and large sudden expansions, and can reduce the large pressure losses associated with these undesirable flow patterns [3].

From this previous study of the current GE tailpipe system design, four different areas were identified where flow improvements could be made. These areas are the strut areas, the 90-deg turn area, the concentric turning vane area, and the sudden expansion into the rectangular plenum area. All four of these areas in the current design produce turbulence in the flow that cause noise, vibration, and flow separation, all of which result in a great loss of total pressure. This high-pressure loss also reduces the expected turbine power output. By making certain design modifications and using the existing rotational transformation flow technology (CRV) and sudden expansion control technology (LAD), this excessive flow turbulence and pressure loss can be minimized, and the power output and efficiency of the turbine can be increased [3].

Objective of New Design

To make a GE frame gas turbine more efficient, an advanced combined cycle such as the ''Advanced Cheng Cycle'' can be used [4]; but high-pressure losses already associated with the current tailpipe design will increase even more; when an advanced combined cycle is used. Therefore, to make an advanced combined cycle work at its highest efficiency, it is absolutely necessary to reduce and keep to a minimum the pressure losses occurring in the gas turbines exhaust system. Based upon a GE frame cycle deck calculation, if the pressure losses are reduced by 40 in. of water (0.10 kgs/sqcm), the turbine efficiency can be increased by up to 5.8%, and the power output can be increased by up to 6.2% (at ISO conditions). To accomplish this, design improvements will have to be made to the struts, 90-deg turn, turning vanes, and sudden expansion areas of the exhaust tailpipe, to try and minimize these pressure losses, increase the flows, reduce the noise and vibration, and increase the turbines efficiency. The new design concepts are described below. They show how flow improvements can be made in the areas of the struts, 90-deg turn, turning vanes, and sudden expansion.

Improvement of Flow in the Strut Region

The current strut design consists of a metal sheet covering a post and it has been shown that this design causes flow turbulence which leads to high pressure losses. The shape of the struts show an airfoil design with the following characteristics: a thickness to cord length ratio of 18%; the strut is positioned at a 15-deg angle with respect to the turbines axis; and the strut has a chord length to space between the tips ratio (known as solidity) of 1. (A high value of solidity increases the flow interaction between struts and thus creates a flow channel for the exhaust gas to go through.) If the solidity of the struts can be increased (which can be achieved by either increasing the chord length or decreasing the spacing between the struts), then the flow interaction between the struts can be increased and the angle at which ''stall'' occurs is delayed [5].

The computation fluid dynamics code STAR-CD software was used to analyze the strut design, in terms of effectiveness in controlling the different swirl angles, and minimizing the drag and flow separation effects. This code is used to calculate the flow field around the struts and in a large expansion, using the industry standard Reynolds number k-ε model. This turbulence model was chosen based on the wide experience the industry has had with this model and software.

As the flow exits the last stage of the turbine it has a swirling flow angle. The angle that the flow develops depends on the load

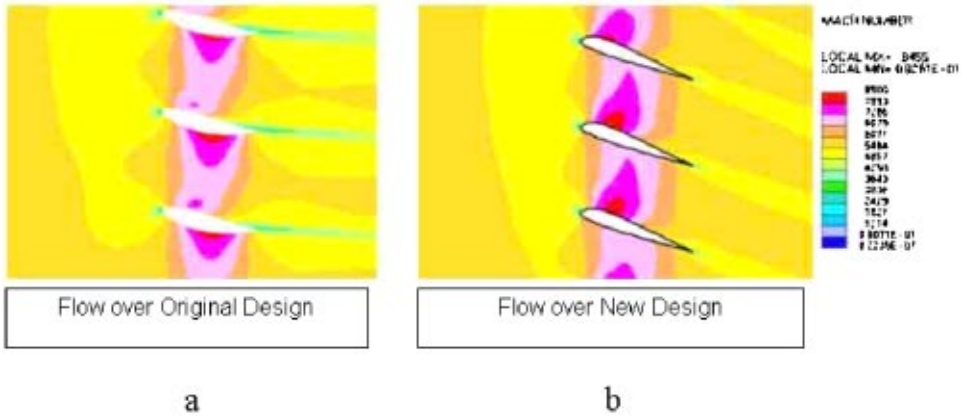

Fig. 2 Differences in flow behavior between (*a*) the current strut design, and (*b*) new strut design. The inlet conditions represent full speed full load operation. The turbulence caused by the current design leads to large pressure losses and removes the swirl that leads to large pressure losses downstream of the struts.

conditions. For the frame 9E gas turbine this angle can vary anywhere from −50 to 14 deg [1]. (Positive swirl angles are clockwise and negative swirl angles are counterclockwise.) The swirling flow also leads to a flow separation and turbulence at the surfaces of the struts.

As the gas flows from the turbine blade area at full speed and full load conditions (see Fig. 2(*a*)), it passes through and over the current designed struts; the struts create a flow turbulence that is applied at right angles to the turbines axis. This flow turbulence leads to a flow separation from the outside walls of the struts. When this happens, the flow accelerates due to the reduction in the core-flow cross-sectional area, and this causes a high-pressure drop and flow non-uniformities to occur. The CFD results also show that the current strut design removes some of the swirl from the flow.

Several airfoil designs [6] were considered to improve the flow in this section. Each airfoil design was analyzed to determine which of their geometric shapes had the maximum angle of attack and lift characteristics, before stall occurred. Figure 2(*b*) shows the flow through a set of newly designed struts. These struts have the same maximum thickness as the original struts; and are positioned at a 15-deg angle with respect to the turbines axis. The new struts are 1.5 times longer (in the axial direction) than the old design and they will fit in the current design area, thus increasing the solidity by 50%. With this new design, the flow separations off of the surfaces of the struts and their trailing edge are minimized. This new strut design also preserves the swirl in the flow and it will be shown in the next section that the swirl in the flow can also be beneficial in helping the exhaust gas navigate the 90-deg sharp turn into the exhaust plenum.

Improvement of Flow Around the 90-Deg Turn

When a fluid flows through an elbow or curved conduit, the flow stream next to the outer radius of the turn must travel a longer distance than the flow stream near the center of the turn. When this happens, the pressure distribution within the flow becomes uneven and the fluid separates into numerous secondary flows that separate, swirl, rotate, and contain accelerated and reverse flows. Thus, the velocity pattern at the exit of the elbow becomes turbulent. This is the reason why a curved conduit will produce a greater pressure loss in a turn, than a straight section of pipe.

Rotation vanes are specifically designed so that they impart a gyroscopic motion to the flowing fluid that counteracts the gyroscopic motion in the fluid that is produced by the 90-deg turn. The guideline for the gyroscopic rotation is designed to make all the flow stream lengths constant throughout the pipe turn. This will allow the fluid to negotiate the 90-deg turn and exit the turn with a flat uniform velocity profile. The benefits of having a flat uniform velocity flow profile at the exit of the 90-deg turn are; elimination of most of the pressure drop through the 90-deg turn; no fluid turbulence; less noise; less vibration; and no fluid separation. The fluid rotation vanes turn the 90-deg turn into the equivalent of a straight length of conduit.

Experimental observations have shown how a flow rotation can remove fluid separation caused by a 90-deg turn. Water and air were used to verify the performance of the rotation vanes. Figure 3 shows water flowing in a piping system with test dyes in the flow stream. This flow visualization test was conducted in a 6-india (15.24 cm) elbow constructed of clear plastic. The flow in the figure is from left to right. Colored dyes were introduced through orifices upstream of the elbow entrance, so that the flow streamlines could be traced. Without rotation vanes there is fluid separation, turbulence, reduction of flow area, and a mixing of the dyes. Separation occurs off the inner and outer walls. To remove this flow turbulence and separation, a set of special designed rotation vanes are placed at the inlet of the elbow. With the rotation vanes there is a uniform flow at the end of the 90-deg turn without any inner mixing of the dyes and any flow turbulence. Rotation of the fluid has stopped at the exit of the elbow. Manometer measurements of the elbows wall static pressure distribution were also taken. The pressure readings showed an uneven pressure distribution when no rotation vanes were used, and that the inner radius of the elbow had a region of lower static pressure, while the outer radius of the elbow had a region of higher static pressure distribution. When rotation vanes were used the pressure was distributed evenly throughout the entire 90-deg turn. Figures 3 and 4 show the benefits of using vanes to pre-rotate the fluid. The rotation allows the innermost stream to be routed to the outer extreme at the elbow exit and at the same time the outermost stream is routed to the innermost layer. The pre-rotation results in equal length streamlines and removes the problem of fluid particle acceleration.

Figure 4 shows the measured cross-stream velocity profiles for an elbow in which air was used as the fluid in a 2-in-dia (5.08 cm) short radius elbow, at a Reynolds number of 100,000. Measurements of the flow were made at the exit of the elbow and at five additional positions each 0.25 diameters downstream from the proceeding position. For the case without rotation vanes, a separated flow can be seen at the inner wall and at 0.25 diameters downstream. A strong velocity gradient is also seen downstream of the elbow with the highest velocities near the outer wall. The velocity gradient diminishes slightly because of the mixing of the fluid, but is still evident at 1.25 diameters downstream of the elbow. The velocity profiles with the rotation vanes show that no separated flow exists and the flow at 1 diameter downstream of

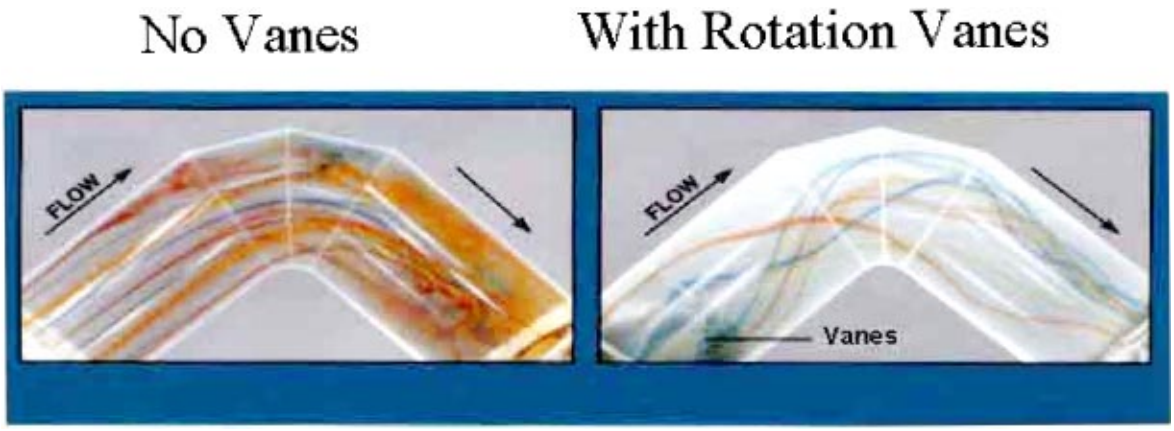

Fig. 3 When water flows through an elbow, separation and turbulence occur. Using specially designed vanes to pre-rotate the fluid, the fluid negotiates the turn with all streamlines traveling in equal flow paths.

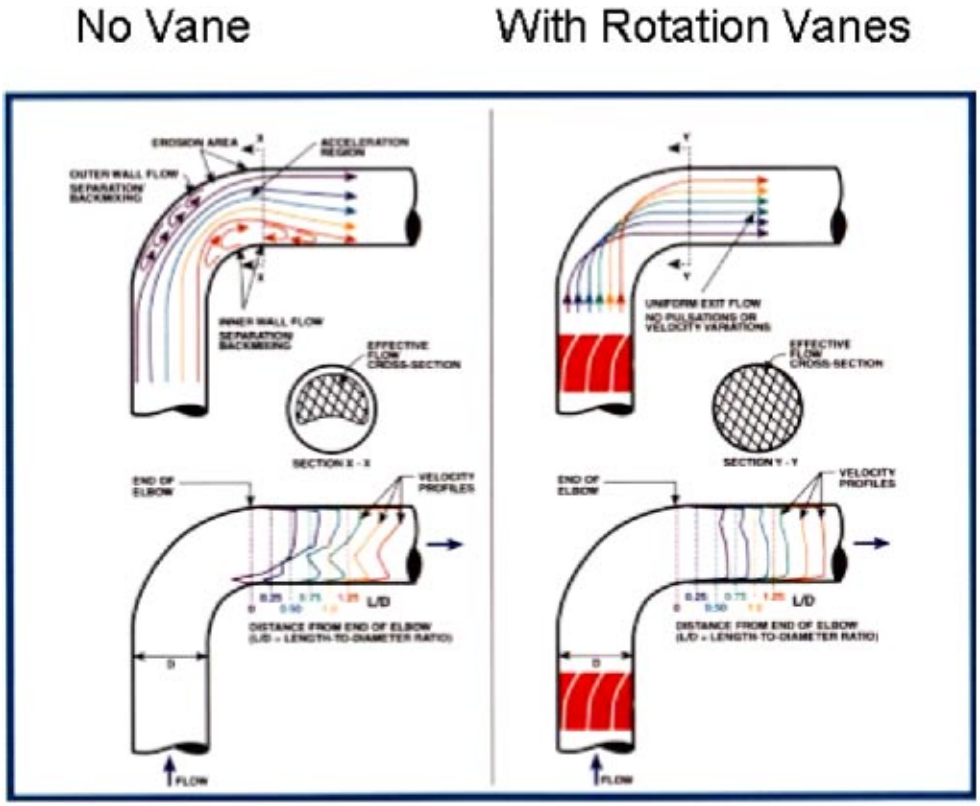

Fig. 4 In a plain elbow with air flowing through, a skewed velocity profile results at the exit. With pre-rotation vanes, there is a flat velocity profile.

the elbow is nearly uniform. These same elbow flow results are obtained when the turning vane technology is used on the inside of a vertical pump at the pumps ninety degree turn discharge area. The turning vanes have the vertical pumps drive shaft going through its center, just as the drive shaft for the turbine would be positioned.

The struts will be redesigned around the turbines drive shaft, using the rotational vane concept to keep the positive swirling flow that exists at full load conditions. This flow rotation will neutralize the swirl produced by the 90-deg turn, resulting in a uniform, constant velocity, non-turbulent flow throughout the 90-deg turn.

Redesign of the Concentric Turning Vanes

Downstream of the struts the exhaust gas is guided by seven concentric turning vanes (which are part of the gas turbines exhaust framework), as it enters the sudden expansion of the exhaust tailpipe. These seven turning vanes are flow restrictive, in that they guide the gas from the back wall of the tailpipe exhaust ducting system and into the back end of the sudden expansion of the tailpipe exhaust ducting. This causes additional flow turbulence and pressure losses, as the turning vanes are not aligned with the flow. By removing all of the interior turning vanes and shaping the sharp inner corner of the exhaust tail pipe to act as an elbow, and repositioning and reshaping the outer most turning vane to conform to the flow path of the outer walls, the flow turbulence can be reduced by a large amount. This was confirmed by calculating the hydraulic diameter ($Dh=4A/P$) (4 times the cross-sectional flow area (A) divided by the wetted perimeter (P)) of the seven concentric turning vanes and the hydraulic diameter of the new design. The calculations showed that the effective flow area of the new design could be increased by 94%, when the interior vanes are removed and the corners are reshaped.

Redesign of Expanding Flow Area Into Exhaust Duct

As the exhaust gasses leave the turbine and enter the sudden expansion of the exhaust plenum, excessive flow separation and back mixing occur. Because the current design forces all of the exhaust gases to the back end of the tailpipe, this leads to large flow separations, reverse and accelerated flows, high flow turbulence, high pressure drops, and increased noise, as the gases reach the sudden expansion. To control this flow turbulence without excessive pressure losses, a maximum expansion angle of 15 deg must be maintained. In most ducting systems including the exhaust ducting for the frame gas turbine systems, this would require an extremely long length of space. Current sudden expansion control technology can correct this problem by using overlapping truncated cones, positioned so that their common focal point is in the center of the smaller originating area (the source). This design is based upon a mathematical point source method, which will cause the exhaust gas to act like it was being issued from a central point in a conical pattern of the desired expansion angle. Figure 5 shows computer simulation results using STAR-CD, showing flow turbulence and back mixing in a sudden expansion area without any cones, and a complete uniform, constant velocity, nonturbulent flow when cones are used. To achieve this will require that this point source concept be placed in the immediate expansion area after the 90-deg turn, before the rectangular exhaust plenum area. Experimental tests have shown that if the theoretical point source of the truncated cones is located within a solid body, it will still produce a uniform constant velocity at the exit of the cones. The resulting benefits of using a sudden expansion control design for this area of the tailpipe will be, a uniform flow of gas, with a constant velocity, and with maximum pressure recovery within the expansion.

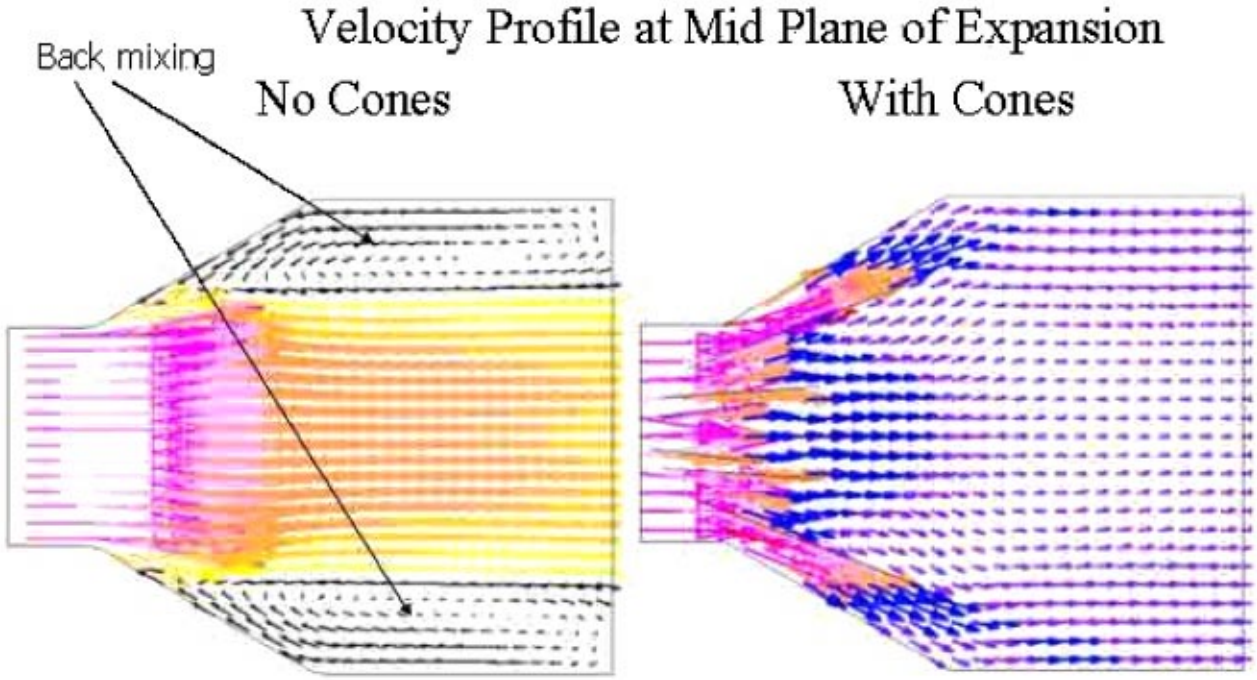

Fig. 5 Without cones in a large expansion, significant back mixing occurs with a high velocity jet in the center. With overlapping concentric cones, the velocity profile through the expansion becomes uniform.

Conclusions

This paper has analyzed the current GE frame 7 exhaust design system. Four areas were identified where large pressure losses can occur. These are the strut areas, 90-deg turn area, concentric turning vane area, and the sudden expansion into the rectangular plenum area. Four changes to the design have been suggested to improve performance in these areas. By making these four changes in the tailpipe design of GE frame gas turbines (see Fig. 6), the flow turbulence can be minimized, while pressure losses can be recovered, and turbine efficiency can be increased. This can be accomplished by creating a new airfoil shape for the struts, which improves their aerodynamic characteristics, and by using rotational flow technology to minimize the flow separations and preserve the flow swirl as the gases enter into the 90-deg turn of the exhaust plenum. Also, by eliminating the interior concentric turning vanes and modifying the internal and external corners of the exhaust system, the flow will remain uniform as it makes the 90-deg turn and enters the exhaust plenum. By changing the outer diffuser walls to form an elbow, a flow path for both the upper-half and lower-half gases can be defined. This elbow will fit into the existing exhaust space and can be easily removed to allow for servicing. Finally, by modifying the transition ducting from the exhaust tailpipe to the exhaust ducting using the sudden expansion control technology, the gas flow can be kept uniform as it enters the large expansion of the rectangular exhaust duct. By making these changes in the exhaust tailpipe design, total pressure recovery will be enhanced and current pressure losses in the tailpipe can be reduced.

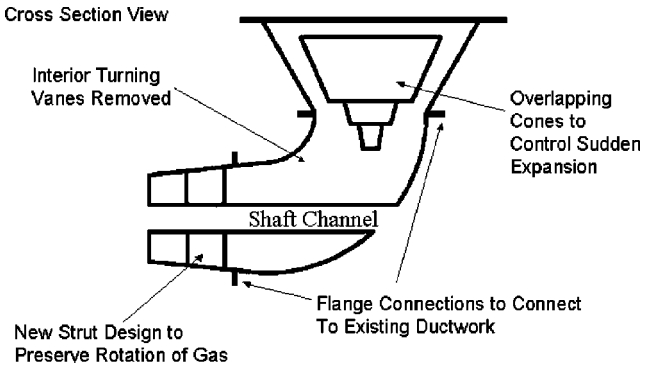

Fig. 6 This is a schematic of a new tailpipe design that fits within the current space of the old design shown in Fig. 1. The struts will be modified to the new shape shown in Fig. 2. Downstream of the struts the wall and turning vanes will be replaced with an elbow.

Nomenclature

CRV = Cheng Rotation Vane
LAD = Large Angle Diffuser
ISO = International Standards Organization
Dh = hydraulic diameter ($Dh = 4A/P$)
A = cross-sectional flow area
P = wetted perimeter
GE = General Electric
CFD = computation fluid dynamics
STAR-CD = software used to analyze strut design
k-ε = industry standard turbulence model used in STAR-CD calculations

References

[1] Sultanian, B. K., Nago, S., and Sakamoto, T., 1999, ''Experimental and Three-Dimensional CFD Investigation in a Gas Turbine Exhaust System,'' ASME J. Eng. Gas Turbines Power, **121**(2), pp. 364–374.
[2] Kosla, L., and Mutsakis, M., 1992, ''New In-Pipe Flow Conditioner Cuts Fluid Problems,'' Chemical Engineering Magazine, Sept.
[3] Sahai, V., and Golomb, R., 2000, ''Improve Condenser Water Flow To Improve Cash Flow,'' Power Magazine, **144**(4), July/Aug., p. 62.
[4] Nelson, A., Vaezi, V., and Cheng, D. Y., 2002, ''A 50% Plus Mid Range Advanced Cheng Cycle,'' IGTI Turbo Expo, Amsterdam, The Netherlands, June 3–6.
[5] Emery, J. C., Herrig, L. J., Erwin, J. R., and Felix, A. R., 1958, ''Systematic Two-Dimensional Cascade Tests of NACA 65-Series Compressor Blades at Low Speeds,'' NACA Technical Report 1386.
[6] Jacobs, E. N., and Sherman, A., 1939, ''Airfoil Section Characteristics as Affected by Variations of the Reynolds Number,'' NACA Technical Report 586.

Evolution of Upstream Propagating Shock Waves From a Transonic Compressor Rotor

Anil Prasad
Aerodynamics Division,
Pratt and Whitney Aircraft Engines,
East Hartford, CT 06108

The evolution of upstream propagating shock waves from the isolated transonic compressor designated NASA Rotor-35 is examined numerically. Results from the numerical simulations are compared with those from a semi-analytical two-dimensional model based on the nonlinear acoustic interaction of shock waves in the axial-tangential plane upstream of the rotor. The evolution determined from a two-dimensional viscous computational solution is found to agree well with the semi-analytical prediction and confirms that shock wave evolution is a primarily inviscid phenomenon. Radial variations are found to increase the rate of decay of the shock wave amplitude in comparison to the prediction from the semi-analytical two-dimensional model. The velocity field from the three-dimensional viscous solution compares well with experimental measurements, indicating that the initial shock strength and shock wave evolution immediately upstream of the rotor blade leading edge are accurately captured. The upstream-propagating shock system is found responsible for nearly 20% of the total loss attributable to the rotor, and is consistent with earlier transonic airfoil cascade studies. The axial decay rate of the upstream induced circumferential static pressure distortion is found to be an order of magnitude slower at spanwise locations with supersonic relative inlet Mach numbers than those at which it is subsonic. As a consequence of this slower decay rate, it is found that the axial gap to the upstream stator would need to be about twice that used for subsonic blade sections.
[DOI: 10.1115/1.1516813]

Introduction

In order to meet the demand by airline customers for more reliable engines with reduced parts count, while maintaining specific fuel consumption as well as thrust-to-weight ratio, aircraft engine manufacturers have been motivated to develop aggressive high-pressure ratio compressors. The required pressure rise is typically achieved in such compressors through the use of higher wheel speeds, which in turn leads to stages that are characterized by high relative inlet Mach numbers. Indeed, in many modern high-pressure ratio compressors, the first and second rotor stages often operate in either the transonic or supersonic regime. The flow field in transonic/supersonic rotors is dominated by a shock that manifests itself in the blade passage. The precise shape and location of the shock depend on the blade leading edge diameter and the operating point on the speedline, although for mass flow rates lower than that corresponding to peak efficiency, the detached shock positions itself in the unguided portion of the blade passage. The shock, which provides a reasonably efficient mechanism through which compression can occur, is responsible for the bulk of the pressure rise that is attained in transonic rotors. Regions of expansion waves develop between adjacent shocks; a necessary condition for periodicity in the circumferential direction is that the change in flow angle across a shock wave is exactly compensated for by a commensurate negative change in angle across its companion expansion wave, as indicated by Ferri [1]. The shock wave system generated by the rotor is not confined to the blade passage; rather, it propagates upstream, unless supersonic axial velocities are encountered. The interaction of rotor-generated shocks with the upstream stator flow field can be potentially detrimental not only to the aerodynamic performance of the stator, but also to its structural integrity, a point that has most recently been experimentally investigated by Probasco et al. [2] using an inlet guide vane with no steady aerodynamic loading. Therefore, an important issue in the design of transonic compressor stages is the management of the shock system. This makes it necessary to accurately and reliably predict the initial shock generated in the blade passage as well as its upstream evolution, and provides the motivation for the present study.

From the perspective of a numerical simulation, the shock wave system described in the previous paragraph could, in general, propagate upstream through the inlet of the rotor computational domain; the propagation of nonlinear waves through a domain boundary poses a challenge to most computational fluid dynamics solvers, and care needs to be exercised in handling such situations in the most physically reasonable manner. Giles [3] has demonstrated the systematic derivation of boundary conditions for propagating waves—commonly referred to as ''nonreflecting boundary conditions''—that are exactly applicable to linear waves in two-dimensional (2-D) flow; although one may continue to utilize the same nonreflecting boundary conditions for the simulation of three-dimensional (3-D) flow fields, spurious reflections can occur at the boundary if the waves are significantly nonlinear. The transonic rotor flow field is further complicated by the fact that at spanwise locations near the hub, the flow on the suction surface either remains subsonic or decelerates from a supersonic state to a subsonic one in the absence of a shock. Consequently, it is not atypical for the rotor shock to be present only in the outer 75% of blade span, resulting in a flow field that may vary quite significantly in the spanwise direction.

The interaction between closely spaced airfoil rows is an important aspect of the flow field in multi-stage turbomachine simulations. Much work has been carried out on rotor-stator interaction, that has largely focussed on the dynamics of wakes impinging on a downstream airfoil row. The transport of wake fluid from a stationary to a rotating airfoil row is an inherently unsteady process and can only be correctly computed using time-accurate simulations. It is this transport that is responsible for the migration of hot fluid from a stator wake towards the pressure surface of the downstream rotor (Kerrebrock and Mikolajczak

Contributed by the International Gas Turbine Institute and presented at the International Gas Turbine and Aeroengine Congress and Exhibition, Amsterdam, The Netherlands, June 3–6, 2002. Manuscript received by the IGTI, October 28, 2001. Paper No. 2002-GT-30356. Review Chair: E. Benvenuti.

Table 1 Summary of topologies and grid discretizations ($i \times j \times k$) for numerical simulations of the NASA Rotor-35 flow field

Case name	Topology	Discretization
2-D inviscid	H grid	$131 \times 49 \times 3$
2-D viscous	O-H grid	$123 \times 49 \times 3$ (for H grid)
		$225 \times 33 \times 3$ (for O grid)
3-D inviscid	H grid	$157 \times 49 \times 21$
3-D viscous	O-H grid	$169 \times 33 \times 81$ (for H grid)
		$189 \times 33 \times 81$ (for O grid)
		$95 \times 17 \times 17$ (for tip grid)

[4]). Transonic compressor rotors introduce another source of unsteadiness between adjacent airfoil rows, through the upstream propagation of rotor-generated shock waves. Since this phenomenon is also basically unsteady, the evolution of shock waves through the rotor computational domain and into that of the upstream stator is critical for predicting the performance of the stator. In the absence of time-accurate multi-stage simulations, some measure of the imposed circumferential distortion generated by a transonic rotor can be obtained from steady isolated rotor simulations, so that preliminary design considerations in a multi-stage environment can be formulated.

This paper commences with an evaluation of the rate of decay of rotor-generated shock waves as predicted by a contemporary second-order Navier-Stokes/Euler solver. The evaluation is performed by making comparisons with a model based on the nonlinear acoustical interaction of shock waves in the axial-tangential plane upstream of the rotor. Attention is then directed to the static pressure distortion induced by the transonic rotor, its variation with distance upstream from the rotor leading edge, and its impact on the issue of axial gapping in high-speed machines.

Computational Details

The flow solver has been described at length by Ni [5] and Davis et al. [6], and been carefully validated in the work of Ni and Bogoian [7], Ni and Sharma [8] and Davis et al. [9]. It utilizes a Lax-Wendroff/multiple grid procedure to compute solutions of the Reynolds-averaged Navier-Stokes (RANS) equations on a structured discretization of the flow field. The algorithm has second-order spatial accuracy and uses a central difference approach for the spatial derivatives with second and fourth-order smoothing for stability. The latter is especially critical in the vicinity of shocks, where nonphysical oscillatory behavior may otherwise occur. The condition of no-slip is implemented at the solid boundaries which are constrained to be adiabatic, and the non-reflecting boundary conditions of Giles [3] are imposed at the inlet and exit of the computational domain.

The solver is normally used to compute the viscous flow field in a 3-D geometry for which purposes an O-H grid topology is used, with a gridded tip clearance gap and turbulence closure being achieved through the use of the k-ω model (Wilcox [10]). The solver may also be used in an inviscid (Euler) mode by enforcing a zero viscous force on all solid boundaries. The inviscid solutions described here for the 3-D geometry are carried out with no tip clearance and an H-grid topology. Finally, the computational solver can be executed on 2-D cascade geometries in both the inviscid and viscous modes; an H-grid topology is utilized for the inviscid cascade simulations and O-H grids are used for the viscous computations.

Computational simulations of the NASA Rotor-35 flow field were performed with the grid discretizations shown in Table 1. The inlet of the domain was located about 2.25 rotor tip axial chord lengths upstream of the leading edge at the hub for the 3-D Navier-Stokes simulation. The inviscid and cascade simulations were carried out with the domain inlet located some 4–5 chord lengths upstream of the rotor leading edge so as to ascertain the behavior of shock waves at large distances from the rotor. The flow field was examined at the peak efficiency condition, which occurs at an inlet corrected mass flow rate of 17.3 kg/s. The viscous and inviscid 3-D simulations were converged to this mass flow rate. In the 2-D cascade simulations, performed on the midspan section of NASA Rotor-35, the exit static pressure was adjusted to best duplicate the midspan pressure distribution obtained from the 3-D viscous calculation.

Nonlinear Model for the Propagation of Shock Waves

The present section is devoted to the brief description of a semi-analytical model based on nonlinear acoustics, which provides a basis for comparison with results from the viscous and inviscid computational solutions.

The problem of shock wave radiation from a 2-D supersonic ducted rotor in an inviscid flow was first addressed by Morfey and Fisher [11]. Employing results from the work of Rudnick [12] on the attenuation of an N-shaped repeated sawtooth shock wave, they predicted the shock strength as a function of axial distance from the leading edge of the rotor. This one-dimensional evolution, derived assuming the occurrence of a weak shock, depends on the initial shock strength as well as the far upstream relative and axial Mach numbers. Morfey and Fisher also derived an expression for the attenuation of these waves propagating in the 2-D axial-tangential plane upstream of the rotor, without the restriction of the weak shock assumption. They demonstrated that the wave evolution predicted by the 2-D method with the caveat of a weak shock, agrees very well with that predicted by the one-dimensional method. In what follows, the complete expression is presented assuming a 2-D evolution with no restriction on shock strength. Under these conditions, the upstream evolution of shock waves is governed by the expression

$$\frac{x}{\tau} = \frac{2\gamma}{\gamma+1}\cos\phi(\sin\phi - \mathrm{M}_x)\left(\frac{1}{\Pi} - \frac{1}{\Pi_0}\right)\times \left[1+\left(\frac{\gamma+1}{4\gamma}\frac{\sin\phi}{\sin\phi-\mathrm{M}_x}\right)^2\frac{\Pi^3}{\Pi_0}\right]^2 \tag{1}$$

where x is the distance from the rotor leading edge, τ is the tangential spacing of the blade, γ is the ratio of specific heats for the gas and Π is the shock strength defined as

$$\Pi = \frac{p^+ - p^-}{\frac{1}{2}(p^+ + p^-)} \tag{2}$$

with p^- and p^+ being the static pressure upstream and downstream of the shock, respectively. The value of shock strength at the initial shock location is labeled Π_0. The far upstream relative Mach number, $\mathrm{M}_{\mathrm{rel}}$, and the axial Mach number, M_x, are used to define the quantity ϕ according to the relation

$$\tan\phi = \frac{\mathrm{M}_x + \mathrm{M}_\theta\sqrt{(\mathrm{M}_{\mathrm{rel}}^2 - 1)}}{\mathrm{M}_\theta - \mathrm{M}_x\sqrt{(\mathrm{M}_{\mathrm{rel}}^2 - 1)}} \tag{3}$$

where the tangential Mach number is calculated from $\mathrm{M}_\theta = \sqrt{\mathrm{M}_{\mathrm{rel}}^2 - \mathrm{M}_x^2}$, assuming axial inlet flow and $\mathrm{M}_x < 1$. It can be shown that Eq. (1) reduces to a quartic equation in Π which, when solved numerically for various values of x/τ, results in the shock strength as a function of axial distance.

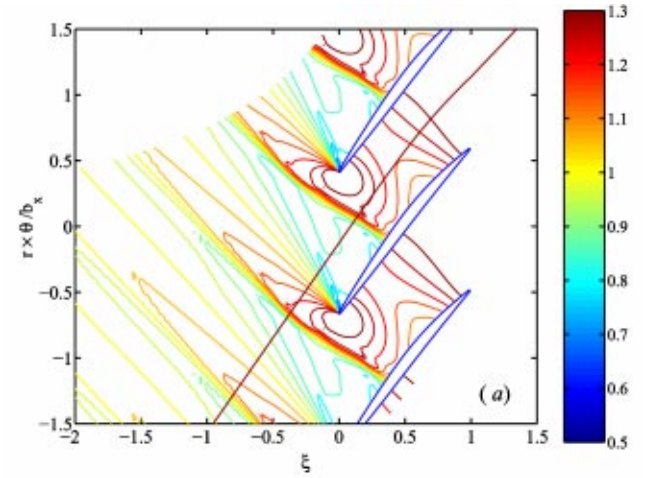

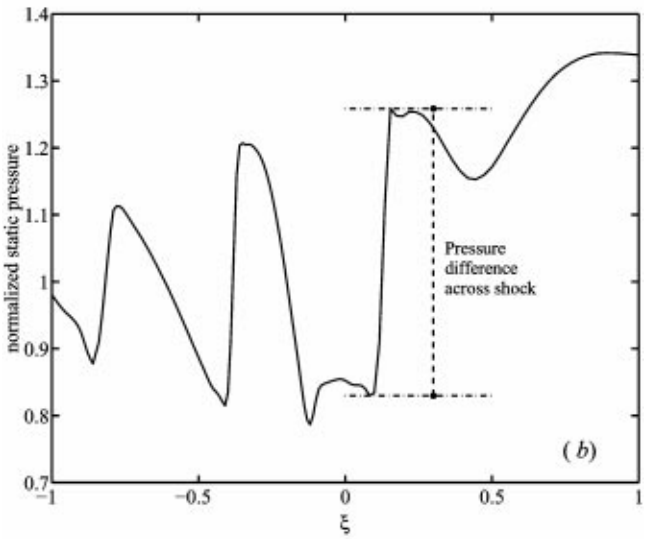

Fig. 1 Locus of the passage centerline overlayed on contours of normalized static pressure in (*a*), and the variation of static pressure along the passage centerline in (*b*), for the 2-D inviscid computation

For the case of weak shocks, $\Pi \ll 1$, the squared term in Eq. (1) reduces to unity and the equation for shock decay can be directly computed from

$$\Pi = \Gamma \frac{\mathcal{F}}{x^*} \times \left(1 + \Gamma \frac{\mathcal{F}}{x^*} \frac{1}{\Pi_0} \right)^{-1} \tag{4}$$

where $\Gamma = 2\gamma/(\gamma+1)$, $x^* = x/\tau$ and the function $\mathcal{F} = \mathcal{F}(\mathrm{M_{rel}}, \mathrm{M}_x)$ is given by

$$\mathcal{F} = \frac{\sqrt{(\mathrm{M}_{\mathrm{rel}}^2 - 1)}}{\mathrm{M}_{\mathrm{rel}}^4} [\mathrm{M}_x \sqrt{(\mathrm{M}_{\mathrm{rel}}^2 - 1)} - \mathrm{M}_\theta]^2 \tag{5}$$

Equation (4) indicates that for large values of $x^* \Pi_0 / \mathcal{F}$, the evolution is given by

$$\Pi = \frac{2\gamma}{\gamma+1} \left(\frac{\mathcal{F}}{x^*} \right) \tag{6}$$

implying that the shock strength decays as x^{-1} at large distances from the rotor. In contrast, it is generally known that for subsonic conditions, disturbances decay exponentially with axial distance from a blade row. It is the nonlinearity of upstream propagating shocks that sustains them for larger distances from their source.

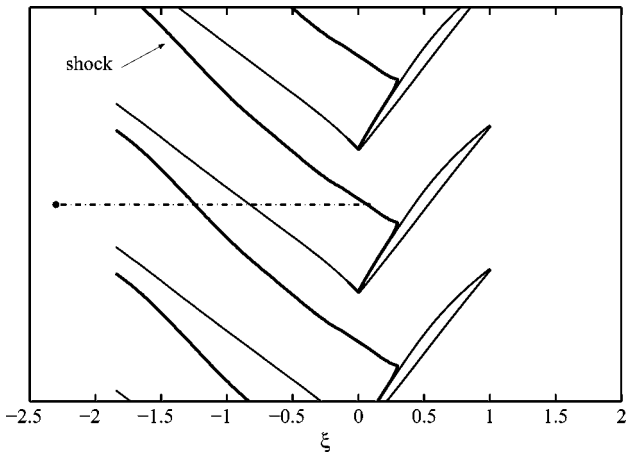

Fig. 2 Definition of axial line along which static pressure is interpolated, with contours of unit relative Mach number

Comparison With Two-Dimensional Simulations

Since the model of Morfey and Fisher is based on 2-D inviscid flow, a reasonable starting point would be to make comparisons with results from inviscid cascade simulations. These inviscid calculations were performed using a grid that was especially refined in the region upstream of the rotor leading edge so as to minimize numerical dissipation of propagating shocks.

The model of Morfey and Fisher requires as input the initial shock strength, the inlet relative Mach number and the inlet axial Mach number. The extraction of these quantities from the computational solution is now described.

Estimation of Initial Shock Strength

The initial shock strength, Π_0, required by the nonlinear model is determined from the static pressure variation along the passage centerline. The passage centerline is defined as one that lies circumferentially midway between the suction and pressure surfaces of the airfoils defining the passage. Upstream and downstream of the blade passage, the centerline is constructed by linear extrapolation at the leading and trailing edge metal angles respectively. The variation of quantities along this centerline represents a quasi-one-dimensional evolution through the passage.

In Fig. 1(*a*) is presented the computed static pressure (p) normalized by its inlet circumferentially averaged value, together with the passage centerline; the radial and angular circumferential coordinate are denoted r and θ, respectively. The axial variation of the normalized static pressure along the passage centerline is shown in Fig. 1(*b*); the axial distance from the rotor leading edge (x) is normalized by the rotor axial chord (b_x) and denoted $\xi = x/b_x$. The shock, identified by the rapid increase in pressure near $\xi = 0.1$, is assumed to support the pressure difference indicated on the figure. It may be noted that the indicated pressure difference is determined by traversing the passage in a direction locally normal to the shock. The initial shock strength is then computed using Eq. (2).

Prediction of Shock Wave Amplitude

The model of Morfey and Fisher requires an estimate of the average relative Mach number and the axial Mach number far upstream of the rotor. Estimates of these two quantities are obtained by circumferentially averaging their constituents at the domain inlet. The averaging was carried out in the manner specified by Dring and Oates [13], with the axial velocity and temperature being density-weighted and the tangential velocity being mass-weighted.

These average Mach numbers at the inlet as well as the initial shock strength from Fig. 1(*b*) and Eq. (2) are now inserted into the

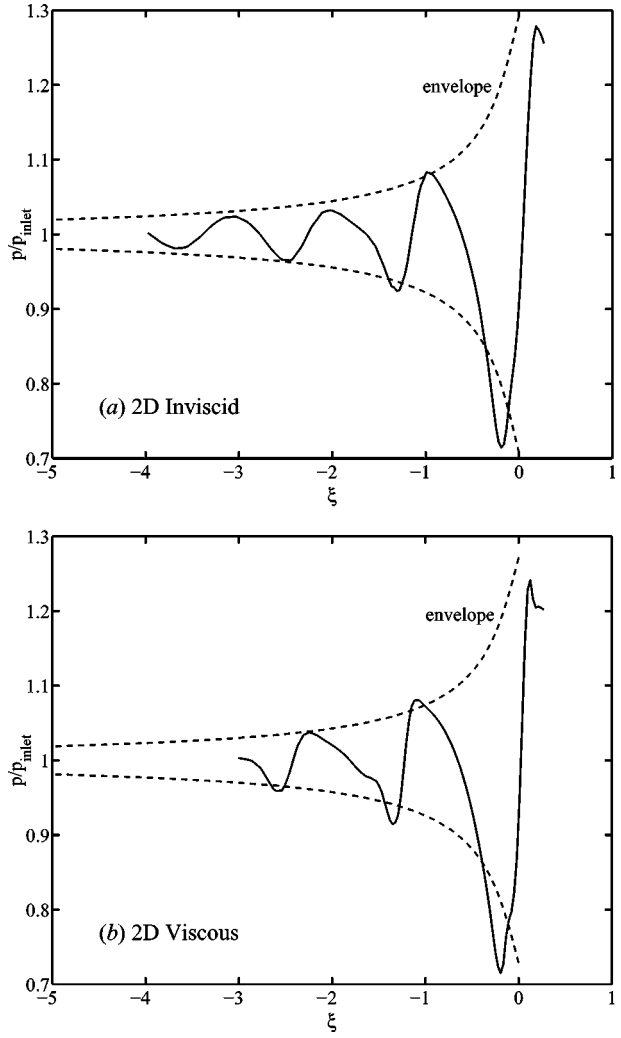

Fig. 3 Axial pressure variations from the 2-D inviscid and viscous simulations are shown as solid lines, with the corresponding envelopes predicted from the semi-analytical model being shown with broken lines

evolution Eq. (1). The quartic equation, solved numerically at several selected values of x, yields the variation of $\Pi=\Pi(x)$, along a line such as that shown in Fig. 2. The amplitude envelope at a given location is computed from the shock strength using Eq. (2) with the denominator being taken as the undisturbed static pressure far upstream of the leading edge, $p_{-\infty}$, such that

$$\Delta p(x)=p^{+}-p^{-}=\Pi(x)\times p_{-\infty} \tag{7}$$

The broken line in Fig. 3(*a*) is the prediction of the shock wave amplitude from the 2-D model of Morfey and Fisher. An equivalent variation was computed using their one-dimensional result and was found to be marginally different in the immediate vicinity of the shock and virtually identical everywhere else. The variation in pressure along the axial line shown in Fig. 2 is determined from the numerical solution by interpolation and plotted in Fig. 3(*a*) as the solid line. The interpolated pressure oscillation from the computational solution is found to agree remarkably well with the envelope predicted from Morfey and Fisher, and provides confidence in the ability of the underlying inviscid flow solver to capture the evolution of upstream propagating shock waves in a 2-D flow. Although a systematic grid resolution study was not conducted, it is found that typically 3–4 points are sufficient to define the initial shock and that about 18 points are required to define one period of oscillation of the pressure variation along the passage centerline. It is this grid resolution that is maintained in the 3-D simulations described in the followling discussion.

The model of Morfey and Fisher implicitly assumes that the attenuation of shock waves emitted from a rotor is governed largely by inviscid effects. To verify the validity of this statement in the presence of viscosity, a 2-D viscous cascade simulation was conducted with an H-grid resolution away from the solid surfaces similar to that used in the inviscid simulations, and a well resolved O-grid surrounding the airfoil. The results from the viscous cascade simulations are interrogated in a manner identical to that described previously for the inviscid case. The axial variation of pressure from the viscous solution, shown in Fig. 3(*b*) as the solid line, is found to compare well with the envelope from the semi-analytical nonlinear model of Morfey and Fisher. This observation substantiates the original assumption of the model, that viscosity plays a minor role in the propagation of shock waves from a blade row.

Comparison With Three-Dimensional Simulations

The evidence, in the preceding section, of the good agreement between the nonlinear acoustical model of Morfey and Fisher and the 2-D viscous and inviscid cascade simulations provides confidence in the ability of the solver to capture the evolution of shock waves in the absence of spanwise variations. The remainder of the paper is concerned with the simulated flow field in the full 3-D geometry. Although the model of Morfey and Fisher is based on 2-D flow, it is expected that some insight will be gained by making comparisons with results obtained from the midspan computational plane of the 3-D simulation. This plane, with an inlet relative Mach number of 1.04, is selected so as to ensure that the direct effects of the endwall and tip clearance flow are negligible. The operations described previously for the calculation of initial shock strength and far upstream Mach numbers are directly applicable to the flow field on the midspan plane.

Before proceeding, it is appropriate to demonstrate the accuracy of the initial shock strength prediction from the 3-D Navier-Stokes simulations by making careful comparisons with experimental data. High-resolution laser-Doppler anemometer (LDA) measurements on the NASA Rotor-35 geometry have been carried out by van Zante et al. [14]. In particular, the ensemble-averaged axial velocity, v_x, and absolute tangential velocity, v_θ, are available at about 92% span. The relative total velocity, V_e, based on these measurements is defined according to

$$V_e=\sqrt{v_x^2+(v_\theta-r_e\Omega)^2} \tag{8}$$

where Ω is the angular speed of the rotor and r_e is the local radius at which the experimental measurement is made. Note that since the LDA system does not yield reliable flow velocities in the immediate vicinity of the blade, the experimental flow field exhibits ''gaps'' in these regions of the flow. By carefully shifting the computational grid blade coordinates nearest to the 92% span location in the azimuthal direction so that they lie to best approximation within these gaps, it is possible to determine the blade locations relative to the experimentally measured flow field. One may then interpolate V_e along the passage centerline (defined in a manner identical to that used in the foregoing) to make direct comparisons with computational results; to do so, a consistent total flow velocity, ignoring its radial component, is defined similarly from the computational results. The experimental data are found to lie between two consecutive computational (k) planes and in what follows the variation along the passage centerline on both these planes is displayed, since the flow displays some sensitivity to radial location at this spanwise location. The variation along the passage centerline of the total velocity normalized by the blade tip speed, U, is displayed in Fig. 4(*a*) and indicates that the initial shock near $\xi=0.15$ is captured to good accuracy by the simulation as is the expansion region near $\xi=-0.25$. It is interesting to note that the small overspeed near $\xi=-0.10$ visible in the measurements is resolved by the computation. The peak near

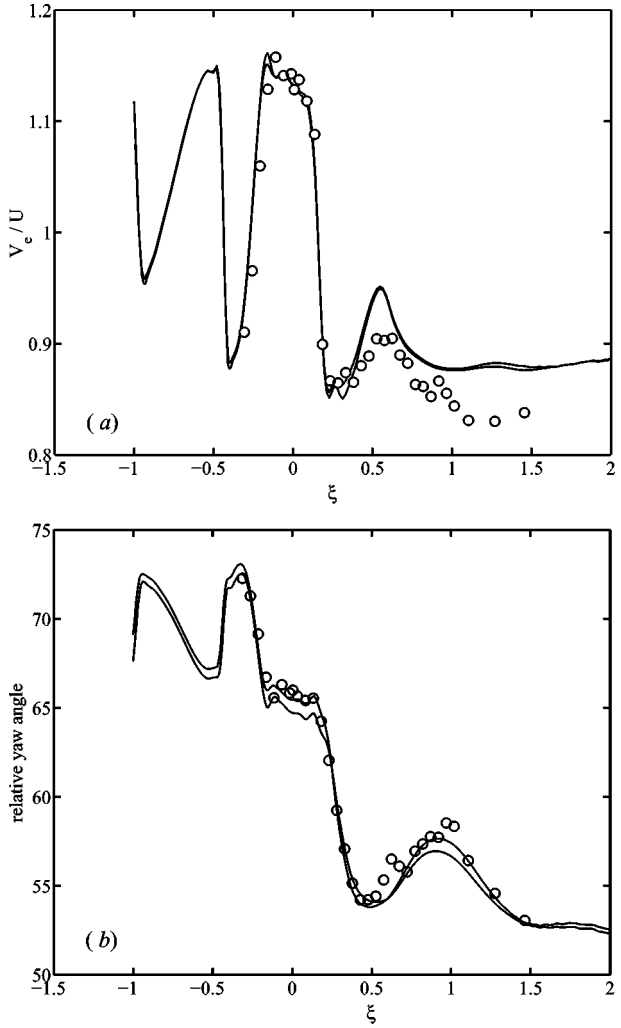

Fig. 4 Comparison between measurement and 3-D viscous computation along the passage centerline at 92% span of (*a*) normalized total velocity, and (*b*) relative yaw angle. Experimental data are denoted by symbols and the solid lines correspond to the two consecutive computational planes between which the measurements lie.

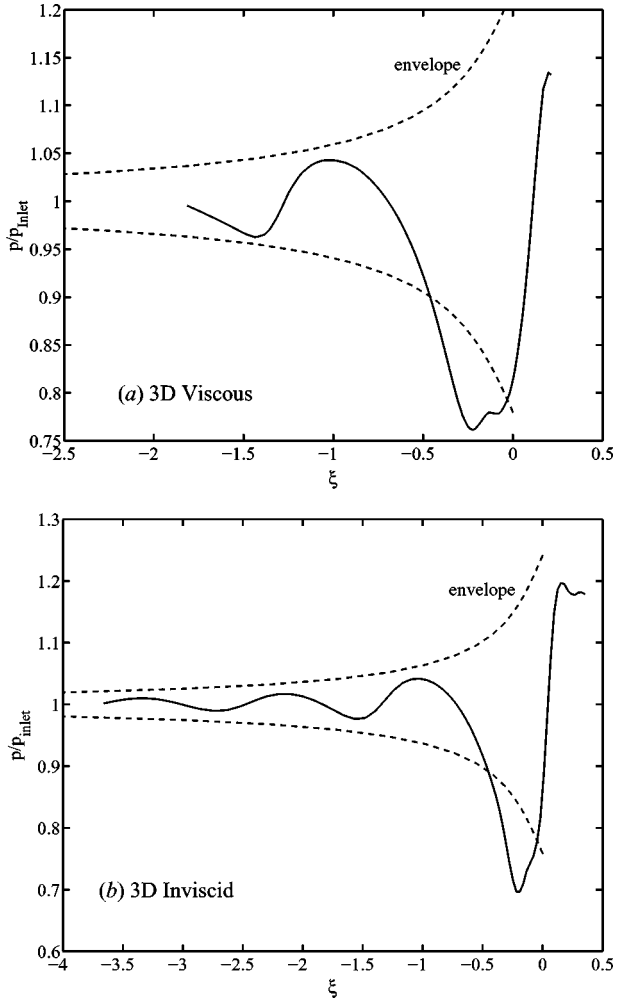

Fig. 5 Axial pressure variations from the 3-D viscous and inviscid simulations are shown as solid lines, with the corresponding envelopes predicted from the semi-analytical model shown with broken lines

$\xi = 0.60$ results from a combination of local acceleration in the blade passage and the descending tip clearance vortex. The reason for the discrepancy in total velocity at locations near and downstream of the trailing edge $\xi \geqslant 1.0$ is not clear since it is observed in wake profiles (not shown) only at the 92% span but not at lower spanwise locations.

The relative yaw angle, defined by $\beta = \tan^{-1}(w_\theta / v_x)$ where $w_\theta = v_\theta - r_e \Omega$, and interpolated along the passage centerline from the experimental data, is found to compare very well with its computational counterpart, shown in Fig. 4(*b*). The minimum visible near $\xi = 0.50$ occurs due to the locus of the passage centerline being in close proximity to the lower periphery of the tip vortex.

The agreement demonstrated in Fig. 4 between the experimental measurement and the computational result suggests that the initial shock strength and its local evolution immediately upstream of the leading edge are determined accurately by the simulation of NASA Rotor-35 at the peak-efficiency condition considered here. Attention will now be directed to the analysis of upstream shock wave evolution as was done in the foregoing 2-D cases.

The pressure along an axial line such as that shown in Fig. 2 is interpolated from the 3-D viscous flow solution at midspan. Using the far upstream Mach numbers and the initial shock strength, the envelope predicted from the model of Morfey and Fisher is displayed as the broken line in Fig. 5(*a*). The interpolated pressure oscillation from the computation is found to be exceeded by the envelope predicted from the 2-D nonlinear acoustical model. This suggests that the pressure oscillation interpolated from the 3-D viscous solution is slightly more attenuated than is suggested by the model of Morfey and Fisher, unlike the 2-D simulations where the agreement was found to be quite good. The variation in Fig. 5(*a*) therefore suggests that the increased attenuation of shock waves is primarily due to spanwise effects. This hypothesis is further supported by the pressure oscillation at midspan, extracted from the 3-D inviscid simulation and shown in Fig. 5(*b*); the attenuation rate is found to be similarly smaller than the prediction from the 2-D model, and confirms the role of three-dimensionality in upstream shock wave propagation. It is conceivable that the misalignment of a shock surface with the computational grid has a more severe impact on numerical dissipation of the shock in the 3-D simulation than in the 2-D simulation. A reduction in the number of radial (k) planes to 65 was found to deliver a virtually identical pressure variation to that shown in Fig. 5(*a*), suggesting that insufficient spanwise resolution did not result in unphysical numerical dissipation.

Since the flow entering the rotor passes through the shock wave system, prediction of the latter field directly influences estimates of rotor performance. The axial variation of the total mass-

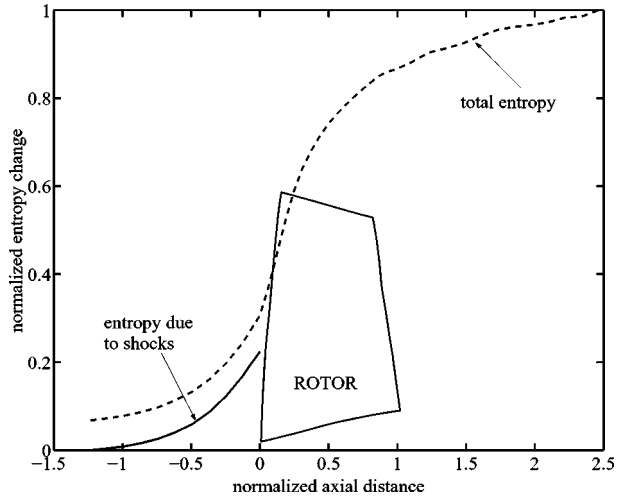

Fig. 6 Axial variation of normalized mass-averaged entropy due to the upstream propagating shock system (——) and the total entropy generated by the rotor (— — —). Results from the 3-D viscous simulation are displayed.

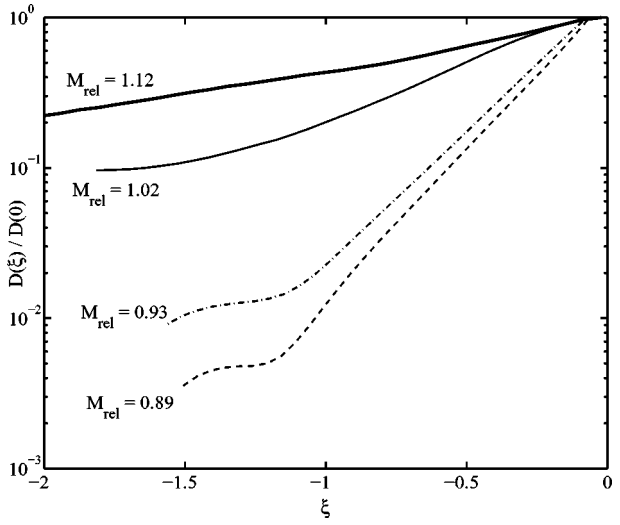

Fig. 7 Upstream variation of normalized circumferential static pressure distortion at four spanwise locations with the indicated inlet relative Mach numbers, from the 3-D viscous simulation

averaged entropy, normalized to unity at the exit, is shown in Fig. 6 as the broken line. The flow entering the computational domain possesses endwall boundary layers, and consequently displays a nonzero total entropy far upstream of the rotor. By retaining that region of the incoming flow from 10 to 90% span, thereby omitting the endwall boundary layer region, it is possible to estimate to good approximation the entropy increase due only to the presence of the shock system; the entropy excluding this endwall region is assumed to be close to zero at the inlet. The surprising result from Fig. 6 is that nearly 20% of the total loss attributable to the rotor, at this peak-efficiency condition, occurs upstream of the leading edge and emphasizes the importance of capturing these waves accurately. Based on measurements in transonic compressor cascades, Chauvin et al. [15] have found that about 15% of the loss associated with the cascade occurs in the upstream propagating shocks, which is in general agreement with the present results from the NASA Rotor-35 simulation. Note that a lack of sufficient grid resolution in the region upstream of the rotor leading edge would artificially dissipate the shock system, and therefore influence the total loss attributable to the rotor.

Upstream Induced Circumferential Distortion

The presence of any airfoil row induces a static pressure distortion on the incoming flow: for subsonic inlet relative Mach numbers an exponentially decaying pressure field is generated whereas in the presence of supersonic inlet relative Mach numbers, the induced distortion persists for longer distances upstream of the airfoil row. The upstream induced pressure distortion assumes significant importance in multi-stage steady and time accurate RANS simulations of closely spaced turbomachinery airfoil rows. The bulk of the pressure distortion induced by a rotor is expected to occur at the blade-passing frequency, and may be estimated from the steady computational solution. Since the computed static pressure $p=p(\xi,\theta,r)$, at a fixed axial location $\xi=\Xi$ and given radius $r=R$, the pressure assumes the form $P(\theta)=p(\Xi,\theta,R)$. The static pressure distortion is defined as

$$D(\xi)=\left[\frac{1}{\Theta}\int_0^{\Theta}(P(\theta)-\overline{P})^2 d\theta\right]^{1/2} \tag{9}$$

where

$$\overline{P}=\frac{1}{\Theta}\int_0^{\Theta}P(\theta)d\theta \tag{10}$$

and Θ is the angular pitch of the airfoil. These operations, carried out for a series of axial locations, deliver the circumferential static pressure distortion upstream of the rotor leading edge.

Figure 7 contains the axial variation of the root-mean-square pressure distortion, $D(\xi)$, for the NASA Rotor-35 geometry, extracted from the 3-D viscous simulation. The evolution at four spanwise locations is displayed, at which the inlet relative Mach numbers (M_{rel}) range from high subsonic to supersonic values. It is to be noted that for each Mach number, the pressure distortion is normalized by its value at the rotor leading edge, $D(0)$. At the two subsonic Mach numbers, the pressure distortion is found to decay rapidly as one moves away from the leading edge. However, the variations obtained at supersonic inlet relative Mach numbers clearly demonstrate the persistence of the distortion induced by upstream propagating shock waves, as evidenced by the more gradual rate of decay.

A brief digression is now made to verify that the circumferential variation induced by the rotor-generated shock wave system is accurately predicted by the 3-D viscous computation. The velocity field, detailed measurements of which have been carried out by van Zante et al. [14], should also exhibit circumferential variations due to the upstream propagating shock wave system. The azimuthal variation of V_e/U, where V_e is computed from Eq. (8), is used to quantify the circumferential velocity distortion at two disparate axial-radial location pairs, shown in Fig. 8. The agreement between the measurement and the computational prediction in Fig. 8, implies that the shock wave pattern generated by the rotor establishes itself to good accuracy in both the radial and axial directions upstream of the leading edge. The lack of agreement in Fig. 8(*a*) near the zero abscissa is probably due to the inability of seeding particles used in the LDA technique to rapidly adapt to local conditions in a region of high velocity gradient.

Returning now to Fig. 7, the following discussion attempts to examine the effect of axial spacing between stator-rotor combinations in compressors, with the implicit assumption that the evolution of upstream propagating waves is not significantly altered by the stator flow field. If one considers the variation at the relative Mach number $M_{rel}=0.89$ to be representative of that found in typical subsonic compressors, and using a value of $\xi=0.4$ as the average axial spacing in these compressors (Sharma and Tan [16]), the normalized distortion from Fig. 7 at the trailing edge of the upstream stator is estimated to be about 0.2. If this value is deemed to be that which the boundary layer on the upstream stator

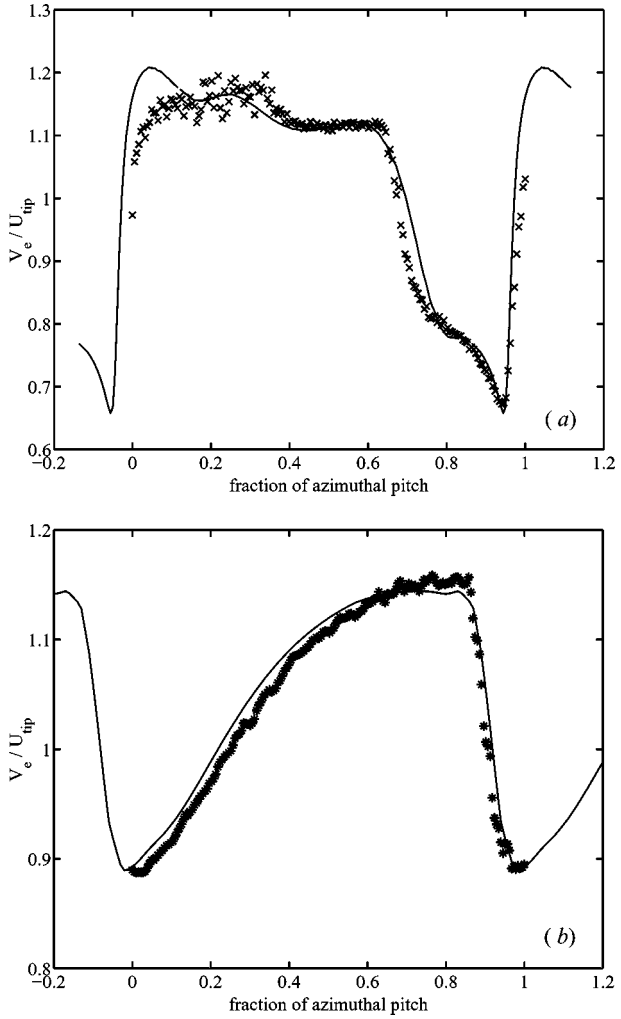

Fig. 8 Circumferential variation of normalized total velocity at (*a*) 80% span and 5% chord upstream of the leading edge, and (*b*) 92% span and 38% chord upstream of the leading edge. The solid line is the prediction from the 3-D viscous simulations and the symbols represent experimental data.

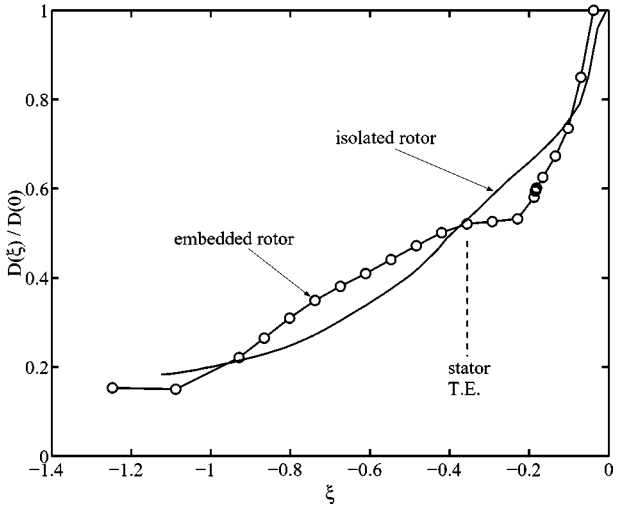

Fig. 9 Variation of the induced circumferential pressure distortion from an (steady) isolated rotor calculation compared to the same rotor embedded in a (time-accurate) multi-stage simulation. Results from 3-D viscous simulations are shown.

can withstand, then for transonic compressors (represented by the variation at $M_{rel}=1.02$), with the same level of normalized distortion, the axial spacing would need to be increased to $\xi=0.8$; furthermore, for supersonic compressors (represented by the variation at $M_{rel}=1.12$) an axial gap in excess of $\xi=1.8$ would be required for a similar level of normalized pressure distortion at the trailing edge of the upstream stator. Note that the occurrence of leading edge sweep in transonic and supersonic rotors provides a mechanism for inserting axial gap without increasing the physical spacing between airfoil rows to unacceptable values.

Smith [17] has demonstrated in a low-speed compressor rig that decreased axial spacing delivered enhanced performance; Mikolajczak [18] presented comparable experimental results, also conducted in a low-speed research compressor. Hetherington and Moritz [19] carried out experiments in a four-stage high-pressure ratio compressor and demonstrated that at 100% speed, increased performance was obtained when the axial gap upstream of all rotors was increased. Although precise experimental details are not available from their study, the shape of the 100% speedline indicates that the compressor was choked at the higher mass flow rates suggesting that some or all of the blade rows were subjected to relative inlet Mach numbers near or above unity. Based purely on the moderate attenuation rate of the shock-induced circumferential pressure distortion generated by transonic rotors, one would expect that enhanced performance would occur with increased axial gap between stator-rotor combinations for such machines. Interestingly, at a lower corrected wheel speed, where the compressor was operating in the subsonic regime (as evidenced by the shape of the speedline), Hetherington and Moritz [19] found a variation consistent with that of Smith [17] and Mikolajczak [18]. More recently, using carefully designed experiments, Gorrell et al. [20] have demonstrated improvement in the performance of a transonic compressor stage with increased axial gap between the rotor and its upstream stator. In summary, it appears from the available experimental measurements in high-speed machines, that the interaction of a rotor-generated shock wave system with the upstream stator is a dominant factor in the perceived unsteadiness and production of loss, whereas other factors, such as transport of wake fluid [17], dominate in low-speed multi-stage compressors.

Much of the previous discussion has focused on the distortion induced by an isolated rotor, and one may question its utility in an examination of the rotor embedded in a multi-stage compressor. In Fig. 9 is shown the axial variation of the distortion induced by a transonic blade row simulated as an isolated rotor, as well as the distortion induced when it is embedded in a multi-stage compressor simulation, both at 92% span. The latter is extracted from the full 3-D time-accurate simulation of the flow field and the comparison with the steady simulation of the isolated rotor is made at a nominally identical mass flow rate. The initial decay rate from the two simulations is reasonably similar and demonstrates that the evolution immediately upstream of the rotor leading edge is approximately independent of the flow exiting the stator. Further upstream near $\zeta=-0.2$, the distortion induced by the isolated rotor is found to be larger than that generated by the embedded rotor, primarily due to the interaction of upstream propagating shock waves with the stator exit flow field. As one moves into the stator passage, the pressure distortion determined from the multi-stage simulation exceeds that from the isolated rotor calculation due to the occurrence of shock reflections in the stator passage. The comparison of the two variations displayed in Fig. 9 indicates that one may use the induced pressure distortion generated by an isolated rotor to obtain conservative preliminary estimates for the distortion experienced by the upstream stator trailing edge flow in a multi-stage environment.

Conclusions

A numerical analysis of the flow field in the isolated transonic compressor designated NASA Rotor-35 has been carried out, with a focus on the upstream propagation of shock waves generated by the rotor. Their propagation has been examined using the flow solver not only in its usual viscous mode but also in an inviscid mode, on both the 3-D geometry as well as the midspan geometry simulated as a 2-D cascade. The decay of upstream propagating shocks from the computational solutions was compared to predictions from a model due to Morfey and Fisher [11], based on the nonlinear evolution of shock waves propagating in a inviscid 2-D flow through an annular duct upstream of the rotor. The results from the 2-D viscous cascade simulation are found to be in good agreement with the predicted envelope from the nonlinear acoustical model, confirming that the decay of upstream propagating shock waves is largely an inviscid phenomenon. This property may be used to efficiently construct adequate flow field discretizations, through the requirement that nonphysical numerical dissipation of these waves be minimized; in the present case, about 18 grid points for one wavelength of pressure oscillation was found to be adequate. The presence of spanwise variations is found to increase the decay rate of shock wave propagation when compared to results from the nonlinear acoustical model. The initial shock strength and shock wave evolution immediately upstream of the rotor leading edge are predicted to good accuracy by the 3-D viscous simulation when compared to the high-resolution experimental measurements of van Zante et al. [15]. The decay of upstream propagating shock waves observed in the present work is found to be in qualitative agreement with the results of Probasco et al. [2] and Koch et al. [21].

The upstream-induced circumferential static pressure distortion is found to decay about an order of magnitude slower at spanwise locations with supersonic inlet relative Mach numbers than for those at which the Mach numbers are subsonic. Based solely on the circumferential pressure field generated by an isolated rotor, it is found that for the same level of induced distortion, the axial gap required between a supersonic blade section and its upstream stator is nearly twice that required for a subsonic blade section. This suggests that for transonic/supersonic compressor rotors, enhanced performance may be achieved by inserting more axial gap than is normally used in subsonic compressors, which is consistent with the observation of Hetherington and Moritz in a high-speed multi-stage compressor. The induced static pressure distortion from an isolated rotor simulation near the location of the upstream stator trailing edge is found to be conservatively estimated in comparison to the value determined from a time-accurate calculation of the rotor when it is embedded in a multi-stage simulation.

The ability of a flow solver to capture the proper upstream evolution of blade row induced pressure disturbances is a fundamental requirement for the simulation of transonic flow fields. For under these conditions, upstream disturbances are known to propagate with weak attenuation, and may thus impact not only the performance of an upstream stator in a multi-stage simulation, but also have implications in predicting the generation of ''buzz-saw'' noise in supersonic fans, as explained in McAlpine and Fisher [22].

Acknowledgments

The author thanks Pratt and Whitney for granting permission to publish the results presented here, and is indebted to Om Sharma for several stimulating discussions and Gary Stetson for his encouragement and support. Akil Rangwalla provided extremely valuable input regarding the numerical flow solver. The author owes his gratitude to Dilip Prasad for suggesting the reference by Morfey and Fisher. Dale van Zante of NASA Glenn Research Center kindly shared his experimental measurements.

References

[1] Ferri, A., 1964, ''Aerodynamic properties of supersonic compressors,'' *Aerodynamics of Turbines and Compressors, High Speed Aerodynamics and Jet Propulsion*, Vol. X, ed., W. R. Hawthorne, Princeton University Press, Princeton, NJ.

[2] Probasco, D. P., Leger, T. J., Wolff, J. M., Copenhaver, W. W., and Chriss, R., 2000, ''Variations in Upstream Vane Loading with Changes in Back Pressure in a Transonic Compressor,'' ASME J. Turbomach., **122**, pp. 433–441.

[3] Giles, M. B., 1988, ''Non-Reflecting Boundary Conditions for Euler Equation Calculations,'' AIAA J., **28**, pp. 2050–2058.

[4] Kerrebrock, J. L., and Mikolajczak, A. A., 1970, ''Intra-stator Transport of Rotor Wakes and its Effect on Compressor Performance,'' ASME J. Eng. Power, **92**, pp. 359–368.

[5] Ni, R.-H., 1982, ''A Multiple-Grid Scheme for Solving Euler Equations,'' AIAA J., **20**, pp. 1565–1571.

[6] Davis, R. L., Ni, R.-H., and Carter, J. E., 1986, ''Cascade Viscous Flow Analysis Using Navier-Stokes Equations,'' AIAA Pap., Paper No. 86-0033.

[7] Ni, R.-H., and Bogoian, H., 1989, ''Predictions of 3-D Multistage Turbine Flow Fields Using a Multiple-Grid Euler Solver,'' AIAA Pap., Paper No. 89-0233.

[8] Ni, R.-H., and Sharma, O. P., 1990, ''Using a 3-D Euler Flow Simulation to Assess Effects of Periodic Unsteady Flow Through Turbines,'' AIAA Pap., Paper No. 90-2357.

[9] Davis, R. L., Shang, T., Buteau, J., and Ni, R.-H., 1996, ''Prediction of 3-D Unsteady Flow in Multi-stage Turbomachinery using an Implicit Dual Time-Step Approach,'' AIAA Pap., Paper No. 96-2565.

[10] Wilcox, D. C., 1998, *Turbulence Modeling for CFD*, DCW Industries, Inc.

[11] Morfey, C. L., and Fisher, M. J., 1970, ''Shock-wave Radiation from a Supersonic Ducted Rotor,'' Aeronaut. J., Royal Aeronautical Society, **74**, pp. 579–585.

[12] Rudnick, I., 1953, ''On the Attenuation of a Repeated Sawtooth Shock Wave,'' J. Acoust. Soc. Am., **25**, pp. 1012–1013.

[13] Dring, R. P., and Oates, G. C., 1990, ''Throughflow Theory for Nonaxisymmetric Turbomachinery Flow—Part I: Formulation,'' ASME J. Turbomach., **112**, pp. 320–327.

[14] van Zante, D. E., Strasizar, A. J., Hathaway, M. D., and Okiishi, T. H., 2000, ''Recommendations for Achieving Accurate Numerical Simulation of Tip Clearance Flows in Transonic Compressor Rotors,'' ASME J. Turbomach., **122**, pp. 733–742.

[15] Chauvin, J., Sieverding, C., and Griepentrog, H., 1970, ''Flow in Cascades with a Transonic Regime,'' *Flow Research on Blading*, ed., L. S. Dzung, pp. 151–189, Elsevier.

[16] Sharma, O. P., and Tan, C. S., 1999, ''Impact of Unsteadiness Induced by Adjacent Airfoil Rows on the Performance, Structural Integrity and Stalling Characteristics of Axial Flow Compressors,'' *Blade Interference Effects in Axial Turbomachinery Stages*, von Karman Institute.

[17] Smith, L. H., 1970, ''Casing Boundary Layers in Multistage Axial-flow Compressors,'' *Flow Research on Blading*, ed., L. S. Dzung, 275–304, Elsevier.

[18] Mikolajczak, A. A., 1976, ''The Practical Importance of Unsteady Flow,'' AGARD Conf. Proc., on Unsteady Phenomena in Turbomachinery, **177**.

[19] Hetherington, R., and Moritz, R. R., 1976, ''Influence of Unsteady Flow on the Design and Operation of Aero Engines,'' AGARD Conf. Proc., on Unsteady Phenomena in Turbomachinery, **177**.

[20] Gorrell, S. E., Okiishi, T. H., and Copenhaver, W. W., 2002. ''Stator-Rotor Interactions in a Transonic Compressor: Part 1—Effect of Blade-Row Spacing on Performance,'' ASME Paper GT-2002-30494.

[21] Koch, P. J., Probasco, D. P., Wolff, J. M., Copenhaver, W. W., and Chriss, R., 2000, ''Transonic Compressor Influences on Upstream Surface Pressures with Axial Spacing,'' J. Propul. Power, **117**, pp. 474–476.

[22] McAlpine, A., and Fisher, M. J., 2000, ''On the Prediction of ''Buzz-Saw'' Noise Generated by an Aeroengine,'' AIAA Pap., Paper No. 2000–2095.

Aerodynamic Design and Performance of Aspirated Airfoils

Ali Merchant
e-mail: merchant@mit.edu
Gas Turbine Laboratory,
Department of Aeronautics and Astronautics,
Massachusetts Institute of Technology,
Cambridge, MA 02139

The impact of boundary layer aspiration, or suction, on the aerodynamic design and performance of turbomachinery airfoils is discussed in this paper. Aspiration is studied first in the context of a controlled diffusion cascade, where the effect of discrete aspiration on loading levels and profile loss is computationally investigated. Blade design features which are essential in achieving high loading and minimizing the aspiration requirement are described. Design studies of two aspirated compressor stages and an aspirated turbine exit guide vane using three dimensional Navier-Stokes calculations are presented. The calculations show that high loading can be achieved over most of the blade span with a relatively small amount of aspiration. Three dimensional effects close to the endwalls are shown to degrade the performance to varying degrees depending on the loading level. [DOI: 10.1115/1.1519834]

Introduction

Historically, the work capacity of modern axial compressors has been advanced primarily by increasing the blade speed while staying well within the established limits for blade loading to satisfy efficiency, stall margin, and other performance requirements. As a departure from this conventional design paradigm, the blade loading can be increased by exploiting boundary layer suction to control separation on the blades and endwalls. Aspiration, or suction, has been used as the basis for the very high-work aspirated compressor stages developed at MIT. The aspirated stages, at a given tip speed, have demonstrated about twice the work capacity of conventional stages with comparable through flow efficiency.

Higher blade loading is attractive as it has the potential of reducing compressor weight, length, and other aspects which ultimately impact the efficiency and cost of a compressor. Wennerstrom [1] discusses approaches taken over many years to achieve very high loading levels in axial compressors. Low aspect ratio blades and splitter blade configurations have been important contributers to increasing diffusion levels, and he also notes the limited success of boundary layer control methods. Recently, there has also been a renewed interest in flow control opportunities in gas turbine engines, in general, and various approaches have been surveyed by Lord et al. [2]

An experimental investigation on the use of boundary layer control on a transonic compressor stage was carried out at MIT by Reijnen [3]. The experiment demonstrated an increase in flow turning and higher static pressure ratio which were attributed to thinner boundary layers due to suction. A delay in the formation of rotating stall cells in the rotor was also observed. Recently, a fully aspirated stage, with suction on the rotor and stator, was successfully tested by Schuler [4]. The experimental results were in good agreement with the design intent. The stage achieved a pressure ratio of 1.59 at a blade speed of 750 ft/s, and the predicted adiabatic efficiency was 89%. Computational design studies and some interesting applications of aspiration are presented in Kerrebrock [5]. Investigations into the impact of suction on engine efficiency can be found in Kerrebrock et al. [6], Kerrebrock [5], and McCabe [7].

The quasi-3-D calculations presented in this paper were carried out using the MISES code. Details of the code are given in a report by Youngren [8]. An integral boundary layer method is used in the code to model viscous effects, and a suction model developed by Merchant [9] was implemented in the code. The model assumes that the suction slot is flush with the blade surface. Comparisons between the predictions of this suction model and experimental data have been carried out for a variety of low speed and isolated transonic airfoils. Hence, the model is expected to be reliable for applications to low-speed and high-speed cascades.

The focus of this paper is to present a discussion on the aerodynamic design aspects and performance of aspirated blade rows. First, a simplified analysis of the boundary layer development subjected to discrete suction is presented. The performance of a controlled diffusion cascade with aspiration is studied next, followed by a discussion on the design features of aspirated blade sections. Finally, application of aspiration to two compressor stages and an exit guide vane are presented, and the effectiveness of aspiration in the context of these three-dimensional applications is examined.

Aspiration and suction are used interchangeably in this paper.

Effect of Suction on Boundary Layer Development

The mass flow removed from the boundary layer by suction can be conveniently quantified in terms of a fraction of the inlet flow into a cascade

$$C_{\mathrm{ms}} = -\frac{1}{\dot{m}_{\mathrm{inlet}}} \int_{s_1}^{s_2} \rho_w \nu_w ds \tag{1}$$

where s_1 and s_2 define the length of the slot and $\rho_w \nu_w$ is the normal mass flux into the slot. C_{ms} is a positive fraction since the sign is implied by $\rho_w \nu_w$. A more intrinsic measure of the effectiveness of suction is the displacement length associated with the suction mass defect. This is defined as

$$\delta_s^* = -\int_{s_1}^{s_2} \frac{\rho_w \nu_w}{\rho_e u_e} ds \tag{2}$$

Note that δ_s^* as it is defined above will be positive for suction. The effects of boundary layer suction can be divided into a local effect, where the boundary layer is modified by the suction slot, and the effect of that change on the downstream development of the boundary layer. These two effects can be examined via the incompressible integral momentum equation as shown in Merchant [10]. For weak suction, where the effect of the pressure gradient across the slot may be neglected, the change in the momentum thickness $\Delta\theta_{21}$ is proportional to δ_s^*. For strong suction, Eq. (3) shows that the change in $\Delta\theta_{21}$ will decrease exponentially with increasing suction.

Contributed by the International Gas Turbine Institute and presented at the International Gas Turbine and Aeroengine Congress and Exhibition, Amsterdam, The Netherlands, June 3–6, 2002. Manuscript received by the IGTI, October 11, 2001. Paper No. 2002-GT-30369. Review Chair: E. Benvenuti.

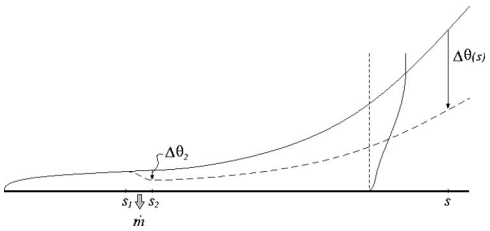

Fig. 1 Effect of suction on boundary layer growth

$$\frac{\Delta\theta_{21}}{\theta_1} \simeq -\frac{\delta_s^*}{\theta_1}$$

$$\frac{\Delta\theta_{21}}{\theta_1} \simeq \left(\frac{u_{e2}}{u_{e1}}\right)^{-(2+H_{\text{avg}})} \exp\left(-\frac{\delta_s^*}{\delta_{\text{avg}}}\right) - 1 \tag{3}$$

The contribution from the shear stress has been neglected since the width of the suction slot Δs is small. The integral momentum equation can be integrated from just downstream of the slot to some distance downstream of the cascade so that the change in momentum thickness can be expressed in terms of a local change produced by suction.

$$d(\ln\theta) = \frac{C_f}{2\theta} ds - (2+H) d(\ln u_e)$$

$$\theta(s) \simeq \theta_2 \exp \int_{s_2}^{s} \left\{ \frac{C_f}{2\theta} - (2+H) \frac{1}{u_e} \frac{du_e}{ds} \right\} ds$$

$$\Delta\theta(s) \simeq \Delta\theta_{21} \exp \int_{s_2}^{s} \left\{ \frac{C_f}{2\theta} - (2+H) \frac{1}{u_e} \frac{du_e}{ds} \right\} ds \tag{4}$$

Here, $\Delta\theta_{21}$ is the change across the suction slot given by Eq. (3) and $\Delta\theta(s)$ is the corresponding change at some distance s downstream of the slot. For completeness, the incompressible integral energy equation can be similarly integrated to give

$$\Delta\theta^*(s) \simeq \theta_{21}^* \left(\frac{u_e}{u_{e2}}\right)^{-3} \exp \int_{s_2}^{s} \frac{2C_D}{\theta^*} ds \tag{5}$$

where $\Delta\theta_{21}^*$ is the change in kinetic energy thickness across the slot.

It is apparent from Eqs. (4) and (5) that the changes across the suction slot are ''magnified'' by an exponential factor. Thus, a large amount of control can be exercised over the downstream boundary layer thickness by bleeding a small amount of mass flow in the appropriate location. This effect is illustrated in Fig. 1. The exponential terms in Eqs. (4) and (5) are close to unity in a weak pressure gradient. However, the magnification effect, which depends on the pressure gradient term, is appreciable in a strong pressure gradient even if the flow is attached. In the case of the integral momentum equation, where the shape parameter H may be large on the suction side of a compressor cascade, the magnification due to the exponential term can easily exceed 10 near the trailing edge.

To illustrate the preceding arguments, the boundary layer development on a controlled diffusion cascade is computationally examined at two different loading levels. The first is a lightly loaded case which corresponds to the design flow conditions, and the second is a highly loaded case where the diffusion factor is increased by approximately 30%. The design flow conditions and cascade geometric parameters are summarized in Table 1. The cascade used in this study has nearly identical design flow conditions and geometrical parameters compared to the cascade tested in an experiment by Hobbs and Weingold [11]. The chord Reynolds number is 500,000, and the boundary layer is tripped to a fully turbulent condition near the leading edge. The mixed-out loss one chord downstream from the trailing edge is 0.024 without aspiration. The highly loaded condition is simulated by lowering the AVDR to 1.03 and the chord to pitch ratio to 1.05. The corresponding diffusion factor is 0.63, and the total pressure loss coefficient is 0.056 without aspiration. At both loading conditions, aspiration is applied at a discrete slot located on the suction surface at 30% chord. The computed pressure distribution for the highly loaded case is shown in Fig. 2. Separation of the suction side boundary layer is seen at 60% chord.

Table 1 Cascade design flow conditions and geometric parameters

M_{inlet}	0.63	x_{suct}/c	30%
α_{inlet}	43.2 deg	$c/p=\sigma$	1.44
AVDR	1.12	$t_{\max}/c$	7.1%
DF	0.48	$\theta_{\max}/c$	12%
ω	0.024	t_{te}/c	1.7%

The change in momentum thickness across the suction slot $\Delta\theta_{21}$, at the trailing edge, and one chord downstream of the trailing edge with increasing suction for the design loading condition are plotted in Fig. 3. The suction displacement thickness defined in Eq. (2) is normalized by the displacement thickness just upstream of the slot δ_1^*. The decrease in θ one chord downstream is nearly 5 times the decrease at the slot. The momentum thickness decreases linearly with increasing suction up to $\delta_s^*/\delta_1^* \simeq 1$ consistent with the assumption used in Eq. (3). The change in momentum thickness levels off once the boundary layer is strongly attached, and further increase in suction results in a slight increase in momentum thickness due to increase in skin friction downstream of the slot. Figure 4 shows the corresponding behavior of the momentum thickness for the highly loaded condition. The de-

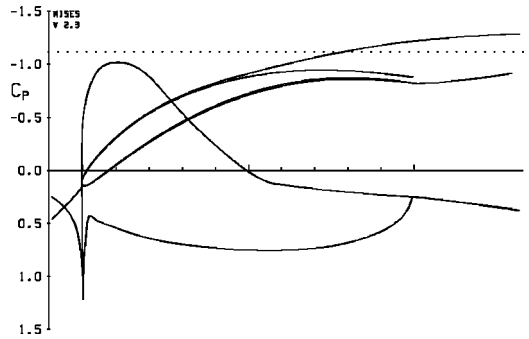

Fig. 2 Controlled diffusion cascade at a highly loaded condition with no suction

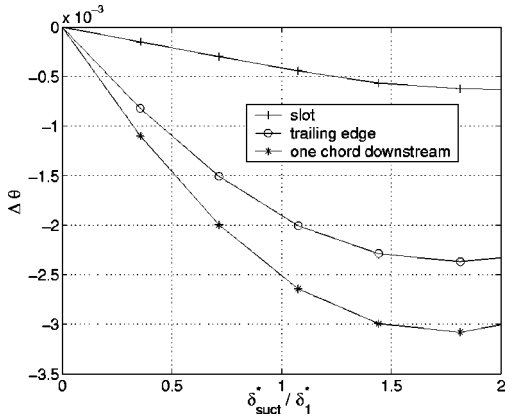

Fig. 3 Decrease in momentum thickness with suction at design loading conditions

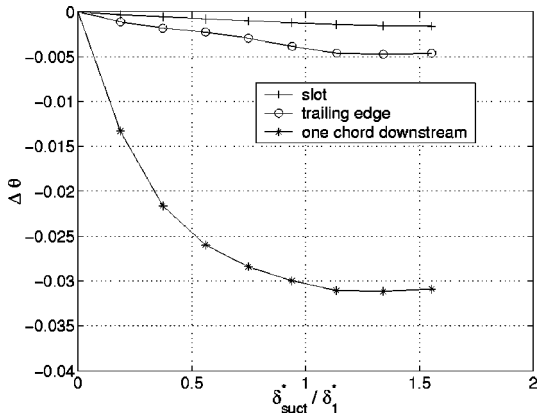

Fig. 4 Decrease in momentum thickness with suction at high loading conditions

crease in downstream momentum thickness is nearly 17 times the decrease at the slot. The sensitivity of $\Delta\theta$ to suction is also seen to be larger compared to the lightly loaded condition. The decrease in momentum thickness for both cases begins to level off for $\delta_s^*/\delta_1^* > 1$. This provides a reasonably good criterion for estimating the suction mass flow requirement for a given application. Experimental results reported by Pierpont [12] and Loughery et al. [13] indicate that the optimum bleed rates in their experiments correspond to $\delta_s^*/\delta_1^* \simeq 1$, which is in agreement with the trend observed in Figs. 3 and 4. The minimum loss ω for the lightly loaded and highly loaded cases are 0.016 and 0.011, and the corresponding suction mass fractions are 0.5 and 0.6%, respectively. The suction side separation for the highly loaded case was completely suppressed at this value, and the exit angle deviation was reduced from 6 to 2 deg. It is interesting to note that the difference in the minimum loss at the two loading conditions is proportional to the difference in the chord to spacing ratios.

The nature of the boundary layer development gleaned from the above analysis can provide insight into positioning the suction slot on the blade. For the greatest control authority with the least amount of mass removal, the best range of positions to apply suction is close to the start of a strong pressure-recovery region; the exponential magnification is then the greatest over the downstream part of the flow. Equation (3) shows that, for strong suction, δ_s^*/θ_{avg} is a measure of the effectiveness of suction, and hence shows that suction will quickly lose its effectiveness if the slot is positioned in the pressure recovery region where the boundary layer has already begun diffusing. In other words, a large H or θ upstream of the slot will require a larger suction mass fraction to achieve the same effect.

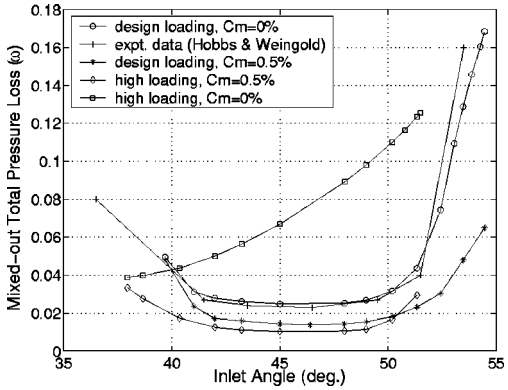

Fig. 5 Effect of aspiration on the loss variation with incidence at design and high loading conditions

Figure 5 shows the effect of aspiration on the loss variation with incidence at the two loading conditions. The loss versus incidence curve at the design loading conditions with no suction is also compared for reference to the experimental data of [11]. The loss curve at design loading with 0.5% suction shows an increase in the incidence range by approximately 2 deg and lower loss over the incidence range compared to the case with no suction. The loss curve for the higher loading condition shows approximately the same incidence range as the case at design loading with no suction. The minimum loss incidence angle for the highly loaded cascade shows a decrease compared to the cascade at design loading conditions. A substantial increase in the loss is seen over the range of incidence angles for the high loading case without suction. At both loading conditions with suction, the loss increases gradually with increasing flow angle, and no abrupt change in loss is observed even for the highly loaded cascade. At high incidence angles, δ_s^*/δ_1^* decreases due to growth of the boundary layer upstream of the slot, but the overall effectiveness of suction is still maintained until δ_s^*/δ_1^* decreases significantly below 1.

Blade Design Considerations

The application of aspiration has focused primarily on increasing the loading capability of transonic and supersonic compressors. The combination of high Mach numbers and large flow turning makes the design of aspirated blades a very challenging task. This section discusses some of the important design features of aspirated blades. A more detailed discussion can be found in [10].

Aspiration places a severe constraint on the blade thickness, which has to be sufficient to accommodate the suction passages inside the blade as well as meet structural requirements. The thickness distribution must be sufficient to accommodate the required suction flow at least at design conditions. Therefore, aspirated blades are generally thicker than conventional blades that are designed for a similar flow regime. The location of the maximum thickness for subsonic sections is not critical and is driven mainly by the desired pressure distribution. For transonic and supersonic blades, the location of the maximum thickness is more critical to the performance, and cannot be too far forward on the blade as this increases the thickness of the blade in the supersonic region. Figure 6 shows an example of a relatively thick supersonic blade section. The optimum location of the maximum thickness in this case was found to be the location where the bow shock impinged on the suction side.

The thickness requirement on aspirated blades also constrains the thickness of the leading edge region. Therefore, considerable attention has to be given to the design of the leading edge region to achieve good performance, especially for transonic and supersonic blades. A poorly designed leading edge region may result in spikes or overspeeds in the pressure distribution. This may cause local separation of the flow resulting in higher losses and lower useful incidence range. The local separation may be particularly detrimental for supersonic blades which are sensitive to blockage. In recent years more attention has been given to the leading edge design in the context of controlled diffusion blading. This can be attributed to better blade representation and improved inverse design methods as discussed by Stow [14], Starken [15], and Hobbs and Weingold [11]. A distinctive characteristic of these blades is a smooth pressure distribution on the suction and pressure sides near the leading edge region. In contrast, overspeeds in the pressure distribution on supersonic compressor blades, which require separate specification of leading circles or ellipses to close the blade shape, are almost unavoidable. The primary consideration in the design of the leading edge region for aspirated cascades has been to obtain a smooth pressure distribution near the leading edge region. This has resulted in leading edge shapes which are not always symmetric with respect to the camberline, and therefore cannot be accurately represented using separate camberline

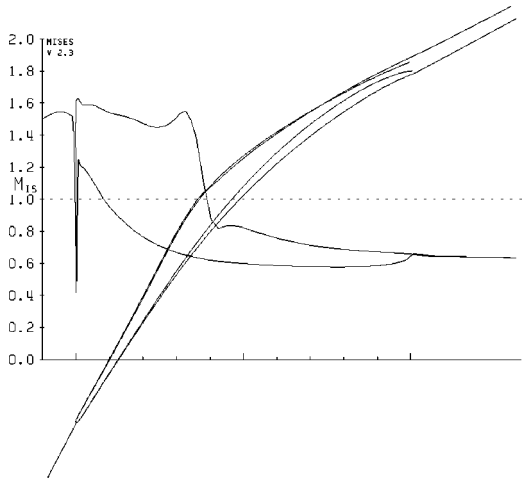

(*a*)

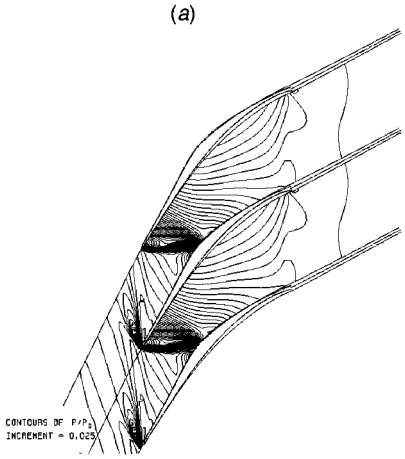

(*b*)

Fig. 6 Aspirated blade section with supersonic precompression—(*a*) surface mach, (*b*) pressure contours

and thickness distributions. The leading edge shock loss relation presented by Koch and Smith [16] has also been used to guide the leading edge thickness requirement for supersonic blades.

Precompression was judiciously used on the supersonic aspirated blades to decrease the bleed requirement and increase the subsonic diffusion downstream of the passage shock. Excessive precompression, where the flow is decelerated to nearly sonic conditions has resulted in unsuccessful designs (Creagh and Klapproth [17]). However, cascades with moderate precompression have been successfully tested by Tweedt et al. [18]. Figure 6 illustrates the degree of precompression used on aspirated blades. Lowering the Mach number upstream of the passage shock to between 1.3 and 1.4 was found to be sufficient to achieve good performance. The modest acceleration seen just upstream of the shock is due to the presence of suction at the foot of the shock. The position of the suction slot at the throat of the blade passage is beneficial since the throat margin is increased by bleeding the flow. Numerical studies at off-design conditions have shown that suction delays the ''spilling'' of the passage shock as the exit pressure is increased, and also delays boundary layer separation after the shock has moved upstream of the throat.

The diverging trailing edge concept, illustrated in Fig. 7, has been used to increase the aft loading of aspirated blades. The increase in loading on the pressure side from a to c is shown by the dashed lines for the corresponding change of the blade pressure surface close to the trailing edge. Besides increasing the aft loading, another advantage of this concept is that the pressure

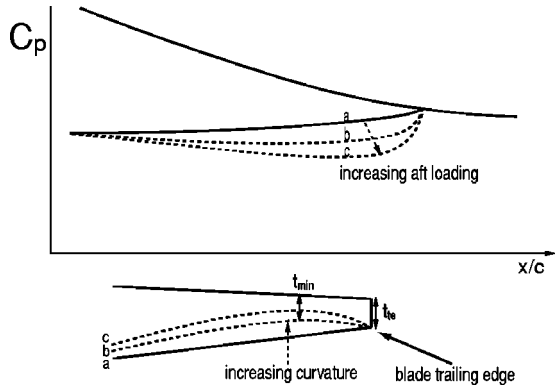

Fig. 7 Diverging trailing edge concept

gradient on the suction side can be relaxed close to the trailing edge. The deviation, which is critical in high turning blades, is significantly reduced by employing this method. The diverging trailing edge design for transonic airfoils was first studied by Henne and Gregg [19], and an example of its use on compressor cascades is given by Korn [20]. The trailing edge thickness t_{te} essentially controls the loading increase that can be obtained, but also has the potential of increasing the profile loss due to the base pressure acting on t_{te}. Therefore, the effectiveness of the diverging trailing concept has to be weighed against the overall performance of the blade. Gostelow [21] provides useful references on trailing edge thickness studies, and he concludes that moderate trailing edge thicknesses up to 2% for compressor cascades do not significantly affect profile loss and also decrease the deviation in exit angle. The criterion used to determine t_{te} for aspirated blades was that the boundary layer remain attached up to the trailing edge, and in addition, that $t_{te} \leqslant \delta^*_{te}$. An integral boundary layer formulation for modeling blunt trailing edges developed by Drela [22] is implemented in the MISES solver.

The pressure surface shape, although usually determined by structural constraints, requires special attention in the case of aspirated blades. The large turning combined with relatively high inlet Mach numbers leads to severe adverse pressure gradients on the blade pressure side up to mid-chord. The leading edge overspeed discussed earlier can also exacerbate this situation. For supersonic rotor and stator blades, as shown in Fig. 8, the impingement of the passage shock on the pressure side may lead to separation of the pressure side boundary layer. The pressure side shape is much more critical in a three dimensional environment where separation of the endwall boundary layer may be initiated along the pressure side corner by a strong adverse pressure gradient. Pressure side separations have been studied extensively for turbine cascades and recently by Brear et al. [23]. Pressure side separations have not been an issue for conventional compressor blades since the turning and camber are limited by separation of the suction side boundary layer, however the design of the pressure side is an important feature of the aspirated blade designs.

Three-Dimensional Applications

The design principles presented above have been applied in the design of several high-work aspirated stages and highly loaded aspirated vanes. The blade performance of two compressor stages and an exit guide vane have been selected for discussion here. The compressor stage calculations were performed using the multistage Navier-Stokes code APNASA developed by Adamczyk et al. [24], and the exit guide vane calculations were performed using a Navier-Stokes finite volume solver with a Baldwin-Lomax algebraic turbulence model. The typical mesh size used in these calculations has 80 axial mesh points within the blade, and 51 mesh points in the spanwise and circumferential directions, respectively.

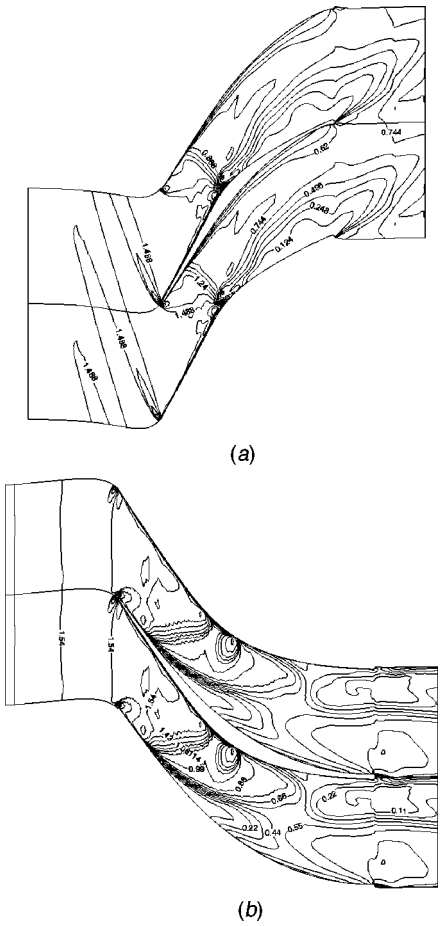

(*a*)

(*b*)

Fig. 8 High-speed stage contours of Mach number—(*a*) rotor 95% span, (*b*) stator 10% span

1 High-Speed Stage. The high-speed aspirated stage was designed to achieve a total pressure ratio of 3.5:1 at a blade speed of 1500 ft/s. One of the objectives of designing this stage was to explore the loading limit that could be achieved for a supersonic stage with aspiration. The preliminary design of the blade rows was carried out using an axisymmetric solver coupled with the quasi-3-D blade design code MISES. The complete aerodynamic design of the stage is described in [10]. The rotor has a work coefficient of 0.7, and peak diffusion factors exceed 0.7 in the rotor and stator. Evaluation of the stage using three dimensional calculations predicted a peak adiabatic efficiency of 86%, and a peak total pressure ratio of 3.4:1. Despite the fact that the blade design was carried out using a quasi-3-D approach, the performance predicted by the three dimensional calculations was found to be in good agreement with the design intent. The exception was near the rotor tip and stator hub where the flow behavior was strongly influenced by the endwall boundary layer.

Figure 8(*a*) shows the contours of Mach number of a rotor section at 95% span. The shock position is in agreement with the quasi-3-D calculation, and the effect of suction at the foot of the passage shock can be seen in the plot. Suction was also found to restrain the shock movement as the exit pressure was increased above the design value. The rotor shows a region of low-momentum fluid in the subsonic section of the passage. The radial extent of the low momentum flow on the rotor suction side can be seen in Fig. 9(*a*). It interesting to note that the boundary layer is well attached over most of the span due to aspiration resulting in relatively thin wakes. The design intent performance, in terms of pressure ratio and mass flow, could not be obtained in calculations with no aspiration. The aspiration slot extended from 40% span up

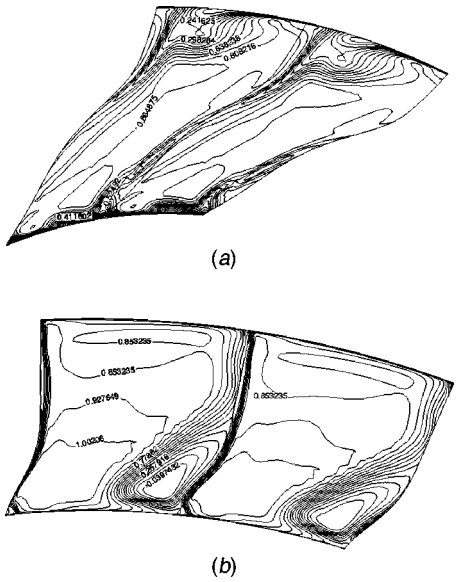

(*a*)

(*b*)

Fig. 9 High-speed stage contours of axial speed—(*a*) rotor exit, (*b*) stator exit

to the tip bleeding 1.5% of the inlet mass flow. The core flow adiabatic efficiency of the rotor for this calculation is 93%.

Figure 8(*b*) shows the contours of Mach number of a stator section at 10% span. With an inlet Mach number close to 1.5 and an inlet angle of 60 deg, the flow conditions near the stator hub were found to be far more severe than the rotor tip. The stator design included flaring the chord near the hub to provide some degree of back sweep, as described by Wennerstrom [25], as well as to relieve the endwall loading. However, no bowing or leaning was applied to the stator. The effect of the bleed can be seen on the suction side just downstream of the passage shock. The aspiration slot extended from hub to tip on the suction side at approximately 40% chord, and a bleed fraction of 2% was used. The impingement of the passage shock on the pressure surface of the stator and the high level of diffusion initiates a corner separation, which then migrates toward the suction side as well as grows radially. The extent of the separation can also be seen in Fig. 9(*b*). Several endwall boundary layer suction schemes were tried to suppress the separation but none were completely successful. The scheme adopted in the present calculations is described in Merchant et al. [26].

Figure 10 shows the mass averaged total pressure and temperature profiles at the rotor and stator exit. The rotor achieves the design intent pressure ratio over most of the span. The loss in the hub region can be attributed to flow separation in the acute corner near the rotor trailing edge, which is due to the high camber and spanwise twist in the blade. Near sonic conditions also contribute to high losses near the hub. The reduction in pressure ratio at the tip can be attributed to the growth of the endwall boundary layer subjected to a very high static pressure rise, exceeding nearly 2.7 at the tip. The total pressure ratio increase very close to the tip is due to the work input by the tip shroud. The stator profiles show that the performance suffers near the hub region for the reasons discussed above, but the rest of the stator performance is acceptable despite the high loading.

2 Low-Reaction Stage. In contrast to the high-speed stage, a low-reaction aspirated stage with a total pressure ratio of 2.3:1 was designed with the objective of increasing the loading as well as improving the stage core flow efficiency. Another motivation was to explore the loading level that could be achieved by using aspiration only on the stator. The stage reaction was decreased by lowering the tip speed, which is normally close to 1500 to 1250

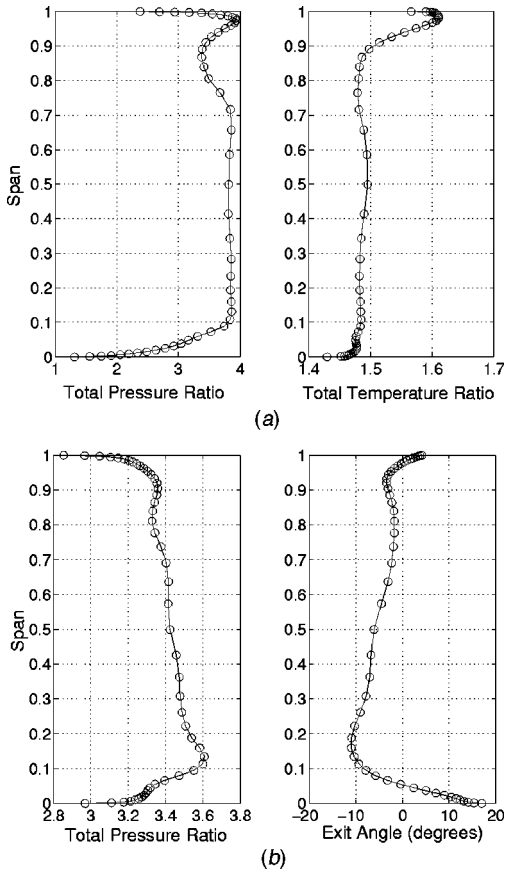

Fig. 10 High-speed stage mass averaged exit profiles—(*a*) rotor exit, (*b*) stator exit

ft/s. This resulted in a decrease in flow Mach number and attendant shock losses in the rotor. The rotor achieved a mass-averaged adiabatic efficiency of 94%. The average diffusion factor of the stator increased to 0.6 as a result of the lower stage reaction. The three-dimensional viscous evaluation of the stage predicted a mass averaged pressure ratio of 2.35 at an adiabatic efficiency of 91%.

The stator midspan flow conditions are summarized in Table 2. An aspiration mass fraction of 0.5% was applied along the stator span on the suction surface at approximately 30% chord. No aspiration was used on the flowpath. It was found that aspiration resulted in a strongly attached boundary in the mid-span region, and decreasing the stator chord resulted in lower losses due to reduction in the wetted surface area. The stator chord was moderately flared near the hub and tip to relieve the endwall boundary layer loading. The loss in the outer 10% span was managed by increasing the stator camber and stagger angle to account for the increase in inlet angle caused by the rotor tip leakage flow.

Figure 11 shows the Mach contours from the three-dimensional viscous calculation at a mid-span section of the stator, and Fig. 12 shows the flow at the stator exit plane. No separation is seen at any spanwise location, however regions of loss due to secondary flow are seen near the hub and tip. Calculations on the design speed line showed that the stator performance did not deteriorate at the different flow conditions despite the high loading. The mass

Table 2 Stator midspan flow conditions

M_{inlet}	0.95
$\Delta\alpha_{\text{inlet}}$	50 deg
DF	0.6
C_{ms}	0.5%

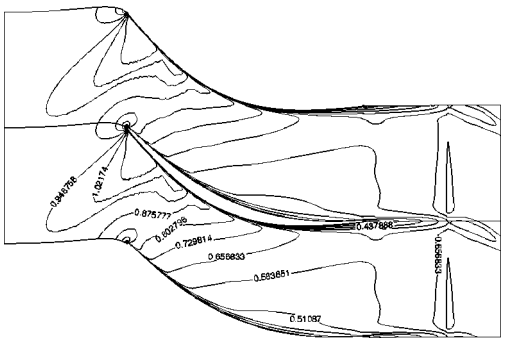

Fig. 11 Low-reaction stage stator mid-span Mach contours

averaged total pressure loss across the stator varied from approximately 3% to a minimum of 2% at peak efficiency.

The mass averaged total pressure and flow angle profiles at the stator exit are shown in Fig. 13. The stator was designed to over turn the flow by 5 deg at the tip, and a linear spanwise variation in exit angle resulting in under turning by the same amount at the hub. The design intent was clearly achieved over most of the span. The rotor total pressure profile is also included in the plot for reference.

3 Turbine Exit Guide Vane. An aspirated exit guide vane (EGV) was designed for a highly loaded turbine stage, where the objective was to minimize the vane count in an effort to reduce weight. The flow conditions for the EGV are summarized in Table 3. The average solidity of the vane is 1.1 with a vane count of 14. The maximum thickness is 16.5% chord and is almost uniform in the spanwise direction. Aspiration was applied at 40% chord on the suction side and extended spanwise from hub to tip.

Figure 14 shows the Mach contours at mid-span from the three-dimensional viscous calculation. A substantial diffusion of the

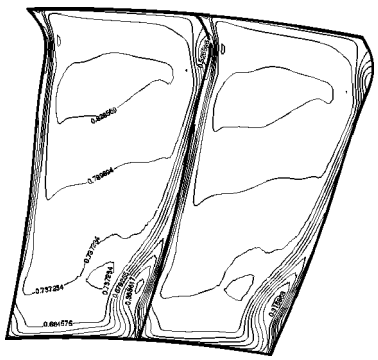

Fig. 12 Low-reaction stage stator exit axial speed contours

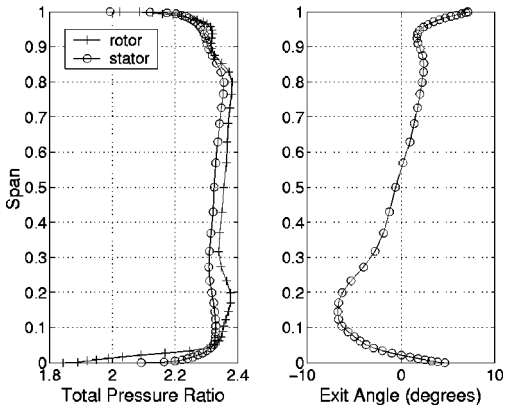

Fig. 13 Low-reaction stage mass averaged stator exit profiles

Table 3 EGV flow conditions

M_{inlet}	0.52
$\Delta\alpha$	45 deg
DF	0.60
C_{ms}	1.0%

flow is seen downstream of the suction location. Although the average diffusion factor is 0.6, it is not a sufficiently good indicator of the loading level for a thick airfoil, where the flow diffusion on the suction surface is more severe than on a thinner airfoil with the same degree of turning. Massive separation of the flow was observed when the calculations were performed without suction. The vane count would have to be significantly increased to achieve acceptable diffusion levels for a nonaspirated design.

Figure 15 shows the contours of axial speed downstream of the EGV. The thickening of the wake and strong secondary flow on the suction side can be attributed to several factors. Examination of the flowfield revealed that corner separation was initiated at the hub and tip by the strong adverse pressure gradient just downstream of the slot. In addition, the curvature of the blade passage and the high loading lead to formation of strong secondary flow. Pitchwise suction slots on the hub and casing had a negligible effect on the corner separations. The corner separation and secondary flow were suppressed either at the hub or the tip by leaning the blade $+5$ or -5 deg, respectively. However, bowing of the blade to include both these effects was ruled out from a practical standpoint of accommodating the suction plumbing within the blade.

The mass-averaged profiles at the EGV inlet and exit are shown in Fig. 16. The impact of suction side separation and secondary flow can be seen in the total pressure profile near the hub and overturning in the exit angle profile. The mass averaged total pressure loss across the EGV was approximately 2%.

Conclusions

The computational studies presented in this paper illustrate the effectiveness of aspiration in controlling the boundary layer development on turbomachinery blade rows. The magnification effect, shown in the boundary layer analysis and cascade study,

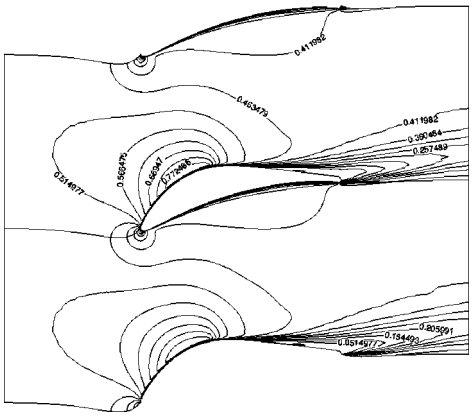

Fig. 14 3-D viscous solution mid-span Mach contours

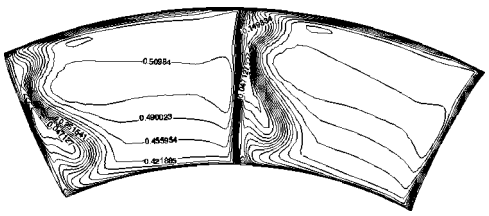

Fig. 15 3-D viscous solution exit axial speed contours

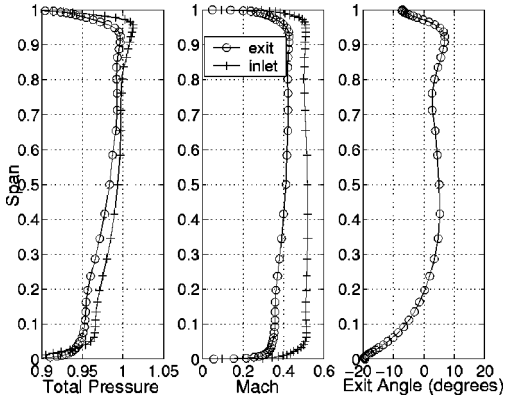

Fig. 16 3-D viscous solution EGV exit profiles

makes aspiration particularly attractive since the blade loading can be significantly increased with relatively small bleed mass fractions on the order of 0.5 to 1% of the inlet mass flow. Computational studies indicate that the useful Lieblein diffusion factor range can be extended to 0.7 or more with aspiration. At moderate loading levels, the thinner boundary layer profile achieved with aspiration can result in a reduction in profile loss. In contrast, increasing the loading capability of conventional cascades, which do not use any method of boundary layer control, will necessarily lead to an increase in profile loss due to a higher solidity requirement and a higher local diffusion factor ($V_{\max}/V_{\text{exit}}$).

The design features of the aspirated blade shapes are an essential ingredient for achieving high loading while minimizing the aspiration requirement. The greater thickness requirement of aspirated blades also demands a more careful design of the blade shape, especially for transonic and supersonic applications. A thickness and camber line description of the blade shape may not be suitable for accurately representing some of the design features of aspirated blades. Design studies have shown that the quasi-3-D design approach can be used quite effectively to design highly loaded blade sections that also perform adequately in three-dimensional calculations. The aspiration requirement on the blade surface predicted by the quasi-3-D code is also consistent with the aspiration requirement in the three-dimensional calculations.

Application of aspiration to three-dimensional blade rows has shown that while aspiration is very effective in controlling the blade boundary layer, the role of the endwall cannot be neglected in achieving high loading. The application of aspiration on the flowpath needs to be investigated and combined with three-dimensional design features such as stator bowing and flowpath contouring to improve loading capability of the endwall boundary layers. In contrast to the very highly loaded high-speed stage and exit guide vane, the low-reaction stage demonstrates the possibility of using aspiration to achieve a moderate increase in loading as well as improving the core flow efficiency. The increase in core flow efficiency has the potential of offsetting the penalty of aspirating the core flow on stage efficiency, and could result in a net gain in stage efficiency. The use of aspiration exclusively on the stator is also an important aspect of this design from an implementation standpoint.

Acknowledgment

I would like to thank Mark Drela and Jack Kerrebrock for their guidance during this research. I would also like to thank John Adamczyk and his team at NASA for many contributions to this research and for carrying out the APNASA calculations. Research presented in this paper was funded by DARPA and NASA Glenn Research Center.

Nomenclature

AVDR = axial velocity density ratio
C_D = dissipation coefficient $=(1/\rho_e u_e^3)\int \tau(\partial u/\partial \eta)d\eta$
C_f = skin friction coefficient $=2\tau_w/\rho_e u_e^2$
C_{ms} = suction mass fraction $=\dot{m}_s/\dot{m}_{\mathrm{inlet}}$
C_p = pressure coefficient
c = blade chord
DF = Lieblein diffusion factor
H = shape parameter $=\delta^*/\theta$
M = Mach no.
P_t = total pressure
p = blade pitch
s = boundary layer arc length
T_t = total temperature
t = thickness
u, v = velocity components
x = axial distance
$\dot{m}$ = mass flow rate
α = absolute flow angle
β = relative flow angle
δ^* = displacement thickness $=\int(1-\rho u/\rho_e u_e)d\eta$
δ_s^* = suction mass defect thickness
η_a = adiabatic efficiency
η = boundary layer normal coordinate
ρ = density
σ = chord to pitch ratio, solidity
θ = momentum thickness $=\int(\rho u/\rho_e u_e)(1-u/u_e)d\eta$
θ = blade camber
θ^* = kinetic energy thickness $=\int(\rho u/\rho_e u_e)(1-u^2/u_e^2)d\eta$
τ = shear stress
ω = mixed out total pressure loss coefficient
ξ = stagger angle
MISES = quasi-3-D design/analysis code

Subscripts

e = boundary layer edge
s = suction
te = trailing edge
w = wall

References

[1] Wennerstrom, A. J., 1990, ''Highly Loaded Axial Flow Compressors: History and Current Development,'' ASME J. Turbomach., **112**, Oct. pp. 567–578.
[2] Lord, W. K., MacMartin, D. G., and Tillman, G., 2000, ''Flow Control Opportunities in Gas Turbine Engines,'' AIAA Pap., June.
[3] Reijnen, D. P., 1997, *Experimental Study of Boundary Layer Suction in a Transonic Compressor*. Ph.D. thesis, MIT, Cambridge, MA, January.
[4] Schuler, B. J., 2001, *Experimental Investigation of an Aspirated Fan Stage*. Ph.D. thesis, MIT, Cambridge, MA.
[5] Kerrebrock, J. L., 2000, ''The Prospects for Aspirated Compressors,'' AIAA Pap., June.
[6] Kerrebrock, J. L., Reijnen, D. P., Ziminsky, W. S., and Smilg, L. M., 1997, ''Aspirated Ccompressors.'' ASME Paper 97-GT525.
[7] McCabe, N., 2001, ''A System Study on the Use of Apirated Technology in Gas Turbine Engines.'' Master's thesis, MIT, June.
[8] Youngren, H. H., 1991, Analysis and Design of Transonic Cascades With Splitter Vanes. Report 203, MIT Gas Turbine Laboratory, Cambridge, MA.
[9] Merchant, A. A., 1996, ''Design and Analysis of Supercritical Airfoils With Boundary Layer Suction.'' Master's thesis, MIT, June.
[10] Merchant, A. A., 1999, *Design and Analysis of Axial Aspirated Compressor Stages*. Ph.D. thesis, MIT, Cambridge, MA, June.
[11] Hobbs, D. E., and Weingold, H. D., 1984, ''Development of Controlled Diffusion Aerofoils for Multistage Compressor Applications,'' ASME J. Eng. Gas Turbines Power, **106**, pp. 271–278.
[12] Pierpont, K., 1947, ''Investigation of Suction-Slot Shapes for Controlling a Turbulent Boundary Layer.'' Technical Note 1292, NACA, June.
[13] Loughery, R. J., Horn, R. A., and Tramm, P. C., 1971, ''Single-Stage Experimental Evaluation of Boundary Layer Blowing and Bleed Techniques for High Lift Stator Blades.'' Contractor Report 54573, NASA, Mar. 71N18749.
[14] Stow, P., 1989, ''Blading Design for Multi-Stage hp Compressors,'' AGARD Conf. Proc., AGARD-LS-167.
[15] Starken, H., 1989, ''Design Criteria for Optimal Blading Design,'' AGARD Conf. Proc., AGARD-LS-167.
[16] Koch, C. C., and Smith, Jr., L. H., 1976, ''Loss Sources and Magnitudes in Axial Flow Compressors,'' ASME J. Eng. Power, July pp. 411–424.
[17] Creagh, J. W. R., and Klapproth, J. F., 1953, ''Utilization of External Compression Diffusion Principle in Design of Shock-in-Rotor Supersonic Compressor Blading,'' research memorandum NACA-RM-E53F18, NACA.
[18] Tweedt, T. L., Schreiber, H. A., and Starken, H., 1988, ''Experimental Investigation of the Performance of a Supersonic Compressor Cascade.'' ASME 88-GT-306.
[19] Henne, P. A., and Gregg, R. D., 1989, ''New Airfoil Design Concept,'' AIAA Pap.,
[20] Korn, D., 1975, ''Numerical Design of Transonic Cascades.'' Technical Report C00-3077-72, ERDA Research and Development.
[21] Gostelow, J. P., 1984, *Cascade Aerodynamics*. Pergamon Press, Oxford.
[22] Drela, M., 1989, ''An Integral Boundary Layer Formulation for Blunt Trailing Edges,'' AIAA Pap., August.
[23] Brear, M. J., Hodson, H. P., and Harvey, N. W., 2001, ''Pressure Surface Separations in Low Pressure Turbines: Part 1—Midspan Behavior.'' ASME Paper 2001-GT-0437, June.
[24] Adamczyk, J. J., Celestina, M. L., and Mulac, R. A., 1986, ''A Model for Closing the Inviscid Form of the Average-Passage Equation System,'' ASME J. Turbomach., **108**, Oct pp. 180–186.
[25] Wennerstrom, A. J., 1984, ''Experimental Study of a High-Throughflow Transonic Axial Compressor Stage,'' ASME J. Eng. Gas Turbines Power, **106**, July pp. 552–559.
[26] Merchant, A. A., Drela, M., Kerrebrock, J. L., Adamczyk, J. J., and Celestina, M., 2000, ''Aerodynamic Design and Analysis of a High Pressure Ratio Aspirated Compressor Stage.'' ASME Paper 2000-GT-619.

Simon Coldrick

Paul Ivey

School of Engineering,
Cranfield University,
Bedford, United Kingdom

Roger Wells
Alstom Power Limited,
Lincoln, United Kingdom

Considerations for Using 3-D Pneumatic Probes in High-Speed Axial Compressors

This paper describes preparatory work towards three-dimensional flowfield measurements downstream of the rotor in an industrial, multistage, axial compressor, using a pneumatic pressure probe. The probe is of the steady-state four-hole cobra probe type. The design manufacture and calibration of the probe is described. CFD calculations have been undertaken in order to assess the feasibility of using such a probe in the high-speed compressor environment where space is limited. This includes effects of mounting the probe in close proximity to the downstream stator blades and whether it is necessary to adjust the calibration data to compensate for these effects. [DOI: 10.1115/1.1515334]

Introduction

Pneumatic pressure probes can be used to make flow measurements in two or three dimensions, for quantities such as flow angle and Mach number. Probes are calibrated in a known flow in a wind tunnel, in the application of the probe to an unknown flow, the data produced is related to the calibration data and the flow conditions determined. Despite their simplicity, basic pneumatic probes have many advantages over techniques such as hot wire probes, laser anemometry and fast response probes; they can be used at high temperatures, give pressure data and do not require any optical windows to be installed in the machine unlike laser anemometry. The main disadvantage of these pneumatic pressure probes is that they are an intrusive method, that is the disturbance effect of the probe contaminates the measurements. This study is centered on measurements in an industrial, multi-stage axial compressor. Two locations were under consideration for the measurements in the compressor; downstream of the rotor at stage 5 and downstream of the rotor at stage 9. Blockage presents a problem particularly at stage 9 since the axial gaps are very small and the probe must be set close to the downstream stator. This paper aims to present some of the problems encountered when making measurements in close coupled compressor stages.

Probe Design

Three hole probes are usually used for 2-dimensional flow measurements and five hole probes for 3-dimensional measurements. The main disadvantage with five hole probes is that redundant data is gained and the probe is larger than it needs to be. Four holes is the minimum number needed to make 3-dimensional measurements.

The four-hole probes used in the current investigation are a miniaturisation of those used by Lyes [1]. The design consists of a three-hole probe with a fourth pitch angle sensing port mounted above the yaw sensing holes. Although this design is not symmetrical, it does allow yaw angle measurements to be made independently of the pitch angle. The probes used by Lyes were for a low-speed, large-scale facility. The current investigation necessitated a smaller probe due to the space limitations. A 3-mm diameter was used, as this was the smallest that could be feasibly manufactured with the available methods and still obtain accurate forming of the probe head.

Since the whole probe must fit in the 3-mm envelope to enable it to be passed through the casing, the probe head can not be extended clear of the probe body. Ideally, the probe head should extend well upstream of the body. Studies by Thomas [2] showed that compacting the probe head has little effect on the performance of a four-hole probe. Figure 1 is a schematic of the probe. Figure 2 shows a comparison of the existing four-hole probes used by Lyes and the new probes for the high-speed testing.

Manufacture

The probe head consists of four stainless steel hypodermic tubes of 0.8-mm OD. These are formed into a swan neck shape then brazed into a 3-mm OD shaft. Finally the chamfers are milled onto the head at 45 deg on the side ports. Due to problems on the previous low speed four hole probes with the chamfer of the upper port almost merging with the neck of the probe, it was decided to omit the chamfer from the upper port ($U1$) altogether. Different flow characteristics around the upper and lower ports mean that a pressure difference between the two ports is still registered when the probe is pitched.

Calibration

Calibration was carried out in a 200-mm-dia suction wind tunnel (Fig. 3). Air is drawn through an inlet filter and bellmouth and then passes through the test section before exiting to the atmosphere. The test section is fitted with a tilting table that can be set between −15 and −15 deg in 5-deg steps. Attached to this table is a traverse gear that yawed the probe between −30 and −30 deg. The probe enters the wind tunnel through a longitudinal slot. Yaw angle is set using an automatic control box, though pitch angle is set manually after each yaw sweep. The Mach number of the test section can be varied between 0 and 0.7 by adjusting the motor power. Mach number was varied between 0.2 and 0.7 in steps of 0.1. Calibrations were performed at 17 yaw angles and 7 pitch angles for each Mach number step, giving a total of 714 calibration points.

It was not possible to vary the Reynolds number of the wind tunnel independently of the Mach number. To do so requires a closed circuit wind tunnel that can be pressurised or a system for heating the air. Thus, it was not possible to determine Reynolds number effects on the probe independently of Mach number. Dominy and Hodson [3] showed that calibration often falls into an area of significant Reynolds number effect, this causes a change in the pressures indicated at the probe port and a change in the angular measurement. Construction of the probe head with well-defined edges minimizes Reynolds number effects, due to the flow separation at these edges [4]. Additionally, positioning the pressure ports on flat edges means that the positioning of the holes is less critical than with a conical or spherical probe.

Contributed by the International Gas Turbine Institute and presented at the International Gas Turbine and Aeroengine Congress and Exhibition, Amsterdam, The Netherlands, June 3–6, 2002. Manuscript received by the IGTI, October 15, 2001. Paper No. 2002-GT-30045. Review Chair: E. Benvenuti.

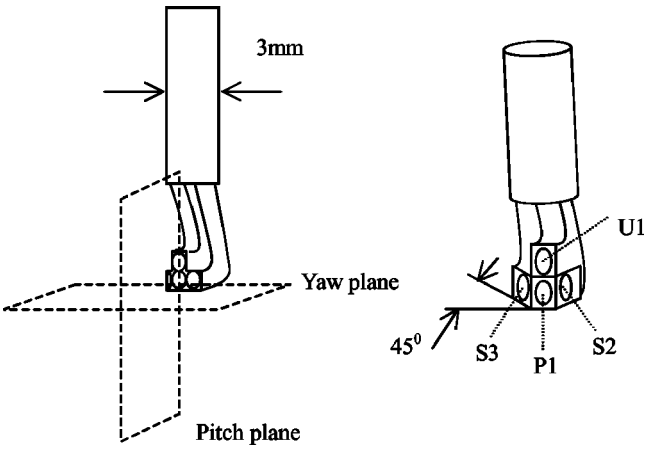

Fig. 1 Probe head schematic and hole numbering convention

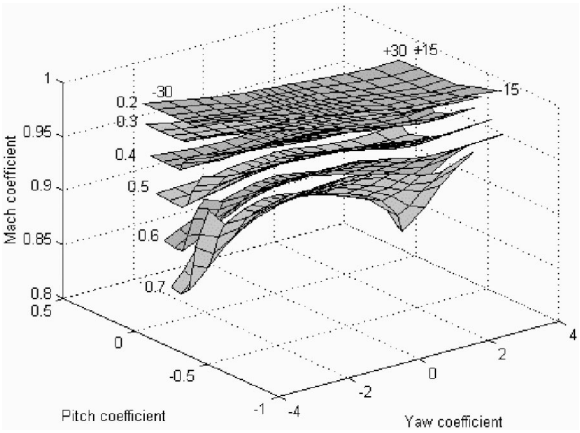

Fig. 4 Calibration graph for all Mach numbers and angles

Calibration Coefficients. Each quantity to be measured requires a corresponding dimensionless coefficient that varies strongly with the quantity to be measured and weakly with the other quantities. For a 3-D probe these are yaw angle, pitch angle. Mach number, and total pressure. There are several options on the formulation of these coefficients, which use the dependent hole pressure difference as the numerator nondimensionalised by a dynamic pressure or a ''probe indicated dynamic pressure'' as the denominator.

A review of calibration coefficients was carried out and coefficients were defined for this investigation according to Dudzinski [5], with the addition of a Mach number coefficient [3] as follows:

$$C_{\text{yaw}} = \frac{S2 - S3}{B} \tag{1}$$

$$C_{\text{pitch}} = \frac{P1 - U1}{B} \tag{2}$$

where $B = P1 - 1/2(S2 + S3)$

$$C_{\text{mach}} = \frac{(U1 + S2 + S3)/3}{P1} \tag{3}$$

$$C_{\text{total}} = \frac{P1 - PT}{B} \tag{4}$$

Although B corresponds to only about half of the true dynamic pressure Dudzinski found that using these coefficients gave less interdependence between the coefficients. Additionally the flow angle can be found only from pressures measured at the probe head. If the dynamic pressure PT-PS is used as B and it is unknown, then it must be determined through an iterative method of guesses and checks. This has the disadvantage that the accuracy of any angular measurements relies upon determining the static pressure correctly. A comparison of the different forms of coefficients is given in [6], where little difference was found between the different forms. Other calibration methods such as zoning [7] were not considered due to the unnecessary complexity, as they are more suited to wide angle measurements with probes with many holes.

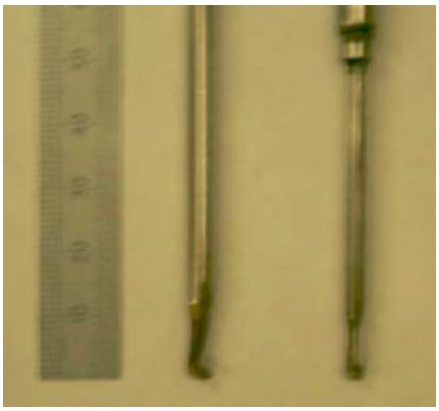

Fig. 2 Four-hole probe for low speed (left), current probe for high speed (right)

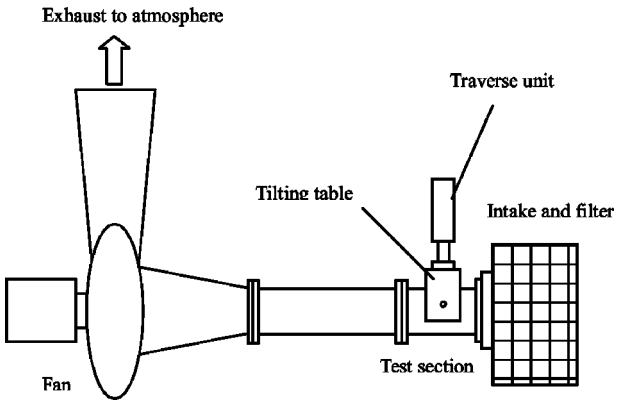

Fig. 3 Wind tunnel layout

Calibration Results and Discussion. Figure 4 shows the calibration graphs for one of probes between Mach 0.2 and 0.7. The uniform shape of the graph in the yaw and pitch angle directions indicate that the probes have calibrated cleanly with respect to these parameters. Yaw coefficient appears to vary evenly with yaw angle. The sensitivity (the per degree change in coefficient with angle) is approximately 0.15. The probes show less sensitivity to pitch angle giving a value of 0.015. This compares to a value of 0.02 found by Lyes for the similar 4-hole probes, the reason for this is the omission of the chamfer on the upper port, which means that a smaller pressure difference is recorded between $P1$ and $U1$ when the probe is pitched.

Yaw coefficient, is relatively unchanged with pitch angle (Fig. 5). This lack of interdependence is beneficial in that the yaw angle can be determined almost independently of pitch angle. However, pitch coefficient shows dependence on yaw angle. This was traced to a manufacturing misalignment of the upper sensing port although not a serious problem it does highlight the sensitivity of small probes to fabrication imperfections. This would seem to be

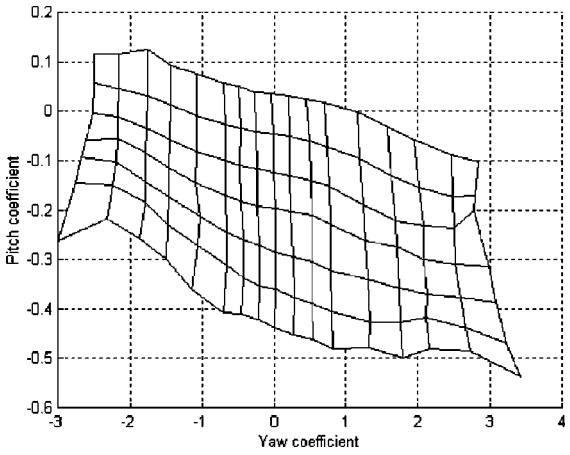

Fig. 5 Calibration graph at Mach 0.7

a particular problem with cobra probes that rely on the formation of the brazing around the probe head, as well as accurate machining of the chamfers on the probe head. Mach coefficient varies in an orderly manner with Mach number, especially at the lower Mach numbers. At higher values there appears to be some effects arising from interdependence with the yaw and pitch coefficients.

Accuracy and Uncertainty. The propagation of errors that arise at the calibration stage has an impact of any subsequent data reduction and angle determination. Kline and McClintock [8] proposed that all experiments fall into two categories; single-sample and multi sample. With a multi-sample experiment an individual measurement is repeated enough times that errors can be determined statistically. In the calibration of pneumatic probes, such a large number of individual measurements are taken that it is not practical to repeat them. In this case the error analysis for single sample experiments has been used.

The approach is the based on that given by Trieber et al. [9]. The method recognises that all measurement uncertainties during calibration can be converted to a total angular error. At present the error analysis is only extended as far as the calibration. Table 1 gives the measurements made during the calibration and their associated errors at Mach 0.5. The measurement errors in column 1 correspond to the basic uncertainties in pressure and probe position. In turn, these give uncertainties in the coefficients, shown in column 2. Through the slope of the calibration curves, the coefficient uncertainties are translated into angular errors. The uncertainty in pressure measurements was mainly due to fluctuations in the static pressure in the test section of the wind tunnel. In comparison with the results of [9], similar pressure uncertainties have been found, but the positioning appears to be less accurate.

Blockage Effects

Among the problems encountered in using a probe in confined spaces are blockage and the effects of the proximity of the probe to solid surfaces. Since in the compressor the probe would be within the downstream stator passage, a computational fluid dynamics (CFD) analysis was conducted to assess the foregoing effects. It is worth mentioning that the probe for large scale testing was 4 mm diameter and used with a blade pitch of 40 mm. The current investigation uses of a 3-mm-dia probe with a blade pitch of 15 mm.

Table 1 Sources of error and their effects

Measurement Error		Consequences	Total Angle Error
Yaw Position	$\Delta\alpha_s = \pm 0.1^0$	$\Delta\alpha_p = 0.019$	$\Delta\alpha = \Delta\alpha_p + \Delta\alpha_s$
Pitch position	$\Delta\beta_s = \pm 0.85^0$	$\Delta\beta_p = 0.019$	$\Delta\beta = \Delta\beta_p + \Delta\beta_s$
P1	$\Delta P1 = \pm 10$ Pa		$\Delta\alpha = 0.27^0$
S2	$\Delta S2 = \pm 50$ Pa		$\Delta\beta = 1.3^0$
S3	$\Delta S3 = \pm 50$ Pa		
U1	$\Delta U1 = \pm 10$ Pa		
PT	$\Delta PT = \pm 1$Pa		
PS	$\Delta PS = \pm 50$ Pa		

Wyler [10] identified that blockage had different effects in closed channels and open jets. By rotating a cylindrical probe with one pressure tapping through a complete revolution in both open and closed jets. Wyler was able to conclude that in closed channels, the presence of the probe caused an increase in speed and a corresponding decrease in pressure indicated at the tapping, whilst in the open jet the opposite was true. A similar method was used in the current investigation to assess the effects of using the 3 mm probe in stage 9 of the compressor, through a numerical simulation of a cylindrical probe fixed at the leading edge of a stator at mid passage. The aim being to provide a means to compare the blockage effects of the 2 and 3-mm probes and a reference against which to judge them. The advantage of using a cylindrical probe in this case is that only one ''calibration'' needed be run, as pressure distribution is gained at all angles around the circumference of the probe. The compromise is that the cobra probe is approximated as a cylinder, which is known to be highly Reynolds number dependent, though for each simulation the Reynolds number is the same (50,000).

The simulation was carried out using the commercial code CFX TASCflow [11]. TASCflow uses a pressure correction method to solve the Navier Stokes equations. Structured grids were used. Converged solutions were obtained using modified linear profile discretization which was used due to the large velocity difference encountered. Standard K-ε turbulence model was used.

Stator vane geometry from a high speed research compressor (HSRC) at Cranfield University was representative of the stators under consideration in the industrial compressor, as the actual blade geometry was unavailable for open publication. The HSRC is a 3-stage, high-speed axial compressor intended for core compressor studies. The blading is representative of modern designs and standard in terms of aerodynamic and geometric parameters, the profiles are controlled diffusion, with no end bends. A cascade of four stator vaness was set up to allow the flow in the blocked passage and the two neighboring passages to be studied. The upstream rotor was not considered in the investigation for a number of reasons. Firstly, the size of the problem would have been prohibitive to run as an unsteady case. Secondly, using a mixing plane upstream of the probe would average out any effects the probe may have on the upstream rotor. Additionally, the HSRC uses enlarged axial blade gaps, which would not give a true representation of the situation. As a result, the scope of this investigation is limited to that of blockage effects and does not include the averaging process of using a steady state probe in an unsteady environment.

Each cascade grid was produced by connecting together 8 individual grid blocks. Thus the empty cascade consisted of four blade grids, and 4 blank spacer grids. For the cascade with the probes, the central spacer grid was replaced with the probe grid. The advantage of this method is that the grid surrounding the probe is the same for each test case. The total number of nodes in the completed grids was approximately 320,000 nodes.
Four of these grids were produced:

- an unblocked cascade
- cascade with a 3-mm cylindrical probe
- cascade with a 2-mm cylindrical probe
- 3-mm probe in a grid with no blades, to act as a reference ''calibration.''

The inlet conditions to stator 3 were available from a full machine simulation. The inlet condition being a distribution of total pressure, total temperature, direction vector and turbulence information in the form of a profile input file. Since the inlet of the

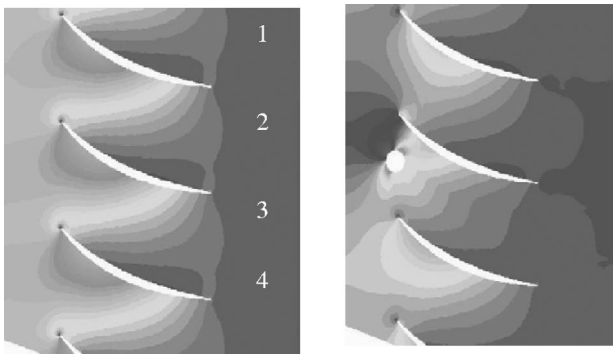

Fig. 6 Pressure through the unblocked cascade (left) and the cascade with a 3-mm cylindrical probe (right)

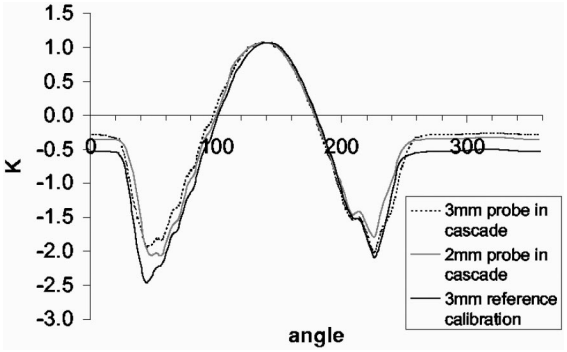

Fig. 8 Pressure coefficient *K* with angle at mid height

cascade grid differed from the mixing plane simulation in both the pitchwise and radial directions it was necessary to modify this input file. Each of the flow quantities was averaged in the pitchwise direction, to give variation only in the radial direction. In the radial direction the flow quantities were individually interpolated from the full simulation grid to the cascade grid. In this way the profile in the hub to shroud direction was preserved, but there was no pitchwise variation. A modified input profile file was attached to each of the grids in the cascade. Outlet of the cascade was set at an average static pressure. The ends of the cascade were periodic and wall boundary conditions applied to all the solid surfaces.

Verification. Figure 6 shows a plot of pressure at midheight in the cascade and the passage numbering convention. Total mass flow through the compressor, when considered as a whole, that is multiplied by 29 gives a value of 10.8 kg/s. This is in reasonable agreement with the design mass flow of 10.64 kg/s and the previous simulation result of 10.6 kg/s. The averaging process used for the inlet conditions accounts for the difference. Inlet flow angle is specified so that the inlet velocity and static pressure in addition to the mass flow are calculated.

Effects of Mounting a Probe in the Flow. Figure 7 shows the mass flow through each passage as a fraction of the total mass flow through each cascade. Mass flow through each passage is as one would expect, that is a reduction in the blocked passage and an increase in the neighboring passages. This means the blockage problem is not as that of a closed duct.

Figure 6 shows the cascade at mid height and with 3-mm-dia probe. It is evident that the overall flow is changed in comparison with the empty cascade. The reason for this is that the total mass flow through the cascade is reduced with the presence of the probe. This is a result of the periodic boundary conditions, which effectively means that there are 29 probes mounted in the compressor, giving a reduction in the overall mass flow. This is unavoidable without simulating the entire stator row. The data are therefore presented in suitable nondimensional form.

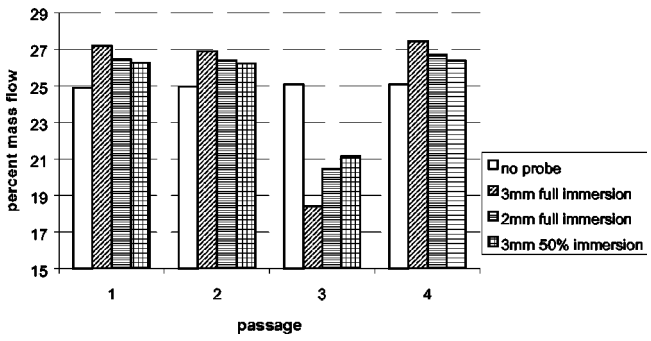

Fig. 7 Percent of cascade total mass flow through each passage

Nodes corresponding to 3 lines around the circumference of the probe were identified and the pressure at each node and its angular position recorded. One line at near casing one at near the hub and one at mid height. The pressure was formed into the following pressure coefficient:

$$K = \frac{Ph - PS}{PT - PS} \tag{5}$$

The value of static pressure was taken at the inlet to the cascade, as this is an explicit result of the calculation. Using this coefficient means that the differences of speed and pressure are removed from the comparison. By plotting the value of this coefficient against angle around the circumference of the probe, the distribution can be compared for the cases of the probe in a free stream and the probe in the cascade.

The three cases studied were:

- the 3-mm-dia cylinder probe in the cascade
- the 2-mm-dia probe in the cascade
- the 3-mm-dia probe in a free stream.

Figure 8 shows the change in pressure coefficient *K* with angle around the probe. From 0 to 100 deg is the side of the probe adjacent to the suction side of the vane. A standard pressure distribution for a cylinder in a steady flow has been obtained. The point at which the lines cross the *x*-axis corresponds to the state where $Ph = PS$. In comparison to the reference calibration, for the 2-mm and 3-mm probes in the cascade, there is a shift in the entire pressure distribution around the probe, towards the suction side of the vane. The effect of the 2-mm probe is similar but to a lesser degree. Figures 9–11 show speed plots in the region of the probe and blade leading edge. The presence of the blades interferes with the flow in the region in front of the probe, causing a slowing of the flow. The result of this appears to be a relative increase in the pressure between the probe and the suction side of the blades. A similar trend was also noticed near the casing and near the hub.

Chue [12] cited that the cause of erroneous readings when the probe was mounted near to a flat surface was due to the nozzle effect of the flow being accelerated between the probe and the surface. Although Heneka and Bubeck [13] found that the cause of errors was due to the fact that the probe head was within the boundary layer, and a steep velocity gradient. In the present investigation, the probe is well outside the boundary layer. The change in pressure around the probe can be explained by the slowing of the flow at the leading edge of the blade and probe and subsequent velocity biasing.

The entire pressure distribution up to approximately 90 deg either side of the stagnation point of the probe is moved by approximately 3 deg, though the effect is less serious on the side of

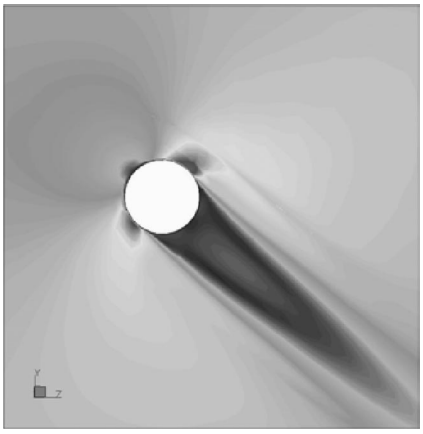

Fig. 9 Speed plot in the reference flow

the probe away from the suction side of the blade. The result of this on a cobra probe would be an increase in pressure at the hole adjacent to the suction side of the blade in addition to a small change in the pressure measured at the center port ($P1$).

Smout [14] investigated the effects of the proximity to the walls through which the probe is introduced. It was found that the effect was to alter the static pressure field in the region of the probe head at different immersions. Smout was able to calculate the errors in the static pressure and adjust the static pressure calibration accordingly. Because calibration coefficients for angles were dependent static on pressure. Smout was able to correct any angular errors arising from the static pressure error. Since the coefficients used in the this investigation depend only on the pressure differences recorded at the probe head, the angular error is directly a result of a ''false'' pressure reading at the side port on the probe nearest to the blade and to a shift in the stagnation point.

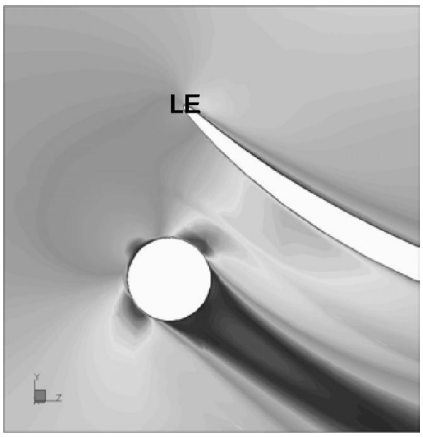

Fig. 10 Speed around the 3 mm probe in the cascade

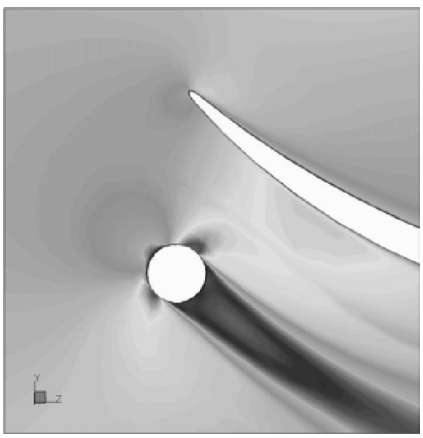

Fig. 11 Speed around the 2-mm probe in the cascade

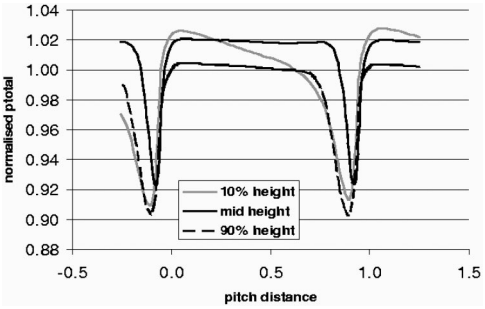

Fig. 12 Total pressure 25% chord downstream of stator row

Downstream Effects. It is noticeable from Figs. 9, 10, and 11 that the wake from the probe is substantial. Wakes from upstream stators have an effect on the downstream rotors, in the form of forcing functions [15]. This is due to the velocity deficit in the wake region. An undesirable effect of pressure probes is that the wake generated is often much more severe than that of the blades.

Figure 12 shows total pressure at 25% chord downstream of the stator, for the undisturbed cascade. The wakes are clearly visible, as is the increased separation on the suction side of the blades. Figure 13 is a total pressure plot at the same axial location, although the blade wakes remain largely unchanged, the wake from the probe is evident in being of greater magnitude than the blade wakes, despite being 125% chord downstream of the probe itself.

Summary and Conclusions

Miniature multi-hole pressure probes have been manufactured and calibrated in order to take measurements downstream of a compressor rotor. The design has shown the limitation of lower pitch angle sensitivity.

The CFD has allowed visualisation of the affects of placing a probe near to the downstream stator vanes. These are presenting a substantial blockage, a change in pressure distribution around the probe and a large wake formed by the probe. The main problem with the analysis of probes in blade rows is that more passages need to be modeled to resolve the problem of the mass flow reduction, ideally the entire stator row. Some of the variation in the mass flow is due to the computational model and the way the quantities are calculated because the mass flow is an explicit result of the calculation. The effect of this mass flow reduction is an

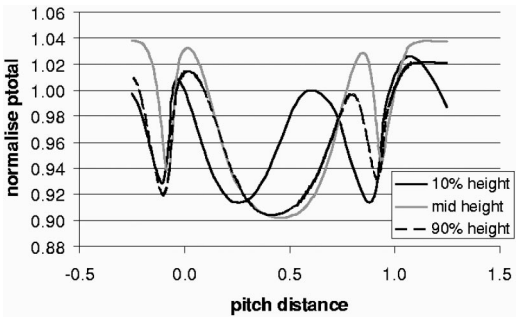

Fig. 13 Total pressure 25% chord downstream of stator row with 3-mm probe

untrue representation of the problem, as such a reduction is in effect a change in position on the compressor map.

It can be concluded that the proximity to the stator vane causes an increase in pressure and a decrease in speed in the region between the blade and the probe, leading to a shift in the stagnation point and an erroneous reading on the adjacent probe pressure port. The addition of the measuring uncertainty from Table 1 would lead to approximately 3.3 deg total uncertainty. This can be resolved in part by moving the probe away from the center of the passage or to a lesser degree by using a smaller probe.

The effect of the probe wake on any downstream rotor blades is in the form of a once per revolution forcing function due to the total pressure deficit.

Acknowledgments

The authors would like to thank the United Kingdom Engineering and Physical Sciences Research Council and also Alstom Power UK limited for supporting the project.

Nomenclature

α = yaw angle
β = pitch angle
P = pressure (Pa)
PT = static pressure
PS = total pressure
$S2$ = probe left side port
$S3$ = probe right side port
$P1$ = probe center port
Ph = nodal pressure value
$U1$ = probe upper port
C = probe pressure coefficient

Subscripts

P = uncertainty of pressure value
S = uncertainty of position

References

[1] Lyes, P. A., 1999, ''Low Speed Axial Compressor Design and Evaluation, High Speed Representation and Endwall Flow Control Studies,'' PhD thesis, Cranfield University, UK.
[2] Thomas, C. C., 1999, ''High Bandwidth Aerodynamic Measurements in Gas Turbine Stages,'' D.Phil thesis, Oxford University, UK.
[3] Dominy, R. G., and Hodson, H. P., 1993, ''An Investigation of the Factors Influencing the Calibration of Five Hole Probes for Three Dimensional Flow Measurements,'' ASME J. Turbomach., **115**, July, pp. 513–519.
[4] Main, A. J., Day, C. R. B., Lock, C. D., and Oldfield, M. L. G., 1996, ''Calibration of a Four Hole Pyramid Probe and Area Traverse Measurements in a Short-Duration Transonic Turbine Cascade Tunnel,'' Exp. Fluids, **21**(4), pp. 302–311.
[5] Dudzinski, T. J., and Krause, L. N., 1969, ''Flow Direction Measurement With Fixed Position Probes,'' NASA TM X 1904.
[6] Cabitza, S., and Mandas, N., 1990, ''An Investigation into the Influence of the Different Calibration Coefficients upon Measurements with Aerodynamic Pressure Probes,'' Proc., 10th symposium on measuring techniques for transonic and supersonic flows in cascades and turbomachines Von Karman Institute.
[7] Schaub, U. W., Sharp, C. R., and Bassett, R. W., 1964, ''An Investigation of the Three Dimensional Flow Characteristics of a Non Nulling Five Tube Probe,'' NRC LR 398.
[8] Kline, S. J., and McClintock, F. A., 1953, ''Describing Uncertainties in Single Sample Experiments,'' Mech. Eng. (Am. Soc. Mech. Eng.), **75**(1), Jan., pp. 3–8.
[9] Treiber, M., Kupferschmied, P., and Gyamarthy, G., 1998, ''Analysis of the Error Propagation Arising from Measurements with a Miniature Pneumatic Five Hole Probe,'' Proc., 14th symposium on measuring techniques for transonic and supersonic flows in cascades and turbomachines, Limerick, Ireland.
[10] Wyler, J. S., 1975, ''Probe Blockage Effects in Free Jets and Closed Tunnels,'' ASME J. Eng. Power, **97**(4), pp. 509–515.
[11] Advanced Scientific Computing Ltd, 1995, Waterloo, Ontario, Canada.
[12] Chue, S. H., 1975, ''Pressure Probes for Fluid Measurement,'' Prog. Aerosp. Sci., **16**(2), pp. 147–223.
[13] Heneka, A., and Bubeck, H., 1983, ''Measuring Errors of Pneumatic Multihole Probes,'' Proc., 7th symposium on measuring techniques for transonic and supersonic flows in cascades and turbomachines, Aachen
[14] Smout, P. D., 1995, ''The Measurement of Near Wall Flows Using Pneumatic Wedge Probes,'' Ph.D. thesis, Cranfield University, UK.
[15] Manwaring, S. R., and Wisler, D. C., 1993, ''Unsteady Aerodynamics and Gust Response in Compressors and Turbines,'' ASME J. Turbomach., **115**, Oct..

Robust Optimal Positioning of Strain Gages on Blades

Marc P. Mignolet
Fellow ASME
Department of Mechanical and Aerospace Engineering,
Arizona State University,
Tempe, AZ 85287-6106
e-mail: marc.mignolet@asu.edu

Byeong-Keun Choi
Gyeongsang National University,
School of Mechanical and Aerospace Engineering,
The Institute of Marine Industry,
Tongyoung, Kyongnam 650-160, Korea
e-mail: bg_choi@nongae.gsnu.ac.kr

This paper focuses on the formulation and validation of an automatic strategy for the selection of the locations and directions of strain gages to capture at best the modal response of a blade in a series of modes. These locations and directions are selected to render the strain measurements as robust as possible with respect to random mispositioning of the gages and gage failures. The approach relies on the evaluation of the signal-to-noise ratios of the gage measurements from finite element strain data and includes the effects of gage size. A genetic algorithm is used to find the strain gage locations-directions that lead to the largest possible value of the smallest modal strain signal-to-noise ratio, in the absence of gage failure, or of its expected value when gage failure is possible. A fan blade is used to exemplify the applicability of the proposed methodology and to demonstrate the effects of the essential parameters of the problem, i.e., the mispositioning level, the probability of gage failure, and the number of gages. [DOI: 10.1115/1.1509076]

Keywords: Sensor Placement, Strain Measurement, Blade Vibration, Optimization, Strain Gage

Introduction

Measuring vibrations of turbomachine blades is a substantially harder task than it is for most other structures. The difficulties encountered stem in particular from the harsh operating conditions of the blades, e.g., the rotation, the fluid flow, as well as their structural peculiarities, e.g., sharply peaked modal strain distributions and mistuning effects.

While there exists a variety of devices to measure vibrations in general, e.g., strain gages, accelerometers, proximity probes, LVDTs, laser vibrometer, etc., the need to not perturb the aerodynamics around the blades and the high centripetal loading they are subjected to limit the choice for blades to strain gages and, more recently, light probes systems. Further, the rotation of the system considered necessitates the use of a slip ring to transmit the strain gage signals to the nonrotating environment. It thus restricts the number of these devices to only a few, typically many fewer than the product of the number of modes of interest by the number of blades on the disk.

In principle, the rotational symmetry of the bladed disk should ease the instrumentation process. Indeed, since the modes of vibration of this system consist in fact of harmonic waves of constant amplitude traveling forward and backward around the disk, the resonant responses of two different blades should have the same amplitude, but be out of phase with respect to each other. In the case of a perfectly tuned disk, it would thus be sufficient to instrument a single blade. Unfortunately, manufacturing variability and in-service wear generally create a small level of blade-to-blade variation in their structural/material properties referred to as mistuning which incurs dramatic differences in the amplitudes of the resonant response of different blades. Accordingly, it would be desirable to instrument a series of blades in order to capture the one yielding the largest resonant response. Given the limitations of slip rings, the instrumentation of several blades is possible only by using p strain gages per blade to obtain the modal strain amplitudes of m different modes, and $p<m$.

With such a small number of strain gages, it is not possible to obtain an accurate perspective of the strain field from the measurements alone. The standard resolution of this issue is then to rely on finite element analyses to obtain the overall shape of the strain field and use the measurements as scale factor of the computational results. To achieve the largest accuracy given the inherent gage error, quantization noise, etc., it would best to position the strain gages at the peaks of the strain distribution of the different modes considered. Clearly, this is in general not possible with $p<m$; but even if it was, it may not always be advisable to do so. Indeed, the peaks of the strain distribution are often very sharp and a slight mispositioning of the strain gage, in location and/or direction, may result in a measured strain much less than the maximum value. The location of the strain gages thus appears as a compromise between high strain levels and low sensitivity to mispositioning.

Another important practical consideration that affects the selection of the strain gage locations is their potential failure. The combination of the large centripetal loading, the entraining fluid flow, and possibly high temperatures represents a particularly harsh environment in which it is not unusual that a strain gauge debonds. The potential loss of a measurement may have dramatic effects on the prediction of the modal strains, especially if there is little overlap between the modes that are captured by different strain gages. The optimization of strain gage placement must then include also the potential loss of one or several of the strain gages.

Surprisingly, given the practical importance of this issue, there has been only a few investigations focusing on the positioning of strain gages on blade. Among these, Yang and Griffin [1] proposed a strain gage positioning strategy aimed in particular at the difficult task of recognizing closely spaced modes. On the contrary, Sensmeier and Nichol [2,3] approached the strain gage placement from a variety of data processing perspectives including mode identification and visibility.

The approach proposed in this paper is complementary of these earlier efforts as it is statistical in nature considering the random effects of mispositioning and gauge failure on the measured strains.

The Max-Min-Max Optimization Principle

No Gage Failure. In the absence of gage failure, the selection of the strain gage locations is dictated by the modal strain distribution and by the ''measurement noise'' (intrinsic gage error, quantization error, electrical interference, etc.) and potential mispositioning of the gauges. While the noise and mispositioning do not affect the strain measurements in similar manners, they have one common effect, i.e., to produce variability in the obtained

Contributed by the International Gas Turbine Institute and presented at the International Gas Turbine and Aeroengine Congress and Exhibition, Amsterdam, The Netherlands, June 3–6, 2002. Manuscript received by the IGTI, March 4, 2002. Paper No. 2002-GT-30454. Review Chair: E. Benvenuti.

strain values. That is, if the instrumentation and measurement processes were repeated over and over on the same blade in the same excitation conditions, different strain measurements would be obtained reflecting different noise values and the effect of a slight variation in the actual positions of the strain gauges around the desired ones. The quantification of the variability present is most conveniently achieved through the signal-to-noise ratio (SNR) which is defined as

$$\mathrm{SNR}(\varepsilon)=\frac{\mu_\varepsilon}{\sigma_\varepsilon} \tag{1}$$

In this equation, μ_ε denotes the mean value of the strain, i.e., the average of the measurements that would be obtained in a series of instrumentation and measurement processes as defined in the foregoing. Further, σ_ε represents the corresponding standard deviation which involves the contributions of the noise, $\sigma_\varepsilon^{(n)}$, and of the mispositioning, $\sigma_\varepsilon^{(m)}$. While the former term is dependent on the type of gage selected, the data acquisition system, and the test conditions, the latter one is a function of the strain gage placement hardware and the skills of the operator. Since the processes involved in the two variability terms are different, it is reasonable to assume that the noise and mispositioning effects be statistically independent, so that

$$\sigma_\varepsilon^2=\sigma_\varepsilon^{(n)2}+\sigma_\varepsilon^{(m)2} \tag{2}$$

Note further that the mispositioning effects depend on the strain distribution around the location of interest at the contrary of the standard deviation of the noise component which may be expressed as a fixed percentage of the measured or maximum strain.

From its definition, Eq. (1), the signal-to-noise ratio can be viewed as a measure of confidence on the observed strains, i.e., the larger this value is, the smaller the variability is in relation to the strain level. On this basis, the overall strain gage placement strategy proposed here focuses on maximizing the signal-to-noise ratios. The specifics of the optimization approach are dependent on how the measurements are used to estimate the modal strain distributions. In the present effort, it has been assumed that the scaling factor of the finite element results for a specific mode are evaluated from the gage yielding the largest signal-to-noise ratio of all p gages for that mode. That is, let $\mathrm{SNR}(i,j,\underline{X})$ be the signal-to-noise ratio of the measurement at location i in the jth mode of response (resonance with the jth natural frequency) when the gages are located at coordinates $'\underline{X}$. Then, the best estimate of the forced response in that mode will be obtained from the gage i that gives the largest value of $\mathrm{SNR}(i,j,\underline{X})$ so that the signal-to-noise ratio of the response in the jth mode is

$$\mathrm{SNR}(j,\underline{X})=\max_i \mathrm{SNR}(i,j,\underline{X}) \tag{3}$$

The appropriateness of a given set $\underline{X}$ of strain gage locations can then be characterized by the values $\mathrm{SNR}(j,\underline{X})$, $j=1,2,\ldots,m$, and more succinctly by the lowest of these signal-to-noise ratios taken over all modes considered, i.e.,

$$\mathrm{SNR}(\underline{X})=\min_j \mathrm{SNR}(j,\underline{X}) \tag{4}$$

On this basis, it is proposed here to select the strain gage locations $\underline{X}$ to maximize $\mathrm{SNR}(\underline{X})$. This process results in the following max-min-max optimization principle

$$\textbf{maximize}\ \min_j\{\max_i[\mathrm{SNR}(i,j,\underline{X})]\}\quad \textbf{with respect to}\ \underline{\mathbf{X}} \tag{5}$$

Multiplicity of Solutions. It should be noted that the max-min-max optimization problem stated above quite often yields a multiplicity of solutions that tends to grow as the number of gages increases. This multiplicity of solutions is most clearly seen when the number of gages equals the number of modes. In this case, the solution that would be expected from the optimization is the one in which each gage is placed at the peak location of the signal-to-noise ratio of a different mode. The corresponding value of the objective function, i.e., $\mathrm{SNR}(\underline{X})$, is the smallest of the peak modal signal-to-noise ratios on the blade. Let that value be S and the corresponding gage location-direction be $\underline{X}_S$. Denote also by d the mode in which S is achieved. Then, a series of solutions exists each of which yields the same best min-max signal-to-noise ratio S. These different solutions can be constructed as follows. First, select $\underline{X}_S$ as the first gage location-direction. Then, select the second gage location-direction to provide a signal-to-noise ratio of mode 1 (if $d\neq 1$, mode 2 otherwise) larger than S. Similarly, choose the third gage location-direction to yield a SNR of mode 2 (if $d\neq 2$, mode 3 otherwise) that is larger than S, etc., In this fashion, the minimum of the modal signal-to-noise ratios will be the best possible value, S, regardless of the exact locations-directions of the gages 2,3, . . . , $p=m$.

The multiplicity of solutions can be resolved by turning to an objective function that involves signal-to-noise ratios of all gages, e.g., a weighed average across different gages. However, the smallest of the modal SNR obtained for such objective functions is often much smaller than the one obtained with the max-min-max principle as weighted average objective functions can be biased by large values of the signal-to-noise ratio of some mode at the detriment of one or several others.

To resolve the multiplicity issue within the max-min-max framework, it was decided to proceed with a sequential optimization approach the first step of which is the one described above. Once the largest minimum modal signal-to-noise ratio has been identified, the corresponding location-direction is held for gage 1. The max-min-max optimization process is then repeated to maximize the *second* smallest modal SNR of the combined p gages (including the fixed first one). If, at the completion of this second step, it is found that the second smallest modal signal-to-noise ratio is also obtained by gage 1, the third smallest modal SNR is then considered. The process is repeated in this fashion until all gage locations-directions have been selected.

Potential Gage Failure. The failure of a gage is a random event that leads to a loss of measurement and thus to zero signal-to-noise ratios for the failed gage. In general, this sudden change of SNR values of a gage will also affect the overall signal-to-noise ratios of Eqs. (3) and (4) rendering them random variables depending on the state, failed or intact, of the gages. The optimization problem of Eq. (5) is then no longer well posed and will be replaced by the maximization of the *expected value* of SNR $(\underline{X})$, i.e., the average signal-to-noise ratio that would be observed in a series of identical tests with gages randomly failing or staying intact. Denoting by P_f the probability of failure of a gage and assuming that the state (failed/intact) of different gages are statistically independent random variables, it can be shown that

$$\begin{aligned}E[\min_j\{\max_i[\mathrm{SNR}(i,j,\underline{X})]\}]&=(1-P_f)^p\mathrm{SNR}mM^{(p)}+P_f(1-P_f)^{p-1}\left[\sum_{l=1}^{p}\mathrm{SNR}mM_l^{(p-1)}\right]\\&\quad+P_f^2(1-P_f)^{p-2}\left[\sum_{\substack{k,l=1\\k\neq l}}^{p}\mathrm{SNR}mM_{kl}^{(p-2)}\right]+\cdots\end{aligned} \tag{6}$$

where $E[\cdot]$ is the expected value operator. Further, $\mathrm{SNR}mM^{(p)}$ denotes the smallest of the modal signal-to-noise ratios of the intact strain gages set, i.e., as computed from Eq. (5). Similarly, $\mathrm{SNR}mM_l^{(p-1)}$ is also the smallest modal signal-to-noise ratio but for the set of $p-1$ strain gages remaining after the lth one has failed. Next, $\mathrm{SNR}mM_{k,l}^{(p-2)}$ is the smallest modal signal-to-noise ratio for the set of $p-2$ strain gages remaining after the kth and lth ones have failed, etc.,

Note that the value of the above expected SNR is a function of the signal-to-noise ratios of all gages, at the contrary of Eq. (4). The multiplicity of solutions discussed in connection with the no gage failure case is thus removed by considering the probability of gage failure.

It should be noted that Eq. (6) has been obtained under the assumption of an equal probability of failure for all gages, but it is readily extendable to the situation where this probability varies with gages, e.g., is dependent on either the gage number or its location on the blade.

Strain Interpolation and SNR Computation

The evaluation of the effects of mispositioning requires the knowledge of the strain distribution on the blade surface in a small neighborhood around the target location of the gage. This information is not directly available from a finite element analysis which only yields modal strains at the nodes in a global reference frame. Thus, the evaluation of the modal signal-to-noise ratios at the nodes (the data required for the first optimization phase, see the forthcoming) can be decomposed into three separate tasks.

1. The determination of the normal to the blade at the node considered. This step is necessary for the definition of local axes in the plane locally tangent to the blade.
2. The definition of an interpolation strategy of the modal strains in the neighborhood of the node considered.
3. The evaluation of the means and standard deviations of the modal strains considering mispositioning and a finite gage size.

These three separate steps are described next.

Determination of the Normal to the Blade at a Node. The components of the normal to the blade surface in the fixed frame of reference can be obtained using elementary analytic geometry. Specifically, expressing one of the coordinates, z say, in terms of the other two in the form $z=z(x,y)$, it can be shown that the normal vector can be written as

$$\underline{\boldsymbol{n}}=\frac{(\partial z/\partial x,\partial z/\partial y,-1)}{\sqrt{(\partial z/\partial x)^2+(\partial z/\partial y)^2+1}} \tag{7}$$

To maintain the smoothness of the normal in the neighborhood of the node considered, a Lagrange interpolation of the z coordinates was carried out using the 8 surrounding nodes, see Fig. 1. That is, the function $z=z(x,y)$ was locally approximated by the polynomial

$$\begin{aligned} z=z(x,y)=&z_0+a_1(x-x_0)+a_2(y-y_0)+a_3(x-x_0)(y-y_0)\\ &+a_4(x-x_0)^2+a_5(y-y_0)^2+a_6(x-x_0)^2(y-y_0)\\ &+a_7(x-x_0)(y-y_0)^2+a_8(x-x_0)^2(y-y_0)^2 \end{aligned} \tag{8}$$

where (x_0,y_0,z_0) are the coordinates of the node considered and the coefficients a_1, a_2, a_3, a_4, a_5, a_6, a_7, and a_8 are such that Eq. (8) is exactly satisfied at the 8 surrounding nodes. With the foregoing representation

$$\left(\frac{\partial z}{\partial x}\right)_{(x_0,y_0,z_0)}=a_1 \quad \text{and} \quad \left(\frac{\partial z}{\partial y}\right)_{(x_0,y_0,z_0)}=a_2 \tag{9}$$

and the components of the normal vector are readily evaluated from Eq. (7).

The above procedure is not applicable for border nodes as the number of neighbors is less than 8. This issue could be resolved by reducing the orders of the polynomial to have as many unknown coefficients as neighboring nodes, but this approach might lead to inaccuracies in the normal which would propagate through the entire signal-to-noise ratio computation. Accordingly, it was decided not to compute directly the signal-to-noise ratios at border nodes but rather to interpolate these values from their counterparts at the surrounding nodes as will be described further.

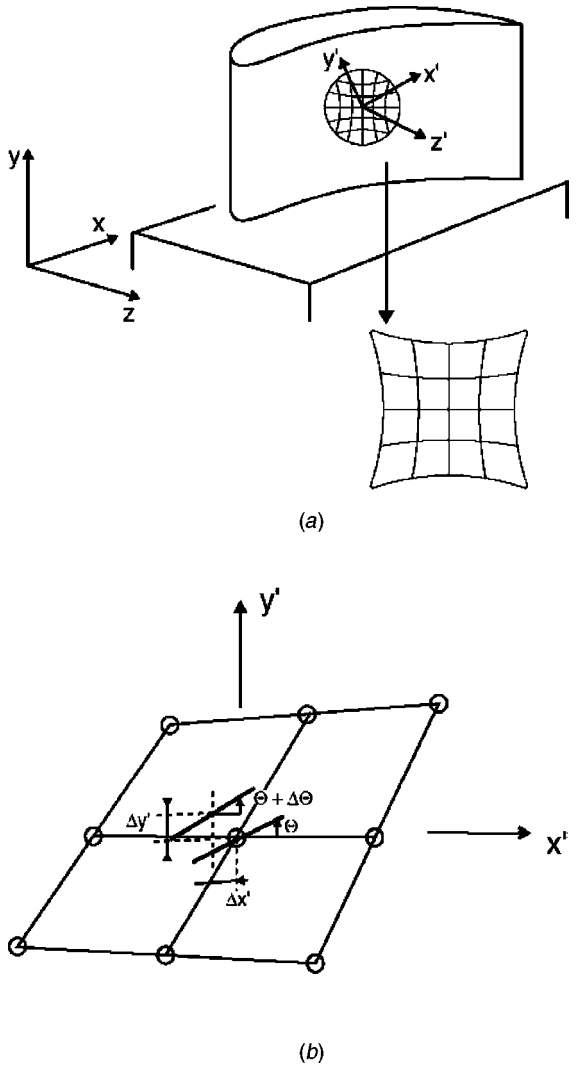

Fig. 1 Blade finite element modeling, surrounding nodes and mispositioning definition

It should be noted that the polynomial approximation of Eq. (8) can exhibit singularities, e.g., when the x, y pairs of coordinates of two or more of the nodes are very close to each other but the corresponding z values are not. To remedy this situation, polynomial approximations of the functions $z=z(x,y)$, $y=y(x,z)$, and $x=x(y,z)$ were all determined and the one yielding the smallest condition number of the corresponding 8×8 system of linear equations for the coefficients a_1, a_2, a_3, a_4, a_5, a_6, a_7, and a_8 was selected for the evaluation of the components of the normal vector.

In-Plane Strains Determination and Interpolation. Once the normal is determined, two tangent vectors $\underline{\boldsymbol{t}}_1$ and $\underline{\boldsymbol{t}}_2$ can be constructed to be perpendicular to $\underline{\boldsymbol{n}}$ and to each other to form the frame of reference (x',y',z') with x' and y' in the plane and z' perpendicular to it, see Fig. 1(a). The strain components $\underline{\boldsymbol{\varepsilon}}'$ in this new frame are related to their counterparts $\underline{\boldsymbol{\varepsilon}}$ in the (x, y, z) axes through the similarity transformation

$$\underline{\boldsymbol{\varepsilon}}'=T\underline{\boldsymbol{\varepsilon}}T^T \tag{10}$$

where T is the transformation matrix of the change of coordinates, from (x, y, z) to (x',y',z'), and the superscript ^{T} denotes the operation of matrix transposition. Note in Eq. (10) that care should be taken to account for the factor of 2 involved in the transformation between engineering and elasticity shear strains.

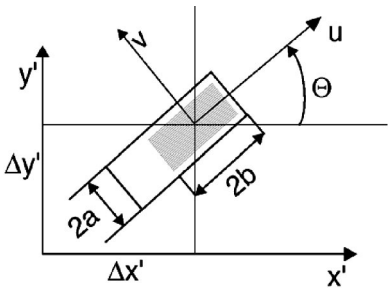

Fig. 2 Strain gage and mispositioning parameters

The in-plane strain components can then be grouped in the vector $\underline{\boldsymbol{\varepsilon}}$ defined as

$$\underline{\overline{\boldsymbol{\varepsilon}}}=(\varepsilon_{x'x'}\ \ \varepsilon_{y'y'}\ \ \gamma_{x'y'})^T \tag{11}$$

As stated in the foregoing, the consideration of mispositioning requires the definition of the strains in the neighborhood of the nodes, not simply at these locations. Proceeding as in the estimation of the normal vector, the in-plane strain vector $\underline{\overline{\boldsymbol{\varepsilon}}}$ will be interpolated by a polynomial of the form

$$\begin{aligned}\underline{\overline{\boldsymbol{\varepsilon}}}=&\underline{\overline{\boldsymbol{\varepsilon}}}_{\mathbf{0}}+\underline{\overline{\boldsymbol{\varepsilon}}}_{,X}(X-X_0)+\underline{\overline{\boldsymbol{\varepsilon}}}_{,Y}(Y-Y_0)+\underline{\overline{\boldsymbol{\varepsilon}}}_{,XY}(X-X_0)(Y-Y_0)\\&+\underline{\overline{\boldsymbol{\varepsilon}}}_{,XX}(X-X_0)^2+\underline{\overline{\boldsymbol{\varepsilon}}}_{,YY}(Y-Y_0)^2+\underline{\overline{\boldsymbol{\varepsilon}}}_{,XXY}(X-X_0)^2(Y-Y_0)\\&+\underline{\overline{\boldsymbol{\varepsilon}}}_{,XYY}(X-X_0)(Y-Y_0)^2+\underline{\overline{\boldsymbol{\varepsilon}}}_{,XXYY}(X-X_0)^2(Y-Y_0)^2\end{aligned} \tag{12}$$

In Eq. (12), the coordinates (X, Y) are either the global coordinates used in the approximation of the surface, e.g., (x, y) as in Eq. (8), or the in-plane local coordinates (x', y'). While the latter set of variables would seem most appropriate, it is felt that the use of global coordinates might be justified, in particular for blades exhibiting large curvatures. The ensuing formulation will be general so that both cases can be considered.

Mean and Standard Deviation of the Measured Strain. The determination of the signal-to-noise ratio requires the evaluation of both the mean and the standard deviation of the measured strain, see Eq. (1), in the presence of a random mispositioning. To this end, let $\Delta x'$ and $\Delta y'$ be the mispositioning in location, see Figs. 1(*b*) and 2, and assume that the orientation of the gage is given by the angle Θ which differs from the desired one θ. Then, neglecting the transverse sensitivity, the measured strain is (see Fig. 2)

$$\varepsilon_m(\Delta x',\Delta y',\Theta)=\frac{1}{4ab}\int_{-a}^{a}\int_{-b}^{b}\underline{\boldsymbol{\beta}}^T\underline{\overline{\boldsymbol{\varepsilon}}}(\hat{x}',\hat{y}',\Theta)dudv \tag{13}$$

where

$$\underline{\boldsymbol{\beta}}^T=(\cos^2\Theta\ \ \sin^2\Theta\ \ \sin\Theta\cos\Theta) \tag{14}$$

$$\hat{x}'=\Delta x'+u\cos\Theta-v\sin\Theta \tag{15}$$

and

$$\hat{y}'=\Delta y'+u\sin\Theta+v\cos\Theta \tag{16}$$

The integration of Eq. (13) will be carried out with the interpolation scheme of Eq. (12). Specifically, if X and Y denote the coordinates in the global frame of reference, then

$$\begin{pmatrix}X-X_0\\Y-Y_0\end{pmatrix}=\begin{pmatrix}T_{11}&T_{12}\\T_{21}&T_{22}\end{pmatrix}\begin{pmatrix}\hat{x}'\\\hat{y}'\end{pmatrix} \tag{17}$$

while

$$X=\hat{x}'\qquad\text{and}\qquad Y=\hat{y}' \tag{18}$$

if X and Y are the coordinates in the tangent plane. A common formulation for these two cases can be obtained by assuming

$$\begin{pmatrix}X-X_0\\Y-Y_0\end{pmatrix}=\begin{pmatrix}t_{11}&t_{12}\\t_{21}&t_{22}\end{pmatrix}\begin{pmatrix}\hat{x}'\\\hat{y}'\end{pmatrix} \tag{19}$$

where $t_{ij}=T_{ij}$ or $t_{ij}=\delta_{ij}$, the Kronecker symbol, if X and Y are the coordinates in the global or the local frame of reference, respectively. Combining Eqs. (15), (16), and (19), it is found that

$$X=X_0+X_N+a_{11}u+a_{12}v \tag{20}$$

and

$$Y=Y_0+Y_N+a_{21}u+a_{22}v \tag{21}$$

where

$$X_N=t_{11}\Delta x'+t_{12}\Delta y' \tag{22}$$

$$Y_N=t_{21}\Delta x'+t_{22}\Delta y' \tag{23}$$

$$a_{11}=t_{11}\cos\Theta+t_{12}\sin\Theta\qquad a_{12}=-t_{11}\sin\Theta+t_{12}\cos\Theta \tag{24}$$

and

$$a_{21}=t_{21}\cos\Theta+t_{22}\sin\Theta\qquad a_{22}=-t_{21}\sin\Theta+t_{22}\cos\Theta \tag{25}$$

Introducing Eqs. (20) and (21) in the interpolation rule and integrating over the gage area, Eq. (13) yields

$$\varepsilon_m(\Delta x',\Delta y',\Theta)=\underline{\boldsymbol{\beta}}^T\left[\xi\,\underline{\overline{\boldsymbol{\varepsilon}}}_{,XXYY}+\sum_{i,j=0}^{2}\underline{\boldsymbol{\alpha}}_{ij}X_N^iY_N^j\right] \tag{26}$$

where the vectors $\underline{\boldsymbol{\alpha}}_{ij}$ and the coefficient ξ are defined in the Appendix.

To obtain the mean of the measurement strain, it remains to evaluate the expected value of Eq. (26) with respect to the random variables X_N, Y_N, and Θ. The dependency of the measured strain with respect to the first two of these variables is limited to the terms $X_N^i\ Y_N^j$, but Θ is present in $\underline{\boldsymbol{\beta}}$, see Eq. (14), and in the vectors $\underline{\boldsymbol{\alpha}}_{ij}$ and the coefficient ξ, see Eqs. (37)–(44). To clarify the Θ effects, note from Eqs. (37)–(43) that the vectors $\underline{\boldsymbol{\alpha}}_{ij}$ can be written in the form

$$\underline{\boldsymbol{\alpha}}_{ij}=\underline{\boldsymbol{\alpha}}_{ij,0}+\underline{\boldsymbol{\alpha}}_{ij,cc}\cos^2\Theta+\underline{\boldsymbol{\alpha}}_{ij,cs}\cos\Theta\sin\Theta+\underline{\boldsymbol{\alpha}}_{ij,ss}\sin^2\Theta \tag{27}$$

Similarly, the coefficient ξ can be expressed as

$$\xi=\sum_{l=0}^{4}\omega_l\cos^{4-l}\Theta\sin^l\Theta \tag{28}$$

Substituting Eqs. (14), (27), and (28) in Eq. (26) and taking the expected value with respect to the random variables $\Delta x'$, $\Delta y'$, and Θ, assumed statistically independent, yields

$$\begin{aligned}&E[\varepsilon_m(\Delta x',\Delta y',\Theta)]\\&=\left[\sum_{l=0}^{4}\omega_l(D_{6-l,l}\ \ D_{4-l,2+l}\ \ D_{5-l,1+l})^T\right]\underline{\overline{\boldsymbol{\varepsilon}}}_{,XXYY}\\&\quad+\sum_{i,j=0}^{2}E_{ij}[\underline{\boldsymbol{\beta}}_0^T\underline{\boldsymbol{\alpha}}_{ij,0}+\underline{\boldsymbol{\beta}}_{cc}^T\underline{\boldsymbol{\alpha}}_{ij,cc}+\underline{\boldsymbol{\beta}}_{cs}^T\underline{\boldsymbol{\alpha}}_{ij,cs}+\underline{\boldsymbol{\beta}}_{ss}^T\underline{\boldsymbol{\alpha}}_{ij,ss}]\end{aligned} \tag{29}$$

Further, the vectors $\underline{\boldsymbol{\beta}}_0$, $\underline{\boldsymbol{\beta}}_{cc}$, $\underline{\boldsymbol{\beta}}_{cs}$, and $\underline{\boldsymbol{\beta}}_{ss}$ are defined as

$$\underline{\boldsymbol{\beta}}_0=(D_{2,0}\ \ D_{0,2}\ \ D_{1,1})^T\qquad\underline{\boldsymbol{\beta}}_{cc}=(D_{4,0}\ \ D_{2,2}\ \ D_{3,1})^T \tag{30}$$

$$\underline{\boldsymbol{\beta}}_{cs}=(D_{3,1}\ \ D_{1,3}\ \ D_{2,2})^T\quad\text{and}\quad\underline{\boldsymbol{\beta}}_{ss}=(D_{2,2}\ \ D_{0,4}\ \ D_{1,3})^T \tag{31}$$

In all of the foregoing equations, the coefficients E_{ij} and $D_{i,j}$ are defined as

$$E_{ij}=E[X_N^iY_N^j]\qquad\text{and}\qquad D_{i,j}=E[\cos^i\Theta\sin^j\Theta] \tag{32}$$

In the special case of uniform distributions of the random variables $\Delta x'$, $\Delta y'$, and Θ, of respective standard deviations $\sigma_{x'}$, $\sigma_{y'}$, and σ_Θ it is found that

$$E_{ij}=\frac{1}{3\sigma_{x'}\sigma_{y'}}\int_{-\sqrt{3}\sigma_{x'}}^{\sqrt{3}\sigma_{x'}}\int_{-\sqrt{3}\sigma_{y'}}^{\sqrt{3}\sigma_{y'}}(t_{11}x'+t_{12}y')^i \times(t_{21}x'+t_{22}y')^j dy'dx' \tag{33}$$

and

$$D_{i,j}=\frac{1}{\sqrt{3}\sigma_\Theta}\int_{-\sqrt{3}\sigma_\Theta}^{\sqrt{3}\sigma_\Theta}\cos^i\phi\sin^j\phi d\phi. \tag{34}$$

Given these expressions, tables of the necessary coefficients E_{ij} and $D_{i,j}$ were produced with the algebraic manipulator MAPLE.

The computation of the second-order moment $E[\varepsilon_m^2(\Delta x',\Delta y',\Theta)]$ proceeds in a manner completely similar to the mean value determination and thus will be omitted here for brevity. The variance of the measured strain is then finally found as

$$\sigma^2_{\varepsilon_m}=E[\varepsilon_m^2(\Delta x',\Delta y',\Theta)]-\{E[\varepsilon_m(\Delta x',\Delta y',\Theta)]\}^2 \tag{35}$$

Optimization Algorithms

The proposed strain gage placement strategy is based on the selection of the locations-directions on the blades that yield an optimum signal-to-noise ratio. This process may be accomplished in two stages. First, a search over a discrete set of locations and directions is conducted to find the best positioning of the strain gages within this set. Then, if desired, a more refined positioning could be accomplished by allowing the strain gages to be located in the neighborhood of the optimum solution corresponding to the discrete set.

The discrete set of locations and directions was obtained here by considering each internal node (the border nodes were excluded because of the interpolation rule, Eq. (8)) and a series of equidistant angles from 0 to 180 deg. Accordingly, a very large discrete set was obtained in which many local maxima of the signal-to-noise ratio could be expected. This situation led to: 1) a strategy for the reduction of the set size of locations and directions that are potentially solution of the optimization problem; and 2) the formulation of a genetic algorithm.

1 Set Size Reduction Strategy. Consider two different locations and directions each having its own set of signal-to-noise ratios for the modes of interest. If the SNRs of the second location-direction are all lower than the corresponding values for the first one then the second location-direction cannot be part of the optimum solution if the probability of gage failure is the same for both locations-directions. This simple observation led to a two-pass scanning through the set of locations-directions. In the first (forward) pass, the signal-to-noise ratios of all locations-directions were compared with the corresponding values of previously scanned and kept locations-directions. The second (backward) pass proceeded similarly but starting from the last location-direction of the set already reduced by the first pass. Although simple, this exact reduction process was found to be particularly efficient.

2 Simple Genetic Algorithm. Genetic optimization algorithms are based on the evolution of a population of individual objects/designs (here strain gage locations-directions) through a series of generations. As in nature, the population at a given generation is obtained from the one before by random reproduction and includes the selection of the parents and the genetic operations of crossover and mutation, as described in the forthcoming. Genetic algorithms are particularly well suited for the present effort because the design variables only admit discrete values (i.e. the locations-directions in the discrete set) and there might be multiple optima; see [4,5] for additional details. Note further that recent applications of genetic algorithm in the context of blades and bladed disks were found to be quite successful (see [2,3,6,7] and references therein).

The simple genetic algorithm used here relies on a population of n_{pop} directions-locations (referred to as "chromosomes") each of which is characterized by a binary sequence of N "genes," i.e., 01011000111 . . . , which evolves from one generation to the next until all the chromosomes yield essentially similar values of the fitness or objective function (selected here as the smallest modal signal-to-noise ratio).

The selection of those members of the population that participate in the production of the next generation is based on the value of the fitness of the individual members and is such that members with greater fitness levels (the largest value of the minimum modal SNR if there is no potential gauge failure) tend to survive. To this end, each individual direction-location i in the population is first assigned a probability of selection $p_s(i)$ given as (fitness proportionate selection)

$$p_s(i)=\frac{\text{SNR}(\underline{X}_i)}{\sum_{j=1}^{n_{\text{pop}}}\text{SNR}(\underline{X}_j)} \tag{36}$$

where SNR $(\underline{X}_i)$ is the minimum modal signal-to-noise ratio corresponding to the set $\underline{X}_i$ of strain gauge locations-directions. Next, n_{pop} individuals (not necessarily all different) are randomly selected according to the probabilities $p_s(i)$ to undergo the genetic operations of crossover and mutation to produce the population at the next generation.

Crossover (or recombination) is the general process by which two chromosomes (the "parents") are split into segments and recombined to form two new chromosomes (the "offspring"). The present investigation relied on the single point crossover technique (see Fig. 3) in which the original chromosomes are sliced into two segments only at a randomly selected location (crossing site). In general, this process need not necessarily take place for all pairs of chromosomes forming the population, rather it occurs only with probability p_c. When crossover does not take place, the two offspring are simply identical to the parents.

The offspring resulting from the crossover process undergo the final stage of mutation in which some of their genes may be altered. In the present binary situation, the mutation was accomplished by independently allowing, with probability p_m, each of the genes to switch type, i.e., from 0 to 1 or vice versa. Note that the probability of mutation plays a very important role in the convergence of the genetic algorithm to an optimum, or near optimum, solution as it controls the diversity of the population. This parameter must be sufficiently high to ensure that the optimization process will cover a large enough part of the set of directions-locations to find the optimum.

Experimentation with the above algorithm has shown that the chromosome with the highest fitness (directions-locations with the largest minimum modal SNR) may disappear from one generation to the next due to the operations of crossover and mutation thereby negatively impacting the convergence of the algorithm. To remedy this situation, the chromosome with the highest fitness

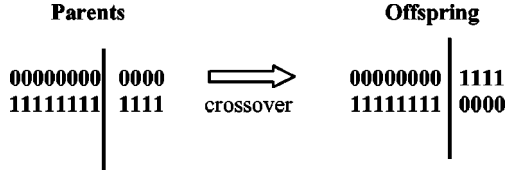

Fig. 3 Graphical description of the single-point crossover technique

Table 1 Values of the parameters of the simple genetic algorithm

Population size (n_{pop})	65
Chromosome length (N)	21-23
Crossover probability (p_c)	1.00
Mutation probability (p_m)	0.05
Max. number of generations ($g_{\max}$)	5000

level was retained unchanged (i.e., no mutation or crossover) from one generation to the next according to the ''one elite reservation'' strategy.

The selection, crossover, and mutation operations were performed from an initially random population for a fixed number ($g_{\max}$) of generations. At each generation, the minimum, maximum, and average objective function value (largest minimum modal SNR) were determined to provide insight in the convergence of the process.

Shown in Table 1 are the values of the algorithm parameters that led to the results presented in this paper. These values were obtained after several trials and were retained because they led to the largest value of the smallest modal signal-to-noise ratio.

3 Fine Tuning of the Optimum. It may be desired in some circumstances to dispose of a finer positioning capability than that provided by the finite element mesh. Such a freedom can be obtained by proceeding first with the search through the discrete set, as described in the foregoing, and using the optimum locations and directions thus found as an initial condition for a refined optimization. While the signal-to-noise ratio computations could be carried out as described in Eqs. (13)–(35), an alternate approach was implemented in which the SNR were directly interpolated from their values at the nodes surrounding the optimum locations. For this task, the Lagrangian interpolation polynomial of Eq. (8) was again used and the optimization process was implemented in the MATLAB(v5.0) environment with the function constr.

It was found that this fine optimization is a particularly convenient way to handle the border nodes that were automatically discarded from the discrete set of locations-directions because of the interpolation rule. The extrapolation of the signal-to-noise ratios from the neighboring nodes to the border or corner did seem to be fairly well conditioned.

4 Refinements and Changes. It should be emphasized that the optimization described in the foregoing is a general framework that can easily be varied to suit different problems. For example, constraints can be added to exclude (or automatically include) some nodes as possible locations-directions. Such constraints could stem from a desire to have gage ratios (measured strain divided by peak strain) to always exceed a certain minimum threshold, etc.

Example

To demonstrate the application of the proposed robust positioning of strain gages, a fan blade from a Honeywell engine was considered. The ANSYS finite element consisted of 4830 8-node blocks, 7560 nodes (2520 on each suction and pressure sides, 208 of which per side were border nodes), and the first five modes were considered. The strain distributions on the pressure side of the blade are shown in Figs. 4(*a*)–(*e*) for each of these five modes.

The discrete set of locations-directions was formed by the 4624 internal nodes of the pressure and suction sides and 36 different angles (5 deg apart). Accordingly, there was a total of 166,464 considered locations and angles to position the strain gages. The modal signal-to-noise ratio of the five modes were computed at

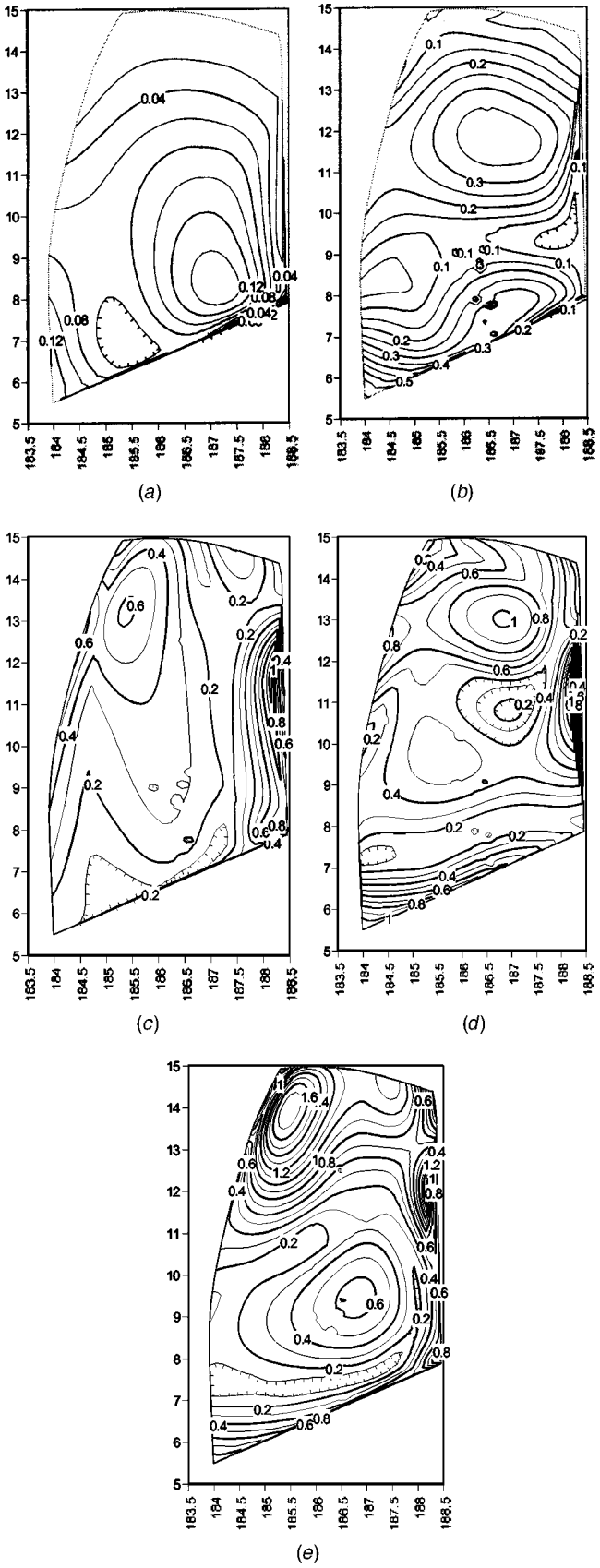

Fig. 4 Modal strain distributions for the first five modes of the fan blade; pressure side

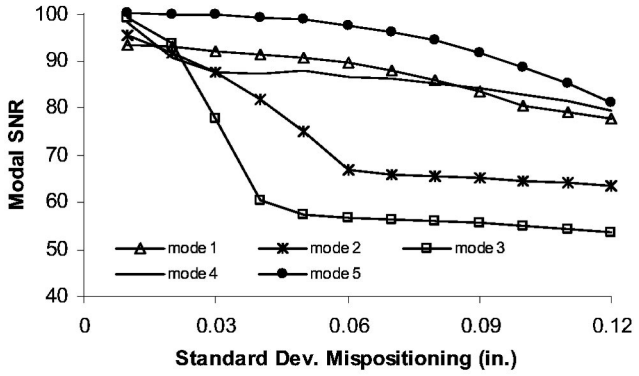

Fig. 5 Evolution of the peak modal signal-to-noise ratios as a function of the standard deviation of mispositioning

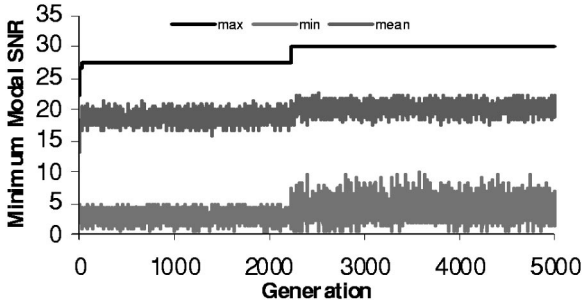

Fig. 7 Convergence plot of the genetic algorithm—maximum, mean, and minimum value of the smallest modal SNR as a function of the generation number

each of these locations-directions according to Eqs. (7)–(35) with the in-plane coordinates in Eq. (12). The standard deviation of mispositioning (in position only, not in angle) was varied from 0.01 in. (0.254 mm.) to 0.12 in. (3.048 mm.). To exemplify the process, the measurement noise was assumed to have a standard deviation equal to 1% of the peak strain value for each mode. Thus, in the absence of any mispositioning effect, the largest SNR ratio would be 100 on each mode.

The largest SNR value obtained for each mode is shown in Fig. 5. Note the difference in behavior exhibited by modes 1 and 5 as compared to 2 and 3. For the former modes, the peak signal-to-noise ratio decreases slowly and smoothly as a function of the mispositioning level. On the contrary, for modes 2 and 3, there is initially a rapid decrease of the SNR; but this trend suddenly changes and an almost constant behavior is observed. To understand these trends, the distribution of signal-to-noise ratio on the blade was analyzed, e.g., see Figs. 6(*a*), (*b*) for the third modes. As done in connection with the strain distributions of Fig. 4, these figures were obtained by keeping for each location on the blade the largest SNR computed as the angle was varied through its 36 different values. Note from Figs. 6(*a*), (*b*) that the SNR distribution exhibits, as the corresponding strain distribution of Fig. 4(*c*), two dominant peaks, one very close to the trailing edge and one toward the leading edge. For the smaller mispositioning level, 0.03 in., see Fig. 6(*a*), it is the sharp trailing edge peak that yields the largest SNR while the situation is reversed for the 0.06 in. mispositioning of Fig. 6(*b*). Note from Fig. 5 that the 0.03 in. mispositioning level is in the rapidly decaying zone while the 0.06 in. case falls in the flat region of the curve. An analysis of the SNR distribution plots for 0.04 in. and 0.05 in. mispositioning levels demonstrates that in fact the break in the curve of Fig. 5 does occur when the peak SNR shifts from one maximum (trailing edge) to the other (leading edge). The different rates of decay of the SNR with mispositioning level before and after the break can be understood from the strain distribution plot of Fig. 4(*c*). Specifically, since the trailing edge peak is very sharp, mispositioning will greatly affect the measured strains and thus the SNR will rapidly decrease with increasing mispositioning. On the contrary, since the leading edge peak is quite broad, mispositioning will only produce a mild effect as seen by the almost flat zone of Fig. 5. A similar situation occurs for mode 2 but also for mode 1, but it is not seen in Fig. 5 because the shift occurs at a mispositioning level below 0.01 in. Indeed, the strain distribution for mode 1, see Fig. 4(*a*), exhibits two almost equal peaks both on the pressure side with the largest one at the root of the blade on the leading edge. Note that the SNR peak shifting explains in particular why the curve of Fig. 5 for mode 1 does not seem to converge to 100 at 0 mispositioning as required from the 1% measurement noise.

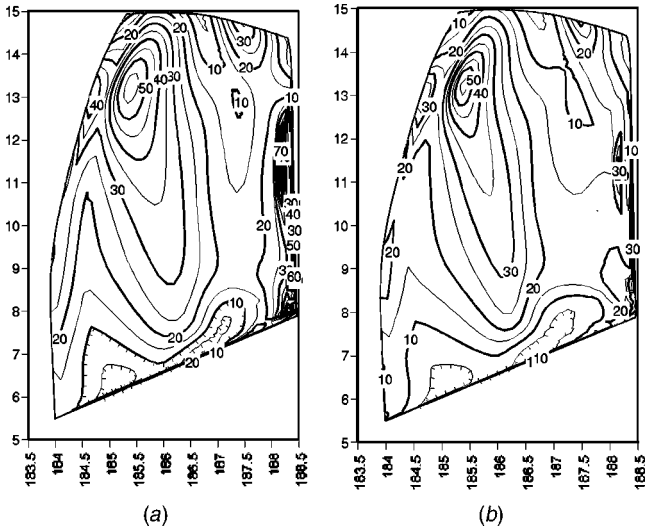

Fig. 6 Distribution of signal-to-noise ratio on the pressure side of the blade for the third mode and for a standard deviation of mispositioning in location only of (*a*) 0.03 in, and (*b*) 0.06 in.

These first results support the choice of the signal-to-noise ratio as the appropriate metric for the selection process of gage location-direction. Thus, the max-min-max principle is expected to follow the intuitive rule of selecting the peak strain location if the peak is not ''too sharp'' but it will *quantify* at what mispositioning level the shift in location-direction must take place.

Having validated the usefulness of the signal-to-noise ratio for the gage positioning process, the optimization of the minimum modal SNR was undertaken, first without gage failure, then with a nonzero probability of such an event. It was first observed that the simple two-pass reduction strategy was particularly efficient in reducing the number of locations-directions to be considered. For a 0.06 in. standard deviation of mispositioning, the first pass reduced the size of the set from 166,464 locations-directions to 15,264. The second pass further reduced this number to only 5020 or 3% of the original size! (note that the correspondence with the number of nodes is fortuitous). While genetic algorithms have a series of advantages over traditional gradient-based techniques, they are also known to occasionally suffer from a lack of convergence to the absolute optimum. It was thus desired to first assess the convergence behavior of the genetic algorithm. The two limiting cases of 1 and 5 gages were thus considered first. The optimum for 1 gage could easily be obtained by an exhaustive search through the 5020 directions-locations. Further, the five-gage optimum solution was also readily determined as it corresponds to the gages being located on the peaks of the five modal signal-to-noise

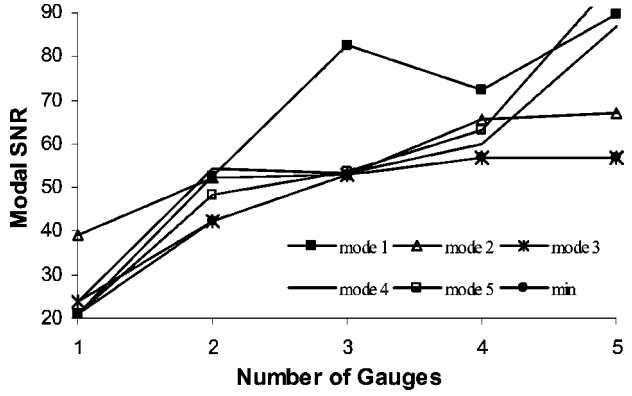

Fig. 8 Evolution of the modal signal-to-noise ratios as a function of the number of strain gages, standard deviation of mispositioning=0.06 in.; $P_f=0$

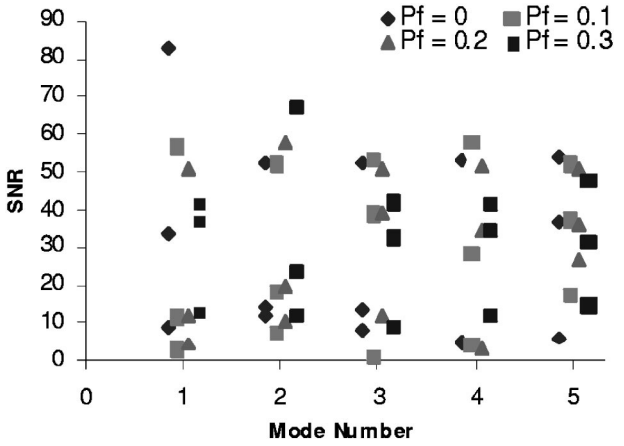

Fig. 10 Signal-to-noise ratios for three gages as a function of the mode number for different probabilities of failure

ratio distributions. In both cases, the genetic algorithm recovered exactly the expected optimum solution. A typical convergence plot is shown in Fig. 7.

The optimum positioning of two, three, and four gages was then considered and the corresponding modal signal-to-noise ratios are shown in Fig. 8. It is seen from this figure that an increase in the number of gages leads, as expected, to a monotonic increase in all modal signal-to-noise ratios. However, the objective function, i.e., the minimum modal SNR appears to rapidly converging, i.e., it is almost constant for three or more gages. Certainly, the consideration of four or five gages leads to improvements but only on modes (e.g., one, four and five) that are already well captured as they exhibit large modal signal-to-noise ratios. From a pragmatic point of view, the return on investment is low for more than three gages for five modes, a result that appears to match some practical experience. These results also demonstrate that the max-min-max principle has forced the efficient use of the strain gages and thereby validate its use. For completeness, shown in Fig. 9 are the locations on the blade of the strain gages.

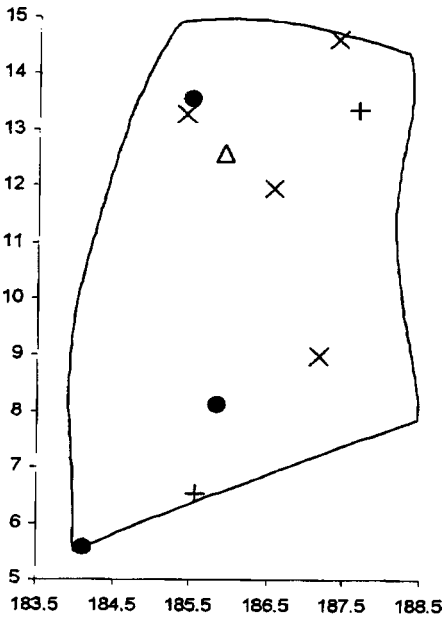

Fig. 9 Optimum strain gage locations for 1(Δ), 2 (+), 3 (●), and 4 (X) strain gages, standard deviation of mispositioning =0.06 in.; $P_f=0$

The influence of potential strain gage failure was considered next for three gages and a mispositioning standard deviation of 0.06 in. Beside the case $P_f=0$ treated in the foregoing, the values 0.1, 0.2, and 0.3 were also considered. Intuitively, it is expected that the possibility of gage failure should promote the evenness of the signal-to-noise ratios of the gages across the different modes. To validate or invalidate this expectation, the signal-to-noise ratios of the three gages for the four different probabilities of failure were plotted as a function of the mode number; see Fig. 10. This figure does indicate a trend of increase of the smallest signal-to-noise ratio and decrease of the largest one as the probability of failure increases, but this trend is certainly not as clear as intuitively thought. In this regards, it should be recognized that: 1) not all signal-to-noise ratios are present in the objective function, i.e. the expected minimum modal SNR, only 7 of the 15 values appear in Eq. (6); and 2) the signal-to-noise ratios that are present in Eq. (6) are not equally weighted. In light of these observations, it was decided to reprocess the data of Fig. 10 emphasizing only the seven signal-to-noise ratios of Eq. (6) and considering separately $\mathrm{SNR}mM^{(p)}$, the three $\mathrm{SNR}mM_l^{(p-1)}$ values, and the three $\mathrm{SNR}mM_{k,l}^{(p-2)}$ terms. To display these signal-to-noise ratios on the same plot while separating them arbitrary shifts of 200 and 100

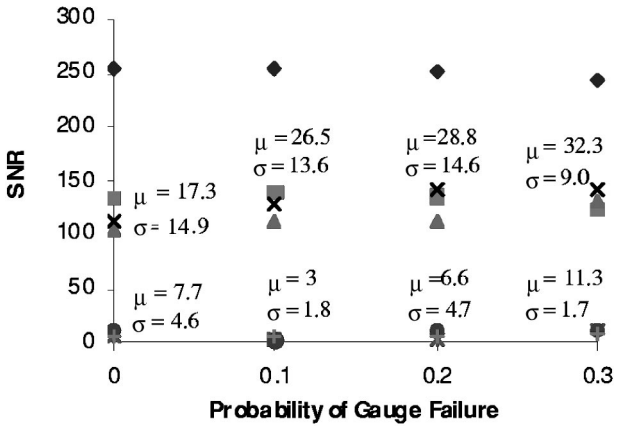

Fig. 11 Minimum modal signal-to-noise ratios corresponding to the optimum solutions for three gages as functions of the probability of gage failure. The top level corresponds to all three gages intact (SNR raised by 200 for display purposes only), the second level represents the signal-to-noise ratios when one gage has failed (SNR raised by 100), the bottom level corresponds to a single remaining gage. The mean and standard deviations are taken by groups of three only.

were added, respectively, to $\mathrm{SNR}mM^{(p)}$ and the three terms $\mathrm{SNR}mM_l^{(p-1)}$. The result of this process is Fig. 11. Several important observations can be drawn from this plot.

First, as the probability of failure remains small, the dominant contribution to the objective function is still the minimum modal signal-to-noise ratio. Thus, this value (the diamonds of Fig. 11) only slightly decrease at first, i.e. it equals 52.8 for $P_f=0$, 51.9 for $P_f=0.1$, 50.7 for $P_f=0.2$, and then drops to 41.5 for $P_f=0.3$. Thus, the consideration of a probability of failure as large as 0.2 does not significantly alter the reliability of the measured strains if failure does not occur. On the contrary, if failure does occur once, the mean smallest modal SNR decreases from 28.8 for the optimal solution considering $P_f=0.2$ to 17.3 for the one obtained with $P_f=0$. This drop is equivalent to an increase by 66% of the measurement error on the strains, from $1/28.8=3.5\%$ to $1/17.3=5.8\%$. It thus appears in this case that the safe approach, i.e., to consider a potential gage failure even when it is unlikely, is appropriate if the probability of gage failure is 0.2 or less. For higher values of this probability, the optimal solution becomes overly conservative and the accuracy of the measured strains is affected.

Consider next the signal-to-noise ratios obtained with one failed gage, i.e., $\mathrm{SNR}mM_l^{(p-1)}$. It is found from Fig. 11 that these values increase monotonically on average and that their standard deviation (variability) decreases as the probability of failure increases. Thus, the optimum solution is driven to yield a minimum modal signal-to-noise ratio; that is, 1) fairly high, and 2) quite insensitive to which gage has failed. This behavior is in fact the evenness expected in the foregoing.

Finally, although the signal-to-noise ratios obtained with two failed gages, $\mathrm{SNR}mM_{k,l}^{(p-2)}$, do not affect significantly the objective function for the low probabilities of failure considered, it is nevertheless seen from Fig. 11 that these terms do exhibit the behavior of increasing mean and decreasing standard deviation already observed in connection with $\mathrm{SNR}mM_l^{(p-1)}$.

The clarity of the trends shown in Fig. 11 as opposed to the rather unclear ones of Fig. 10 demonstrates that the strain gage positioning strategy with potential gage failure is intuitively simple and logical but that obtaining the optimal solution without an efficient search algorithm is not.

The effect of the gage size on the optimum strain gage placement was investigated by considering a square gage of 0.06 in. with standard deviations of mispositioning equal to 0.03 in. and 0.06 in. In both cases, it was found that the distribution of signal-to-noise ratio was almost identical to the one obtained by a zero-size gage and thus no change in the optimal gage locations-directions was observed.

Finally, the refined optimization effort was not conducted for the present, but was performed in another example of a square plate not discussed here for brevity. The convergence of the strain gage locations-directions was achieved very quickly and remained within the neighborhood of the solution provided by the genetic algorithm and used as initial condition.

Summary

This paper focused on the formulation and validation of an automatic strategy for the selection of the locations and directions of strain gages to capture at best the modal response of a blade in a series of modes. The approach seeks the strain gage locations-direction that lead to the maximum robustness (signal-to-noise ratio) of the measured strain values with respect to the inherent system measurement noise and the mispositioning of the gage in location and direction. This task was accomplished through the following steps:

1 The selection of the signal-to-noise ratio of the measured strains (average of strain divided by its standard deviation, see Eq. (1)) as the appropriate metric to assess robustness.

2 The formulation of two optimization problems, one when gage failure is not possible and the other one when it is. In the former case, a sequential max-min-max principle, see Eq. (5), was defined. When gage failure is possible, the objective function was replaced by its expected value with respect to the failure events and the search was found to be non-sequential.

3 The derivation of expressions for the mean value and standard deviation of the measured strain at any location on the blade from the finite element modal strain results, see Eqs. (7)–(35) and (37)–(44). These expressions depend explicitly on the standard deviations of the mispositioning (in location and direction), but also the gage size.

4 The formulation of a multi-step optimization strategy to search for the best (in the sense of the principle of step 2) strain gage locations-directions. The first step of the approach is a simple, but efficient, reduction strategy that eliminates locations and directions which cannot be optimal solutions. The second step is a true optimization effort based on a genetic algorithm and aims at the best placement of strain gages on the nodes of the finite element mesh. The final step is a fine optimization that searches for the optimal placement of the strain gages within the finite elements.

The proposed strategy for the selection of strain gage locations-directions was finally exemplified and validated on a full finite element model of a fan blade. The trends of the optimal strain gage locations were found to be in complete agreement with intuitive expectations but were able to *quantify precisely* the effects of mispositioning and gage failure.

Acknowledgments

The support of this work by the AlliedSignal/Honeywell Foundation is gratefully acknowledged. In addition, the authors wish to thank Mr. Jeff Lentz from Honeywell Engines for his continuous support of and interest in this project.

Appendix

$$\underline{\boldsymbol{\alpha}}_{00}=\overline{\underline{\boldsymbol{\varepsilon}}}_0+\frac{b^2}{3}(a_{11}a_{21}\overline{\underline{\boldsymbol{\varepsilon}}}_{,XY}+a_{11}^2\overline{\underline{\boldsymbol{\varepsilon}}}_{,XX}+a_{21}^2\overline{\underline{\boldsymbol{\varepsilon}}}_{,YY})+\frac{a^2}{3}(a_{12}a_{22}\overline{\underline{\boldsymbol{\varepsilon}}}_{,XY}+a_{12}^2\overline{\underline{\boldsymbol{\varepsilon}}}_{,XX}+a_{22}^2\overline{\underline{\boldsymbol{\varepsilon}}}_{,YY}) \tag{37}$$

$$\underline{\boldsymbol{\alpha}}_{10}=\overline{\underline{\boldsymbol{\varepsilon}}}_{,X}+\frac{b^2}{3}(2a_{11}a_{21}\overline{\underline{\boldsymbol{\varepsilon}}}_{,XXY}+a_{21}^2\overline{\underline{\boldsymbol{\varepsilon}}}_{,XYY})+\frac{a^2}{3}(2a_{12}a_{22}\overline{\underline{\boldsymbol{\varepsilon}}}_{,XXY}+a_{22}^2\overline{\underline{\boldsymbol{\varepsilon}}}_{,XYY}) \tag{38}$$

$$\underline{\boldsymbol{\alpha}}_{01}=\overline{\underline{\boldsymbol{\varepsilon}}}_{,Y}+\frac{b^2}{3}(2a_{11}a_{21}\overline{\underline{\boldsymbol{\varepsilon}}}_{,XYY}+a_{11}^2\overline{\underline{\boldsymbol{\varepsilon}}}_{,XXY})+\frac{a^2}{3}(2a_{12}a_{22}\overline{\underline{\boldsymbol{\varepsilon}}}_{,XYY}+a_{12}^2\overline{\underline{\boldsymbol{\varepsilon}}}_{,XXY}) \tag{39}$$

$$\underline{\boldsymbol{\alpha}}_{11}=\overline{\underline{\boldsymbol{\varepsilon}}}_{,XY}+\frac{4}{3}(b^2a_{11}a_{21}+a^2a_{12}a_{22})\overline{\underline{\boldsymbol{\varepsilon}}}_{,XXYY} \tag{40}$$

$$\underline{\boldsymbol{\alpha}}_{02}=\overline{\underline{\boldsymbol{\varepsilon}}}_{,XX}+\frac{1}{3}(b^2a_{21}^2+a^2a_{22}^2)\overline{\underline{\boldsymbol{\varepsilon}}}_{,XXYY} \tag{41}$$

$$\underline{\boldsymbol{\alpha}}_{20}=\overline{\underline{\boldsymbol{\varepsilon}}}_{,YY}+\frac{1}{3}(b^2a_{11}^2+a^2a_{12}^2)\overline{\underline{\boldsymbol{\varepsilon}}}_{,XXYY} \tag{42}$$

$$\underline{\boldsymbol{\alpha}}_{21}=\overline{\underline{\boldsymbol{\varepsilon}}}_{,XXY}\quad \underline{\boldsymbol{\alpha}}_{12}=\overline{\underline{\boldsymbol{\varepsilon}}}_{,XYY}\quad \underline{\boldsymbol{\alpha}}_{22}=\overline{\underline{\boldsymbol{\varepsilon}}}_{,XXYY} \tag{43}$$

and

$$\xi = \frac{b^4}{5} a_{11}^2 a_{21}^2 + \frac{a^2 b^2}{9} (a_{11}^2 a_{22}^2 + 4 a_{11} a_{12} a_{21} a_{22} + a_{12}^2 a_{21}^2) + \frac{a^4}{5} a_{12}^2 a_{22}^2 \quad (44)$$

References

[1] Yang, M.-T., and Griffin, J. H., 1998, ''Theory and Methodology of Optimally Measuring Vibratory Strains in Closely Spaced Modes,'' ASME J. Eng. Gas Turbines Power, **120**(4), pp. 801–807.

[2] Sensmeier, M. D., and Nichol, K. L., 1998, ''Optimum Placement of Sensors for Vibration Measurements on Turbine Engine Blades,'' *Proc. 39th AIAA/ASME/ASCE/AHS/ASC Structures. Structural Dynamics, and Materials Conference*, Long Beach, CA, April 20–23, AIAA Pap., 98-1849.

[3] Sensmeier, M. D., and Nichol, K. L, 2000, ''Improved Vibration Monitoring Through Optimization of Sensor Placements,'' presented at the International Gas Turbine & Aeroengine Congress and Exposition, Munich, Germany, May 8–11, ASME Paper 2000-GT-612.

[4] Gen, M., and Cheng, R., 1997, *Genetic Algorithms & Engineering Design*, Wiley-Interscience, New York, NY

[5] Goldberg, D. E., 1989, *Genetic Algorithms in Search, Optimization & Machine Learning*, Addision Wesley, New York, NY.

[6] Choi, B.-K., Lentz, J., Rivas-Guerra, A. J., and Mignolet, M. P., ''Optimization of Intentional Mistuning Patterns for the Reduction of the Forced Response Effects of Unintentional Mistuning,'' 2001-GT-0293 ASME J. Eng. Gas Turbines Power, to be published.

[7] Petrov, E. P., Vitali, R., and Haftka, R., 2000, ''Optimization of Mistuned Bladed Discs Using Gradient-Based Response Surface Approximations,'' *Proc. 41st AIAA/ASME/ASCE/AHS/ASC Structures, Structural Dynamics and Materials Conference and Exhibit*, Atlanta, GA, Apr., Paper AIAA-2000-1522.

Measurement and CFD Prediction of the Flow Within an HP Compressor Drive Cone

Christopher A. Long
Alan B. Turner
Guven Kais
Kok M. Tham

Thermo-Fluid Mechanics Research Center,
University of Sussex,
Brighton, BN1 9QT, U.K.

John A. Verdicchio
Rolls-Royce plc,
Derby, DE24 8BJ, U.K.

In some gas turbine aeroengines, the HP compressor is driven by the H.P. turbine through a conical shaft or drive cone. This drive cone is enclosed by a stationary surface that forms the supporting material for the combustion chambers. Air used to cool the turbine blades is directed into the space around the drive cone, and a major concern to an engine designer is the temperature rise in this air due to frictional dissipation and heat transfer. This paper presents results from a combined experimental and CFD investigation into the flow within an engine representative HP compressor drive cone cavity. The experimental results show similarities in flow structure to that found in classic rotor-stator systems. Both 2-D and 3-D CFD simulations were carried out using the FLUENT/UNS code. The 3-D model which included the actual compressor blade tip clearance gave the best agreement with the experimental data. However, the computational resource required to run the 3-D model limits its practical use. The 2-D CFD model, however, was found to give good agreement with experiment, providing care was exercised in selecting an appropriate value of initial tangential velocity. [DOI: 10.1115/1.1516195]

1 Introduction

The internal air system of a modern gas turbine provides air to cool and seal various components around the engine. Such air is bled from the compressor and is parasitic to the main cycle, ultimately leading to an increase in fuel consumption. It is therefore the task of designers to minimize the amount of air extracted, while at the same time providing an adequate supply for sealing and cooling.

The drive cone cavity is the space between the HP compressor drive cone and the combustor casing. This is one of the hottest uncooled components in the engine. It is not uncommon for surface temperatures to reach 900 K at 10,000 rpm, so the material used in the drive cone operates at the edge of its safe working temperature. The elastic limit of this material is very sensitive to temperature changes at these high temperatures (a 10 K rise in surface temperature can halve its life). So modelling techniques must be able to accurately predict component surface temperatures. Although this may be obtained from a conduction analysis (Monico and Chew [1], Dixon [2]), knowledge is required of the local heat transfer coefficients, which in turn can be obtained from experiment and CFD (computational fluid dynamics) results. With the increasing sophistication required to match experiments to engine conditions, there is a trend towards using CFD as a predictive tool. However, given the uncertainties associated with simulating the actual boundary conditions and turbulence modeling, CFD results require validation, which can only be obtained from experimental data.

There exists an extensive body of knowledge on different classes of flows in rotating systems (see Owen and Rogers [3,4]). These are generally classified as one of the following:

- Free disk system—a disk rotating in an infinite environment.
- Rotor-stator system—a rotating disk adjacent to a stationary casing, there may also be a superposed flow either radially inward or radially outward.
- Rotating cavity system—two disks rotating with a common angular speed and bounded at their periphery by a circumferential shroud. Flow may be supplied to the cavity either radially inward or outward, or axially through the cavity.

The first two of these have particular relevance to this study. The fluid adjacent to the surface of a rotating disk is pumped radially outward, and is balanced by an ''entrainment'' of fluid towards the disk. The dimensionless entrainment rate is governed by the rotational Reynolds number and the tangential velocity of the fluid away from the disk. For a rotor-stator system without any superposed flow, fluid is pumped radially outward in the rotor boundary layer, and to satisfy continuity, there is radially inward flow in the boundary layer adjacent to the stator. For a sufficiently large axial gap between the rotor and stator, these boundary layers do not merge, but are separated by an inviscid core region (where the radial and axial velocity components are zero). The tangential velocity of this core region has a value of about 40% of the rotor speed. The effect of a superposed radial *inflow* into the rotor-stator cavity is, since angular momentum is conserved, to create a free vortex and increase the core rotational speed.

Much of the work on rotating cones (as opposed to disks) has focused on the free cone (see, for example, Wu [5]). For a cone of outer radius, b, rotating with angular speed, Ω, in a quiescent fluid of density, ρ, and dynamic viscosity, μ, the flow field has similarity with free disk flow providing the rotational Reynolds number, Re_ϕ, is defined using the cone half-angle, θ, viz.

$$\mathrm{Re}_\phi = \rho \Omega b^2 / \mu \sin\theta \tag{1}$$

Chew [6,7] applied von Kármán's [8] momentum integral method to a free cone of nonzero hub radius, and found that the nondimensional entrainment, $C_{w,\mathrm{ent}}$, was given by

$$C_{w,\mathrm{ent}} = \frac{\dot{m}_{\mathrm{ent}}}{\mu b} = 0.2186\left[1 - \left(\frac{a}{b}\right)^5\right]\mathrm{Re}_\phi^{4/5} \tag{2}$$

where $\dot{m}_{\mathrm{ent}}$ is the mass flow rate entrained by a cone of inner and outer radii a and b, respectively. The leading constant in Eq. (2) is the same as for a free disk, and the factor in the square brackets takes account of the nonzero inner radius, $r = a$.

A cone rotating within a stationary casing has obvious geometric similarities with the rotor-stator system mentioned above. The experimental work of Yamada and Ito [9] showed that Taylor vortices were suppressed by increasing the superposed flow, the ro-

Contributed by the International Gas Turbine Institute and presented at the International Gas Turbine and Aeroengine Congress and Exhibition, Amsterdam, The Netherlands, June 3–6, 2002. Manuscript received by the IGTI, October 31, 2001. Paper No. 2002-GT-30239. Review Chair: E. Benvenuti.

tational Reynolds number, and the gap between rotor and stator. It is however, very unlikely that Taylor vortices occur for the conditions reported in this current paper. May et al. [10] finite difference solution of the Reynolds-averaged Navier-Stokes equations predicted a flow structure similar to that in rotor-stator systems: a boundary layer with radial outflow on the rotating cone, a boundary layer with radial inflow on the stator, and an inviscid core region. However, both these studies considered the effects of a superposed radial outflow, there appears to be no work associated with a cone rotor-stator system with superposed radial inflow as investigated here. These studies also make use of an idealized geometry, which although valuable, begs the question ''are these results of use in the real geometry of a gas turbine engine?''

This paper discusses results obtained from a combined experimental and numerical investigation into the flow in the conical space between a HP compressor drive cone and its stationary casing. A future paper will discuss the heat transfer results.

2 Experimental Apparatus

A general assembly of the test rig is shown in Fig. 1. A full description of this may be found in the thesis of Kais [11]. The rig uses real engine parts, taken from a Rolls-Royce RB211-535, for the HP compressor stack, drive cone, turbine disk, and bearing assemblies. A mild steel casing forms a pressure casing around the rotor assembly. This design choice gives the advantage of a true engine representative geometry.

Referring to Fig. 1, the rotor assembly comprises six stages of the HP compressor stack, the HP drive cone, a mini-disk, and the HP turbine disk. The inner radius, a, of the drive cone is 189.50 mm and the outer radius, b, is 328.57 mm, giving the radius ratio at the drive cone hub radius as, $a/b=0.58$. The outer radius of the central drive shaft is 85 mm and the inner radius of the sixth stage compressor disk is 91.95 mm. For simplicity, the simulated intermediate pressure (IP) drive shaft rotates at the same speed as the drive cone. This differs from normal engine practice where the LP system rotates at a lower speed (7000 rpm) than the HP system (10,000 rpm). However, this is not considered to be an influential factor governing the heat transfer from the outer surface of the drive cone. (When in a convection regime dominated by buoyancy forces, the relationship between shaft and rotor speed is known to affect the heat transfer from the inner surface of the cone (see Alexiou et al. [12]), it will, however, have very little influence on that from the outer surface which experiences a forced convection regime.)

The rig was designed to operate at engine representative values of nondimensional flow rate, rotational Reynolds number, and speed parameter with a design speed of 7300 rpm. As in an engine, the HP compressor stack is driven by the HP turbine stage. However, in the rig in order to reduce the compressor work, only the sixth stage HP compressor blades were retained. This was found to be sufficient to maintain engine representative conditions at the inlet of the drive cone cavity. In order to achieve engine representative conditions in mainstream flow, with the flow rate available, the annulus area was scaled down. Consequently, the height of these 80 original HP compressor blades was reduced to a height of 8.3 mm at the leading edge of the blade and 7.02 mm at the trailing edge.

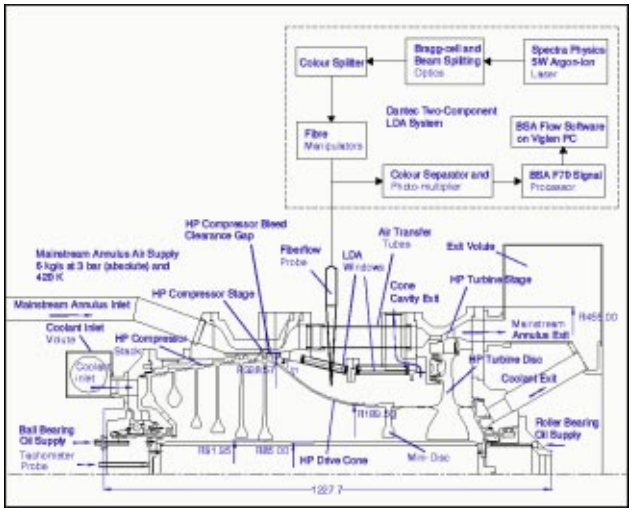

Fig. 1 General assembly of the HP compressor drive cone rig

The mainstream flow enters the rig via a conical diffuser and then (to eliminate any undesired swirl into the HP compressor stage) through ten 60.2-mm-inside-dia stainless steel tubes. After the HP compressor stage, some of the mainstream flow will be ingested into the cone cavity. The remainder of the mainstream flow was used to drive the rig, by the turbine stage with a set of 92 reduced height turbine blades, as the power requirements for the rig was much lower than the engine. The cone cavity flow leaves though an annular wall with 30 radial holes of 12 mm diameter, after which it is collected in an annular collection chamber, and finally leaves via a 52-mm-inside-dia cast iron pipe.

For the mainstream air supply, the rig has access to two independent compressed air supplies. One being a Rolls-Royce Dart RDa7 compressor, providing 6 kg/s of air at 3 bar (absolute) and 420 K, driven by a Rolls-Royce Dart RDa12 engine. For a detailed description of this novel gas turbine driven centrifugal compressor, the reader is referred to Turner et al. [13]. Alternatively, the mainstream flow was provided by two Keith-Blackman compressors, capable of supplying up to 1.6 kg/s at 1.3 bar (absolute) and 378 K. An additional air supply to pressure balance the bearing chamber, was provided by a Hydrovane model 250 PU rotary vane compressor.

The air inlet temperature into the cone cavity, T_m, was measured by two half-shielded total temperature probes (see Fig. 1), with a recovery factor of 0.96 (Benedict [14]), each containing a Kapton-insulated chromel-alumel thermocouple. The thermocouple was held in a 1.6-mm-inside-dia, 3.2-mm-outside-dia, stainless steel tube, positioned in the mid-plane of the cavity, aligned normal to the inner surface of the upstream casing.

The dimension of the gap perpendicular to the surface at the cone entrance was measured by a capacitive transducer, previously calibrated and compensated for temperature changes. During testing this gap varied from 2.89 to 3.10 mm, depending on rotational speed. The rotational speed of the drive cone was measured using a magnetic pick-up sensor, connected to a Graham & White Instruments MT-7602B tachometer (accuracy ± 1 rpm).

The mainstream air supply from the Dart, and that into the test rig, was measured with a venturi with inlet and throat diameters of 250 and 176 mm, respectively. For the Blackman compressors, this was measured using another venturi with inlet and throat diameters of 150 and 86 mm. The flow rate from the cone cavity itself was measured by an orifice plate in the exit pipe with an inner diameter of 31.2 mm and a diameter ratio of 0.6. All the flow meters conform to British Standards (BS 1042) [15]. The pressures and temperatures from the flow meters are measured by a Scanivalve system (Model SSS-48C MK4, resolution ± 10.5 Pa) and a National Instruments data acquisition system (resolution ± 0.12 K), respectively.

Measurements of the tangential and axial components of velocity in the cone space were obtained using a two-component Dantec laser Doppler anemometer (LDA) system. A schematic diagram of the LDA system is shown in Fig. 1. The LDA system was used in backscatter arrangement and comprised:

1. a 5 W water-cooled Spectra-Physics Argon-Ion laser;
2. transmitting optics that included a Bragg-cell, a color splitter, and a 50-mm beam spacing, 2.2-mm beam diameter, two-component FiberFlow probe, with a focal length of either 300 or 600 mm;

Table 1 Measurement volume dimensions for blue (488 nm) and green (514.5 nm) beams

Beam Wavelength (nm)		Focal Length (mm)	Diameter (mm)	Length (mm)	Fringe Spacing (μm)
488	(for V_ϕ)	300	0.0847	1.017	2.938
488	(for V_ϕ)	600	0.169	4.067	5.861
514.5	(for V_z)	300	0.0893	1.072	3.098
514.5	(for V_z)	600	0.179	4.288	6.179

3. receiving optics which comprised a focusing lens, a color separator (488 nm and 514.5 nm interference filters), and a photo-multiplier;
4. a BSA F70 signal processor (160 MHz Doppler frequency with 120 MHz bandwidth);
5. BSA flow software;
6. a Viglen Contender P3-800 PC.

Optical access into the cone cavity was achieved through BK7 fused silica glass windows, mounted using mild steel flanges on the outer casing. The measurement volume dimensions for the blue (used to measure the tangential velocity) and green (used to measure the axial velocity) beams are given in Table 1; in each case there were 28 fringes present.

Mineral oil was used as the seeding material, with an estimated mean particle size of less than 1 μm and produced from a TS1 model 9306 six-jet atomizer.

Table 2 Experimental conditions in the drive cone cavity for the CFD simulations

	low speed	high speed	Engine
inlet pressure (Pa)	115642 ± 415	250058 ± 662	
inlet temperature (K)	346 ± 1.3	416 ± 1.3	
main annulus mass flow (kg/s)	1.12	4.5	
drive cone mass flow (kg/s)	0.071 ± 0.0016	0.226 ± 0.01	
seal flow at Exit 3 (kg/s, % of main annulus)	0.0056, 0.5	0.0225, 0.5	
rotational speed (rad/s)	203 ± 1.3	530 ± 1.3	
metal temperature (K)	346 ± 1.4	430 ± 1.4	
rotational Reynolds number, Re_ϕ[1]	2.8 x 10^6	10.7 x 10^6	76 x 10^6
dimensionless flow rate, C_w[2]	-10113	-28574	-136636
turbulent flow parameter, $\lambda_T = C_w/Re_\phi^{0.8}$	-0.071	-0.068	-0.068
speed parameter, $N/\sqrt{T}$ (rev/min / $K^{1/2}$)	105	246	348

[1] $\theta = 27$ deg.
[2] It is convention to define this as negative for a superposed radial inflow.

3 CFD: General Description of CFD Models

Full details of the CFD model can be found in the Thesis by Verdicchio [16]. All CFD computations are based on the FLUENT/UNS code previously validated against a number of benchmark rotating flow problems. A standard k-ε turbulence model with standard wall functions was used, although some work was also carried out with a two-layer zonal model, which was found to agree with the wall function approach. In order to investigate the trade off between accuracy of CFD predictions and computational resources, both 2-D and 3-D models were run. Comparisons were made with LDA data at low speed (1938 rev/min) and at high speed (5061 rev/min), see Table 2 for further details.

3.1 The 2-D CFD Model. The mesh for the 2-D model is shown in Fig. 2. The discrete holes at the exit of the cone space (marked as ''Exit 2'' on this figure) are replaced by an axisymmetric slot of equivalent area. Although the solution domain extends into the main annulus flow region, the rotor blades are not included in the 2-D model. In all the computations reported here, it is assumed that the flow is incompressible. This is considered to be a reasonable assumption since the flow reaches a maximum Mach number of about 0.5 only in limited regions of the gap at the rim, and a value of 0.3 in a small fraction of the cone cavity. It was important to retain this assumption to avoid computational difficulties. However, subsequent work has revealed that including compressibility effects makes little difference to the velocities in the LDA measurement plane. The boundary conditions follow standard practice for this class of flow. No slip conditions are applied at solid walls. Specified temperatures and (when appropriate) velocities are applied at the inlet boundary (Inlet 1). The inlet turbulence intensity is taken as 3% with a length scale of 10 mm. This value of turbulence intensity is judged to be representative of the low turbulence in this region, the value of length scale chosen as being similar to the annulus height. The mass flow, as measured in the experiment, is specified at Inlet 1 and Exit 2. The mass flow through Exit 3 was determined using a 1-D network model based on Rolls-Royce correlations for labyrinth seals as 0.5% of the annulus flow, and this value was used in the CFD. Zero derivative (normal to the exit) conditions are applied to variables at all exits, except pressure, which is interpolated from the nearest upstream values.

The 2-D mesh used for both high and low speed test cases had either 10670 cells for the standard model, or 39824 cells for a refined model. All y^+ values were in the range of 30 to 100, which is within the accepted limits.

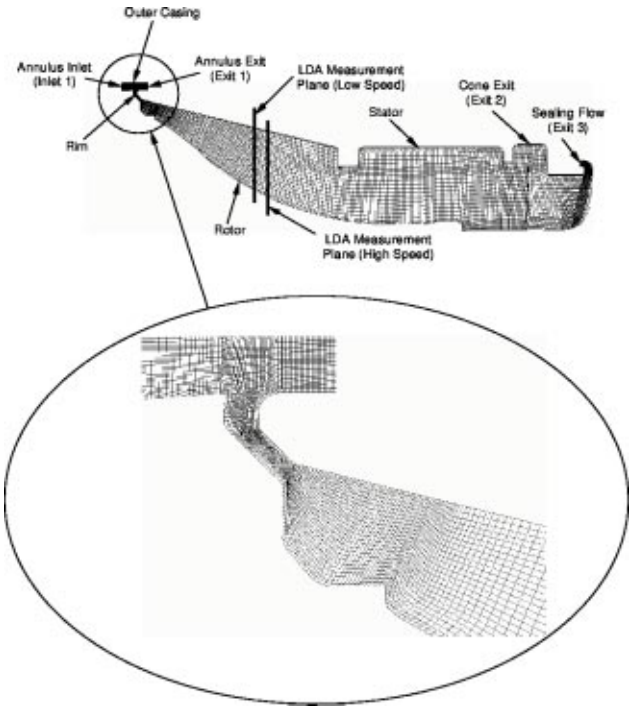

Fig. 2 The CFD mesh for the standard (10670 cells) 2-D model

The standard 2-D model was run at the conditions of the low speed case and was found to converge (normalized residuals all less than 3.7×10^{-7}) within 10^4 iterations. Comparison with the results obtained from the refined mesh showed very little difference (within $\pm1\%$) between the predicted values of axial and tangential velocities. The two-layer zonal model with 40675 cells required a similar number of iterations but took four times as long to converge and gave similar results (within $\pm1\%$) to the standard model. Consequently, this too was considered to offer very little advantage and all the 2-D computations discussed here use the standard model.

3.2 The 3-D CFD Models. The asymmetry due to the row of compressor blades was modelled using a 3-D mesh. The blade and passage geometry were taken from the CAD file and so give an accurate representation of the full 3-D features. As good boundary layer resolution was required and, in general, the cavity has relatively simple geometry, hexahedral cells were used. Two different 3-D models were created. In the first, the compressor blade tip clearance was neglected and a blade-to-blade sector modelled. The second 3-D model took account of the measured blade tip clearance of 20% of the annulus height, and modelled a sector with a central blade.

The 3-D model without tip clearance comprised two parts: i) the blade with main annulus, and ii) the drive cone cavity. The two meshes were joined using a nonconformal interface. The main reason for adopting this meshing approach was so that the different regions could have different mesh densities, resulting in a smaller mesh size. A key consideration was keeping the FLUENT model to around 400,000 cells so that it would run on a 512 MB workstation. The blade passage was also meshed several times to obtain the correct near-wall spacing and a mesh with acceptable cell aspect and expansion ratios and skewness. Use of the nonconformal interface avoided the need to mesh the cone cavity each time. Since the main body of the physical drive cone cavity is axisymmetric, this was meshed using a similar strategy and near wall spacing as the 2-D model. The final mesh had 350425 cells, with 191864 in the cone cavity, and 158561 in the main annulus and blade region. This model required about 7000 iterations to converge, taking about 12 days on a Unix workstation.

The second 3-D model, which included the blade tip clearance, used a different meshing approach to avoid the need for the nonconformal interface, and resulted in a more even mesh spacing. This model used the same near wall spacing as the first and was significantly larger with 481364 cells. Apart from the newly created tip gap, the second 3-D model was run to the same boundary conditions as the first. The solution was initialised with a zero initial flow field in the absolute frame. The second model required over 18,000 iterations to converge, about eight days on an 8 node P.C. cluster.

4 Results From LDA Measurements and Comparison With the 2-D CFD Model

The main features of the flow structure in the cone cavity are illustrated by the streamlines of Fig. 3. This plot was obtained from running the standard 2-D model at the low speed condition, but the features are common to the high speed case as well. The flow structure has similarities to the classic ''rotor-stator'' system (see Owen and Rogers [3]). Fluid near to the rotor surface is pumped radially outward due to the action of centrifugal pumping. Whereas, adjacent to the stator surface there is radial inflow. The widening of the streamlines in the central region indicates a ''core region'' where viscous effects are negligible, and the radial pressure gradient is in equilibrium with the centrifugal force. The insert in Fig. 3 shows a close up of the computed streamlines in the gap region. A strong recirculation is seen to exist, which (in the 2-D model) prevents egress of flow from the rim gap region of the cone cavity.

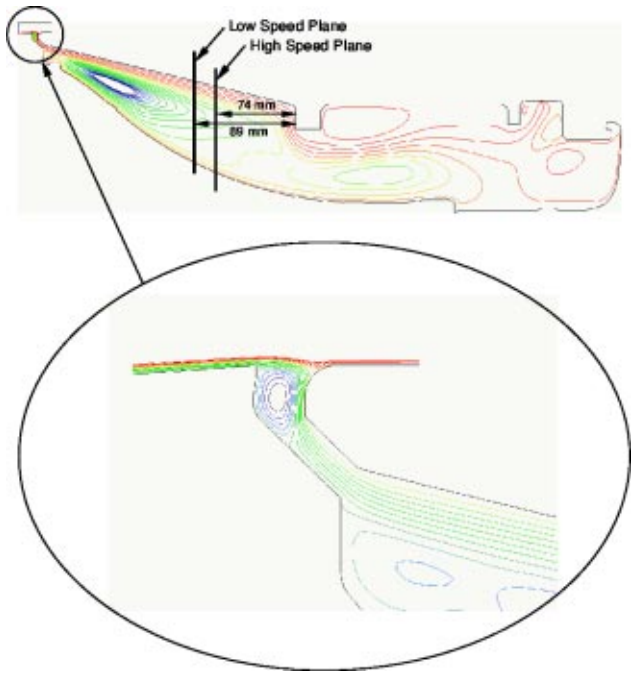

Fig. 3 Computed streamlines from the standard 2-D model at low speed conditions ($\Omega=203$ rad/s, $\dot{m}_{cone}=0.071$ kg/s)

Measured values of tangential velocity, normalized with respect to the local rotor velocity, $V_\phi/\Omega r$, and their variation with radius ratio, $x=r/b$, are shown in Fig. 4. The tests were carried out at low speed conditions, with and without superposed inflow and also at high speed conditions with superposed flow. In both cases, the superposed inflow is significantly less than (about 1/3 of) the free cone entrainment rate (Eq. (2)). The location of the two measurement planes is shown in Fig. 3. The cone rotor surface is located at $x\approx0.69$ and that of the stationary casing at $x\approx0.889$. For no flow into the cavity ($C_w=0$), the tangential velocity in the core region ($0.71<x<0.85$) is approximately 40% of the rotor speed, which is consistent with the theoretical value for turbulent flow given in [3]. For $|C_w|>0$ ($C_w=-10^4$ at the low speed case and $C_w=-2.86\times10^4$ at high speed), the tangential velocity increases with increasing $|C_w|$, which for radial inflow is consistent with conservation of angular momentum. The line $V_\phi/\Omega r=$ constant implies that a forced vortex flow occurs. When inflow is supplied, $V_\phi/\Omega r$ decreases with r/b, which indicates an influence of free vortex behavior.

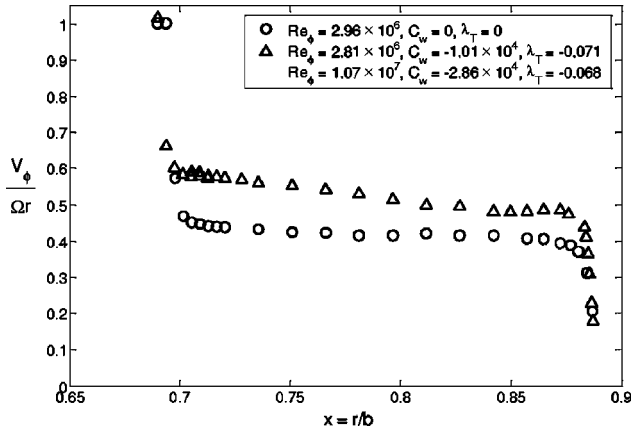

Fig. 4 Measured variation of dimensionless tangential velocity with radius ratio

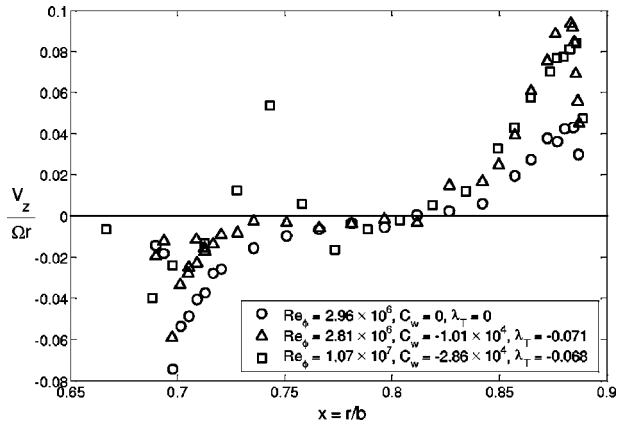

Fig. 5 Measured variation of dimensionless axial velocity with radius ratio

Experimentally measured values of dimensionless axial velocity, $V_z/\Omega r$, and their variation with x, are shown in Fig. 5. As can be seen, the magnitude of the axial velocities in the boundary layers is an order of magnitude less than the tangential component. In the core region the measured axial velocities are close to zero. A positive value of V_z indicates the flow moves away from the inlet—so fluid is seen to move towards the inlet and radially outward in the rotor boundary layer ($x<0.73$) and radially inward in the stator boundary layer ($x>0.82$).

The radial variation of tangential and axial velocity at the LDA measurement plane from various 2-D CFD models and experimental data, for the low speed ($\Omega=203$ rad/s) case, are compared in Fig. 6. The tangential velocity component is shown in Fig. 6(*a*), the axial component in Fig. 6(*b*). The CFD results are for a number of different conditions of tangential velocity specified at Inlet 1 (Fig. 2). The standard model uses a uniform value of 3.931 m/s, which is derived from the measured (by a yaw probe) flow angle 4.5 ± 1 deg and mainstream flow velocity of 49.96 m/s. There is fair agreement between this and the LDA data, but using this value of inlet tangential velocity results in a lower than measured value of tangential velocity in the core region ($0.23<r<0.29$ m) and also under prediction of the peak axial velocity in the stator boundary layer ($r=0.29$ m). As shown in Fig. 6, an inlet condition of a uniform tangential velocity of 15 m/s, is in much better overall agreement with the LDA data. So, clearly the results obtained from the 2-D model are sensitive to this specified value of tangential velocity. Results are also shown in Fig. 6 for two other values of inlet tangential velocity. Both of these use a 1/7th power law boundary layer profile for both the axial and tangential velocities at inlet. The thickness of the boundary layer is taken as 5 and 10% of the height between inner and outer annulus walls at the cone cavity inlet. This boundary layer approach leads to an improvement in the predicted values of peak axial velocity in the stator boundary layer. However, there appears to be significant over prediction of the tangential velocity in the core.

Comparison is made in Fig. 7 between CFD predictions and experimental values of tangential and axial velocity for the high speed test ($\Omega=530$ rad/s). It may also be seen that the radial location of the measurements in this figure is not identical to that in the previous one. This is because the LDA probe was moved slightly from one set of tests to the other. There is some degree of scatter present in the LDA measurements of axial velocity for $r<0.245$ m, which is considered due to greater experimental uncertainty at this higher rotational speed.

The LDA equipment used here was provided on loan for a limited period. So time constraints did not permit a separate series of experiments to be carried out to specifically evaluate the uncertainty in the actual measurements. It is therefore not possible to

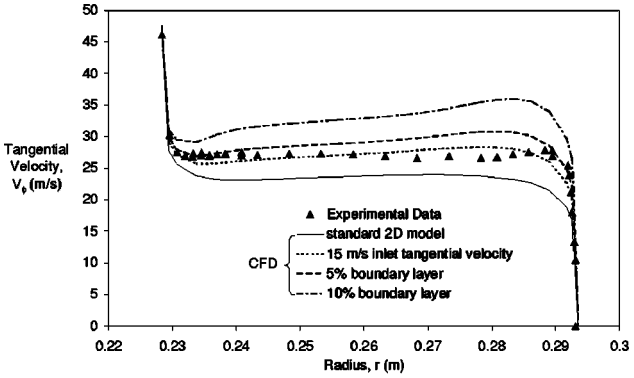

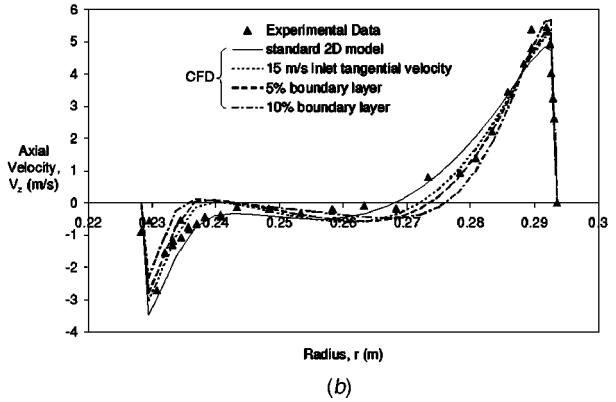

Fig. 6 Comparison between experimental data and 2-D CFD models with various inlet boundary conditions (low speed case, $\Omega=203$ rad/s, $\dot{m}_{cone}=0.071$ kg/s)—(*a*) tangential velocity, (*b*) axial velocity

provide a numerical estimate of this. However, the mean velocity measurements obtained from the Dantec Burst Spectrum Analyser were transit time weighted, which is claimed to eliminate velocity bias. The validated data rate was more than adequate (from 0.2 to 1 kHz), and the seeding generator and material had previously been used with success on a number of rotating test rigs. Overall confidence in the LDA measurements is then relatively good. The relatively large scatter evident in the measurements of axial velocity can be explained as being due to relatively small uncertainties in the location of the probe alignment. A relatively small off-axis misalignment will measure a component of, the much larger, tangential velocity. Nonetheless, the measurements of axial velocity show features consistent with the formation of separate boundary layers on the cone and stator surface, and also a core region of zero axial velocity between them.

Comparison with the low speed case CFD results shows thinning of the rotor and stator boundary layers at the high speed. As in the previous figure, a number of different values are specified for the tangential velocity at Inlet 1. The standard model uses a uniform value of 55 m/s (derived from experimental data), and two other uniform values of 70 m/s and 90 m/s were also investigated. Results using the boundary layer approach are not shown, as they did not give a significant improvement. As was found to occur at low speed, the predicted velocities are sensitive to this inlet condition. A value which is consistent with the experimentally measured flow angle and annulus mainstream velocity gives significant under prediction of the tangential velocity (but as will be explained later, confidence in this measurement is low). Increasing the inlet swirl to 70 m/s improves the match, but the best agreement is obtained with a value of 90 m/s.

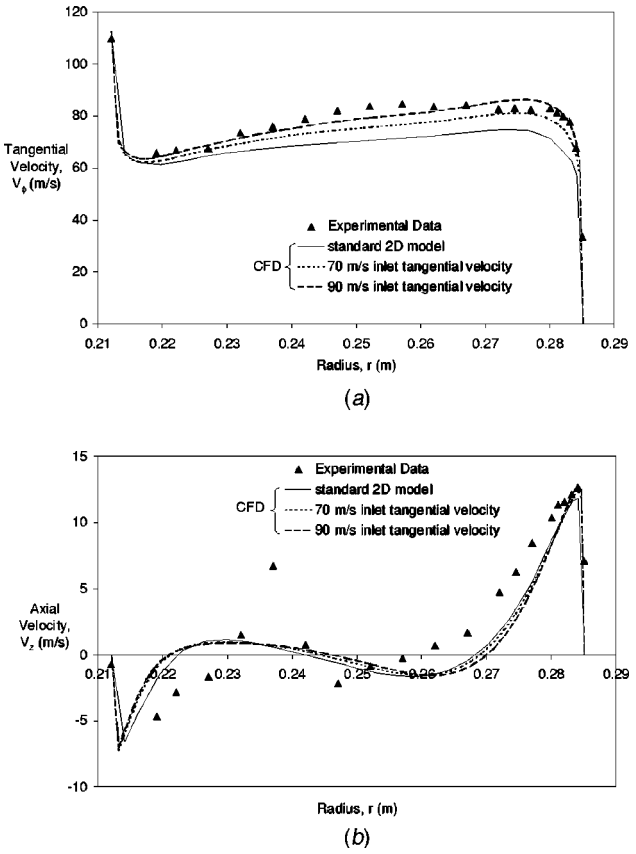

Fig. 7 Comparison between experimental data and 2-D CFD models with various inlet boundary conditions (high speed case, $\Omega = 530$ rad/s, $\dot{m}_{cone} = 0.226$ kg/s)

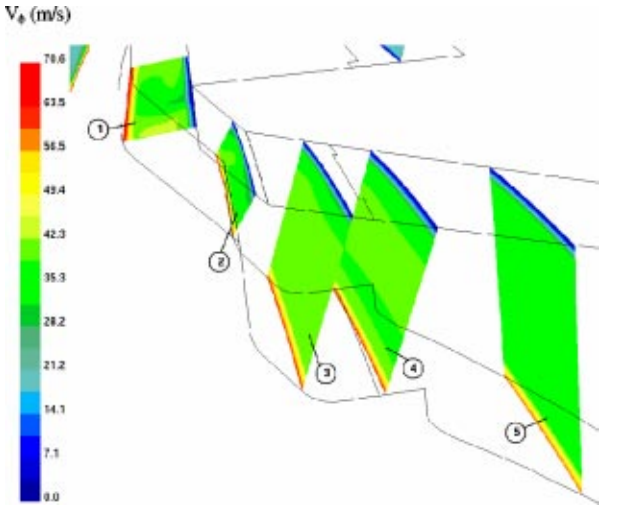

Fig. 8 Values of tangential velocity, V_ϕ, obtained from the 3-D model without tip clearance at the low speed case ($\Omega = 203$ rad/s, $\dot{m}_{cone} = 0.071$ kg/s)

5 Results From the 3-D Model

5.1 Running the 3-D Model. The 3-D model was run at the low speed condition as given in Table 2. The radial and tangential velocities were set to zero in a rotating frame of reference (at rotor speed), the turbulence intensity was 1.0% and the turbulence length scale 0.01 m. The standard k-ε turbulence model was used with the standard log-law wall functions. The initial solution strategy was slightly different to that used in the 2-D work. In order to model the rotating blade, the 3-D model assumes a rotating reference frame, so the solution was initialised with zero velocity in that frame. A uniform initial pressure field was assumed as in the 2-D work. The LDA measurement plane was used in the 3-D model to monitor the solution and to compare with experimental data. After 5000 iterations the solution on this plane showed no signs of converging and the mass averaged tangential velocity on this plane remained at over 50.0 m/s. Despite trying different meshes, changing the under-relaxation factors and also the discretisation scheme, the problem was eventually traced to the initial value of the tangential velocity. The solver was changed from SIMPLE to the coupled implicit solver, and by initialising the velocities to zero in the stationary frame of reference, a converged solution was obtained in 7000 iterations.

5.2 The 3-D CFD Model Without Tip Clearance. Figure 8 shows contours of tangential velocity at several planes cut through the rim region of the cone cavity. The 3D effect from the blade is significant at Plane 1, it decreases through Plane 2 and can still be seen to be present on Plane 3 where there is a protrusion due to a welded seam. The flow becomes axisymmetric by the time it reaches Plane 4: Plane 5 indicates where the LDA measurements were made. Although not shown here, comparison between the predicted 3-D velocity vectors in an r-z plane with the 2-D streamlines indicates a very similar flow pattern. The main annulus flow coupled with rotor entrainment causes a strong recirculation in the rim entrance, and flow moves radially inward adjacent to the stator.

The 3-D model so far, revealed two particular inconsistencies. Firstly, the flow angle (calculated from circumferentially averaged values of axial and tangential velocity at the blade mid-height) at the blade exit was found to be 22.0 deg in the stationary frame (and close to the blade exit angle of 48 deg in a rotating frame of reference). Clearly, there is a significant discrepancy with the experimentally measured value of 4.5 deg. Secondly, the boundary layer thickness (calculated from the circumferentially-averaged absolute tangential velocity) is about 28% of the annulus height. This is much higher than the values assumed in the 2-D analysis.

5.3 The 3-D CFD Model With Tip Clearance and Comparison With 2-D CFD and Experimental Data. These inconsistencies may be resolved when the blade tip clearance is modelled. Figure 9 shows the variation across the annulus height of the circumferentially averaged tangential and axial velocities at the blade exit plane. As shown, including the blade clearance in the 3-D CFD model causes a reduction (from around 22 to 15 m/s) in the predicted tangential velocity at the mid-height of the blade exit plane; since this allows flow to pass the blade with little affect on its tangential velocity. There is also a corresponding increase in the maximum axial velocity (from 57 to 61 m/s) at the blade exit plane. Using these axial and tangential velocities gives a blade exit angle of 14.0 deg (compared to 22.0 deg for the 3-D model with no tip clearance and a measured value of 4.5 deg). The difference between these predicted angles may seem surprisingly large, but the reader is reminded that the tip clearance was measured as 20% of the annulus height (1.6 in 8.3 mm). This gap, and the significant flow that passes relatively unaffected by the blade, obviously affects conditions in the annulus. There are also considered to be relatively large uncertainties in the blade exit angle measured by the yaw probe (uncertainties in radial location as well as those due to a highly swirling flow with blade passing effects), so confidence in the measured blade exit angle is low.

When the tip clearance is modeled, the 3-D results are considered to accurately represent the physics of the flow. So it is both interesting and supportive of this to note that the predicted value of tangential velocity at the blade exit plane (of 15 m/s), is consistent with the value used in the 2-D model to obtain the best fit with velocity measurements in the cone cavity.

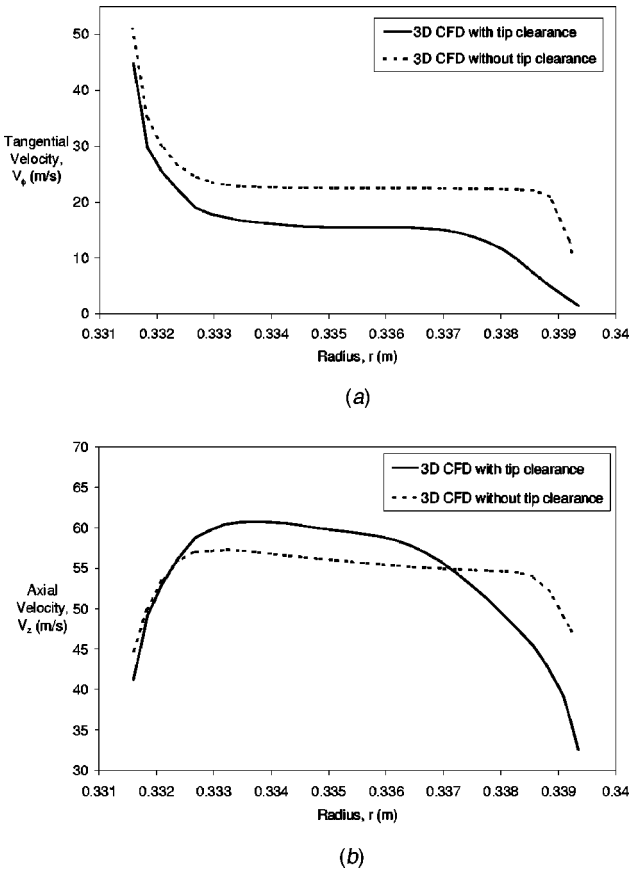

Fig. 9 Variation of tangential and axial velocities with annulus height, at the blade exit plane (low speed case, $\Omega = 203$ rad/s, $\dot{m}_{cone} = 0.071$ kg/s)—(*a*) tangential velocity, (*b*) axial velocity

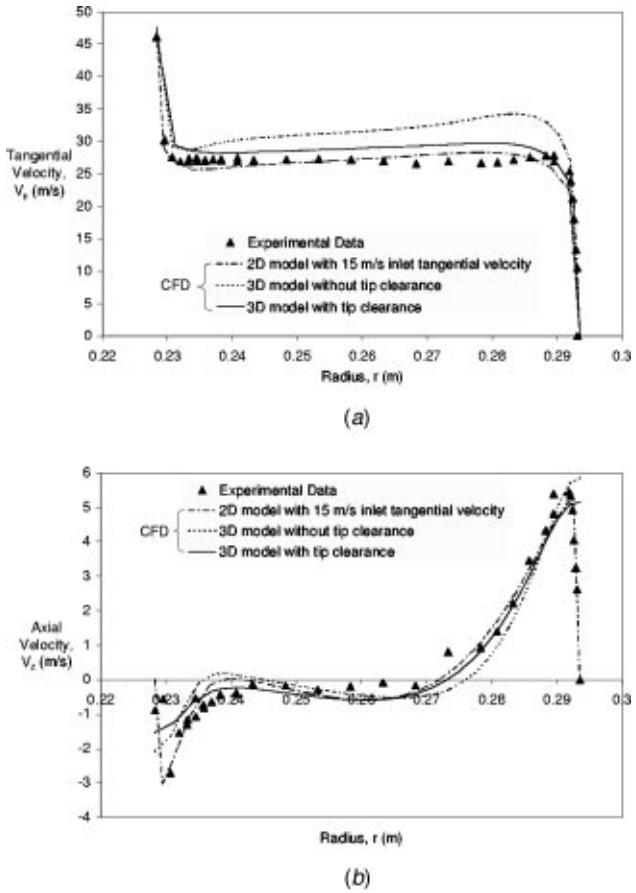

Fig. 10 Comparison between experimental data, 2-D and 3-D CFD models (low speed case, $\Omega = 203$ rad/s, $\dot{m}_{cone} = 0.071$ kg/s)—(*a*) tangential velocity, (*b*) axial velocity

Figure 10 shows a comparison at low-speed conditions of tangential and axial velocities obtained from both the 3-D models, experimental data and the best 2-D result—for a uniform tangential velocity at Inlet 1 of 15.0 m/s. The axial velocity profiles of the 2-D and 3-D results are similar which supports the idea that the axial velocity is relatively insensitive to the inlet boundary conditions. The tangential velocity in the 3-D model without tip clearance is significantly (around 20%) greater than the 2-D prediction. Including the tip clearance in a 3-D model has a marked affect on the tangential velocity. The agreement with the data is better than the other models, except the 2-D model. However, the overall shape of the 3-D result is in slightly better agreement with the experimental data than the 2-D prediction (the 2-D results show an increase of V_ϕ with radius not shown in the 3-D results, nor experimental data).

6 Conclusions

This paper has reported on a combined experimental and numerical (CFD) investigation of the flow inside an HP compressor drive cone cavity. The experimental work was carried out using an engine parts test rig which operated at engine representative nondimensional conditions. Measurements of the axial and tangential velocities were obtained from a 2-D laser doppler system. The CFD work, which used both 2-D and 3-D models, was carried out using the FLUENT/UNS code. A standard k-ε turbulence model with standard wall functions was used, although some work was also carried out with a two-layer zonal model. In the 2-D model different inlet tangential velocities were specified; the compressor blade tip clearance was included in one of the 3-D models and excluded in the other.

The experimental data have shown similarities in the flow to those of a classic rotor-stator system. Boundary layers form on the cone and on the stationary casing, and these are separated by an inviscid ''core'' region. For no superposed flow, the core between the rotating cone and stationary casing rotates at about 40% of the rotor speed. A superposed radial inflow of air is shown to increase this rotation.

The 3-D CFD models have shown the importance of the asymmetries created by the compressor blades in determining the inlet conditions for the cone cavity. The results are encouraging in that when tip clearances is included, then the 3-D model does give reasonable agreement with experiment. But it must be noted that the computational requirements of the 3-D model currently severely limit its use in practice. However, with a suitable choice of inlet tangential velocity, the 2-D CFD model gives similar results to the 3-D solution. Thus careful use of the 2-D approximation is justified.

Acknowledgments

The authors wish to express their thanks to the following organisations that have supported this research work: The Engineering and Physical Sciences Research Council, Rolls-Royce plc, the European Union and participating companies in the 4th Framework of the BRITE-EURAM scheme of the European Union. We are also grateful to Mr. J. D. Edmonds of Rolls-Royce plc for carrying out the LDA measurements.

Nomenclature

a, b = inner and outer radii, respectively
$C_w = \dot{m}/\mu b$ = dimensionless mass flow
$\dot{m}$ = mass flow
p = pressure
r = radius
$\mathrm{Re}_\phi = \rho\Omega b^2/\mu \sin\theta$ = rotational Reynolds no.
T = temperature
V_ϕ = tangential velocity
V_z = axial velocity
$x = r/b$ = radius ratio
μ = dynamic viscosity
$\lambda_T = C_w/\mathrm{Re}_\phi^{0.8}$ = turbulent flow parameter
ρ = density
θ = cone half-angle
Ω = angular speed of rotor

Subscripts

ent = entrained value
in = inlet value

References

[1] Monico, R. D., and Chew, J. W., 1992, ''Modeling Thermal Behavior of Turbomachinery Disc and Casings,'' AGARD Conf. Proc., pp. 24.1–24.9, Oct.
[2] Dixon, J. A., 1999, ''Gas Turbine Critical Component Temperature Predictions for Life and Integrity Considerations,'' 14th Int. Symp. Air Breathing Engines, pp. 99–105, Sept.
[3] Owen, J. M., and Rogers, R. H., 1989, ''Flow and Heat Transfer in Rotating-Disc Systems Volume 1—Rotor-Stator Systems,'' Research Studies Press Ltd, Taunton, Somerset, England.
[4] Owen, J. M., and Rogers, R. H., 1995, ''Flow and Heat Transfer in Rotating-Disc Systems Volume 2—Rotating Cavities,'' Research Studies Press Ltd, Taunton, Somerset, England.
[5] Wu, C.-S., 1959, ''The Three Dimensional Incompressible Laminar Boundary Layer on a Spinning Cone,'' Appl. Sci. Res., Sect. A, **8**, pp. 140–146.
[6] Chew, J. W., 1985, ''Moment Coefficients and Flow Entrainment Rate for a Cone Rotating in an Infinite Environment,'' Rolls-Royce Report No. TSG0225.
[7] Chew, J. W., 1988, ''The Effect of Hub Radius on the Flow Due to a Rotating Disk,'' ASME J. Turbomach., **110**, pp. 417–418.
[8] von Kármán, T., 1921, ''Uber Laminare und Turbulente Reibung,'' Z. Angew. Math. Mech., **1**, pp. 244–249.
[9] Yamada, Y., and Ito, M., 1979, ''Frictional Resistance of Enclosed Rotating Cones With Superposed Throughflow,'' ASME J. Fluids Eng., **101**, pp. 259–264.
[10] May, N. E., Chew, J. W., and James, P. W., 1994, ''Calculation of Turbulent Flow for an Enclosed Rotating Cone,'' ASME J. Turbomach., **116**, pp. 548–554.
[11] Kais, G., 1998, ''The Design and Commissioning of an Experimental Rig to Investigate the Heat Transfer and Fluid Flow in the High Pressure Compressor Drive Cone Cavity of an Aeroengine,'' D.Phil. thesis, School of Engineering, University of Sussex.
[12] Alexiou, A., Hills, N. J., Long, C. A., Turner, A. B., and Millward, J. A., 2000, ''Heat Transfer in H.P. Compressor Gas Turbine Internal Air Systems: a Rotating Disc-Cone Cavity with Axial Throughflow,'' Exp. Heat Transfer, **13**, pp. 299–328.
[13] Turner, A. B., Davies, S. J., Childs, P. R. N., Harvey, C. G., and Millward, J. A., 2000, ''Development of a Novel Gas Turbine Driven Centrifugal Compressor,'' Proc. Inst. Mech. Eng., IMechE Conf., **214**, pp. 423–437.
[14] Benedict, R. P., 1984, *Fundamentals of Temperature, Pressure, and Flow Measurements*, Third Edition, John Wiley & Sons, Inc, New York, NY.
[15] British Standards Institute, 1992, ''BS1042 Measurement of Fluid Flow in Closed Conduits, Section 1.1: Specification for Square-Edged Orifice Plates, Nozzles, and Venturi Tubes Inserted in Circular Cross-Section Conduits Running Full.''
[16] Verdichhio, J. A., 2001, ''The Validation and Coupling of CFD and FE Codes for Solving ''Industrial Problems'','' D.Phil. thesis, School of Engineering and Information Technology, University of Sussex.

A Study on Impeller-Diffuser Interaction—Part I: Influence on the Performance

Kai U. Ziegler[1]
e-mail: kai.ziegler@muc.mtu.de

Heinz E. Gallus

Reinhard Niehuis
e-mail: niehuis@ist.rwth-aachen.de

RWTH Aachen,
University of Technology,
Institute of Jet Propulsion and Turbomachinery,
52062 Aachen, Germany
www.ist.rwth-aachen.de

The interaction between impeller and diffuser is considered to have strong influence on the flow in centrifugal compressors. However, the knowledge about this influence is still not satisfying. This two-part paper presents an experimental investigation of the effect of impeller-diffuser interaction on the unsteady and the time averaged flow field configuration in impeller and diffuser and the performance of these components. The flat wedge vaned diffuser of the investigated compressor allows an independent adjustment of diffuser vane angle and radial gap between impeller exit and diffuser vane inlet. Attention is mainly directed to the radial gap, as it determines the intensity of the impeller-diffuser interaction. Part I deals with the integral flow losses and the diffusion in impeller, diffuser and the entire compressor. An extensive test series with steady probe measurements at impeller exit and diffuser exit was performed at 10 different diffuser geometries and different operating points. The results show that in most cases smaller radial gaps are leading to a more homogeneous flow field at diffuser vane exit and to a higher diffuser pressure recovery resulting in a higher compressor efficiency. On the other hand, impeller efficiency is hardly affected by the radial gap. In Part II, measurements with a laser-2-focus velocimeter are presented illuminating the reasons for the effects found. The experimental results are published as an open CFD test case under the name "Radiver."
[DOI: 10.1115/1.1516814]

Introduction

Impeller-diffuser interaction in a centrifugal compressor can be defined as the group of mechanisms which cause the differences in flow phenomena and performance of the two components between isolated and coupled operation, including unsteady and other effects. The interaction has two main aspects. The first and more important one is the influence of the impeller on the diffuser flow. It is characterized mainly by viscous and to a smaller degree by potential effects. But also the significance of the potential repercussion of the diffuser on the impeller flow was pointed out early (Pfleiderer [1], Dean [2]). The two main aspects can be further subdivided as follows:

1. *Impeller→diffuser (vaned or vaneless):*
(a) Unsteady effects due to the highly distorted relative impeller flow field and the blade wakes play a dominating role including intensive mixing processes.
(b) The shape of the axial profile of Mach number and angle at diffuser inlet, which would remain after a circumferential averaging of the impeller flow field, is a fundamental diffuser inlet condition also including mixing processes.

2. *Diffuser→impeller:*
(a) The diffuser vanes cause an unsteady pressure disturbance for the relative impeller flow.
(b) After an imaginary circumferential averaging of the diffuser flow field the diffuser vanes would still have an upstream potential effect. Even the shape of the vaneless diffuser inlet region (Hayami and Umemoto [3], Japikse [4]) or the presence of a vaneless diffuser at all influences the impeller flow.

These effects are difficult to isolate for research purposes. In experimental investigations on the repercussion of the diffuser on the impeller flow often measurements with vaned and vaneless diffuser are compared (e.g., Krain [5], Inoue and Cumpsty [6]), including the unsteady and time averaged potential repercussion of the diffuser vanes (2(a) and 2(b)). Fowler [7] investigated the exit flow field of a rotating channel, exhausting into a large box rotating with it, compared to discharging into a vaneless diffuser (only 2(b)). Cascade testing of radial diffusers allows a variation of the inlet profiles (only 1(b), e.g., Filipenco et al. [8], Deniz et al. [9]). Here, it is a difficult task to ensure realistic testing conditions.

Numerical investigations provide better possibilities to separate the different aspects of impeller-diffuser interaction. Often a steady calculation with a mixing plane between impeller and vaned diffuser is compared with an unsteady stage calculation (e.g., Yamane et al. [10], Dawes [11]) showing clearly the influence of unsteady effects in impeller and diffuser (1(a) and 2(a)). Effect 1.b can be easily isolated by a separate diffuser calculation with varied inlet profiles. Another interesting variant for research purposes is the frozen rotor calculation (e.g., Liu and Hill [12]). Steady calculations are performed in a number of fixed (''frozen'') impeller-diffuser positions, and are then averaged, probably overestimating the losses caused by flow unsteadiness.

Another possibility to investigate the interaction between impeller and vaned diffuser experimentally and numerically, is a variation of the radial gap between impeller exit and diffuser vane inlet. The disadvantage here is that in radial machines not only all aforementioned aspects of impeller-diffuser interaction are included, but also important additional parameters. For example, an increase of the radial gap leads to a decrease of the Mach number at the vane leading edges and to a significantly longer flow path in the vaneless space. The growth of boundary layer thickness caused thereby increases the blockage in the diffuser throat, and by that impairs the performance of the following diffuser channel. So it is even more difficult to attribute the found effects to single causes. On the other hand a variation of the radial gap has a high practical relevance. The radial gap is an often discussed design parameter influencing pressure ratio, efficiency, mass flow range, mechanical loading, noise emissions and size of a centrifugal

[1]Current address: MTU Aero Engines GmbH, 80995 Munich, Germany

Contributed by the International Gas Turbine Institute and presented at the International Gas Turbine and Aeroengine Congress and Exhibition, Amsterdam, The Netherlands, June 3–6, 2002. Manuscript received by the IGTI, October 26, 2001. Paper No. 2002-GT-30381. Review Chair: E. Benvenuti.

compressor. Many researchers presented investigations varying the radial gap (e.g., Rodgers [13], Inoue and Cumpsty [6], Jin et al. [14], Shum et al. [15], Salvage [16]); but corresponding recommendations to find an optimum radial gap do not exist yet due to the large number of contradicting parameters influenced by it.

The objective of the experimental investigation presented in this two-part paper is to achieve a better understanding of the flow phenomena connected with a variation of the radial gap and their influence on the performance of impeller, diffuser and the entire compressor. Furthermore, the general knowledge about the highly unsteady flow field between the impeller exit region and diffuser throat shall be improved. Both impeller and wedge vaned diffuser of the investigated 4:1 pressure ratio compressor have high-subsonic inlet flow conditions. The presented work is based on a preceding project of unsteady pressure measurements at the same test rig reported by Justen et al. [17]. An overview of the research work conducted at the test rig up to now is given by Ziegler et al. [18]. The strategy was to combine an extensive parameter study with the help of steady probe measurements, presented in part I, and detailed time resolving laser-2-focus measurements, presented in Part II, in order to get to an overall result. The probe measurements were conducted for the vaneless diffuser and at two different diffuser vane angles, each combined with a number of radial gaps.

Centrifugal Compressor Test Rig

The compressor is run in a closed loop using air and allowing a variation of inlet pressure and temperature (Fig. 1). The compressor stage (Fig. 2) consists of an unshrouded impeller made of aluminum with 15 backswept blades and a diffuser with 23 wedge vanes. The impeller was provided by MTU Aero Engines, whereas the wedge vaned diffuser was designed at the institute by Rothstein [19] based on the characteristic parameters for flat diffusers of Runstadler et al. [20]. The diffuser allows a continuous and independent adjustment of the vane angle, indicated by the vane suction side angle α_{4SS}, and the radial gap between impeller exit and diffuser vane inlet, indicated by the radius ratio r_4/r_2 (Fig. 3). The most important data of the compressor is collected in Table 1. A detailed description of the development and the technical realization of the compressor and the test rig is given by Rothstein [19], a short summary is given by Ziegler et al. [18]. Varying α_{4SS} and r_4/r_2, other important geometry parameters of the vaned diffuser change. Their values are listed in Table 2 for all diffuser geometries investigated. It should be considered that the very important diffuser channel divergence angle 2θ (see Fig. 3) is invariant.

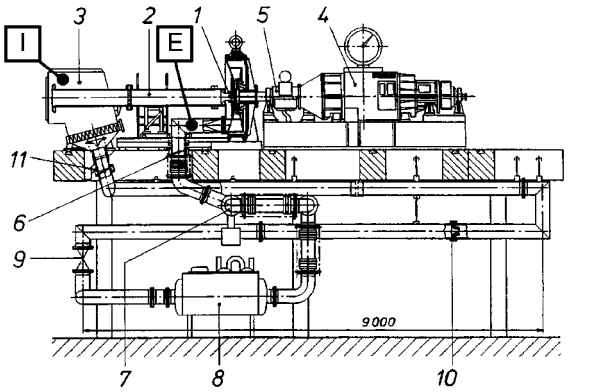

1 Centrifugal compressor stage	6, 11	Fast-opening butterfly valves
2 Suction pipe with honeycomb	7, 9	Slide valves
3 Settling chamber with air filter	8	Heat exchanger
4 500 kW d.c. motor	10	Flow nozzle (DIN 1952)
5 Planetary gearbox		

Fig. 1 Test bed

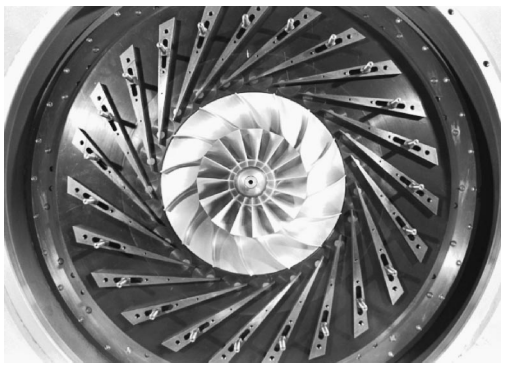

Fig. 2 Stage with dismounted front wall

Figure 4 shows details of the flow path inside the compressor (see also Fig. 1). Leaving the suction pipe, the flow is accelerated strongly in the inlet (1) before entering the impeller (2), in order to reduce boundary layer thickness. At the exit of the parallel walled diffuser (3), the flow discharges into a collector (10), which is designed as a mixture of a simple collector and a volute and which guides the flow to the pressure pipe. Figure 4 also shows the circumferential adjustment mechanism for probe mea-

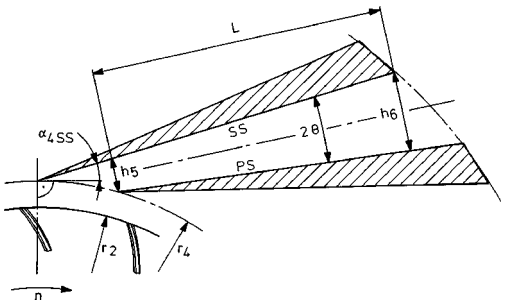

Fig. 3 Adjustable geometry parameters α_{4SS} and r_4/r_2

Table 1 Technical data for nominal speed and diffuser reference geometry

Compressor:		
- Shaft speed:	n_0	= 35200 1/min
- Impeller tip speed:	u_2	= 498 m/s
- Relative tip Mach number impeller inlet:	Ma_{w1}	= 0.95
- Absolute Mach number impeller exit:	Ma_2	= 0.94
- Maximum total pressure ratio:	$\pi_{t,max}$	= 4.07
- Maximum corrected mass flow:	$\dot{m}_{red,max}$	= 2.50 kg/s
- Maximum isentropic efficiency (total/total):	$\eta_{stt,max}$	= 83.4%
- Specific speed:	n_s	= 0.69
	N_s = 89 rpm(ft³/s)$^{1/2}$/ft$^{3/4}$	
Impeller:		
- Tip radius:	r_2	= 135 mm
- Number of blades:	z_I	= 15
- Blade backsweep angle at impeller exit:	β_b	= 38°
Diffuser: (Nomenclature see Fig. 3)		
- Constant meridional diffuser height:	b	= 11.1 mm
- Number of vanes:	z_D	= 23
- Vane angle:	α_{4SS}	= 16.5°
- Radial gap:	r_4/r_2	= 1.10
- Thickness of angular leading edge:	d_{LE}	= 0.45 mm
- Vane wedge angle:	α_V	= 6.615°
- Length of vane pressure side:	l_{PS}	= 178 mm
- Length of vane suction side:	l_{SS}	= 190 mm
- Invariant diffuser channel divergence angle:	2θ	= 9.037°
- Diffuser channel length-width ratio:	LWR	= L/h_5 = 9.31
- Diffuser channel area ratio:	AR	= h_6/h_5 = 2.47
- Diffuser channel aspect ratio:	AS	= b/h_5 = 0.68

Table 2 Geometry parameters depending on α_{4SS} and r_4/r_2

α_{4SS} [°]	r_4/r_2	h_5 [mm]	L/h_5	h_6/h_5	b/h_5	r_7/r_2	α_7 [°]
16.5	1.18	17.481	8.501	2.344	0.635	2.080	57.692
	1.14	16.873	8.889	2.405	0.658	2.049	58.381
	1.10	16.265	9.306	2.471	0.682	2.018	59.091
	1.06	15.657	9.755	2.542	0.709	1.987	59.824
	1.04	15.354	9.993	2.580	0.723	1.972	60.199
12.5	1.18	14.671	10.065	2.591	0.757	2.028	55.904
	1.14	14.158	10.530	2.664	0.784	1.998	56.645
	1.10	13.646	11.029	2.743	0.813	1.968	57.409
	1.06	13.133	11.567	2.828	0.845	1.938	58.197

surements at diffuser exit, which has been integrated into a new diffuser front wall (4). Two turning rings in the diffuser front wall (5) and rear wall (9) respectively, coupled at four circumferential positions, are driven simultaneously by a stepping motor (8).

Test Program

In order to give an overview, here the program of the complete test series is listed, including the laser-2-focus measurements, which will be discussed later in Part II. Figures 5 and 6 show the measurement planes as thick black lines. In the project measurements were performed in these planes normal to the casing only. The following measurements were conducted:

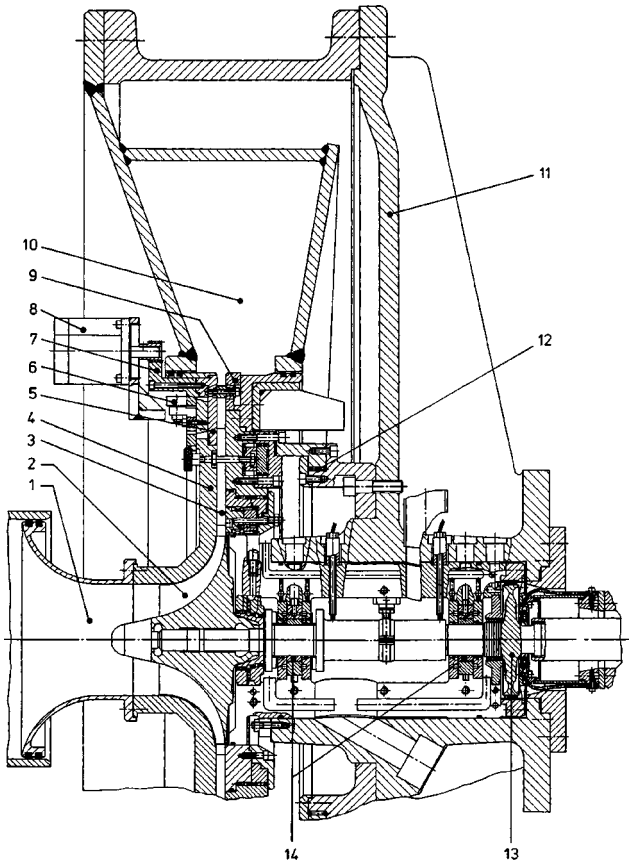

Fig. 4 Sectional view of the centrifugal compressor

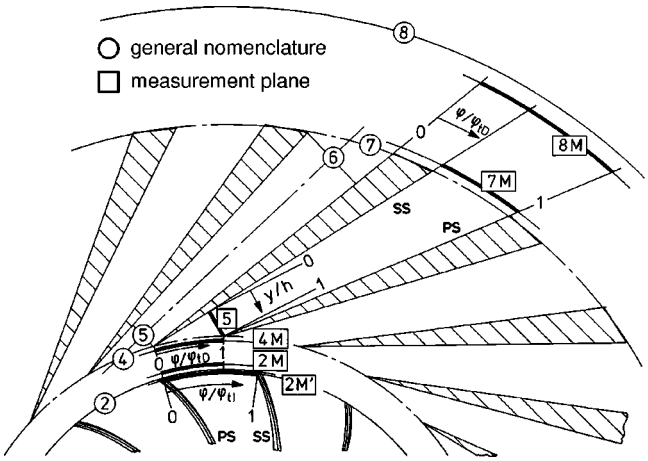

Fig. 5 Measurement planes

Steady Probe Measurements.

- 1M: *Static wall pressure*
- 2M: *-Static wall pressure*: 4 taps on front, 4 on rear wall *-Pitot probes*: $5\times4=20$ points/pitch, $z/b=(0.1|0.3|0.5|0.7|0.9)$
- 7M: *3-hole cobra probe*: $7\times18=126$ points/pitch, $z/b=(0.071|0.214|0.357|0.5|0.643|0.786|0.929)$, measuring radius depends on diffuser geometry.
- 8M: *3-hole cylinder probe, temperature probe and static wall pressure*: $7\times25=175$ points/pitch, $z/b=(0.071|0.214|0.357|0.5|0.643|0.786|0.929)$, additional measuring plane with fixed radius, so that the same endwall friction is balanced for all diffuser geometries.

The probe measurements in the above mentioned planes were conducted exclusively at 80% speed. Figure 7 shows the compressor characteristics of the investigated diffuser geometries at this speed. The measured operating points are indicated by big symbols. At $\alpha_{4SS}=16.5$ deg (group of curves on right-hand side) five

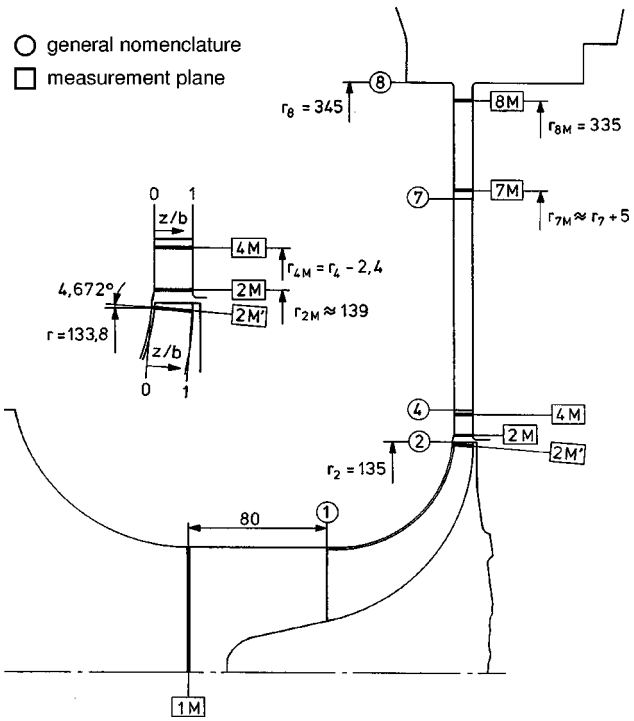

Fig. 6 Measurement planes in sectional view

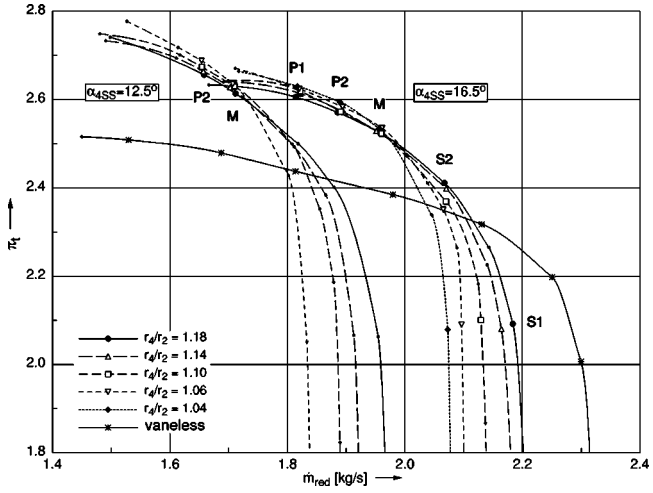

Fig. 7 Operating points of probe measurements ($n_{red}/n_0 = 0.8$)

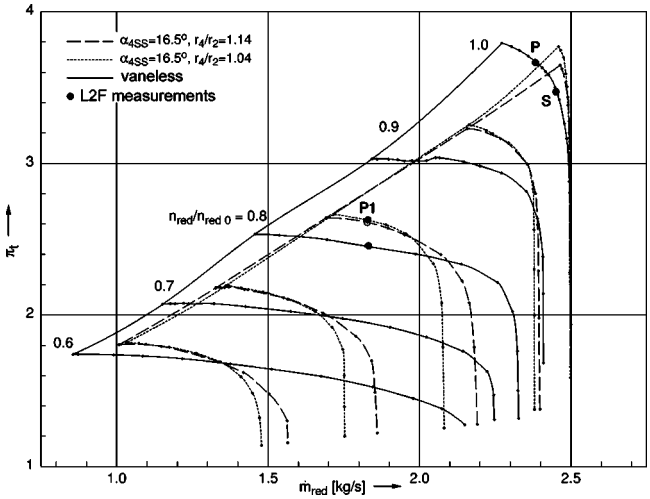

Fig. 8 Operating points of L2F measurements

radial gaps between 4 and 18% have been investigated, each in five operating points. The points P1, P2, M, and S2 are defining particular corrected mass flow rates, whereas S1 can be regarded as the choke limit of each diffuser geometry. S2 and S1 coincide for the geometry combination [$\alpha_{4SS}=16.5$ deg, $r_4/r_2=1.04$]. For all five radial gaps the operating point nearest to the surge limit (P1) is roughly the best point of the compressor, though the efficiency does not drop significantly up to P2 (compare Fig. 16). In order to investigate also the influence of the vane angle, the probe measurements were conducted at a second angle ($\alpha_{4SS}=12.5$ deg, group of curves on left-hand side) for two operating points (P2 and M). For reasons of design, here the radial gap could be varied between 6 and 18% only. Finally, the probe measurements were performed with the vaneless diffuser as a comparative basis. For these tests the diffuser vanes were replaced by small spacers.

Time Resolving Laser-2-Focus Measurements.

- 2M′: $5\times15=75$ points/pitch
- 2M: vaneless diffuser: $5\times15=75$ points/pitch vaned diffuser: $5\times12=60$ points/pitch
- 4M: absolute frame of reference: $5\times8=40$ points/pitch, relative frame of reference: $5\times12=60$ points/pitch, measuring radius depends on diffuser geometry, 2M and 4M coincide for [$\alpha_{4SS}=16.5$ deg, $r_4/r_2=1.04$]
- 5: $5\times5=25$ points/pitch

For all L2F measurements the resolution is $z/b=(0.15|0.3|0.5|0.7|0.85)$. Figure 8 shows the compressor maps of the diffuser geometries investigated with the laser-2-focus velocimeter. Again, the measured operating points are indicated by big symbols. At 80% speed the L2F measurements were performed in the best point (P1). For the diffuser geometries [$\alpha_{4SS}=16.5$ deg, $r_4/r_2=1.14$] and [$\alpha_{4SS}=16.5$ deg, $r_4/r_2=1.04$] the planes 2M′, 4M, and 5 were measured. For the vaneless diffuser the measurements were carried out in 2M′ and 2M. At 100% speed investigations were conducted exclusively for the vaneless diffuser. Here the plane 2M was measured in two operating points (P and S).

Flow Visualization With Dye Injections on the Casing.

Measurement of the Compressor Characteristics (Figs. 7, 8) The total pressure ratio is calculated between the settling chamber, where inlet total pressure and total temperature are measured (index I, see Fig. 1), and the pressure pipe (index E), where the exit total pressure is measured with four total pressure probes. The last measured points of the characteristics represent the surge limit. Minimal further throttling was leading to surge.

The small total pressure losses in the suction pipe are included in the performance data of the impeller. The exit total temperature was measured exclusively in plane 8M, and is assigned to all planes downstream the impeller. The tests were conducted with an inlet condition of about 0.6 bar and 296 K. All quantities shown in Parts I and II were then corrected to the standard inlet condition of $p_{tI}=1.013$ bar and $T_{tI}=288.15$ K.

Probe Measurement Technique and Evaluation

Figure 9 shows details of the probes and their fitting positions. Due to the narrow flow channels in the compressor the use of probes required special efforts. The probes were designed and manufactured at the institute with the goal to achieve as small dimensions as possible. The pitot probes at impeller exit are a compromise between small dimensions and strength due to mechanical safety reasons. In order to realize symmetrical flow conditions, the probes in 8M and 2M rise over the entire flow channel. For that purpose the circumferential adjustment mechanism in 8M simultaneously drives two rings in the diffuser front and rear

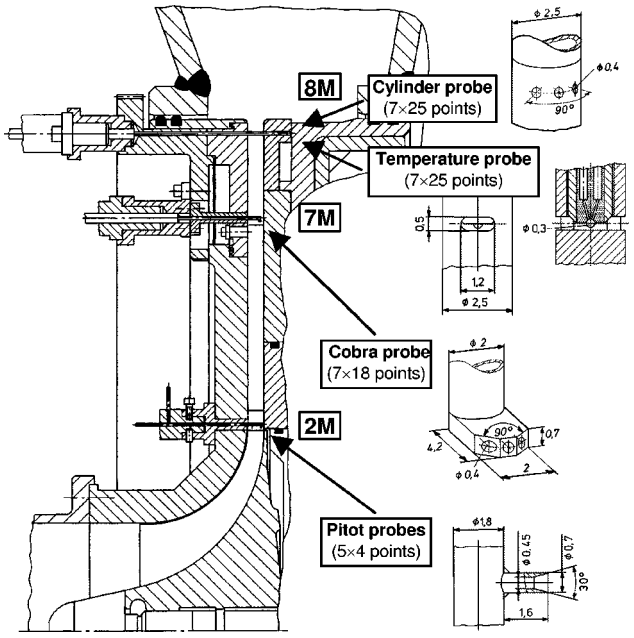

Fig. 9 Probe measurement technique

wall, respectively, (see also Fig. 4). The temperature probe with a NTC sensor (*N*egative *T*emperature *C*oefficient) was specially designed for a high resolution in axial direction.

The insertion of the pitot probes into the sensitive transonic flow field in plane 2M was critical concerning compressor stability. For that reason the probe measurement series was conducted at 80% speed, and the pitot probe measurements were performed only for two diffuser geometries: [$\alpha_{4SS}=16.5$ deg, $r_4/r_2=1.18$] and [$\alpha_{4SS}=16.5$ deg, $r_4/r_2=1.04$]. The five pitot measuring heads are distributed to three different probes, which were mounted one after another during the measurements, each at four different circumferential positions. It was important to measure the total pressure in several circumferential positions due to the maximum difference measured by that variation being 1.75% (compare Epstein et al. [21] and Copenhaver et al. [22]). The pitot probes were adjusted to the flow direction manually. Due to the missing flow angle information only an area averaging of the total pressure is possible in 2M. An integral flow angle is calculated in this plane using the mass flow measured in the flow nozzle (Fig. 1).

The flow in plane 8M is characterized by low Mach numbers and even backflow regions in the wakes of the thick vane trailing edges. Due to these reasons a thorough mass averaging including the backflow regions was essential. A ''compound mass average'' was used: The static pressure is area averaged, and the static temperature is mass averaged. With these values together with the mass averaged velocity components the Mach number and then the total flow quantities are calculated. The advantage in comparison with a direct mass averaging of the total pressure is that the static portion of the total pressure is area averaged correctly. Though a detailed analysis showed that the differences are small. The necessity of measuring properly also the backflow regions made the measurements in 8M extremely time consuming. On account of a significant heat flux through the diffuser front wall the total temperature used to calculate work input and efficiencies is determined in a special way, called ''Hi3 method'': The three highest values of the measured total temperature field in 8M are averaged and defined to be the total temperature, which would be measured in the diffuser, if the diffuser was adiabatic. Due to the nearly adiabatic diffuser rear wall the highest total temperature values are always located close to this wall, and the difference between the total temperature at impeller exit and the Hi3 total temperature can be assumed to be small. Due to the lack of measured temperature values in the flow field in 7M the described compound mass average was calculated in a simplified version, assuming constant static temperature and static pressure in the flow field.

The calibration of the two 3-hole probes and the flow calibration of the temperature probe was carried out in an open jet. The Reynolds numbers at calibration and measurements agree well due to the lowered compressor inlet pressure during the tests. In order to minimize the measurement errors of the 3-hole probes due to flow gradients a special measurement procedure was used. Each of the three holes was positioned individually exactly at the given measuring point.

Results of the Steady Probe Measurements

Influence of the Impeller-Diffuser Gap on the Performance of the Compressor Components. Already the compressor maps shown in Figs. 7 and 8 give some information about the influence of the radial gap on the integral performance of the entire compressor. The choke mass flow rate decreases with reduced radial gap. On the one hand, this is due to the diffuser throat area becoming smaller (h_5 in Fig. 3). On the other hand, the Mach number at the diffuser leading edges is rising with reduced radial gap, so that already a smaller suction sided incidence is leading to choke. In Table 3 the incidence to the diffuser vanes is given for different operating points. It was calculated from total tempera-

Table 3 Diffuser vane incidence measured at 2M

α_{4SS} [°]	16.5						12.5		
operating point	surge	P1	P2	M	S2	S1 (18% gap)	surge	P2	M
i [°]	+1.5	-0.2	-1.2	-2.2	-4.1	-6.1	+0.2	-2.0	-2.7

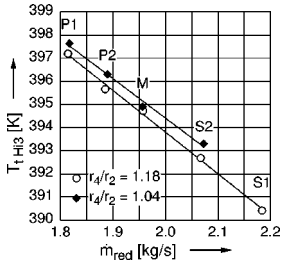

Fig. 10 Maximum total temperature (Hi3) at 8M ($\alpha_{4SS}=16.5$ deg, $n_{red}/n_0=0.8$)

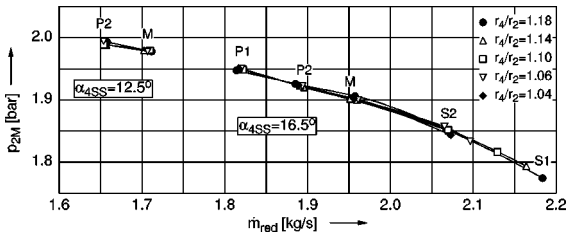

Fig. 11 Averaged static pressure at 2M ($n_{red}/n_0=0.8$)

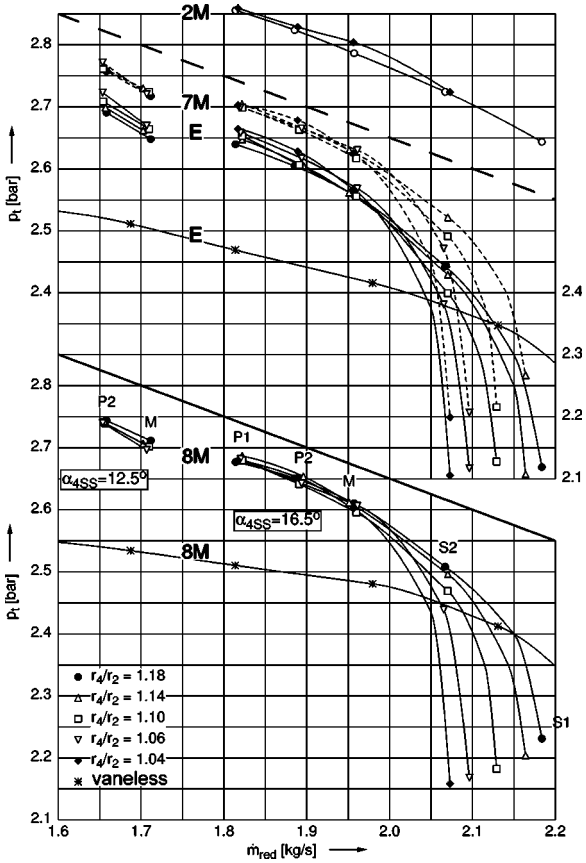

Fig. 12 Averaged total pressures in four measurement planes ($n_{red}/n_0=0.8$)

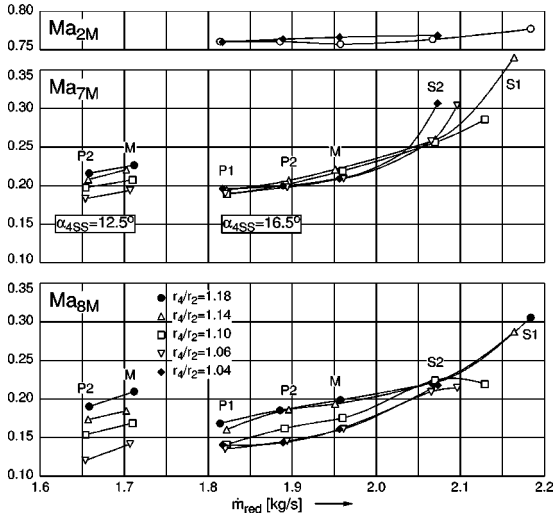

Fig. 13 Averaged Mach numbers in three measurement planes ($n_{red}/n_0=0.8$)

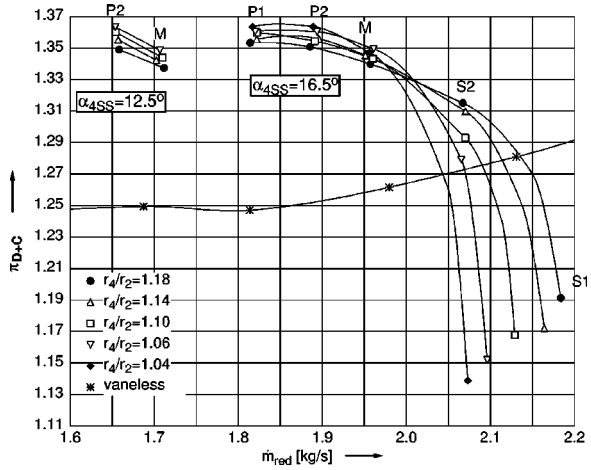

Fig. 15 Static pressure ratio of [diffuser+collector] ($n_{red}/n_0=0.8$)

ture, total and static pressure measured in 2M and the mass flow rate. Throttling the compressor, the total pressure ratio at smaller radial gaps exceeds the ratios at larger gaps. At 80% speed and $\alpha_{4SS}=16.5$ deg, the difference in the total pressure ratio is rising up to the surge limit to a value of 1.5% (6% radial gap compared to 18%). Figure 8 clearly shows that the effect becomes stronger with rising corrected speed. At design speed the compressor achieves with 4% radial gap a 2.9% higher total pressure ratio compared to 14% radial gap at the same mass flow rate. The following discussion concentrates on the operating points P1, P2, and M, where the described effect is visible.

Figures 10 to 13 show the Hi3 total temperature and averaged static and total pressures and Mach numbers in different planes in the compressor. The impeller makes a slightly higher work input at 4% radial gap compared to 18% (Fig. 10) resulting in a higher total pressure (Fig. 12), while impeller efficiency hardly changes. The achieved static pressure in 2M does not show significant differences either (Fig. 11). It can be said that the influence of the radial gap on impeller performance is negligible. At diffuser exit, as well in 7M as in 8M, a variation of the radial gap leads only to small differences in the mass averaged total pressures in the operating points P1, P2, and M (Fig. 12). But at compressor exit (E), the total pressure curves clearly indicate smaller flow losses at smaller radial gaps. Figure 13 reveals the reason for this effect: At $\alpha_{4SS}=16.5$ deg the diffuser decelerates the flow up to the variable plane 7M at smaller radial gaps to the same Mach number level, although the vane exit is on smaller radii then. In consequence, the mass averaged Mach number level in the fixed measurement plane 8M is lower for smaller radial gaps, since then the flow can make use of a bigger radius ratio between 7M and 8M for further general deceleration and wake mixing. At $\alpha_{4SS}=12.5$ deg the described effect is even more distinctive. Here the Mach number level is already lower in plane 7M at smaller radial gaps indicating a much better diffusion. It can be concluded that the higher total pressure loss from diffuser exit (8M) to compressor exit (E) at larger radial gaps is a result of a worse preceding deceleration inside the diffuser, as the bulk of the remaining kinetic energy at diffuser exit (8M) is dissipating up to compressor exit (E), where the Mach number is about 0.05 independently from the radial gap.

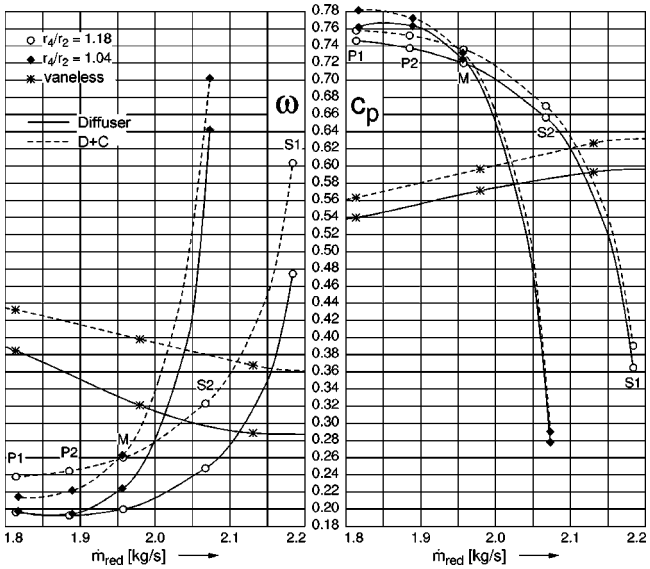

Fig. 14 Total pressure loss (ω) and pressure recovery (c_p) of diffuser and [diffuser+collector] ($\alpha_{4SS}=16.5$ deg, $n_{red}/n_0=0.8$)

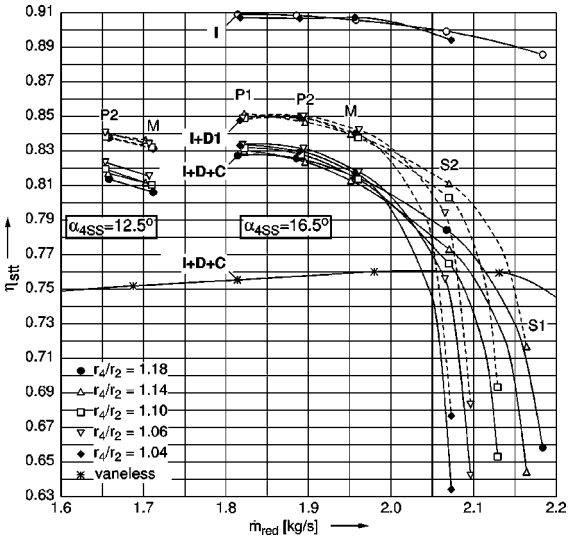

Fig. 16 Isentropic efficiencies (total/total) of impeller, [impeller+diffuser1], [impeller+diffuser+collector] ($n_{red}/n_0=0.8$)

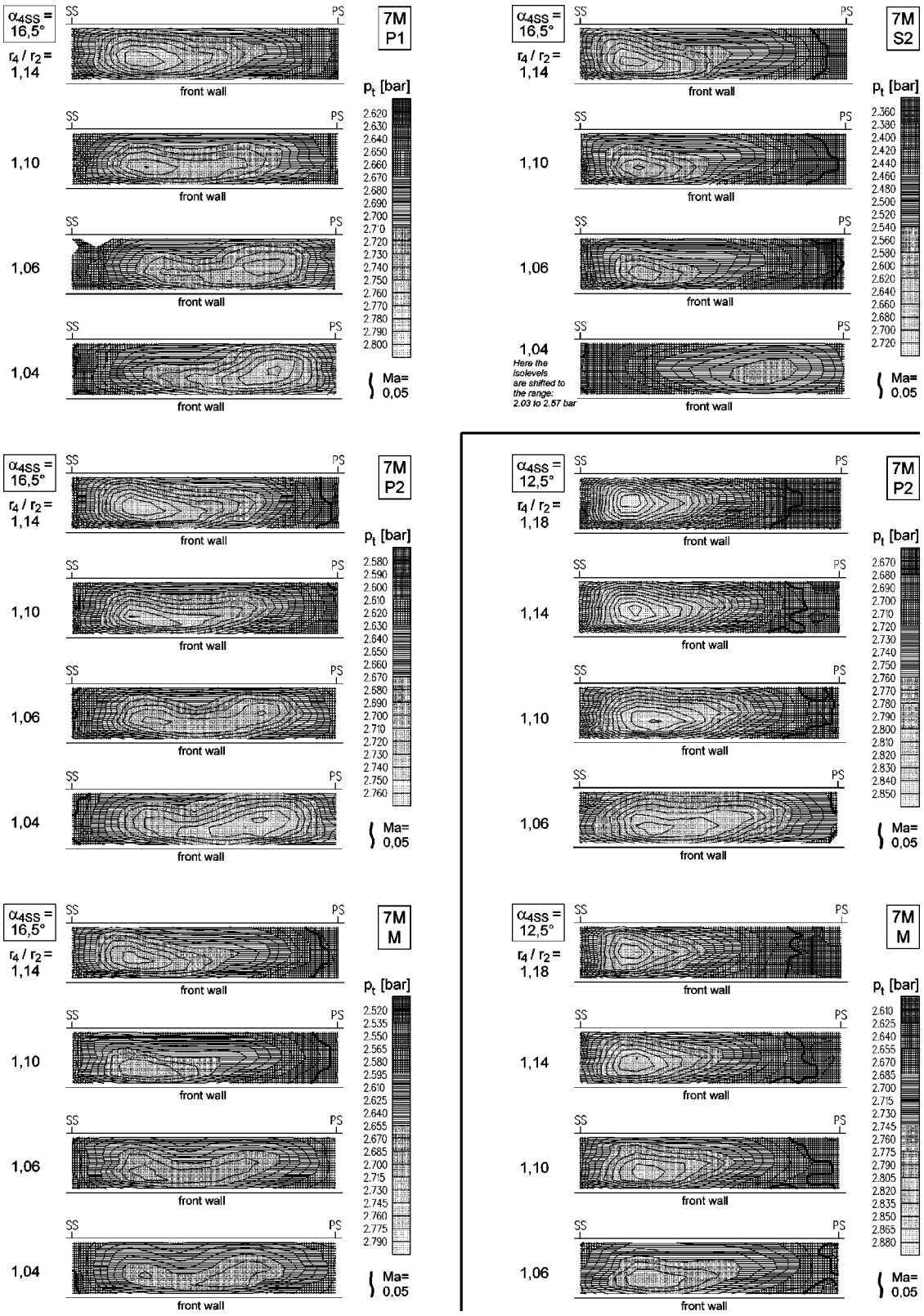

Fig. 17 Comparison of the total pressure distributions at diffuser vane exit (7M, $n_{red}/n_0 = 0.8$)

This effect can be also quantified well with the total pressure loss and pressure recovery coefficients of the diffuser alone on the one hand, and the entire diffusing system [diffuser+collector] on the other hand (Fig. 14). At the operating points P1 and P2 the diffuser with 4% radial gap achieves a 2-point higher pressure recovery with an equal total pressure loss. In consequence, up to compressor exit as well pressure recovery as total pressure loss are 2 points better for 4% radial gap compared to 18%. The coefficients could be calculated only for the two diffuser geometries shown, for which the total pressure in 2M was measured. Figure 15 shows the static pressure ratio from impeller exit (2M) to compressor exit (E), which is available for all diffuser geometries. It

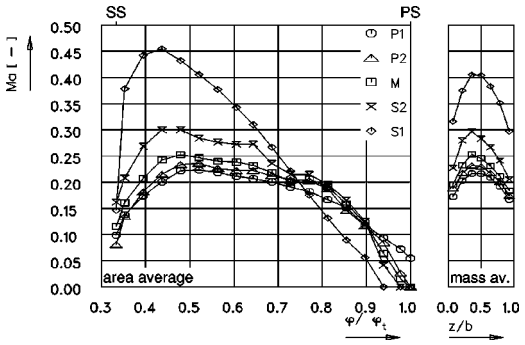

Fig. 18 Mach number at 7M ($\alpha_{4SS}=16.5$ deg, $r_4/r_2=1.14$, $n_{red}/n_0=0.8$)

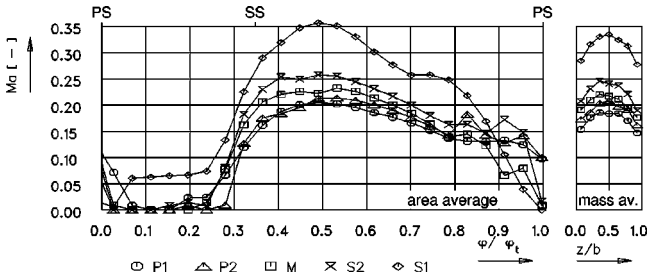

Fig. 20 Mach number at 8M ($\alpha_{4SS}=16.5$ deg, $r_4/r_2=1.18$, $n_{red}/n_0=0.8$)

can be seen that the pressure ratio is rising continuously with a decreased radial gap. The maximum difference in the isentropic compressor efficiency caused by the described effect is measured at $\alpha_{4SS}=12.5$ deg in the operating point P2 (Fig. 16). It amounts to 0.9 points between 6 and 18% radial gap. As shown by the compressor maps, higher values can be expected closer to the surge limit and at higher shaft speeds.

Analysis of the Diffuser Exit Flow Field. Searching for the reasons for the positive effect of smaller radial gaps on diffuser pressure recovery, a first step is the analysis of the flow field at diffuser vane exit. Figure 17 shows the total pressure distributions at 7M for several diffuser geometries and operating points. For $\alpha_{4SS}=16.5$ deg, the operating points P1, P2, M, and S2, and for $\alpha_{4SS}=12.5$ deg, P2 and M are shown. For each operating point the flow fields for the different measured radial gaps are plotted on top of each other. Comparing the isoplots, it should be noticed that in plane 7M for reasons of design the measured radial gaps for $\alpha_{4SS}=16.5$ deg are 14, 10, 6, and 4%, and for $\alpha_{4SS}=12.5$ deg 18, 14, 10, and 6%. Due to the nearly constant static pressure in 7M the total pressure distributions are interchangeable with the Mach number distributions. Therefore, in the following the region of maximum total pressure is simply called ''flow maximum.'' The thick black lines in the plots are marking the lower calibration limit of the 3-hole cobra probe, which is Ma=0.05. Below that limit the Mach number is set to zero, and total and static pressure are set to the same value, which equals the average of the measured pressures at the three holes of the probe.

The distributions for $\alpha_{4SS}=16.5$ deg reveal that for all measured operating points from surge to choke limit (S1 not shown in Fig. 17) the flow maximum shifts from the vane suction side towards the pressure side, by decreasing the radial gap. That is to say, an increase of the radial gap is leading to a growing loading of the vane pressure side. One could presume that the flow passing the vaneless space gets a more radial flow angle, so that at larger radial gaps the diffuser vanes get a growing suction sided incidence resulting in a higher loading of the vane pressure side. And indeed, the L2F measurements in P1 reveal that the integral flow angle at the diffuser vane leading edges is 1.2 deg more radial at $r_4/r_2=1.14$ compared to $r_4/r_2=1.04$. But it can be proven by the comparison of the flow angles at the different operating points that this small angle difference can not be the main reason for the found effect. For example between P1 and M a difference of 2 deg in the incidence was measured at 2M (compare Table 3). But this difference has a much smaller influence on the flow field in 7M than an increase of the radial gap from 4 to 14%, which is leading to an incidence difference of only 1.2 deg. So the found flow phenomenon must have another reason, possibly an unsteady effect in the diffuser inlet region.

For $\alpha_{4SS}=12.5$ deg (right bottom part of Fig. 17) a reduction of the radial gap has throughout positive consequences. Although separations cannot be proved directly due to the calibration limit of the cobra probe, it can be assumed that the pressure side is separated at least for 18% and 14% radial gap in both measured operating points (P2 and M). By this, the diffusion in the remaining part of the flow channel is reduced significantly. This explains, why the averaged Mach number in 7M shown in Fig. 13 is still very high for the larger radial gaps. In contrast to that, the flow field becomes much more homogeneous up to 6% radial gap indicating a better diffusion up to plane 7M and reducing the downstream mixing losses.

For $\alpha_{4SS}=16.5$ deg the shift of the flow maximum towards the pressure side goes too far in the operating points P1 and P2, so that at 4% radial gap even the suction side is the higher loaded vane surface. Taking into account only the flow field at 7M the optimum radial gaps would be 10 to 6% for P1, 6% for P2 and 4% for M, being reflected weakly also by the minimum mass averaged Mach numbers in 7M (Fig. 13). But at diffuser exit (see 8M in Fig. 13) the smaller radial gaps have a clear advantage over the larger ones due to their bigger radius ratio between 7M and 8M (as discussed in the previous section). In summary, one can say that the reason for the better diffusion in the diffuser at smaller radial gaps is an unloading of the typically (e.g., Kenny [22]) highly loaded vane pressure side.

Figures 18 and 19 are comparing the Mach number distribu-

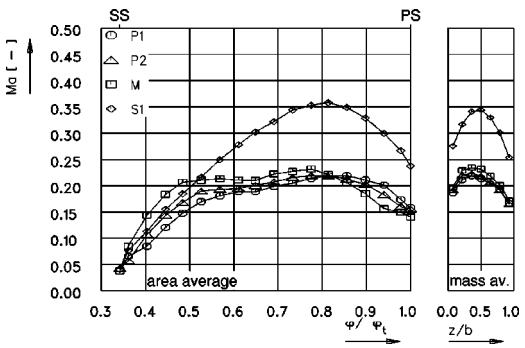

Fig. 19 Mach number at 7M ($\alpha_{4SS}=16.5$ deg, $r_4/r_2=1.04$, $n_{red}/n_0=0.8$)

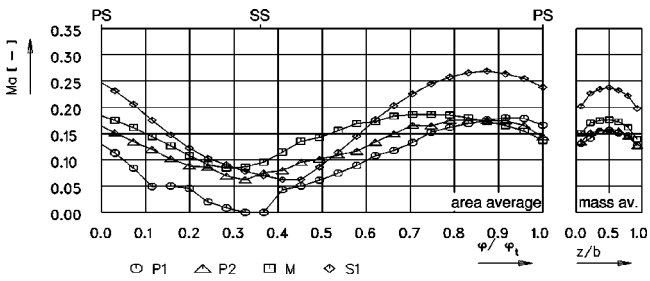

Fig. 21 Mach number at 8M ($\alpha_{4SS}=16.5$ deg, $r_4/r_2=1.04$, $n_{red}/n_0=0.8$)

tions at 7M for $\alpha_{4SS}=16.5$ deg and the largest and smallest measured radial gaps. The figures clarify once again the remarkable result that the general location of the flow maximum is hardly affected by the operating point, but determined by the radial gap. Figures 20 and 21 show the Mach number distributions at 8M again for $\alpha_{4SS}=16.5$ deg and the largest and smallest radial gaps. (It should be noticed that here the largest measured radial gap is 18%.) The comparison reveals the better diffusion up to plane 8M for the smaller radial gap due the bigger radius ratio. Furthermore, it can be observed that the wake of the diffuser vane has been mixed out already to a higher degree.

Conclusions

In this first part of a two-part paper results of an extensive test series with steady probe measurements at impeller exit and diffuser exit of a 4:1 pressure ratio centrifugal compressor are presented. In order to investigate the impeller-diffuser interaction, the radial gap between impeller exit and diffuser vane inlet was varied between 4 and 18% of the impeller tip radius for two different vane angles. The main results are:

1 Already the compressor maps show a rising total pressure ratio with decreasing radial gap. The maximum measured differences are 1.5% at 80% speed and 2.9% at design speed. The maximum measured improvement of the isentropic compressor efficiency at 80% speed is 0.9 points.

2 The impeller has a slightly higher work input at smaller radial gaps (up to 0.5%), while impeller efficiency hardly changes.

3 In most cases the flow field at diffuser vane exit is more homogeneous at smaller radial gaps indicating a much better diffusion. The reason is that a decrease of the radial gap is leading to an unloading of the typically highly loaded vane pressure side. Surprisingly the general location of the flow maximum at diffuser vane exit is hardly affected by the operating point, but determined by the radial gap possibly due to an unsteady effect at diffuser inlet.

4 In consequence, the diffusion up to diffuser exit (downstream of diffuser vane exit) is in all cases better at smaller radial gaps. The maximum measured difference in the diffuser pressure recovery coefficient is 2.0 points with the total pressure loss coefficient being equal.

5 Due to the lower Mach numbers at diffuser exit at smaller radial gaps the total pressure loss in the collector is smaller. As a result of that, up to compressor exit as well pressure recovery as total pressure loss are 2 points better for 4% radial gap compared to 18%.

The reasons for points 2 and 3 will be investigated in detail in Part II, analyzing the results of time resolving laser-2-focus measurements between the impeller exit region and diffuser throat. Also, the final interpretation and conclusions will be given in Part II.

Steady and unsteady experimental results of the presented project are published as an open CFD test case under the name "Radiver." The compressor geometry, figures, animations and supplementary information have been put together on a test case CD-ROM. Interested researchers are asked to contact the authors.

Acknowledgments

The investigations presented in this paper were funded partly by the German Research Association (Deutsche Forschungsgemeinschaft, DFG). The Institute of Jet Propulsion and Turbomachinery and the authors would like to thank DFG for this promotion. We are also grateful to MTU Aero Engines for the donation of the impeller.

Nomenclature

c = velocity in absolute frame of reference
c_m = meridional component of c
c_p = pressure recovery coefficient, $c_p=(p_{out}-p_{in})/(p_{t,in}-p_{in})$
c_u = circumferential component of c
i = incidence to diffuser vane camber line (positive: towards pressure side)
F = unsteadiness coefficient (Eqs. (1) and (2) in Part II)
Ma = Mach no.
$\dot{m}_{red}$ = mass flow rate corrected to ISA inlet conditions ($p_{tI}=1.013$ bar, $T_{tI}=288.15$ K)
n_0 = design shaft speed
n_{red} = shaft speed corrected to ISA inlet conditions
PS = pressure side
p = pressure
r = radius [mm]
r_4/r_2 = "radial gap" (Fig. 3)
SS = suction side
T = temperature
u = circumferential velocity
w = velocity in relative frame of reference
y/h = relative coordinate in diffuser throat (Fig. 5)
z/b = relative coordinate normal to the casing (Fig. 6)
α = flow angle in absolute frame of reference (from positive tangential, Fig. 2 in Part II)
α_{4SS} = diffuser vane suction side angle (Fig. 3)
α_7 = angle of diffuser channel centerline (= angle of vane camber line) in plane 7 (from positive tangential)
α_f = deviation angle in diffuser channel (positive: towards pressure side)
β = flow angle in the relative frame of reference (from positive tangential, Fig. 2 in Part II)
η_{stt} = isentropic efficiency (total/total)
π = pressure ratio
φ/φ_{tD} = circumferential coordinate relative to diffuser pitch (Fig. 5), indicating also unsteady diffuser position
φ/φ_{tI} = circumferential coordinate relative to impeller pitch (Fig. 5), indicating also unsteady impeller position
ω = total pressure loss coefficient, $\omega=(p_{t,in}-p_{t,out})/(p_{t,in}-p_{in})$

Subscripts

max = period maximum value of unsteady quantity
min = period minimum value of unsteady quantity
t = total

Superscripts

— = time-averaged value

Plane Definitions (Figs. 1, 5, and 6)

I = compressor inlet
1 (1M) = impeller inlet
2 (2M′,2M) = impeller exit/diffuser inlet
4 (4M) = diffuser vane inlet
5 = diffuser throat
6 = diffuser channel exit
7 (7M) = diffuser vane exit
8 (8M) = diffuser exit
E = compressor exit

Compressor Components

I = impeller (total: I→2M, static: 1→2M)
D = diffuser (2M→8M)
D1 = diffuser component 1 (2M→7M)
C = collector (8M→E)

Operating Points (Figs. 7 and 8)

80% speed = P1 (best point), P2, M, S2, S1 (choke)
100% speed = P (more throttled), S (more unthrottled)

References

[1] Pfleiderer, C., 1961, *Die Kreiselpumpen für Flüssigkeiten und Gase*, Springer-Verlag, Berlin, Göttingen, Heidelberg.

[2] Dean, R. C., 1971, ''On the Unresolved Fluid Dynamics of the Centrifugal Compressor,'' Advanced Centrifugal Compressors, ASME Gas Turbine Division.

[3] Hayami, H., Umemoto, A., 1995, ''Effects of Inlet Passage Width Contraction of Low Solidity Cascade Diffusers on Performance of Transonic Centrifugal Compressor,'' 95-YOKOHAMA-IGTC-15, *Proc. Yokohama International Gas Turbine Congress*.

[4] Japikse, D., 1996, *Centrifugal Compressor Design and Performance*, Concepts ETI, Inc.

[5] Krain, H., 1981, ''A Study on Centrifugal Impeller and Diffuser Flow,'' ASME J. Eng. Power, **103**, pp. 688–697.

[6] Inoue, M., and Cumpsty, N. A., 1984, ''Experimental Study of Centrifugal Impeller Discharge Flow in Vaneless and Vaned Diffusers,'' ASME J. Eng. Gas Turbines Power, **106**, pp. 455–467.

[7] Fowler, H. S., 1968, ''The Distribution and Stability of Flow in a Rotating Channel,'' ASME J. Eng. Power, **90**, pp. 229–236.

[8] Filipenco, V. G., Deniz, S., Johnston, J. M., Greitzer, E. M., and Cumpsty, N. A., 1998, ''Effects of Inlet Flow Field Conditions on the Performance of Centrifugal Compressor Diffusers—Part 1: Discrete-Passage Diffuser,'' ASME Paper 98-GT-473.

[9] Deniz, S., Greitzer, E. M., and Cumpsty, N. A., 1998, ''Effects of Inlet Flow Field Conditions on the Performance of Centrifugal Compressor Diffusers—Part 2: Straight-Channel Diffuser,'' ASME Paper 98-GT-474.

[10] Yamane, T., Fujita, H., and Nagashima, T., 1993, ''Transonic Discharge Flows Around Diffuser Vanes From a Centrifugal Impeller,'' ISABE Paper 93-7053.

[11] Dawes, W. N., 1994, ''A Simulation of the Unsteady Interaction of a Centrifugal Impeller with its Vaned Diffuser: Flow Analysis,'' ASME Paper 94-GT-105.

[12] Liu, Z., and Hill, D. L., 2000, ''Issues Surrounding Multiple Frames of Reference Models for Turbo Compressor Applications,'' *Proc. 15th Int. Compressor Engineering Conference at Purdue University, West Lafayette*, IN.

[13] Rodgers, C., 1982, ''The Performance of Centrifugal Compressor Channel Diffusers,'' ASME Paper 82-GT-10.

[14] Jin, D., Jiang, Z., Hasemann, H., Haupt, U., and Rautenberg, M., 1995, ''Influence of Vaned Diffuser on Dangerous Blade Vibration Due to Blade Flow Interactions in a Centrifugal Compressor,'' ASME Paper 95-GT-122.

[15] Shum, Y. K. P., Tan, C. S., and Cumpsty, N. A., 2000, ''Impeller-Diffuser Interaction in Centrifugal Compressor,'' ASME Paper 2000-GT-428.

[16] Salvage, J. W., 1999, ''Development of Centrifugal Compressor With a Variable Geometry Split-Ring Pipe Diffuser,'' ASME J. Turbomach., **121**, pp. 295–303.

[17] Justen, F., Ziegler, K. U., and Gallus, H. E., 1999, ''Experimental Investigation of Unsteady Flow Phenomena in a Centrifugal Compressor Vaned Diffuser of Variable Geometry,'' ASME J. Turbomach., **121**, pp. 763–771.

[18] Ziegler, K. U., Justen, F., Rothstein, M., Gallus, H. E., Niehuis, R., 2000, ''Research on a Centrifugal Compressor of Variable Geometry,'' *Proc., 15th Int. Compressor Engineering Conference at Purdue University, West Lafayette, IN*.

[19] Rothstein, M., 1993, ''Entwicklung und experimentelle Untersuchung eines Radialverdichters mit beschaufeltem Diffusor variabler Geometrie,'' doctoral thesis, RWTH, Aachen.

[20] Runstadler, P., Dolan, F., and Dean, R., 1975, ''Diffuser Data Book,'' CREARE Technical Note 186.

[21] Epstein, A. H., Giles, M. B., Shang, T., and Sehra, A. K., 1990, ''Blade Row Interaction Effects on Compressor Measurements,'' AGARD CP-468.

[22] Copenhaver, W. W., Puterbaugh, S. L., Cunningham, C. C., and Hah, C., 1997, ''Intra-Stage Measurement Probe Influence on Transonic Fan Performance,'' ISABE Paper 97-7072.

[23] Kenny, D. P., 1969, ''A Novel Low-Cost Diffuser for High-Performance Centrifugal Compressors,'' ASME J. Eng. Power, **91**, pp. 37–47.

A Study on Impeller-Diffuser Interaction—Part II: Detailed Flow Analysis

Kai U. Ziegler[1]
e-mail: kai.ziegler@muc.mtu.de

Heinz E. Gallus

Reinhard Niehuis
e-mail: niehuis@ist.rwth-aachen.de

RWTH Aachen,
University of Technology,
Institute of Jet Propulsion and Turbomachinery,
52062 Aachen, Germany
www.ist.rwth-aachen.de

The interaction between impeller and diffuser is considered to have strong influence on the flow in centrifugal compressors. However, the knowledge about this influence is still not satisfying. This two-part paper presents an experimental investigation of the effect of impeller-diffuser interaction on the unsteady and the time-averaged flow field in impeller and diffuser and the performance of these components. The flat wedge vaned diffuser of the investigated compressor allows an independent adjustment of diffuser vane angle and radial gap between impeller exit and diffuser vane inlet. Attention is mainly directed to the radial gap, as it determines the intensity of the impeller-diffuser interaction. In Part I it was shown that smaller radial gaps improve diffuser pressure recovery, whereas impeller efficiency is hardly affected. Part II focuses on the reasons for these effects. Measurements with a laser-2-focus velocimeter in the highly unsteady flow field between the impeller exit region and diffuser throat were performed at three different diffuser geometries allowing a detailed flow analysis. Especially the unsteady results show that for a smaller radial gap more impeller wake fluid is conveyed towards the highly loaded diffuser vane pressure side reducing its loading and leading to a better diffusion in the diffuser channel. Concerning the impeller flow, it was found that a smaller radial gap is leading to a noticeable reduction of the wake region at impeller exit. The experimental results are intended to be published as an open CFD test case under the name "Radiver." [DOI: 10.1115/1.1516815]

Introduction

Trying to attain a better understanding of the mechanisms related to impeller-diffuser interaction, investigations of the unsteady flow field between the impeller exit region and at least diffuser throat are of particular relevance. Unsteady flow field measurements in that region are rare due to the great demands on the measurement techniques, especially concerning high-speed machines. Here important work was done for example by Krain [1–3], Fradin and Janssens [4,5] and Stahlecker [6]. Inoue and Cumpsty [7] showed instructive results from a low speed test rig. The first unsteady 3-D Navier-Stokes calculations of centrifugal compressor stages were presented only a few years ago (e.g., Yamane et al. [8,9], Dawes [10], Sato and He [11,12], Shum et al. [13] and Peeters and Sleiman [14]). To this day, reliable predictions of the flow field in the interaction region of a centrifugal compressor must be regarded as a challenge. All mentioned experimental and numerical investigations delivered valuable contributions partly showing similar trends, partly contradicting. Still much work has to be done in the field of impeller-diffuser interaction.

A variation of the radial gap between impeller exit and diffuser vane inlet implies a change of all aspects of impeller-diffuser interaction. The objective of the experimental investigation presented in this two-part paper is to achieve a better understanding of the flow phenomena connected with a variation of the radial gap and their influence on the performance of impeller, diffuser and the entire compressor. Furthermore, the general knowledge about the highly unsteady flow field between the impeller exit region and diffuser throat shall be improved. Both impeller and wedge vaned diffuser of the investigated 4:1 pressure ratio compressor have high-subsonic inlet flow conditions. The strategy was to combine an extensive parameter study with the help of steady probe measurements, presented in Part I, and detailed time resolving laser-2-focus measurements, presented in Part II, in order to get to an overall result. The L2F measurements were conducted for two different radial gaps and for the vaneless diffuser.

The description of the test rig and the test program is given in part I including the information on the L2F measurement planes and operating points. All quantities shown in Part I and II are corrected to the standard inlet condition of $p_{tI}=1.013$ bar and $T_{tI}=288.15$ K.

L2F Measurement Technique and Evaluation

Laser measurement techniques are most suitable for flow investigations in the narrow flow channels of high-speed centrifugal compressors, especially if the very sensitive transonic flow in the region between impeller exit and diffuser throat is concerned. The laser-2-focus technique working on the light barrier principle goes back to the work of Schodl [15]. The data acquisition of the 2-D Polytec L2F system of the Institute of Jet Propulsion and Turbomachinery was optimized by Bramesfeld [16]. Before the beginning of the test series the velocimeter was inspected and calibrated by the Schodl group from DLR Cologne. Mainly due to the small diffuser height of 11.1 mm, the measurements were in parts extremely time consuming.

Figure 1(*d*) shows the adaptation of the velocimeter to the compressor and Fig. 1(*a*) the irradiation into the flow channel with a deviation mirror. The advantage of this configuration compared to the use of a fiber optic is that the luminous intensity of the back scattered light is almost not decreased. The optical system positioned close to the hot compressor had to be cooled during the measurements. Figure 1(*b*) shows the laser windows used for the measurements. In order to avoid big corners in the double curved casing contour at impeller exit, one diffuser pitch to be covered was distributed to three individual windows. For flow seeding a resin-free oil was used sprayed with a commercial particle generator (Palas AGF 2.0). The diameters of the oil droplets are between 0.2 and 0.3 μm. They are supplied to the flow in the suction

[1]Current address: MTU Aero Engines GmbH, 80995 Munich, Germany

Contributed by the International Gas Turbine Institute and presented at the International Gas Turbine and Aeroengine Congress and Exhibition, Amsterdam. The Netherlands, June 3–6, 2002. Manuscript received by the IGTI, October 26, 2001. Paper No. 2002-GT-30382. Review Chair: E. Benvenuti.

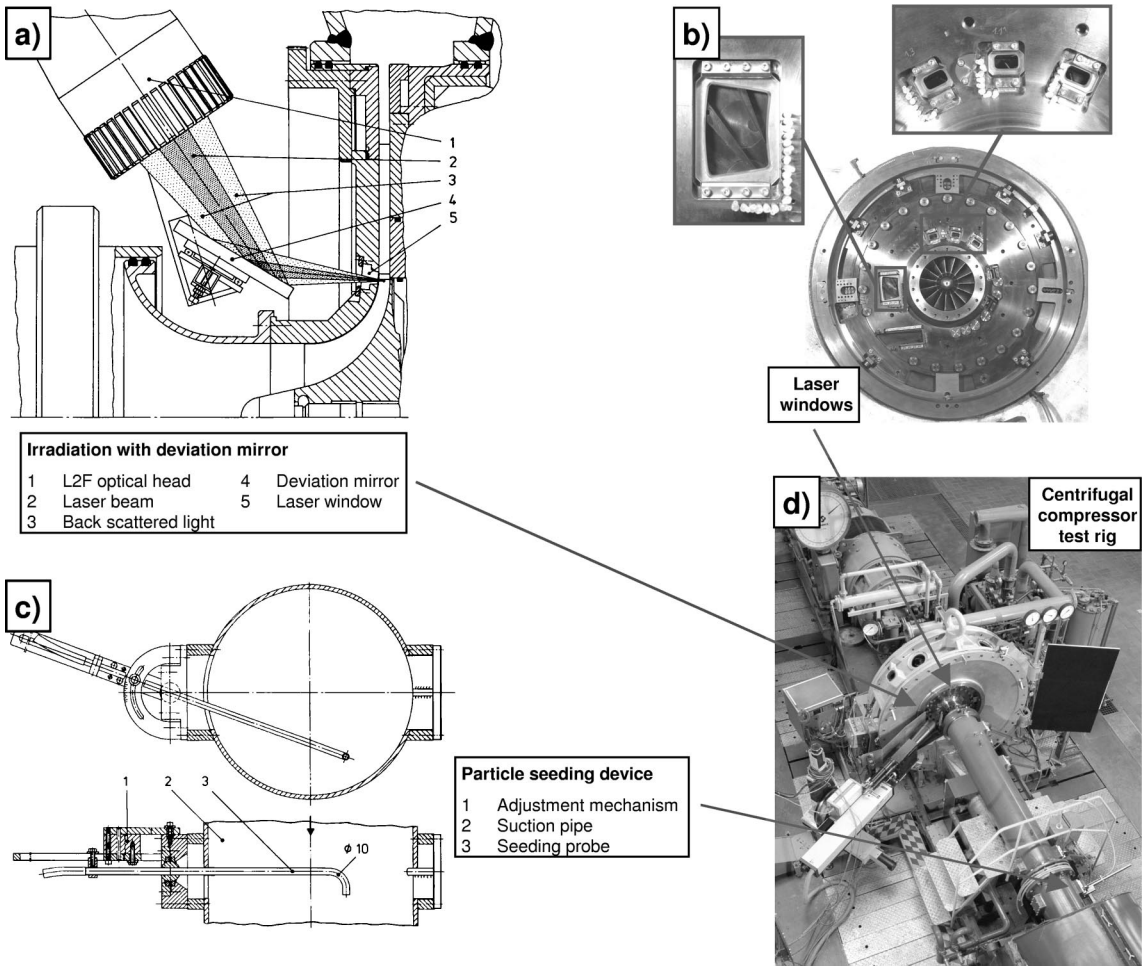

Fig. 1 Laser-2-focus measurement technique

pipe upstream of the honeycomb (Fig. 1(*d*)). To be able to find the optimum seeding stream line, it was necessary to design an adjustment mechanism for the seeding probes (Fig. 1(*c*)).

The statistical evaluation of the measured data was done with the boundary-value distribution method proposed by Schodl [17]. The velocimeter is measuring magnitude and direction of the absolute velocity component perpendicular to the laser beam axis. From these values the 2-D velocity vector is calculated assuming the flow being congruent between hub and casing contour. Additionally the 2-D turbulence intensity of the flow is evaluated from the measured histograms. Generally, the uncertainty of the measured values is less than $\pm 1\%$ in velocity and ± 1 deg in angle. In wake regions with high turbulence levels these errors may rise up to $\pm 3\%$ and ± 3 deg, respectively. All averaged velocities or angles shown in this paper are calculated from the two area averaged velocity components.

Results of the Laser-2-Focus Measurements

Analysis of the Impeller Exit Flow Field. Figure 2 shows the velocity triangle and Fig. 3 the relative velocity and angle shortly before impeller exit (plane $2M'$). In the isoplots the measurement points are indicated by small dots. If the isoplot is representing a time averaged flow field in the relative frame of reference (e.g., $r_4/r_2=1.14$ and 1.04 in Fig. 3) this indication is not possible any more, as the measurement points have different locations within the impeller pitch for the different time steps.

Before the influence of impeller-diffuser interaction on the impeller flow is discussed, first a short introduction on the general flow configuration at impeller exit is given. The relative velocity shows a configuration of the jet-wake structure quite typical for impellers with backswept blades (e.g., Krain [18]). The center of the wake is located close to suction side and casing, but it is spread distinctly towards the channel center due to the influence of tip clearance flow and the relative motion of the casing. Also, the revealed distribution of the relative angle is well known. A strong passage vortex is leading to a more tangential jet flow and a much more radial wake flow. Again, due to tip clearance flow and relative motion of the casing, the wake flow gets more tangential close to the casing. In the absolute frame of reference, the wake has high kinetic energy and a more tangential flow angle (Fig. 4). Figure 5 shows a 3-D plot of the resulting meridional velocity at $2M'$. In plane 2M, shortly downstream of impeller exit (Fig. 6), the wake region can still be identified by high absolute velocities and more tangential absolute flow angles. For the vane-

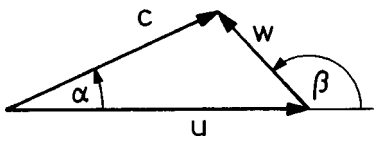

Fig. 2 Velocity triangle at $2M'$ (area average over the measured region, $\alpha_{4SS}=16.5$ deg, $r_4/r_2=1.04$, $n_{red}/n_0=0.8$, P1)

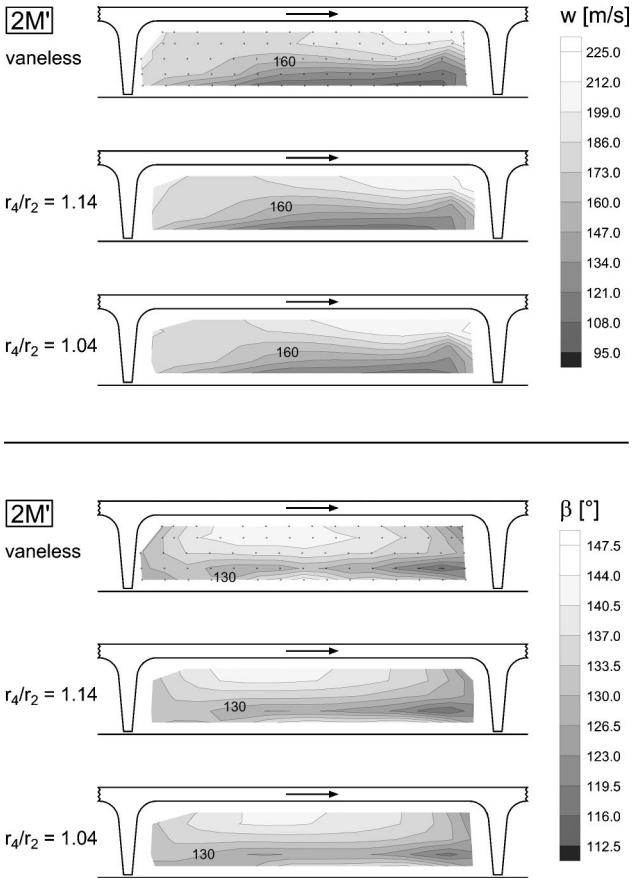

Fig. 3 Time-averaged relative velocity and angle at 2M′ (α_{4SS} = 16.5 deg, n_{red}/n_0 = 0.8, P1)

less diffuser the flow field in 2M was measured at the operating point P1 at 80% corrected speed (''80%/vaneless'' in Fig. 6) and at two operating points at design speed, one of them more throttled (''100%/P'') and the other one more unthrottled (''100%/S''; see Fig. 8 in Part I). A comparison between ''80%/vaneless'' and ''100%/P'' reveals that the jet-wake structure becomes more pronounced, increasing the speed. An even sharper separation between jet and wake flow can be observed, unthrottling the compressor up to operating point S (compare especially the flow angle distributions). The absolute flow angle getting distinctly more radial towards the pressure side is not a result of impeller flow physics, but caused by a strong acceleration of the relative flow leaving the impeller in that region.

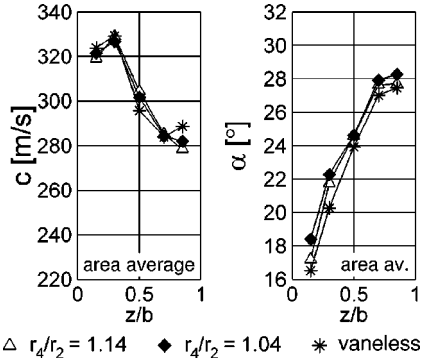

Fig. 4 Absolute velocity and angle at 2M′ (α_{4SS} = 16.5 deg, n_{red}/n_0 = 0.8, P1)

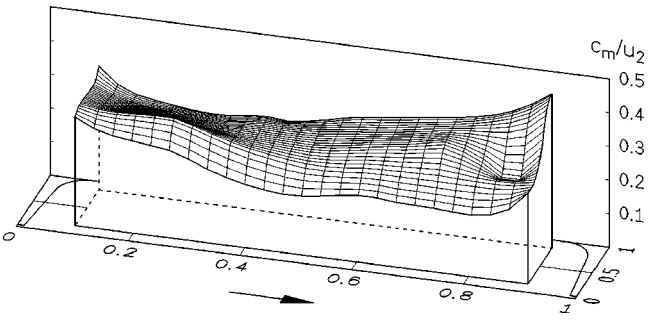

Fig. 5 Meridional velocity at 2M′ (vaneless diffuser, n_{red}/n_0 = 0.8, P1)

A more detailed discussion of the impeller flow is renounced in favor of the analysis of impeller-diffuser interaction in the following. The distributions of the relative velocity in Fig. 3 show a significant reduction of the wake region at impeller exit with vaned diffuser (r_4/r_2 = 1.14) compared to the vaneless, and a smaller but still noticeable further reduction, if the radial gap is reduced from 14 to 4%. This is accompanied by the absolute flow angle getting distinctly more radial (Fig. 4), also visible shortly downstream of impeller exit (Fig. 6, compare ''80%/1.04'' with ''80%/vaneless''). Dye injections on the casing at impeller exit region confirm this result (not shown here). With vaned diffuser at 14% radial gap and especially at 4%, a remarkably more radial absolute angle of the time-averaged casing boundary layer flow

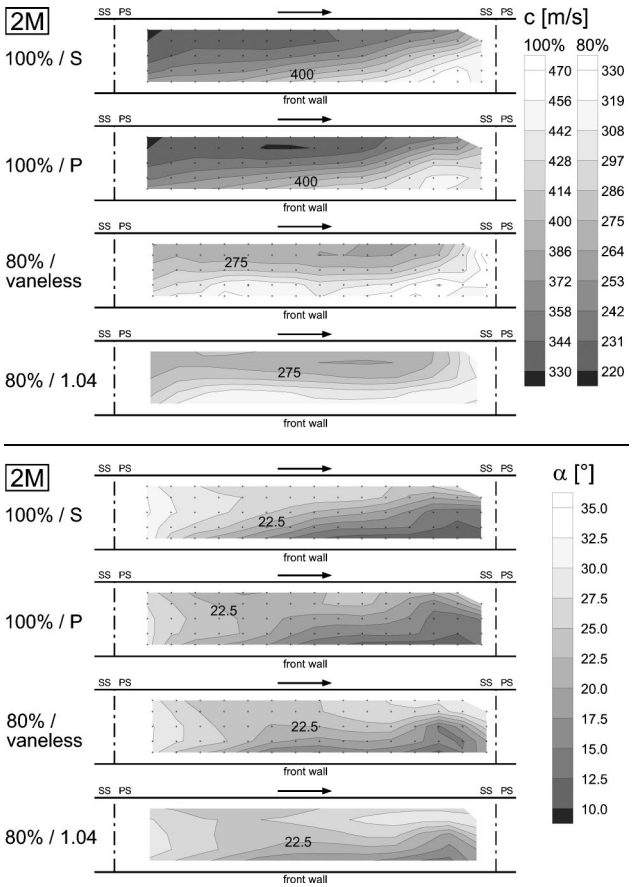

Fig. 6 Absolute velocity and angle at 2M in the relative frame of reference

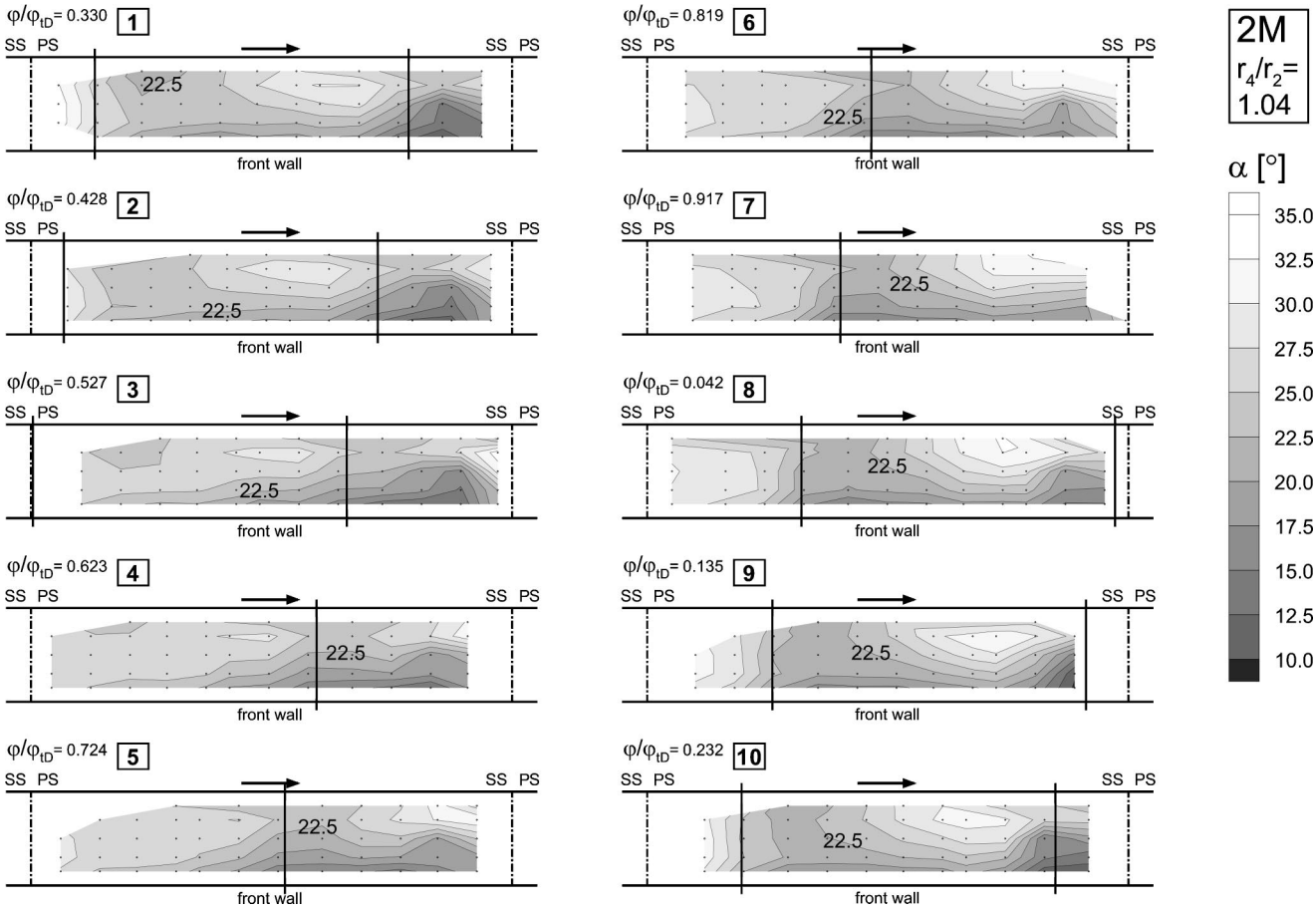

Fig. 7 Unsteady absolute angle at 2M in the relative frame of reference (α_{4SS}=16.5 deg, r_4/r_2=1.04, n_{red}/n_0=0.8, P1)

can be observed compared to the vaneless diffuser. Several effects could be the reason for that phenomenon found also by other authors (e.g., Krain [1], Yamane et al. [9]):

1 The unsteadiness induced by the diffuser vanes could have enhanced the mixing process between jet and wake already inside the impeller, as pointed out by Inoue and Cumpsty [7] and Sato and He [11].

2 It should be considered that the diffuser vanes have the tendency to increase the much more tangential absolute angle of the wake flow already upstream of the vane leading edges due to their potential repercussion.

3 Even more simple, the diffuser vanes provide additional blockage being able to reduce an upstream casing separation or backflow due to the accelerating influence on the meridional velocity (Balje [19], Kirtley and Beach [20]). This is not an unsteady effect, but would be still visible after an imaginary circumferential averaging of the diffuser flow field.

4 Also the influence of the unsteady vane pressure field on the impeller tip clearance flow could be responsible. Information on that influence is given by Shum et al. [13], and in the field of axial flow compressors by Graf et al. [21].

The points one and two are now discussed in more detail. Figure 7 shows the unsteady absolute flow angle 2.4 mm upstream of the diffuser vane leading edges in 2M. The data is plotted in the relative frame of reference between impeller pressure and suction side. The thick black lines are representing the radial projections of the diffuser vane leading edges on the measurement surface. The impeller is fixed, so that the diffuser vanes are crossing the impeller pitch from the right to the left. As a basic aerodynamic effect due to diffuser vane blockage the absolute velocity is decreased and the absolute angle gets more radial in a zone left from the vane leading edge. In a zone right from the leading edge it is the other way round. Due to impeller kinematics, in the left zone the relative velocity rises and the relative angle gets more tangential (compare Fig. 2). Again it is the other way round for the right zone. In plane 2M′ and for 4% radial gap this effect can be visualized very well by the unsteady isoplots of c and β (β shown in Fig. 8), but not so clear by w and α. For the following discussion the absolute flow angle was therefore plotted in plane 2M closer to the vane leading edges. Comparing the unsteady angle distribution (Fig. 7) with the time averaged one (Fig. 6, ''80%/1.04''), it can be observed that the center of the wake has a more radial angle than the time average, when the diffuser vane leading edge is in front of it (time indices 4 to 8). At time index 7 the center of the wake can not even be identified any more. When the diffuser vane leading edge is passing the center of the wake (time indices 9 to 3), the angle is more tangential than in the time average. Only at time index 1 the wake is more pronounced than that one with vaneless diffuser (Fig. 6, ''80%/vaneless''). Considering the flow field still inside the impeller, it is conceivable that the increasing influence of the diffuser vanes on the flow angle is outweighing the decreasing effect, so that in the time averaged flow field the wake region gets smaller (''reason number 2''). In order to investigate, if an enhanced mixing between jet and wake could be the reason for the diminished wake region (''reason number 1''), the relative velocity and angle should be examined. Figure 8 visualizes the strong fluctuations of the relative angle at plane 2M′ due to the diffuser vanes passing by. In order to quantify the fluctuation level, local unsteadiness coefficients for the relative velocity (Eq. (1)) and angle (Eq. (2)) were defined.

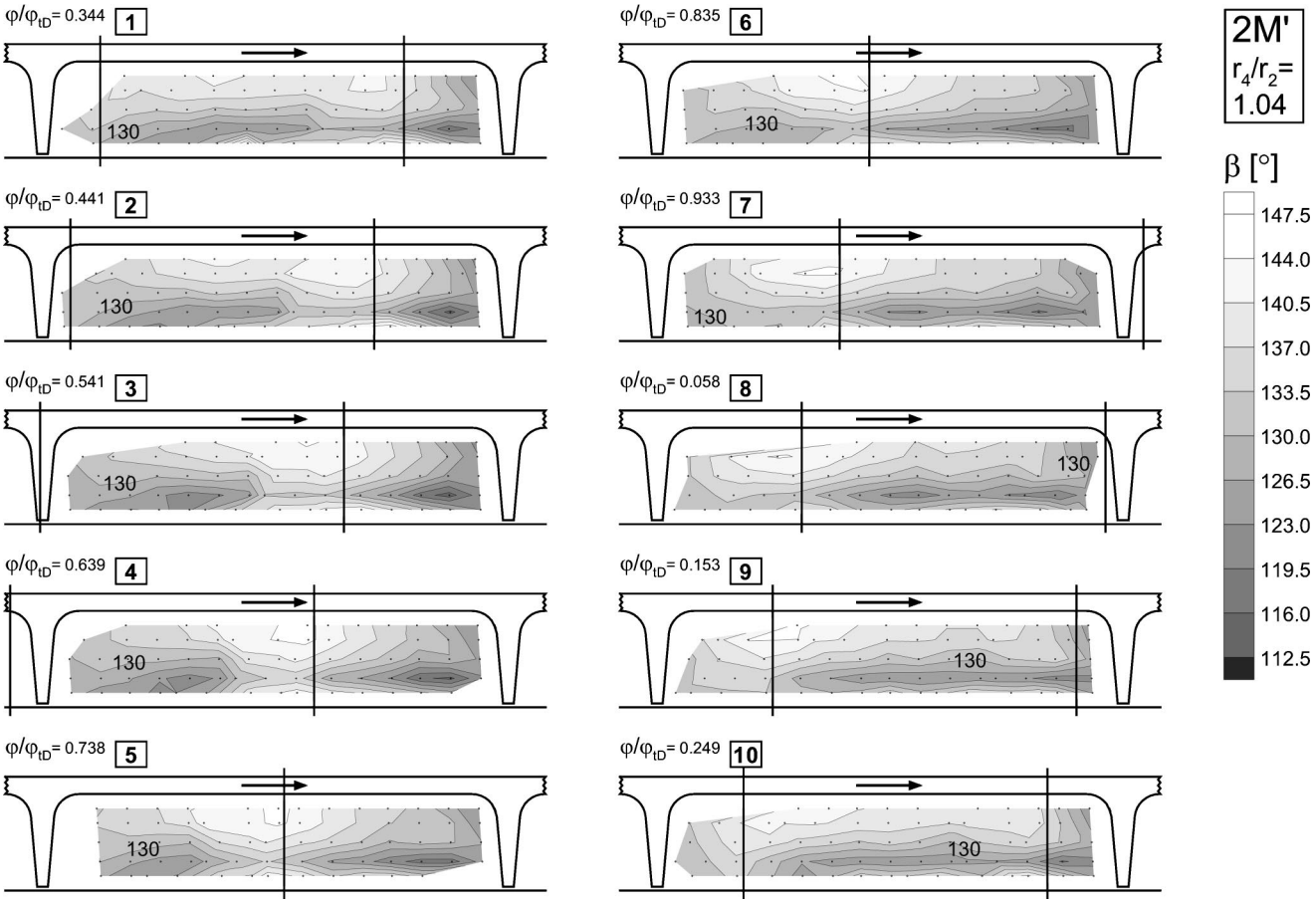

Fig. 8 Unsteady relative angle at 2M′ ($\alpha_{4SS}=16.5$ deg, $r_4/r_2=1.04$, $n_{red}/n_0=0.8$, P1)

$$F_w=\frac{w_{\max}(z,\varphi)-w_{\min}(z,\varphi)}{\overline{w}(z,\varphi)} \tag{1}$$

$$F_\beta=\beta_{\max}(z,\varphi)-\beta_{\min}(z,\varphi) \tag{2}$$

Figure 9 compares on the left-hand side the distributions of these coefficients in plane 2M′ for 14 and 4% radial gap. As expected, the fluctuations are higher for the smaller radial gap. Here maximum values of $F_w=31.4\%$ and $F_\beta=13.2$ deg are found, compared to $F_w=24.2\%$ and $F_\beta=9.5$ deg for $r_4/r_2=1.14$. In the measured flow field the area averaged values are $F_w=11.8\%$ and $F_\beta=7.3$ deg for $r_4/r_2=1.04$ and $F_w=6.4\%$ and $F_\beta=2.7$ deg for $r_4/r_2=1.14$. The high fluctuation levels and the fact that the highest fluctuations are found in the wake region could be arguments for the mixing theory. But these unsteady experimental observations of course can not give a definitive answer, which of the four effects, or which combination of them, causes the observed reduction of the wake region. As outlined in the introduction of Part I, CFD may provide better possibilities to isolate the different aspects of impeller-diffuser interaction. It is an important result that the reduction of the wake region is not leading to or is not the result of an improved impeller efficiency (see Part I). It can be concluded that the region inside the impeller, which is influenced by the repercussion of the diffuser vanes, is too small to affect impeller efficiency. The repercussion seems to be merely cosmetic for the impeller exit flow field.

It is often reported that slip and recirculation are influenced by impeller-diffuser interaction (Pfleiderer [22], Traupel [23], Japikse [24], Balje [19]). Figure 3 reveals at impeller exit a slightly more tangential relative flow angle in the jet region for the vaneless diffuser compared to the vaned one with 14% and especially with 4% radial gap. But comparing the two radial gaps, the averaged values of β in the measured flow field are identical ($\beta=133{,}0$ deg). So the higher work input at smaller radial gaps found by the total temperature measurements cannot be explained with reduced slip. It could more likely be due to an increased recirculation into the impeller at smaller radial gaps. Because recirculation causes an additional work input, which cannot be identified by an increased Δc_u, but only by a higher difference of the total enthalpy. As shown above, the time averaged absolute flow angles close to the casing at 2M′ and 2M are more radial for smaller radial gaps indicating even a smaller tendency for backflow. But recirculation is a highly unsteady mechanism as described for example by Chen et al. [25]. Material from the impeller jet region crosses the blade trailing edge and then travels backwards into the wake region, being ''reflected'' by a diffuser vane. It was shown in Fig. 7 that the diffuser vanes are ''forcing back'' the wake flow, when the vane leading edge is passing the wake. Although in these situations neither at 2M′ nor at 2M backflow was measured, it is conceivable that in the region closer to the casing, not covered with L2F measurements, negative angles are reached, especially for smaller radial gaps.

Analysis of the Flow in the Diffuser Inlet Region. The most important finding of the probe measurements was that a decrease of the radial gap is leading to an unloading of the typically highly loaded diffuser vane pressure side, in most cases resulting in a much better diffusion in the diffuser channel. It was found that the general location of the flow maximum in the diffuser channel is hardly affected by the operating point, but determined by the ra-

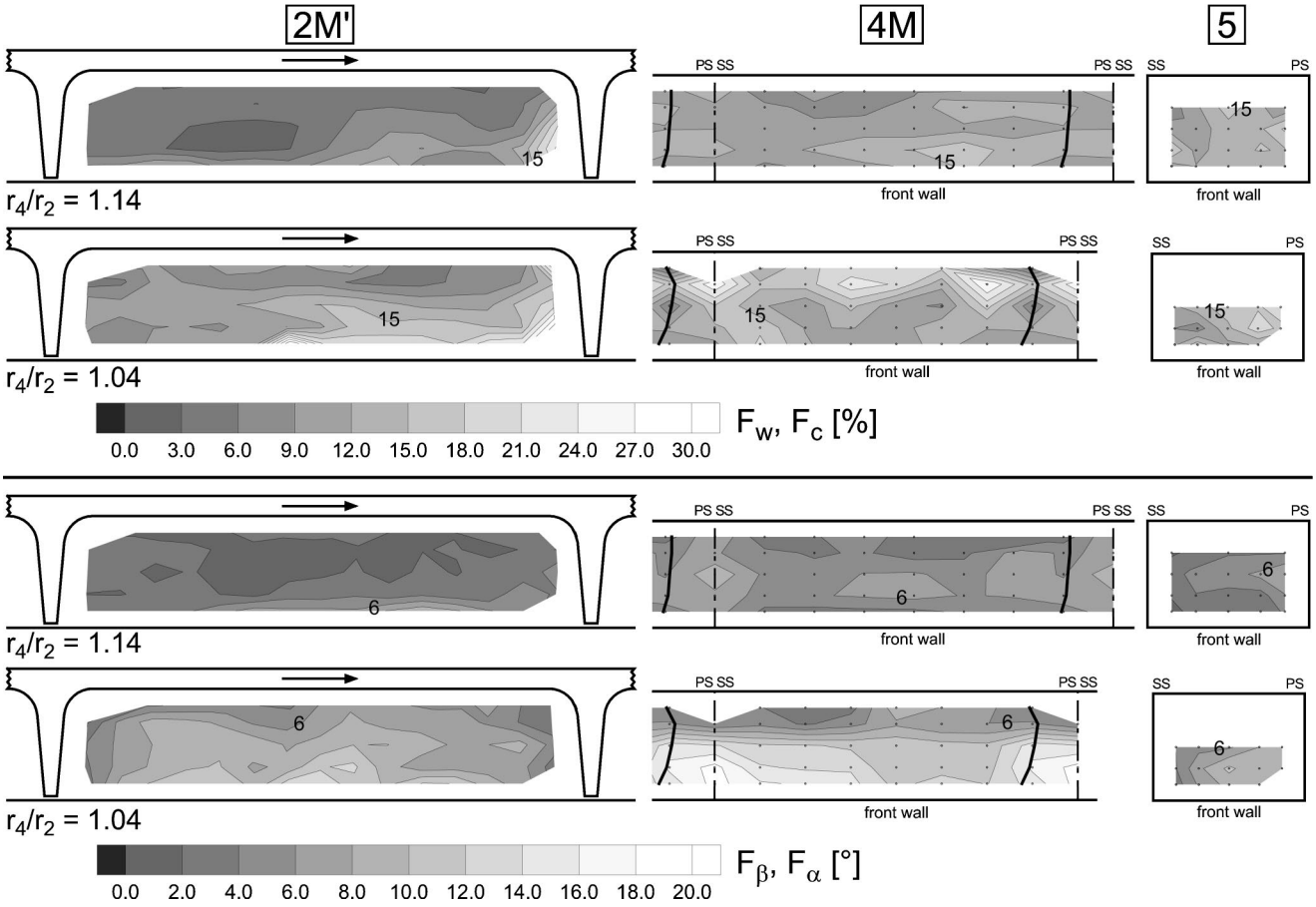

Fig. 9 Unsteadiness coefficients of relative velocity and angle at 2M′ and absolute velocity and angle at 4M and 5 (α_{4SS} = 16.5 deg, n_{red}/n_0 = 0.8, P1)

dial gap, possibly due to an unsteady effect at diffuser inlet. This will be investigated by the following analysis of the L2F results.

Figure 10 shows the time-averaged flow fields in the measurement planes 4M, 2.4 mm upstream of the vane leading edges, and 5, the diffuser throat. (It should be noticed that 4M and 2M are identical for $r_4/r_2 = 1.04$). Besides the absolute velocity, the incidence to the vane camber line is shown in 4M, and in plane 5 a ''deviation angle'' is defined between the actual flow direction and the locally ideal channel flow. (For example, in the center of the throat the ideal channel flow has the direction of the channel centerline, and in the vane suction side boundary layer it has the direction of the suction surface.) A positive incidence or deviation angle means that the flow vector has a component towards the vane pressure side. In Figs. 11 and 12 the area-averaged values of the mentioned quantities are plotted, and in Fig. 13 additionally the flow angle. Unfortunately, in the diffuser throat the laser measurements were possible only up to $z/b = 0.7$ for $r_4/r_2 = 1.14$ and up to $z/b = 0.5$ for $r_4/r_2 = 1.04$ due to strong reflections from the rear wall and the vane surfaces. In order to be able to compare the axially averaged values for the two radial gaps in Figs. 11–13, for both gaps the averages were calculated only up to $z/b = 0.5$.

In Fig. 10 the results in 4M are plotted as well in the absolute as in the relative frame of reference (''abs'' and ''rel''). The time averaged plots in the relative frame of reference allow an analysis, how far advanced the mixing process between jet and wake is, before the flow reaches the diffuser vane leading edges. It is remarkable that the typical distribution of the absolute velocity in the impeller pitch is still visible clearly at 14% radial gap. Here, the measurement plane 4M is on the radius $r/r_2 = 1.122$ compared to $r/r_2 = 1.022$ for 4% radial gap. The mixing process in circumferential direction seems to be not more effective than that one in axial direction, as reported by many authors. A comparison of the angle (here: incidence) distributions in the relative frame of reference reveals that at 14% radial gap the originally small flow angle in the wake region has become significantly more radial due to the momentum exchange process with the much more radial jet flow region on the one hand, and due to wall friction on the other hand. In contrast, at 4% radial gap in the center of the wake up to 5.5 deg positive incidence was measured. These results are reflected also by the resulting unsteadiness coefficients in the absolute frame of reference shown in Fig. 9 on the right-hand side. They are defined in the same way as the coefficients for the relative flow in Eqs. (1) and (2). It is remarkable that as well in 4M as in 5 F_c has quite similar levels for the two radial gaps, whereas F_α shows much bigger differences. At $r_4/r_2 = 1.04$ for F_α maximum values of 18.8 deg in 4M and 10.5 deg in 5 are found, compared to 9.6 deg in 4M and 8.0 deg in 5 for $r_4/r_2 = 1.14$. In the measured flow field the area averaged values in 4M are $F_\alpha = 10.4$ deg for $r_4/r_2 = 1.04$ and $F_\alpha = 5.4$ deg for $r_4/r_2 = 1.14$.

Plotting the data in the absolute frame of reference over one diffuser pitch, the influence of the diffuser vanes on the flow field becomes visible (Fig. 10, compare also Figs. 11, 12, and 13). The dash-dot lines in the isoplots ($\varphi/\varphi_{tD} = 0.0$ and 1.0 in the diagrams) are the radial projections of the diffuser vane leading edges on the measurement plane. Additionally, the ''stagnation point stream surfaces'' have been estimated and plotted as thick black lines in the isoplots and also in the diagrams. They were calculated iteratively with the simplifying assumption that the flow starting from the measurement plane is following a logarithmic spiral up to the vane leading edges. Of course, in reality the flow angle between 4M and the leading edges is not constant, and the stagnation point

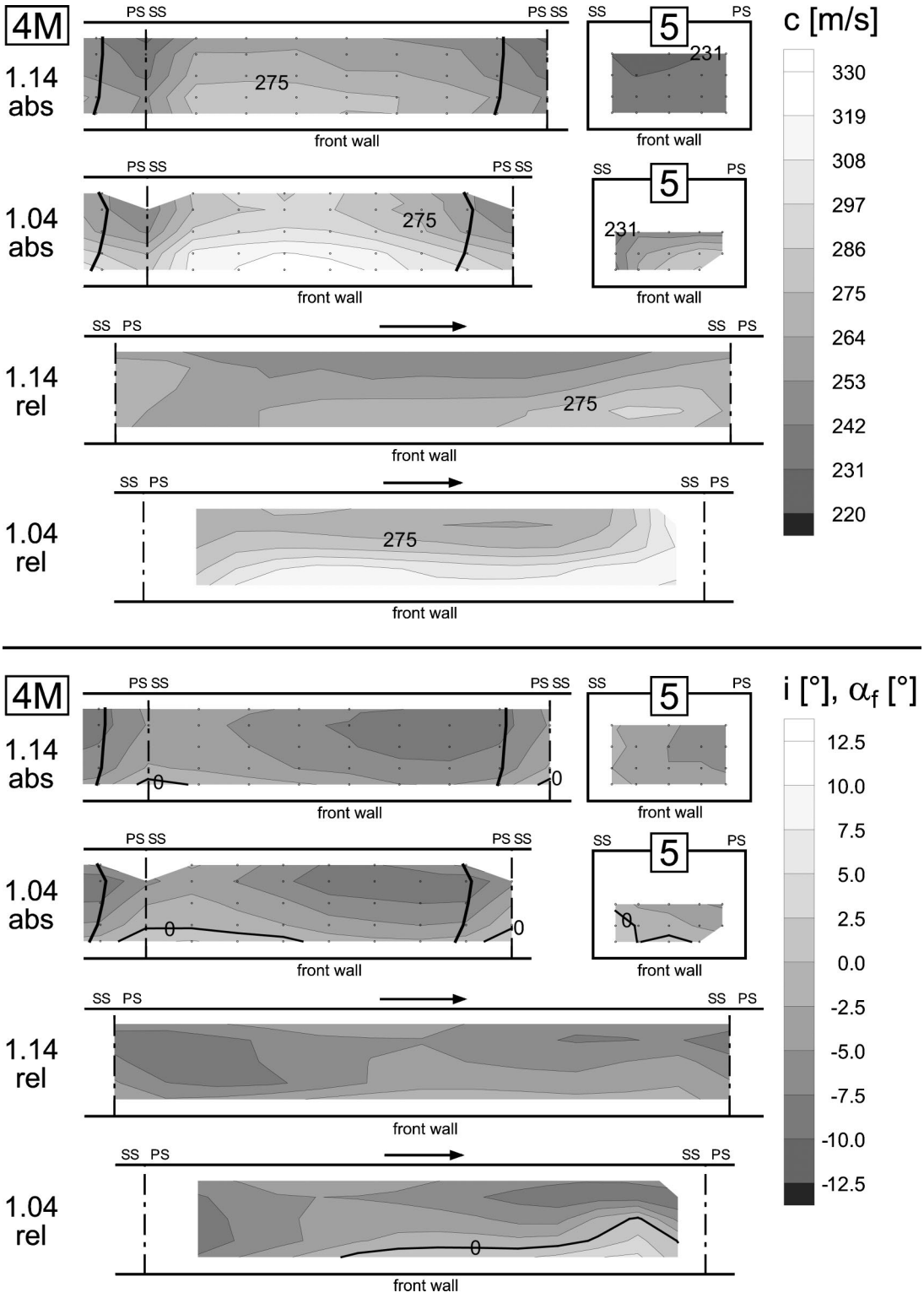

Fig. 10 Time-averaged absolute velocity (4M and 5), incidence (4M) and deviation angle (5) in the absolute and relative frame of reference (α_{4SS}=16.5 deg, n_{red}/n_0=0.8, P1)

possibly will not be exactly on the leading edges. But here just an impression should be given, which is roughly the material entering the diffuser pitch. Close to the leading edges the stagnation zones are represented by reduced velocities. Corresponding to the impeller exit flow the highest velocities are found near the casing. Figure 11 reveals that the deceleration of the flow in the semivaned space is much stronger for the smaller radial gap, especially close to the suction side. Also, close to the vane suction side the flow is forced to a more tangential flow angle (Figs. 10 and 12), whereas in the rest of the flow field a significant suction sided incidence is found. The maximum measured incidence angle is for both radial gaps nearly −10 deg and is located close to pressure side and diffuser rear wall. The stagnation point stream surfaces reveal maximum incidences to the leading edges of −8.1 deg for

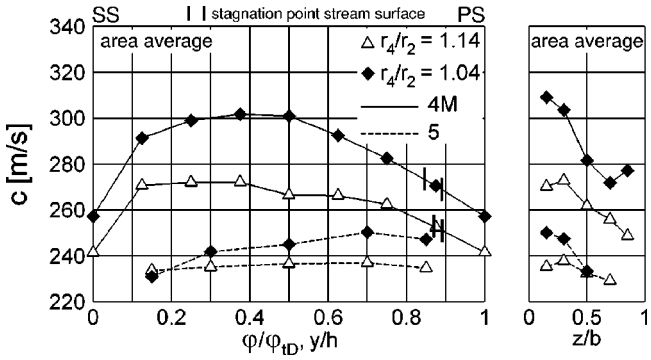

Fig. 11 Absolute velocity at 4M and 5 (α_{4SS}=16.5 deg, n_{red}/n_0=0.8, P1)

$r_4/r_2=1.14$ and -9.0 deg for $r_4/r_2=1.04$, resulting in -4.8 or -5.7 deg incidence relative to the vane pressure side. The area averaged incidences in the measured region are -5.7 deg for $r_4/r_2=1.14$ and -4.5 deg for $r_4/r_2=1.04$. (But it should be noticed that these values are representing only 70% of the flow field.) These suction sided incidences in the best point of the compressor explain, why typically the diffuser vane pressure side is the higher loaded vane surface. The mentioned values are quite similar for $r_4/r_2=1.14$ and $r_4/r_2=1.04$. But the important difference between the two radial gaps is that at $r_4/r_2=1.04$ there is a relatively narrow strip with a distinct pressure sided incidence and high kinetic energy close to the diffuser front wall, which originates in the impeller wake region and is also visible in the diffuser throat (Fig. 10). Comparing the circumferentially averaged flow angles for the two radial gaps in 4M (Fig. 13), it can be observed that they are starting at the same value close to diffuser rear wall. But the longer radius ratio at 14% radial gap is leading to a significantly increased angle close to diffuser front wall. As

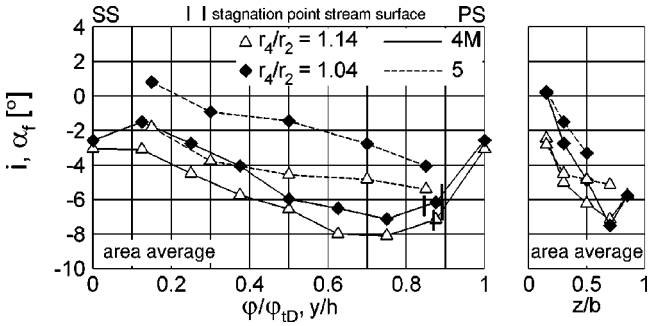

Fig. 12 Incidence (4M) and deviation angle (5) (α_{4SS}=16.5 deg, n_{red}/n_0=0.8, P1)

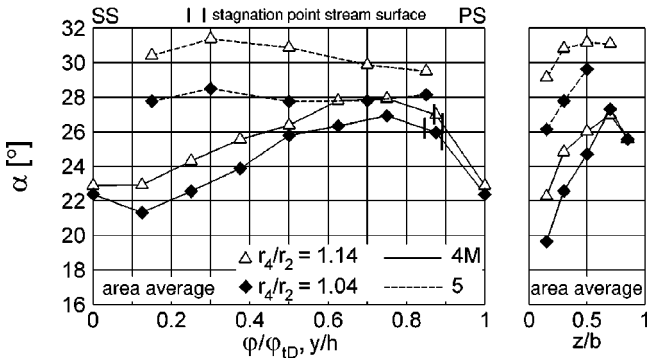

Fig. 13 Absolute angle at 4M and 5 (α_{4SS}=16.5 deg, n_{red}/n_0=0.8, P1)

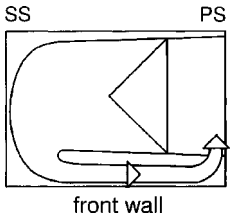

Fig. 14 Vortex in the diffuser throat

already discussed, this is to some extent due to an exchange of momentum between the more radial impeller jet flow and the more tangential wake flow. The fact that the angle of the jet flow hardly decreases during that momentum exchange process, can be explained by the much higher mass flow in the jet region compared to the wake region. The circumferential averages in Fig. 12 allow an extrapolation of the incidence and deviation angle, which can roughly be expected at the diffuser front wall. In the measurement point nearest to the front wall ($z/b=0.15$) incidence and deviation angle are about zero for 4% radial gap and will reach a value of roughly $+4$ deg on the front wall. In contrast, for 14% radial gap presumably only zero incidence is reached on the front wall. Additionally, the fluid close to the front wall has a lower kinetic energy (Fig. 10). At $r_4/r_2=1.04$ a strong vortex must develop in the diffuser throat helping the vane pressure side not to separate in the middle and rear span region (Fig. 14), or more generally, which is reducing the loading of the highly loaded vane pressure side. (Stahlecker [6] shows excellent 3-D LDA measure-

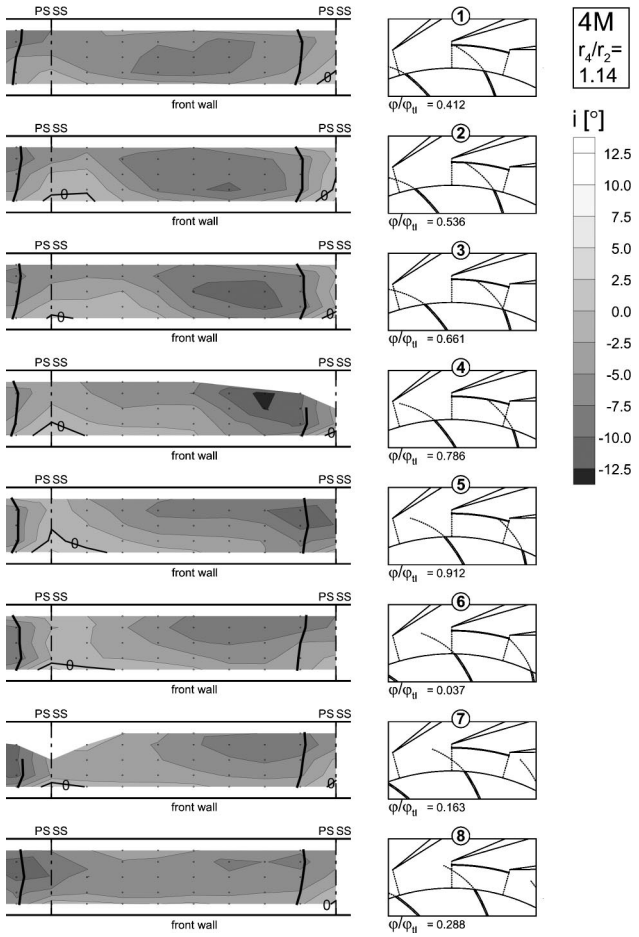

Fig. 15 Unsteady incidence at 4M (α_{4SS}=16.5 deg, r_4/r_2=1.14, n_{red}/n_0=0.8, P1)

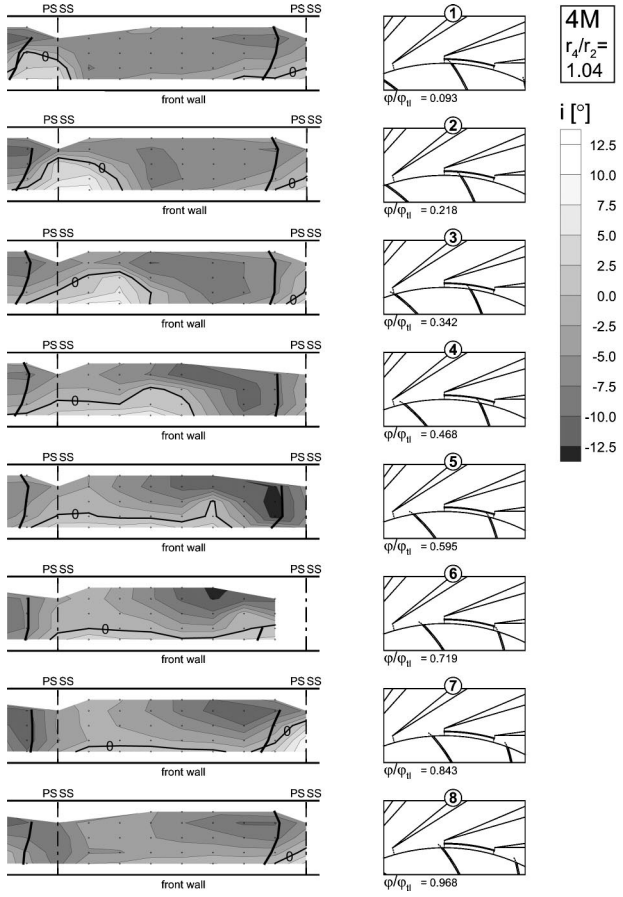

Fig. 16 Unsteady incidence at 4M ($\alpha_{4SS}=16.5$ deg, $r_4/r_2=1.04$, $n_{red}/n_0=0.8$, P1)

ments of this kind of throat vortex.) With growing radial gap this vortex gets weaker due to the flow close to diffuser front wall getting more radial, and the vane pressure side begins to suffer from the distinct suction sided incidence in the channel center and close to the rear wall. This mechanism must be the reason for the shift of the flow maximum towards the suction side with increasing radial gap, as observed at diffuser vane exit in Part I.

But 2-deg difference of the deviation angle in the front half of the diffuser throat seems to be not enough to explain the completely different flow configurations at diffuser vane exit for 14% and 4% radial gap. The full substantiation is given by the unsteady incidences in 4M shown in Figs. 15 and 16. At 14% radial gap (Fig. 15) the maximum measured negative incidence is −13.3 deg (time index 4) close to vane pressure side surely leading to a separation on the pressure side. Regions with positive incidence are found close to the suction side only, which of course forces flow angles more tangential than the camber line angle. In contrast, at 4% radial gap (Fig. 16) the characteristic angle distribution of the impeller flow field can still be observed travelling through the measurement plane from the left to the right. Only when the center of the wake, indicated by a strong positive incidence, is passing the region close to the pressure side, where the diffuser vanes have a strong steepening effect on the flow. Nevertheless, the presumably temporarily occurring separations on the vane pressure side (e.g., time index 5) are filled up again and again with high energy fluid (time index 6) moving towards the pressure side and then rolling up in the direction of the diffuser rear wall. So, at larger radial gaps not only the generally more radial flow angle close to diffuser front wall causes problems for the vane pressure side, but also the homogeneous angle distribution in circumferential direction in the relative frame of reference close to diffuser front wall (compare the incidence distributions in the relative frame of reference in Fig. 10). At 14% radial gap a ''peak'' of higher positive incidence is missing, which can be found at 4% gap in the center of the impeller wake, interrupting again and again a pressure sided separation. Obviously, a steady calculation with a mixing plane between impeller and diffuser will hardly be capable of correctly predicting the flow configuration in the diffuser channel. So it is recommended to concentrate the efforts on unsteady calculations. In this context the results of Yamane [8] and Peeters and Sleiman [14] are very promising. They found a lower loaded vane pressure side in their unsteady calculations compared to the steady ones.

Conclusions

Results of laser-2-focus measurements between the impeller exit region and diffuser throat of a 4:1 pressure ratio centrifugal compressor are presented in this second part of a two-part paper. In order to investigate the impeller-diffuser interaction, the measurements were performed for two radial gaps between impeller exit and diffuser vane inlet (4 and 14% of impeller tip radius) and for the vaneless diffuser. The main results are:

Impeller flow:

1. At impeller exit a typical jet-wake structure was found getting more pronounced at higher rotational speed and at higher mass flow rate (at constant speed).
2. A significant reduction of the wake region at impeller exit was found with vaned diffuser ($r_4/r_2=1.14$) compared to the vaneless, and a smaller but still noticeable further reduction, if the radial gap is reduced from 14 to 4%. Several mechanisms could be the reason for this effect, which hardly influences impeller efficiency (see Part I).
3. Slip is hardly influenced by the diffuser.
4. The slightly higher work input at smaller radial gaps found in Part I is probably due to an enhanced recirculation.

Diffuser flow:

1. The mixing process of the impeller jet-wake flow in the vaneless space is not more effective in the circumferential direction compared to the axial direction.
2. Angle non-uniformities mix out better than differences in velocity.
3. Already in the best point the diffuser vanes have a time and area averaged suction sided incidence of about 5 deg (in the measured area) indicating a generally highly loaded vane pressure side. At small radial gaps the loading is reduced by impeller wake fluid with pressure sided incidence. In a highly unsteady process temporarily occurring separations on the vane pressure side are filled up again and again with this high energy fluid. At large radial gaps the angle of the impeller wake flow gets significantly more radial in the vaneless space minimizing the positive effect for the vane pressure side. This mechanism is the reason for the higher loaded vane pressure side and worse diffusion in the diffuser channel at larger radial gaps, found at diffuser vane exit in Part I.

So, generally small radial gaps can be recommended, if not a wide mass flow range has higher priority. Of course, the optimum value of 4 to 6% for this particular compressor can not be a general recommendation. The essential result of the presented investigation is rather that in each individual case the flow configuration in the diffuser channel can be optimized by the adjustment of the radial gap. With the radial gap the loading of vane pressure and suction side should be balanced for an optimum diffusion. For that, unsteady calculations of the stage must be performed in the design process. At present, the prediction of the flow configuration in the diffuser channel depending sensitively on the radial gap is surely a challenge. For that reason, steady and unsteady experi-

mental results of the presented project are published as an open CFD test case under the name ''Radiver.'' The compressor geometry, figures, animations and supplementary information have been put together on a test case CD-ROM. Interested researchers are asked to contact the authors. At the Institute of Jet Propulsion and Turbomachinery steady calculations of the impeller have been already performed with PANTA. Unsteady stage calculations are in preparation.

Acknowledgments

The investigations presented in this paper were funded partly by the German Research Association (Deutsche Forschungsgemeinschaft, DFG). The Institute of Jet Propulsion and Turbomachinery and the authors would like to thank DFG for this promotion. We are also grateful to MTU Aero Engines for the donation of the impeller and to Dr. Schodl and Mr. Beversdorff from DLR Cologne for their support, when the laser-2-focus technique was established at the centrifugal compressor test rig.

Nomenclature

The Nomenclature is given in Part. I.

References

[1] Krain, H., 1981, ''A Study on Centrifugal Impeller and Diffuser Flow,'' ASME J. Eng. Power, **103**, pp. 688–697.
[2] Krain, H., 1984, ''Experimental Observations of the Flow in Impellers and Diffusers,'' VKI Lecture Series 1984–07.
[3] Krain, H., 1999, ''High Pressure Ratio Centrifugal Compressor with Transonic Flow,'' FEDSM99-7801.
[4] Fradin, C., 1988, ''Detailed Measurements of the Flow in the Vaned Diffuser of a Backswept Transonic Centrifugal Impeller,'' ICAS-88-2.6.2, 16th ICAS, Jerusalem, Israel.
[5] Fradin, C., and Janssens, G., 1990, ''Detailed Measurements of the Flow Field at the Outlet of a Backswept Transonic Centrifugal Impeller Equipped with a Vaned Diffuser,'' ASME Cogen Turbo Power, pp. 249–254.
[6] Stahlecker D., 1999, ''Untersuchung der instationären Strömung eines beschaufelten Radialverdichterdiffusors mit einem Laser-Doppler-Anemometer,'' doctoral thesis ETH Zürich Nr. 13228, Verlag Mainz Aachen.
[7] Inoue, M., and Cumpsty, N. A., 1984, ''Experimental Study of Centrifugal Impeller Discharge Flow in Vaneless and Vaned Diffusers,'' ASME J. Eng. Gas Turbines Power, **106**, pp. 455–467.
[8] Yamane, T., Fujita, H., and Nagashima, T., 1993, ''Transonic Discharge Flows Around Diffuser Vanes From a Centrifugal Impeller,'' ISABE Paper 93-7053.
[9] Yamane, T., Fujita, H., and Nagashima, T., 1995, ''An Investigation of Impeller and Diffuser Interaction in a Transonic Centrifugal Compressor,'' *Unsteady Aerodynamics and Aeroelasticity of Turbomachines*, Elsevier Science B. V; 1994, Proc., ISUAAAT.
[10] Dawes, W. N., 1994, ''A Simulation of the Unsteady Interaction of a Centrifugal Impeller with its Vaned Diffuser: Flow Analysis,'' ASME Paper 94-GT-105.
[11] Sato, K., He, L., 1998, ''Effect of Rotor-Stator Interaction on Impeller Performance in Centrifugal Compressors,'' Proc., ISROMAC Conf.
[12] Sato, K., and He, L., 2000, ''A Numerical Study on Performances of Centrifugal Compressor Stages with Different Radial Gaps,'' ASME Paper 2000-GT-462.
[13] Shum, Y. K. P., Tan, C. S., and Cumpsty, N. A., 2000, ''Impeller-Diffuser Interaction in Centrifugal Compressor,'' ASME Paper 2000-GT-428.
[14] Peeters, M., and Sleiman, M., 2000, ''A Numerical Investigation of the Unsteady Flow in Centrifugal Stages,'' ASME Paper 2000-GT-426.
[15] Schodl, R., 1977, ''Entwicklung des Laser-Zwei-Fokus-Verfahrens für die berührungslose Messung der Strömungsvektoren, insbesondere in Turbomaschinen,'' doctoral thesis, RWTH Aachen.
[16] Bramesfeld, W., 1995, ''Optimierung eines Laser-Zwei-Fokus-Meßsystems zur berührungslosen Geschwindigkeitsmessung in Turbomaschinen,'' doctoral thesis RWTH Aachen, VDI Fortschritt-Berichte, Reihe 9, Nr. 505, VDI Verlag.
[17] Schodl, R., 1981, ''Verfahren und Programm zur Auswertung der von einem L2F-Geschwindigkeitsmeßgerät gelieferten Meßdaten,'' Internal Report IB 325/2/1981, Institut für Antriebstechnik, DFVLR Köln, Germany.
[18] Krain, H., 1988, ''Swirling Impeller Flow,'' ASME J. Turbomach., **110**, pp. 122–128.
[19] Balje, O. E., 1981, *Turbomachines*, John Wiley and Sons, New York, Chichester, Brisbane, Toronto.
[20] Kirtley, K. R., and Beach, T. A., 1991, ''Deterministic Blade Row Interactions in a Centrifugal Compressor Stage,'' ASME Paper 91-GT-273.
[21] Graf, M. B., Greitzer, E. M., Marble, F. E., Sharma, O. P., 1999, ''Effects of Stator Pressure Field on Upstream Rotor Performance,'' ASME Paper 99-GT-99.
[22] Pfleiderer, C., 1961, *Die Kreiselpumpen für Flüssigkeiten und Gase*, Springer-Verlag, Berlin, Göttingen, Heidelberg.
[23] Traupel, W., 1988, *Thermische Turbomaschinen*, Springer-Verlag, Berlin, Heidelberg, New York, London, Paris, Tokyo.
[24] Japikse, D., 1996, *Centrifugal Compressor Design and Performance*, Concepts ETI, Inc.
[25] Chen, Y. N., Seidel, U., Haupt, U., and Rautenberg, M., 1996, ''Jet, Wake and Intrinsic Motion in Impellers of Centrifugal Compressors,'' ASME Paper 96-GT-261.